THE UNIVERSITY OF ADELAIDE

DEPARTMENT OF MECHANICAL ENGINEERING

ESTABLISHING VERY LOW SPEED, DISTURBANCE-FREE FLOW FOR ANEMOMETRY IN TURBULENT BOUNDARY LAYERS

presented by

Peter Vernon Lanspeary, B.E.(Hons)

for the Degree of Doctor of Philosophy

December 1997

Contents

List of Figures

List of Tables

Summary

This document addresses problems encountered when establishing the very low air-flow speeds required for experimental investigations of the mechanisms of low-Reynolds-number boundary-layer turbulence. Small-scale motions in the near-wall region are important features of turbulent boundary-layer dynamics, and, if these features are to be resolved by measurements in air with conventionally-sized hot-wire probes, a well-behaved canonical turbulent boundary layer must be developed at free stream flow speeds no higher than 4 m/s. However, at such low speeds, the turbulent boundary layers developed on the walls of a wind tunnel are very susceptible to perturbation by non-turbulent time-dependent flow structures which originate upstream from the test section in the laminar flow at the inlet and in the contraction.

Four different non-turbulent flow structures have been identified. The first is a result of quasi-two-dimensional separation of the laminar boundary-layer from the surfaces of the wind-tunnel contraction. Potential flow simulations show that susceptibility to this form of separation is reduced by increasing the degree of axisymmetry in the cross-section geometry and by decreasing the streamwise curvature of the concave surfaces. The second source of time-dependence in the laminar boundary-layer flow is an array of weak streamwise vortices produced by Görtler instability. The Görtler vortices can be removed by boundary-layer suction at the contraction exit. The third form of flow perturbation, revealed by visualisation experiments with streamers, is a weak large-scale forced-vortex swirl produced by random spatial fluctuations of temperature at the wind-tunnel inlet. This can be prevented by thorough mixing of the inlet flow; for example, a centrifugal blower installed at the inlet reduces the amplitude of temperature nonuniformity by a factor of about forty and so prevents buoyancy-driven swirl. When subjected to weak pressure gradients near the start of a wind-tunnel contraction, Görtler vortices in laminar wall layers can develop into three-dimensional separations with strong counter-rotating trailing vortices. These trailing vortices are the fourth source of unsteady flow in the test-section. They can be suppressed by a series of appropriately located screens which remove the low-speed-streak precursors of the three-dimensional separations. Elimination of the above four contaminating secondary flows permits the development of a steady uniform downstream flow and well-behaved turbulent wall layers.

Measurements of velocity in the turbulent boundary layer of the test-section have been obtained by hot-wire anemometry. When a hot-wire probe is located within the viscous sublayer, heat transfer from the hot-wire filament to the wall produces significant errors in the measurements of both the mean and the fluctuating velocity components. This error is known as wall-proximity effect and two successful methods are developed for removing it from the hot-wire signal. The first method is based on the observation that, if all experimental parameters except flow speed and distance from the wall

are fixed, the velocity error may be expressed nondimensionally as a function of only one parameter, in the form $\Delta U^+ = f(y^+)$. The second method, which also accommodates the effect of changing the hot-wire overheat ratio, is based on a dimensional analyis of heat transfer to the wall.

Velocity measurements in the turbulent boundary layer at the mid-plane of a nearly square test-section duct have established that, when the boundary-layer thickness is less than one quarter of the duct height, mean-velocity characteristics are indistinguishable from those of a two-dimensional flat-plate boundary layer. In thicker mid-plane boundary layers, the mean-velocity characteristics are affected by stress-induced secondary flow and by lateral constriction of the boundary-layer wake region. A significant difference between flat-plate and duct boundary layers is also observed in momentum-balance calculations. The momentum-integral equation for a duct requires definitions of momentum and displacement thickness which are different from those given for flat-plate boundary layers. Momentum-thickness growth rates predicted by the momentum-integral equation for a duct agree closely with measurements of the newly defined duct momentum thickness. Such agreement cannot be obtained in terms of standard flat-plate momentum thickness.

In duct boundary layers with Reynolds numbers (Re_{θ_2}) between 400 and 2600, similarity in the wake-region distributions of streamwise turbulence statistics has been obtained by normalising distance from the wall with the flat-plate momentum thickness, θ_2. This result indicates that, in contrast with the mean velocity characteristics, the structure of mid-plane turbulence does not depend on the proportion of duct cross-section occupied by boundary layers and is essentially the same as in a flat-plate boundary layer. For Reynolds numbers less than 400, both wall-region and wake-region similarity fail because near-wall turbulence events interact strongly with the free stream flow and because large scale turbulence motions are directly influenced by the wall. In these conditions, which exist in both duct and flat-plate turbulent boundary layers, there is no distinct near-wall or wake region, and the behaviour of turbulence throughout the boundary layer depends on both wall variables and on outer region variables simultaneously.

Acknowledgments

This project would never have been completed without the assistance of many other people. My most sincere thanks must go to Dr. M. K. Bull for acting as my supervisor and for obtaining financial support from the Australian Research Council. His friendly advice has always been useful and has contributed significantly to the quality of my work. Discussions with Professor R.E. Luxton have been most interesting and are much appreciated. I also thank Drs. G. J. Nathan and R. M. Kelso for instruction on flow topology, for their friendship and for helping me whenever I asked. Drs. C. H. Hansen and J. M. Pickles have provided welcome assistance in negotiating the bureaucratic maze.

The research findings of this project have arisen almost entirely from experimental work and so, in the manufacture and maintenance of equipment, the willing assistance of technicians and tradesmen has been particularly valuable. Most technical staff in the Department of Mechanical Engineering have contributed in some way to my work and to my education. Rod Curtin, Eric Browne, Alan Mittler and Jonathan May have provided vital support for the computer hardware and systems software. Initial low-level graphics software for the Visual 500 display terminal came from Rod. The data acquisition hardware was designed and built by Rod Curtin, Alan Mittler and Silvio DeIeso. Alan and Silvio also designed and assembled much of the analogue instrumentation. George Osborne made the all-important anemometer probes and most of the associated fittings. The workshop staff: Ron Jager, Craig Price, Malcolm Bethune, Dudley Morrison, Doug Smith, Bill Doble and Werner Eidam have manufactured or modified numerous wind-tunnel components for me. Their support and practical advice are highly appreciated. I have particular gratitude for Herwig Bode who, in providing access to innumerable items of equipment and in many other ways, has given absolutely first-class service.

Statement of originality

This work contains no material which has been accepted for the award of any other degree or diploma in any university or institution and, to the best of my knowledge and belief, contains no material previously published or written by another person except where due reference has been made in the text.

Peter Vernon Lanspeary

Permission to copy

I consent that this copy of my thesis be made available for loan and photocopying when it is deposited in a library of the University. Photocopies of some diagrams may be of inferior quality if the photocopy machine cannot faithfully reproduce the shades of grey in monochrome images.

Peter Vernon Lanspeary

Part I

Wind-tunnel flow at very low speeds

Chapter 1

Introduction

This thesis is concerned primarily with establishing flow conditions suitable for experimental investigation of the properties and mechanisms of low-Reynolds-number boundary-layer turbulence. Such an investigation requires the resolution and measurement of the small-scale turbulent motion very close to the solid boundary. In particular, there is a need for measurements in the very thin viscous sublayer region, which is in contact with the wall, and also in the adjacent so-called "buffer-region" of the boundary layer. Some elements of the small-scale turbulence are dynamically significant and participate directly not only in the production of turbulence but also in the viscous dissipation of turbulent kinetic energy. Turbulence fluctuations have maximum amplitude in the buffer region which, in a boundary layer with a typical growth-rate angle of about one degree, extends from the wall for a distance equivalent to only a few percent of the boundary-layer thickness.

In order to have adequate spatial resolution, a probe in the buffer region of the boundary layer must have a sensing volume no larger than the smallest dynamically significant turbulence motion. The length scale of near-wall turbulence is proportional to the ratio of kinematic viscosity and friction velocity[1] (ν/U_τ) and, as a first approximation, the friction velocity (U_τ) is proportional to the speed of the external flow (U_0). The requirement for a particular level of spatial resolution can therefore be expressed as a maximum permissible nondimensional sensor length,

$$l^+ = \frac{lU_\tau}{\nu}, \tag{1.1}$$

or as an upper limit on the Reynolds number of the sensor,

$$Re_l = \frac{lU_0}{\nu}. \tag{1.2}$$

For a specified flow medium, the spatial resolution of an anemometer sensor is clearly improved by making it smaller or by developing the turbulent boundary layer at a lower flow speed. In order to

[1] Symbols are explained in Section 1.4 on page 25.

avoid the known difficulties of making and using extremely small probes, the length scales of near-wall boundary-layer turbulence were enlarged by reducing the flow rate in an existing open-circuit wind tunnel. This wind tunnel was originally designed and used for studying the behaviour of turbulent boundary layers at test-section flow speeds of 20 m/s to 30 m/s. Such flow speeds are far too high for measurement of small-scale turbulence with conventionally-sized anemometer probes. At the very low speeds required for resolution of small-scale turbulence, inlet contractions in wind tunnels of this kind can produce several different unsteady secondary flows. These secondary flows are undesirable because they are unrelated to wall turbulence and they can have dramatic effects on the behaviour of the downstream boundary layers. The first of four such contaminating secondary flows is associated with quasi two-dimensional laminar boundary-layer separation in the wind-tunnel contraction. Görtler vortices formed on the concave contraction surfaces are the second source of unsteadiness in the boundary-layer flow. The third is a large-scale buoyant swirl produced by the combination of naturally occurring temperature nonuniformity and extremely low inlet flow speeds. The fourth source of contamination in the wind-tunnel flow is a pair of streamwise counter-rotating vortices which is initially produced by Görtler instability, but gains most of its strength from the action of small pressure gradients near the start of the contraction.

This introductory chapter contains a review of the research literature on the mechanisms of turbulence in flat-plate boundary layers and channel flows. From the information provided in the review it is possible to quantify the flow speeds required for resolution of small-scale turbulence events. The wind tunnel, instrumentation and anemometry techniques used in the experimental work are described in Chapter 2. The initial evidence of an unsatisfactory test-section flow is presented in Chapter 3. In accordance with the aims of the project, this is followed in Chapter 4 by a description of the experiments leading to the identification of quasi two-dimensional separation in the wind-tunnel contraction. From guidance provided by numerical modelling of the flow, it was possible to modify the contraction in a manner which eliminated this separation. Chapter 5 describes the experimental diagnosis, theoretical analysis and suppression of buoyant swirl generated by spatial temperature nonuniformities in the inlet air flow. Chapter 6 gives an account of experiments which demonstrate the existence of a large counter-rotating streamwise vortex pair in the test-section flow. These experiments show that the vortex pair is part of a flow structure created during the growth of three-dimensional laminar separation from the concave contraction surface. The topology and dynamics of this flow structure, and a method of interrupting its early stages of development are discussed in some detail. After appropriate remedial action, further velocity measurements and flow visualisation experiments indicate that test-section boundary layers are free of unsteady secondary flows. The characteristics of the now well-behaved test-section boundary layer are explored in Chapter 7. The measurements required for this work were also sufficient to determine the speeds and locations at which the flow was suitable for further study of turbulence in flat-plate turbulent boundary layers. Even in a well-behaved turbulent

boundary layer, hot-wire anemometry in the viscous sublayer produced values of mean velocity which were consistently and obviously in error. This error, which is known as wall-proximity effect, is due to heat transfer from the hot-wire filament to the wall. Wall-proximity effect is studied in Chapters 8 to 10. The process of correcting the hot-wire signals demonstrates that wall-proximity effect also produces significant errors in the measurements of velocity fluctuations within the viscous sublayer. The conclusions and research findings of the thesis are detailed in Chapter 11.

1.1 Background: the nature of boundary-layer turbulence

Since the existence of fluid turbulence was demonstrated in 1883 by Osborne Reynolds' dye-streak visualisation of a pipe flow, a great deal of effort has been expended on study of the phenomenon. Turbulence in a boundary layer, which is a thin region of flow adjacent to a solid surface where flow is retarded by the action of fluid viscosity, is of particular engineering interest because the functioning of so many mechanical devices depends on the behaviour of the turbulent boundary layers developed on their surfaces. The main features of a boundary layer are that its thickness is usually two or three orders of magnitude less than its streamwise development length and that its development is influenced by the nature of the main (potential or free stream) flow. As revealed by even a small part of the immense body of research literature on the subject, the mechanisms of wall turbulence are extremely complex and at best are incompletely understood. This complexity is not only produced by the wide variety of surface geometries and flow conditions but, more importantly, is a direct consequence of the fundamental physical laws governing the flow field, and exists even in the simplest surface/turbulent-fluid interactions.

Turbulence has been defined by Bradshaw (1971) as

> "... a three-dimensional time-dependent motion in which vortex stretching causes velocity fluctuations to spread to all wavelengths between a minimum determined by viscous forces and a maximum determined by the boundary conditions of the flow. It is the usual state of fluid motion except at low Reynolds numbers."

"Vortex stretching" is the process by which an element of fluid with vorticity about an axis is stretched in the direction of this axis by the local strain rate and is compressed in directions normal to the axis. Conservation of angular momentum during the compression results in the transfer of kinetic energy from the larger-scale turbulent motion, which provides the stretching, to smaller-scale turbulent motion in the plane of compression [Bradshaw, 1971]. The process of transferring energy to smaller and smaller scales of motion by successive vortex stretching is generally known as the "turbulence

energy cascade". At the smallest scales, where the Reynolds number of the turbulence eddies is in the order of 1 to 10, strain rate produces dissipation of turbulence energy rather than further stretching.

Measurements of flow-field variables such as velocity and pressure inevitably contain errors or uncertainties. If the measurements are used as a set of initial conditions for the prediction of individual turbulent fluctuations, the effects of the errors eventually grow rapidly to dominate the results of the calculations, and so impose limits on the prediction. The fluctuating part of a turbulent flow field can therefore appear to be random. To an experimentalist who can measure only a few point variables, the randomness seems to be of a high order because the turbulent motion is complex and because the quantity of information required for any deterministic prediction of individual turbulence motions is in practice never available. This means that the results of any anemometric study must be presented in a statistical form.

Turbulence develops from laminar shear flows which become unstable and, through the growth of what may be infinitesimally small disturbances, pass through a stage of transition to turbulence. In nearly all instances of fully developed turbulence, the scales of motion containing most of the turbulence energy are at least several orders of magnitude larger than scales at which dissipation occurs. Typically, large-scale turbulent motion is sustained by extraction of energy from the mean flow. It is anisotropic and has other characteristics which depend on the driving force and the boundary conditions of the flow. On the other hand, small-scale and dissipation-scale motion tends to be isotropic and tends (so the theory goes) to have universal characteristics. A major exception to this is the region of maximum turbulence intensity close to the wall in a turbulent boundary layer where very energetic eddies are also those responsible for significant dissipation [Klebanoff, 1957]. In experimental studies of near-wall turbulent boundary-layer structure it is therefore important to resolve all but the smallest scales of turbulence. If anemometers do not have adequate spatial resolution, significant turbulence events may not be detected and measurements may contain serious errors.

At least two sets of length, time and velocity scales are required to describe the behaviour of a turbulent boundary layer. The scales of the largest turbulence motions are determined by the thickness of the boundary layer and the speed of the free stream flow; i.e. the large-motion length, time and velocity scales are δ, δ/U_0 and U_0 respectively. The length, time and velocity scales of turbulence near the wall are determined by the mean wall-shear stress and the kinematic viscosity of the fluid; these wall scales are ν/U_τ, ν/U_τ^2, and U_τ respectively where U_τ is the friction velocity defined in terms of the mean wall shear stress τ_w and fluid density ρ as $U_\tau = \sqrt{\tau_w/\rho}$.

Because boundary-layer turbulence is a very complex phenomenon, in experimental investigations it is important to retain the essential characteristics of wall turbulence and eliminate as many other parameters as possible. Traditionally, this has been done by studying the canonical problem where the

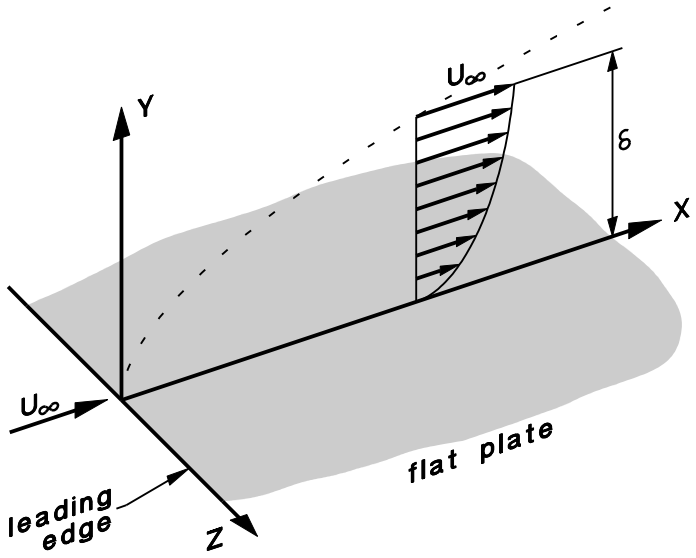

Figure 1.1: The canonical flat plate boundary layer and coordinate directions

boundary layer is developed on a flat plate which is placed at zero incidence in a uniform steady free stream flow. As shown in Figure 1.1, the leading edge of the infinite-width plate is perpendicular to the free stream so that the boundary layer is two dimensional; i.e. its properties are independent of lateral (or spanwise) location.

Some basic features of the canonical turbulent boundary layer can be described with a typical mean velocity profile such as that shown in Figure 1.2. According to long-established practice, the mean fluid speed and distance from the wall in this graph are nondimensionalised using the wall variables (U_τ and ν) and distance from the wall is plotted on a logarithmic axis. Generally the boundary layer can be divided into an outer and an inner region. In the outer (or wake-like) region, there are large-scale long-lived turbulence motions which interact only indirectly with the wall [Townsend, 1951], and the mean flow satisfies a "velocity defect law" of the form

$$\frac{U_0 - U}{U_\tau} = f_1\left(\frac{y}{\delta}\right). \tag{1.3}$$

For well-developed boundary layers, the defect law is valid in a region extending from the outer edge into the inner region until viscosity (i.e. dissipation) begins to have a direct effect on the largest scales of turbulence. In the inner region the velocity scales directly on wall variables so that

$$\frac{U}{U_\tau} = f_2\left(\frac{yU_\tau}{\nu}\right). \tag{1.4}$$

Where the two regions overlap, both Equation 1.3 and Equation 1.4 are valid, and the mean velocity gradient ($\partial U/\partial y$) is a function of only y and U_τ because it cannot depend on viscosity (ν) or boundary-layer thickness (δ). Application of the Buckingham Pi theorem then shows that the existence of a

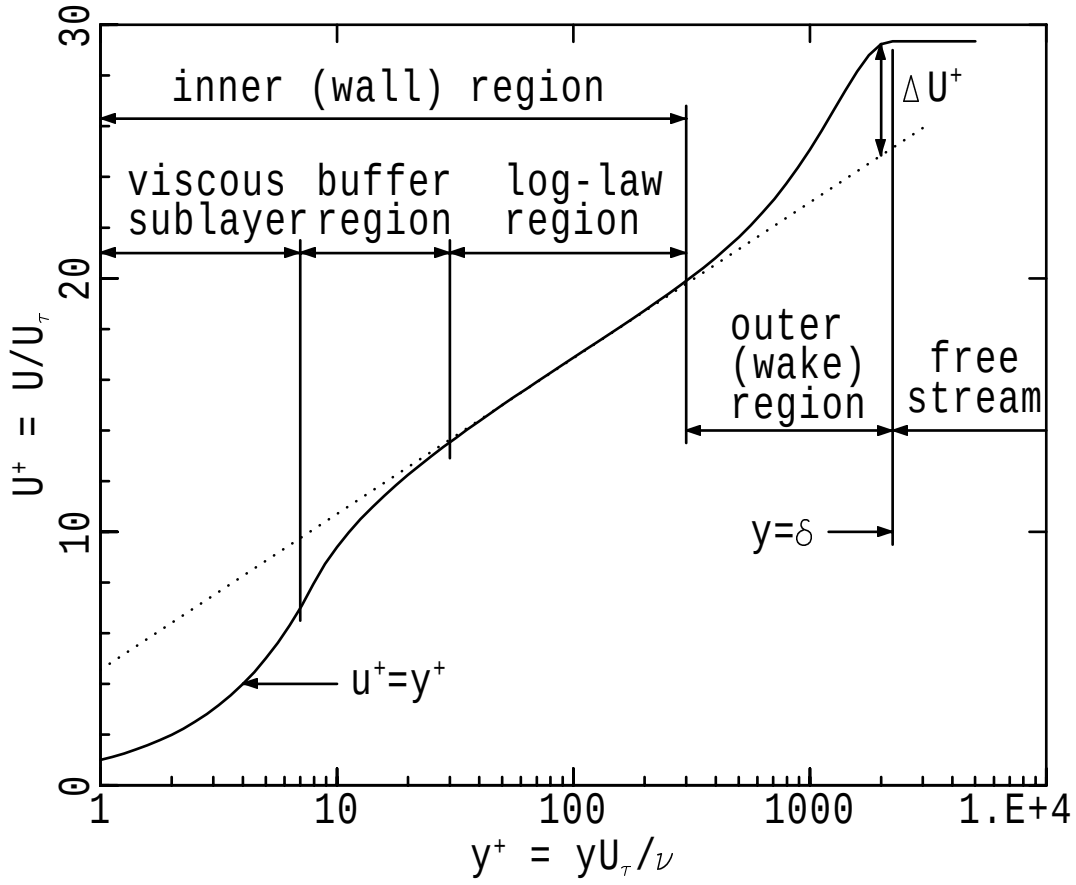

Figure 1.2: Mean velocity profile of a typical two dimensional turbulent boundary layer

"logarithmic" region (Figure 1.2) is a direct consequence of this overlap. In the extremely thin viscous sublayer ($0 < yU_\tau/\nu \lesssim 7$) closest to the wall, the fluid viscosity has significant direct effects on the largest scales of turbulence and in the absence of an externally applied pressure gradient the mean velocity is proportional to distance from the wall ($U/U_\tau = yU_\tau/\nu$). The largest velocity fluctuations and the peak in turbulence energy production [Laufer, 1954] occur in the buffer region between the viscous sublayer and the logarithmic region.

1.2 The structure of turbulent boundary layers

There are already many excellent reviews of turbulent-boundary-layer studies (e.g. Kovasznay, 1970; Willmarth, 1974; Willmarth, 1975; Cantwell, 1981; Robinson, 1991), and so there is little purpose in attempting yet another comprehensive survey. However, salient features of turbulent-boundary-layer structure need to be identified for their particular relevance to this project. Hence, in this review attention is focussed mainly on flow visualisation studies and conceptual models of near-wall turbulence.

In the partial differential equations which govern behaviour of incompressible fluids (i.e. the Navier-Stokes and continuity equations) the unknown variables, which must be solved for in order to predict the behaviour of a flow, are the velocity-vector and pressure fields. If the non-turbulent component of the flow is steady, the time dependence of these variables can be removed by time-averaging the equations. However, time averaging also has the effect of generating 6 unknown fluctuating-velocity product terms of the form $-\rho\overline{u_i u_j}$, the so-called Reynolds stresses, which represent exchange of momentum between the turbulent and the mean flows. Therefore, the time-averaged equations, called the Reynolds equations, can be solved only with the assistance at least 6 extra equations which define the relationship between the Reynolds stress terms and the mean velocity field. These extra relationships are typically supplied by a mathematical model of turbulence. Ideally such theoretical models of turbulence should be based on an understanding of the structure and physical mechanisms of the turbulence.

Early theoretical models of turbulence were developed during the 1920s and the 1930s from the notion of turbulence as an essentially stochastic phenomenon and relied on an analogy between the random molecular motion in a fluid and the larger-scale turbulence motions. These models used the concept of a “mixing length” analogue of molecular mean-free-path over which some property of the fluid is conserved. Mixing length models have been largely replaced by more modern (e.g. $k-L$ and $k-\varepsilon$) turbulence models because closer examination shows that turbulent and molecular motions behave quite differently. However “eddy viscosity”, which is the turbulence analogue of molecular viscosity, is still used in these newer models. An early indication that wall turbulence has some organised structure and is not merely stochastic was obtained by Fage and Townend (1932) who observed and measured the velocity of microscopic particles in a water channel flow. They showed that in such a flow the maximum velocity fluctuation varies and the anisotropy of the turbulence increases as distance from the wall is reduced. Within the viscous sublayer, which was usually referred to as the laminar sublayer, they observed an unsteadiness in the flow consisting mainly of a small-scale wavelike motion but also showing the presence of occasional large-scale lateral disturbances.

During the 1940s, a great deal of attention was given to the decay of homogeneous isotropic turbulence. At about the same time it was observed that, in high Reynolds number turbulence, the behaviour of large-scale energy-containing eddies does not depend directly on fluid viscosity and is different from the behaviour of the small scale turbulence motions where energy is dissipated by the action of viscosity. In the resulting theoretical model, turbulence energy is transferred through a cascade of smaller and smaller scales of motion, with negligible direct coupling between the largest and smallest eddies.

In the 1940s and 1950s, it was shown that the outer edges of turbulent wakes, jets and boundary layers [Klebanoff, 1957, Townsend, 1951, Corrsin and Kistler, 1954] have well-defined but irregular edges so

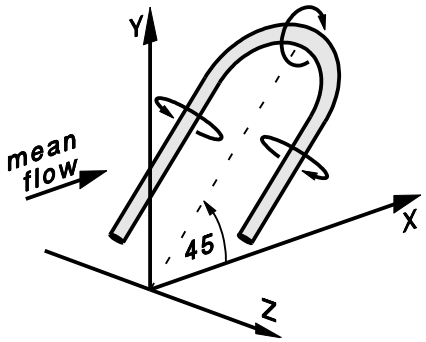

Figure 1.3: Alignment of a typical hairpin vortex in the turbulent boundary layer

that an appropriately located probe detects intermittently turbulent and laminar flow. Townsend (1951) suggested that this distortion of the edge of the boundary layer is caused by the existence of large-scale eddies which are not directly affected by the presence of the wall. He suggested that closer to the surface, where the characteristics of the turbulence are determined by the presence of the wall, the dominant eddies should lose energy by direct viscous dissipation and should have a shape which supports the high shear rate. In this sense such eddies would be "attached to the wall". He also observed that vortex stretching should cause preferential alignment of vorticity at an angle of 45° to the wall. Theodorsen (1952) proposed that turbulent boundary layers are fundamentally composed of horseshoe vortices (Figure 1.3) which, by the process of vortex stretching, grow outward from the wall at a downstream inclination of 45°, and both produce and dissipate turbulence energy. Vortex loops of this kind were actually observed in a pipe flow at transition Reynolds numbers by Weske and Plantholt (1953).

1.2.1 Near-wall "bursting"

Measurements of high turbulence levels and very high dissipation rates in the buffer region of the boundary layer [Klebanoff, 1957, Laufer, 1954] focussed attention on turbulence in the near-wall region. Measurements of two point velocity correlations near the wall [Grant, 1958] revealed a streamwise elongated structure. This was observed by several workers as alternate high and low speed streaks when dye was introduced through the wall into the viscous sublayer.

In particular, Kline and Runstadler (1959) observed that such streaks always appeared in turbulent but never in laminar boundary layers, and that at intervals a low speed streak was lifted slowly from the wall by a predominantly streamwise vortex and then broken up by turbulence at a larger distance from the wall. More detailed visualisation experiments with electrolytic generation of hydrogen bubbles from a spanwise wire [Kline et al., 1967] showed that elongated low-speed streaks occur only in the viscous

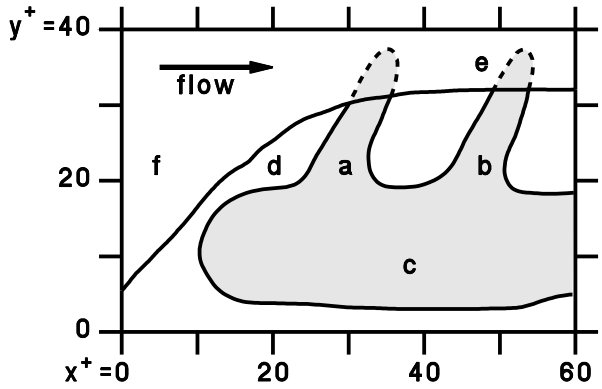

Figure 1.4: Schematic diagram of fluid ejections from a low speed streak [Corino and Brodkey, 1969]. (a) ejection in progress, (b) second ejection, (c) decelerated region, (d) high shear region, (e) violent interaction region, (f) large-scale disturbance.

sublayer and have a median spacing of about 100 viscous length units ($\lambda^+ \approx 100$). Several other groups of workers (e.g. Gupta et al., 1971) have measured similar values of streak spacing. The process of lifting and roll-up of a streak followed by its break-up (i.e. distribution throughout the thickness of the boundary layer) is known as "bursting". Kline, Reynolds, Schraub and Runstadler (1967) showed that, along with streak formation, bursting is an essential feature of turbulence production. In a further extension of this work Kim, Kline and Reynolds (1971) confirmed that nearly all turbulence production occurs during the bursting process. They suggested that the primary energy transfer from the mean flow to the turbulence occurs during the roll-up phase and that break-up is the beginning of the cascade to smaller scales of motion. By using a suspension of magnesium oxide particles in a trichloroethylene pipe flow, Corino and Brodkey (1969) observed a bursting sequence which begins with the acceleration of a low-speed zone of fluid in the sublayer and buffer region ($0 \leq y^+ \lesssim 30$) by a much larger mass of fluid which appears from upstream. This is followed by one or more small-scale outward ejections of fluid from the low-speed region (Figure 1.4). The ejected fluid interacts with the higher speed fluid to produce very turbulent and chaotic fluid motion which contributes significantly to Reynolds stress. The bursting sequence ends with a sweep of high speed fluid which re-establishes the usually observed velocity profile, and removes the retarded elements from the field of view. When due allowance is made for the differences in flow visualisation technique these observations are generally consistent with those of Kline and Runstadler (1959), Kline et al. (1967) and Kim et al. (1971). Grass (1971) used hydrogen-bubble flow-visualisation to measure the u and v components of the instantaneous near-wall velocity field, and observed that ejection and high-speed sweep events make approximately equal contributions to the total Reynolds stress. He suggested that both types of event are essential features of wall turbulence. Wallace, Eckelmann and Brodkey (1972) split the signal from an X-hot-film probe

into quadrants according to the signs of the fluctuating u and v components and then determined that ejection ($u < 0, v > 0$) and sweep ($u > 0, v < 0$) events are each responsible for about 70% of the total Reynolds stress. Events from the other two signal quadrants have much shorter time-scales and make a total negative contribution to the Reynolds stress of about -40%.

Nychas, Hershey and Brodkey (1973) extended the work of Corino and Brodkey (1969) by using a similar flow visualisation technique over a much larger region of the boundary layer. They observed that the dominant process in the outer region of the boundary layer is the formation and decay of transverse vortices at the shear interface between large-scale high speed and low speed regions. They also observed that the production of near-wall ejections is closely associated with the transverse vortices. The addition of stereo cinematography enabled Praturi and Brodkey (1978) to describe vortical motions more clearly and they suggested a conceptual model of wall turbulence in which transverse vortices are the dominant structural feature. In this model ejections appear just upstream of the recently formed transverse vortex, either as a direct result of the flow due to the vortex or as a result of the interaction of the high-speed and low-speed regions near the wall which also produce intense short-lived transverse and streamwise vortices.

In contrast with Nychas and Brodkey (1973) and Praturi and Brodkey (1978) who proposed that large-scale sweeps from the outer region were responsible for near-wall bursts, Offen and Kline (1974,1975) suggested that the bursts are essentially self-regenerating. Offen and Kline (1974) used a combination of coloured dye and hydrogen-bubble visualisation to investigate turbulence in the near-wall region of a low-Reynolds-number water-channel boundary layer. To explain their observations they proposed a conceptual model of bursting [Offen and Kline, 1975] in which an ejection from a low-speed streak is induced by the adverse pressure gradient produced in the near-wall vicinity of a passing high-speed sweep. They considered such a sweep to be a product of a previous burst cycle. By describing the bursting process in terms of the formation and stretching of a horseshoe vortex, they were able to explain qualitatively most of the patterns observed in their own and earlier hydrogen-bubble experiments. They also suggested that the large-scale motions observed in the outer region of higher-Reynolds-number boundary layers might be the result of repeated pairing or amalgamation of vortices produced by bursting.

1.2.2 Counter-rotating streamwise vortex hypothesis

With the help of a mixing length approximation Bakewell and Lumley (1967) deduced the existence of a characteristic randomly-located near-wall eddy structure from an eigenfunction decomposition of space-time correlation measurements. The eddy structure was interpreted as a pair of elongated counter-rotating streamwise vortices with a lateral separation of $\lambda^+ \approx 100$. Kastrinakis, Wallace, Will-

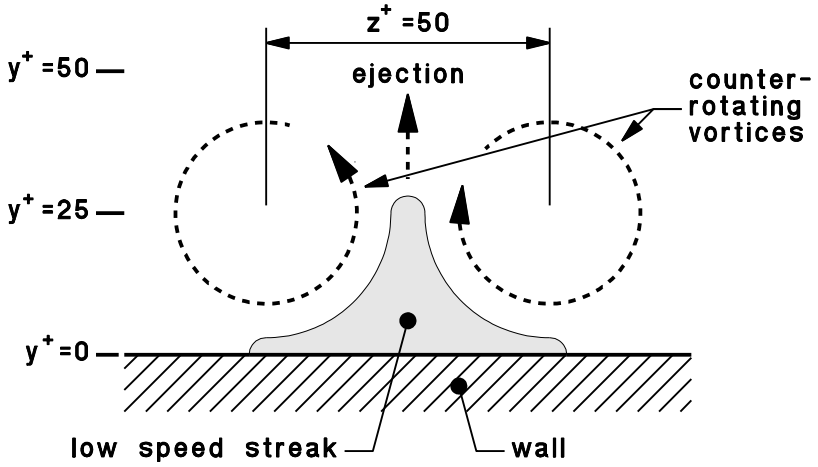

Figure 1.5: Schematic diagram of counter-rotating streamwise vortices and ejection mechanism proposed by Kastrinakis et al. (1977).

marth, Ghorashi and Brodkey (1977) applied the velocity pattern recognition algorithm developed by Wallace, Brodkey and Eckelmann (1977) to conditionally average streamwise vorticity measured from two laterally spaced probes at $y^+ = 30$. They suggested that these results are consistent with a near-wall turbulence model in which ejections from low-speed streaks occur between pairs of intense counter-rotating streamwise vortices (Figure 1.5). In particle visualisation experiments with a spanwise (yz) planar field of view, they observed streamwise vortex rotation but not as identifiable counter-rotating vortex pairs. However in a study where both top and end views of hydrogen-bubble motion were recorded simultaneously, Smith and Schwartz (1983) observed the presence of counter-rotating streamwise structures in at least 20% of all the patterns in the region $10 < y^+ < 45$. Each of such counter-rotating vortex pairs was always accompanied or preceded by a low-speed streak, suggesting that it either generated or was caused by a low-speed streak. Blackwelder and Eckelmann (1979) obtained further evidence supporting the counter-rotating-vortices hypothesis from quadrant classification of two-component shear stress measurements with laterally separated wall-mounted probes. Their conditional sampling measurements suggest that the low-speed streak and streamwise vortices are destroyed by the approach of a high-speed sweep.

1.2.3 Horseshoe vortex models

Willmarth and Tu (1967) observed that pressure-velocity correlations measured in the near-wall region of a turbulent boundary layer are consistent with the existence of convected horseshoe vortex structures inclined downstream from the wall. Correlation measurements between velocity at $y^+ = 5$ and streamwise vorticity at $y^+ = 185$ led Willmarth and Lu (1972) to extend this hypothesis by suggesting

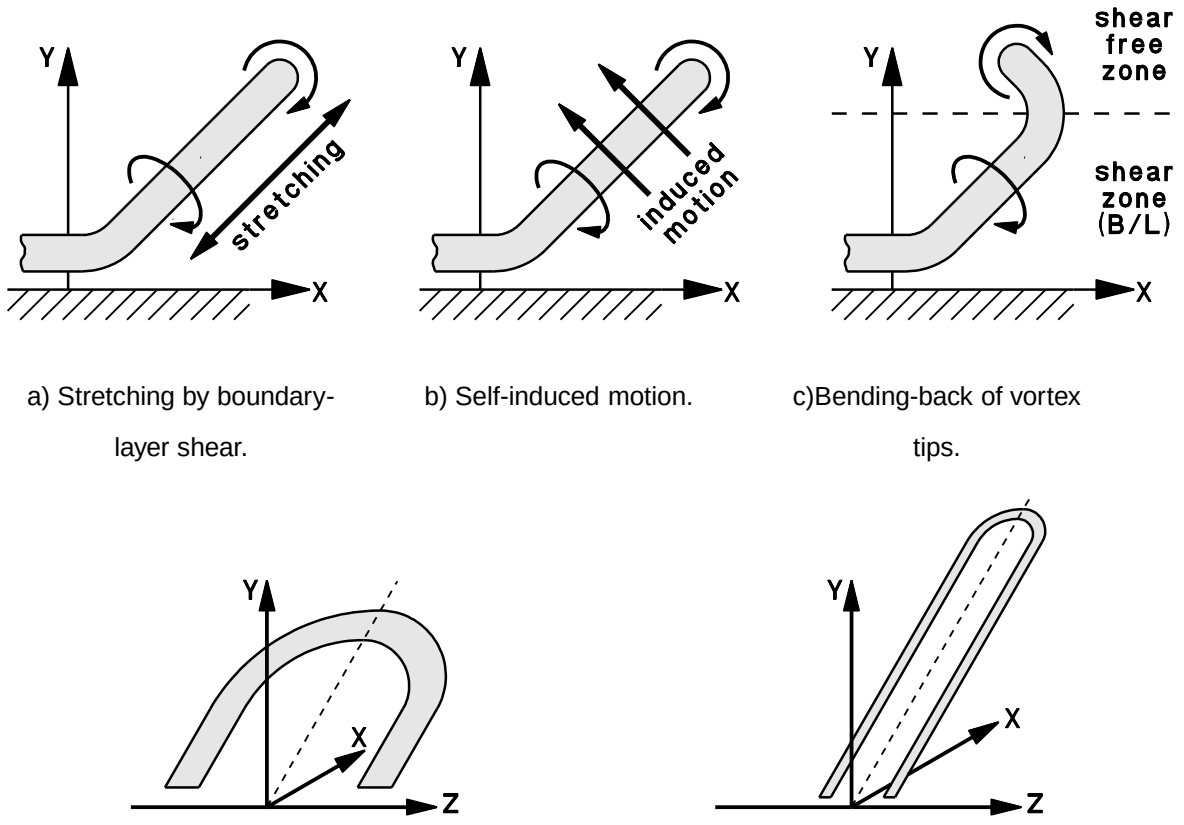

a) Stretching by boundary-layer shear.

b) Self-induced motion.

c)Bending-back of vortex tips.

d) Effect of Reynolds number: low Re_θ.

e) Effect of Reynolds number: high Re_θ.

Figure 1.6: Behaviour of hairpin vortices in the turbulent boundary layer

that such horseshoe vortices are responsible for bursting.

Observations from experiments in which a smoke-filled boundary layer was illuminated by a sheet of laser light, led Head and Bandyopadhyay (1981) to conclude that turbulent boundary layers consist mainly of horseshoe or hairpin vortex loops with legs arranged at approximately 45 degrees to the wall. In this model the vortices, which have an average lateral extent of about 100 viscous units (i.e. $\lambda^+ \approx 100$), grow from the near-wall region to occupy the full thickness of the boundary layer (Figure 1.6(a)). The resulting boundary-layer structure is very Reynolds-number (Re_θ) dependent. At low Re_θ the vortex loops have a relatively low aspect ratio (Figure 1.6(d)) and high rotation rate. At high Re_θ they become extremely elongated (Figure 1.6(e)) and are aggregated randomly to form large scale structures which have an apparent slow rotation due to the mean shear. Head and Bandyopadhyay suggested that the lifetime of the horseshoe vortices would tend to be limited by mutual diffusive cancellation of their legs but might be extended by the pairing of two (or more) vortices.

By modelling the boundary layer as an array of continuously generated random-height vortices which

grow from the wall, Perry and Chong (1982) were able to deduce the distributions of mean velocity, turbulence velocity components, Reynolds stress and streamwise velocity spectrum in the logarithmic region of the boundary layer. In this model vortex loops undergo a process of "eddy death" by diffusive interaction of vortex legs with others of opposite rotation. This limitation on the lifetime (and therefore height) of eddies requires the formation of hierarchies of larger but geometrically similar vortex loops, possibly by the process of vortex pairing between vortex legs rotating in the same direction. With the assistance of Townsend's (1976) attached eddy hypothesis, the model, was refined and extended [Perry et al., 1986] to include the outer (or wake) region of the flow. Dimensional arguments were used to deduce general forms for the power spectrum of all three velocity components. Because the inclined vortex loops (also called attached eddies) do not contribute to turbulent energy dissipation, provision was made for a Kolmogorov spectral region by assuming that the attached eddies are surrounded by fine-scale isotropic turbulence.

These studies [Head and Bandyopadhyay, 1981, Perry and Chong, 1982, Perry et al., 1986] did not examine the mechanism of horseshoe vortex formation. It is simple to show from the Navier-Stokes equations that the normal component of vorticity gradient at the wall depends on the pressure gradient. From this Wallace (1982, 1984, 1985) argued that vortex lines diffusing out from the wall (in accordance with the vorticity transport equation) would inevitably become distorted by local pressure fluctuations. Vortex loops pointing downstream would be lifted from the wall by self-induction according to the Biot-Savart law and would also be stretched by the mean velocity gradient, but vortex loops pointing upstream would would remain anchored to the wall. Wallace suggested that the downstream loops might perturb the wall-pressure sufficiently to produce new vortex loops.

1.2.4 Numerical simulations

In the early 1980s the size and speed of the largest computers became sufficient to simulate canonical wall turbulence by finite difference solution of the governing Navier-Stokes and continuity equations. Such simulations produced databases which are complete time and space descriptions of the velocity and pressure fields — in contrast with laboratory experiments which have so far been limited to velocity measurements within one or two planes [Utami and Ueno, 1987]. The interpretation of these databases has required development of new analysis techniques and has absorbed a major part of the research effort.

The first useful numerical simulations of wall turbulence were large eddy simulations (LES) of a channel flow at $Re = 13800$ [Moin and Kim, 1982] in which, by application of a spatial filter, each flow variable was decomposed into a large scale and a residual component. The large scale components were calculated by solving the filtered Navier-Stokes equations and the influence of the residuals was

obtained using an eddy-viscosity model. In these numerical simulations the solution method was spectral in directions parallel to the wall. Spectral solution methods maximise accuracy at high wavenumbers. The turbulence statistics from the simulation exhibited the same general trends as experimental measurements but were significantly different in the near-wall region, $y^+ < 80$. Several well-known features of wall turbulence such as elongated low-speed sublayer streaks, sweeps and ejections were identified from selected contour plots of flow variables and from simulated particle tracking – although streak spacing was about twice the experimentally measured value. Analysis of this database continued for several years. Kim (1983) performed spatial conditional averaging (VISA) with detection criteria similar to the VITA used by Blackwelder and Kaplan (1976). He produced velocity and Reynolds stress ensemble averages very similar to those of Blackwelder and Kaplan (1976), with ejections downstream of the detection point and sweeps upstream of it. Conditional averaging of streamwise vorticity suggested the presence of counter-rotating streamwise vortices which are lifted away from the wall during the ejection process and have much shorter lifetimes than low-speed streaks. Streamline and velocity-vector cross-sections of the conditionally sampled flow field [Kim, 1985] indicated counter-rotating streamwise vortices on each side of an ejection downstream of the detection point and another pair of streamwise vortices of opposite sign underneath a sweep upstream of the detection point. The complexity of this result raises doubts about whether it is truly representative of a near-wall burst sequence. In retrospect it is clear that this and previous conditionally averaged "pictures" could be a consequence of the lateral symmetry of the mean flow and could be a result of uncorrelated sweep and ejection events. Kim and Moin (1985) found that the most probable inclination of large vorticity values in the middle 60% of the boundary layer thickness is 45°. This implies that production of turbulence vorticity is due mainly to stretching by the mean velocity gradient, and that the x and y components of r.m.s. vorticity are equal [Deissler, 1969]. Both the tracing of vortex lines and projection of the vorticity vector field onto a spanwise plane inclined at 45° to the wall indicated the presence of hairpin vortices, although such vortices were usually asymmetric. Vorticity lines constructed from the conditionally averaged vorticity vector fields had a weak upright horseshoe shape downstream of the detected event and a weak inverted horseshoe shape upstream of the detected event. However, this structure is associated with ejection and sweep events rather than with the existence of true horseshoe vortices.

Improvements in resolution and accuracy of turbulent channel flow simulation were achieved by changing from LES to DNS (direct numerical simulation) and by developing solution methods which were spectral in all directions. Kim, Moin and Moser (1987) have produced very good agreement between the turbulence statistics from a DNS at $Re = 3300$ and experimental measurements. Some discrepancies were observed very close to the wall ($y^+ \lesssim 10$) but most of these were attributed to error in the experimental measurement. This simulation produced the correct low-speed streak spacing ($\lambda^+ = 100$). Kim (1987) ensemble-averaged the database over second quadrant events and used this as the initial flow field for simulating the development of an isolated horseshoe vortex. Enstrophy ($\omega_i^2/2$) contour-

surface plots of the simulation results revealed stretching of the vortex legs (Figure 1.6(a)), self-induced rolling back of the tip (Figure 1.6(c)) and vortex ring formation in the central region of low mean shear. The tip of the vortex was a region of high Reynolds stress and low static pressure. The legs of the horseshoe vortex were also regions of low pressure. Moin and Moser (1989) used one, two and three dimensional orthogonal decomposition techniques to extract characteristic eddy structures from the DNS database. The two-dimensional decomposition yields eddies consisting of a narrow ejection from a low-speed region straddled by a pair of weak counter-rotating streamwise vortices. The three dimensional decomposition provided some streamwise dimensions to this eddy structure. The lengths of the low-speed streak, ejection region and counter-rotating vortices were about 400, 200 and 100 wall units respectively. The inclination of the vortices ranged from 10 degrees near the wall to 60 degrees in the logarithmic region. However, from the observation that streamwise vortices in the DNS results were solitary rather than paired, it became clear that the characteristic eddies were not necessarily representative of eddy shapes in the instantaneous flow fields and their relationship to observable structure was uncertain. The spanwise symmetry of the decomposition was simply a result of the spanwise homogeneity of the flow field. Guezennec, Piomelli and Kim (1989) adapted the burst detection procedure of Kim and Spalart (1987) to remove the lateral symmetry generated by conditional averaging. They observed that, in a $y-z$ plane, the circulation around a path enclosing a detection point had a bimodal probability density (with a local minimum at zero circulation). This showed that the most likely event was strongly asymmetric. By reflecting the flow fields of events with negative circulation in the $x-y$ plane at the detection point they were able to show that the dominant ejection event structure was a single "streamwise" vortex inclined at a small angle to the wall. From measurements with a spanwise array of 10 hot-wires at $y+ = 15$ Antonia and Bisset (1990) have also demonstrated that single-detection-point conditional averaging produces patterns which are not typical of individual turbulence structures because information on the alignment of structures is lost. Jiminez and Moin (1991) attempted to isolate and study the basic unit of wall turbulence by running the channel-flow DNS code of Kim, Moin and Moser (1987) with a very small computational grid. As the grid width was reduced below about 100 wall units turbulence decayed first on one and then on both walls. The grid was too small to simulate the outer region flow correctly, but, provided that the turbulence was sustained, the mean and r.m.s. velocity statistics in the buffer region and viscous sublayer agreed well with experimental measurements. This indicates that the turbulence generation mechanism in the near-wall region is self-sustaining rather than dependent on the outer region flow. Examination of the vorticity field revealed an asymmetric ejection mechanism in which fluid from a low-speed streak is pulled sideways, away from the wall, by a single overlying streamwise vortex.

In comparison with channel flow, the simulation of flat-plate boundary layers is complicated by the streamwise growth of the boundary-layer thickness. Spalart and Leonard (1987) overcame this difficulty and enabled the use of periodic upstream/downstream boundary conditions by replacing the

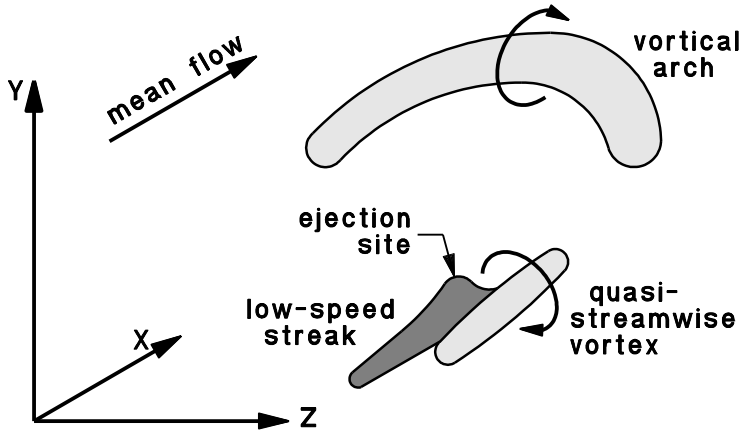

Figure 1.7: Typical vortex structures of the turbulent boundary layer and the relationship with low-speed sublayer streaks and ejections — as described by Robinson (1991) .

normal coordinate y with a similarity coordinate η which expands with the growth of the boundary layer. Boundary-layer and sublayer thicknesses expressed in terms of η then become independent of x. This approach also required a change of the dependent variables (velocity, pressure) and reformulation of the governing equations. The numerical method was spectral in all directions. The simulations, which were obtained for a number of pressure gradients [Spalart and Leonard, 1987] and Reynolds numbers [Spalart, 1988], produced features long recognised as typical in turbulent boundary layers; for example, low-speed sublayer streaks, an irregular turbulent/non-turbulent interface at the edge of the boundary layer, and identifiable viscous sublayer, buffer, logarithmic and wake regions in the mean velocity profile. Boundary-layer properties such as friction coefficient (C_f), wake strength (ΔU^+), r.m.s. turbulence levels and Reynolds stresses compared well with the results of experimental measurements. However, in the simulation the dependence of velocity components (especially the spanwise component) on Reynolds number extended down into the buffer and viscous sublayer regions even when they were scaled on wall variables. Kim and Spalart (1987) used the simulation databases for $Re_\theta = 300$, 670 and 1410 to determine that the number of bursts per unit wall area is almost independent of Reynolds number when scaled on wall variables. In this case bursts were detected by testing grid points in the $y^+ = 12$ plane against a second-quadrant Reynolds-stress (uv) threshold criterion.

Robinson (1991) used specially developed 2D and 3D graphics tools, which included animation and stereo imagery, to identify, classify and describe turbulence structures produced by Spalart's (1988) boundary-layer DNS software, and studied the spatial-temporal relationships between these structures. Particular attention was given to the role of vortex structures and a number of methods for detecting them were examined. The presence of elongated low pressure surfaces proved to be by far the best indicator of vortex structure because pressure is a function of space-integrated vorticity. Most vortices

identified in this way were single quasi-streamwise vortices (30%) or one-sided (11%) and two-sided (30%) transverse arches (Figure 1.7). Two-sided hairpin vortices were extremely rare and many two-sided structures were strongly asymmetric. Ejections were observed on the updraught side of stronger near-wall (single) quasi-streamwise vortices and on the upstream side of transverse arches. Sweeps were observed on the down-draught side of quasi-streamwise vortices. The population of short-lived near-wall quasi-streamwise vortices producing ejections and sweeps was much larger than the weaker more persistent wake-region transverse vortices. This is consistent with Jiminez and Moin's (1991) deduction that the wake region has a very small effect on near-wall turbulence production. Robinson (1991) also examined a class of structural features known as near-wall shear layers (NWSLs). NWSLs identified by vorticity magnitude contours were found mostly in the region $y^+ < 80$, typically inclined at a shallow angle to the wall, and located between lifted low-speed streaks and the surrounding higher-speed fluid. The downstream tips of NWSLs were frequently observed to roll up into transverse vortices. NWSLs have been studied experimentally by Kreplin and Eckelmann (1979) and Johansson, Alfredsson and Eckelmann (1986). These experiments, which were performed in the Göttingen oil channel at $Re_\theta = 7500$, indicated the presence of inclined shear layers with a characteristic length of about 100 wall units in the buffer and logarithmic regions of the boundary layer. Ensemble averages showed that in the buffer region these structures are preserved and convected over distances of more than 500 wall units at a convection velocity of about $13U_\tau$. The inclination angle increased from 7° at the wall to 20° in the buffer region. From his own observations Robinson (1991) concluded that vortex structures are the central feature of wall turbulence and almost all observed structural elements could be explained in terms of them. Vortices were observed to produce shear layers in various ways and shear layers "rolled up" to produce vortices.

In a channel-flow large-eddy simulation Piomelli et al. (1993) superimposed the tracks of fluid moving out of the viscous sublayer on velocity, Reynolds stress and enstrophy contours and showed that ejections occur on the updraught side of single and counter-rotating paired quasi-streamwise vortices. This is consistent with their conditionally averaged laboratory measurements and LES data showing that a peak in enstrophy (i.e. squared vorticity amplitude) leads a peak in Reynolds stress by $t^+ \approx 3$.

1.2.5 Flow-structure components of near-wall turbulence

In the 1980s a research group led by C. R. Smith at Lehigh University published a series of papers on the characteristics and behaviour of recognised elements of wall turbulence such as low-speed streaks, streamwise vortices and horseshoe vortices. These reports were the result of flow-visualisation experiments which involved the simultaneous recording of two orthogonal views of hydrogen-bubble motion near the wall. The dual views made it possible to observe the three dimensionality of the turbulence motion. Careful measurements of low-speed-streak characteristics over a wide range of Reynolds

numbers ($740 < Re_\theta < 5830$) [Smith and Metzler, 1983] showed that the distribution of streak spacing is log-normal and verified that the mean spacing is $\lambda^+ \approx 100$ [Kline et al., 1967, Gupta et al., 1971]. Also, individual streaks are traceable for time periods much longer than the time between bursts. The log-normality of streak spacing is significant because it indicates that streak spacing is self-dependent, and so implies that streaks are indirectly self-regenerating. In the region $10 < y^+ < 45$ at least 40% of all the patterns observed in top and end views [Smith and Schwartz, 1983] indicated the presence of streamwise rotation and at least 20% indicated the presence of counter-rotating streamwise structures. These counter-rotating vortices, which were believed to be stretched legs of horseshoe vortices, were always accompanied or preceded by low-speed streaks, suggesting that they were either necessary for or the result of low-speed streak formation. Smith and Metzler (1982) observed the lifting of fluid from low-speed streaks between counter-rotating vortices. Lifting and roll-up of fluid from low-speed streaks was sometimes observed to form sequences of between 2 and 5 horseshoe vortex loops. This led to the tentative hypothesis that, through stretching by the mean velocity gradient in the buffer region, the counter-rotating legs of a vortex loop are oriented mainly in the streamwise direction and so create a new (or reinforce an existing) low-speed streak. The coalescing of the legs from a succession of vortex loops would strengthen and extend the life of the counter-rotating vortices and enhance the low-speed streak.

Acarlar and Smith (1987a) carried out a detailed investigation of the formation, development and behaviour of horseshoe vortices shed periodically from a surface-mounted hemisphere in a laminar boundary layer. These experiments established that a very wide variety of patterns can be generated by a horseshoe vortex as the location of the visualisation tracer is changed relative to the vortex. Striking similarities were found between the bubble patterns generated by regular vortex shedding and those observed in a turbulent boundary layer. Several behavioural features of horseshoe vortices previously found in turbulent boundary layers were also observed in these experiments. These features were streak regeneration by near-wall quasi-streamwise parts of the counter-rotating vortices, rapid mutual cancellation of vortex legs relative to the persistence of the transverse vortex tips, and backward curling of vortex tips which grow beyond the region of boundary-layer shear. It was also demonstrated [Acarlar and Smith, 1987b] that a similar train of horseshoe vortices could be generated spontaneously from a synthetic low-speed streak produced by fluid injection through a wall slot. In the subcritical laminar boundary layer far downstream of the vortex loop source, the mean and r.m.s. velocity profiles generated by the train of horseshoe vortex loops and associated secondary vortices were very like those measured in a turbulent boundary layer or channel flow.

Hon and Walker (1991) used the Biot-Savart law to calculate the evolution of an isolated hairpin from a slightly distorted line vortex in a uniform-shear boundary layer. In these numerical simulations the developing head of the vortex rose away from the wall and bent back as it emerged into the shear-free

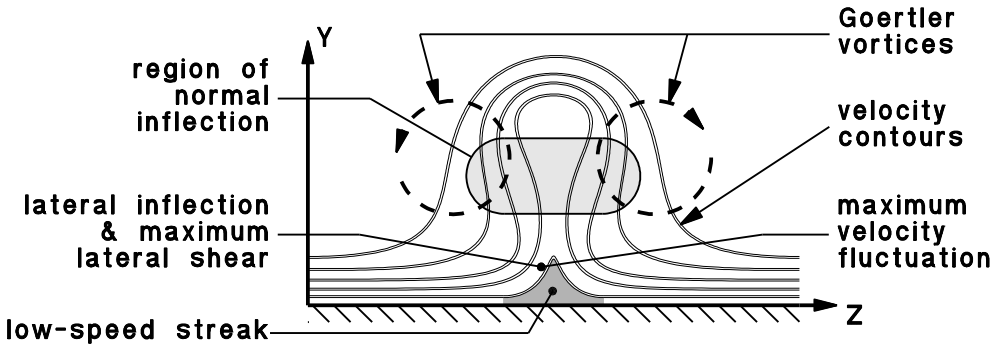

Figure 1.8: Normal and lateral shear due to streamwise vortices in a laminar boundary layer [Swearingen and Blackwelder, 1987].

region while the vortex legs stretched and extended towards the wall. As in the experiments of Acarlar and Smith (1987a, 1987b), the main vortex loop generated subsidiary hairpin vortices which spread and multiplied in the spanwise direction. Similar behaviour has been observed in the simulated development of asymmetric hairpin vortices from an asymmetric stepped line vortex [Smith et al., 1991b]. Also, in a mean shear profile equivalent to that of a turbulent boundary layer, the head of the vortex became broader and the descending legs approached each other; that is, the spacing between the vortex legs was inversely related to the background shear.

The effect of spanwise shear ($\partial u/\partial z$) in the generation of boundary-layer turbulence has been observed in several investigations. Komoda (1967) suspended a lateral array of winglets above a laminar boundary layer in order to produce periodic lateral variations in thickness and used a vibrating ribbon [Schubauer and Skramstad, 1943, Schubauer and Skramstad, 1947] to excite periodic velocity fluctuations. He then showed that the most rapid growth of velocity and vorticity fluctuations occurred within intense lateral shear (i.e. large $\partial u/\partial z$) which developed between the regions of maximum and minimum boundary-layer thickness. Swearingen and Blackwelder (1987) studied the development and breakdown of streamwise vortices arising from Görtler instability in a laminar boundary layer and used the results to infer by analogy some of the characteristics of near-wall quasi-streamwise vortices in the turbulent boundary layer. Measurements with a hot-wire array demonstrated that low-speed streaks are formed on the updraught side of Görtler vortices. Upstream of breakdown to turbulence, velocity profiles are inflectional, and therefore unstable in both the normal and lateral directions. The peak r.m.s. velocity fluctuations occur at the *sides* of the low speed streaks (Figure 1.8). These locations coincide with peak values of lateral shear ($\partial u/\partial z$) rather than with the regions of maximum normal shear ($\partial u/\partial y$). Elongated regions of high lateral shear with accompanying inflectional lateral velocity profiles have also been detected at $y^+ = 15$ in turbulent boundary-layer experiments [Antonia and Bisset, 1990].

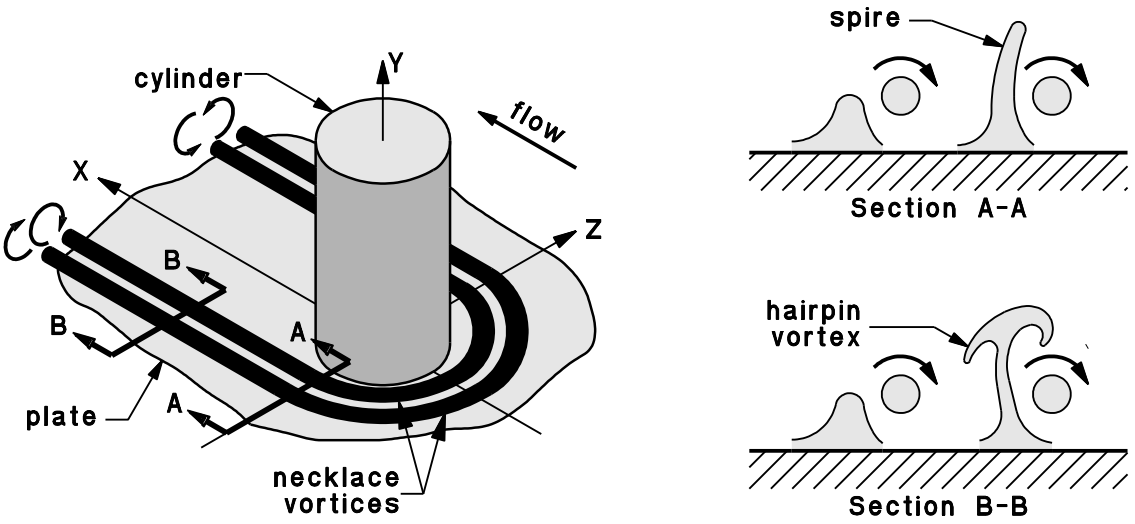

Figure 1.9: Necklace vortices at a cylinder-wall junction in a laminar boundary layer — as observed by Smith Fitzgerald and Greco (1991)

Several numerical studies [Doligalski and Walker, 1984, Ersoy and Walker, 1985, Ersoy and Walker, 1987, Peridier et al., 1991a, Peridier et al., 1991b] have shown that the interaction between a vortex and a surface will always produce a discrete eruptive separation if the development time and vortex strength are sufficient. In such flows the eruptions develop into very narrow spikes. Because of the extreme flow distortion, numerical solutions based on conventional Eulerian methods (i.e. fixed mesh) are much less successful than those which use Langrangian coordinates (i.e. mesh which distorts with the fluid motion). However, even with Langrangian methods the simulations proceed only until the development of the separation singularity and do not include the final eruptive stage [Peridier et al., 1991a]. Similarly, the most useful theoretical discussions of unsteady separation have been based on Langrangian descriptions of the flow [Cowley et al., 1990, van Dommelen and Cowley, 1990]. In the model arising from this discussion, the fluid "particles" on the separating zero-vorticity surface are compressed horizontally to almost zero width and, as a consequence of continuity, are rapidly elongated in the direction normal to the wall. Fluid arriving from upstream is deflected around this region and away from the wall to form an eruption which, in its final development stage, becomes independent of the initiating adverse pressure gradient [Elliot et al., 1983]. Van Dommelen and Cowley (1990) examined the asymptotic scaling of coordinates on the approach to separation and concluded that, as measured by the thickness of the separating fluid layer, a typical three dimensional eruption has a long and thin crescent shape.

It is well known that horseshoe (or necklace) vortices with extended trailing legs are formed in the laminar flow around a cylinder-plate junction (Figure 1.9). Hydrogen-bubble visualisation experi-

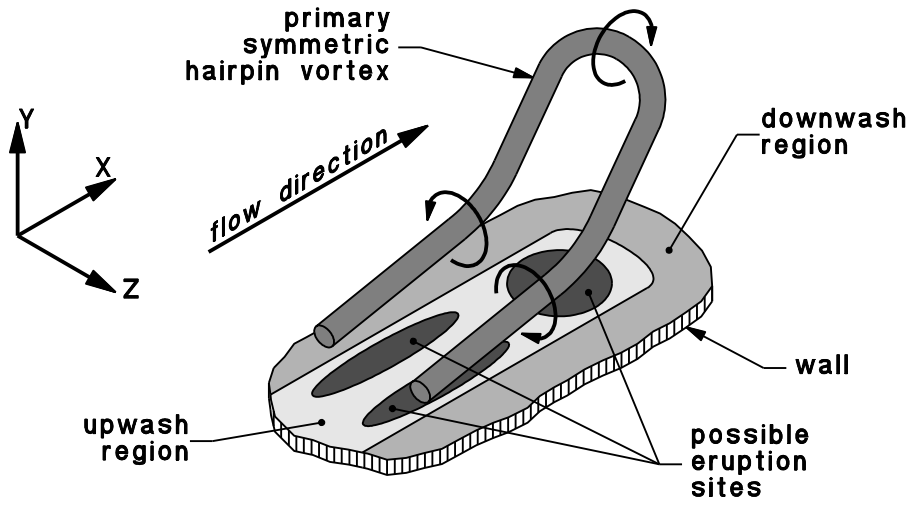

Figure 1.10: Locations where the interaction between a convected symmetric hairpin vortex and a wall can induce eruptive separation from low-speed streaks — as described by Smith et al. (1991a).

ments have revealed the eruption of spire separations from the thickened boundary layer adjacent to these vortex legs [Smith et al., 1991a]. At cross-sections further downstream the eruptive spires were observed to have developed into mushroom shaped patterns characteristic of hairpin vortices. A similar technique has also shown that the characteristic height and thickness of the spires in a turbulent boundary layer are approximately 100 and 10 wall units respectively [Smith et al., 1991b].

A number of studies examining the behaviour of simple flow-structure components in various degrees of isolation have been reviewed in this section. The most important of these components are the ejection event (or eruptive separation), the quasi-streamwise vortex and the low-speed streak. Quasi-streamwise vortices are the legs of usually asymmetric horseshoe vortices. Using knowledge gained from a series of such “kernel” flow investigations Smith et al. (1991) assembled a model of near-wall turbulence which describes the evolution and interaction of the various flow components. In this model the updraught sides of near-wall hairpin vortex legs create or enhance low speed streaks. The low-speed streaks are inactive except where they are thickened by the regions of adverse pressure gradient which exist on the updraught sides of near-wall hairpin vortex legs or, less frequently, upstream of hairpin vortex heads (Figure 1.10). These pressure gradients generate the initial streak thickening which eventually develops into the narrow crescent-shaped eruptive separations described in previous paragraphs. As shown in Figure 1.11, the shear layer produced by the ejected fluid then rolls up, creating secondary hairpin vortices which are initially almost symmetric but, in a typically chaotic and highly sheared environment, rapidly become asymmetric or one-legged. This conceptual model of the mechanism for regenerating hairpin vortices was tested by a set of experiments in which single symmetric hairpin vortices were generated by Acarlar and Smith’s (1987b) method of controlled fluid injection

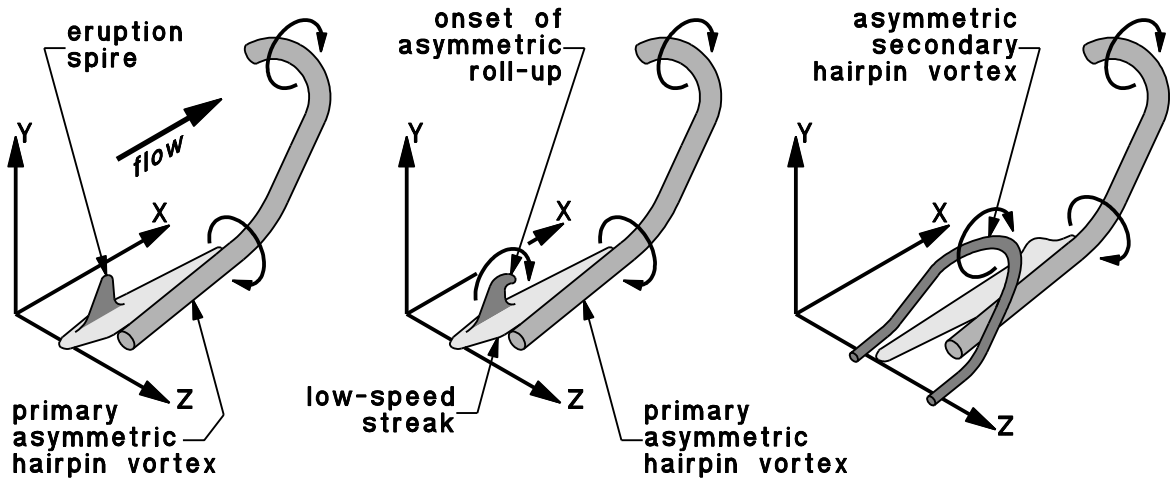

Figure 1.11: Mechanism for near-wall generation of hairpin vortices [Smith et al., 1991b].

from the wall. Through very careful positioning of a hydrogen-bubble wire and an appreciation of the theory of unsteady separation [Cowley et al., 1990], it was possible to observe the formation of secondary hairpin vortices at three sites: one symmetric roll-up behind the head of the primary hairpin vortex, and, as shown in Figure 1.11, one asymmetric or skewed roll-up on the updraught side of each leg of the primary hairpin vortex [Smith et al., 1991b].

Except for one significant detail, the dynamical model of wall turbulence proposed by Smith et al. (1991) is consistent with the kinematic structure revealed by Robinson's (1991) study of DNS databases. The difference is in the nature of the ejection event. In the dynamical model a typical ejection is an explosive bursting (i.e. very rapid) process with a lateral length scale in the order of $10\nu/U_\tau$ or less. In its later stages this unsteady separation has dynamics which are quite distinct from the direct effects of adjacent low-speed streaks, shear layers or quasi-streamwise vortices. Direct simulations [Jiminez and Moin, 1991, Robinson, 1991] indicate that an ejection from a low-speed streak is a more gradual process induced by an adjacent quasi-streamwise vortex. Zang (1991) suggests that although the DNS of Spalart (1988) and Kim et al. (1987) produced velocity statistics which agree with experiment, they might not have resolved the smallest-scale motions in a manner independent of the finite-difference grid spacing. Therefore there is some doubt that the shapes and dynamics of instantaneous turbulence structures were simulated reliably, but this does not necessarily mean that all Eulerian simulations are unsuitable for dynamical studies. In x-z and x-y cross sections of the flow from more recent large eddy simulations of turbulent channel flow [Piomelli et al., 1993], the distributions of "particles" marked by simulated dye injection indicate an eruptive flow structure which is remarkably similar in scale and shape to the ejections revealed by hydrogen-bubble experiments.

1.3 The flow speeds required for study of small-scale turbulence in wind-tunnel boundary layers

The literature review in Section 1.2 has shown that dynamically important features of near-wall turbulence such as eruptive spires may have a lateral extent as small as $\Delta z^+ \approx 5 - 10$. At a free stream speed of 10 m/s, which may be the lower limit of a typical low-speed wind tunnel, these turbulence events would have a width of from 0.2 to 0.4 mm, and so would not be detected by conventional hot-wire probes with a filament length of about 1 mm. Hot-wires as short as 0.1 mm have been manufactured and used, but the difficulties of doing so are severe [Willmarth et al., 1976, Willmarth and Sharma, 1984, Ligrani and Bradshaw, 1987b, Watmuff, 1989] and these difficulties are amplified still further if multi-probe arrays are needed. Hot-wire probes of conventional size are therefore preferred even though this choice incurs the added difficulty of developing a turbulent boundary layer at much lower flow speeds. The required flow speed depends on the nature of the data processing and the required spatial resolution of the measurements. At one extreme, selection rules developed by Ligrani and Bradshaw (1987) indicate that hot-wires with a length of 1 mm and a diameter of 5 μm can accurately measure near-wall r.m.s. turbulence levels in air at free stream speeds up to about 9 m/s. At the other extreme, measurements which resolve the dissipation scales of turbulence in the viscous sublayer and buffer region would only be obtained with hot-wire filaments shorter than 2 or 3 Kolmogorov lengths [Wyngaard, 1968, Ligrani and Bradshaw, 1987a]. From the estimates of Kolmogorov length provided in Appendix A ($\eta^+_{\text{min}} = 1.35$), resolution of the highest turbulence wavenumbers would therefore require a free stream speed no higher than about 1 m/s. While the resolution of Kolmogorov scales might be useful for verifying the accuracy of measurements at higher speeds, it would not be considered essential for investigation of turbulence mechanisms because the smallest dynamically significant events are believed to have a width in the order of 10 Kolmogorov lengths. Hot-wires with a length of 1 mm may therefore have sufficient spatial resolution for the more important measurements, such as those which detect the effects of ejection-type events, at flow speeds as high as 3 or 4 m/s.

1.4 Notation

C_f	Local skin friction coefficient
f_1	function representing the velocity defect law
f_2	function representing the law of the wall
l	length of a hot-wire filament
Re	hU_0/ν, channel Reynolds number based on half-width h
Re_l	lU_0/ν, Reynolds number of hot-wire length

Re_θ	$U_0\theta/\nu$, Reynolds number of a boundary layer — based on momentum thickness θ.
U	x component of mean fluid velocity
ΔU	Strength of boundary-layer wake (outer) region – maximum amount by which velocity exceeds the law of the wall value
U_0	mean speed of free stream external to boundary layer
U_τ	$\sqrt{\tau_w/\rho}$, friction velocity of the boundary layer
u, v, w	x, y and z components of fluctuating velocity
x, y, z	streamwise, normal and spanwise components of the position vector
x	distance downstream of the flat plate leading edge
y	distance from a wall on which a boundary layer is developed
Δz	width of an ejection spire
δ	boundary-layer thickness
η	Kolmogorov dissipation length scale
λ	spanwise distance between low-speed sublayer streaks
ν	kinematic viscosity of the fluid
ρ	density of the fluid
$-\rho\overline{u_i u_j}$	Reynolds stress tensor. In a canonical boundary layer the only non-zero component is $-\rho uv$.
τ_w	wall shear stress
ω_i	vorticity tensor component

Superscripts

Variables which have a superscript $^+$ are nondimensionalised using the viscous flow variables U_τ and ν, e.g. $U^+ = U/U_\tau$ and $y^+ = yU_\tau/\nu$.

Chapter 2

Wind tunnel and instrumentation

The literature review in Chapter 1 establishes that, in the near-wall region of the turbulent boundary layer, dynamically important features such as eruptive spires may have lateral dimensions in the order of $\Delta z^+ \approx 5 - 10$. Detection of these events with conventionally sized hot-wire probes requires an air flow speed of not more than 3 to 4 m/s. A general description of the wind tunnel which was available for investigations of near-wall turbulence is given in Section 2.1; the modifications needed to satisfy the constraint on flow speed are included in this description. The hot-wire anemometry techniques used for measurements within the low-speed turbulent boundary layer of the wind-tunnel test section are also explained in this chapter. This is followed by an outline of the data acquisition system and other necessary instrumentation.

2.1 Boundary-layer wind tunnel

The wind tunnel used by Lim (1971) and Thomas (1976) was modified to operate over a much lower flow-speed range than the original 19 m/s to 35 m/s. This is an open-circuit induced-flow wind tunnel driven by a centrifugal compressor which, in turn, is driven through two step-up gear boxes by an SCR-controlled 60kW d.c. electric motor (Figure 2.1). The boundary layer under investigation is developed on the walls of the wind-tunnel test section.

The flow rate in the wind tunnel is controlled by a variable-throat-area sonic choke between the test section and the drive compressor. The sonic choke was redesigned and rebuilt to reduce the regulated flow rate and to increase the "turndown" speed ratio. Further details of the sonic choke and auxiliary inlet may be found in Appendix B. The exhaust diffuser and exhaust silencer are described in Appendix C.

Air enters the wind tunnel through a contoured bell-mouth, and passes through 2 honeycombs, 6 fine wire mesh screens and a settling chamber. A contraction then reduces the cross-section of the flow from $1.15\,\mathrm{m} \times 1.15\,\mathrm{m}$ to $228\,\mathrm{mm} \times 228\,\mathrm{mm}$ at the start of the test section. The general arrangement of the inlet section and contraction is shown in Figure 2.1, and further details are contained in Tables 2.1 and 2.2.

The open area ratio of the screens in the inlet section, $\beta = 38\%$, is much lower than the minimum value of 57% recommended by Bradshaw (1965). This recommendation is the result of experiments which found that, for $\beta < 57\%$, the flow emerges from the pores in the screen as a pattern of jets which coalesce irregularly and produce significant nonuniformities in the downstream flow. In such cases Bradshaw measured lateral variations of up to 20% in mean shear stress on the wall of the test section, but a similar effect was not found in the test section of the present tunnel because the Reynolds number of flow through the screens is much lower than in Bradshaw's investigation, and is also much lower than the minimum value required for vortex shedding [Kovasznay, 1949, Nishioka and Sato, 1974, Gerich and Eckelmann, 1982].

The test section of the wind tunnel (Figures 2.1 and Figure 2.2) is constructed from rigid, heavy aluminium C-section. Fifteen instrumentation ports with a diameter of 152.4 mm are spaced 304.8 mm apart along the centreline of the upper surface. The lower surface is a flexible stainless steel sheet which can be raised or lowered on screw jacks to adjust the streamwise pressure gradient of the flow.

2.2 Hot-wire anemometry technique

Experimental measurements within the turbulent boundary layer of the wind-tunnel test section were obtained almost entirely by hot-wire anemometry. The principles, theory and broad practical aspects of hot-wire anemometry have been described in many reviews and books on the subject (for example, Compte-Bellot, 1976; Blackwelder, 1981; Perry, 1982; Smoliakov and Tkachenko, 1983; Lomas, 1986). This section of Chapter 2 discusses aspects of hot-wire anemometry which are affected by the aims of the data analysis and by the flow conditions in low-speed turbulent boundary layers. In particular, it was necessary to resolve small-scale velocity fluctuations in circumstances where a high r.m.s. turbulence level of 30% to 40% was combined with an unusually low mean flow speed.

2.2.1 Boundary-layer hot-wire probe

A hot-wire probe used for measurements within the viscous sublayer should satisfy several requirements. The most important of these are that

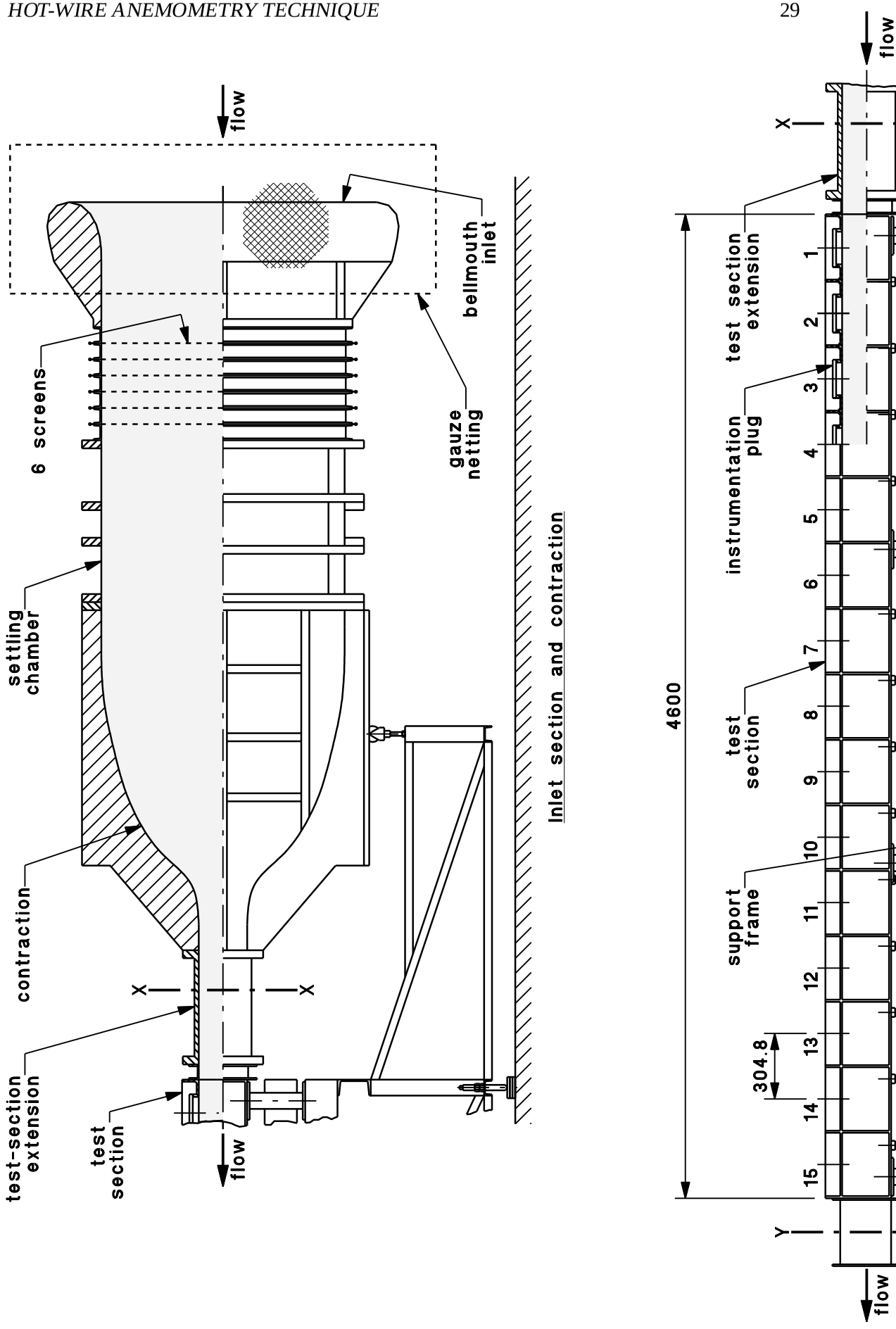

Figure 2.1: The boundary-layer wind tunnel. Scale 1:25.

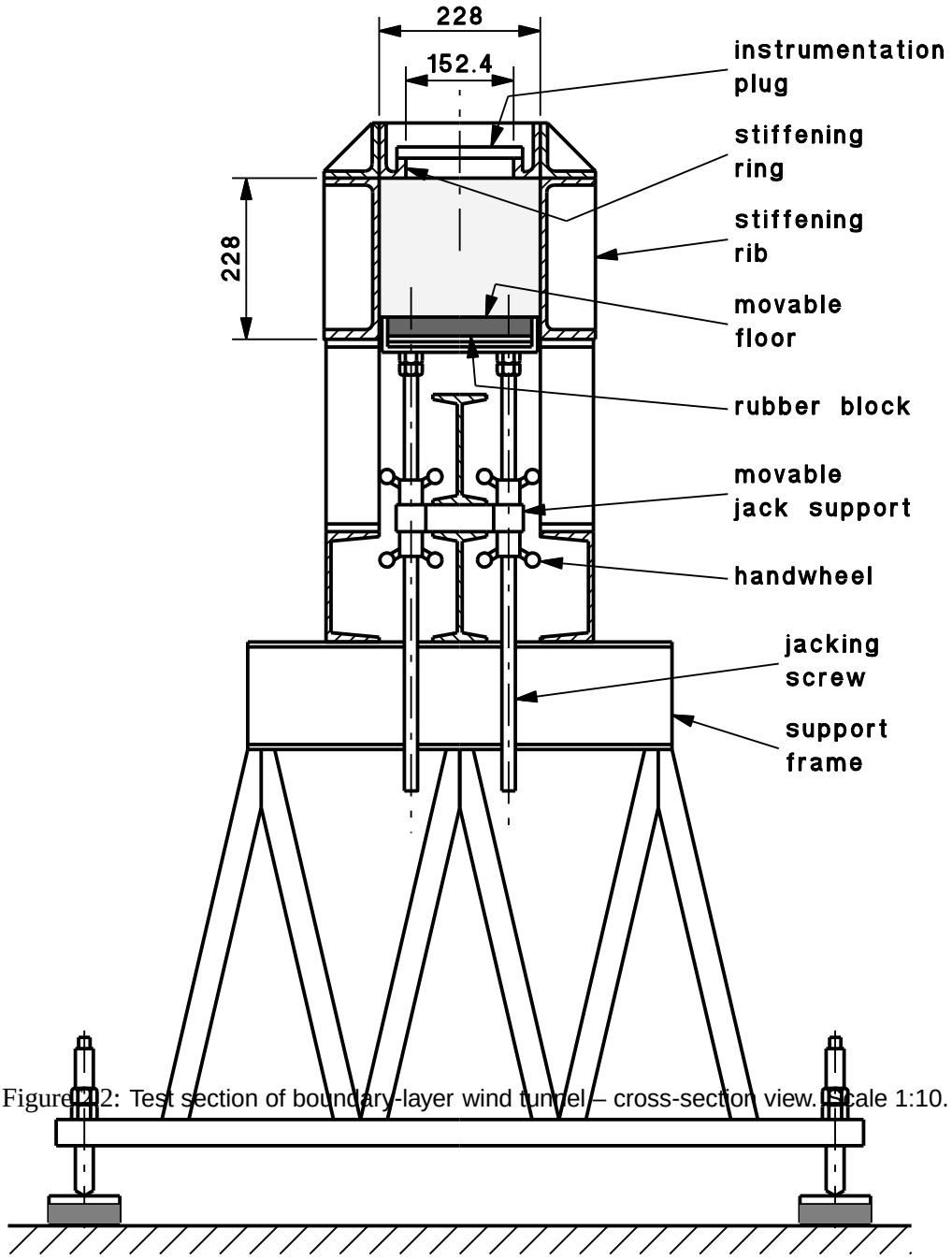

Figure 2.2: Test section of boundary-layer wind tunnel – cross-section view. Scale 1:10.

Table 2.1: Principal Dimensions of Boundary Layer Wind Tunnel

(partly from Lim (1971))

Inlet		
Bell-mouth	Internal cross-section	1.15 m × 1.15m
Honeycombs	Number	2
	Thickness	100 mm
	Cell size	6.5 mm
	Separation	Variable
Gauze Screens	Number	6
	Number of mesh per cm	13
	Wire diameter	0.315 mm
	Separation	76 mm
	Open area ratio	38%
Settling Chamber	Internal cross-section	1.15 m
	Length	0.76 m
Contraction	Internal cross-section —	
	at upstream end	1.15 m × 1.15m
	at downstream end	228 mm × 228 mm
	Contraction-ratio	25:1
	Length	1.4 m
Test Section	Length	500 mm
Extension	Cross-section	228 mm × 228 mm
Test Section	Height - variable	228 mm (max)
	Width	228 mm
	Length	4.5 m
	Instrumentation ports —	
	Number	15
	Separation	304.8 mm
	Diameter	152.4 mm
Flow Control	Sonic choke flow rate	
	large centrebody	0.067 kg/s to 0.61 kg/s
	small centrebody	0.73 kg/s to 1.3 kg/s
	Bypass choke flow rate	0.35 kg/s
Compressor	Manufacturer	General Electric (U.S.A.)
	Type	Turbosupercharger B-22
	Rated maximum speed	24000 rpm
	Speed in wind tunnel	12000 rpm
Electric motor	Manufacturer	British Thomson-Houston
	Type	d.c.
	Number of poles	6
	Continuous ratings —	
	output power	60 kW
	current, voltage	136 Amps, 440 Volts
	speed	790 rpm
Gear-boxes	Total step-up ratio	17:1

Continued on the next page

Table 2.2: Principal Dimensions of Boundary Layer Wind Tunnel (continued)

(partly from Lim (1971))

Exhaust	Height	1300 mm
Diffuser	Inlet cross-section	200 mm × 150 mm
	Outlet cross-section	452 mm × 418 mm
	Area ratio	6.3
	$\frac{1}{2}$ angles	5.54^o & 5.89^o
Exhaust	Height	800 mm
Silencer	External cross-section	470 mm × 462 mm
	Splitter plates —	
	number	6
	thickness	44 mm
	spacing	22 mm
	Noise attenuation	more than 40dB

(1) the length of the filament should be small enough to resolve small-scale turbulence events accurately and be long enough to avoid the effects of heat conduction to the prongs. This is detailed in Section 2.2.5.

(2) it should be possible to put the filament very close to the wall; for example $y \approx 0.04$ mm or $y^+ \approx 0.5$. This means not only that the prongs must be at a non-zero angle of incidence to the flow, but also that any curvature of the filament must not significantly increase the uncertainty in distance from the wall.

(3) the prongs, probe body and probe stem should produce minimal disturbance to the flow around the filament. As explained in Chapter 8, probes satisfying this criterion avoid aerodynamic wall-proximity effect. In high-speed subsonic and supersonic flows the required slenderness of the probe is in conflict with the need for sufficient rigidity to avoid excitation of wire vibration by the flow, but this is not the case for air speeds less than 10 m/s.

The hot-wire probes used in this project have 5-μm-diameter tungsten filaments. Tungsten filaments are physically stronger and easier to prepare than those of either platinum or platinum/rhodium-alloy Wollaston wire. Also, if operated at the same overheat ratio, a tungsten wire is at a lower temperature than wires of these alternative materials because of its higher temperature coefficient of resistivity. A number of smaller-diameter (platinum and platinum/rhodium alloy) Wollaston wires were tested in the initial stages of the experimental work, but the resolution advantage of the smaller available diameters was largely cancelled by greater difficulty in manufacture, greater fragility and greater persistence of output-voltage drift than encountered with tungsten-wire probes. In addition, the reduction in wall-proximity effect, which results from decreasing the wire diameter [Zemskaya et al., 1979, Krishnamoorthy et al., 1985], was to a large extent eliminated by the higher operating temperature of the Wollaston wires.

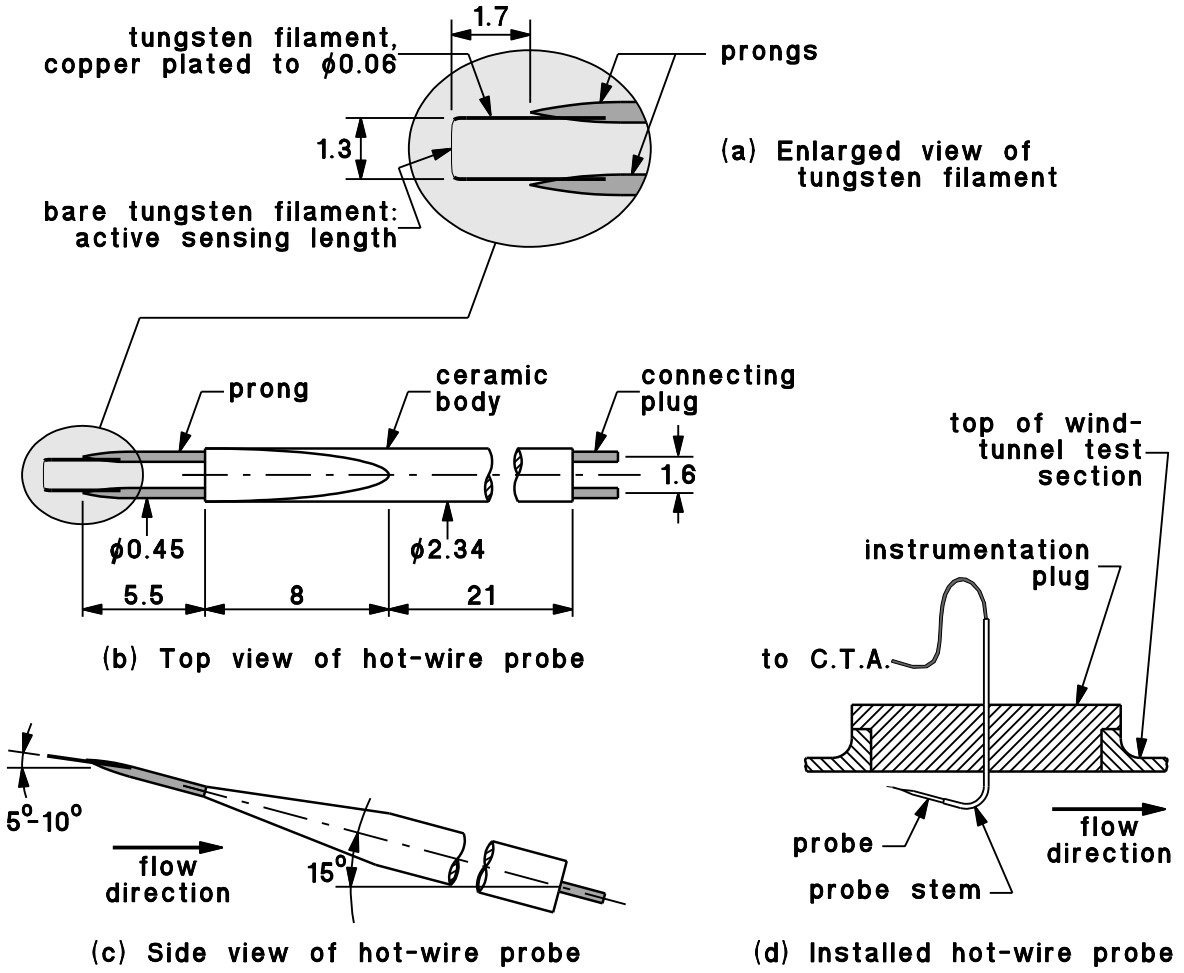

Figure 2.3: The boundary-layer hot-wire probe

The ends of the tungsten-wire filaments in the boundary-layer probes are copper plated to a diameter of about 60 μm and are bent back at right angles to form a flat bottomed U before being soldered to the prongs. The dimensions of the probe are shown in Figure 2.3. When mounted in the probe stem, the prongs are inclined at an angle of 15 degrees to the flow, but the final angle of incidence of the copper-plated tungsten wire is between 5 and 10 degrees. The purpose of this probe design, which is similar to that used by Willmarth (1976), is to keep the prongs well away from the active part of the hot wire and also to allow the wire to be placed very close to the wall. The length of the active part of the filament is 1.3 mm which, in the velocity range 1.5 to 10 m/s, is equivalent to $6.5 \lesssim l^+ \lesssim 35$. At a free stream speed of about 5 m/s the length of the hot-wire filament ($l^+ \approx 20$) is small enough to avoid loss of r.m.s. signal by spatial averaging, and is long enough ($l/d = 260$) to avoid the effects of heat conduction from the ends of the wire [Ligrani and Bradshaw, 1987a].

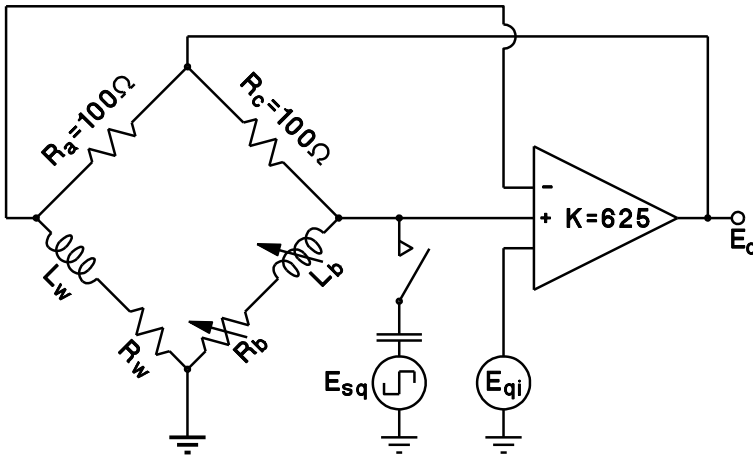

R_w — cold resistance of the hot-wire filament,
L_w — inductance of the hot-wire probe and its cable,
R_b — overheat resistor,
L_b — balance inductance,
K — gain of d.c.-coupled amplifier,
E_o — bridge output voltage,
E_{qi} — offset voltage source,
E_{sq} — 1 kHz square-wave source.

Figure 2.4: Constant temperature anemometer bridge – schematic circuit diagram

2.2.2 Constant temperature anemometer bridge

All hot-wire probes are operated at constant temperature by electronic bridge circuits which were designed in accordance with the recommendations of Perry & Morrison (1971) and were built by technical staff of the Department of Mechanical Engineering. The basic elements of the constant temperature anemometer (C.T.A.) bridge are shown in Figure 2.4. The operating temperature of the wire is set by adjusting the value of the overheat ratio to $R_b/R_w = 1.5$. The amplifier input offset voltage, E_{qi}, supplies the error signal which allows the bridge to operate [Perry and Morrison, 1971, Blackwelder, 1981] and, together with the balance inductance L_b, is an important factor in determining the frequency response of the circuit. The gain of the d.c.-coupled amplifier is limited by internal feedback to $K = 625$, giving a frequency response which is flat to about 50 kHz. The most serious problems with these C.T.A. bridges are high frequency instability when operating 0.6 μm Platinum-Rhodium hot wires [Watmuff, 1989] and occasional component failure.

2.2.3 Anemometer frequency response

The square-wave test is commonly used to optimize the frequency response of a hot-wire probe. Typically, a 1 kHz square-wave signal is introduced at the non-inverting input of the bridge amplifier (Figure 2.4), and the output from the anemometer circuit is monitored on an oscilloscope. The effect of the feedback loop in the circuit is to differentiate the square-wave test signal, and so produce an impulse-like output. The shape and duration of the output pulse, which may be altered by adjusting the offset-voltage (E_{qi}) and balance-inductance (L_b) controls of the C.T.A., are a measure of

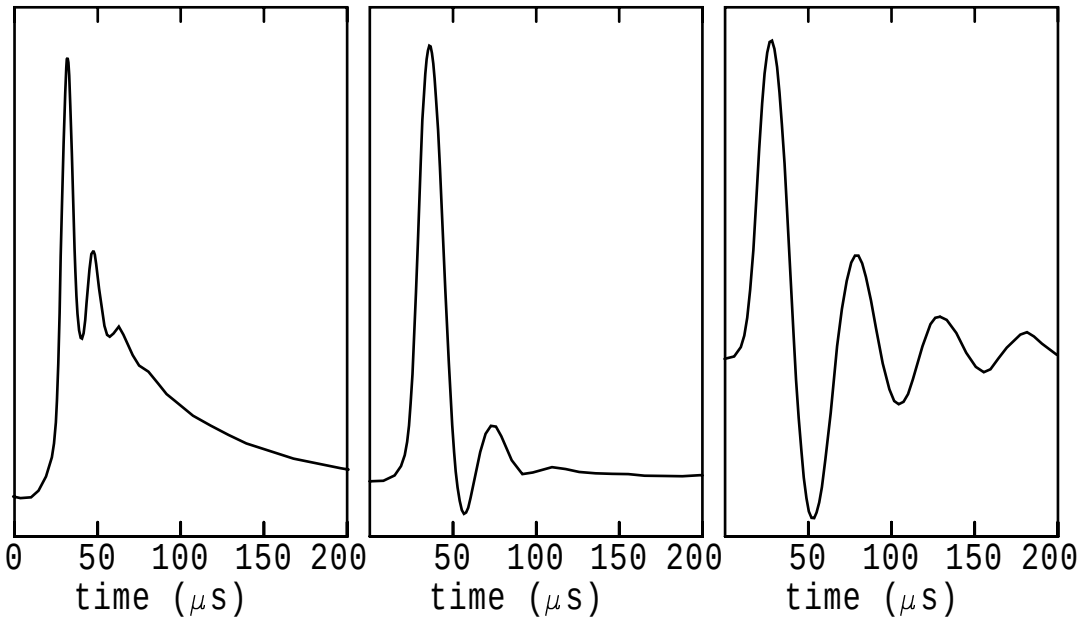

a) $E_{qi} = 70.0$ mV overdamped

b) $E_{qi} = 24.6$ mV optimum response

c) $E_{qi} = 16.8$ mV underdamped

Figure 2.5: Variation in square wave response of a tungsten hot wire (5 μm diameter, 1.3 mm length) at an air speed of 4.0 m/s for different values of offset voltage E_{qi} and optimum balance inductance L_b.

the C.T.A. frequency response. Optimal frequency response is obtained for an output pulse with 13% overshoot [Freymuth, 1977, Freymuth and Fingerson, 1977]. The 3 dB bandwidth of the C.T.A. is then $(1.3\Delta t)^{-1}$ Hz, where Δt is the time measured from the start of the pulse until it first returns to less than 3% of its maximum value. The presence of oscillations in the decay of the pulse indicates insufficient damping.

Results from a series of square-wave tests with the boundary-layer hot-wire probe (Section 2.2.1) are shown in Figure 2.5. These tests indicate that the 3dB cut-off frequency of the frequency response of the properly-adjusted C.T.A. is almost constant at 22 kHz over flow speeds ranging from 2.0 m/s to 8.0 m/s, and exceeds the maximum signal frequency by a factor of at least 4.

2.2.4 Stability; use of offset voltage and balance inductance

In their third-order analysis of the C.T.A., Perry & Morrison (1971) have included the effects of lead inductance, offset voltage and amplifier gain on frequency response. The transfer function for this model of the C.T.A. has two complex-conjugate poles and a single real pole. The complex poles generally have a much lower frequency than the real pole, and so they control the frequency response of the bridge. Their location is strongly influenced by the input offset voltage E_{qi} and the balance

inductance L_b (Figure 2.4). With this model of the C.T.A., which assumes flat amplifier frequency response, stable operation can usually be ensured by using only the offset voltage adjustment, but such stability is obtained at the expense of bandwidth. A much better frequency response is obtained if the balance inductance is adjusted together with the offset voltage. In this way both the bandwidth and the stability margin can be controlled. Adjusting amplifier gain K has only a weak effect on frequency response.

The C.T.A. bridges described in Section 2.2.2 have adjustable balance inductance, adjustable offset voltage but fixed amplifier gain. As revealed by the square-wave test, the behaviour of these C.T.A.s is broadly in accordance with Perry and Morrison's (1971) analysis. The square-wave test also reveals a departure from the behaviour predicted by the third-order model when the circuit is highly damped (Figure 2.5(a)). This departure is clearly due to the presence of a much higher frequency complex pole. Watmuff (1989) explained this behaviour by extending Perry's analysis. He found that modelling the limited amplifier frequency response as a simple 40 dB per decade roll-off produces another pair of s-plane poles. These new poles are much further from the origin than the those described by Perry. They move almost vertically away from the negative real axis of the s-plane as offset voltage E_{qi} increases and, as shown in Figure 2.5(a), eventually become underdamped. Watmuff also found that, with limited amplifier frequency response, the optimum system stability is achieved with a balance inductance considerably larger than the bridge balance value of $L_w R_c/R_a$, and that satisfactory operation of sub-micron-diameter hot-wires requires an amplifier response which is flat up to frequencies in excess of 1 MHz.

2.2.5 The effects of filament length

Ligrani and Bradshaw (1987a,1987b) have studied the effect of hot-wire filament length on the measurement of turbulence levels and spectra in the boundary layer. From measurements at $y^+ = 17$ with a large number of different probes, they have shown that, for determination of broadband turbulence levels to an accuracy of 5% or better, the length-to-diameter ratio l/d of the hot wire should be greater than 150 to 200 and the non-dimensional length l^+ should be less than about 20. If the dimensions of a hot-wire filament violate the first criterion (i.e. if $l/d < 150 - 200$), the signal fluctuations are attenuated by the "heat sink" effect of heat conduction to the prongs[1]. Ligrani and Bradshaw also found that, for hot wires longer than 200 diameters and longer than about $20\nu/U_\tau$, the measured turbulence level

[1]The primary effect of heat conduction to the prongs is to produce a non-uniform temperature distribution along the hot-wire filament. As the air speed over the wire (i.e. the convective heat transfer coefficient) varies with time, the rate of heat generation in the wire and the rate of heat conduction to the prongs also varies, and so the temperature distribution in the filament changes. The time required for the change in temperature distribution to occur is governed by the rate at which heat becomes available for that purpose and the thermal capacity of the wire.

is a strongly decreasing function of l^+. This dependence of turbulence level upon l^+ arises because, if the length of the hot wire exceeds the size of small-scale turbulence events, it performs spatial "eddy" averaging of the small-scale motion. In experiments with probe of lengths $l^+ = 14$ and $l^+ = 33$, Johansson and Alfredsson (1983) concluded that spatial averaging also significantly affects skewness, flatness and probability density of the velocity fluctuations because the effect of spatial averaging on ejection events (negative velocity fluctuations) is much greater than on the larger sweep events (positive velocity fluctuations).

While a hot-wire filament length of $l^+ \approx 20$ is small enough for accurate measurement of r.m.s. turbulence level in the buffer and viscous sublayer regions of the turbulent boundary layer, it is too large to resolve dissipation-scale turbulence. By assuming local isotropy of dissipation-scale turbulence and using Pao's (1965) expression for the high wavenumber part of the spectrum, Wyngaard (1968) calculated the attenuation effect of spatial averaging on spectral measurements with hot wires and showed that measurements of dissipation-scale turbulence are significantly attenuated by hot wires longer than 2 or 3 Kolmogorov lengths (2–3η). Ligrani and Bradshaw (1987a) were able to verify Wyngaard's (1968) result for locations where the turbulence may be considered locally isotropic (e.g. $y^+ = 169$), but at $y^+ = 17$ where the small-scale motions are anisotropic and are more energetic, they found that attenuation by spatial averaging is more severe than predicted by Wyngaard. This inability to correct spectral data for spatial averaging in the buffer region and viscous sublayer of a turbulent boundary layer implies that the hot-wire filament should not be longer than about 3η if the dissipation scales are to be resolved.

Ligrani and Bradshaw's criteria for the measurement of the r.m.s. turbulence level can be satisfied by using a typical 1.3-mm-long, 5-μm-diameter hot wire at a free stream speed of about 5 m/s or less. Operation in this speed range requires special procedures for calibration of the hot-wire probes and for the measurement of dynamic pressure, but avoids the considerable difficulties associated with manufacturing and using subminiature hot-wire probes ($l < 0.5$ mm, $d < 2$ μm). The estimates of Kolmogorov microscales provided in Appendix A allow the $l/\eta \lesssim 3$ requirement for accurate spectral measurements at dissipation frequencies to be placed in the context of the more familiar "wall units" or viscous scaling. If we assume $\eta^+ \approx 1.7$ in or near the viscous sublayer it becomes clear that the criterion $l/\eta \lesssim 3$ cannot be satisfied unless the product of free-stream speed and hot-wire length is less than approximately 0.0017 m^2/s.

2.2.6 Hot-wire calibration

The inherent non-linearity, complexity and variability of hot-wire anemometer probes makes them quite difficult to calibrate for use over a wide speed range. Some of the many variables which in-

fluence calibration are C.T.A. settings (e.g. overheat ratio, offset voltage, balance inductance), room temperature, filament dimensions, material properties, annealing history and cleanliness. If a probe is to be used in the viscous sublayer, it should ideally be calibrated over a speed range which extends from the friction velocity U_τ to a little in excess of the free stream speed U_0. In practice, calibrating down to speeds of $2U_\tau$ to $3U_\tau$ has produced satisfactory results, but is not without risk as the non-linearity of hot-wire probes is likely to reduce the reliability of measurements requiring extrapolation beyond the calibrated speed range. Careful and frequent (at least daily) calibration is required while the probes are in use.

Hot-wire calibrations were performed in the test section of the wind tunnel (i.e. *in situ*), and so it was not necessary to switch off the C.T.A. or remove the probe from its traverse mechanism between calibration and boundary-layer measurements. Three different methods were used to measure the very wide range of air speeds required for calibration of hot wires. Each of these is discussed separately in Sections 2.2.6.1, 2.2.6.2 and 2.2.6.3. An indirect pitot-tube method was generally used for flow speeds between 10 m/s and 3 m/s. From approximately 3 m/s to 0.3 m/s, air speed was determined from the frequency of laminar vortex shedding from a cylinder. Wall-proximity effect was used to extend the range of calibration down to about 0.03 m/s. Details of the calibration formulae are explained in Section 2.2.6.4.

2.2.6.1 Measurement of dynamic pressure in the wind-tunnel test section

With the available instrumentation, it was not possible to measure the dynamic pressure of an air speed less than about 5 m/s with both sufficient rapidity and sufficient accuracy to perform a hot-wire calibration. Downstream of the wind-tunnel test section, the flow passes through a conical contraction (of area ratio 6.40) into a cylindrical pipe. The relationship between the centreline dynamic pressure in the cylindrical pipe and the free stream dynamic pressure in the wind-tunnel test section has been determined experimentally over the full operating speed range of the wind tunnel. This allows free stream speed at any port in the test section to be determined by a dynamic pressure measurement in the pipe, and avoids frequent, lengthy and error-prone measurement of extremely small dynamic pressures (down to about 1 Pa) in the test section. It allowed convenient and reliable measurement of free stream speeds down to about 2 m/s without the introduction of a pitot tube in the test section.

Dynamic pressures were measured with a pitot-static tube coupled initially to an MKS 10 Torr Baratron and later to a Microswitch (Honeywell) 170PC pressure transducer. Comparison with a 100 Torr Barocel over the pressure range 0–1.3 kPa revealed a 0.2% nonlinearity in the output from the Microswitch transducer. When a suitable cubic polynomial was applied to the digitised transducer output, the final nonlinearity error decreased by factor of about eight and became only slightly larger than the

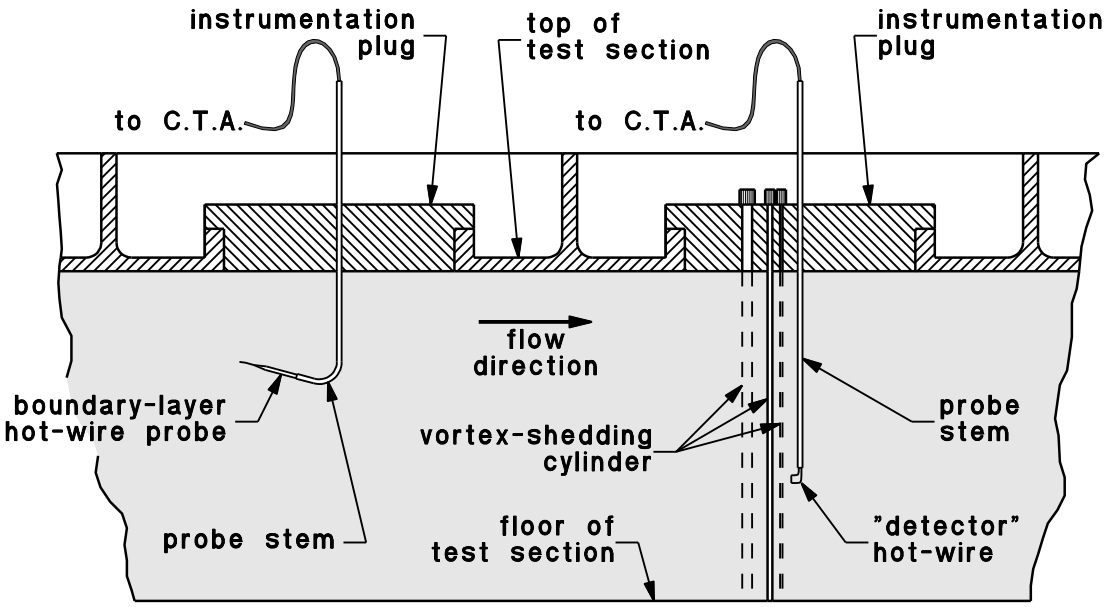

Figure 2.6: Use of a vortex shedding anemometer for hot-wire calibration

discretisation error of the available 12-bit analogue-to-digital converters.

2.2.6.2 Vortex-shedding anemometer

During the calibration of hot wires, air speeds between about 3 m/s and 0.3 m/s were determined from the frequency of laminar vortex shedding from a cylinder. For each air-speed measurement, a vortex-shedding cylinder with a diameter of 0.90 mm, 1.59 mm, 3.18 mm or 6.35 mm was inserted through an eccentric hole in the test-section plug immediately downstream of the boundary-layer probe (Figure 2.6). Vortex shedding was detected by placing a hot-wire probe in the wake approximately four diameters downstream from the cylinder. The hot-wire filament was parallel to the cylinder axis and its location within the width of the wake was adjusted by minutely rotating the instrumentation plug. It was also kept well clear of any wake from the boundary-layer probe. The vortex-shedding frequency was determined by spectral analysis of the signal from the "detector" probe in the cylinder wake. Signals from the detector probe and the boundary-layer probe were recorded simultaneously by a data acquisition system and the analysis was performed with custom-built calibration software. This practice was made necessary by initial experience which showed that the vortex-shedding signal from the detector probe often consisted of two or more nearly pure tones of comparable amplitude and was rarely simple harmonic.

The most often quoted relationship between Strouhal number of laminar vortex shedding, $St = f_S d/U_0$,

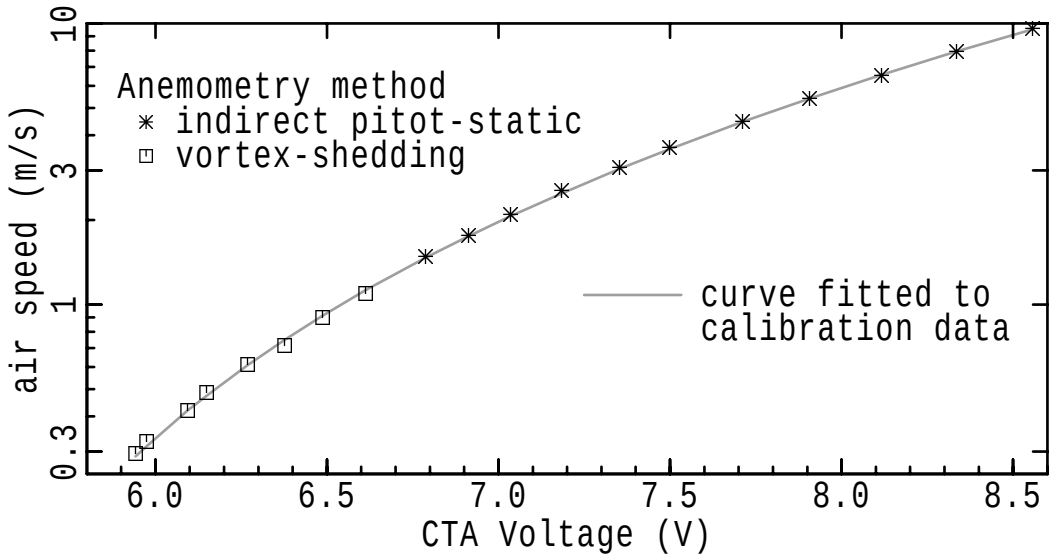

Figure 2.7: A hot-wire calibration determined from vortex-shedding anemometry and indirect pitot-tube anemometry

and the Reynolds number of the cylinder, $Re_d = U_0 d/\nu$, is that due to Roshko (1954):

$$St = 0.212\left(1 - \frac{21.2}{Re_d}\right) \tag{2.1}$$

for $50 < Re_d < 150$. However, Gerich and Eckelmann (1982) have concluded that the boundary conditions at the ends of a cylinder alter the mechanism of vortex shedding and, in a region near each end, produce a shedding frequency (f_e) up to 15% lower than given by Equation 2.1. Their experimental results show that, when the l/d ratio of a cylinder between end-plates is larger than about 30, the main features of the vortex-shedding spectrum are one peak at the boundary-affected frequency f_e and another peak at a frequency f_S which is more consistent with Equation 2.1. The relative amplitudes of the spectral peaks depend on spanwise distance from the "detector" hot-wire probe to the ends of the cylinder. In the boundary-affected regions near each end of the cylinder the highest spectral peak is at frequency f_e, but in the central region of the cylinder the dominant spectral peak is at f_S.

For the purpose of measuring air speed during a hot-wire calibration, it was therefore assumed that, if the main feature in the vortex shedding spectrum were a double peak, the lower frequency component of the signal was due to shedding from the boundary-affected region. The higher frequency component was assumed to come from the central region of the cylinder where the Strouhal number of vortex shedding agrees with Equation 2.1 and is unaffected by end-conditions. In order to be consistent with the findings of Gerich and Eckelmann (1982), Equation 2.1 was used to calculate air speed from the higher frequency in a double peak. As shown in Figure 2.7, calibration data obtained from this analysis of the vortex-shedding signal can be successfully combined with data from indirect pitot-tube

measurements (Section 2.2.6.1).

Experimental evidence, which has accumulated since Roshko's (1954) investigation, shows that laminar vortex shedding from a cylinder can contain a significant quantity of fine detail which is not taken into account by Equation 2.1. The fine detail includes features such as variations and discontinuities in the Strouhal-number/Reynolds-number relationship, oblique vortex shedding and the existence of discrete vortex cells along the length of the cylinder[Tritton, 1959, Gaster, 1971]. Williamson (1988,1989) found that the frequency of vortex shedding in the central region of the cylinder span is given by

$$\frac{St}{\cos\theta} = \frac{-3.3265}{Re_d} + 0.1816 + 0.00016Re_d \tag{2.2}$$

where θ is the angle of oblique shedding. This relationship, fitting the experimental data with an r.m.s. error of 0.06%, is universal in the sense that, for a specified Reynolds number, it correlates variations and spatial discontinuities in Strouhal number with changes in shedding angle (θ), and it is consistent with the step-changes which occur across the boundaries between vortex cells. The angle of oblique vortex shedding is related to the difference between the conditions which produce shedding instability at the ends of the cylinder and the conditions near the centre of the span. If these conditions are so dissimilar that oblique shedding cannot produce the compatibility necessary for spanwise-continuous vortices, vortex dislocations occur and discrete vortex cells are formed, each with a different frequency and a different oblique angle of shedding. Williamson (1989) has shown that the presence of different shedding frequencies (or discrete vortex cells) along the cylinder span depends on Reynolds number and on the flow conditions at the ends of the cylinder. König, Eisenlohr and Eckelmann (1990) have extended these findings to show that the shedding frequencies and the locations of the boundaries between vortex cells also depend on the length-to-diameter ratio of the cylinder. Their experimental examples demonstrate that, with various end conditions, three or four types of vortex cells, each with a different characteristic Strouhal number, can be formed simultaneously from different parts of the cylinder span.

In a trial hot-wire calibration, air-speed values estimated on the basis of the examples provided by König, Eisenlohr and Eckelmann (1990) were, at 2.5 m/s, about 2% larger than values determined from Roshko's formula. At the lower end of the useful air-speed range (i.e. 0.2 m/s to 1 m/s), the average increase was about 4%. This adjustment in the calibration data produced a corresponding change in the curve-fitted hot-wire calibration relation. The effects on the measurements of test-section boundary-layer characteristics were examined by reprocessing a small proportion (20%) of the experimental data from Section 7.5. In these tests, the various measurements of velocity and Reynolds number were increased by an average of 2.5%. The average changes in the measurements of boundary-layer thickness, displacement thickness, momentum thickness and skin-friction coefficient were between five and ten times smaller. Inspection of the corresponding standard deviations showed that these changes were not statistically significant. In this re-evaluation of the calibration data, the estimates of oblique vortex-

shedding angle were no better than first order approximations, and so the adjustments to the hot-wire calibrations should, in a strict sense, not be treated as corrections. They do, however, indicate that the errors introduced by vortex-shedding anemometry are small in comparison with the total experimental error, especially since most results contain or are presented as nondimensional velocity ratios.

Papangelou (1993) avoided the problem of unknown shedding angle by measuring the frequency of parallel vortex shedding from a cylinder between two end-spheres spaced 19 cylinder diameters apart. This development, which provides a reliable method of measuring very low air speeds, was published after the completion of the laboratory work described in this thesis.

2.2.6.3 Use of wall-proximity effect to extend the calibration range

In hot-wire anemometry, wall-proximity effect is observed as an error which is due to additional heat transfer from the hot wire to a nearby surface. The measured air speed (U_m) is larger than the actual air speed (U) by an amount which depends on distance (y) between the hot wire and the wall. Janke (1987) has shown that wall-proximity effect can be used to extend the calibration of hot wires down to air speeds much lower than those which were measured by the vortex-shedding anemometer. This method of extending the hot-wire calibration range arises from the observation that the apparent Reynolds number $U_m y/\nu$ approaches a constant value of about 4 as the actual Reynolds number Uy/ν approaches zero. Janke (1987) therefore concluded that, in still air ($U = 0$), the uncorrected velocity signal (U_m) produced by wall-proximity effect is inversely proportional to distance from the wall.

The additional data required for extending the calibrated speed range were obtained by reducing the flow speed to zero and then recording the C.T.A. output voltage (E_i) as a function of distance from the wall (y_i). Useful wall-proximity data were obtained with the hot wire at distances between 0.02 mm and 1 mm from the wall. Air speeds measured by the vortex-shedding technique were then plotted as a function of C.T.A. output voltage, and the wall-proximity data coordinates ($E_i, 1/y_i$) were plotted on the same axes as if the reciprocal of distance from the wall ($1/y_i$) were equivalent to air speed; i.e., as if

$$U_m = \frac{k_0}{y}, \tag{2.3}$$

where the constant of proportionality was initially $k_0 = 1$. The value of k_0 was then adjusted until the wall-proximity data coincided with the vortex-shedding data in the region where the C.T.A. output voltages from each set of data overlapped. This process is illustrated in Figure 2.8. The final step is to fit a single calibration curve to the vortex-shedding and wall-proximity data.

The wall-proximity relation (Equation 2.3) can be used to extend the range of a hot-wire calibration down to about 0.03 m/s. At air speeds lower than 0.03 m/s, free-convective heat transfer from the hot wire was responsible for large and unacceptable curve-fitting errors. This lower limit is consistent with

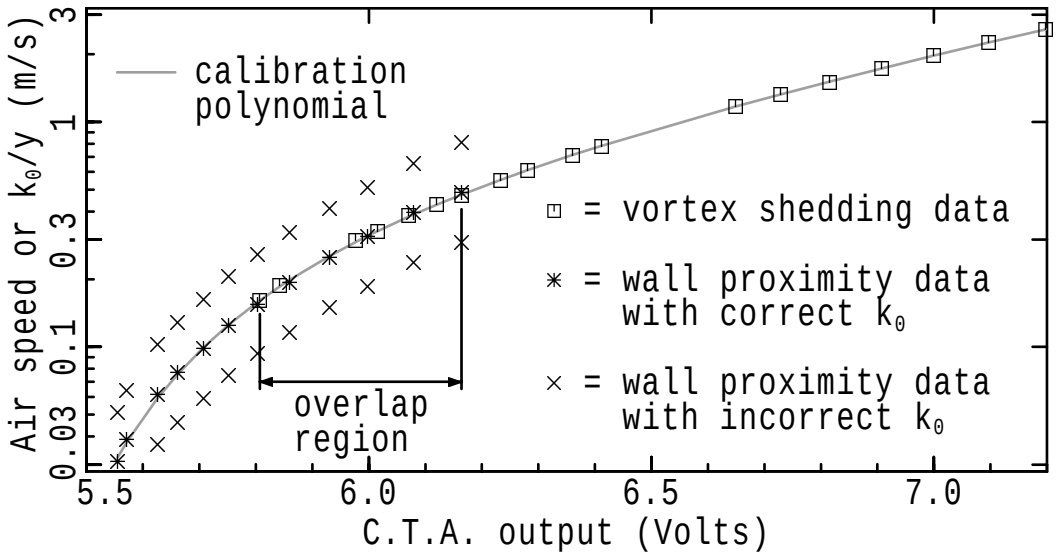

Figure 2.8: A hot-wire calibration determined from the frequency of vortex shedding and from wall-proximity effect

the criterion, $Re_d > Gr_d^{1/3}$ [Collis and Williams, 1959, Hollasch and Gebhart, 1972], for avoiding the effects of buoyant convection.

2.2.6.4 Calibration formulae

Calibration between the free stream speed and 0.2–0.3 m/s did not make use of the proximity relation (Equation 2.3) identified by Janke (1987). In these cases, a relation of the form

$$E^2 = a + bU^n + cU^{2n}, \tag{2.4}$$

which is similar to that used by Siddall and Davies (1972), was fitted to the calibration data. This formula has more flexibility than the King's law formula [King, 1914], and so can be used over a wider range of air speeds. The exponent n can be selected to minimize the sum of the squared fitting error. That is, for m calibration data coordinates $\{(U_i, E_i) : 1 \leq i \leq m\}$, the objective function for the optimization is

$$e(n) = \sum_{i=1}^{m} (E_i'^2 - E_i)^2, \tag{2.5}$$

where $E_i'^2 = a + bU_i^n + cU_i^{2n}$. For a typical set of calibration data, the function $e(n)$ is very "flat" in the region of its minimum and its value varies by only about 25% in the range $0.4 < n < 0.55$ usually adopted for a King's law calibration.

When Equation 2.3 is used for extending the hot-wire calibration down to speeds near the buoyant-

convection regime, the Siddall-Davies relation (Equation 2.4) can no longer be adjusted to fit the calibration data in a satisfactory manner. In such cases, satisfactory results can be achieved by expressing air speed as a polynomial of C.T.A. output voltage,

$$U = P(E - E_o), \tag{2.6}$$

where $P()$ is a fourth or fifth order polynomial selected to minimize the sum of squared fitting errors and E_o is an offset constant. For a typical C.T.A. output in the range of 5.5 to 7.0 volts, an offset constant of $E_o = 5$ ensures that the polynomial is calculated only for small values of $(E - E_o)$. If the value of E_o is inappropriate, (for example, if $E_o = 0$,) round-off errors can produce a significant loss of precision because successive terms in the polynomial may have alternating signs and may be much larger than the air speed value itself. The polynomial P is determined by a method which calculates a set of successively higher order orthogonal polynomials from the calibration data [Liu et al., 1983], and so avoids inverting a potentially ill-conditioned Vandermonde matrix [The Mathworks, Inc., 1995, Kreyszig, 1972, Chapter 18.11]. In this curve-fitting process, each calibration coordinate (E_i, U_i) is assigned a weight or bias-factor of $1/U_i$ in order to produce a curve-fitting error which is approximately proportional to the air speed.

2.2.6.5 Conversion of unsteady hot-wire signals into velocity

It has been a traditional practice to separate the signal from the C.T.A. into mean and fluctuating components and then multiply the fluctuating voltage by the probe sensitivity at the mean output voltage to obtain a fluctuating velocity signal. Perry (1982) reported that this technique produces an error of 5% in the measurement of a sinusoidal velocity fluctuation with an r.m.s. intensity of 40%. When expressed in terms of the local mean velocity, the maximum r.m.s. level of turbulence in a boundary layer is also about 40%, and so one might expect a similar effect upon the measurement of boundary-layer turbulence statistics. In Figure 2.9 turbulence statistics produced by this linearisation technique are compared with those produced by applying the hot-wire calibration directly to each individual data sample. These measurements were made in the viscous sublayer of a turbulent boundary layer and were *not* corrected for wall-proximity effect. The error in the measurement of turbulence level shown in Figure 2.9(b) agrees substantially with Perry's (1982) result. Figure 2.9(a) shows that there is a similar error in measuring the mean velocity. Figures 2.9(c) and (d) reveal that the effect on the measurement of skewness and flatness factors in the viscous sublayer is quite large. This is to be expected because these higher order statistical moments depend very heavily upon extreme signal values which are not correctly linearised. In order to avoid such errors, all data from calibrated hot-wires are first converted to velocity before subjecting them to any other processing.

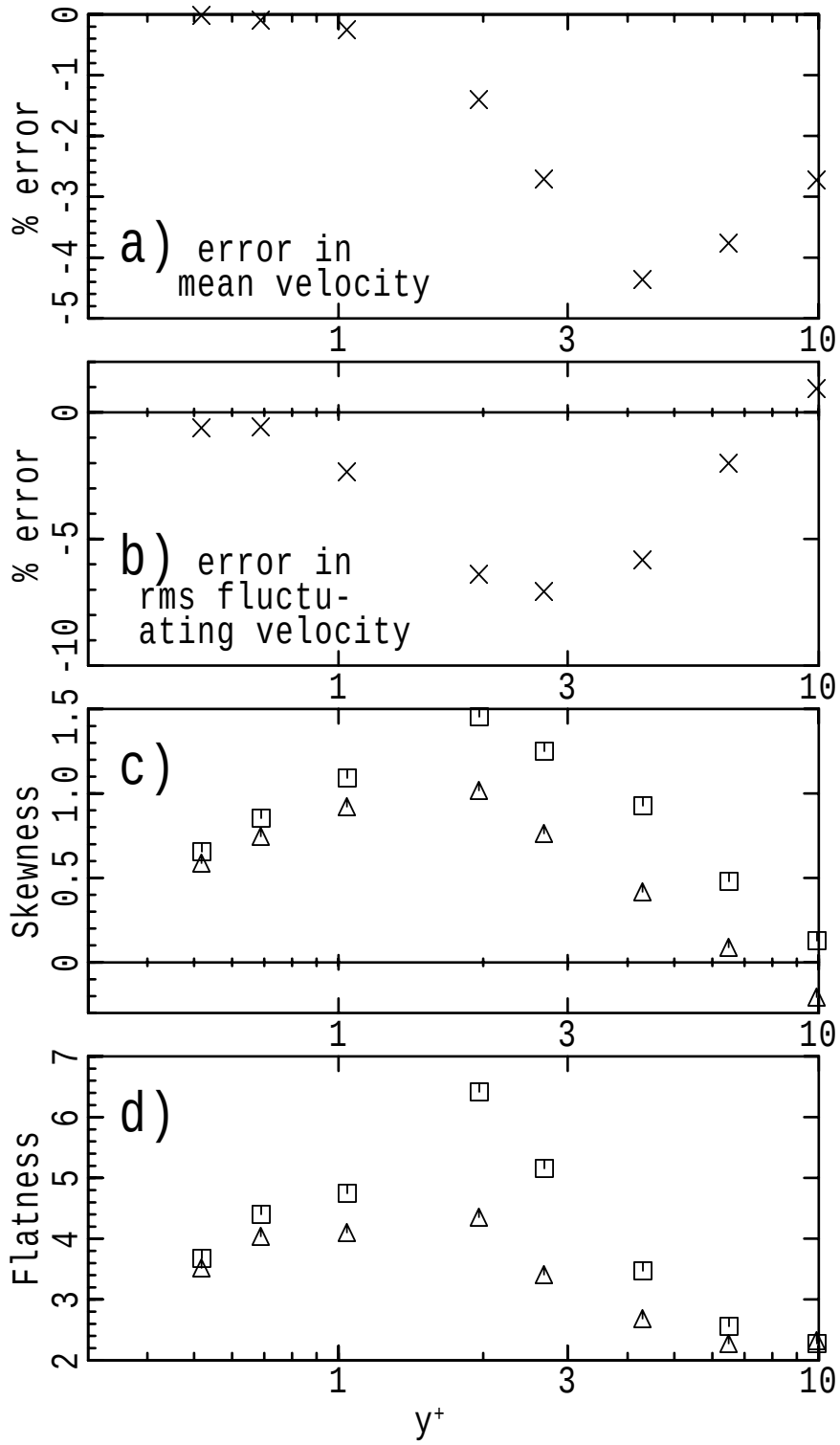

Figure 2.9: Effect of linearisation technique upon measurement of turbulence statistics in the viscous sublayer; □, linearisation of each data sample using the full hot-wire calibration; △, separation of C.T.A. output voltage into mean and fluctuating components followed by conversion into fluctuating velocity with the calibration slope; ×, percentage difference between the two methods. N.B. Error is dominated by wall-proximity effect for $y^+ < 2$.

2.2.7 Probe-traverse mechanism

The traverse described by Lim (1971) was used for experiments in which a single hot-wire probe was held stationary or needed only to be moved in the vertical direction. This traverse (Figure 2.10) was mounted on an instrumentation plug which could be placed in any of the ports along the top of the wind-tunnel test section. The traverse carriage was driven over a maximum displacement of 90 mm by a 3-Watt reversible synchronous motor and a lead screw.

In experiments which measured characteristics of the test-section boundary layers, the traverse was under direct control of the data acquisition system which recorded the hot-wire signals. The data acquisition system determined the location of the hot-wire probe by reading the output of a linear potentiometer connected to the traverse carriage. The potentiometer was calibrated with the aid of limit switches at the extremes of the traverse motion. The accuracy with which the probe could be positioned in this way was limited by electronic drift and by the resolution of the 12-bit analogue-to-digital converter which was used to sample the potentiometer output. The loss of resolution by the analogue-to-digital converter was equivalent to a error of ± 0.025 mm. Electronic drift was capable of causing an additional error of up to about ± 0.025 mm. If necessary, feedback from a dial indicator mounted on the traverse made it possible to adjust the position of the carriage manually with a precision no worse than ± 0.005 mm.

A datum for the distance between the wall and hot-wire filament of a probe installed in the traverse was established by measuring the distance between the hot-wire and its reflection in the wall with a travelling microscope. The distance between the hot-wire and the wall could then be measured to an accuracy of better than 0.005 mm with the dial indicator.

A multidirectional traverse mechanism was also built for investigations which required three-dimen-sion-al adjustments to the position of a hot-wire probe, or required calibration of two-wire or three-wire probes. This traverse, which was not required for work presented in this thesis, is described briefly in Appendix D.

2.3 Data acquisition system

Virtually any anemometric study of turbulence phenomena requires a means of gathering, storing and analysing large amounts of data. For example, in boundary-layer experiments at air speeds near 10 m/s, it may be necessary to obtain continuous data records with lengths in the order of one million samples, at sampling rates in the order of 100 kHz. The experimental data for this thesis were recorded and stored by a data acquisition system which was designed and constructed by technical staff of the

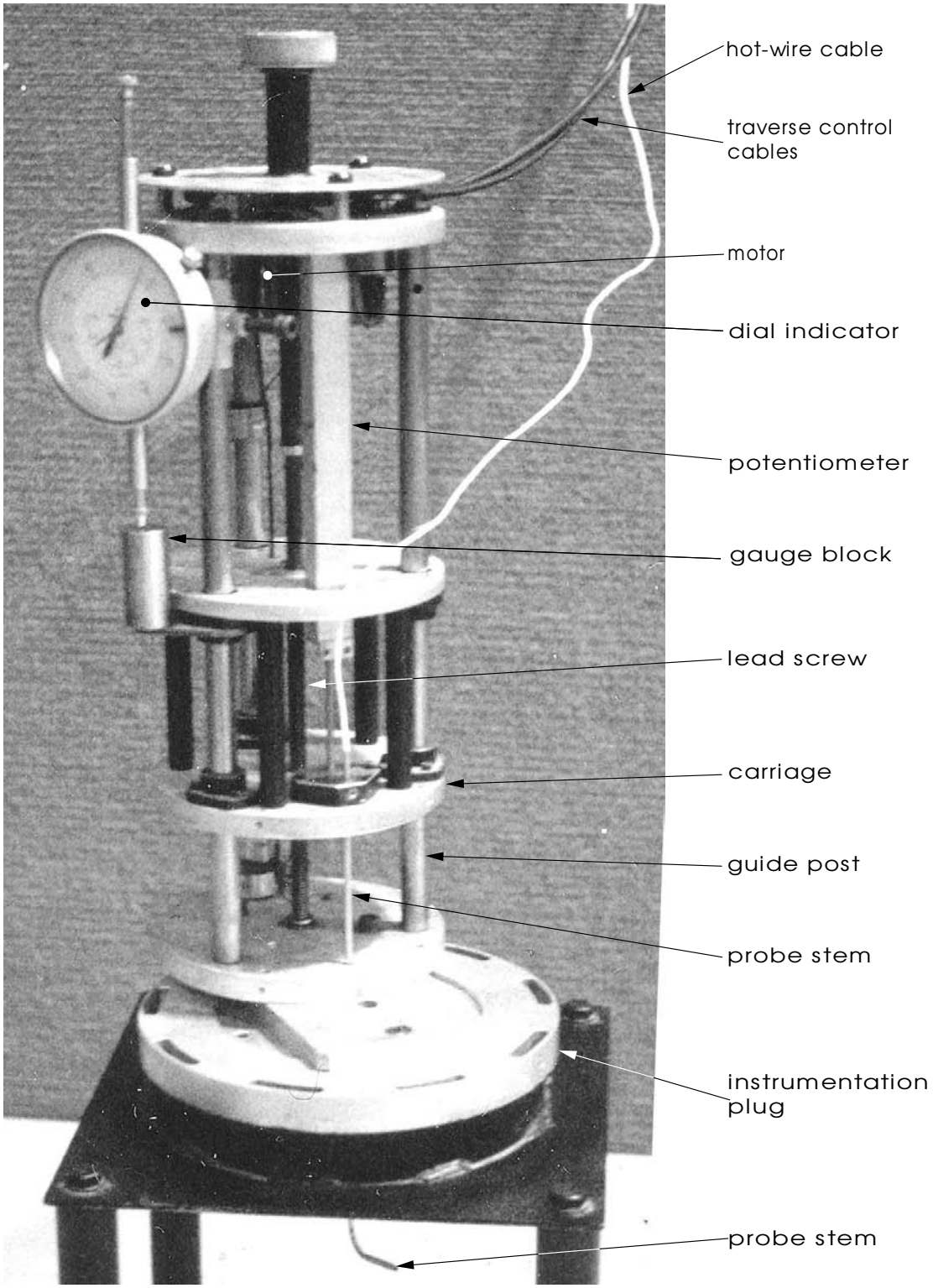

Figure 2.10: Probe-traverse mechanism

Department of Mechanical Engineering. The system was designed specifically for turbulence experiments. At the time of construction (mid 1980s) such systems were not commercially available for an affordable price.

At the centre of the data acquisition system was an SBC100M microcomputer which controlled two analogue-to-digital (A/D) converters and 2 megabytes of external RAM which was used for temporary data storage. An MS-DOS personal computer with an Intel 8088 processor was used for control of the SBC100M. The SBC100M was based on an 8-bit Zilog Z80A microprocessor with 64 kilobytes of RAM and an S100 bus. In addition to providing real-time, low-level control of the A/D converters and external RAM, it also drove probe-traverse mechanisms and transmitted data to the personal computer.

The data acquisition system was equipped with a 4-microsecond 16-channel A/D converter, which was used for sampling the rapidly fluctuating signals from hot-wire probes. The other much slower A/D converter was used for sampling signals from electronic manometers and the probe-traverse potentiometers. Instrumentation amplifiers were used to ensure that the signal voltages from hot-wire probes and other sensors were well matched with the input voltage range of the A/D converters. Between -10 volts and +10 volts of offset was available at the input of each amplifier and gain could be varied continuously from 1 to 125. Low-pass anti-aliasing filters were not used because, in the rare cases where spectral analysis was required, the sampling rate of the A/D converter always exceeded twice the maximum signal frequency.

Further details of the data acquisition system may be found in Appendix E.

2.4 Data processing

Experimental data recorded by the data acquisition system were processed on VAX computers running under the VMS operating system and on Sun Microsystems SPARC workstations. The software required for analysis and presentation of the data was written in Fortran. A brief introduction to this software is available in Appendix F. The source code and documentation is supplied on the diskettes which are included with this volume.

2.5 Notation

a,b,c	polynomial coefficients for Kings's law or Siddall & Davies hot wire calibration relation
d	diameter of a hot-wire filament or cylinder

E	C.T.A. output voltage
E_i'	$= a + bU_i^n + cU_i^{2n}$, C.T.A. output calculated using the hot-wire calibration at air speed U_i.
E_o	offset constant for the hot-wire calibration polynomial $P(E - E_o)$
E_{qi}	offset voltage at the input of the amplifier in a C.T.A.
$e(n)$	$\sum_{i=1}^{m}(E_i'^2 - E_i)^2$, objective function for optimizing a hot wire calibration relation
f_S	frequency of vortex shedding from the central region of a cylinder
f_e	frequency of vortex shedding from the end-affected region of a cylinder
Gr_d	$\frac{g\Delta T d^3}{T\nu^2}$, Grashof number of a horizontal cylinder in air, where g is gravitational acceleration and ΔT is temperature of the cylinder surface relative to the absolute ambient air temperature T
K	voltage gain of the amplifier in the C.T.A.
k_0	constant of proportionality for Janke's (1987) wall-proximity relation (Equation 2.3)
L_b	C.T.A. balance inductance in series with the overheat resistor
L_w	inductance of a hot wire probe and its cable
l	length of a hot-wire filament
m	number of hot-wire calibration coordinates
n	exponent of velocity for Siddall & Davies (1972) hot-wire calibration relation
$P(E - E_o)$	hot-wire calibration polynomial
R_b	overheat (or balance) resistor in the C.T.A. bridge
R_c, R_a	fixed values for resistors in the "top legs" of the C.T.A. bridge
R_w	cold resistance of the hot-wire filament
Re_d	$U_0 d/\nu$, Reynolds number of a hot-wire filament or Reynolds number of a cylinder normal to an air stream
St	$f_S d/U_0$, Strouhal number of vortex shedding from a cylinder
U	air speed
U_0	free stream air speed
U_m	measured mean air speed — *not* corrected for wall-proximity effect
U_τ	$\sqrt{\tau_w/\rho}$, friction velocity of the boundary layer
y	distance between the hot-wire filament and the wall
β	open area ratio of a wire-mesh screen
Δt	duration of C.T.A. output pulse during a square-wave test
Δz	typical spanwise dimension of small-scale turbulence features
θ	angle of laminar vortex shedding from a cylinder
η	Kolmogorov length scale
ν	kinematic viscosity (of air)

ρ	air density
τ_w	wall shear stress

Superscripts

Variables which have a superscript $^+$ are nondimensionalised using the viscous flow variables U_τ and ν, e.g. $U^+ = U/U_\tau$ and $y^+ = yU_\tau/\nu$.

Subscripts

Subscript *i* indicates a measured value of C.T.A. output voltage (E_i), air speed (U_i) or distance from the wall (y_i), which is used for calibration of a hot-wire probe.

Chapter 3

Initial examination of the boundary layer

3.1 Required characteristics of the test-section boundary layer

The purpose of this project was to establish a canonical flat-plate turbulent boundary layer with free-stream air speed in the range 1 m/s to 4 m/s. As part of this process it was necessary to verify that the boundary layer was genuinely turbulent and the turbulence mechanisms were due entirely to the presence of the wall. Bradshaw and Wong (1972) have shown that other kinds of turbulence, such as turbulence from mixing layers, can contaminate the boundary layer significantly, with the effects persisting for extremely long downstream distances. Extraneous turbulence must therefore not be generated from, for example, a distant upstream tripping device. Also, the free-stream flow must not contain long-term unsteadiness, swirl or excessive turbulence [Coles, 1962]. It will be shown in later chapters that non-turbulent free-stream unsteadiness can make it impossible to measure the characteristics of the boundary layer reliably. The streamwise pressure gradient imposed by the free stream should not be large enough to have a significant effect on the growth of the boundary layer. The turbulent boundary layer must also be two-dimensional in the sense that the behaviour of the turbulence is not affected by secondary flows. Two-dimensionality is usually achieved by making the width of the test surface much greater than the thickness of the boundary layer. Finally, the ideal fully-developed experimental boundary layer should satisfy the similarity defect law (Equation 1.3) in its outer region and so be an equilibrium layer[Clauser, 1954]. In practice this requires a Reynolds number based on momentum thickness (Re_θ) of more than about 6000, a value which is not easily attained at flow speeds less than about 10 m/s.

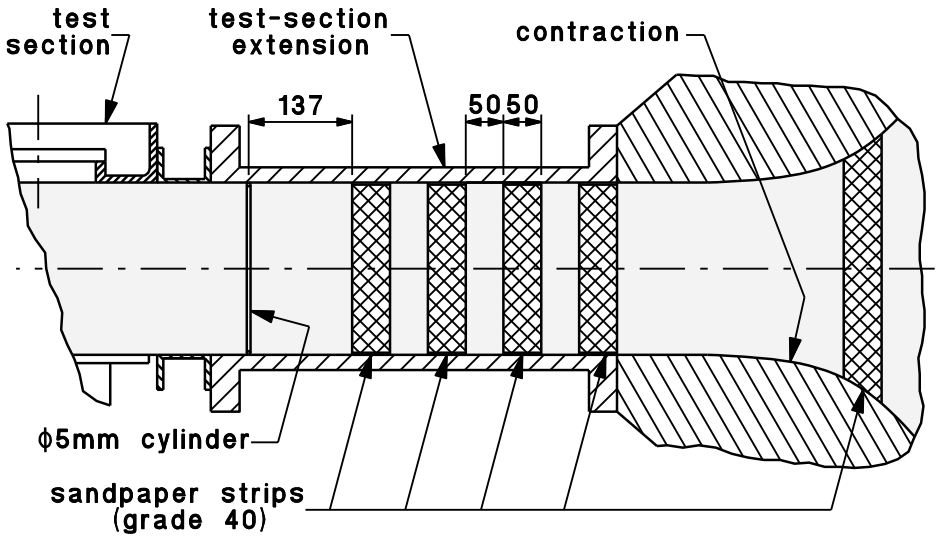

Figure 3.1: Boundary-layer trips in the test-section extension. Scale 1:10.

3.2 Preliminary examination of the test-section flow

3.2.1 Boundary-layer trip

Coles (1962) has established that it is desirable to allow natural transition from a laminar to a turbulent boundary layer, because momentum equilibrium of a tripped boundary layer can easily be destroyed by long-lived eddies which are generated by a trip and then convected downstream as a thickened wake region. Thomas (1977) found that even at 20 m/s in a 130 mm $\times$ 228 mm test section, it was not possible to obtain a steady transition without the use of a boundary-layer trip. He placed a 50-mm-wide strip of 40-grade sandpaper 310 mm upstream of the contraction exit in order to prevent a wandering separation in the contraction, and another sandpaper strip at the start of the test section to generate the transition.

At lower speeds it was correspondingly more difficult to produce boundary-layer transition. With only the sandpaper strips used by Thomas, a turbulent boundary layer was not obtained for free-stream speeds less than about than 3 m/s in the test section. Consequently, a 500-mm-long extension was added to the upstream end of the test section in order to provide a greater development length for the boundary layer, and to accommodate tripping devices. As shown in Figure 3.1, sandpaper strips were placed around the perimeter of the extension to thicken the low-speed laminar boundary layer, and a 5-mm-diameter cylindrical trip was placed 50 mm from its downstream end. This combination of tripping devices generated transition for free stream speeds down to 1.4 m/s. Cylindrical trips of much larger diameter (e.g. 10 mm) produced a turbulent wake extending well beyond the edge of the

boundary layer and into the free-stream flow. Except in the final set of boundary-layer measurements, which is described in Chapter 7, the size of the trip was not varied as flow speed changed.

3.2.2 Static pressure distribution

For the initial boundary-layer measurements, the flexible stainless-steel floor of the test section was adjusted to give a zero streamwise pressure gradient at a flow speed of about 6 m/s. Extreme care was required when adjusting the position of the test-section floor because it was necessary to resolve static pressure changes which were sometimes more than 100 times smaller than the dynamic pressure of the test-section flow. In order to achieve the required divergence of the test section duct, it was necessary to have an initial contraction of about 20% in the first one metre of the duct length.

3.2.2.1 A criterion for negligible pressure gradient

As part of establishing a canonical boundary layer in the test section, it was necessary to check that the static pressure had a negligible effect on the growth of the boundary layer. The effect of streamwise pressure gradient on the growth of a boundary layer can be described in terms of the differential form of the momentum integral equation [Duncan et al., 1970, p 256]:

$$\frac{d\theta}{dx} + \frac{\theta}{U_0}\frac{dU_0}{dx}(H+2) = \left(\frac{U_\tau}{U_0}\right)^2 \tag{3.1}$$

where θ is the momentum thickness of the boundary layer, U_0 is the free stream speed and H is the ratio of displacement and momentum thicknesses. If Bernoulli's equation along a streamline,

$$-U_0\frac{dU_0}{dx} = \frac{1}{\rho}\frac{dP_0}{dx}, \tag{3.2}$$

is used to convert the free-stream velocity gradient into a pressure gradient, Equation 3.1 becomes

$$\left(\frac{U_0}{U_\tau}\right)^2\left[\frac{d\theta}{dx} - (H+2)\frac{\theta}{2q_0}\frac{dP_0}{dx}\right] = 1, \tag{3.3}$$

where P_0 is static pressure in the free stream, ρ is air density and $q_0 = \frac{1}{2}\rho U_0^2$ is the free-stream dynamic pressure. The significance of the pressure gradient in the process of boundary-layer growth can then be expressed as the non-dimensional term

$$\alpha = (\frac{1}{2}H+1)\left(\frac{U_0}{U_\tau}\right)^2\frac{\theta}{q_0}\frac{dP_0}{dx}; \tag{3.4}$$

so that

$$\left(\frac{U_0}{U_\tau}\right)^2\frac{d\theta}{dx} = 1+\alpha. \tag{3.5}$$

This indicates that the effect of pressure gradient upon the growth rate of the boundary layer is insignificant if $|\alpha| \ll 1$.

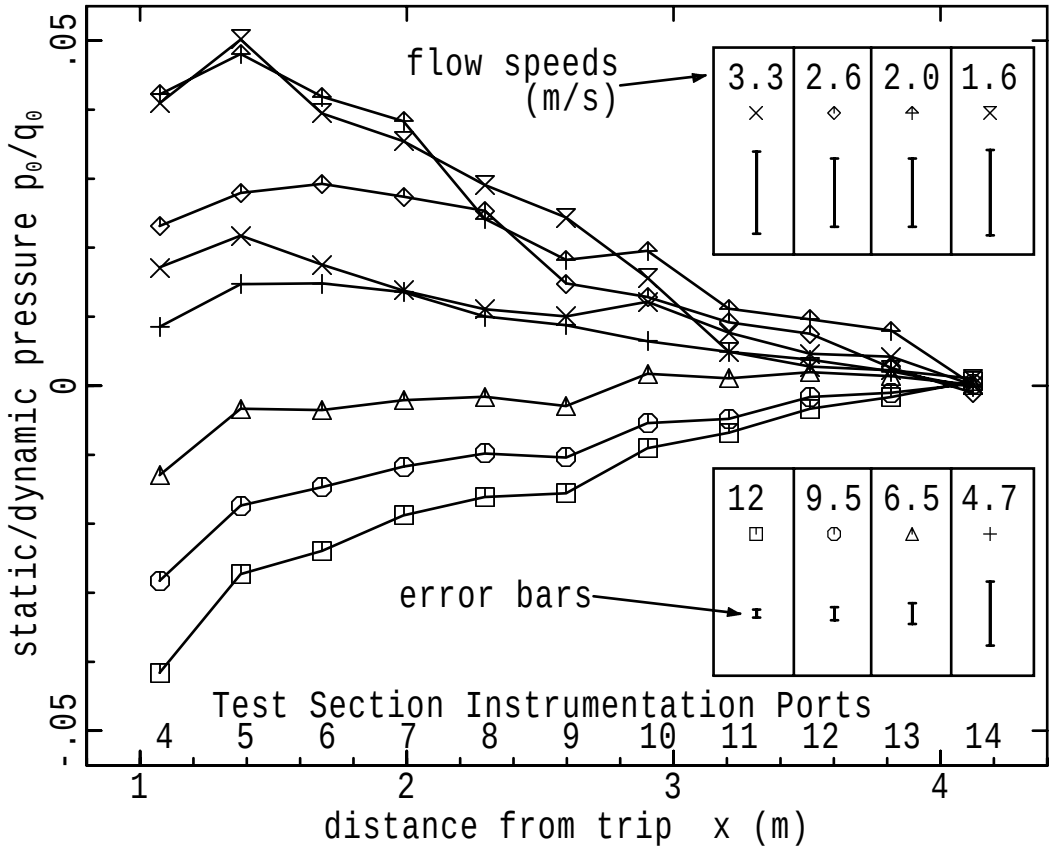

Figure 3.2: Static pressure distribution along the test section for flow speeds ranging from 1.6 m/s to 12 m/s. The plotting symbol and error bar for each flow speed are shown in the legends.

3.2.2.2 Measurements of streamwise pressure distribution

After the flexible lower surface of the test section was adjusted to minimise the pressure gradient at $U_0 \approx 6$ m/s, the distribution of static wall-pressure along the length of the test section was measured at eight free-stream speeds ranging from 1.6 m/s to 12 m/s. The results plotted in Figure 3.2 have been normalized with the free stream dynamic pressure, and the measurement at test-section Port 14 was used as a convenient reference datum. The graph shows that, at the highest speeds, the pressure gradient was unfavourable (i.e. positive). As speed was reduced, the pressure gradient decreased, passed through zero at $U_0 \approx 6$ m/s, and then became negative at lower speeds. This change in pressure gradient was due to a speed-dependent variation in the growth rate of boundary-layer displacement thickness. The apparent increase in erratic pressure variations and the larger error bars at the lower speeds are due to the experimental difficulties in measuring extremely small pressures of less than 0.1 Pa. Acceptable results were obtained only by extensive amplification, low-pass filtering and ensemble averaging of the electronic manometer output. It was also necessary to monitor instrumentation drift continually and to

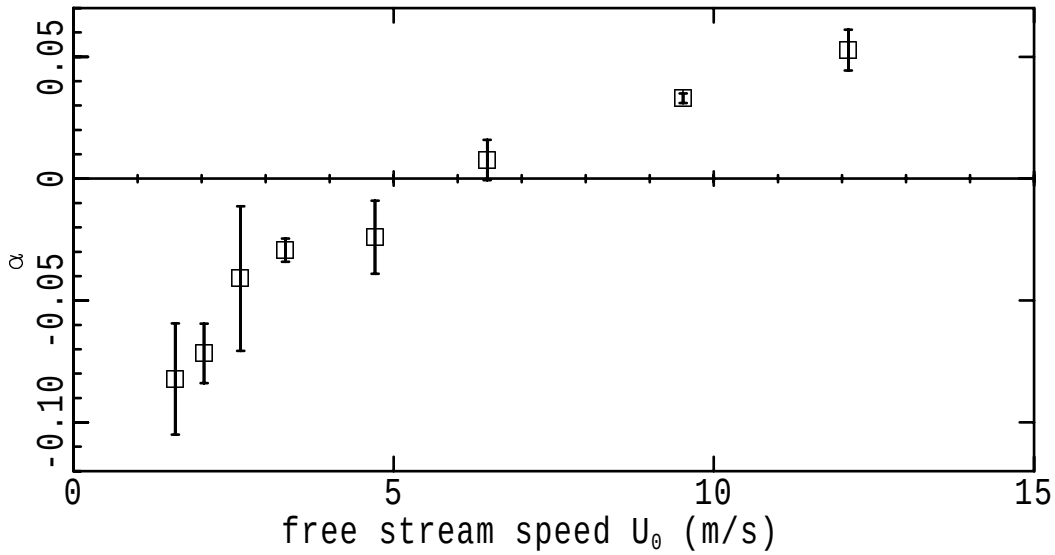

Figure 3.3: Pressure gradient growth parameter (α) as a function of flow speed. Error bars indicate variation in α along the test section from Port 5 to Port 14.

compensate for this drift in the processing of the results. The overall resolution of these measurements is believed to be about 0.05 Pa.

The experimental error in the measurement of the static pressure makes it very difficult to estimate the pressure gradient at each port in the test section with acceptable accuracy. However, at each free-stream air speed, it is possible to estimate the mean value of the pressure gradient growth parameter α over the useful length of the test section. These values (Figure 3.3), which range from about 0.05 at a flow speed of 12 m/s to about -0.09 at 1.6 m/s, are small enough to establish that the effects of streamwise pressure gradient on the growth of the boundary layer are very small over a region in the test section extending from instrumentation Port 5 to Port 14.

3.2.3 Secondary flow

In experimental studies, contamination of the flat-plate boundary layer by side-wall boundary layers is usually avoided by restricting the location of measurements to a region where boundary-layer thickness is at least an order of magnitude smaller than plate width. In this case the duct cross-section was almost square and this criterion would have confined measurements to the upstream 30% of the test-section length. In an effort to justify use of the downstream end of the test section, where the turbulent boundary layer was thicker and more fully developed, it was necessary to examine the effects of cross-section two-dimensionality a little more closely.

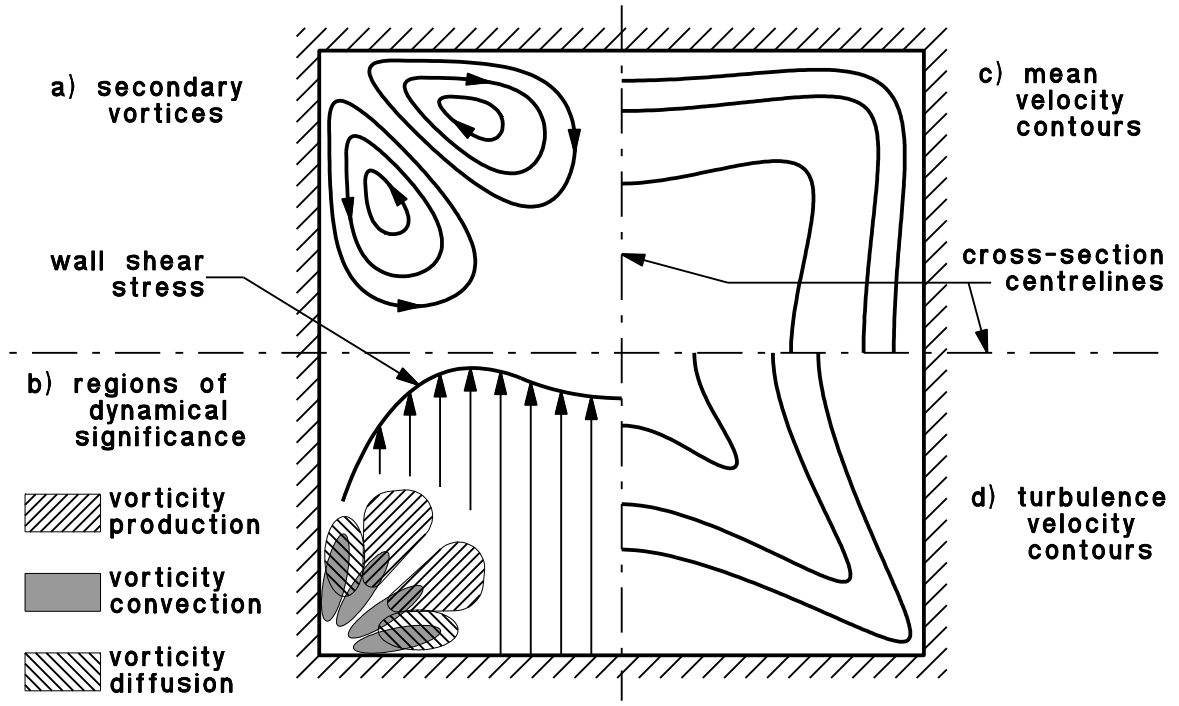

Figure 3.4: Schematic diagram of secondary flow in a straight square cross-section duct with fully developed turbulent primary flow; (a) secondary vortices; (b) regions of dynamical significance; (c) mean velocity contours; (d) turbulence velocity contours [Schlichting, 1968, Leutheusser, 1963, Brundrett and Baines, 1964, Melling and Whitelaw, 1976].

Turbulent flow in straight ducts with a non-circular cross-section has non-zero time-averaged velocity components within the cross-section planes normal to the free stream. The presence of this secondary flow implies streamwise vorticity. In 1930 Nikuradse demonstrated that secondary flow in a straight rectangular duct takes the form of counter-rotating streamwise vortex pairs near each corner (Figure 3.4(a)) [Schlichting, 1968]. Detailed examination of the time-averaged vorticity transport equations[1] [Bradshaw, 1987] shows that there are two mechanisms for generating mean streamwise vorticity. The first is an inviscid "skew-induced" rotation of existing mean vorticity by the mean velocity gradient and it can be found in both laminar and turbulent flows. In non-circular ducts the Reynolds stresses produced by the turbulence of the main flow give rise to a second "stress-induced" mechanism for producing secondary flow.

Compared with the main flow, the mean secondary flow velocities are quite small. In an investiga-

[1]Time-averaged vorticity transport equations:

$$U_j \frac{\partial \Omega_i}{\partial x_j} + \frac{\partial}{\partial x_j}\left(\overline{u_j \omega_i}\right) = \Omega_j S_{ij} + \overline{\omega_j s_{ij}} + \nu \frac{\partial^2 \Omega_i}{\partial x_j^2}$$

tion of fully developed turbulent flow in a rectangular duct, Brundrett and Baines (1964) used "X" hot-wire probes to measure a maximum mean secondary-flow speed of about 1.4% of the centreline speed. The turbulence kinetic energy contours in a cross-section are much more distorted by the secondary flow than the mean velocity contours. The contour maps of mean streamwise vorticity, vorticity convection, vorticity production and vorticity diffusion [Brundrett and Baines, 1964] show that these quantities, which represent dynamics of the secondary flow, are most significant in the corner 25% of the cross-section area and are negligible at or near the cross-section centrelines (Figure 3.4(b)). In an examination of fully developed laminar and turbulent flow in ducts with rectangular cross-sections, Leutheusser (1963) found that mean velocity profiles on the cross-section centrelines obey the same logarithmic "law of the wall" as do two-dimensional duct flows. He calculated friction velocity by averaging wall shear stress over the perimeter of the duct cross section, and obtained coefficients A and B [Leutheusser, 1963] in $U^+ = A\ln y^+ + B$ which were within the range of commonly accepted values[2]. Direct numerical simulation (DNS) at a duct Reynolds number of 4410 [Gavrilakis, 1992] also produced a logarithmic "law of the wall", but with coefficients $A = 3.2$ and $B = 3.9$ which are quite different from the usual two-dimensional channel-flow and boundary-layer values. In this case, the friction velocity was determined from assuming $U^+ = y^+$ in the viscous sublayer.

The measurements of Brundrett and Baines (1964) suggest that, on the cross-section centrelines, the boundary-layer dynamics are dominated by the wall-turbulence mechanism and that the dynamics of the "Reynolds-stress-induced" secondary flow are of significance only near the corners of the duct. This hypothesis is supported by the existence of a logarithmic region along the cross-section centrelines [Gavrilakis, 1992, Leutheusser, 1963] and by the agreement of turbulence statistics along the cross-section centrelines with channel-flow data [Gavrilakis, 1992]. The secondary flow in these regions consists of a very slow mean-flow convection away from the walls ($V > 0$) which is mainly due to the requirements of continuity and takes no significant part in the secondary-flow dynamics. It is therefore expected that the main effects of secondary flow on the centreline boundary-layers would be to change the coefficients A and B of the logarithmic mean velocity distribution.

For all of the experimental investigations cited in the previous two paragraphs [Leutheusser, 1963, Brundrett and Baines, 1964, Gavrilakis, 1992], measurements were made in a flow where the whole flow field was turbulent and the flow was sustained by a negative streamwise pressure gradient rather than by momentum loss through boundary-layer growth. Such conditions, i.e. fully developed duct flow, usually only exist further than about 40 hydraulic diameters[3] downstream from the duct inlet. In the present work, the 15 instrumentation ports of the wind-tunnel test section are between 0.6 and 19.2 hydraulic diameters downstream of the test-section inlet, and so secondary-flow effects are likely to be less severe than in a fully-developed duct flow. Melling and Whitelaw (1976) have measured

[2] $A = 2.46$ and $B = 5.51$

[3] hydraulic diameter $= 4 \times$ (cross-section area)/(cross-section perimeter)

the mean velocity and most Reynolds stress components over cross-sections of turbulent flow in a square duct at locations ranging from $x/D_H = 5.6$ to $x/D_H = 36.8$[4]. Although turbulence extends over the whole duct cross-section at $x/D_H \approx 22$, streamwise variation of the centreline turbulence intensity indicates that the flow is not quite fully developed even at $x/D_H = 36.8$. Melling and Whitelaw found that at $x/D_H = 5.6$, which is equivalent to $x/L = 0.3$ in the wind-tunnel test section[5], distortion of the streamwise turbulence-velocity contours is confined to the corner region of a relatively thin turbulent boundary layer. At $x/D_H = 20.7$, which is a position equivalent to just beyond the downstream end of the test section, this distortion is very strong but is confined to a narrow region around the diagonals where mean velocity contours were highly curved. At $x/D_H = 29.0$ the distortion is spread over the entire cross section, and the mean secondary flow near the cross-section centrelines pushes the mean velocity contours further away from the wall (Figure 3.4(c,d)).

Experimental evidence of stress-induced secondary flow may be obtained by measuring the lateral distribution of mean wall shear stress. Leutheusser (1963) measured a local minimum at the centre of the wall and a local maximum about half way between the centre and each corner (Figure 3.4(b)). He measured wall-shear-stress variations of about 8% in the central region between the local maxima. In the present work, the wall shear stress at $x/D_H = 13.9$ and $x/D_H = 17.9$ in the wind-tunnel test section varied by about 5% as a Preston tube was traversed across the central 100 mm of the test wall. At $x/D_H = 6.0$ a variation of less than 2% in wall shear stress was almost completely obscured by signal noise and turbulence. Although these measurements were rather crude, the similarity between the results and those obtained by Leutheusser (1963) is sufficient to verify the development of secondary flow in the test section.

In summary, it is likely that the effects of secondary flow near the downstream end of the wind-tunnel test section are only about half as large as in a fully-developed turbulent duct flow, and that, in the vicinity of the cross-section centreline, the main effect is a small change in the mean velocity distribution of the turbulent boundary layer.

3.2.4 Free-stream turbulence level

Measurements with a hot-wire about half way along the test section indicated an r.m.s. free-stream turbulence level ranging from $u'/U_0 \approx 0.9\%$ at $U_0 = 1.5$ m/s to $u'/U_0 \approx 0.25\%$ at $U_0 = 10$ m/s. Also, a small increase in free-stream turbulence level was observed at positions further downstream. Platinum/rhodium alloy Wollaston wires of 0.6 μm diameter were used for these measurements because, with the low-pass filtering provided by the instrumentation amplifier (Appendix E.7), it was possi-

[4] x = distance from the duct inlet; D_H = hydraulic diameter

[5] L = the length of the wind-tunnel test section

ble to obtain a lower signal-noise amplitude than with the more conventional 5-μm-diameter tungsten hot-wire filaments. The difficulties in using the 0.6-μm-diameter hot-wires made more extensive free stream turbulence measurements impracticable.

3.3 Measurements of boundary-layer characteristics

Many characteristics of a turbulent boundary layer can be determined by measuring the distribution of the streamwise velocity component over the thickness of the boundary layer. These measurements have been made over the length of the test section from Port 5 to Port 14 and for flow speeds ranging from 1.45 m/s to 9.3 m/s. The results include measurements of thickness, local skin-friction coefficient, mean velocity, r.m.s. velocity fluctuation and higher-order moments of fluctuating velocity.

3.3.1 Experimental technique

The streamwise component of velocity was measured with a single 5-μm-diameter, 1.3-mm-long "U" tungsten hot-wire which was operated at constant temperature with an overheat ratio of 0.5. The analogue instrumentation required for operating the hot-wire probe and the probe traversing mechanism are described briefly in Section 2.2.2, Section 2.2.7 and Appendix E.7. The geometry of the hot-wire probe is described in Section 2.2.1 and the calibration technique is described in Section 2.2.6. The hot-wire probe was calibrated at least twice daily, immediately before and immediately after each set of measurements.

For each measurement of the velocity distribution in the boundary-layer, about 40,000 data samples were obtained at each of 26 distances from the wall. These distances were distributed in geometric progression from $y = 0.1$ mm to $y = 80$ mm. The data sampling rate was varied from $f = 2.08$ kHz down to 300 Hz over the free stream speed range 9.3 m/s to 1.45 m/s, so that the ratio U_0/f remained approximately constant. These sampling rates were considered too low for spectral analysis, but this did not affect the suitability of the data for calculating mean values and moments of the distribution because the analogue signal was not low-pass filtered before digital sampling.

3.3.2 Momentum thickness

The normalised momentum thicknesses shown in Figure 3.5 were calculated from the mean air-speed measurements by the parabolic interpolation method of Coles (1968). Irregular variations were very large and, at up to $\pm 20\%$ of the expected momentum thickness, they were between one and two orders of magnitude larger than the error in the measurement. Only the most general trends of the

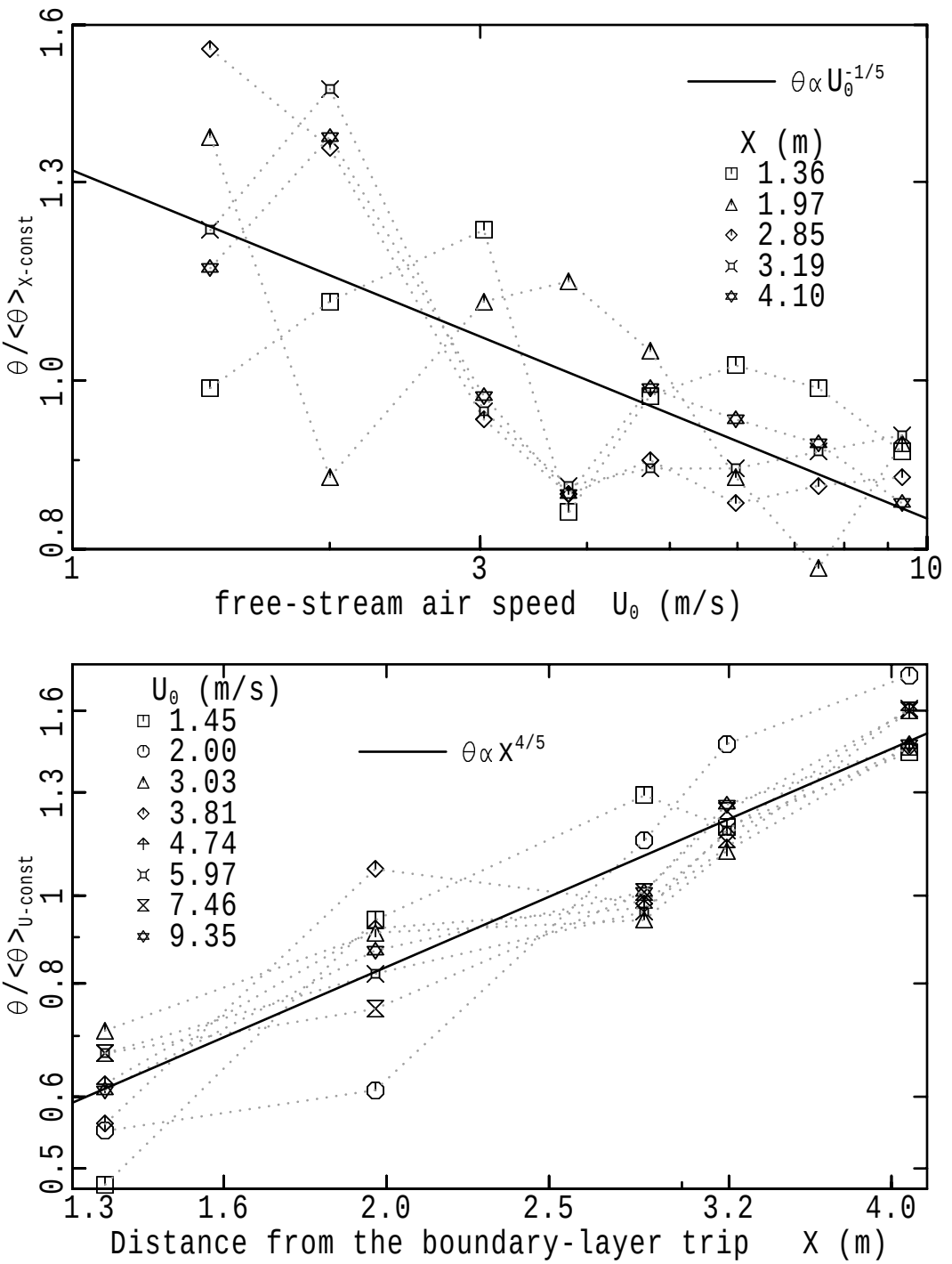

Figure 3.5: Momentum thickness, θ, of the test-section mid-plane boundary layer. The scales are logarithmic in both coordinate directions. **(a)** θ at selected streamwise locations, x, as a function of free-stream speed, U_0. At each location, θ is normalised by its geometric mean over the speed range, $< \theta >_{\text{x-constant}}$. The relationship $\theta \propto U_0^{-1/5}$ is shown as a solid black straight line. **(b)** θ at selected free-stream speeds, U_0, as a function of streamwise location, x. At each speed, θ is normalised by its geometric mean over the length of the test section, $< \theta >_{\text{u-constant}}$. The relationship $\theta \propto x^{4/5}$ is shown as a solid black straight line.

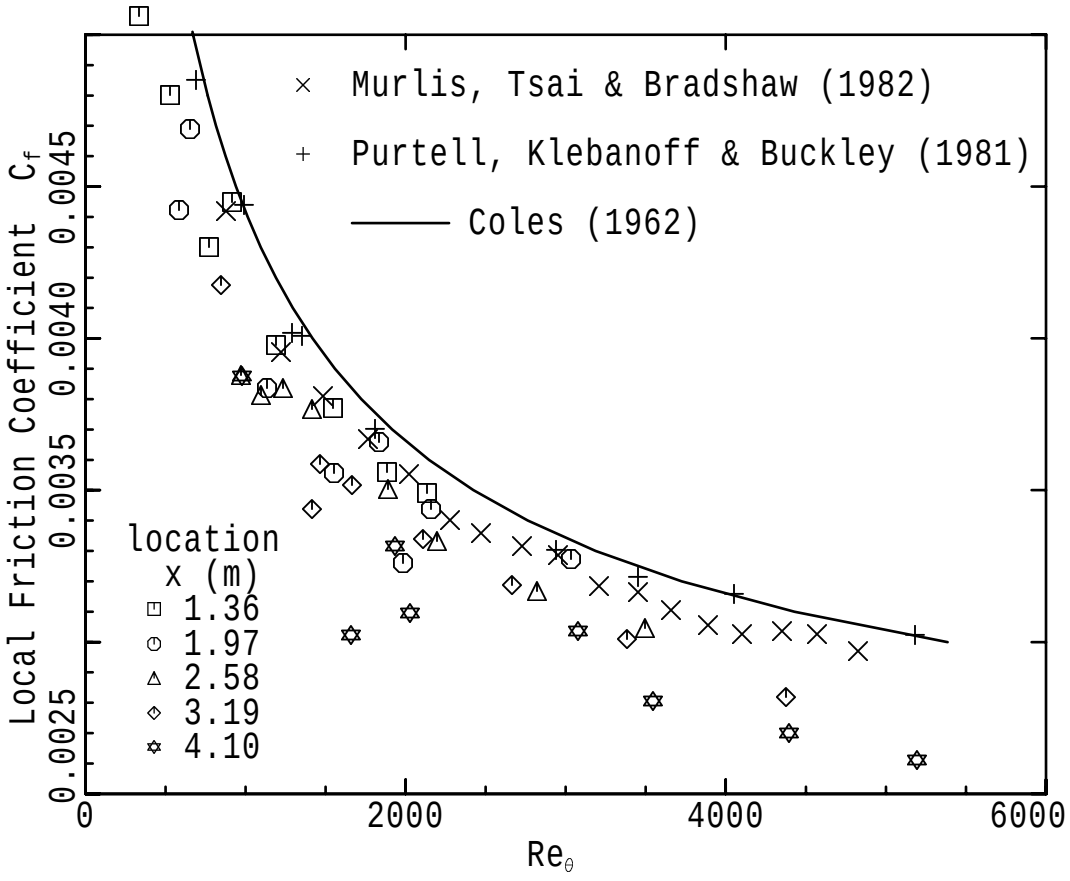

Figure 3.6: Local friction coefficient along the test-wall centreline. A different closed symbol (□, ◯, △, ◇, ✡) is used for each of the test section ports.

results conformed to the proportionality relationships $\theta \propto x^{4/5}$ and $\theta \propto U_0^{-1/5}$, which are derived from the empirical one-seventh power-law velocity distribution [von Kàrmàn, 1921] and are shown as solid straight lines in Figure 3.5. The sequences of individual momentum-thickness measurements, which are indicated with dotted lines, do not follow the expected proportionality relationships.

3.3.3 Local friction coefficient

In the absence of direct shear stress measurements at the wall, the local friction coefficient (C_f) may be determined from the velocity distribution in the logarithmic region of the turbulent boundary layer [Clauser, 1954]. In these experiments, only three or four data coordinates in each mean velocity profile were within the logarithmic region; so the part of the mean velocity profile which could be used for estimating C_f was extended into the buffer region and viscous sublayer ($y^+ \lesssim 30$) by replacing the

Clauser (1954) mean velocity model,

$$U^+ = \frac{1}{0.40}\ln y^+ + 5.0, \tag{3.6}$$

with Squire's (1948) model:

$$U^+ = \begin{cases} y^+ & \text{if } 0 < y^+ < y_0^+ \\ \frac{1}{\kappa}\ln\left[y^+ - y_0^+ + \frac{1}{\kappa}\right] + C & \text{if } y^+ \geq y_0^+ \end{cases} . \tag{3.7}$$

The constant coefficients $\kappa = 0.407$, $y_0^+ = 7.87$ and $C = y_0^+ + \kappa^{-1}\ln\kappa = 5.66$ were taken from Beattie and Green (1983).

In Figure 3.6, the skin-friction coefficients determined from Equation 3.7 are compared with the Coles (1962) local friction law, with the data of Murlis et al. (1982) ($\times$) and with the data of Purtell et al. (1982) ($+$). Except at the greatest distance from the boundary-layer trip ($x = 4.10$ m) the friction-coefficient values are lower than Coles' (1962) standard curve by $\Delta C_f \approx 0.3 \times 10^{-3}$, and are much more scattered than the previously published data. If allowance is made for the scatter of the results, the difference between skin-friction measurements in the test section and the Coles curve seems to depend primarily on distance from the boundary-layer trip, with the difference increasing to $\Delta C_f \approx 0.5 \times 10^{-3}$ (or about 16%) at $x = 4.10$ m. In terms of streamwise location used by Melling and Whitelaw (1976) $x = 4.10$ m is equivalent to $x/D_H \approx 18$, a position where they found that the near-wall region of the boundary layer is noticeably thickened by stress-induced secondary flow. From this evidence it seems reasonable to conclude that secondary flows are largely responsible for the reduction in skin-friction coefficient as distance from the trip increases. The scatter of the measurements is believed to have the same cause as the irregular variations in momentum thickness already referred to in Section 3.3.2.

3.3.4 Mean velocity distributions in the test-section boundary layer

Measurements of mean velocity in the boundary layer developed on the test wall are shown in Figure 3.7 for a free-stream speed of 2.00 m/s. Scaling on wall-region variables in Figure 3.7(a) reveals the presence of conventional features of a turbulent boundary layer such as viscous sublayer ($y^+ < 7$), buffer region ($7 < y^+ < 30$), logarithmic region ($30 < y^+ < 100$) and turbulent wake region ($y^+ > 100$). Near the downstream end of the test section, the thickness of the boundary layer exceeds the 90 mm of maximum probe movement allowed by the traverse mechanism. The influence of wall-proximity effect on the hot wire is clearly visible for $y^+ < 3$. Some mean velocity measurements in the logarithmic region at $x = 3.19$ m and $x = 4.10$ m are clearly inconsistent with any smooth curve which can be fitted to the data. Close examination of Figure 3.7(b) shows that similar anomalies are present to a lesser degree in all the other mean-velocity distributions. They are believed to have the same cause as the irregularities in measurements of momentum thickness (Section 3.3.2).

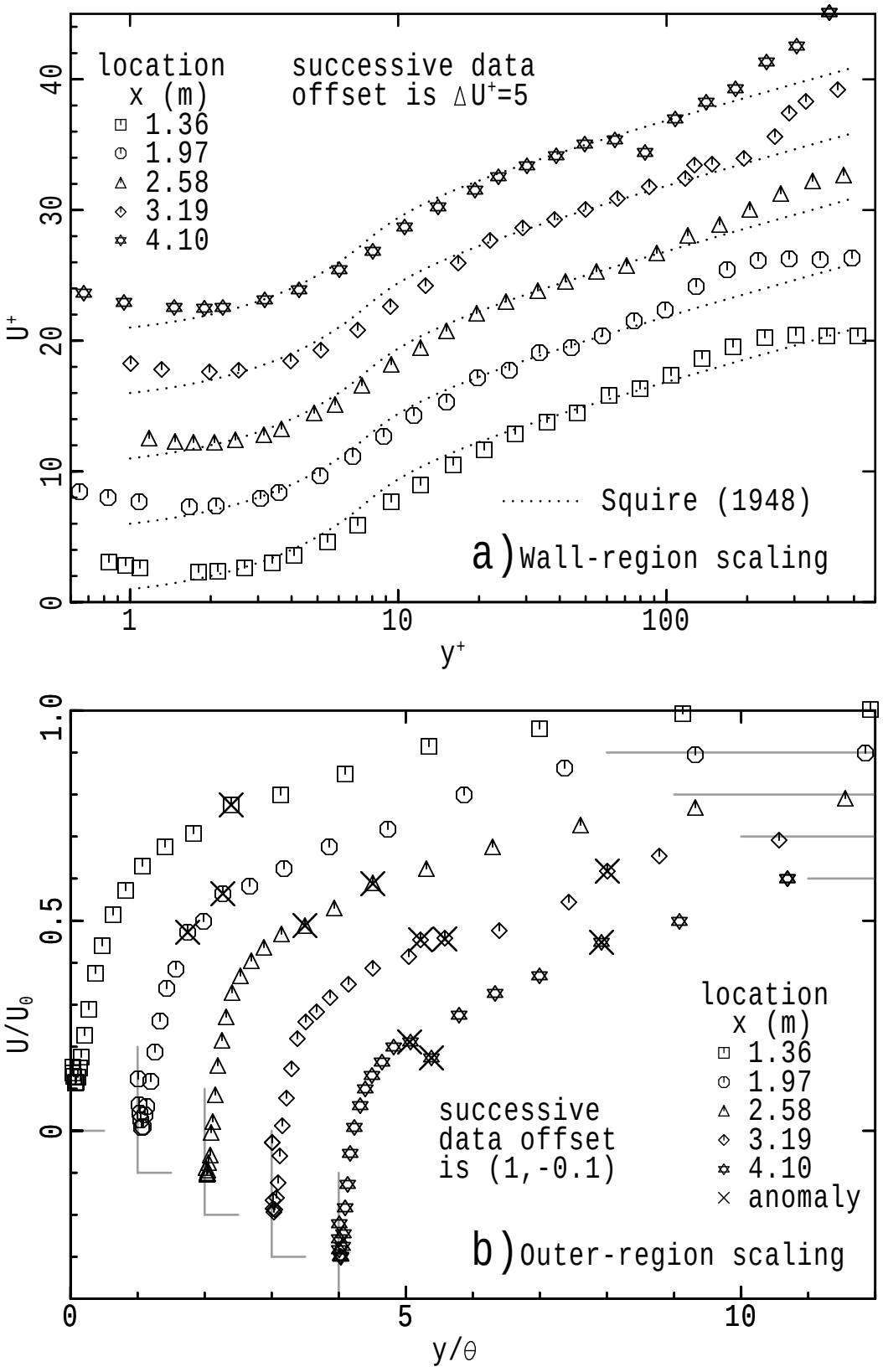

Figure 3.7: Mean velocity distribution in the test-section boundary layer for a free-stream speed of 2.00 m/s; (a) wall-region scaling (y^+, U^+); (b) outer-region scaling $(y/\theta, U/U_0)$, $\times$ is used to indicate anomalous measurements.

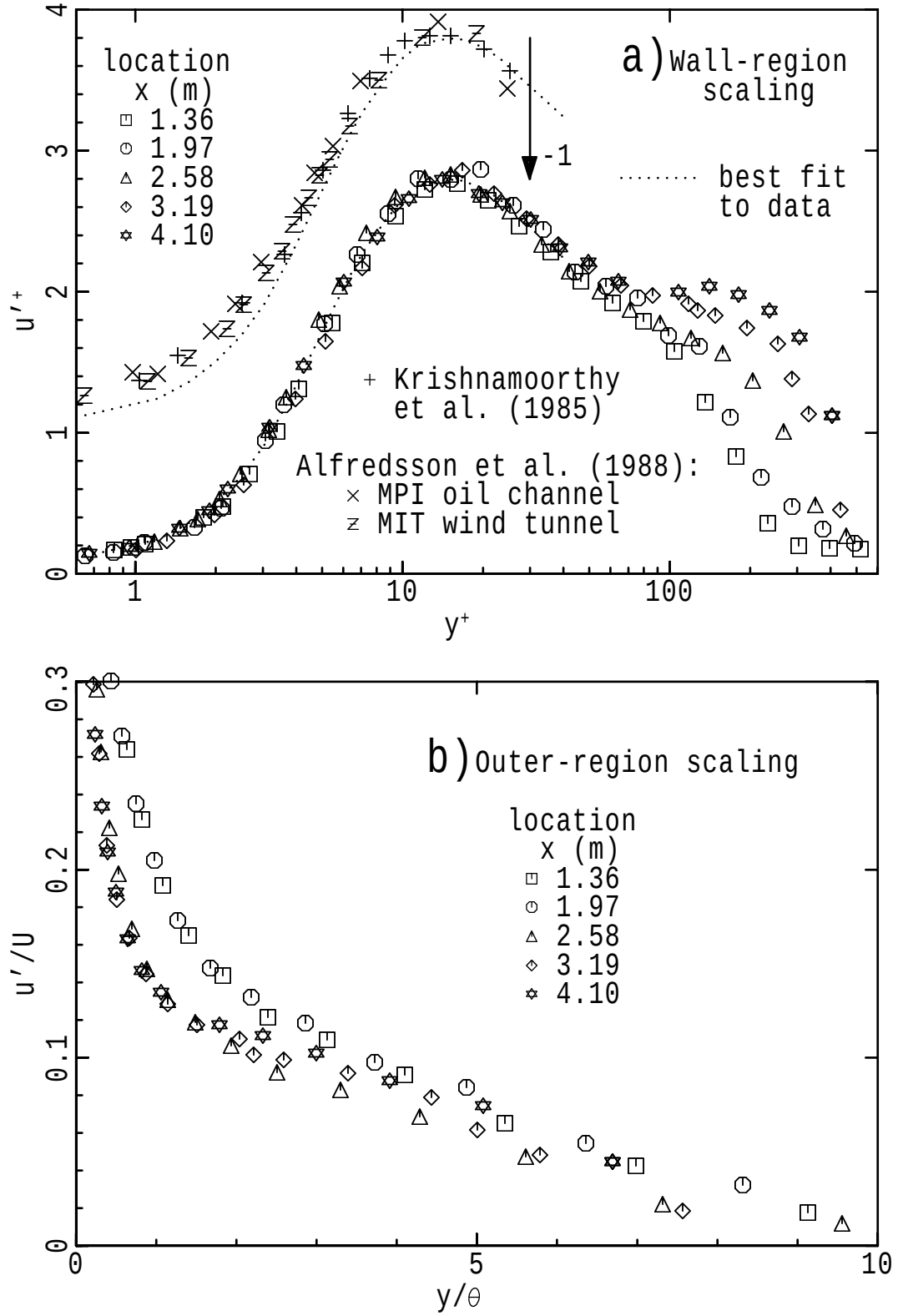

Figure 3.8: R.m.s. velocity distribution in the test-section boundary layer for a free stream speed of 2.00 m/s; (a) wall-region scaling (y^+, u'^+), with data from Krishnamoorthy et al. (1985) and Alfredsson et al. (1988) displaced vertically by $\Delta u'^+ = +1$; (b) outer-region scaling $(y/\theta, u'/U)$.

3.3.5 R.m.s. velocity distributions in the test-section boundary layer

Wall-region scaling of the r.m.s. velocity fluctuations for $U_0 = 2.00$ m/s in Figure 3.8(a) shows the usual collapse of the data onto a single curve (dotted line) for all $y^+ < 30$. For $y^+ > 30$, there is the usual rise in turbulence level as Reynolds number increases. In the buffer region the data are in close agreement with the results of Krishnamoorthy, Wood, Chambers and Antonia (1985) and with the results of Alfredsson, Johansson Haritonidis and Eckelmann (1988).

Scaling distance from the wall with momentum thickness would be expected to produce collapse of the relative turbulence intensity (u'/U) data over at least the wake region of the boundary layer. However, the collapse shown in Figure 3.8(b) is poor. The most likely reason for this is the irregularity in the momentum thickness measurements.

3.3.6 Distribution of skewness and flatness in the test-section boundary layer

Plotting skewness as a function of y^+ (Figure 3.9(a)) collapses the data for the sublayer and buffer regions of the boundary layer ($y^+ < 30$) onto a single curve, which is shown as a dotted line. In the logarithmic region, which is very small at the upstream end of the test section, skewness has a weak Reynolds number (Re_θ) dependence. When flatness measurements are plotted as a function of y^+, they form a single curve (dotted line in Figure 3.10(a)) over the entire "law of the wall" region ($y^+ < 100$). In the wake region, intermittency due to interaction with the free stream flow produces large negative values of skewness and large positive values of flatness. High skewness and flatness in the viscous sublayer are generated by intermittent "sweep" interactions with the wall. In the viscous sublayer and wake regions, the intermittency or scarcity of statistically significant events in the velocity signal greatly reduces the accuracy with which skewness and flatness are measured. However, skewness and flatness data from the viscous sublayer are well within the range of values measured by Krishnamoorthy et. al. (1985) and Alfredsson et. al. (1988).

As in the case of the relative turbulence intensity, scaling the distance from the wall with an outer-region variable such as momentum thickness would be expected to produce collapse of the skewness and flatness data onto single curves in the turbulent wake region of the boundary layer. Figures 3.9(b) and 3.10(b) show that such collapse is only very approximate. The likely reasons for this are almost certainly the same as those given in Section 3.3.5 for the scatter of relative turbulence intensity measurements.

Although they are not reproduced here, distributions of mean velocity, r.m.s. velocity, skewness and flatness have been obtained for other free stream speeds from 1.45 m/s up to 9.35 m/s [Lanspeary, 1986]. Except for the effects of a wider variation in Reynolds number and except for an increase in the scatter

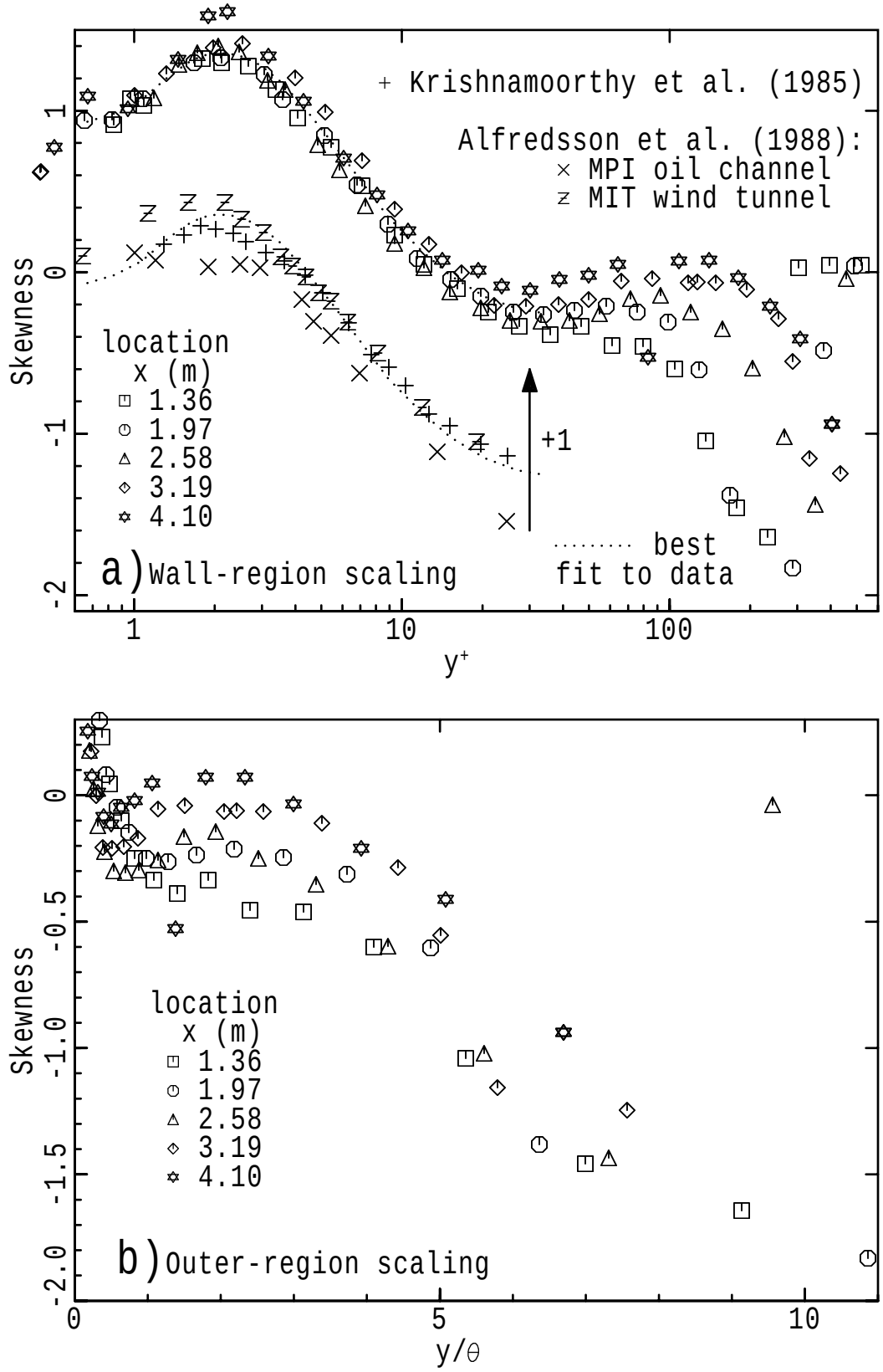

Figure 3.9: Skewness distribution in the test-section boundary layer for a free-stream speed of 2.00 m/s; (a) wall-region scaling (y^+, S), with data from Krishnamoorthy et al. (1985) and Alfredsson et al. (1988) displaced vertically by $\Delta S = -1$; (b) outer-region scaling $(y/\theta, S)$.

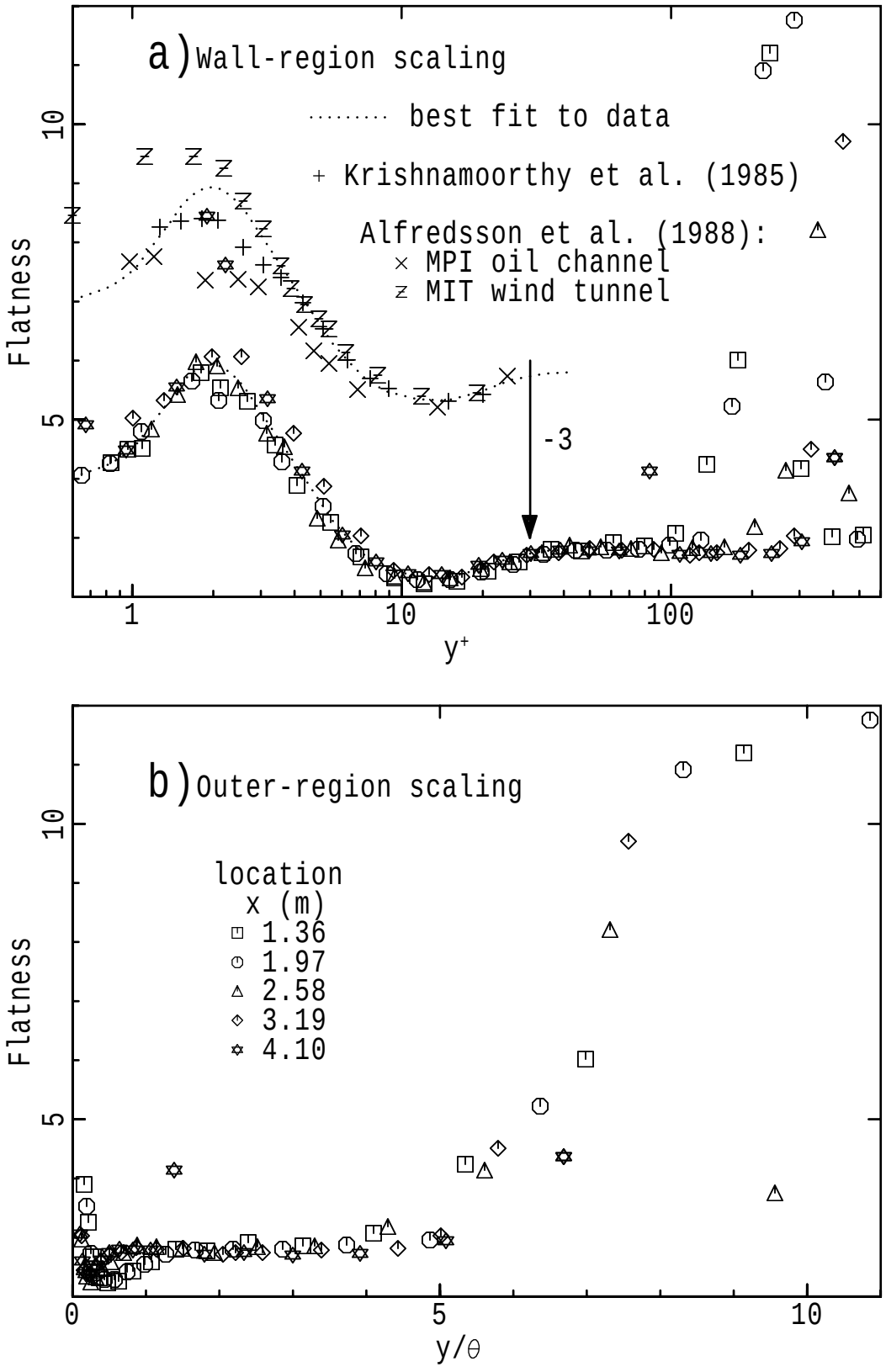

Figure 3.10: Flatness distribution in the test-section boundary layer for a free-stream speed of 2.00 m/s; (a) wall-region scaling (y^+, F), with data from Krishnamoorthy et al. (1985) and Alfredsson et al. (1988) displaced vertically by $\Delta F = +3$; (b) outer-region scaling $(y/\theta, F)$.

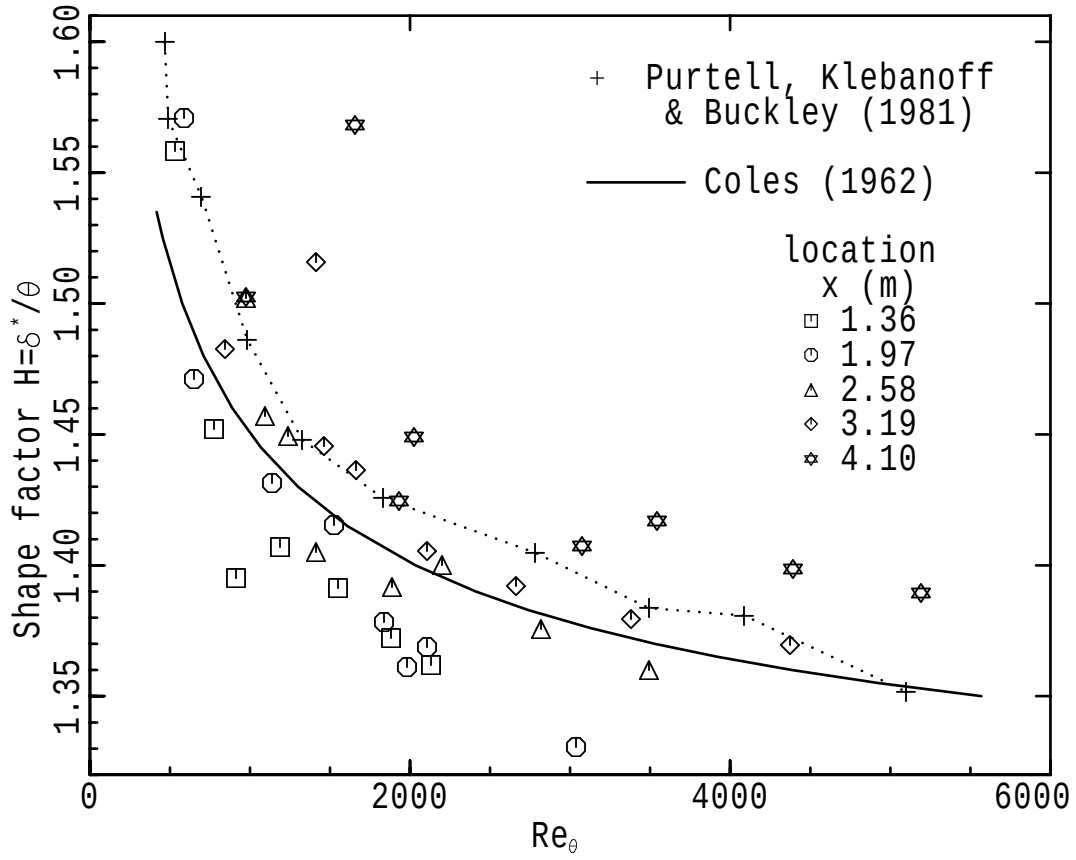

Figure 3.11: Boundary-layer shape factor $H = \delta^*/\theta$ along the test-wall centreline. A different closed symbol (□, ◯, △, ◇, ✡) is used for each of the test section ports. As a visual aid, measurements of Purtell et al. (1981) are joined by dotted straight lines.

of the viscous sublayer results due to deficient hot-wire calibration, these results exhibit essentially the same features as those at 2.00 m/s.

3.3.7 Interpretation of boundary-layer measurements

The irregular variation of the momentum thickness indicates that the boundary layer in the wind-tunnel test section failed to satisfy the criteria which define the canonical turbulent boundary layer. However, measurements of other parameters such as local friction coefficient and distributions of the statistical moments of velocity (mean, r.m.s., skewness and flatness) suggest that the variation in momentum thickness was superimposed on a conventional turbulent boundary layer without producing a fundamental change in the wall turbulence mechanism. From inspection of Figures 3.6 and 3.11, there are clear differences between values of C_f and H measured in the test-section boundary layer and the published results of Purtell et al. (1981) and Murlis et al. (1982). These differences have one component

which may be described as a random scatter and another component which may be thought of as a systematic variation controlled by the streamwise location. It is estimated that experimental error is responsible for less than 20% of the random scatter; the greater part is therefore attributed to the irregular variation in boundary-layer thickness.

3.4 Conclusion

The operating flow speed of the boundary-layer wind tunnel was reduced in order to produce turbulent boundary layers in which small-scale turbulence motions could be resolved by conventionally sized hot-wire probes. Measurements in the mid-plane boundary layer of the test section revealed an irregular variation in boundary-layer thickness superimposed on apparently conventional wall turbulence. In order to ensure the presence of a canonical turbulent boundary layer in the test section of the wind tunnel, it then became necessary to find and eliminate the source of this anomaly.

3.5 Notation

A, B, κ, C	coefficients of the logarithmic mean velocity distribution $U^+ = A\ln y^+ + B$ or $U^+ = (1/\kappa)\ln y^+ + C$
C_f	τ_w/q_0, local skin-friction coefficient
D_H	$4A/\mathcal{P}$, hydraulic diameter of a duct, where A is the cross-section area and $\mathcal{P}$ is the cross-section perimeter
F	$\overline{u^4}/u'^4$, flatness of streamwise air-speed fluctuations
f	data-sampling frequency
H	δ^*/θ, boundary-layer shape factor
L	length of duct
P_0	free stream static pressure
q_0	$\frac{1}{2}\rho U_0^2$, free stream dynamic pressure
Re_θ	$U_0\theta/\nu$, Reynolds number based on boundary-layer momentum thickness θ
S_{ij} (s_{ij})	mean (fluctuating) rate of strain tensor
S	$\overline{u^3}/u'^3$, skewness of streamwise air-speed fluctuations
U	streamwise (i.e. x) component of time-averaged fluid velocity
U_0	speed of the main free-stream flow (outside the boundary layer)
U_i (u_i)	time-averaged (fluctuating) velocity tensor; $U_1 \equiv U$, $U_2 \equiv V$, $U_3 \equiv W$
U_τ	friction velocity of the boundary layer; defined by $\tau_w = \rho U\tau^2$

u'	r.m.s. of the streamwise velocity fluctuations
V	component of time-averaged velocity normal to the wall
x	streamwise location, usually distance downstream from a duct inlet or boundary-layer trip
x_i	location tensor; $x_1 \equiv x$, $x_2 \equiv y$ and $x_3 \equiv z$
y	distance from the wall
y_0^+	virtual-origin parameter for Squire's (1948) wall-region mean velocity distribution (Equation 3.7).
α	dimensionless parameter which indicates the proportion of boundary-layer growth due to pressure gradient
δ^*	$\int_0^\infty (1 - U/U_0)dy$, displacement thickness of the boundary layer
θ	$\int_0^\infty (1 - U/U_0)(U/U_0)dy$, boundary-layer momentum thickness
ν	kinematic viscosity of the fluid
ρ	density of fluid
τ_w	wall shear stress
Ω_i (ω_i)	mean (fluctuating) vorticity tensor

Superscripts

Variables which have a superscript $^+$ are nondimensionalised using the viscous flow variables U_τ and ν, e.g. $U^+ = U/U_\tau$ and $y^+ = yU_\tau/\nu$.

Time-averaging of a variable or expression is indicated by drawing a horizontal line above it; e.g. $\overline{u_j \omega_i}$.

Chapter 4

Classical flow separation in the wind-tunnel contraction

4.1 The unsteady boundary layer in the test section

The first evidence of unsatisfactory behaviour in the boundary-layer wind-tunnel test section has been presented in Chapter 3. To confirm that this was not due to faulty experimental technique, the boundary-layer velocity distributions were measured again, with probe locations distributed uniformly over the boundary-layer thickness at each test-section port. The velocity distribution shown in Figure 4.1(a), which was obtained from the instrumentation port closest to the boundary-layer trip ($x = 0.19$ m), contains many more data points in the outer region of the boundary layer than the results presented in Chapter 3. The irregularity of the plotted data points, each of which is an average of 5000 data samples collected over 20 seconds, clearly remains. Each 5000-sample data record was then split into 8 segments and the data within each segment were averaged separately. These results, which are shown in Figure 4.1(b), strongly suggest boundary-layer properties varying on a time scale (in the order of 2 seconds) much longer than that of the largest eddies in the boundary layer ($2\delta/U_0 \approx 0.02$ s). This suggestion was reinforced by Figures 4.1(c) and 4.1(d) which show clear differences between two distributions of mean and fluctuating velocity obtained under identical experimental conditions. Results similar to those in Figure 4.1 were obtained throughout the length of the test section.

Removal of the sandpaper strips from the test-section extension and wind-tunnel contraction (Figure 3.1) did not eliminate unsteadiness of the type revealed in Figure 4.1. This excluded the possibility that the unsteadiness was being caused by intermittent or wandering transition on any of the sandpaper strips.

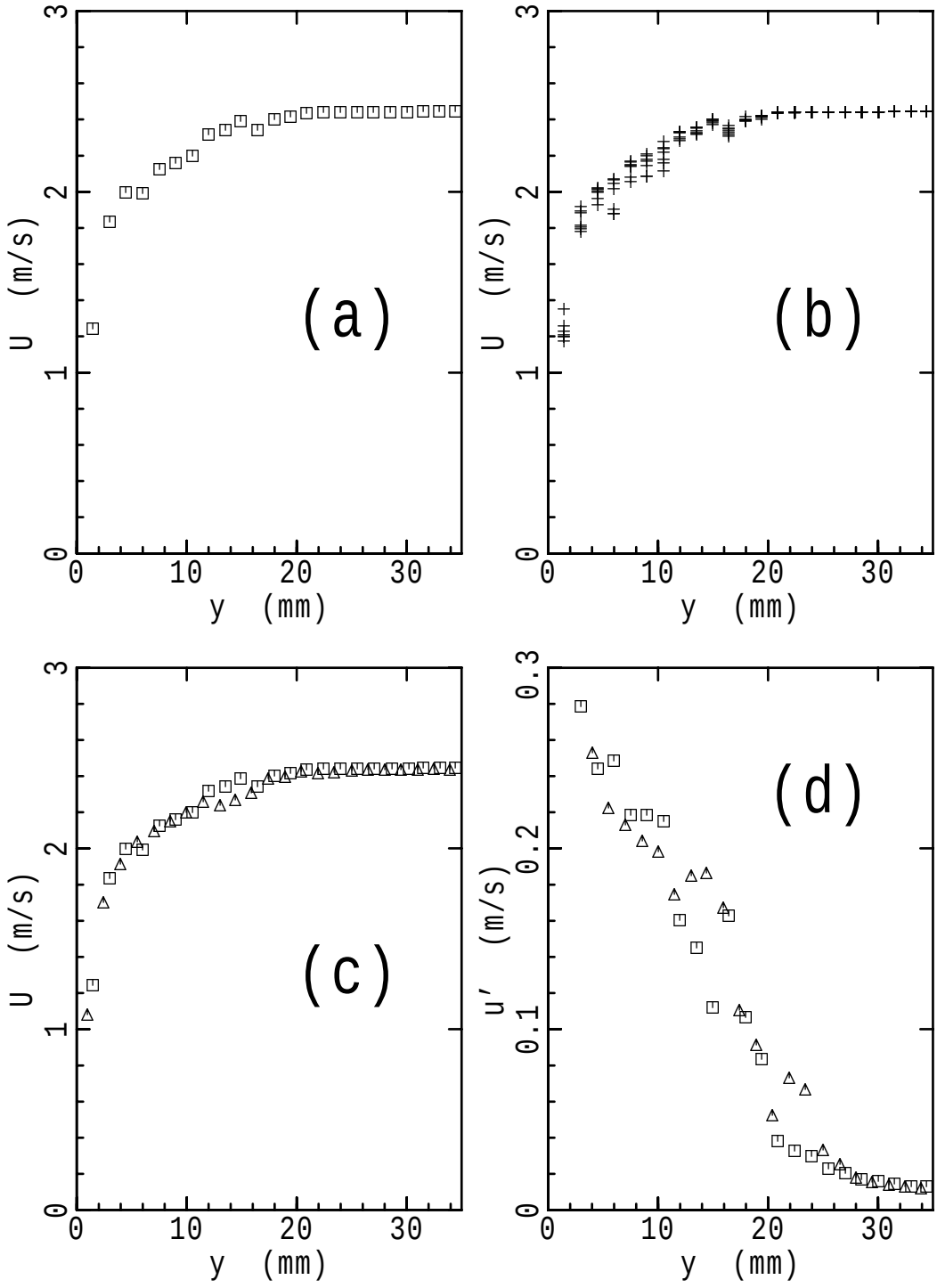

Figure 4.1: Velocity distribution in the unsteady turbulent boundary layer at test-section Port 1, $x = 0.19$ m, $U_0 = 2.45$ m/s. (a) Mean velocity measurement; (b) Each data record from (a) split into 8 segments; (c) Mean velocity from 2 successive measurements; (d) R.m.s. velocity fluctuation from 2 successive measurements.

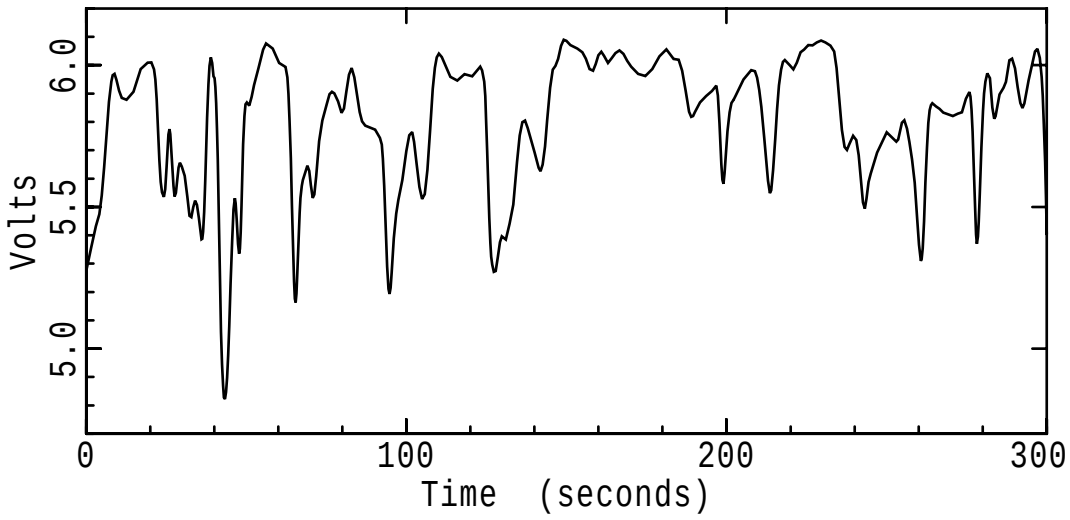

Figure 4.2: Signal from a hot wire in the laminar boundary layer, 100 mm upstream of the boundary-layer trip and 8 mm from the wall; $U_0 = 1.7$ m/s.

Figure 4.2 is an example of the signal from a hot-wire probe located 8 mm from the wall and 100 mm upstream of the boundary-layer trip where the boundary-layer thickness was about 11 mm. This signal was obtained over a period of 5 minutes at a free-stream speed of 1.7 m/s. It demonstrates that the boundary layer upstream of the trip was laminar, and that the air speed within the boundary layer was varying slowly with time. The character of the signal fluctuations did not change as flow speed was varied over the range 1.0 m/s to 9.6 m/s. The distribution of the mean and r.m.s. fluctuation of the hot-wire signal at the same streamwise position (Figure 4.3) shows that the unsteadiness in the flow was confined to $y \lesssim 15$ mm, that is, to within the laminar boundary layer. This evidence led to the conjecture that the source of the unsteadiness was flow instability in the wind-tunnel contraction, and that the instability was caused by laminar boundary-layer separation in regions of adverse pressure gradient on the wall of the contraction. The long-term variations in the characteristics of the test-section boundary layer were clearly not due to wall turbulence.

4.2 Evidence of flow separation in the contraction

A search was then made for direct evidence of boundary-layer separation in the wind-tunnel contraction. For test-section flow speeds ranging from 1.2 m/s to 9.6 m/s, the corresponding extremes of air speed at the inlet of the contraction are 0.05 m/s and 0.4 m/s. Over this speed range the boundary layer was laminar everywhere on the contraction walls. The primary tool for the investigation was a straight, conventional hot-wire probe mounted on a sleeve and inserted though a number of small holes in the

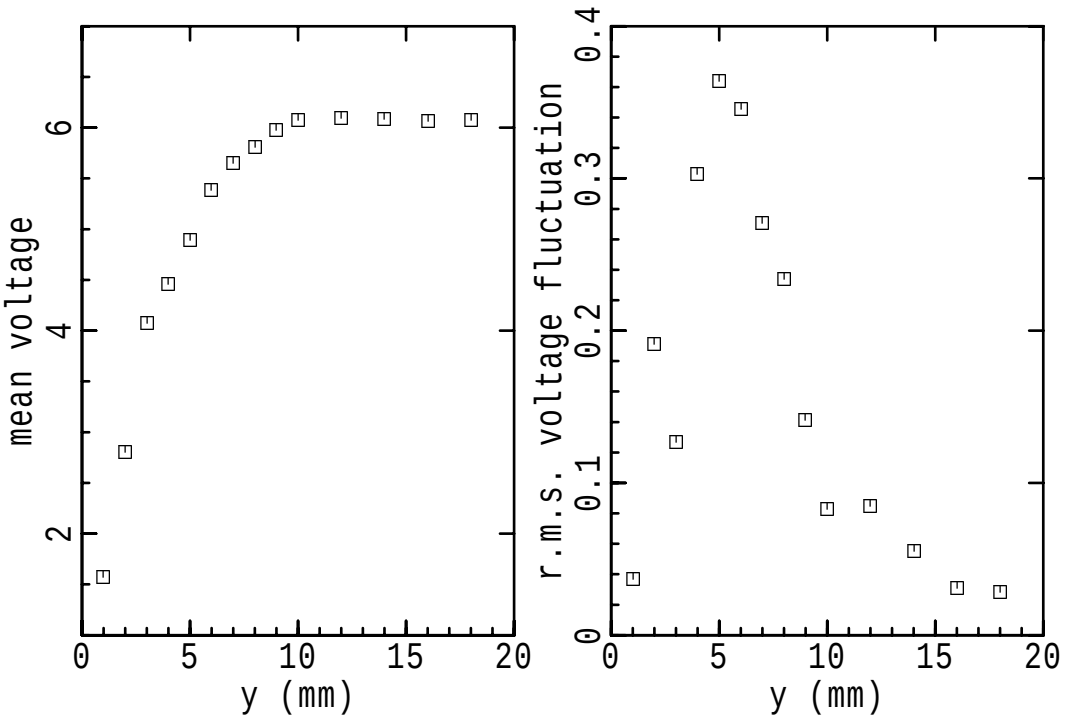

Figure 4.3: Distribution of mean and r.m.s. fluctuation of the signal from a hot-wire in the laminar boundary layer, 100 mm upstream of the boundary layer trip; $U_0 = 1.7$ m/s.

wall of the contraction. As it was not strictly necessary to quantify air speed in the contraction, no attempt was made to calibrate the probe. Figures 4.4(a) and (b) are the distributions of the mean and fluctuating components of the hot-wire signal across the thickness of the laminar boundary layer near the centreline of the upper surface and 220 mm downstream from the start of the contraction. This location is marked as "A" in Figure 4.5. The presence of a separated flow region is revealed in Figure 4.4(a) by a mean voltage which approaches the value corresponding to zero air speed at distances of about 9 mm from the wall.

Signal distributions showing similar evidence of flow separation at locations "B" and "C" (Figure 4.5) indicate that the separation region covered a large proportion of the contraction surface and was typically less than 10 mm thick. Further measurements at location "C" demonstrated that the region of separated flow, which is sketched in Figure 4.5, shrank as flow speed was increased. The signal fluctuations (Figure 4.4(b)) measured within the separated boundary layer were erratic and were much larger than the background noise levels measured outside the boundary layer ($y > 50$ mm). These elevated fluctuation levels were not present at locations where measurements could verify an absence of boundary-layer separation, and so they were believed to be strongly associated with separation. Crude estimates from the data in Figure 4.4 show that the maximum relative intensity of velocity fluctuations

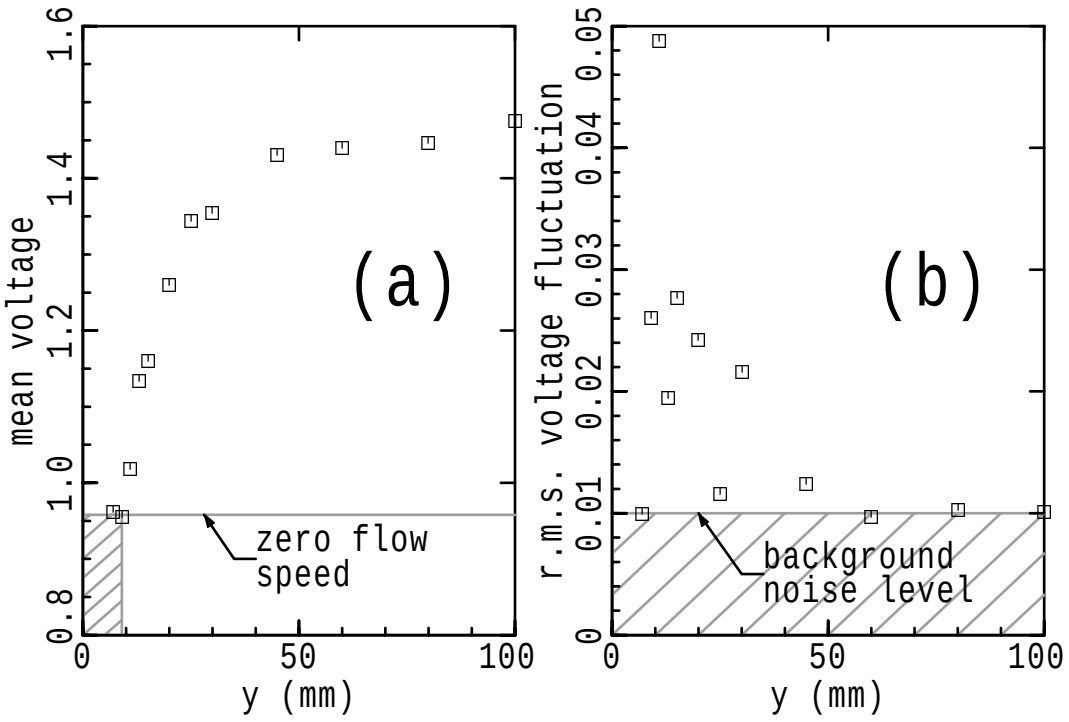

Figure 4.4: Distribution of (a) the mean and (b) the r.m.s. fluctuation of the output from a hot-wire placed in the boundary layer 220 mm downstream from the start of the contraction; $U_0 = 3.5$ m/s.

(u'/U) near the boundary of the separated flow region is similar in magnitude to the value found just upstream of the boundary-layer trip in the test section (Figure 4.3). This, together with the rather long time-scale of the signal fluctuations shown in Figure 4.2, suggests that large scale random movement of the separated flow regions in the contraction was producing variations in boundary-layer thickness which were being convected into the test section.

These experiments indicate that if separation were to be avoided, it would be necessary to modify the shape of the contraction. The data required for an appropriate redesign of the wind-tunnel inlet were obtained by numerical modelling of the potential flow in the contraction.

4.3 Numerical modelling of potential flow

4.3.1 Background

The traditional practice in the design of wind-tunnel contractions has been to model the flow as a potential (incompressible, irrotational and inviscid) flow in two-dimensional axisymmetric or Cartesian coordinates. The velocity distribution within the contraction is typically determined from an analytic or

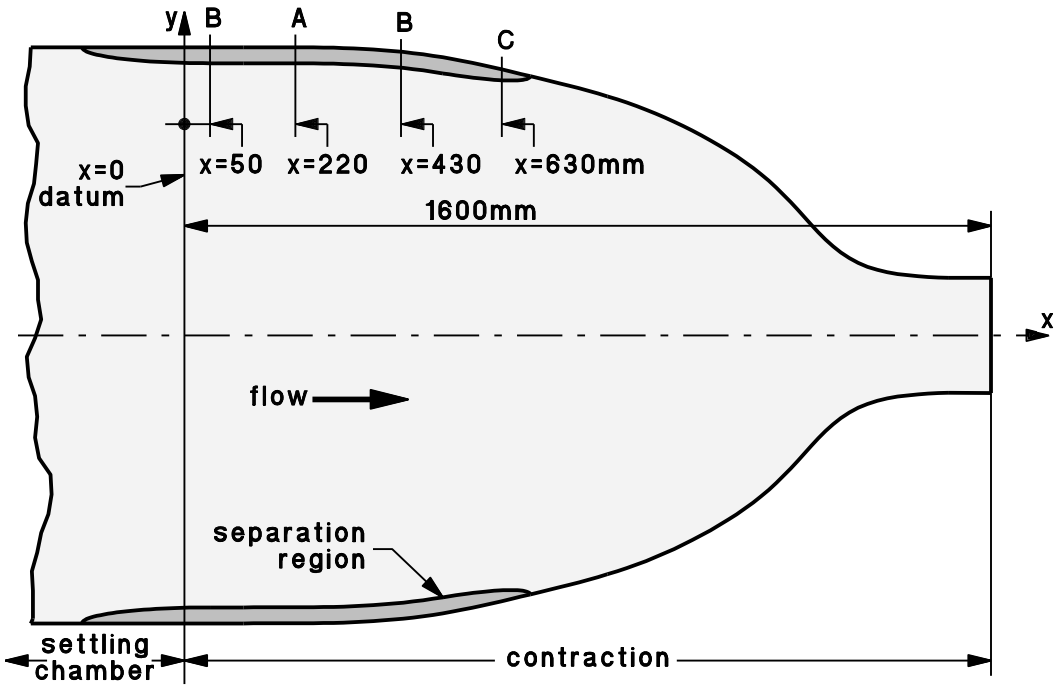

Figure 4.5: Approximate size and location of the separation bubble in the wind-tunnel contraction. The thickness of the separation region is exaggerated by a factor of about 4. Hot-wire probe locations are indicated by "A", "B" and "C". Dimensions are in mm. $U_0 \approx 3.5$ m/s.

numerical solution of Laplace's equation for the Stokes or Cartesian stream function [Mikhail, 1979, Cohen and Ritchie, 1962, Watmuff, 1986]. The boundary layer on the wall of the contraction is assumed to be very thin in comparison with the cross-section dimensions of the contraction, and the likelihood of separation can then be estimated from the wall-pressure distribution.

In the present work, three-dimensional and two-dimensional numerical solutions for the potential flow in the wind-tunnel contraction were obtained using the finite element program Ansys. With the version of Ansys available at the time of this study, the only formulation of Laplace's equation suitable for solving a potential-flow problem was a model for thermal conduction through an isotropic solid. The temperature field T was interpreted as the velocity-potential function ϕ, and thermal flux $\dot{q}$ was interpreted as velocity u. The velocity potential function ϕ was defined by $u = \nabla\phi$, and so for a thermal flux given by $\dot{q} = k\nabla T$, it was convenient to set the thermal conductivity to $k = 1$. Two-dimensional modelling of the flow in the square wind-tunnel contraction would have been inadequate, because, at the very least, the length of streamlines along a surface centreline and along a corner were significantly different. Since the completion of this study several computer programs (e.g. Fidap, Phoenics) capable of simulating fluid flows have become available and the increase in computation required by the direct inclusion of viscous effects has been largely balanced by the increased speed of the machines.

However, judging from experience with Phoenics, it is likely that attempts to simulate very thin and unsteady laminar separation regions with more advanced and more complex software would have greatly increased the difficulty of assuring the reliability of numerical solutions.

Potential-flow solutions were obtained for the existing contraction geometry and for a number of modified geometries. The method of Thwaites (1949) was used to calculate the development of the laminar boundary layer on the contraction surfaces, and thus showed how changes in contraction geometry affect the growth of the laminar boundary layer and the likelihood of boundary-layer separation. The results of the numerical simulation were used as a basis for modifications to the inlet section of the wind tunnel which were then tested experimentally.

4.3.2 Boundary conditions

At the surfaces of the contraction the flow must be parallel to the surface. In terms of the thermal conduction analogy of potential flow, this means that the sides of the contraction must be adiabatic; that is, for surface normal vector n, the heat flow satisfies $\dot{q} \cdot n = 0$.

Solution of the potential-flow problem also requires that one scalar boundary condition be defined over the inlet and outlet surfaces of the model. These boundary conditions, which are usually expressed as a uniform velocity magnitude or direction, are to some extent arbitrary because the actual flow conditions in the wind-tunnel inlet are not known precisely. However, the results of this study have shown that if a sufficient (short) length of parallel-sided duct is added to each end of the model, the effects of these slightly artificial boundary conditions become negligible. When the potential-flow problem is formulated in terms of the two-dimensional stream function ψ, the usual practice has been to specify a uniform horizontal velocity component at the inlet and a zero vertical velocity component at the outlet of the contraction [Chmielewski, 1974, Watmuff, 1986]. In this three-dimensional study, where the solution variable is velocity potential, the inlet and outlet boundaries are more appropriately defined as equipotential surfaces. These boundary conditions were also used by Downie, Jordinson and Barnes (1984). The absence of potential gradient on the inlet and outlet surfaces of the model ensures that the velocity vector is perpendicular to these surfaces. In terms of the analogy between potential flow and heat conduction, the uniform velocity potential condition over the inlet and outlet surfaces translates into uniform temperature.

4.3.3 Contraction profile of the numerical model

The contraction in the boundary-layer wind tunnel had a square cross-section. The contraction profile was adapted from the Cheers (1945) description for contractions of infinite length. The Cheers profile

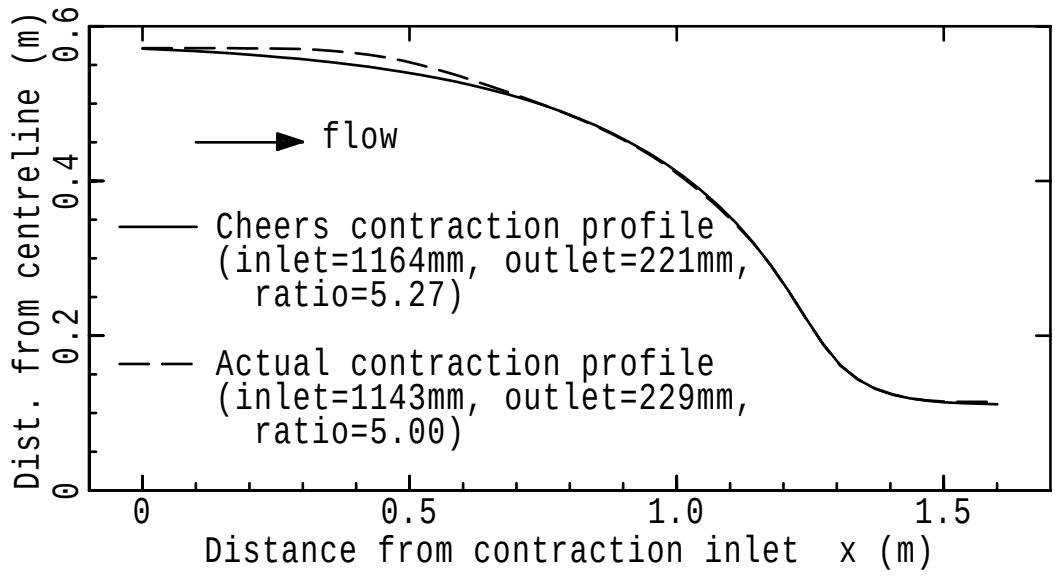

Figure 4.6: Comparison of Cheers' formula and the actual contraction profile. Inlet dimensions, outlet dimensions and the two-dimensional contraction ratio are shown on the figure.

is compared with the actual profile of the wind-tunnel contraction in Figure 4.6. Partly as a result of adapting the Cheers profile to a finite-length contraction, the main difference between the two profiles occurred in the region near the start of the contraction ($x < 0.6$ m) where an adverse pressure gradient was most likely to produce boundary-layer separation [Cohen and Ritchie, 1962, Morel, 1975, Mikhail, 1979].

4.4 Procedure for finite element analysis

4.4.1 Model generation: preprocessing

For each variant of contraction geometry modelled with Ansys a small Fortran program was written to provide the data required by the Ansys pre-processor. These data consisted mainly of node and element definitions for the finite element mesh. The contraction cross-section geometries selected for this study were square, regular octagonal and octagonal-to-square. As shown in Figure 4.7, the symmetry of each geometry was used to reduce the number of nodes and elements. The parameters required for generating the finite element mesh are:

(1) the contraction profile (Figure 4.6),

(2) the geometry of the contraction cross-section (Figure 4.7),

(3) the length of parallel-sided settling chamber, which is upstream of the contraction, and test sec-

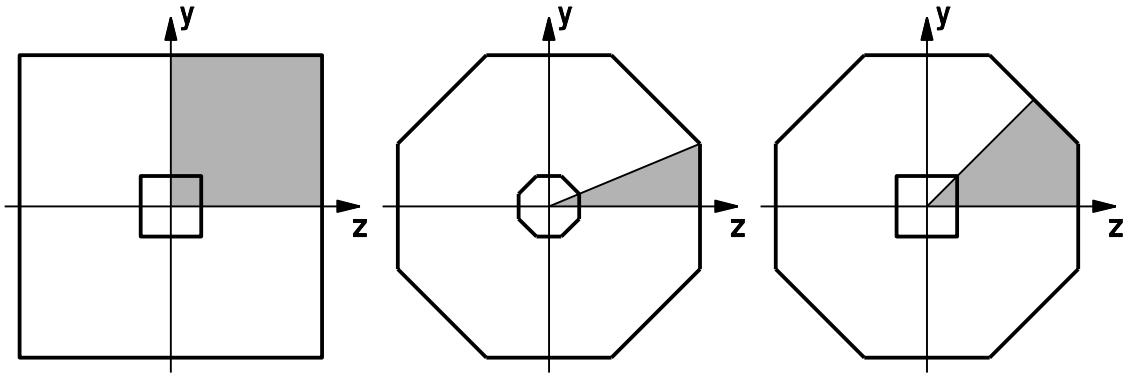

SQUARE
rectangular elements
($\frac{1}{4}$)

REGULAR OCTAGONAL
prismatic elements
($\frac{1}{16}$)

REGULAR OCTAGONAL
TAPERING TO SQUARE
prismatic and tetrahedral
elements ($\frac{1}{8}$)

Figure 4.7: Use of cross-section symmetry to reduce mesh size. The diagrams are end views of the contraction, looking downstream from the inlet. The extent of the finite element mesh is indicated as a shaded region. The shape of the finite elements and the proportion of cross-section in the mesh are shown under each diagram.

tion, which is downstream of the contraction, to be included in the mesh,

(4) the number of finite elements distributed uniformly along the duct "radius", and

(5) the formula describing the taper which effects the streamwise conversion of the regular octagonal inlet cross-section into the square outlet cross-section.

The coordinates of the contraction profile were obtained from Lim (1971). Small portions of the settling-chamber length and test-section length were included in the finite element mesh in order to accommodate regions of non-uniform flow which extended beyond the ends of the contraction [Morel, 1975]. In general the most accurate solution of a finite element problem is likely to be obtained from the mesh with the least irregularly shaped or the most nearly square elements. In this case the irregularity of element shapes was controlled sufficiently by making the streamwise length of each element equal to its radial or dominant cross-section dimension[1]. The details of the taper formulae which convert the octagonal inlet to a square outlet are given in Appendix G.

For the development and verification of the mesh-generation programs only four elements were distributed along the "radius" of each finite-element model, giving a total of between 300 and 700 elements. The main results were obtained with models having "radii" of eight or nine elements and containing between 4000 and 6000 elements.

[1] In Figure 4.7, the "radial" direction is along the z-axis.

4.4.2 Extracting the velocity data: post-processing

After Ansys had solved each finite element model, the post-processor made the velocity data available as a table of heat flux vectors listed in the same order as that in which the mesh elements were defined. A small Fortran program was required to calculate the position of the centroid of each element from separate lists of element definitions, and then to tabulate velocity as a function of location. This table was used for plotting selected parts of the velocity and pressure fields, and for estimating the development of the laminar boundary layer on the walls of the contraction by the Thwaites method. The static gauge pressure $P_0(x)$ was calculated from Bernoulli's equation,

$$P_0(x) = -\frac{1}{2}\rho\,|u(x)|^2 . \tag{4.1}$$

4.4.3 Boundary-layer separation – the Thwaites analysis

The final part of modelling the flow in the contraction was to calculate whether or not the boundary layer would separate from from the surfaces of the contraction. It began with calculation of the laminar boundary-layer momentum thickness, θ, as a function of downstream distance, x_1, using the Thwaites equation,

$$\left[\theta^2 U_0^6\right]_{x_0}^{x_1} = 0.45\nu \int_{x_0}^{x_1} U_0^5(x)\,dx \tag{4.2}$$

[Thwaites, 1949], where U_0 is the air speed calculated by the finite element method. The initial momentum thickness, θ, at the inlet of the finite element model, x_0, was estimated from experimental measurements. The average flow speed over the exit of the contraction was set at 1.2 m/s. The skin-friction parameter,

$$l(m) = \frac{\theta}{U_0}\left.\frac{\partial U}{\partial y}\right|_{y=0}, \tag{4.3}$$

which becomes zero at a two-dimensional separation and depends only on the Thwaites parameter,

$$m = -\frac{\partial U_0}{\partial x}\frac{\theta^2}{\nu}, \tag{4.4}$$

could then be determined from a table of modified universal Thwaites functions [Curle, 1962]. The type of separation predicted by this method, where velocity gradient becomes zero at the point of separation, may be called classical or two-dimensional separation. It is different from the more complicated three-dimensional separation which is discussed in Chapter 6.

In this calculation of the developing laminar boundary layer, there was no attempt to construct and follow flow streamlines. It was simply assumed that a streamline passing through the centroid of an element in the finite element model also passed through the centroid of the adjacent downstream element. In addition, the Thwaites method assumes essentially two-dimensional behaviour of the boundary layer along the near-surface streamlines. In contractions with square and regular octagonal cross-sections,

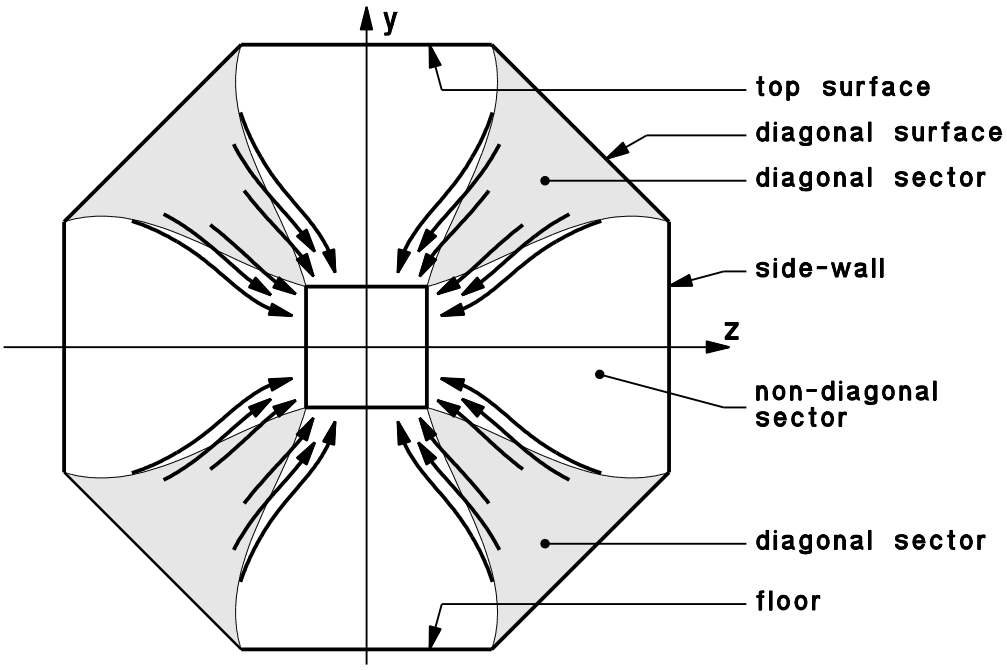

Figure 4.8: Cross-flow for the octagonal-to-square cross-section geometry. In this schematic view from the inlet end of the contraction, arrows show the cross flow from the diagonal sectors (shaded) through the side-faces of the finite elements.

this assumption is not expected to generate significant error because nearly all of the mass flow through each element passes through its upstream and downstream faces. However, for the contractions with a transition from octagonal-to-square cross-section, the diagonal surfaces of the contraction taper to a point. This means that all the flow in these diagonal sectors, which was initially half the total mass flow, passes through the sides of the elements into the other (non-diagonal) sectors of the model. This is illustrated in Figure 4.8. The estimates of momentum thickness may therefore have been less accurate in the regions of high taper rates, but in the regions of adverse pressure gradient, where the greatest accuracy is required from the Thwaites method, the rate of diagonal sector taper was very low and accuracy would not have been degraded significantly by the cross flow.

4.5 Flow in the contraction with a square cross-section

The geometry of the finite element model representing the contraction with the original square cross-section is shown in Figure 4.9. For clarity the model is drawn with only 16 elements in each cross-section and 24 elements along it length whereas the results presented are those obtained from a 9×9×55-element mesh. As indicated in Figure 4.7, only one quadrant of the contraction has been

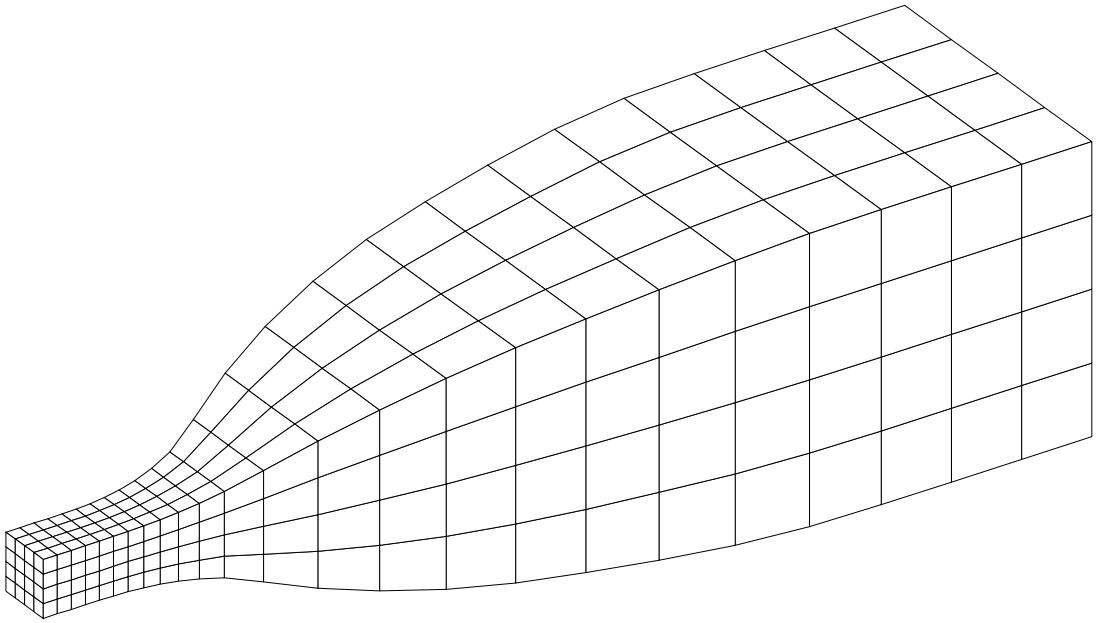

Figure 4.9: Finite element model for the contraction with a square cross-section geometry. For clarity the diagram is of a $4\times4\times24$-element mesh. Results were obtained from a model with $9\times9\times55$ elements.

modelled.

4.5.1 Non-uniformity of flow at inlet and outlet

Figure 4.10 shows the calculated distribution of air velocity at the centroids of the elements at the contraction inlet and outlet. At these locations, which are half an element length from the model boundaries, the ideal of uniform flow is approached very closely. In the distribution of air speed[2] over the inlet end of the model, the extremes are 1.3% higher and 1.3% lower than the average flow speed. The maximum is at the centre and the minima are in the corners of the duct. At the outlet end of the model the air-speed nonuniformity is $\pm0.21\%$ and the maximum air speeds are in the corners of the duct. The cross-flow velocity components are an order of magnitude smaller than the nonuniformity in the air speed.

[2]Air speed, which is the length of air-velocity vector, is almost exactly equal to the axial velocity component because, in comparison, the cross-flow components of velocity are at least two orders of magnitude smaller.

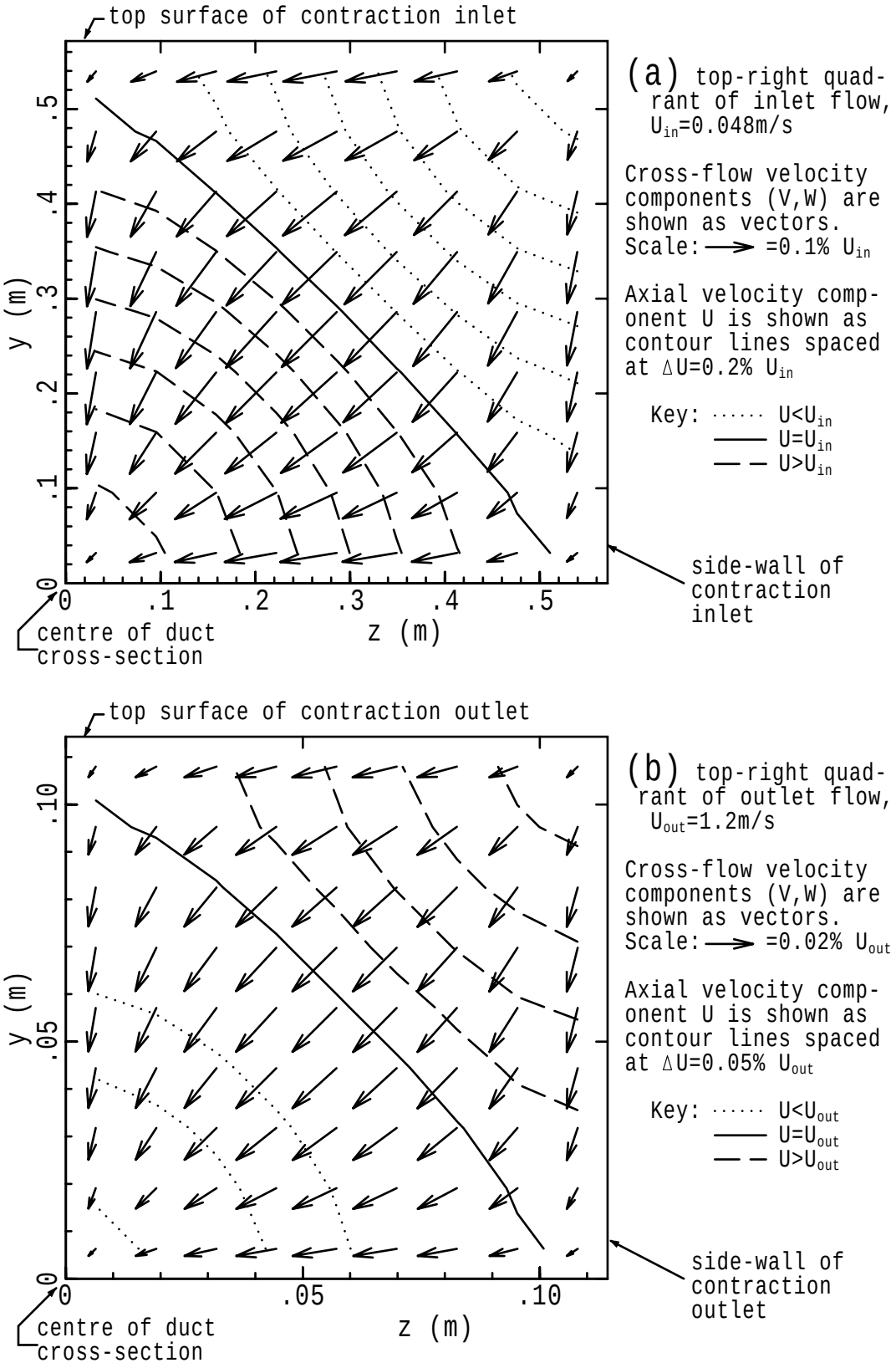

Figure 4.10: Nonuniformity of air velocity at (a) contraction inlet and (b) contraction outlet. N.B. only one quadrant of the duct cross-section is shown, with the duct centre at the coordinate origin.

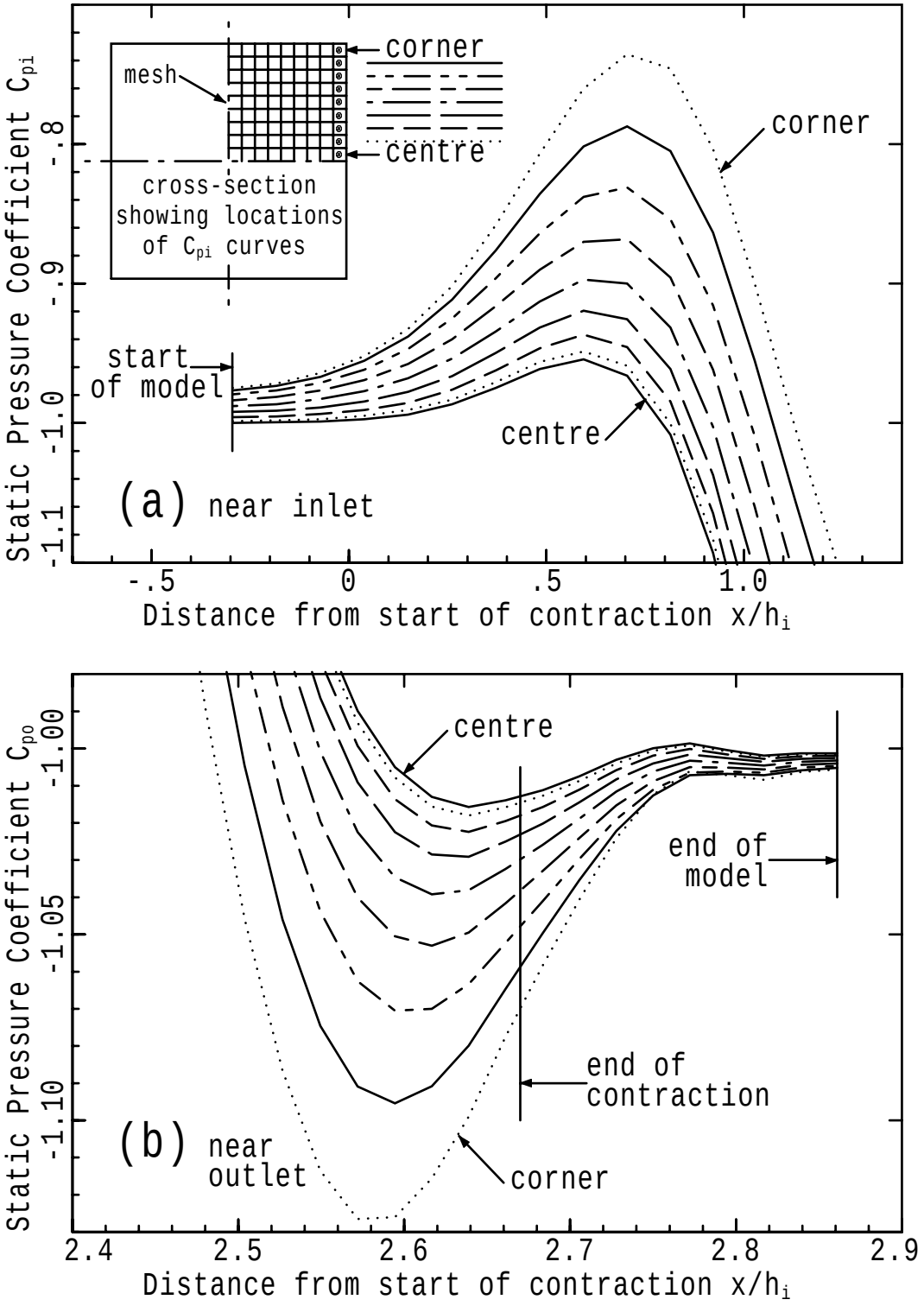

Figure 4.11: Static pressure coefficient near the wall of the square contraction (a) near the start of the contraction and (b) near the contraction outlet. Note that the pressure is calculated at the centroids of the elements adjacent to the contraction surface. The location of the centroid for each curve is indicated by a ● in the cross-section view of the contraction.

4.5.2 Static pressure distribution on the wall

The variation in static pressure over the wall near the start of the contraction is presented in Figure 4.11 as the static pressure coefficient

$$C_{pi}(x) = \frac{P_0(x)}{q_{\text{inlet}}}, \tag{4.5}$$

where the static pressure P_0 is defined in Equation 4.1 and q_{inlet} is the average dynamic pressure over the inlet of the finite element model. Static pressure near the contraction outlet is plotted as

$$C_{po}(x) = \frac{P_0(x)}{q_{\text{outlet}}}, \tag{4.6}$$

where q_{outlet} is the average dynamic pressure over the outlet of the model. The distance from the start of the contraction is expressed as x/h_i, where h_i is one half of the height of the contraction inlet. Each line in Figure 4.11 follows the centroids of the finite elements nearest the surface in the axial direction.

In comparison with the average static pressure over the inlet of the finite element model, the maximum pressure rise near the start of the contraction ranges from 4.5% at the centre, to 24.6% in the corner. This corresponds to a decrease in air speed of 2.3% and 13.2% respectively, and is comparable in magnitude with the 10% pressure rise typically required to cause separation of a laminar boundary layer. The magnitude of pressure undershoot near the contraction outlet varies from 1.4% at the centre to 12.0% in the corner. This is smaller than the rise near the inlet but is still large enough to require testing for boundary-layer separation. The variation in pressure coefficient across the width of the contraction surface reveals significant three-dimensionality in the near-wall pressure and velocity fields. Figure 4.11 also shows that, because the spatial pressure variations extend significantly beyond the ends of the contraction, it is necessary to include some settling chamber length ($x/h_i < 0$) and some test-section length ($x/h_i > 2.67$) in the finite element model. For the contraction with a square inlet cross-section the length of settling chamber in the model was $\Delta x/h_i = 0.35$. For other contraction geometries, this was increased to $\Delta x/h_i = 0.70$ so that the flow uniformity at the inlet of the model would be improved even further.

4.5.3 Development and separation of the boundary layer

The results of applying the Thwaites analysis described in Section 4.4.3 are presented in Figure 4.12. As in Figure 4.11, results are calculated at the centroids of the finite elements adjacent to the side-wall of the contraction, and they are presented as streamwise distributions. Figure 4.12(a) reveals a significant lateral (i.e. spanwise) variation in boundary-layer momentum thickness. As demonstrated by the lateral distribution at $x = 1.0$ m (Figure 4.12(a)), about 75% of this change in momentum thickness, which is due mainly to lateral variation of air speed near the wall, occurs over the half of the surface which is nearer the corner.

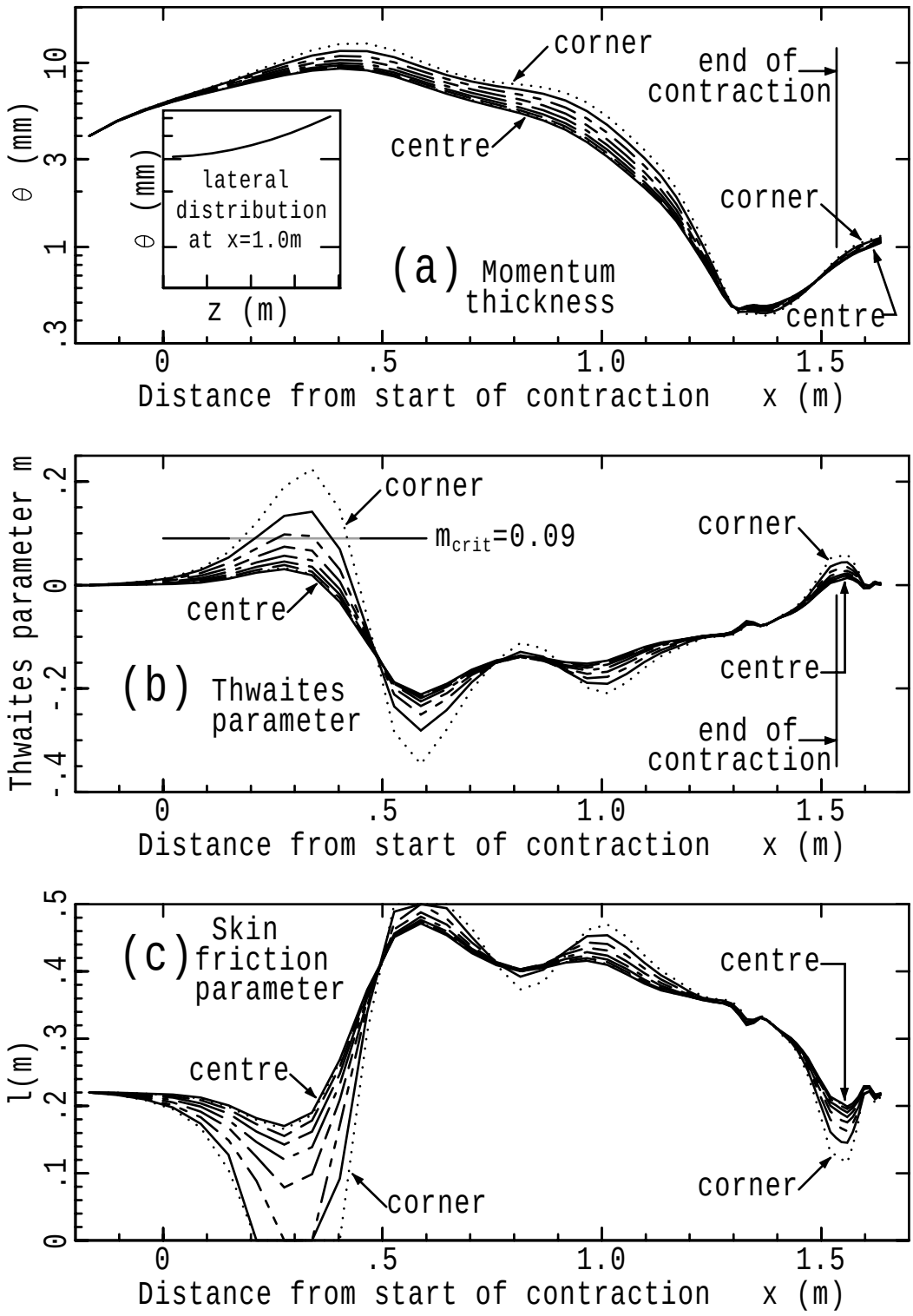

Figure 4.12: Development of the laminar boundary layer throughout the square contraction calculated by the Thwaites method; (a) distribution of momentum thickness (the graph of the lateral distribution at $x = 1.0$ m uses the same scale as the main graph); (b) Thwaites shape parameter, m; (c) skin friction parameter, $l(m)$. The location of each curve is indicated by a • in the cross-section view of Figure 4.11(a).

The existence of values much greater than 0.09 for the Thwaites parameter, m, in Figure 4.12(b) indicates adverse pressure gradients sufficient to initiate boundary-layer separation over large areas near the corners of the contraction inlet. The skin friction parameter, $l(m)$, obtained from the modified universal Thwaites functions is zero in these regions (Figure 4.12(c)). Separation is not indicated in the region of adverse pressure gradient near the exit because the maximum value of m there is less than two thirds of the critical value, $m_{\text{crit}} = 0.09$.

Although Figures 4.11 and 4.12 suggest a significantly three-dimensional near-surface flow, closer examination of the velocity field shows that, in the region of the adverse pressure gradient near the inlet, the cross-flow component of velocity[3] is at most only about 3% of the air speed. This relatively low level of three dimensionality would not be expected to invalidate the prediction of classical separation by the Thwaites method.

Estimation of accuracy is an important part of any application of the finite element method. There is rarely any simple formula or convenient analytical way of making this estimate, and so it was only possible to examine the trends exposed by empirically varying the mesh parameters. Given that the basic rules for generating the elements were fixed and the aspect ratios were already approximately optimal, the main parameter determining the accuracy of the solution was the number of elements in the mesh. This was was limited to about 6000 by the available disk-storage space in the computer and by the maximum number of simultaneous equations permitted by Ansys. In order to assess the accuracy of the solutions given in Section 4.5, it was necessary to model the flow with a mesh height of considerably more than 9 elements. It was not possible to do this for a three-dimensional contraction, but for a two-dimensional contraction planar finite elements could be used and the reduction in computer-memory requirements then allowed a mesh height of up to 30 elements.

4.6 Convergence of the finite element method

The potential flow in a two-dimensional equivalent of the wind-tunnel contraction has been calculated with meshes containing 4×24, 9×55, 19×110 and 29×177 elements. Figure 4.13 shows the mesh with fewest elements, and the results of the calculations are shown in Figures 4.14 and 4.15. As with the three-dimensional contraction, adverse pressure gradients occur near the start and near the exit of the contraction. It is in these regions, where good accuracy is most important, that the finite element analysis has the poorest convergence rate. There is a large decrease in the magnitude of the pressure maximum and minimum as the number of elements in the mesh is reduced. Part of this change is due to the increasing distance between the contraction surface and the centroids of the adjacent

[3] i.e. the flow through the *side* faces of the finite elements

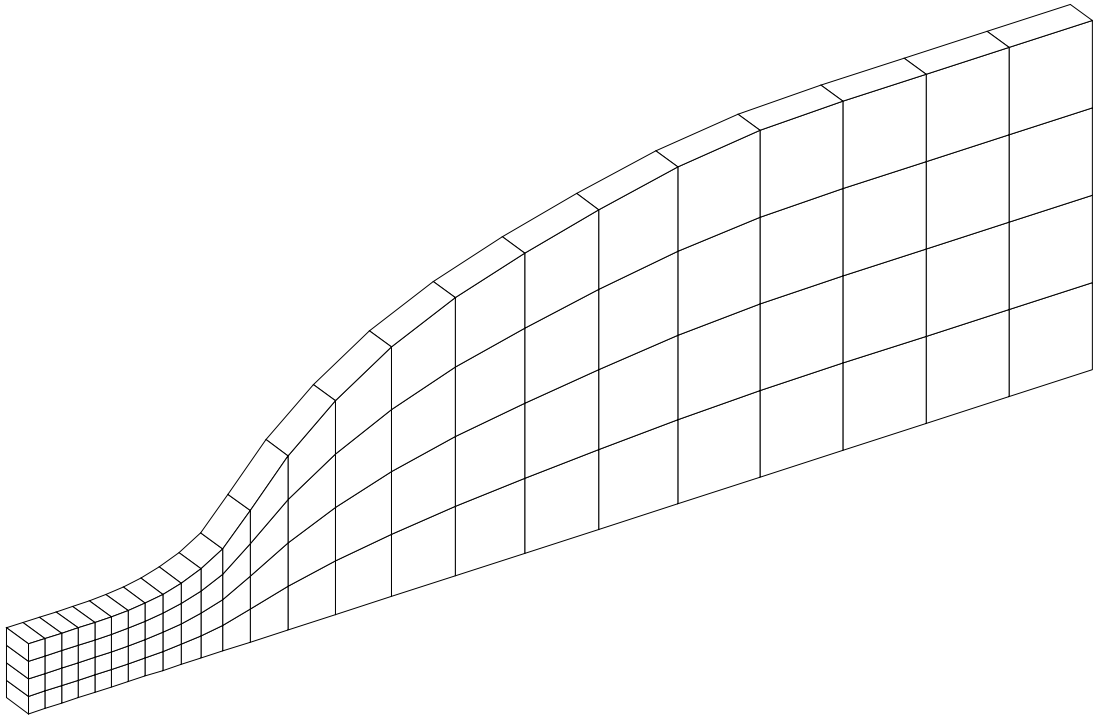

Figure 4.13: Finite element model for a two-dimensional contraction. Results were obtained from models with 4×24 (shown here), 9×55, 19×117 and 29×179 elements.

elements. The remainder is accounted for by the increase in artificial model "stiffness" caused by using elements which, in comparison with the spatial extent of variations in velocity and pressure, are too large. The values of the Thwaites parameter, which are the main result of the analysis, are expected to be less accurate than the wall-pressure distribution because they are calculated from finite difference estimates of velocity gradient. As the number of mesh elements increases, the Thwaites parameter converges more slowly towards an asymptote than the wall pressure. From Figure 4.16, which shows the maximum pressure coefficient C_{pi} and the maximum Thwaites parameter m as a function of the number of elements, it is apparent that the Thwaites parameter obtained for a 9×55-element mesh is significantly in error – probably by about 33%. The corresponding error for the 19×110-element mesh is about 13%. Over the downstream half of the contraction, rapid spatial oscillations are visible in the results obtained for the 29×177-element mesh (Figures 4.14(b) and 4.15). The cause of these oscillations is unknown.

Moving from a two-dimensional to a three-dimensional contraction geometry changes the contraction ratio, introduces lateral near-wall streamline curvature and decreases the "stiffness" of the finite-element solution. In this study, it is not possible to quantify the possibly complex effects of such factors on the finite-element solutions. Some uncertainty is therefore associated with using the two-

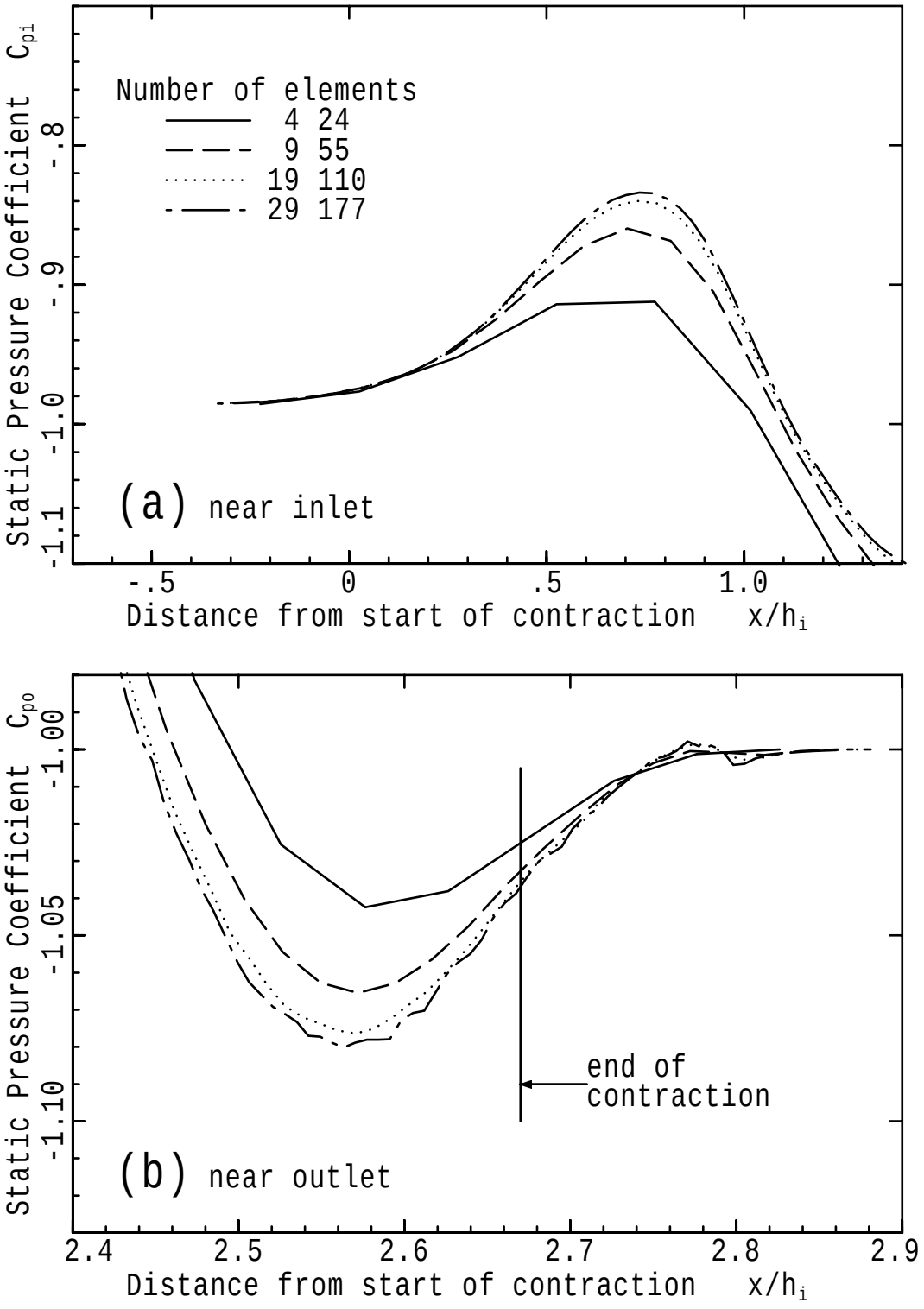

Figure 4.14: Static pressure coefficient near the wall of the two-dimensional contraction: the effects of changing the number of finite elements in the model (a) near the start of the contraction and (b) near the contraction outlet.

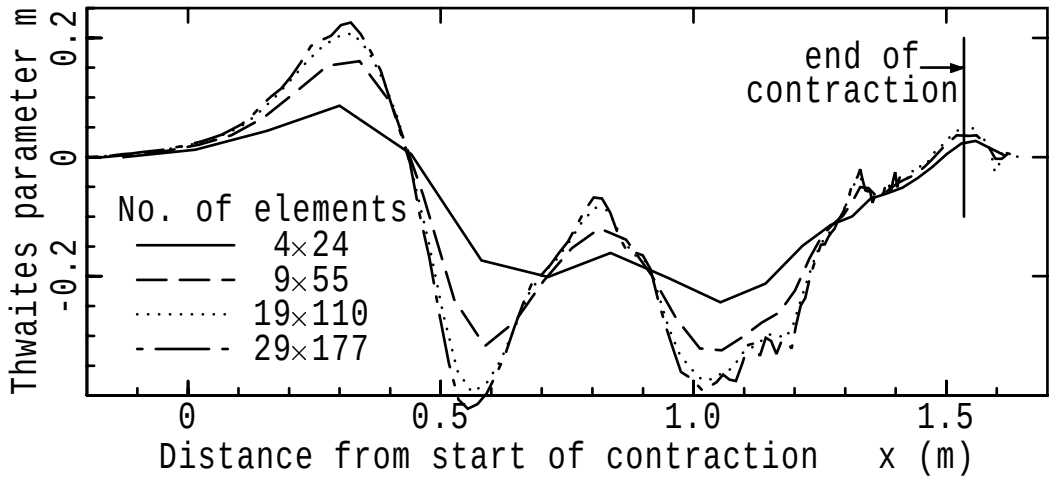

Figure 4.15: Thwaites parameter m in the two-dimensional contraction: effects of changing the number of finite elements. The scale is the same as in Figure 4.12(b).

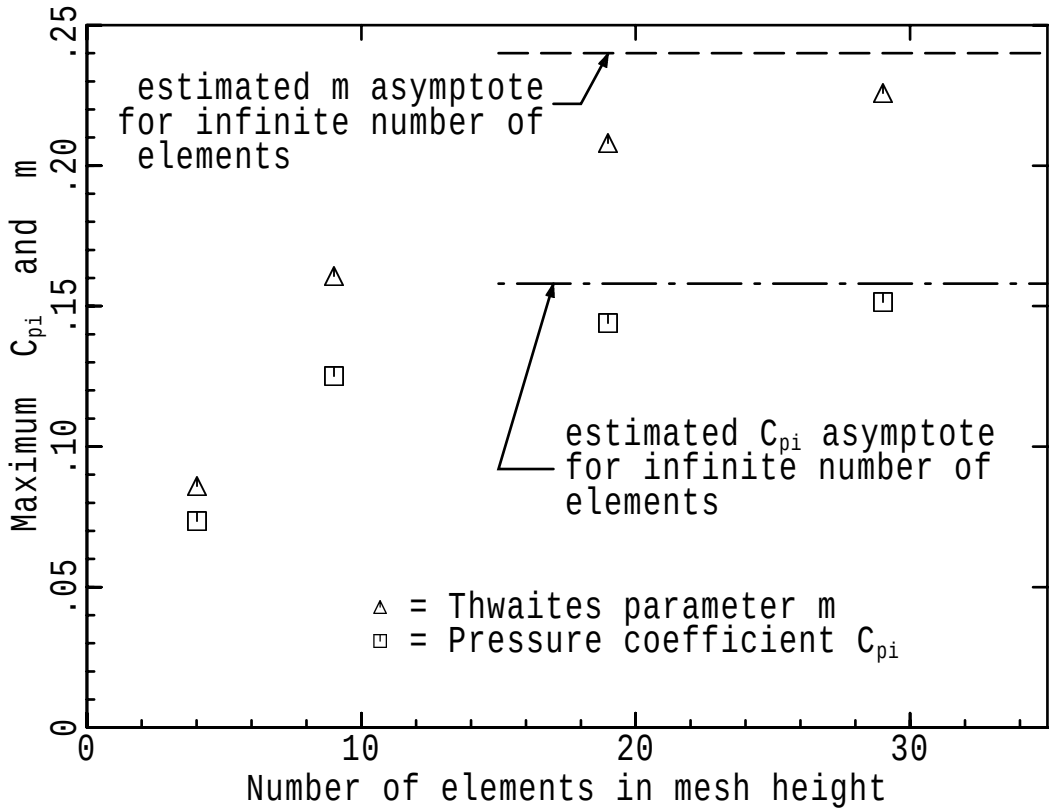

Figure 4.16: Convergence test : Maximum wall-pressure coefficient C_{pi} and maximum Thwaites parameter m as functions of the number of mesh elements.

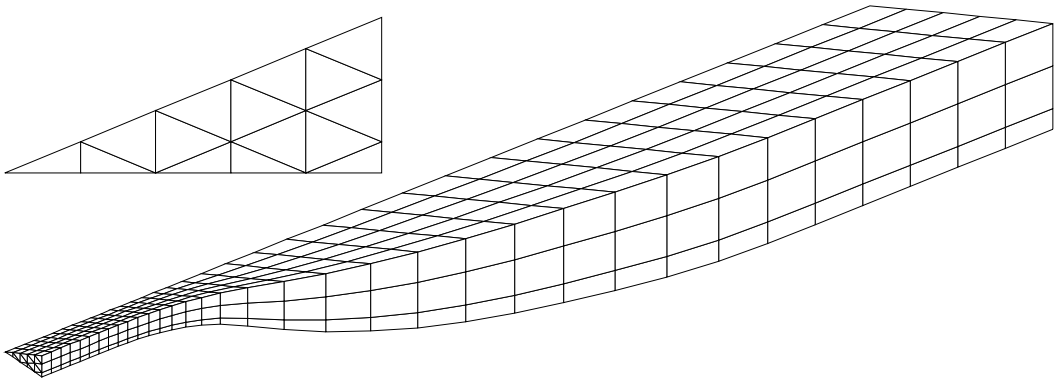

Figure 4.17: Oblique and end views of the finite element model for the contraction with an octagonal cross-section geometry. For clarity the diagram shows a mesh with only 15 elements in each cross-section. Results were obtained from a model with 66 elements in each cross-section.

dimensional finite-element calculations to estimate the accuracy of the results for the three-dimensional contraction. However, this uncertainty is acceptable because it is expected to be much smaller than the effect of changing the number of mesh elements from 9×55 to infinity. On the basis of the results shown in Figure 4.16, where the maximum Thwaites parameter obtained for a 9×55-element mesh is only 67% of the value estimated for an infinite number of mesh elements, it would be reasonable to expect near-inlet separation in the three-dimensional contraction wherever the Thwaites parameter calculated from the results of the finite-element modelling (Figure 4.12(b)) is in excess of 0.06.

4.7 Octagonal cross-section geometry

Modelling of flow in a contraction with a square cross-section geometry indicates that there is significant lateral variation in boundary-layer thickness and that adverse pressure gradients are capable of initiating separation over a large surface area near the corners at the start of the contraction. With the change from a square to an octagonal cross-section, the corners regions, which contain most of the surface where separation can begin, are eliminated. The finite element mesh for the octagonal contraction is wedge-shaped and is built of prismatic elements. This wedge-shaped mesh is shown in Figure 4.17. The contraction ratio is unchanged at 25:1.

4.7.1 Static pressure distribution at the wall

The distributions of static wall pressure near the start and outlet of the contraction are shown in Figure 4.18. The lateral pressure variation in the octagonal contraction is five times smaller than in the

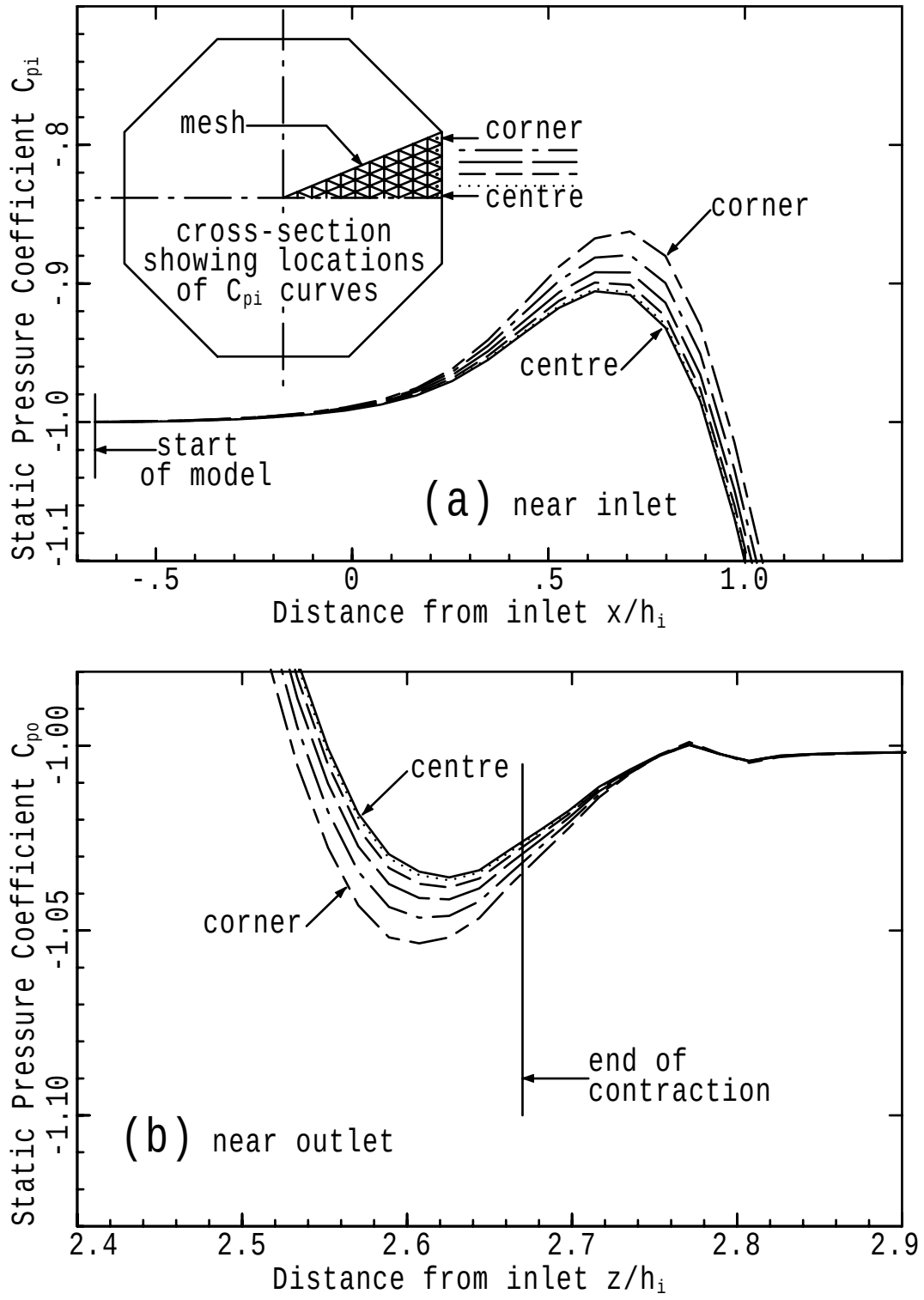

Figure 4.18: Static pressure coefficient near the wall of the octagonal contraction (a) near the start of the contraction and (b) near the contraction outlet. The pressure is calculated at the centroids of the elements adjacent to the contraction surface. The location of the centroids for each curve is indicated by a ● in the cross-section view of the contraction. The scale is the same as in Figure 4.11.

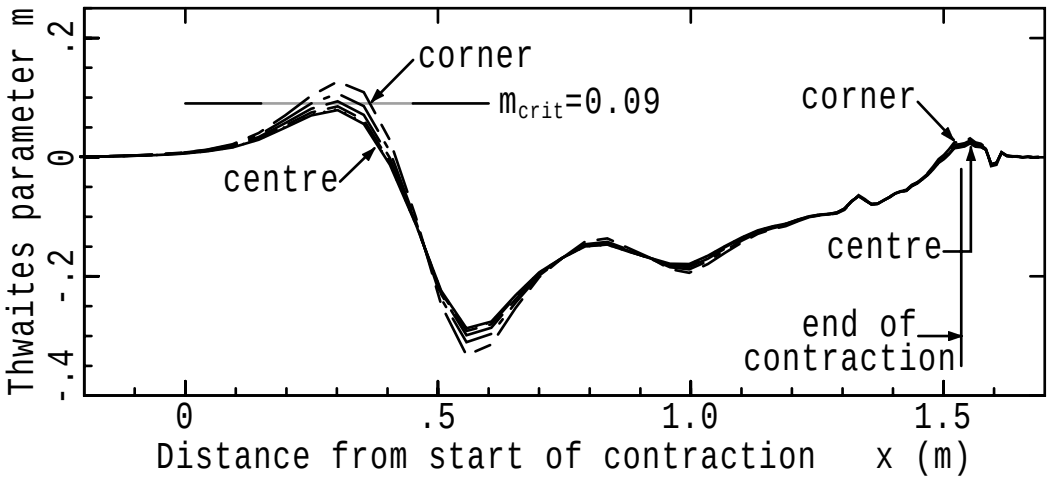

Figure 4.19: Thwaites parameter *m* for the octagonal contraction. The location of each curve is indicated by a • in the cross-section view of Figure 4.18(a). The scale is the same as in Figure 4.12(b).

square contraction. As the number of sides on a cross-section is increased, the cross-section becomes more nearly circular and, with the tendency towards axial symmetry, the three-dimensionality of the flow becomes less pronounced. Even without a Thwaites analysis it is clear that the reduced three-dimensionality of the flow has significantly reduced the maximum Thwaites parameter, although perhaps not enough to prevent separation. When averaged across the width of the surface, the maximum pressure coefficients for square and octagonal contractions are almost the same ($\langle C_{\text{pi,max,square}} \rangle = 0.875$ and $\langle C_{\text{pi,max,octag}} \rangle = 0.890$ respectively). In order to reduce this laterally-averaged pressure it is necessary to improve the contraction profile rather than to increase the cross-sectional symmetry.

4.7.2 Thwaites analysis

The boundary-layer momentum thickness calculated for the octagonal contraction is of similar magnitude to that calculated for the square contraction, except that the variation across the width of the surface, like the variation in static pressure, is much smaller. Figure 4.19 shows that the Thwaites parameter, *m*, also has this characteristic. The maximum value of the parameter *m*, $m_{\text{max}} = 0.127$, exceeds the critical value of 0.09, but it is less than the maximum of 0.224 calculated for the square contraction. Clearly, changing the cross-section of the contraction from square to octagonal cannot be expected to prevent separation of the boundary layer near the start of the contraction, especially as no allowance has been made for the modelling error of 33% which is indicated by the convergence test of Section 4.6.

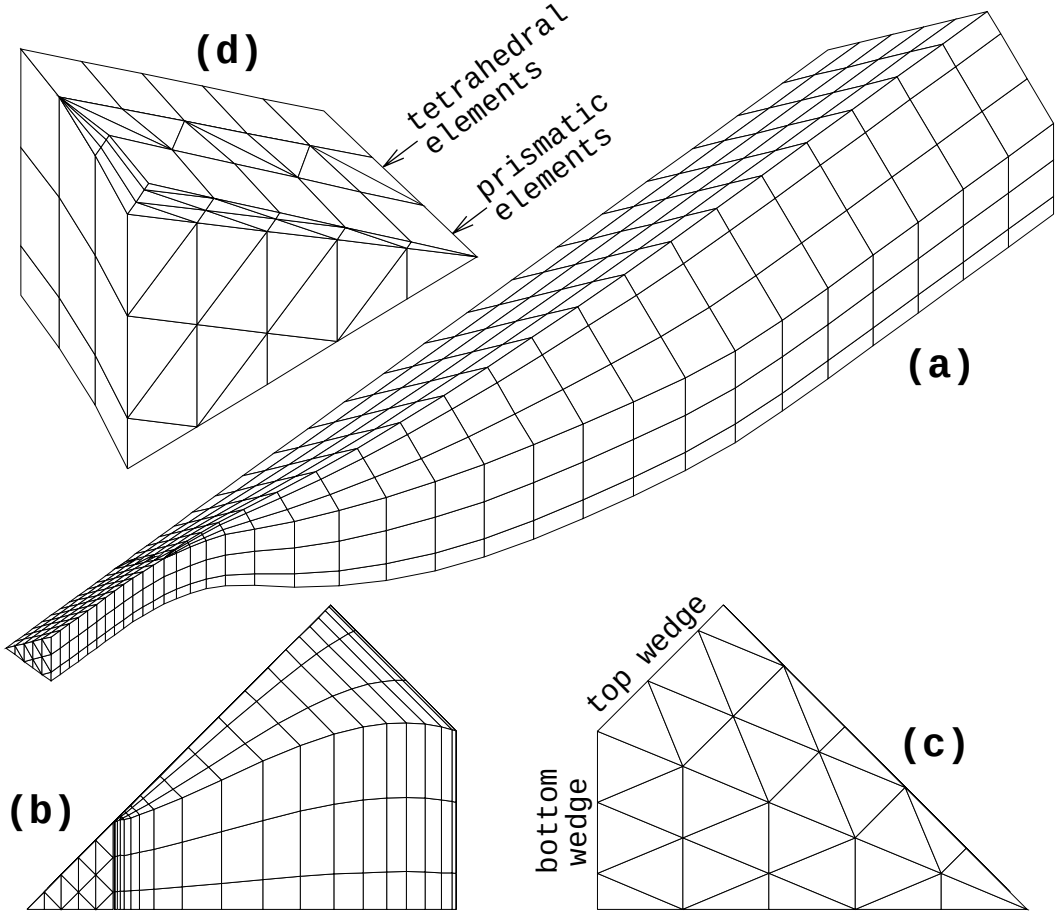

Figure 4.20: Finite element mesh for an octagonal-to-square contraction: mixed taper rule. (a) oblique view; (b) view from outlet end; (c) view from inlet end; (d) oblique view showing tetrahedral elements which terminate the downstream end of the top wedge.

4.8 Octagonal-to-square cross-section geometry

4.8.1 The finite element model

The investigation reported in the previous section shows the extent to which an improvement in contraction performance can be obtained by changing the cross-section of the wind-tunnel inlet from square to octagonal. The absence of boundary-layer separation near the square outlet makes it possible to perform a transition from octagonal-to-square cross-section entirely within the contraction. As shown in Figure 4.20, the model for a contraction which incorporates this transition is formed from two wedges, one lying on top of the other. At the inlet, the cross-section of the top wedge is equal in size to that of the bottom wedge. However, near the outlet, the cross-sectional area of the top wedge tapers to such a small value that it is truncated well short of the outlet. In order to provide as smooth a transition

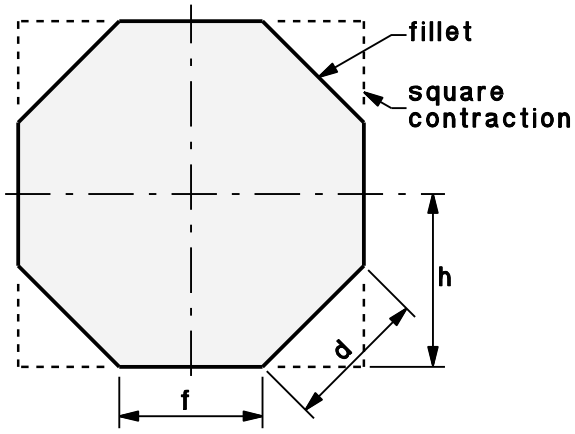

Figure 4.21: Conversion from square to octagonal cross-section in the wind-tunnel contraction.

to square cross-section as possible, the downstream end of the top wedge is terminated by rows of tetrahedral elements (Figure 4.20(d)).

In practice, conversion to an octagonal wind tunnel inlet was achieved by building a fillet in each corner of the original square cross-section. The transition to a square cross-section at the contraction outlet was produced by tapering the width *d* of the corner fillets (Figure 4.21) to zero. Potential flow solutions were obtained for three different kinds of taper, each with a different finite element geometry:

fillet taper, where the diagonal width of the fillet is a linear function of the cross-section height;

floor taper, where the width of the floor of the contraction is a linear function of the cross-section height;

mixed taper, which is a combination of the other two tapers, producing a fillet taper near the contraction inlet and a floor taper near the contraction outlet.

A more detailed description of the tapering methods is provided in Appendix G.

4.8.2 Static pressure distribution on the wall

The distributions of wall pressure near each end of the contraction and for each of the taper methods are presented in Figures 4.22 and 4.23. Near the start of the contraction the pressure distribution for the mixed taper is indistinguishable from the distribution for the fillet taper, and near the outlet it is indistinguishable from the distribution for the floor taper. These comparisons are also true for the Thwaites pressure gradient parameter (Section 4.8.3). On the vertical and horizontal surfaces the

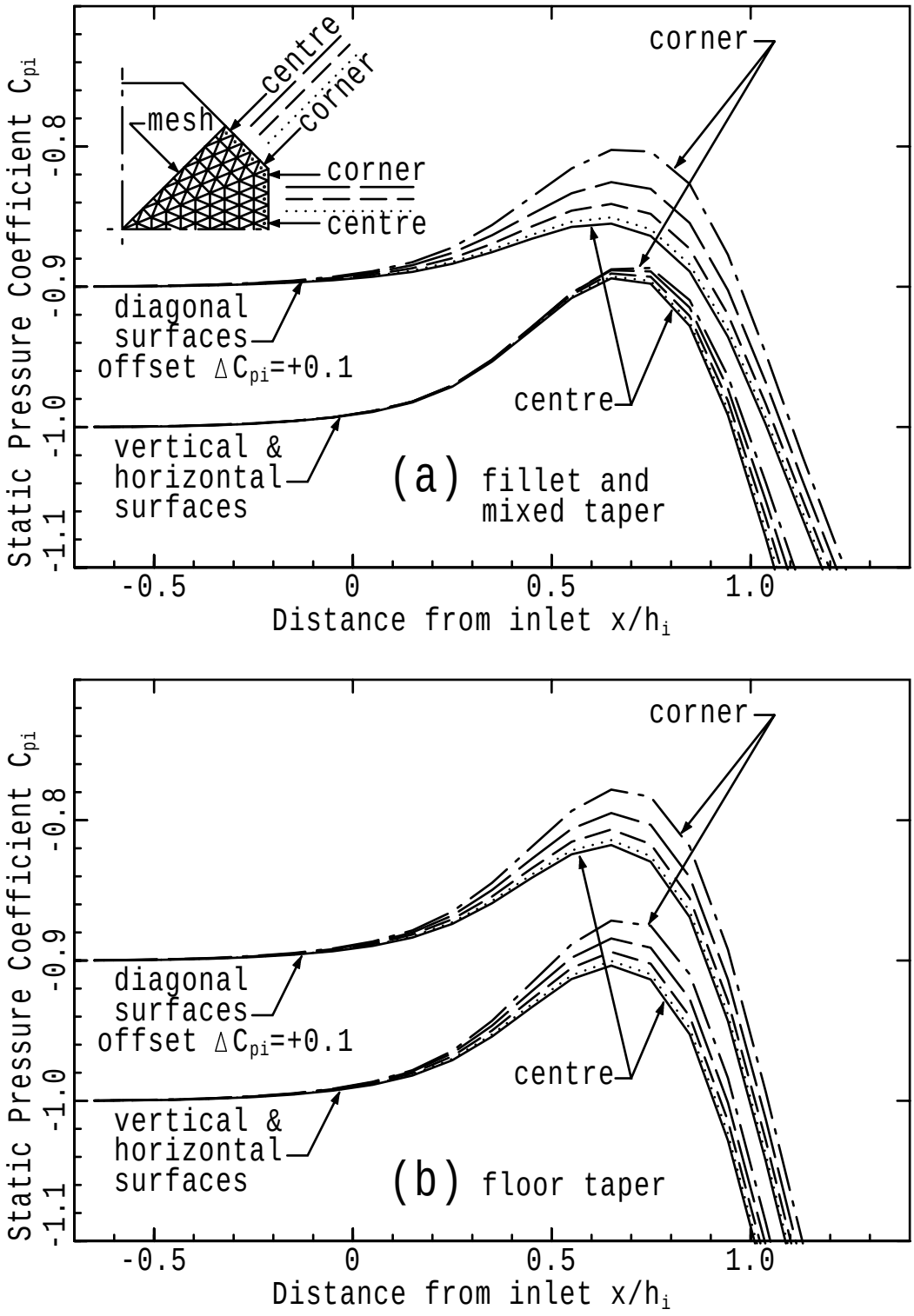

Figure 4.22: Wall static pressure coefficient near the start of the octagonal-to-square contraction (a) fillet and mixed taper rules and (b) floor taper rule. Data for the diagonal surfaces are displaced upward by $\Delta C_{pi} = +0.1$. The pressure is calculated at the centroids of the elements adjacent to the contraction surface. The location of the centroids for each C_{pi} curve is indicated by a • in the cross-section quadrant of the contraction. The scale is the same as in Figure 4.11(a).

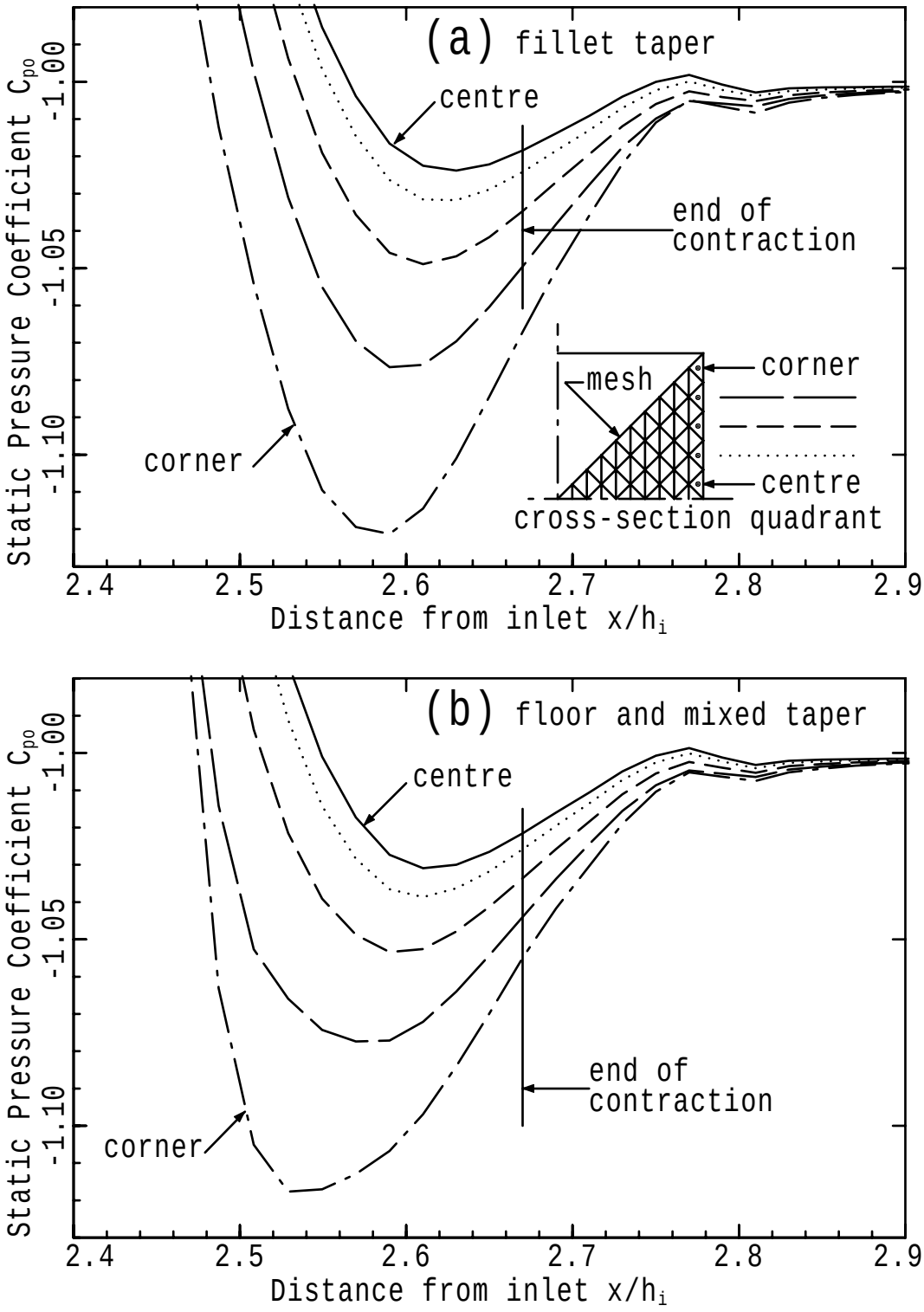

Figure 4.23: Wall static pressure coefficient near the outlet of the octagonal-to-square contraction (a) fillet taper rule and (b) floor and mixed taper rules. The location of the centroids for each C_{po} curve is indicated by a • in the cross-section quadrant of the contraction. The scale is the same as in Figure 4.11(b).

lateral average of the peak pressure is, for all three tapers, the same as for the octagonal contraction. However, most other details vary from case to case. For the floor-taper rule, the pressure distribution near the contraction inlet is nearly the same as for the octagonal contraction and, on all surfaces, the maximum pressures are higher than for the other two tapers. For the fillet and mixed tapers, the lateral pressure variation on the vertical and horizontal surfaces is very small, and so indicates the presence of a nearly two dimensional flow. On the diagonal surfaces the lateral pressure variation is much larger, but the pressure rise is everywhere less than on the adjacent walls.

Near the contraction outlet, the magnitude of wall static pressure variations is almost independent of the taper rule (Figure 4.23) but, by changing from a fillet taper to a mixed or floor taper, the location of the pressure minimum is moved upstream so that the adverse pressure gradients are reduced.

4.8.3 Thwaites analysis

Values of the Thwaites parameter for contractions with a transition from octagonal to square cross-section are shown in Figure 4.24. Without allowing for error in the modelling of the flow, these calculations indicate that near-inlet boundary-layer separation would be expected on all surfaces except the diagonal surfaces of the fillet and mixed taper contractions. The fillet and mixed taper rules produce a lower maximum Thwaites parameter near the start of the contraction ($m_{\max} = 0.101$) than the floor taper rule ($m_{\max} = 0.120$). The peak Thwaites parameter near the exit is slightly less for the floor and mixed taper rules ($m_{\max} = 0.0478$) than for the fillet taper rule ($m_{\max} = 0.0564$).

4.8.4 Selection of the taper formula

The fillet-taper rule is designed to minimise the peak value of Thwaites parameter near the start of the contraction, and so also produces a nearly two-dimensional flow on the vertical and horizontal surfaces in this region. With the floor-taper rule it is possible to reduce slightly the effect of adverse pressure gradient near the outlet, but at the cost of a more adverse wall-pressure gradient near the other end of the contraction. The mixed taper retains the approximately optimal near-inlet behaviour of the fillet taper while also taking advantage of the slightly better performance of the floor taper near the outlet.

4.9 Modification of the contraction profile

The work described earlier in this chapter has indicated that the performance of the initially square wind-tunnel contraction could be improved significantly by converting the inlet cross-section to a regular octagon and by tapering the width of the diagonal surfaces to zero within the contraction. At the low

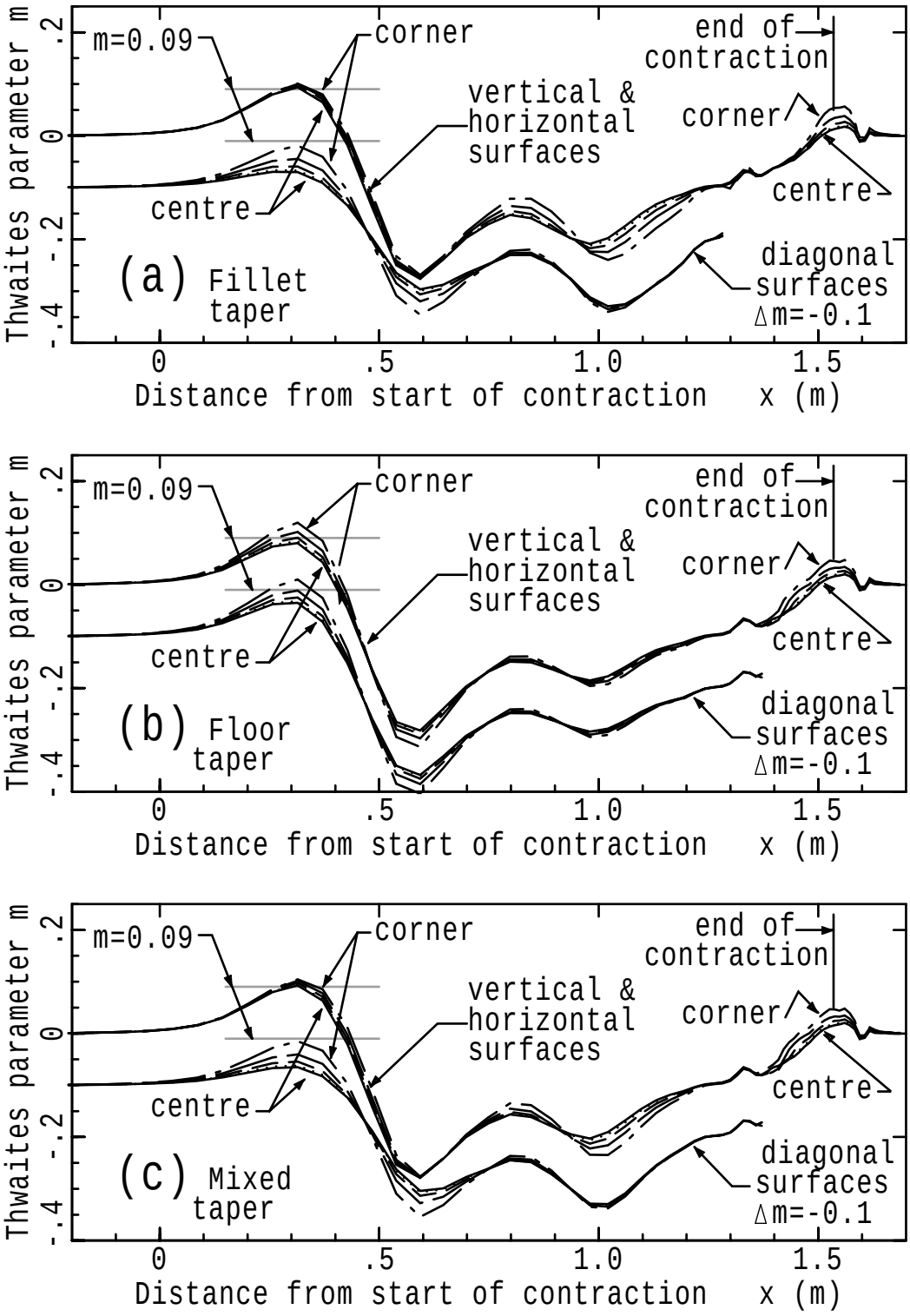

Figure 4.24: Thwaites parameter m for the octagonal-to-square contraction; (a) fillet taper; (b) floor taper; (c) mixed taper. Data for the diagonal surfaces are displaced downward by $\Delta m = -0.1$. The location of each curve is indicated by a ● in the cross-section quadrant in Figure 4.22(a).

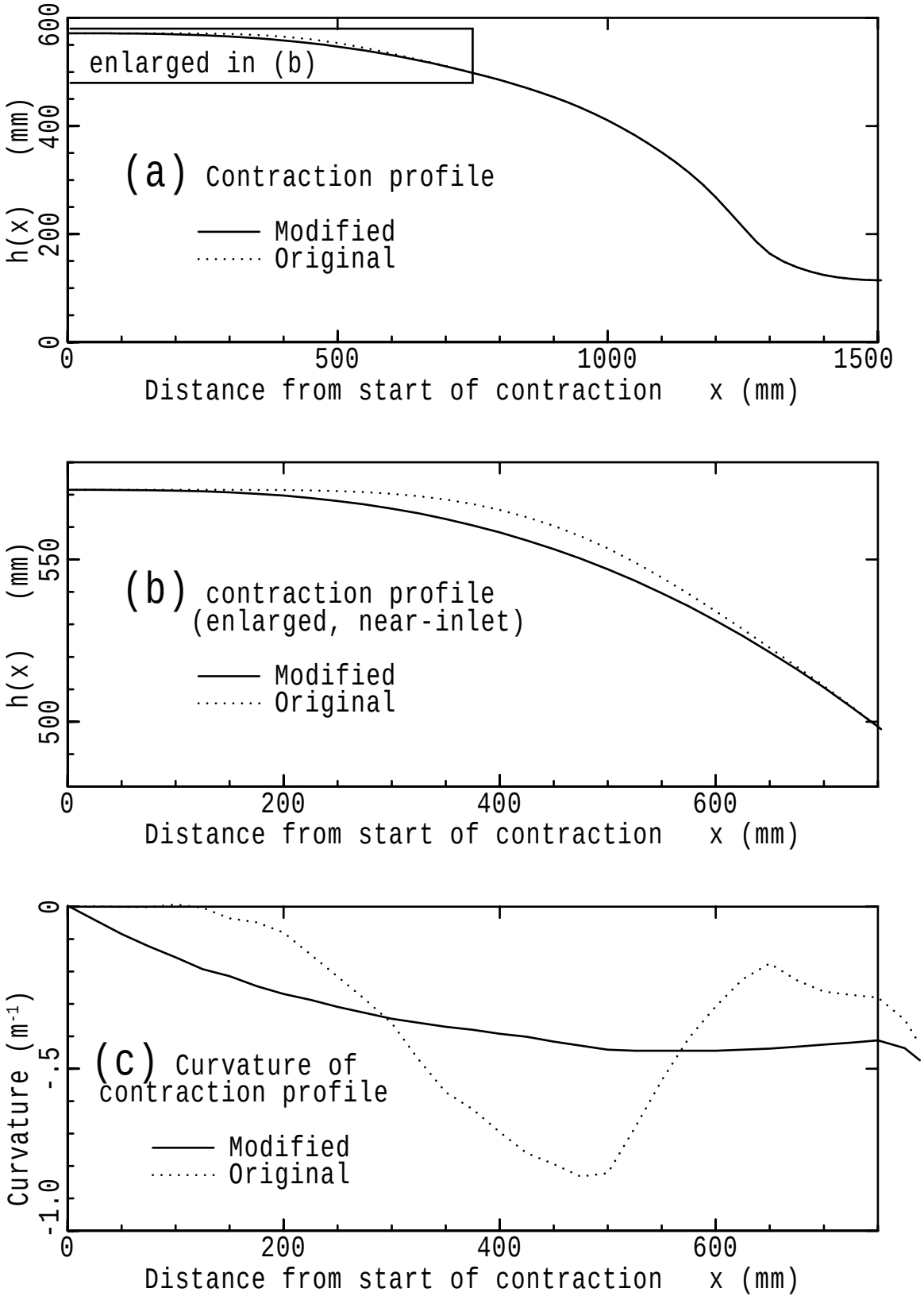

Figure 4.25: Comparison of the original and modified contraction profiles; (a) contraction profiles (true shape); (b) enlarged near-inlet contraction profiles; (c) near-inlet profile curvature.

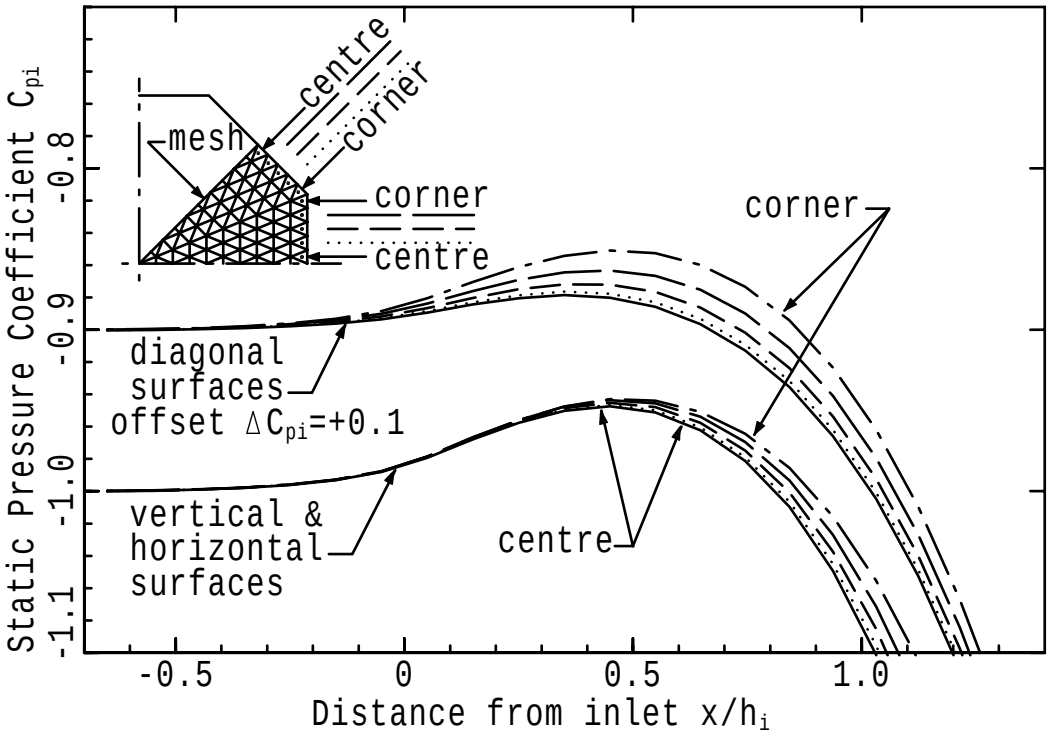

Figure 4.26: Wall static pressure coefficient for the modified contraction profile near the start of contraction. Results for the diagonal surfaces are displaced upward by $\Delta C_{pi} = +0.1$. The location of the centroids for each C_{pi} curve is indicated by a • in the cross-section quadrant of the contraction.

flow speeds required, however, this improvement would be insufficient to entirely prevent boundary-layer separation near the start of the contraction. Complete avoidance of separation therefore dictated a modification to the near-inlet region of the contraction profile. In changing the contraction profile, the main objectives were to minimise the axial variations in profile curvature and to maintain continuity of slope and curvature at the intersections of the modified and original profiles. The curve selected for the new contraction profile, which is drawn in Figure 4.25(a), is a quartic polynomial. Figure 4.25(c) shows that curvature in the first 800 mm of the modified contraction decreases almost monotonically.

4.9.1 Static pressure distribution on the wall

The final potential flow simulation was performed for the octagonal-to-square contraction using the modified profile shown in Figure 4.25(a) and the mixed taper rule. The wall-pressure distribution near the outlet of the modified contraction is the same as for the original mixed taper contraction (Figure 4.23(a)), but the pressure rise near the inlet (Figure 4.26) is only half as large. This is accompanied by almost the same reduction in lateral pressure variation. The fact that such a large improvement

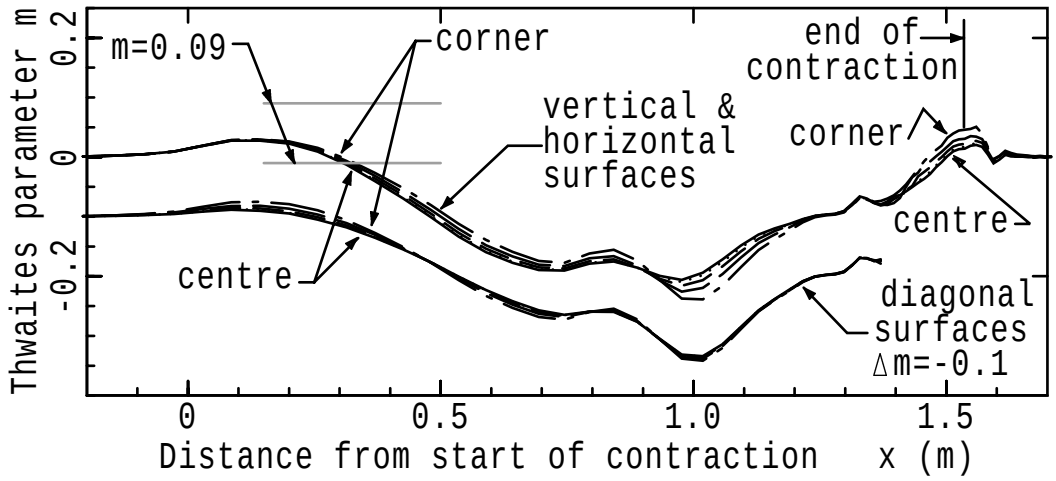

Figure 4.27: Thwaites parameter m for the modified contraction profile. Results for the diagonal surfaces are displaced downward by $\Delta m = -0.1$. The location of each curve is indicated by a • in the cross-section quadrant in Figure 4.26. The scale is the same as in Figure 4.12(b).

is achieved with such a small alteration to the contraction profile indicates the importance of profile curvature in determining the flow conditions near the wall.

4.9.2 Thwaites analysis

Figure 4.27 shows that, in comparison with the unmodified mixed taper rule (Figure 4.24), changing the contraction profile reduces the maximum Thwaites parameter m near the inlet by a factor of 3.4 to 0.030. This improvement is so great that the overall maximum value of m ($m_{\max} = 0.0508$) then occurs in the region of velocity overshoot near the contraction outlet. The alterations to the contraction profile have almost no measurable effect on the flow in the downstream half of the contraction. The convergence tests in Section 4.6 indicate that the actual peak value of the Thwaites parameter could be up to 50% higher than the values derived from the finite element modelling. Even with this "factor of safety" there is a wide margin between the critical value $m = 0.09$ and the peak Thwaites parameter in the inlet region of the contraction. Laminar boundary-layer separation is responsible for the regions of separated flow illustrated in Figure 4.5, and so was believed to be responsible for the velocity fluctuations in the exit boundary layer of the original contraction. The results from the numerical model strongly suggest that separation would not occur in the octagonal-to-square contraction with a modified profile and mixed taper rule.

4.10 Comments on flow in contractions

As already indicated in Section 4.3.2, the boundary conditions applied at the open ends of a finite element or finite difference mesh representing a wind tunnel contraction are usually to some extent arbitrary, because the actual velocity and pressure fields at the inlet and outlet are unknown. If the traditional approach of specifying uniform velocity or velocity potential at inlet and outlet is adopted, it is necessary to add a short length of straight parallel duct to the ends of the contraction model. These extensions are required to prevent the artificial inlet and outlet boundary conditions from influencing the solution in the regions of adverse pressure gradient. Morel (1975), who used extensions with a length of 0.7 local duct radii, found that the use of an outlet extension improved the uniformity of the exit flow, and so considered the outlet extension to be an integral part of the contraction.

The effect of increasing the axial symmetry of a contraction, e.g. changing from a square to an octagonal cross-section, is to reduce the lateral variation of the velocity and pressure fields near the contraction surfaces without significantly changing the lateral averages of these flow variables. The consequent reduction of local adverse pressure gradients might sometimes be sufficient to eliminate laminar boundary layer separation. While a circular cross-section geometry produces optimal flow, it may be difficult to make and, in such cases, an octagonal cross-section shape becomes a reasonable compromise between degree of axial symmetry and ease of construction. However, axial symmetry is unlikely to compensate for a poor choice of contraction profile.

The results from Section 4.9 demonstrate that the curvature of the wall is one of the most important factors determining the wall-pressure distribution near the ends of the contraction. By making an apparently small change to the contraction profile focussed on minimising the variation of wall curvature, it is possible to improve (that is, reduce) the peak Thwaites parameter ($m_{\max}$) by a factor of more than three. The similarity between the wall-pressure distributions for the two-dimensional contraction, where contraction ratio is 5 (Figure 4.14(a)), and the wall pressure for the octagonal contraction, where contraction ratio is 25 (Figure 4.18(a)), indicates that the pressure distribution is influenced much more strongly by wall curvature than by contraction ratio.

4.11 Summary and interpretation of finite element modelling

Preceding sections of this chapter have described how the general purpose finite-element package Ansys was used to model the flow in the wind-tunnel contraction as a potential flow. Small programs were used to prepare the model specifications for Ansys and to process the flow-field results. The laminar boundary layer in the contraction was assumed to be substantially two-dimensional and its development was estimated by the Thwaites method. Convergence tests with a two-dimensional model of the

contraction indicate that the peak Thwaites parameter was probably underestimated by about 33%. Increasing the number of mesh elements from 9×9×55 to 19×19×110 would have reduced the likely error to about 13%, but this worthwhile improvement in accuracy was prevented by data storage and Ansys “wave front” limitations.

However, despite its limitations, the numerical analysis of the existing wind-tunnel contraction reveals much more detail than the anemometry experiments. For example, the adverse pressure gradients are shown to be much more severe in the corners of the square contraction than near the centre of the surfaces. The square cross-section shape produces a significantly three-dimensional flow with adverse pressure gradients which are much larger than would be present in an axisymmetric contraction. Because the boundary layer in the contraction is laminar, it is quite susceptible to separation by an adverse pressure gradient, and application of the Thwaites method clearly shows that such a separation is to be expected near the inlet of the contraction. Anemometry experiments indicate that regions of separated flow formed in this way tend to oscillate in size and position, and so cause the thickness of the downstream boundary layer to vary slowly with time.

By changing the cross-section of the contraction from square to regular octagonal, the calculated maximum value of the Thwaites parameter is reduced by about 50%. This beneficial effect is entirely due to the increase in axial symmetry, but it is not sufficient to avoid separation. Both experimental evidence and the results of numerical simulation indicate that separation occurs only near the inlet, and so the necessary transition to the square cross-section of the test section is incorporated into the contraction. Potential flow simulations were performed with three different types of octagonal-to-square transition:

(1) the fillet taper, where the width of the diagonal surfaces is is a linear function of the cross-section height,
(2) the floor taper, in which the width of the floor surface is a linear function of the cross-section height, and
(3) the mixed taper, which is the same as the fillet taper at the contraction inlet and is the same as the floor taper at the outlet.

The simulation results indicate that the taper rule can be used to exercise some control over the wall-pressure distribution near the start of the contraction. The flow in the regions of adverse pressure gradient at one end of the contraction appears to behave independently of the flow at the other end, and so, by using the mixed taper rule, advantageous features of both the fillet taper and the floor taper can be retained.

By combining the mixed taper rule for octagonal-to-square transition with a new contraction profile which considerably reduces the wall curvature (Figure 4.25), the maximum value of the Thwaites parameter near the start of the contraction is reduced to 0.03. This is so much lower than the critical value of 0.09 that boundary-layer separation would no longer be expected.

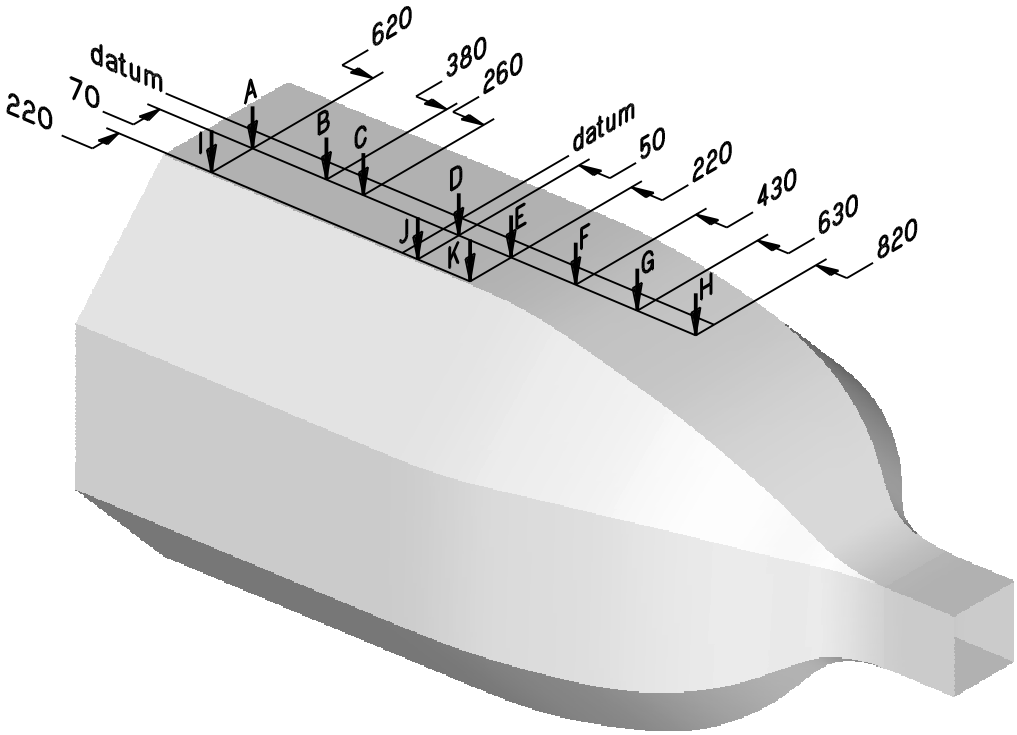

Figure 4.28: Probe locations used in the search for separated flow. Probe locations are indicated by downward-pointing arrows (⏚) labelled **A**–**K**. The datum for dimensions, which are in mm, is at the centre of the start of the contraction.

4.12 Experimental verification of simulation results

4.12.1 Construction of contraction modifications

Plywood fillets were placed in the corners of the square contraction to produce a regular octagonal cross-section at the start of the wind-tunnel contraction. This cross-section was carried upstream through the settling chamber, screens and honeycombs to the bell-mouth inlet of the wind tunnel. The fillets were tapered towards the contraction outlet in accordance with the mixed taper formula. The profiles of the vertical and horizontal surfaces of the contraction were then modified as shown in Figure 4.25 by the application of a fibreglass-epoxy filler.

4.12.2 Boundary-layer measurements in the modified contraction

After the alterations to the inlet, settling chamber and contraction were completed, boundary-layer “velocity” distributions were measured on the top surface of the settling chamber and contraction with

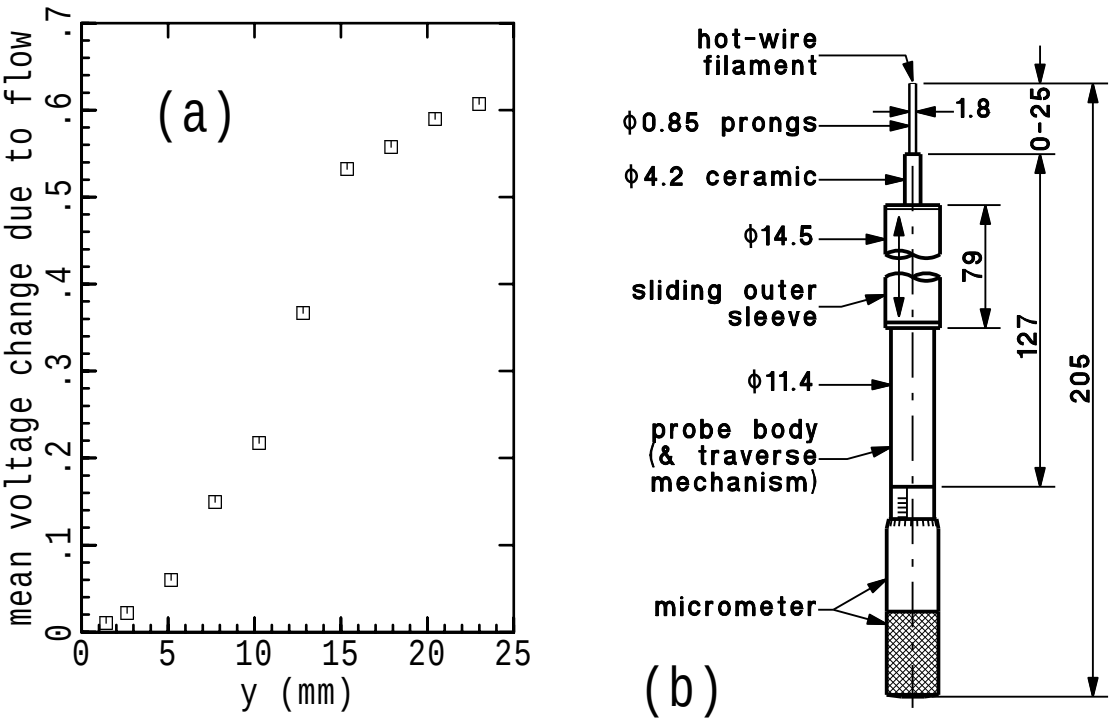

Figure 4.29: Hot-wire measurements in the near-inlet boundary layer of the modified contraction; (a) change in the time-averaged hot-wire signal due to the flow at location **D**. $U_0 \approx 3$ m/s, $x = 50$ mm, $z = 70$ mm. Note the distortion caused by wall-proximity effect when $y < 15$ mm. (b) the plug-mounted, micrometer-traverse probe.

an uncalibrated hot-wire probe. The locations of these measurements are illustrated in Figure 4.28. The purpose of this experiment was to search for boundary-layer separation near the start of the contraction.

Most results were obtained using the plug-mounted probe illustrated in Figure 4.29(b). In this probe the prongs extended directly from a plug installed flush with the wall. The length of the exposed prongs, and hence the distance between the hot-wire filament and the wall (y), was adjusted by turning a micrometer screw. Continuity of the wall surface and the precision of the micrometer adjustment made detection of classically separated flow much easier than with the probe arrangement described in Section 4.2. Unfortunately the measurements were affected by wall proximity and by "strain gauging" which was due to variation of the hot-wire tension with the changing length of the exposed prongs. The measurements at each y position are therefore presented in Figure 4.29(a) as the change in time-averaged C.T.A. output voltage caused by the addition of flow. When distance from the wall was reduced below 15 mm, the signal was significantly distorted by a decreased probe sensitivity which was due to wall-proximity effect. However, none of the signal distributions measured at any of the locations "**A**" to "**K**" in Figure 4.28, of which Figures 4.29(a) is an example, revealed any evidence of flow separation.

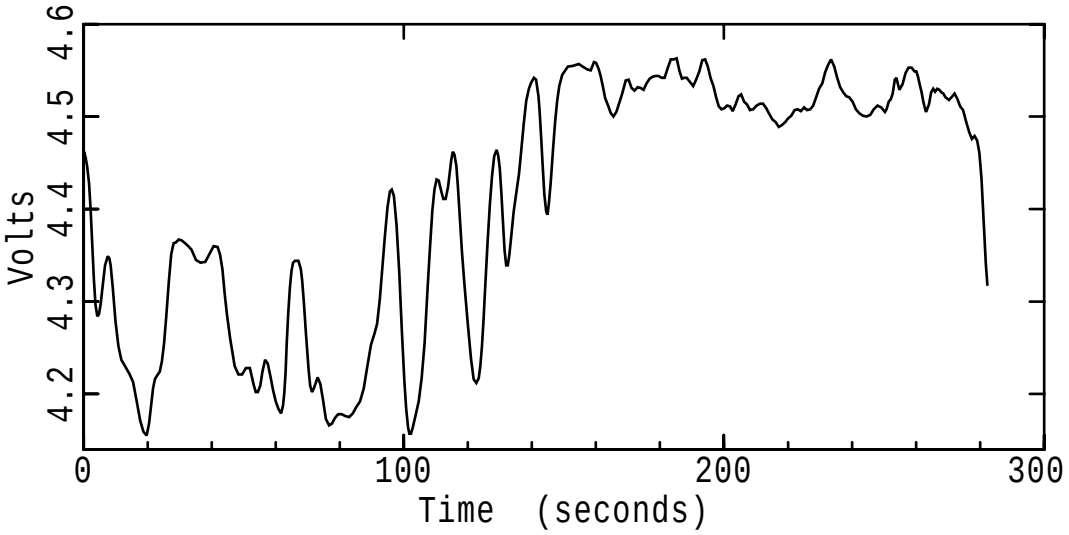

Figure 4.30: Signal from a hot-wire in the outlet boundary layer of the modified contraction. Distance from the wall is 4mm; $U_0 = 1.7$ m/s.

4.12.3 Boundary layer at the contraction exit

The earlier test, in which a signal was recorded from a hot-wire probe in the laminar boundary layer at the contraction exit (Section 4.1), was repeated for the modified contraction. Typical results from this test, such as that shown in Figure 4.30, were qualitatively similar to those obtained from the original square contraction (Figure 4.2). They demonstrate that removing the regions of near-stagnant separated flow from the concave surfaces of the contraction did not prevent the growth of velocity fluctuations within the laminar boundary layer.

It was then suggested that the persisting fluctuations within the laminar boundary layer might be due to the development of Görtler vortices on the concave surfaces of the contraction. Such vortices are the result of an instability arising from the opposition of radial centrifugal and pressure forces within the boundary layer. Görtler (1940) was the first to describe this instability mathematically and predict that it could generate an array of stationary counter-rotating streamwise vortices in the flow over a concave surface. The first direct experimental evidence for the existence of Görtler vortices was produced by Tani (1962) who measured the development of periodic spanwise air-speed variations in the flow over a concave surface. Other more recent investigations [Tani and Aihara, 1969, Bippes and Görtler, 1972, Aihara et al., 1984] have shown that, at sufficiently large distances downstream of the initial Görtler instability, the streamwise vortices develop either sinuous or horseshoe-vortex modes of unsteady secondary instability which then break down into boundary-layer turbulence.

A visualisation study of the laminar boundary layer at the contraction exit was performed in order

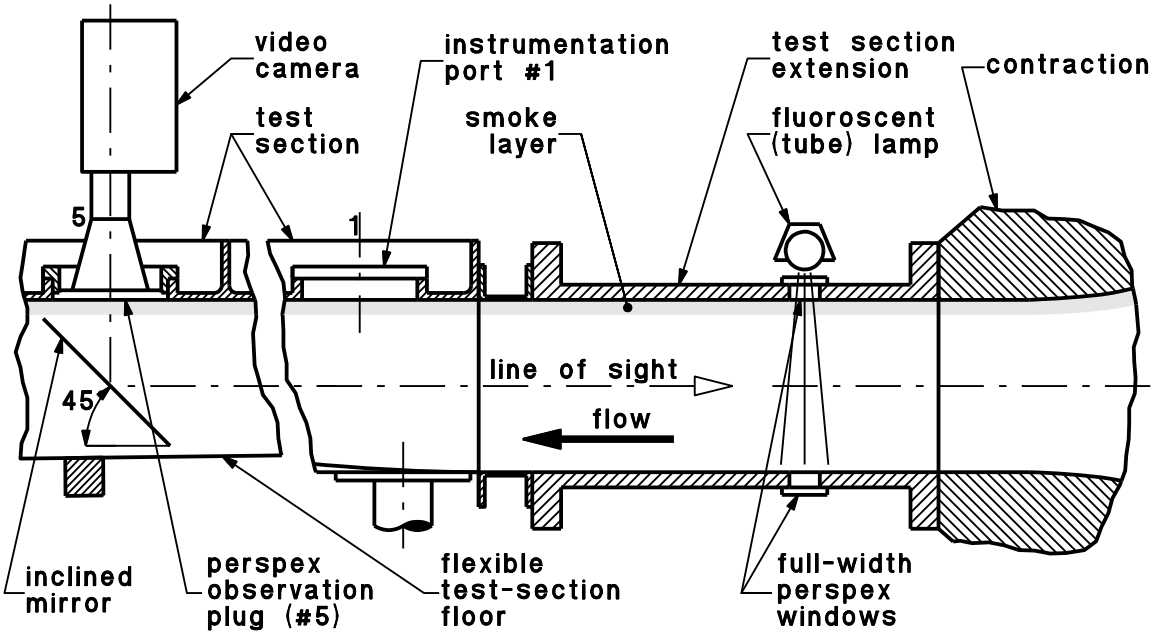

Figure 4.31: Experimental arrangement for flow visualisation of the laminar boundary layer emerging from the wind-tunnel contraction. Scale 1:10

to examine the possibility that the signal fluctuations in Figure 4.30 were caused by the presence of Görtler vortices within the contraction. As illustrated in Figure 4.31, the cross-section of the flow was illuminated through a window which occupied the entire width of the test-section extension. Oil-based smoke was introduced through a horizontal rake at the top surface of the wind-tunnel inlet and video images of smoke in the illuminated cross-section were recorded via an inclined mirror located 1.7 m downstream of the window. In order to prevent density differences from creating significant buoyant convection in the settling chamber and contraction, the smoke generator was driven with nitrogen rather than with carbon dioxide, and the flow rate of smoke was reduced appropriately as air speed in the wind tunnel was decreased. For the purpose of preparing diagrams, selected images were converted into computer bitmaps. Enhancement of any bitmap presented in this thesis was limited to adjusting brightness and contrast and, in some cases, equalizing the image grey-scale.

Results indicate that, at a free stream flow speed of 7.4 m/s (Figure 4.32(a)), smoke within the boundary layer is gathered into an array of nearly circular structures. These structures are occasionally observed to contain rotational features and behave in a manner consistent with that expected of Görtler vortices. Once formed, the circular structures are permanent rather than transient and are always confined within the laminar boundary layer. They wander laterally with a time-scale of oscillation which is compatible with velocity-signal fluctuations of the type shown in Figure 4.30. At lower speeds (Figure 4.32(b)) and with smoke introduced on the floor of the wind-tunnel inlet (Figure 4.32(c,d)), details

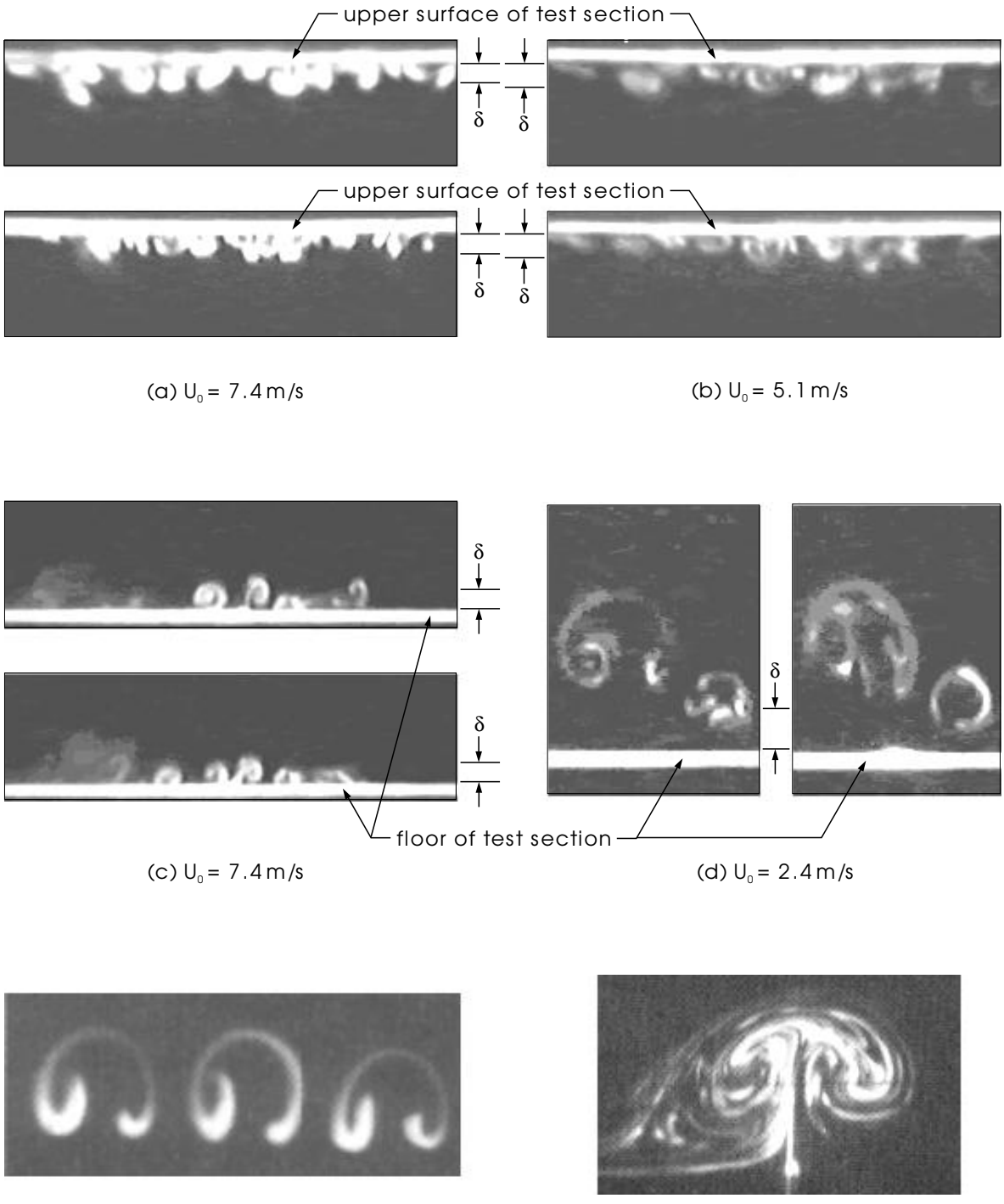

Figure 4.32: Structure of the laminar boundary layer emerging from the wind-tunnel contraction: cross-section views of smoke-marked features for three flow speeds (U_0). The dimension δ indicates the approximate boundary-layer thickness

of the smoke-filled structures are visible as the “mushroom” shapes which are characteristic of counter-rotating vortex pairs. These vortex pairs migrate or oscillate slowly within the vicinity of the surface. The results of this experiments may be compared with Figure 4.32(e) which is the flow visualisation image of a Görtler vortex-pair array observed by Aihara, Tomita and Ito (1984). The structure and motion of the vortex pairs in Figure 4.32(c) is similar to the structure and motion of Görtler vortex cross-sections observed by Peerhossaini and Wesfreid (1988) (Figure 4.32(f)).

At the lowest speed (Figure 4.32(d)) one of the vortex pairs can move away from direct contact with the surface, emerging from the laminar boundary layer and into the free stream flow. This indicates a stronger three-dimensional separation than is usually produced by Görtler vortices. Interpretation of this result is made more complicated by the additional observation that smoke-filled vortex-pair structures on the floor of the test section are further from the wall than vortex pairs on the upper surface, and so appear to have positive buoyancy. The presence of nitrogen, which is three percent less dense than air, as a medium for the smoke might therefore contribute significantly to the migration of a vortex-pair away from the wall and to the strength of three-dimensional separation in the contraction. A further investigation of three-dimensional separation by methods which introduce much smaller density gradients is described in Chapter 6.

The results of this experiment indicate the presence of Görtler instability within the boundary layer of the wind-tunnel contraction, and suggest that lateral movement of streamwise vortex structures is responsible for spatial and temporal variations in the laminar boundary-layer thickness. In principle Görtler instability does not occur if the Görtler number, defined as

$$G = \frac{U_0 \theta}{\nu} \sqrt{\frac{\theta}{R}} \tag{4.7}$$

for radius of curvature R, falls below a theoretical curve of neutral stability which is usually calculated as a function of spanwise wavelength. Many improvements to this theory have been published since the original investigations by Görtler (1941). One of the more recent [Hall, 1983] has shown that, in a developing boundary layer, the behaviour of the neutral stability curve is complicated by a dependence not only on streamwise location but also on the position and form of the initial disturbance. Solutions obtained by Floryan and Saric (1983) suggest that Görtler instability could be suppressed by a very carefully distributed suction through the concave surfaces of the contraction. However, results such as those of Hall (1983) indicate that the difficulties associated with successfully using suction in this manner are likely to be substantial, and so the preferred option is to remove the unsteady laminar boundary layer with a suction manifold located between the contraction exit and the test section of the wind tunnel.

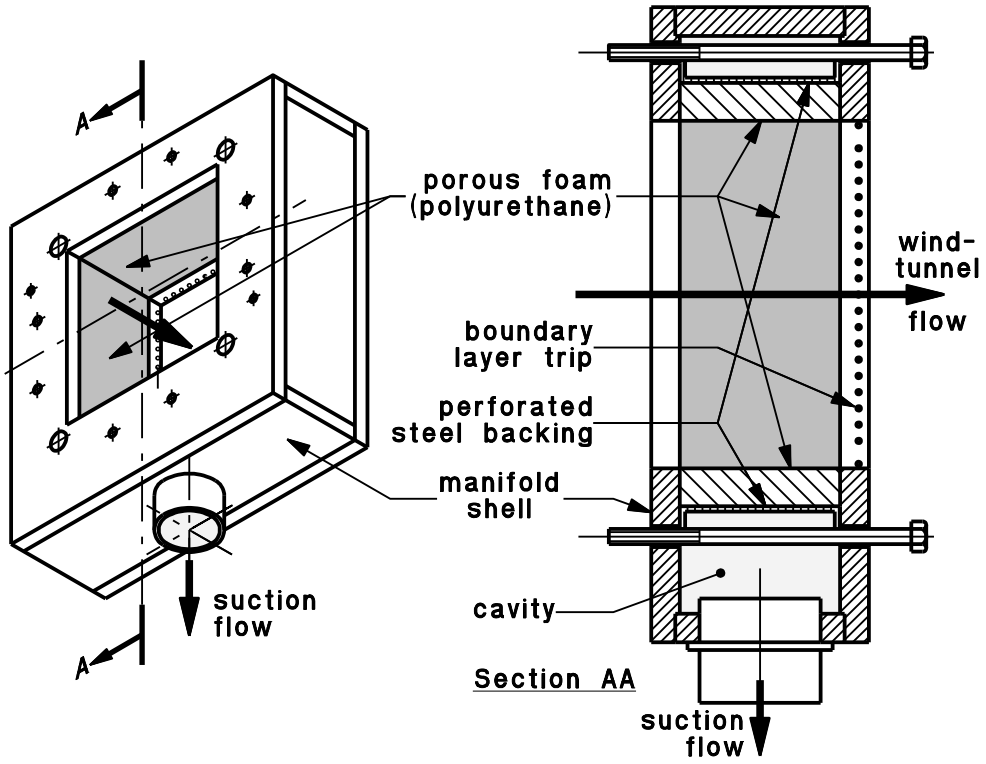

Figure 4.33: Suction manifold for removing the contraction-exit boundary layer and the final location of the boundary-layer trip. The scale of Section AA is 1:5.

4.13 Removal of the contraction-exit boundary layer

4.13.1 Design and construction of the suction manifold

The suction manifold, shown in Figure 4.33, consists primarily of a melamine-coated particle board[4] shell enclosing a porous polyurethane foam surface which has the same internal cross-section as the contraction exit and the test-section inlet. The manifold cavity is connected by 65-mm-diameter P.V.C. pressure pipe to the duct between the main drive compressor of the wind tunnel and the variable-area sonic choke (see Figure 2.1). The flow rate through the porous surface is controlled by a gate valve in the P.V.C. line and is monitored by measuring the static pressure drop in the long straight section of P.V.C. pipe running alongside the wind-tunnel test section. In order to obtain an almost uniform flow through the polyurethane foam, its porosity and thickness are chosen so that the flow resistance of the foam is at least an order of magnitude larger than that of the cavity in the suction manifold. Mechanical support for the foam blocks is provided by perforated steel sheet with a high open area ratio.

[4]Trade name: Laminex

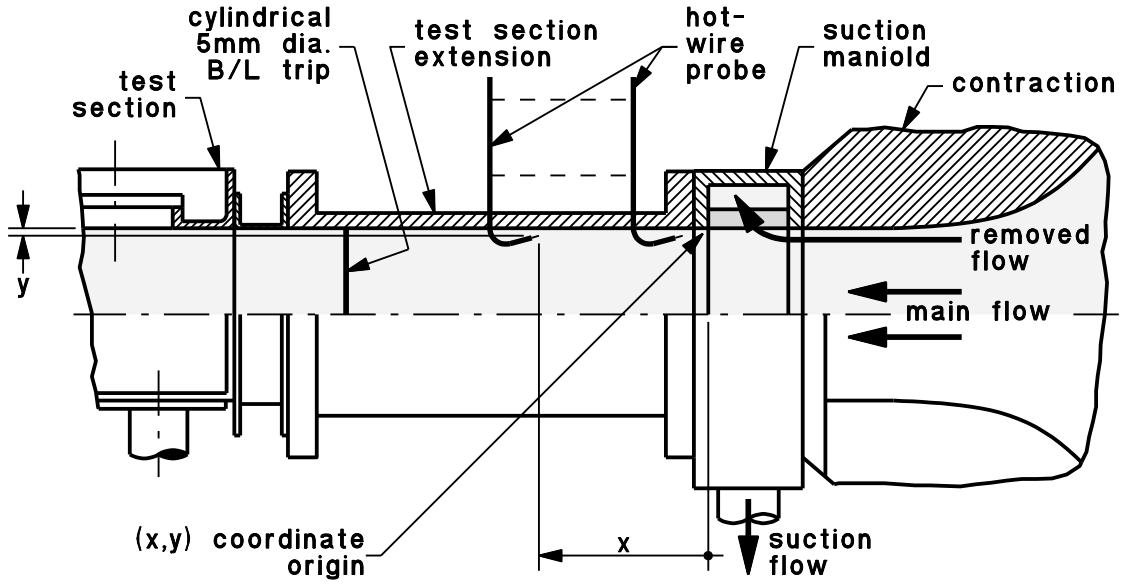

Figure 4.34: Initial installation of the suction manifold for calibration of suction flow rates. Half-section view: scale 1:10.

4.13.2 Calibration of the suction manifold

After installation of the suction manifold, it was necessary to determine the suction flow rate which was required to remove the unsteady contraction-exit boundary layer and then to examine the downstream redevelopment of the laminar boundary layer. For this investigation the suction manifold was placed between the contraction and the test-section extension (Figure 4.34). An uncalibrated hot-wire probe was located 15 mm downstream of the porous surface and 2 mm from the wall. In the initial trials the only measure of suction flow rate was to count the number of turns applied to the hand-wheel of the gate valve. The results of these tests, of which Figure 4.35(a) is a typical example, appeared to demonstrate that removal of the contraction exit boundary layer reduced the velocity fluctuations in the test-section boundary layer to the level of the background noise. However, when the probe was placed further downstream, the presence of new velocity fluctuations was revealed. Signal distributions such as in Figure 4.35(b) showed that, like the fluctuations originating from within the contraction, these existed only within the laminar boundary layer, but they had a smaller amplitude. They also had a much shorter characteristic time scale. Additional measurements showed that velocity fluctuations were present even within the extremely thin boundary layer 15 mm downstream from the porous surface, and that they grew in amplitude as they were carried downstream.

The mechanism responsible for generating the laminar fluctuations downstream of the suction manifold is thought to be similar to the Görtler-type laminar instability mechanism which produces streamwise

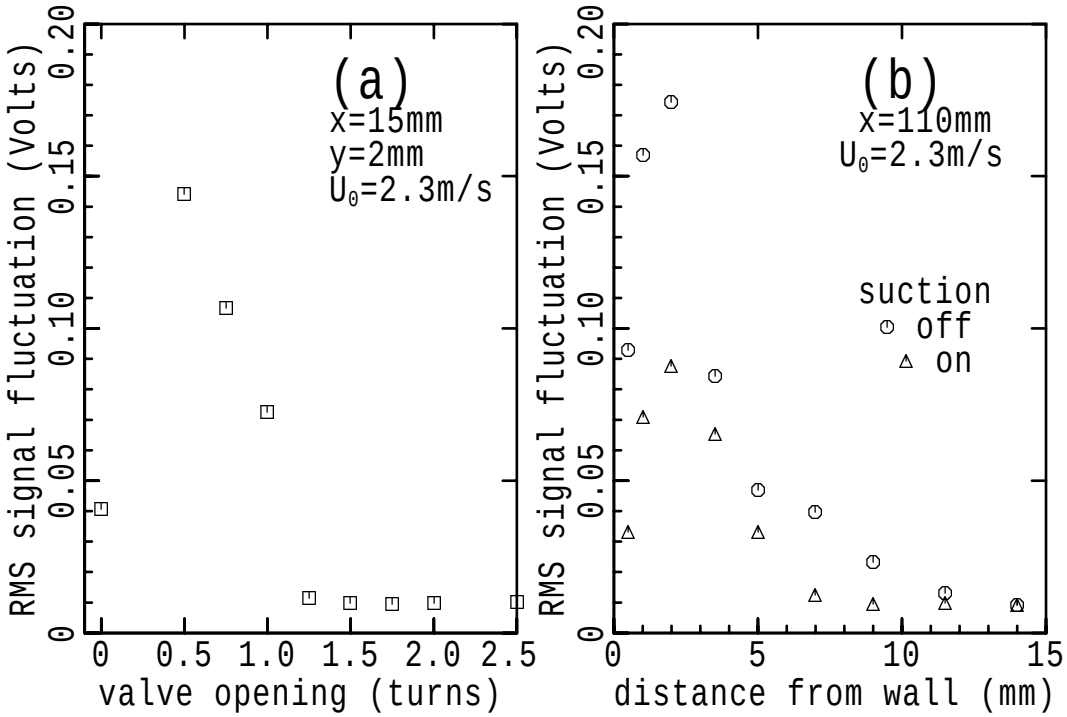

Figure 4.35: R.m.s. of signal fluctuation from a hot-wire probe in the laminar boundary layer downstream of the suction manifold for a free stream speed of $U_0 = 2.3$ m/s; (a) as a function of gate valve opening, with the hot-wire located $x = 15$ mm downstream from the porous surface and $y = 2$ mm from the wall; (b) measurements distributed over thickness of the boundary layer, showing the effect of "1.75 turns" of suction, $x = 110$ mm.

vortices on the concave surfaces of the contraction. The dynamics of this instability mechanism are very weak in comparison with the dynamics of wall turbulence, and so it is possible to avoid the laminar instability problem by inducing boundary-layer transition immediately downstream of the suction manifold.

4.13.3 Transition and the boundary layer trip

With the use of suction and a 5 mm trip-wire near the downstream end of the test-section extension (Figure 4.34), boundary-layer turbulence near the upstream end of the test section, i.e. at Port 1, became intermittent at a free stream speed of 1.2 m/s. By relocating the cylindrical boundary-layer trip from $x = 460$ mm to $x = 60$ mm downstream of the suction surface, the reliability of transition was significantly improved and anemometry statistics[5] from Port 1 of the test section could once again be

[5]Distributions of signal mean, r.m.s. fluctuation, skewness and flatness.

recognised as belonging to a turbulent boundary layer. This result is consistent with the formula

$$\frac{dU_\tau}{\nu} > 20 \tag{4.8}$$

[Schlichting, 1968], which gives the cylindrical trip diameter d required to produce immediate transition to turbulence and suggests that the effectiveness of a trip can be improved by placing it further upstream. In the extreme case, where the trip was located on the downstream edge of the manifold shell (Figure 4.33), transition occurred at the lowest possible flow speed and it effectively suppressed the instability mechanism responsible for unsteady flow in the laminar test-section boundary layer (Section 4.13.2).

Coles (1962) and Erm (1988) have presented ample evidence that the strength of the "wake" or outer region of the turbulent boundary layer (Figure 1.2) depends on the size of the tripping device, and that it is important to select a trip which has the minimum effect on the development of the turbulent boundary layer. Further examination of the flow in the downstream half of wind-tunnel test section revealed a turbulent wake so thickened by the 5 mm diameter cylindrical trip that a potential or free-stream flow could no longer be detected. This thickening of the boundary layer was greatly reduced by removing the test-section extension and reducing the diameter of the cylindrical trip to 3 mm. Even better results were obtained when the cylindrical trip was replaced by a single row of steel balls. Tests were conducted with various ball diameters. The final choice of boundary-layer trip was a single row of 4.97-mm-diameter balls spaced 10 mm apart and glued to all four edges of the suction manifold shell 10 mm downstream from the porous foam surface. This device produced transition at free stream speeds down to 1.7 m/s. At lower speeds the boundary layer was relaminarised by the 20% contraction at the start of the test section[6].

4.14 Summary

The experimental scatter of boundary-layer characteristics measured in the test section of the wind tunnel[7] was due to random fluctuations of the boundary-layer thickness. Further experiments demonstrated that the boundary layer of the inlet contraction was entirely laminar and, at the low end of the wind-tunnel speed range, it was separated from a large proportion of the concave contraction surface. Potential flow simulations using the finite element software Ansys have indicated that this separation was produced by adverse pressure gradients in the region of the contraction inlet. The flow on the surface of a square contraction was found to vary substantially in the lateral direction. Increasing the

[6]This initial contraction, which was formed by jacking up the floor, was required to produce a near-zero streamwise pressure gradient in the remainder of the test section.

[7]see Chapter 3

axial symmetry of the contraction reduced the lateral variation of the surface flow. In a nearly axisymmetric contraction, the maximum pressure increase along a surface streamline and the peak Thwaites parameter were about 50% lower than in a square contraction. The other important factor influencing the surface static pressure distribution was streamwise curvature of the wall. By reducing the concavity (i.e. curvature) of the wall near the contraction inlet, the maximum value of the Thwaites parameter was decreased further by a factor of about 3 to a level well below the critical value of 0.09, thus indicating that separation would not occur. After the contraction was modified in accordance with these findings, measurements in the contraction boundary layer showed no evidence of the near-stagnant separated flow regions which were discovered in the original contraction, but the character of the velocity fluctuations within the laminar boundary layer at the contraction exit remained essentially unchanged. Flow visualisation at the contraction exit indicated that the laminar velocity fluctuations were due to the development of Görtler vortices on the concave parts of the contraction surface. The boundary layer containing the velocity fluctuations was removed by suction at the contraction-exit because suppression of the Görtler instability mechanism by further modification of the wind-tunnel contraction was believed to be impracticable. An inspection of the research literature suggested that any attempt to suppress the Görtler instability mechanism by further modification of the wind-tunnel contraction was unlikely to be successful, and so the contraction-exit boundary layer was removed by suction. A boundary-layer trip was then located at the downstream edge of the suction surface so that any laminar instability in the newly developing boundary layer would be suppressed by immediate transition to turbulence.

4.15 Notation

$C_{pi}(x)$	$P_0(x)/q_{\text{inlet}}$, inlet static pressure coefficient
$C_{po}(x)$	$P_0(x)/q_{\text{outlet}}$, outlet static pressure coefficient
d	diameter of boundary-layer trip
$d(x)$	diagonal width of the fillet insert in the octagonal-to-square contraction
$f(x)$	width of the floor of the octagonal-to-square contraction
G	Görtler number (Equation 4.7, page 110)
$h(x)$	horizontal or vertical distance from the axis of the contraction to the contraction surface
k	thermal conductivity; for thermal conduction/potential flow analogy
$l(m)$	Thwaites skin-friction parameter (Equation 4.3, page 80)
m	Thwaites parameter (Equation 4.4, page 80)
n	unit (outward) normal vector
$P_0(x)$	static pressure of potential flow in the wind-tunnel contraction

$\dot{q}$	heat conduction rate per unit area; for thermal conduction/potential flow analogy
q_{inlet}, q_{outlet}	dynamic pressure at the inlet and outlet of the wind-tunnel contraction
R	radius of curvature of a concave surface
T	temperature; for thermal conduction/potential flow analogy
U_0	free stream air speed or axial (x) component of potential flow velocity
U_τ	friction velocity of the boundary layer; defined by $\tau_w = \rho U_\tau^2$
u'/U	relative intensity of axial velocity fluctuations; i.e. r.m.s. divided by local mean velocity
u	potential flow velocity vector
x	distance in the axial (or streamwise) direction from the start of the wind tunnel contraction or, depending on context, from the start of the test section or from the downstream edge of the suction manifold
x_0, x_1	limits of integration for the Thwaites method
y	distance from a wall or vertical distance from the contraction axis
z	lateral distance from the contraction axis
δ	boundary-layer thickness
θ	$\int_0^\infty (1-U/U_0)(U/U_0)dy$, momentum thickness of a boundary layer
ν	kinematic viscosity
ρ	air density
ϕ	velocity potential function; defined by $v = \nabla\phi$
ψ	two-dimensional streamfunction
τ_w	wall shear stress
$\langle \ldots \rangle$	angle brackets indicate space averaging
∇	gradient operator

Vectors

Vectors are indicated by **bold** typeface.

Subscripts

$_i$	for inlet dimensions of the contraction (h_i, d_i and f_i)
$_{\max}$	maximum value

Chapter 5

Buoyant convection in the wind tunnel

5.1 Introduction

Measurements described in Chapters 3 and 4 have shown that characteristics of the turbulent boundary layer developed on the test-section walls of an open-circuit wind tunnel varied with time. This unsteadiness, which had a time-scale at least two orders of magnitude longer than any belonging to the boundary-layer turbulence, was traced to air-speed fluctuations in the laminar boundary-layer flow emerging from the wind-tunnel contraction. Flow visualisation suggested that the laminar air-speed fluctuations were a result of Görtler instability on the concave surfaces of the contraction. The contraction-exit boundary layer was then removed by a suction manifold and the boundary-layer trip was relocated to the downstream edge of the suction surface so that any laminar instability in the newly developing boundary layer would be suppressed by immediate transition to turbulence.

Further measurements of the velocity distribution in the test-section boundary layer were made to assess the effects of installing the suction manifold and to determine if the boundary-layer characteristics were those of a near-canonical low-Reynolds-number turbulent boundary layer. These measurements provided the initial indication of another type of perturbation in the wind-tunnel flow. The experimental method was similar to that used in Section 3.3, but with data obtained at many more locations within the wake region of the boundary layer. As shown in Figure 5.1, the mean velocity distributions for a free stream speed of 2.0 m/s initially (at $x = 0.70$ m downstream from the boundary-layer trip) have a conventional shape but, at locations ranging from $x = 1.91$ m to $x = 2.52$ m, they develop an inflection and towards the downstream end of the test section they become irregular. The same inflectional characteristics are evident at the higher speed of 8.7 m/s but only at much greater distances downstream from the contraction (Figure 5.2). Such inflections in turbulent shear layers usually indicate multiple sources of turbulence or a severe disturbance to the turbulent flow, as, for example, in the

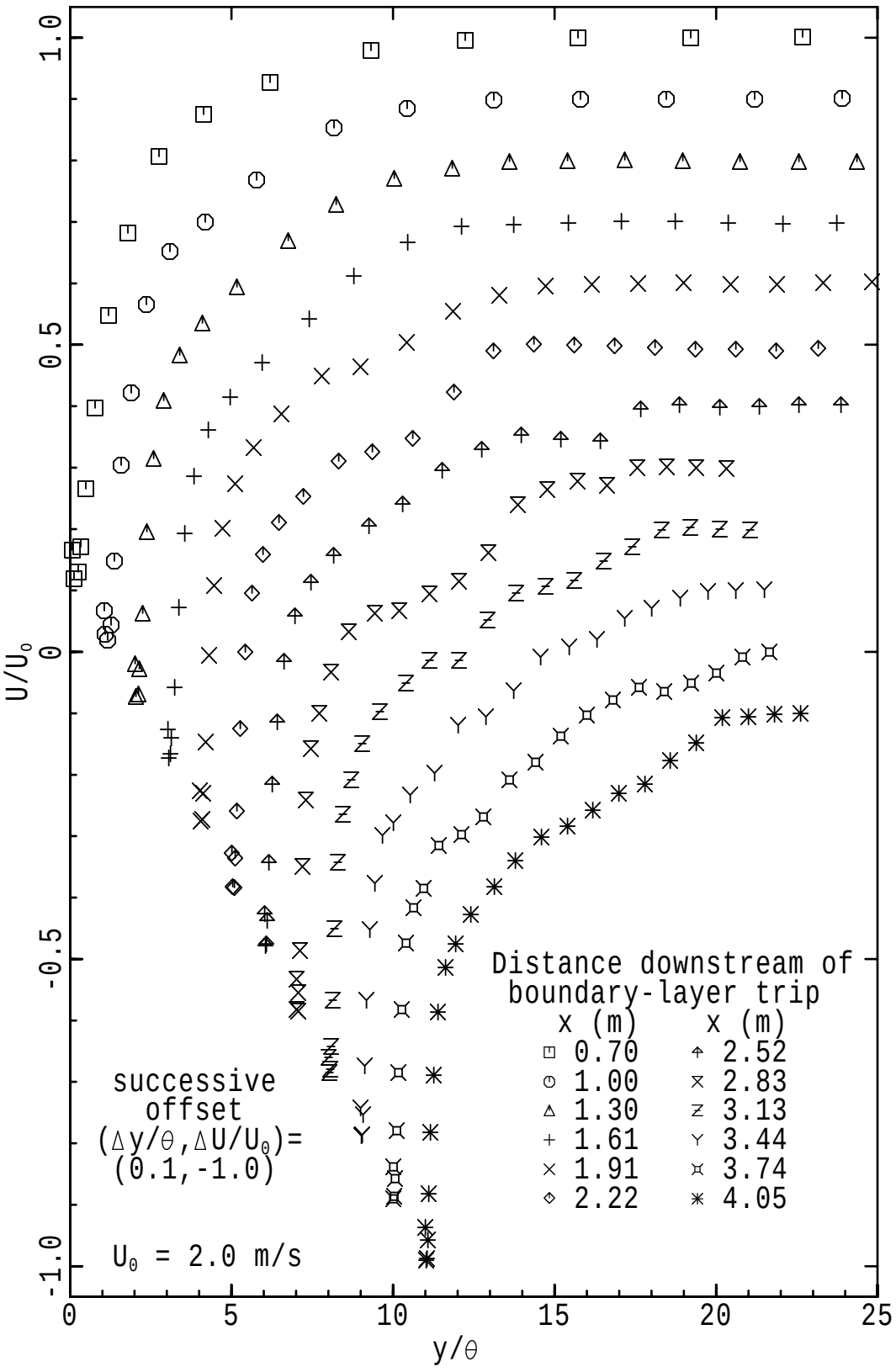

Figure 5.1: Mean velocity distribution in the test-section boundary layer for a free stream speed of 2.0 m/s. The scaling variables are free stream speed U_0 and momentum thickness θ. Data are successively offset by $(\Delta y/\theta, \Delta U/U_0) = (0.1, -1.0)$ as distance from the boundary-layer trip is increased from 0.70 m.

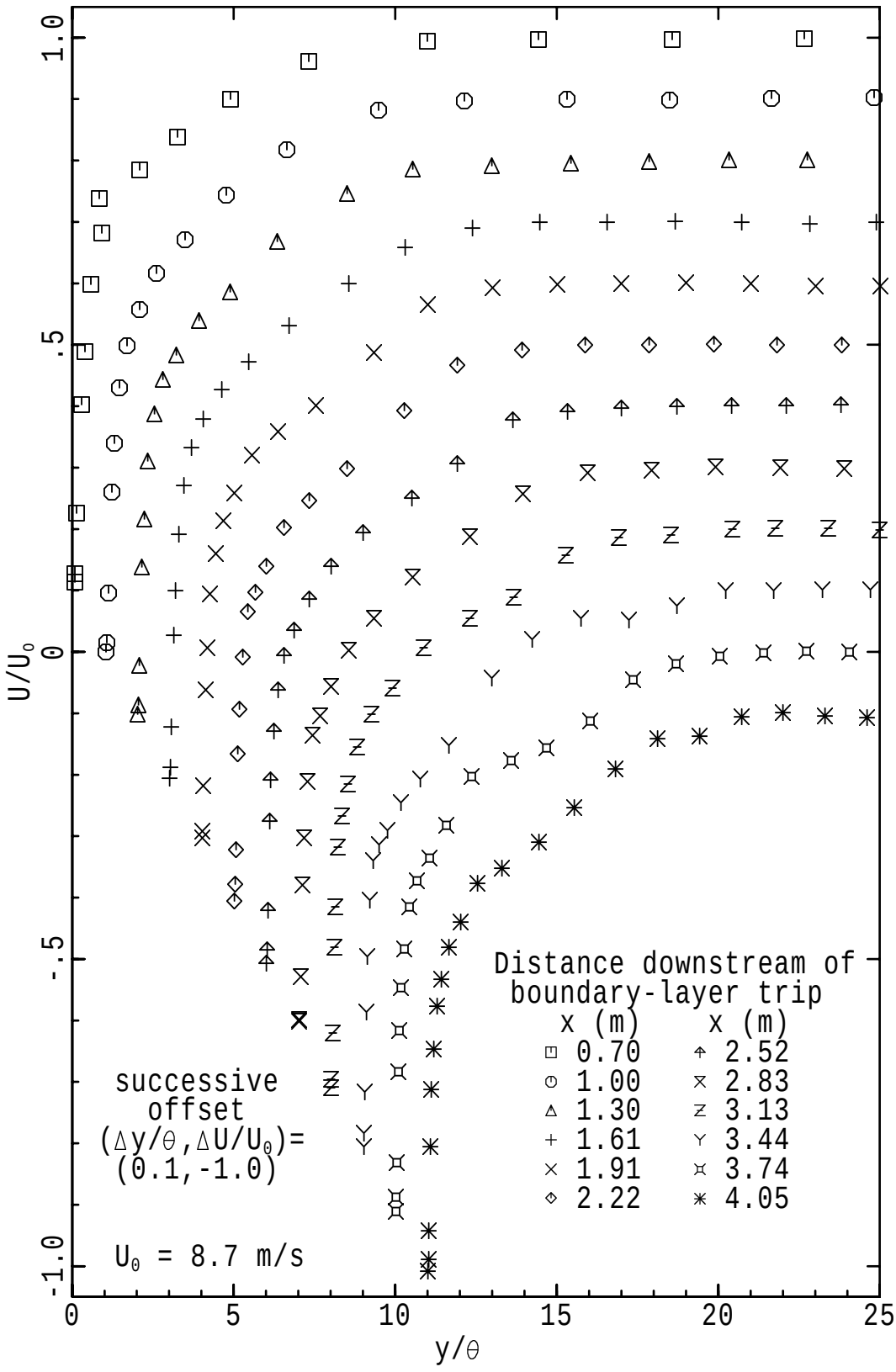

Figure 5.2: Mean velocity distribution in the test-section boundary layer for a free stream speed of 8.7 m/s. The scaling variables are free stream speed U_0 and momentum thickness θ. Data are successively offset by $(\Delta y/\theta, \Delta U/U_0) = (0.1, -1.0)$ as distance from the boundary-layer trip is increased from 0.7 m.

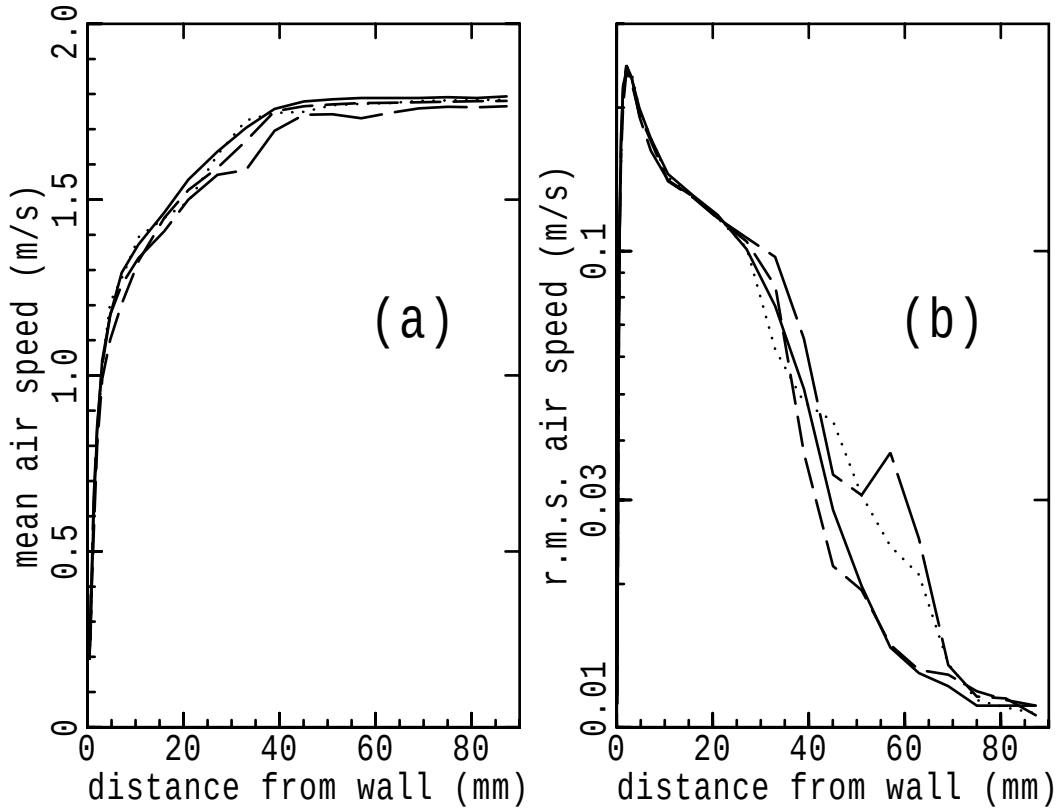

Figure 5.3: Repeated measurements of mean and fluctuating velocity distribution in the turbulent boundary layer at $x = 2.52$ m.

boundary layer and wake of a backward-facing step [Bradshaw and Wong, 1972]. However, repeated measurement of the velocity distribution at $x = 2.52$ m (Figure 5.3) has demonstrated that, in this case, the inflections were caused by very slow variations in boundary-layer thickness. The time scale of these fluctuations was much longer than the 30 seconds of data sampling at each probe position, and so they could not be detected by the record-segmentation technique described in Section 4.1. The conventional nature of the local skin-friction values shown in Figure 5.4 and the disparity between the fluctuation time-scale and the time-scales of boundary-layer turbulence made it most unlikely that the variability arose from within the test-section boundary layer. Large-scale unsteady transverse velocity components in the free stream core of the test-section flow were the most likely cause of the problem: over the length of the test section, a change in flow direction of only a few degrees would be quite sufficient to convect a corner flow to the middle of the test wall and so produce a significant change in the measured characteristics of the boundary layer.

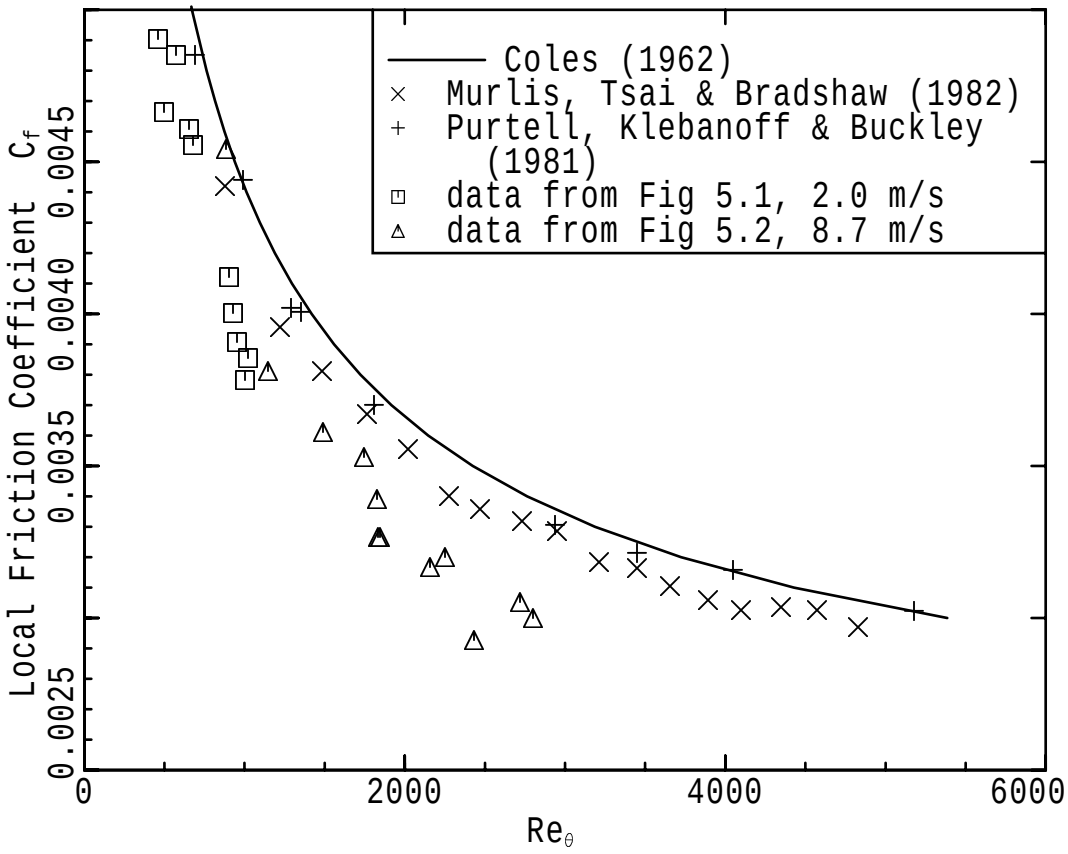

Figure 5.4: Local friction coefficient for the data of Figures 5.1 and 5.2

5.2 Experimental investigation of test-section secondary flow

Further diagnosis of the cause of irregularities in the test-section boundary layer required direct evidence of secondary flows which were capable of perturbing the boundary layer. Because it was believed necessary to detect cross-flow velocity components as much as two orders of magnitude smaller than the air speed, and because the time-scale of the “instability events” seemed to be very long (up to 10 minutes), hot-wire anemometry was discarded in favour of a flow-visualization technique using streamers.

5.2.1 Experimental arrangement

The general arrangement for the flow-visualisation experiments is shown in Figure 5.5. In these experiments, between 8 and 12 lengths of acrylic or silk thread were glued at approximately equal spacings to a stem with a diameter of 3 mm and an exposed length of 230 mm. For tests at flow speeds lower than 8 m/s, the acrylic streamers were replaced with the lighter silk streamers which performed satisfacto-

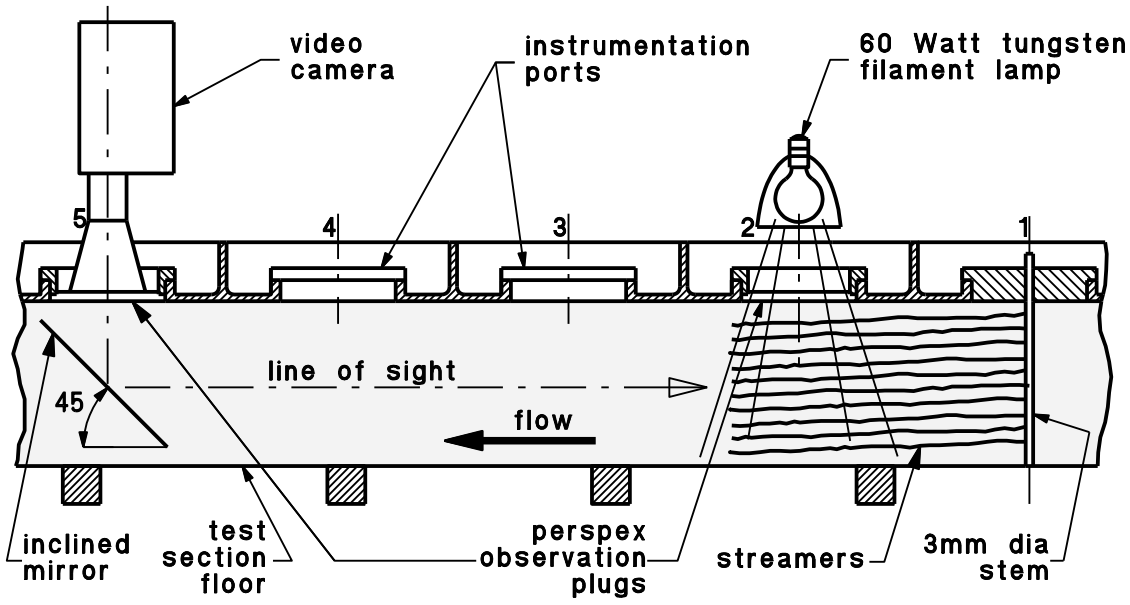

Figure 5.5: General arrangement for visualisation of the test-section flow with streamers. Scale 1:10

rily at speeds as low as 2 m/s. The stem (with streamers attached) was installed in the test-section port closest to the contraction so that it spanned the test section from top to bottom and so that the streamers trailed under the second test-section port. The streamers were illuminated through a perspex plug at Port 2. Their behaviour was observed through a video camera mounted directly on another perspex plug at least 0.9 metres downstream of the illumination. Light from the streamers was reflected into the camera by an inclined mirror in the test section. The pattern formed by the array of streamers was recorded at normal speed on video-tape.

By using the stem as a reference, it was easy to detect sideways streamer deflections of only a few millimetres but the magnitude of the deflections could only be estimated from the television image with an accuracy of perhaps at best $\pm 30\%$. This and the lack of control over the factors producing the secondary flows dictated that the information obtained was qualitative rather quantitative. Because the angles of streamer deflection were quite small, the results obtained with this method of visualisation were very sensitive to misalignment of the camera and mirror. Another minor problem was that vortex shedding from the mirror caused the mirror to vibrate with an amplitude which was sometimes apparent in the video recording. It should also be noted that, due to use of the inclined mirror, all video-taped images were reflections about a vertical axis. The possibility that the presence of the mirror itself might cause some deflection of the streamers was tested by placing the mirror further downstream at Port 11 and then removing it altogether. It was clearly observed that in neither case did this make any difference to the behaviour of the streamers, although it was only possible to observe the streamers through the perspex plug at Port 2 when the mirror was removed.

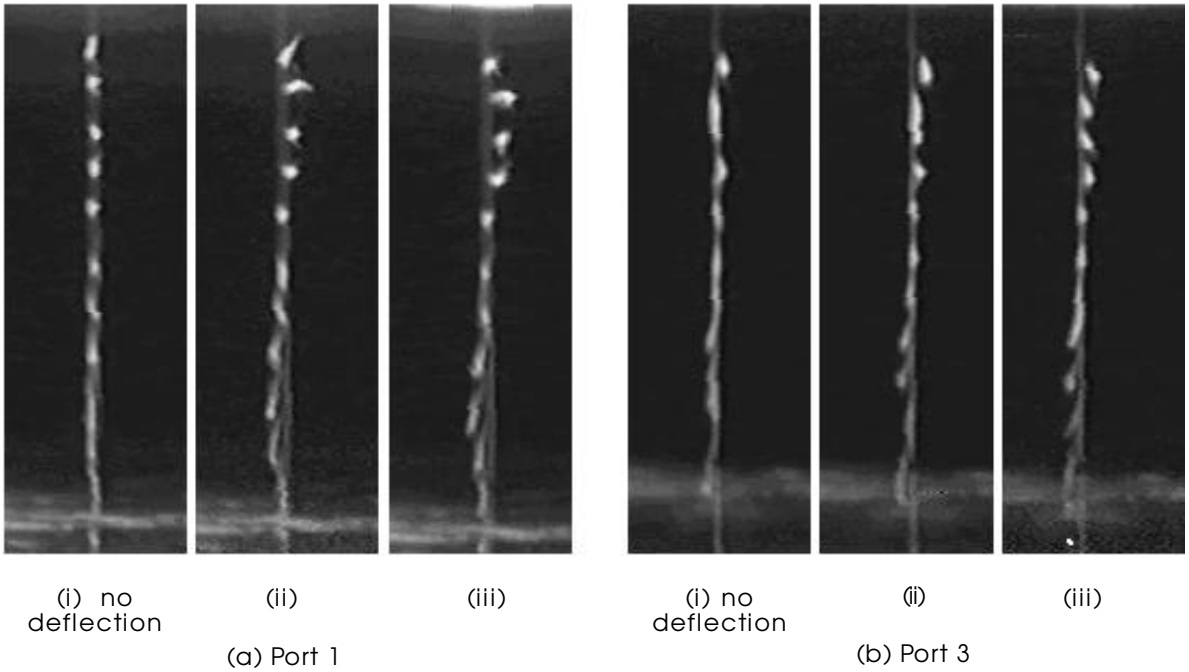

Figure 5.6: Streamer pattern due to natural excitation of a single streamwise vortex for $\langle U \rangle \approx 7.5$ m/s; (a) at Port 1; (b) at Port 3; (i) no vortex; (ii) and (iii) weak streamwise vortex.

5.2.2 Natural excitation of secondary flows

A typical example of the pattern formed by lateral deflection of the streamers at a test-section bulk-flow speed[1] of about 7.5 m/s, is shown in Figure 5.6(a). This pattern indicates the presence of a single, weak streamwise vortex almost completely filling the duct cross-section. The axis of the vortex is located approximately in the centre of the duct. Time histories were obtained from manual measurements of streamer deflection in the videotape images. As recorded in Figure 5.7(a), the amplitude of rotation was found to vary slowly and apparently at random, but changes in the direction of the rotation were very rarely observed. The time-scale of fluctuations in secondary-flow amplitude varied from about 1 minute up to about 10 minutes.

In order to determine whether the vortex extended over a significant proportion of the length of the test section, the streamers were also placed at Ports 3 and 7. Secondary flow of the same kind was observed in both of these cases (e.g. Figure 5.6(b), Figure 5.7(b)), but it was usually of smaller amplitude. The significance of the observed reduction in amplitude is not entirely clear because, even at Port 1, lateral deflection of the streamers could not always be detected and on several occasions the secondary flows were completely absent for periods of several hours. These tests were performed both with and without

[1] Bulk-flow speed $\langle U \rangle$ is the streamwise velocity component averaged over the duct cross-section.

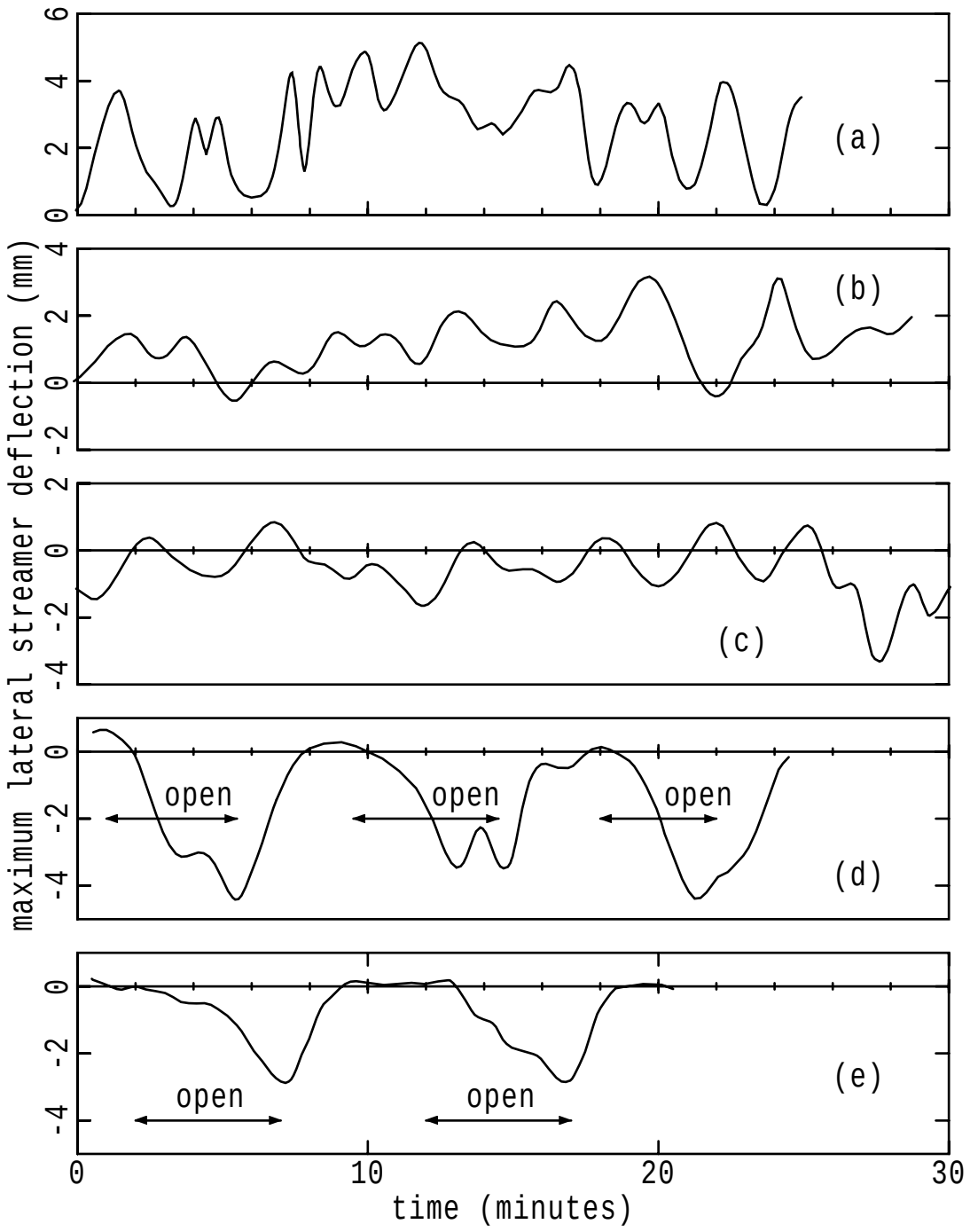

Figure 5.7: Time histories of naturally excited streamer deflection measured from the videotape record; $\langle U \rangle \approx 7.5$ m/s;

(a) streamers at Port 1 — typical time history;

(b) streamers at Port 3 — typical time history;

(c) streamers at Port 1 — effect of a 25mm foam blanket upstream of the honeycomb;

(d) streamers at Port 1 — effect of opening and closing the laboratory door;

(e) streamers at Port 1 — effect of opening and closing the laboratory door after replacing the second honeycomb with drinking straws.

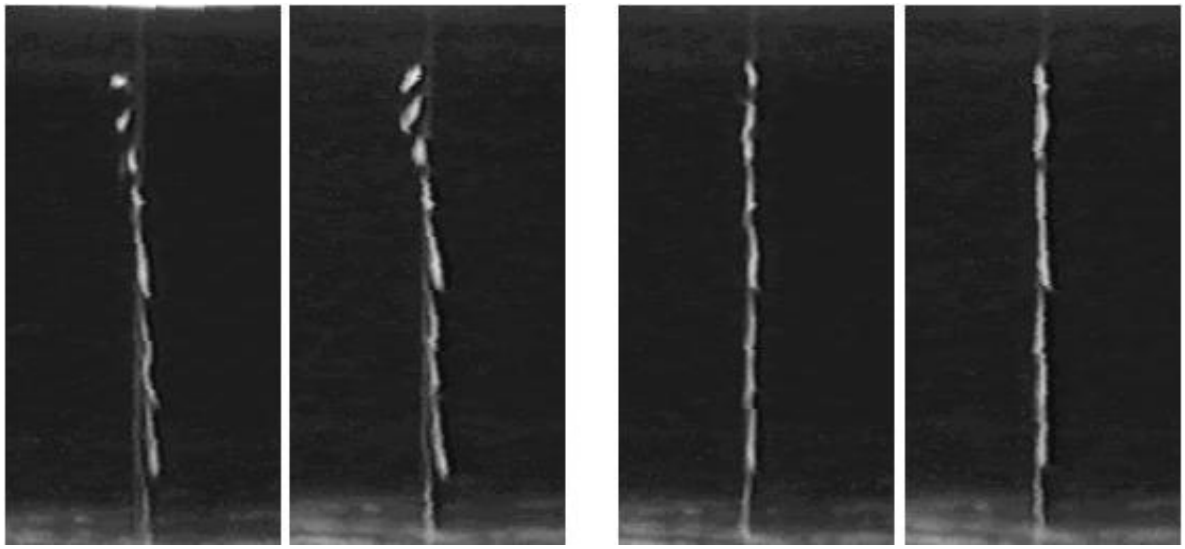

(a) open door (b) closed door

Figure 5.8: Effect of opening and closing the laboratory door on streamer deflection patterns at Port 1, $\langle U \rangle \approx 7.5$ m/s; (a) open door; (b) closed door.

boundary-layer suction at the start of the test section but, although there were differences in detail between individual video recordings, there was no observable correlation between the quantity of air removed by the suction manifold and the nature of the secondary flow.

In the search for the cause of axial rotation in the test-section flow, it was then necessary to check the efficacy of the honeycombs (Figure 2.1, Table 2.1), whose intended function was to remove swirl from the air flowing into the bellmouth inlet of the wind tunnel. Mehta (1977) recommended that the length to diameter ratio l/d of honeycomb cells should exceed 10 and he pointed out that if the flow angle of incidence to the honeycomb cells became too large, the effectiveness of the honeycomb was reduced by stalling within the cells. The two honeycombs in the wind tunnel had $l/d \approx 12$ but the angle of incidence of the flow was unknown. In an effort to preclude a possibly large angle of incidence, a 25 mm thick layer of polyurethane foam was placed against the upstream face of the first honeycomb but, from Figure 5.7(c), it is clear that this produced no significant change in the secondary flows within the test section.

To one side of the bellmouth inlet there was a large roller door which allowed vehicular access to the laboratory, and when the door was opened strong draughts could sweep across the wind-tunnel inlet. The effect of opening the door, which is illustrated in Figures 5.8(a) and 5.7(d), was to generate a rotating secondary flow in the test section after a delay of about two minutes. In every case the flow rotation disappeared shortly after the door was closed (Figure 5.8(b)). This indicated that the

free stream secondary flow in the test section was caused by factors outside the wind tunnel and not by a "random" instability within the wind tunnel. However, the mechanism by which these external factors generated the rotation was still unknown. At this stage, the performance of the honeycombs was under suspicion and it was considered that the length to diameter ratio of the honeycomb cells might still be inadequate. The second honeycomb (with $l/d \approx 12$) was therefore replaced by a honeycomb made of carefully packed drinking straws with $l/d \approx 44$, and the previous test was repeated. This test (Figure 5.7(e)) showed that poor honeycomb performance was not responsible for the secondary flows, and that, while the stimulus for the rotation came from outside the wind tunnel, the rotation itself began and developed within the settling chamber and contraction of the wind tunnel.

Naturally excited secondary flows similar to those in Figure 5.6 were found at test-section bulk-flow speeds ranging from $\langle U \rangle = 7.5$ m/s down to $\langle U \rangle = 1.5$ m/s. It was not possible to resolve details of trends due to changing flow speed because the cause of the secondary flow was not a controlled variable. The most commonly occurring secondary flow pattern, which consisted of a single large-scale small-amplitude axial vortex (Figures 5.9(a) to 5.9(d)), could be found at almost all of the flow speeds examined and was generally observed to increase in strength as flow speed decreased. In the lower half of the speed range more complex streamer patterns could be formed. Some, such as the slowly-changing or steady pattern shown in Figure 5.9(e), could be readily interpreted as pair of counter-rotating vortices. Sometimes, especially when there was rapid motion of the streamers, proper classification of the secondary flow was not possible. Some unsteady flow appeared to be the result of particularly strong excitation. In a few cases, for example, as in Figure 5.9(f), the secondary flow appeared to have completely different characteristics.

In summary, the experiments with an array of streamers verified the presence of secondary flows in the test section of the wind tunnel. These secondary flows extended over a significant proportion of the test-section length and usually took the form of a single streamwise vortex occupying most of the available duct cross-section. The swirl angle was typically one or two degrees. The secondary flow rotation was a result of the air-flow conditions outside the wind tunnel, but it actually began and developed within the settling chamber and contraction of the wind tunnel. It was not prevented or caused by honeycombs at the wind-tunnel inlet.

5.3 Excitation of buoyant convection

5.3.1 The effect of a carbon dioxide jet

The first indication that buoyant convection within the settling chamber and contraction of the wind tunnel might be the cause of the secondary flows was provided by observing that severe flow distur-

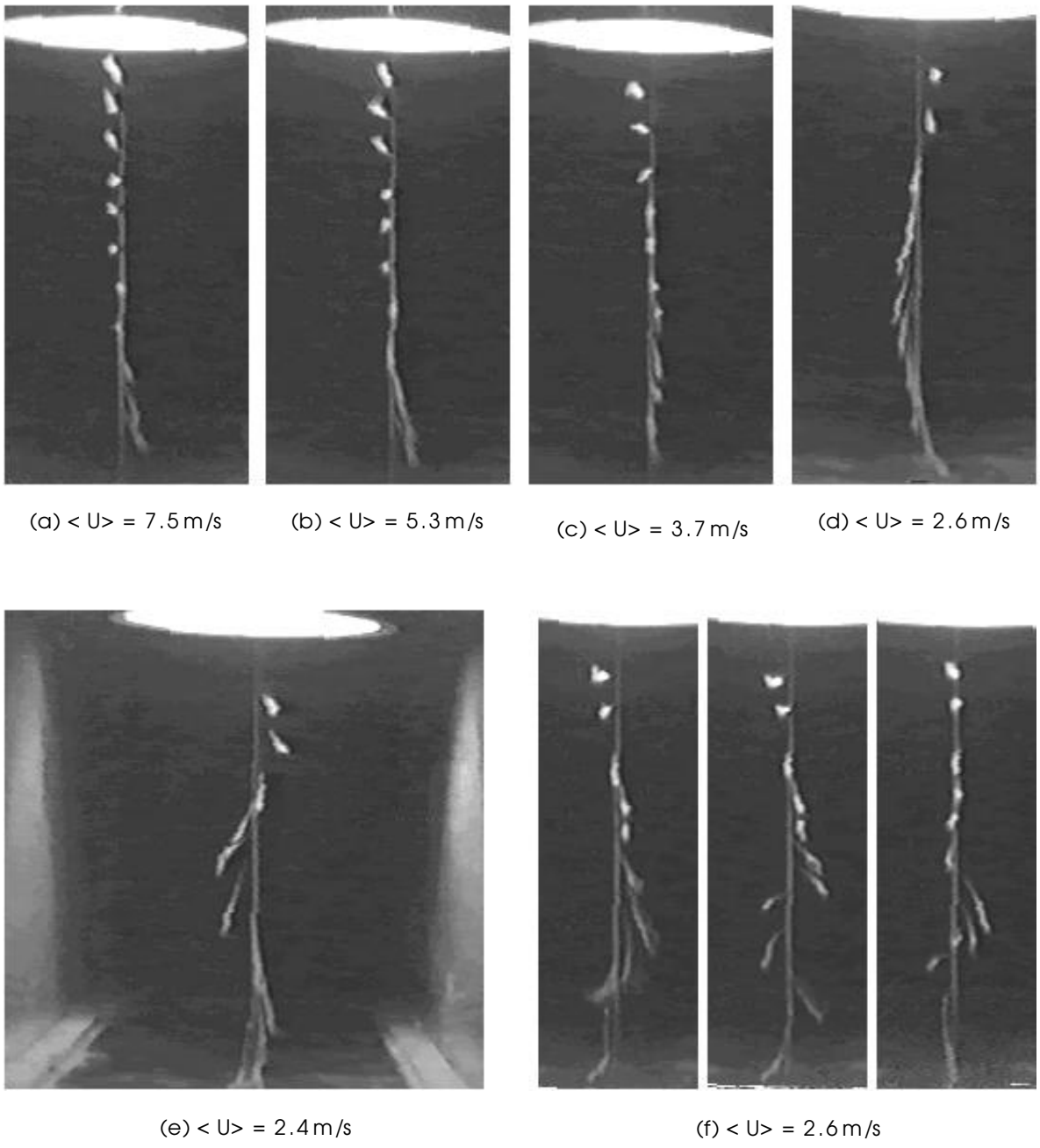

Figure 5.9: Naturally excited streamer-deflection patterns over a range of flow speeds; (a–d) single streamwise vortex; (e) counter-rotating pair of streamwise vortices; (f) three images of unsteady, unclassifiable flow.

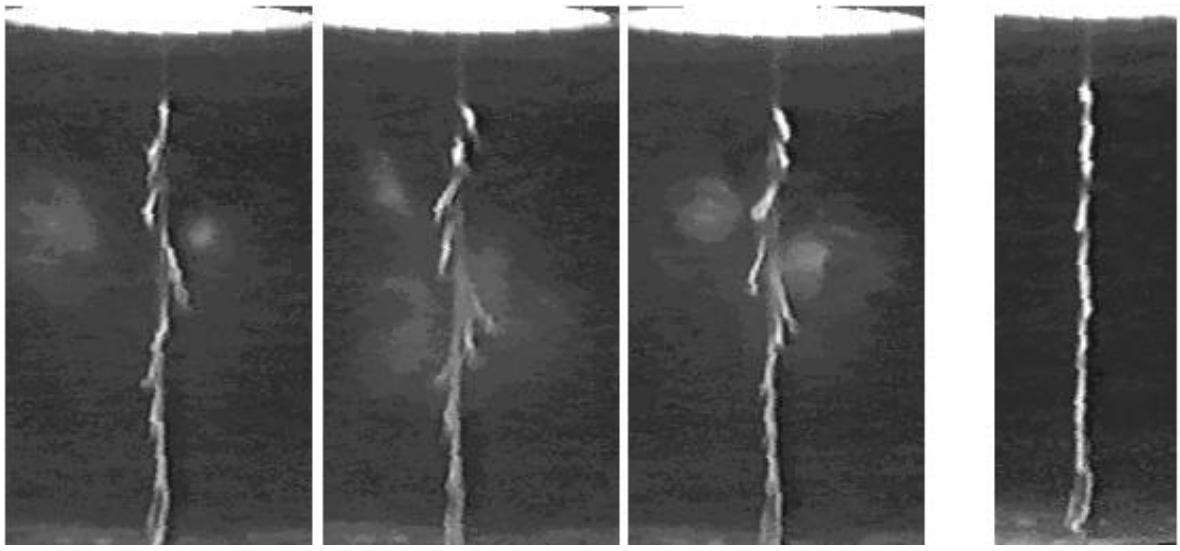

Figure 5.10: Effect on the flow of a CO_2-borne smoke jet; $\langle U \rangle \approx 7.5$ m/s; (a–c) with CO_2; (d) without CO_2.

bances were created in the test section when a narrow jet of CO_2-borne smoke was introduced at the bell-mouth inlet (Figure 5.10). Carbon dioxide is 52% more dense than air and, at low air speeds, the resulting negative buoyancy was sufficient to drive strong convection currents within the settling chamber and contraction. At this point it became clear that buoyant convection due to non-uniformities in the temperature of the inlet air stream might be sufficient to produce the secondary flows described in Section 5.2.2. However, the density differences produced by temperature nonuniformities of just a few degrees are much less than the difference between the densities of air and carbon dioxide, and so it was necessary to test this hypothesis experimentally.

5.3.2 The effect of temperature non-uniformity

The air temperature distribution over the wind-tunnel inlet was easily made nonuniform by placing a small electric fan-heater in front of the wind-tunnel bellmouth and at a height approximately level with the floor of the settling chamber. After a delay of about 2 minutes, which was probably due to the heat capacity of the screens and honeycombs in the wind-tunnel inlet, a single-vortex rotation appeared in the test-section flow. It rapidly became apparent that the “driving force” provided by the fan-heater was considerably greater than the natural stimulus of Section 5.2.2 because, with the heater producing a temperature rise of 7^oC, the rotation slowly grew in strength and eventually became unsteady in the top half of the duct (Figure 5.11(a)). When the temperature rise was increased to 15^oC the region of

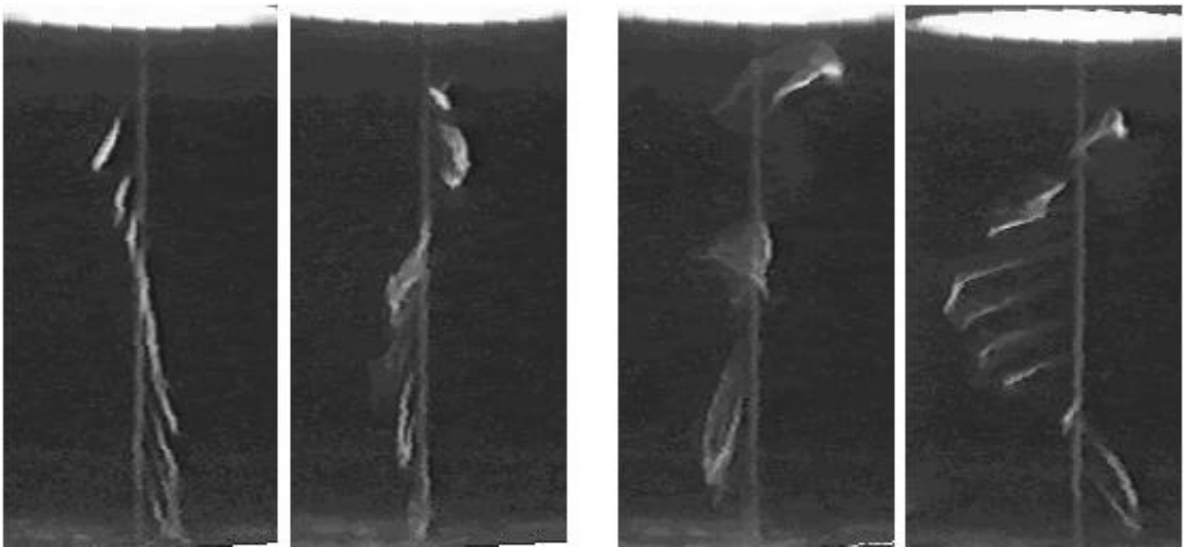

(a) 7 °C temperature rise (b) 15°C temperature rise

Figure 5.11: Effect of nonuniform air temperature at the wind-tunnel inlet. $\langle U \rangle \approx 7.5$ m/s. The temperature nonuniformity was produced by an electric fan-heater.

unsteady flow grew in size to occupy the whole of the duct. The unsteadiness grew in amplitude to about 50 mm of lateral streamer displacement, and became a violent oscillation which might loosely be called a turbulent buoyant convection (Figure 5.11(b)). The response of the flow to opening and closing the laboratory door (Figure 5.8) was clearly a result of the outside air temperature being a few degrees Celsius lower than the temperature inside the laboratory.

If the temperature of a small part of the air flowing in a horizontal duct becomes $\Theta_a + \Delta\theta$, slightly higher than the temperature of the surrounding air Θ_a, the buoyancy force on it is proportional to $g\Delta\theta/\Theta_a$, where g is gravitational acceleration. If the streamwise component of air velocity U remains unchanged, then the time over which this force acts in a duct of length L is L/U. The cross-stream component of impulse on the heated air, hence the secondary flow component of velocity, is proportional to the product of these two quantities: $(g\Delta\theta/\Theta_a)(L/U)$. The air-velocity vector is therefore turned by an angle

$$\alpha = k\frac{\Delta\theta}{\Theta_a} \cdot \frac{gL}{U^2}, \tag{5.1}$$

where k is a constant if the nondimensional temperature distribution $\Delta\theta/\Theta_a$ does not change.

This crude analysis shows that small angles of swirl produced by buoyant convection should be proportional to the temperature nonuniformity across the width of the bellmouth inlet of the wind tunnel. It was easy to verify that, as implied by Equation 5.1, swirl angle increased as flow speed was reduced. By regulating the fan-heater through an autotransformer, measuring the resultant air-temperature rise

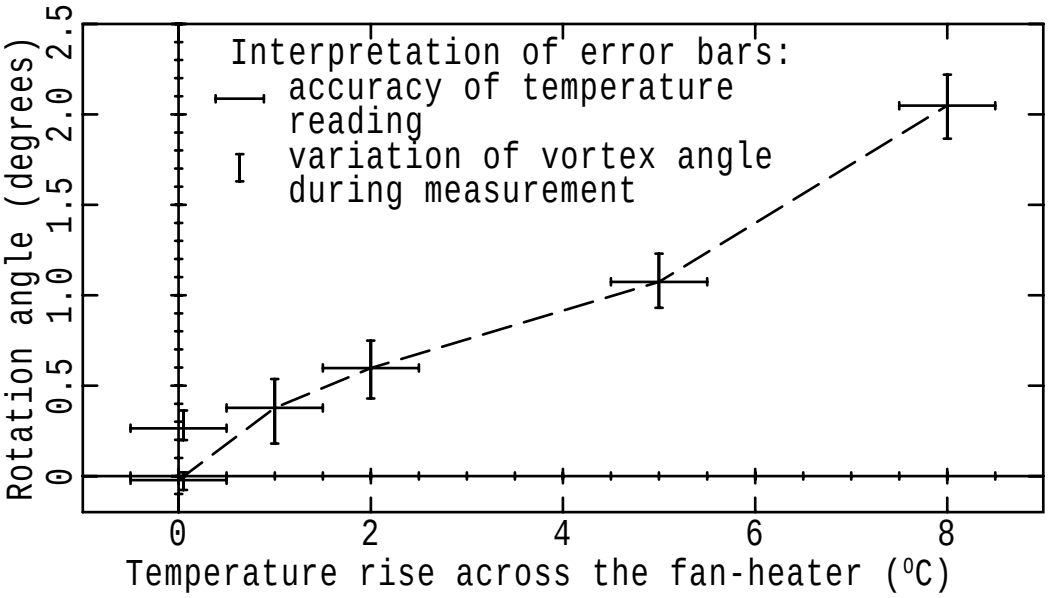

Figure 5.12: Secondary flow-rotation angle in the test section as a function of temperature rise produced by a fan-heater; $\langle U \rangle \approx 7.5$ m/s

at the bellmouth inlet, and observing the lateral deflection of the streamers in the test-section, it was possible to estimate a value k in Equation 5.1. The results of these measurements are shown in Figure 5.12. They give a value for k of about 0.25 degrees of flow rotation per degree Celsius. The rather large uncertainty indicated by the error-bars is due to a combination of measurement error and naturally occurring air temperature nonuniformities at the wind-tunnel inlet. Experimental error might also have been caused by change in the shape of the temperature distribution over the wind-tunnel inlet as the temperature and velocity of the air from the fan-heater was varied.

Figure 5.13 is a typical example of a naturally occurring temperature distribution across the wind-tunnel inlet. This distribution, for which the difference between maximum and minimum temperatures is about 1^oC, produced a lateral streamer deflection of about 3 mm. The isothermal contours in the diagram were estimated from temperature measurements made with a platinum resistance thermometer at the corners and centre of the octagonal duct inlet. The flow-rotation angle of about 0.5 degrees per degree Celsius is in the same order of magnitude as that indicated by Figure 5.12.

To summarise: it was concluded that the free stream secondary flows in the test section were produced by buoyant convection which began within the settling chamber and contraction of the wind tunnel. The density variations driving this convection were a result of air temperature nonuniformities over the wind-tunnel inlet. The principal mode of secondary flow was a single forced vortex occupying the entire cross-section of the duct. For an air speed of about 7.5 m/s in the test section, the swirl angle of

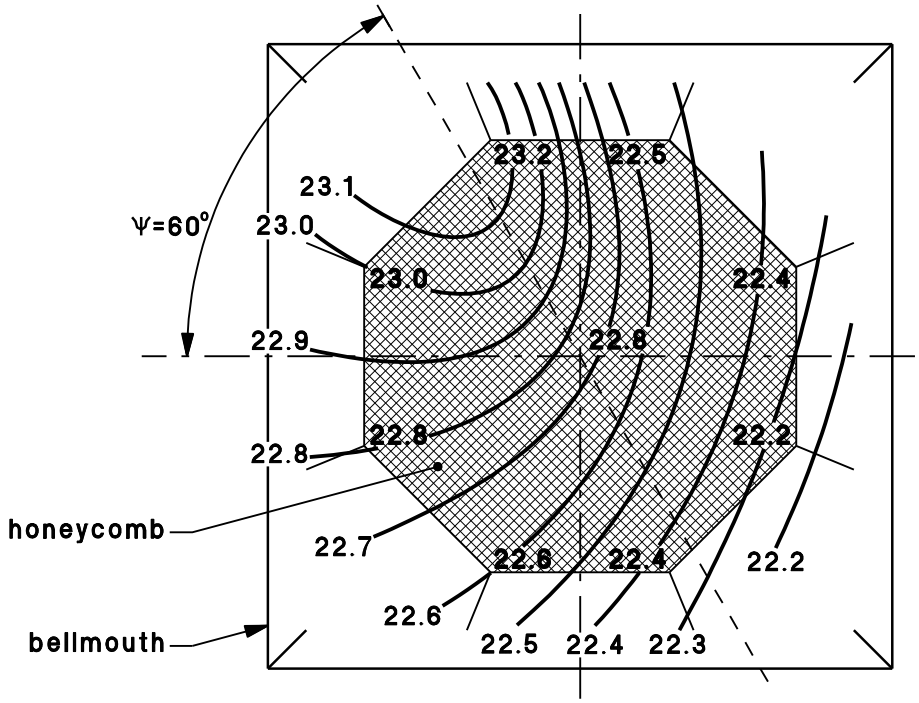

Figure 5.13: Estimate of a typical temperature distribution over the wind-tunnel inlet — end-view of bellmouth inlet and honeycomb. Measurements in the corners and centre of the octagonal duct inlet (i.e. hatched area) are shown in **bold** typeface. $\langle U \rangle \approx 7.5$ m/s. Initial rotation angle $\psi_{\text{in}} \approx 60^o$.

the forced vortex was about 0.5 degrees of arc per degree Celsius of temperature non-uniformity.

5.4 Simple theory for weak buoyancy-driven swirl

The theory presented in this section was derived with the main purpose of developing an understanding of weak buoyancy-driven swirl, and to provide a basis for engineering estimates of whether or not the effects of buoyant convection were likely to influence a duct flow significantly. The strongly non-linear behaviour which results from large driving temperature differences has not been examined.

5.4.1 One dimensional model

For this exercise, the Navier Stokes equations are conveniently written in tensor notation as

$$\tilde{\rho}\left(\frac{\partial \tilde{u}_i}{\partial t} + \tilde{u}_j \frac{\partial \tilde{u}_i}{\partial x_j}\right) = -\frac{\partial \tilde{p}}{\partial x_j} + \mu \frac{\partial^2 \tilde{u}_i}{\partial x_j^2} + \tilde{\rho} F_i, \tag{5.2}$$

where $F_i = g_i$ is the body force due to gravity. The tilde ($\tilde{}$) in $\tilde{u}_i$, $\tilde{p}$ and $\tilde{\rho}$ indicates that the variables are time-dependent. If there is no flow, Equation 5.2 becomes the hydrostatic equation which, in a

time-averaged form, is

$$0 = -\frac{\partial P_a}{\partial x_i} + \rho_a F_i, \tag{5.3}$$

where P_a is the time-averaged ambient air pressure. When this equation is subtracted from Equation 5.2, the result is

$$\tilde{\rho}\left(\frac{\partial \tilde{u}_i}{\partial t} + \tilde{u}_j\frac{\partial \tilde{u}_i}{\partial x_j}\right) = -\frac{\partial}{\partial x_i}(\tilde{p} - P_a) + \mu\frac{\partial^2 \tilde{u}_i}{\partial x_j^2} + (\tilde{\rho} - \rho_a)F_i \tag{5.4}$$

[Townsend, 1976, Chapter 8]. Application of the Boussinesque approximation[2] followed by conversion of density variations to temperature fluctuations using the constant pressure relation

$$\frac{\tilde{\rho} - \rho_a}{\rho_a} = -\frac{\Delta\tilde{\theta}}{\Theta_a}, \tag{5.5}$$

where $\Delta\tilde{\theta}$ is the temperature excess above ambient temperature Θ_a, gives

$$\frac{\partial \tilde{u}_i}{\partial t} + \tilde{u}_j\frac{\partial \tilde{u}_i}{\partial x_j} = -\frac{1}{\rho_a}\frac{\partial}{\partial x_j}(\tilde{p} - P_a) + \nu\frac{\partial^2 \tilde{u}_i}{\partial x_j^2} - \frac{\Delta\tilde{\theta}}{\Theta_a}g_i. \tag{5.6}$$

In the case under consideration, the flow is confined within a horizontal duct. The temperature differences are small, the viscous stress terms $\nu\partial^2\tilde{u}_i/\partial x_j^2$ are significant only within a negligibly thin boundary layer and the flow is steady. Equation 5.6 can now be rewritten as

$$U_j\frac{\partial U_i}{\partial x_j} = -\frac{1}{\rho_a}\frac{\partial}{\partial x_j}(P - P_a) - \frac{\Delta\theta}{\Theta_a}g_i. \tag{5.7}$$

At this point it is convenient to replace the tensor notation by the conventional (x,y,z) space representation in which U, V and W are the streamwise, vertical and lateral components of steady velocity. As a further approximation, if the cross-flow components of velocity (V and W) are small in comparison with a uniformly distributed streamwise component, and if the streamwise pressure gradient is zero, then Equation 5.7 simplifies to

$$U\frac{\partial V}{\partial x} + V\frac{\partial V}{\partial y} + W\frac{\partial V}{\partial z} = -\frac{1}{\rho_a}\frac{\partial P}{\partial y} + \frac{\Delta\theta}{\Theta_a}g \tag{5.8}$$

$$U\frac{\partial W}{\partial x} + V\frac{\partial W}{\partial y} + W\frac{\partial W}{\partial z} = -\frac{1}{\rho_a}\frac{\partial P}{\partial z}. \tag{5.9}$$

With the addition of the continuity equation

$$\frac{\partial V}{\partial y} + \frac{\partial W}{\partial z} = 0, \tag{5.10}$$

and with boundary conditions defined at the inlet, outlet and walls of the duct, this system of equations could, in principle, be solved numerically for V, W and P. If required, Taylor's hypothesis[3] can be used to transform the system into a planar time-dependent model.

[2] Boussinesque approximation: density variations are significant only in buoyancy terms

[3] Taylor's hypothesis:

$$-U\frac{\partial V}{\partial x} = \frac{\partial V}{\partial t} \qquad\qquad -U\frac{\partial W}{\partial x} = \frac{\partial W}{\partial t}.$$

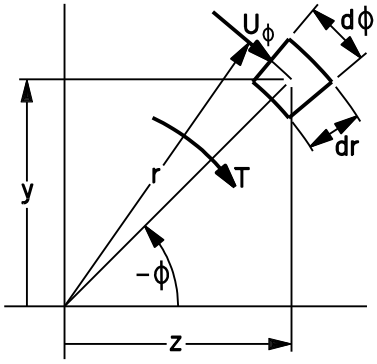

$$z = r\cos\phi, \quad y = r\sin\phi, \quad dA = dy\,dz = r\,dr\,d\phi$$

Figure 5.14: Coordinate system for the duct cross-section

By further simplifying the model to a two-dimensional flow (i.e. $W = 0$, $\partial/\partial z = 0$) which is not constrained in the vertical direction (i.e. $\partial P/\partial y = 0$), Equations 5.8, 5.9 and 5.10 reduce to

$$U\frac{dV}{dx} = \frac{\Delta\theta}{\Theta_a}g. \tag{5.11}$$

This can be integrated over a duct length L to obtain the secondary flow velocity V produced by buoyant convection. The small rotation angle, α, of the velocity vector then becomes the Richardson number,

$$\alpha = Ri = \frac{gL}{U^2}\frac{\Delta\theta}{\Theta_a}, \tag{5.12}$$

which is similar to Equation 5.1. For the inlet conditions of Figure 5.13, where the Richardson number of flow within the wind-tunnel contraction is estimated to be $Ri \approx 0.2$, a small but significant buoyant convection is superimposed on the main flow. With a similar inlet temperature distribution at the lower flow speed of, for example, 2 m/s, the Richardson number is much higher ($Ri \approx 3$) and buoyant convection is expected to completely dominate the flow within the contraction.

5.4.2 Forced-vortex model of buoyant convection

The one-dimensional model of the previous section shows that buoyant rotation of the flow-velocity vector is in the order of the Richardson number. In this section the buoyant rotation within the settling chamber and contraction of the wind tunnel (Figure 2.1) is modelled as a forced vortex at each cross-section of the duct. This, together with a linear temperature distribution at the duct inlet, greatly simplifies the mathematics of the analysis. Experimental measurements and observations indicate that these assumptions are sufficiently realistic to provide useful results.

5.4.2.1 Torque due to a linear temperature distribution

The (vertical) buoyancy force on a fluid element of mass dm is $dF = -g\,d(\Delta m)$ where g is acceleration due to gravity and $d(\Delta m) = (\rho - \rho_a)\,dV$ is the mass excess of the element. By expressing the elemental volume dV as the product of its area dA and length dx, and also using Equation 5.5 to express the buoyancy force as a function of temperature distribution, the streamwise gradient of the buoyancy force on the fluid element becomes

$$d\frac{dF}{dx} = \rho_a g \frac{\Delta\theta(y,z)}{\Theta_a}\,dA, \tag{5.13}$$

where $\Delta\theta(y,z)$ is the temperature distribution over the duct cross-section. For the cross-section coordinate system defined in Figure 5.14, the streamwise torque gradient about the duct axis is

$$d\frac{dT}{dx} = -\rho_a g \frac{\Delta\theta(y,z)}{\Theta_a}\,z\,dA. \tag{5.14}$$

If, as an approximation, the cross-section of the duct is assumed to be circular with radius R and if the torque on the element is written using polar coordinates,

$$d\frac{dT}{dx} = -\rho_a g \frac{\Delta\theta(r,\phi)}{\Theta_a}\,r^2\cos\phi\,dr\,d\phi. \tag{5.15}$$

The total streamwise torque gradient over the cross-section is

$$\begin{aligned}\frac{dT}{dx} &= \int_{r=0}^{r=R}\int_{\phi=0}^{\phi=2\pi} d\frac{dT}{dx} \\ &= -\frac{\rho_a g}{\Theta_a}\int_{r=0}^{r=R}\left(\int_{\phi=0}^{\phi=2\pi}\Delta\theta(r,\phi)\cos\phi\,d\phi\right)r^2 dr.\end{aligned} \tag{5.16}$$

To evaluate this integral, it is necessary to specify the temperature distribution $\Delta\theta(r,\phi)$. For simplicity, an initial temperature distribution which varies linearly with z, from $\Theta_a + \Delta\Theta/2$ at $z = -R$ on one side of the duct to $\Theta_a - \Delta\Theta/2$ at $z = R$ on the other (Figure 5.15) has been adopted. This initial temperature distribution is not a function of vertical position y, and is thought to approximate reality with sufficient accuracy to provide useful results. Following from the initial forced-vortex assumption, at a distance x from the start of the duct the initial temperature distribution will have rotated by some angle $\psi(x)$. The analytical solution for thermal conduction within a disk indicates that the diffusion time-scales responsible for significant distortion of the temperature distribution are much larger than the time required for fluid to pass through the settling chamber and contraction. Therefore, it is also assumed that the diffusion of the temperature distribution is negligible, so that

$$\Delta\theta(r,\phi) = -\frac{\Delta\Theta}{2R}\,r\cos(\phi+\psi), \tag{5.17}$$

and Equation 5.16 can be evaluated to give

$$\frac{dT}{dx} = \frac{\pi}{8}\frac{\Delta\Theta}{\Theta_a}\rho_a g R^3\cos\psi. \tag{5.18}$$

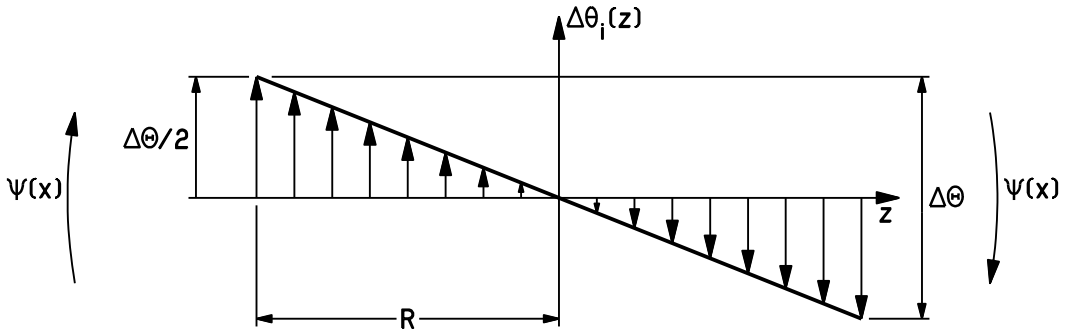

Figure 5.15: Temperature distribution for forced-vortex rotation. Buoyant convection rotates this temperature distribution through angle $\psi(x)$

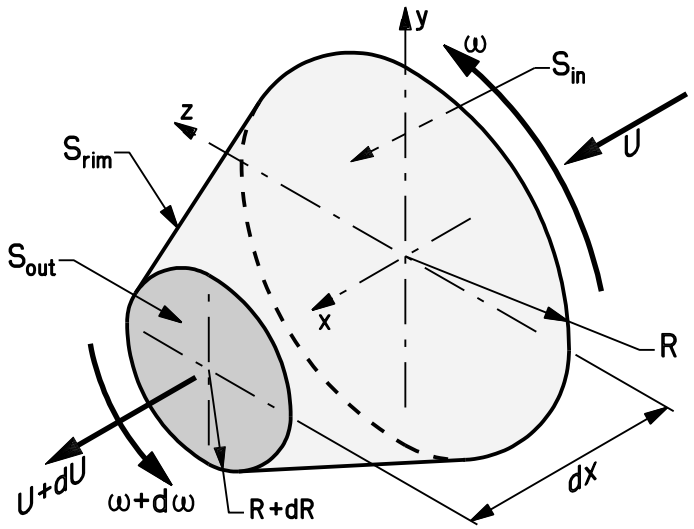

Figure 5.16: Control volume enclosing a duct cross-section of infinitesimal thickness dx. Note the changing radius of the duct. Flow is from upper-right to lower-left.

5.4.2.2 Angular momentum of forced-vortex rotation

If a duct cross-section of thickness dx is considered as a control volume of the kind shown in Figure 5.16, then for steady flow, the torque on the control volume dT is the net flow rate of angular momentum

$$dT = i \cdot \int_S (r \times U)(U \cdot n)\, \rho_a\, dA, \tag{5.19}$$

where S is the surface of the control volume and n is the unit outward normal vector on S. For the coordinate system defined in Figure 5.14, the displacement vector is

$$r = ix + jr\sin\phi + kr\cos\phi, \tag{5.20}$$

and the velocity vector U is

$$U = iU + jU_\phi \cos\phi - kU_\phi \sin\phi. \tag{5.21}$$

For forced-vortex rotation, the tangential component of velocity can be expressed in terms of the angular velocity, ω, of the cross-section "disk" as $U_\phi = r\omega(x)$. Evaluation of Equation 5.19 is simplified by rewriting it as

$$dT = \int_S (U \cdot i \times r)\,(U \cdot n)\,\rho_a\, dA. \tag{5.22}$$

The scalar triple product in the integrand reduces immediately to $U \cdot i \times r = r^2\omega$. The surface S consists of a flat inlet surface S_{in} over which $U \cdot n = -U$, a flat outlet surface S_{out} over which $U \cdot n = U$ and a cylindrical rim S_{rim} over which $U \cdot n = 0$. Equation 5.19 then becomes

$$dT = -\int_{S_{\text{in}}} r^2\omega U\rho_a\, dA + \int_{S_{\text{out}}} r^2(\omega + d\omega)(U + dU)\rho_a\, dA \tag{5.23}$$

All quantities in the integrands except r^2 can be removed from the integration because they are constant over surfaces S_{in} and S_{out}:

$$dT = -\rho_a\omega U \int_{S_{\text{in}}} r^2 dA \;+\; \rho_a(\omega + d\omega)(U + dU) \int_{S_{\text{out}}} r^2 dA. \tag{5.24}$$

After continuity over the control-volume surface, given by

$$0 = \pi(R + dR)^2(U + dU) - \pi R^2 U, \tag{5.25}$$

is used to eliminate the factor $(U + dU)$ and both integrals are evaluated over circular areas[4], Equation 5.24 yields

$$\frac{dT}{dx} = \frac{\pi}{2} R^3 \rho_a U \left(R\frac{d\omega}{dx} + 2\omega\frac{dR}{dx} \right). \tag{5.26}$$

5.4.2.3 Stream rotation due to buoyancy

Equating the torque gradient generated by the non-uniform temperature distribution of Figure 5.15 (Equation 5.18) and the angular momentum gradient (Equation 5.26) gives an expression for the gradient of rotation rate:

$$\frac{d\omega}{dx} = \frac{\Delta\Theta}{\Theta_a} \frac{g\cos\psi}{4RU} - \frac{2\omega}{R}\frac{dR}{dx}. \tag{5.27}$$

The rotation angle ψ of the temperature distribution follows the swirl streamline, and so can be calculated from

$$\frac{r d\psi}{U_\phi} = \frac{dx}{U} \tag{5.28}$$

[4]

$$\int_{S_{\text{out}}} r^2 dA = \int_{\phi=0}^{\phi=2\pi} \int_{r=0}^{r=R+dR} r^2 r dr d\phi = \int_0^{2\pi} d\phi \int_0^{R+dR} r^3 dr = \frac{\pi}{2}(R + dR)^4$$

which, with use of $U_\phi = r\omega$, becomes

$$\omega = U\frac{d\psi}{dx}. \tag{5.29}$$

Equation 5.27 then becomes a differential equation in ψ for buoyant rotation of the flow. With the aid of the continuity equation $d(UR^2) = 0$ it can be written as

$$\frac{d^2\psi}{dx^2} = \frac{\Delta\Theta}{\Theta_a}\frac{g\cos\psi}{4RU^2}. \tag{5.30}$$

The presence of the nonlinear term, $\cos\psi$, and nonuniformity of the duct radius in the wind-tunnel contraction greatly increases the difficulty of finding an analytical solution for Equation 5.30, and so it is instructive to examine the more restricted problems in which these factors can be ignored.

5.4.2.4 Solution for small rotation angle in a cylindrical duct

In the special case where the rotation angle ψ of the temperature distribution is small enough to allow the approximation $\cos\psi \approx 1$ and where the duct radius R is a constant, the solution for Equation 5.27 with the initial conditions $\psi|_{x=0} = 0$ and $\omega|_{x=0} = 0$ is

$$\omega = \frac{1}{4}\frac{\Delta\Theta}{\Theta_a}\frac{gL}{RU} = \frac{U}{4R}Ri. \tag{5.31}$$

At the periphery of the duct outlet, the swirl angle α is then given by

$$\tan\alpha = \frac{R\omega}{U} = \frac{1}{4}Ri. \tag{5.32}$$

Like the one-dimensional model in Section 5.4.1, this solution shows that the peripheral swirl angle α is approximately proportional to the Richardson number of the duct.

Equation 5.31 can be written in a form which is independent of the duct radius:

$$\omega = \frac{gL}{2U\Theta_a}|\nabla\theta|, \tag{5.33}$$

where the length of the temperature gradient vector $|\nabla\theta|$ has the same value throughout the duct. This shows that the linear temperature distribution is compatible with forced vortex rotation.

5.4.2.5 Solution for large rotation angle in a cylindrical duct

In order to examine the case where the duct radius is constant and the flow rotation angle is large enough to invalidate $\cos\psi \approx 1$, Equation 5.30 is nondimensionalised to the form

$$\frac{d^2\psi}{d(x/L)^2} = \psi_0\cos\psi, \tag{5.34}$$

Table 5.1: Accuracy of the solution for small rotation angles: $\tan\alpha = 0.25Ri$

Accuracy	$4\tan\alpha$	1% $0.99Ri$	3% $0.97Ri$	10% $0.90Ri$	30% $0.70Ri$
Control parameter	ψ_0	0.632	1.095	2.00	4.80
Richardson number	Ri	$2.53R/L$	$4.38R/L$	$8.00R/L$	$19.2R/L$
"third term"	$\psi_0^4/1920$	83.3×10^{-6}	0.75×10^{-3}	8.33×10^{-3}	0.236
Flow-rotation angle	ψ (radians)	0.316	0.542	0.967	2.07
	ψ (degrees)	18.1	31.1	55.4	118

where ψ_0 is the constant

$$\psi_0 = \frac{L}{4R}Ri. \tag{5.35}$$

An approximate solution has been found by expressing $\cos\psi$ as a truncated Taylor series, proposing a solution polynomial $\psi = P(\psi_0)$, and then iteratively substituting the proposed solution into the differential equation to obtain higher and higher-order coefficients of the solution polynomial. The solutions obtained in this way for ψ and ω at the duct outlet are

$$\psi|_{x=L} = \frac{\psi_0}{2} - \frac{\psi_0^3}{240} + \frac{\psi_0^5}{19200} - \frac{29\psi_0^7}{20966400}\ldots \tag{5.36}$$

$$\omega|_{x=L} = \frac{U}{4R}Ri\left(1 - \frac{\psi_0^2}{40} + \frac{\psi_0^4}{1920} - \frac{29\psi_0^6}{1497600}\ldots\right). \tag{5.37}$$

Finally, the swirl angle at the periphery of the duct outlet is given by

$$\tan\alpha|_{x=L} = \frac{1}{4}Ri\left(1 - \frac{\psi_0^2}{40} + \frac{\psi_0^4}{1920} - \frac{29\psi_0^6}{1497600}\ldots\right). \tag{5.38}$$

Equation 5.38 shows that the accuracy of the solution for small rotation angle (Equation 5.32) is controlled by the parameter ψ_0. As demonstrated by the examples in Table 5.1, a fairly large flow-rotation angle (ψ) of almost 1 radian is required before Equation 5.32 produces an error of 10%. For flow-rotation angles smaller than about 90 degrees the third term of the series in Equation 5.38 ($\psi_0^4/1920$) is negligible but, as ψ increases beyond 90 degrees, it grows rapidly to a size comparable with the second term ($\psi_0^2/40$). The dependence of ψ_0 on duct radius R does not destroy the compatibility of the linear temperature distribution with the assumption of forced-vortex rotation because the effect of changing R is balanced by a proportionate increase or decrease in $\Delta\Theta$ at the duct periphery.

5.4.2.6 Solution in a convergent or divergent duct without buoyant convection

In the absence of buoyant convection, Equation 5.27 can be simplified to

$$0 = \frac{d\omega}{\omega} + 2\frac{dR}{R}. \tag{5.39}$$

When integrated over the length of the control volume in Figure 5.16, this becomes the well known result for conservation of circulation:

$$U_{\phi,\mathrm{in}} R_{\mathrm{in}} = U_{\phi,\mathrm{out}} R_{\mathrm{out}} \tag{5.40}$$

or, in terms of duct cross-section area A,

$$\frac{\omega_{\mathrm{in}}}{\omega_{\mathrm{out}}} = \frac{A_{\mathrm{out}}}{A_{\mathrm{in}}}. \tag{5.41}$$

According to the continuity equation, $U_{\mathrm{in}} A_{\mathrm{in}} = U_{\mathrm{out}} A_{\mathrm{out}}$, the area ratio $A_{\mathrm{out}}/A_{\mathrm{in}}$ in Equation 5.41 can be replaced by $U_{\mathrm{in}}/U_{\mathrm{out}}$ and so, with use of the definition $\tan\alpha = R\omega/U$,

$$\tan\alpha_{\mathrm{out}} = \frac{R_{\mathrm{out}}}{R_{\mathrm{in}}} \tan\alpha_{\mathrm{in}}. \tag{5.42}$$

This result shows that, in the absence of buoyancy forces, small swirl angles are approximately proportional to duct radius. In the wind tunnel, which has a contraction with an area ratio of 20.7:1, an observed swirl angle of 1 degree in the test section implies a swirl angle of about 4 degrees near the middle of the contraction. In this scenario, buoyancy forces cause the swirl angle to increase as the flow progresses through the settling chamber and initial part of the contraction, and then the swirl angle is reduced in the highly convergent part of the contraction.

5.4.2.7 Numerical solution for wind-tunnel flow

Equation 5.30 has been solved numerically for a duct with the same profile (i.e. "radius") as the wind-tunnel settling chamber and contraction. The cross-section of the duct is circular and the contraction ratio is 25:1. The cross-section of the wind-tunnel contraction has an octagonal-to-square transition, and so the area ratio of 20.7:1 is smaller than that used in the numerical model. The solution for small flow-rotation angles (Equation 5.32) indicates that the production of flow rotation by buoyancy forces occurs almost entirely in the settling chamber and in the upstream half of the wind-tunnel contraction. In the downstream half of the contraction, changes in the flow rotation are dominated by the convergence of the duct. This means that the mismatch between the theoretical model and the experimental measurements would be approximately minimised by comparing the two on the basis of common inlet flow speed. The outlet flow velocities $U_{\mathrm{out,equiv}}$ for the solution of Equation 5.30 are therefore adjusted downwards by a factor equal to the quotient of area ratios, 20.7/25. In order to model the effects of the temperature distribution shown in Figure 5.13, the temperature nonuniformity $\Delta\Theta/\Theta_a$ at the duct inlet of the numerical model is taken as $1/300$ and, as shown in the figure, the initial rotation angle is taken as $\psi = 60$ degrees.

The numerical solutions of Equation 5.30 for distributions of swirl angle and flow-rotation angle along the length of the settling chamber and contraction are shown in Figure 5.17(a) and 5.17(b). Solutions

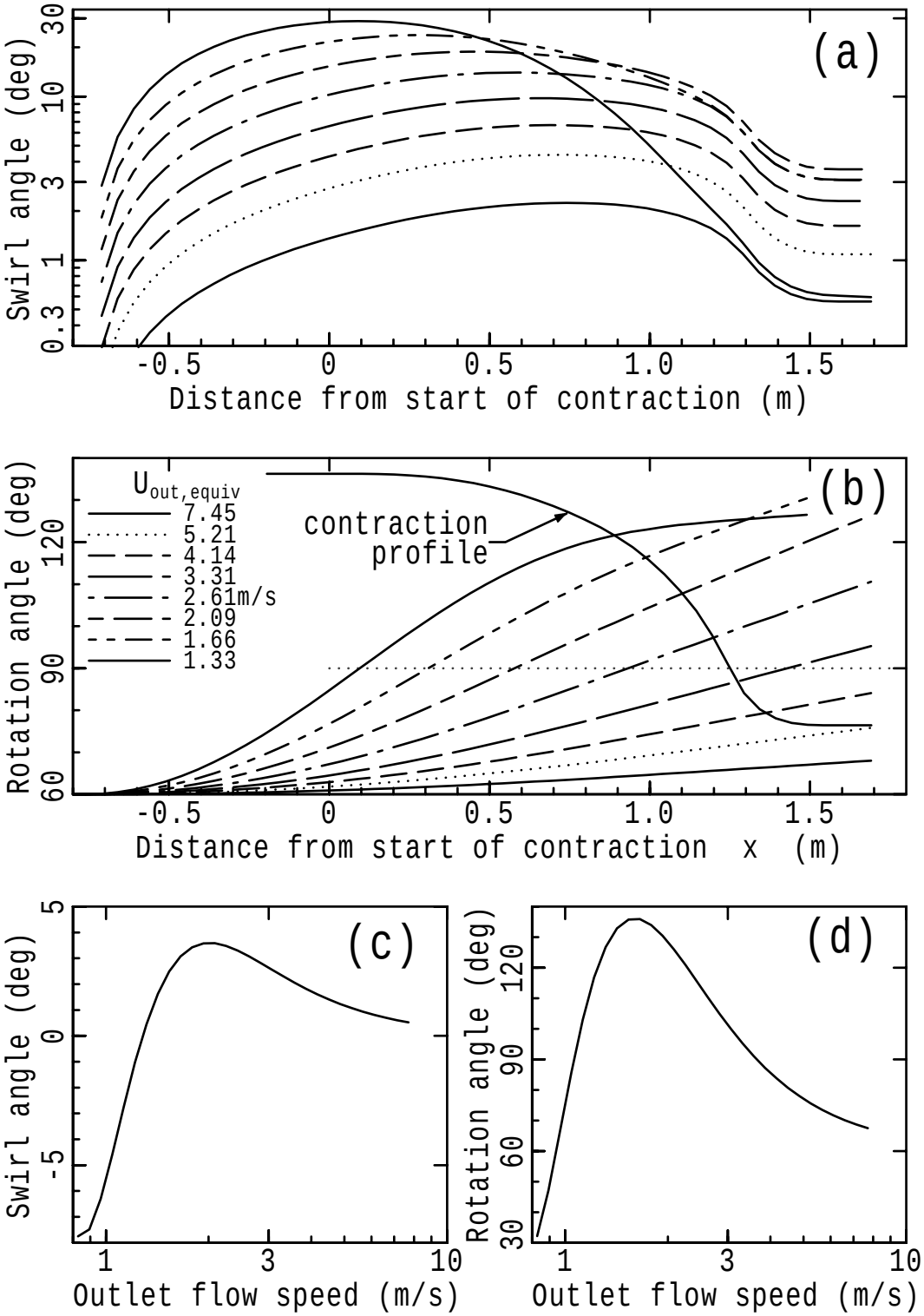

Figure 5.17: Numerical solution for buoyancy-induced swirl in the wind tunnel; (a) peripheral swirl angle α and (b) flow-rotation angle ψ along the settling chamber and contraction; (c) peripheral swirl angle α and (d) flow-rotation angle ψ at the contraction outlet. Outlet flow speeds $U_{\text{out,equiv}}$ have been adjusted to correspond with wind-tunnel flow speeds.

were obtained for test-section flow speeds ranging from 7.45 m/s to 1.33 m/s. A scaled representation of the contraction profile has been provided in Figure 5.17(b) as an aid to interpretation of the results. At all but the three lowest speeds (1.33, 1.66 and 2.09 m/s), the swirl is generated mainly in the region of large cross-section area (-0.76 m $\leq x \leq$ 0.6 m) and then is largely suppressed by the narrowing of the duct (0.8 m $\leq x \leq$ 1.5 m). When flow-rotation angles become larger than 90 degrees the direction of the buoyancy torque is reversed and the angular momentum of the flow decreases. This effect is most clearly visible for the three lowest speeds and appears as a reduction of swirl angle beginning in the region $0 \leq x \leq$ 0.6 m. In particular, at 1.33 m/s the reduction in swirl angle, which has a peak value of 28.5 degrees, is due mainly to torque reversal.

The reduction in swirl angle brought about by the strong contraction in the duct (0.8 m $\leq x \leq$ 1.5 m) might intuitively be expected to produce a corresponding decrease in the streamwise gradient of flow rotation angle ($d\psi/dx$). However, this does not happen because it would require the second derivative of ψ to be negative, and examination of Equation 5.30 reveals that, regardless of changes in duct radius, the second derivative of ψ cannot be negative unless there is a torque reversal due to $\cos\psi < 0$.

The swirl conditions at the contraction outlet are plotted as functions of equivalent outlet flow speed $U_{\text{out,equiv}}$ in Figure 5.17(c) and 5.17(d). At the highest speed ($U_{\text{out,equiv}} = \langle U \rangle = 7.45$ m/s) the calculated outlet swirl angle of 0.56 degrees is remarkably close to the 0.5 degrees of swirl measured for the temperature distribution in Figure 5.13. As speed is reduced the flow rotation and swirl angles calculated from the theoretical model increase until torque reversal causes them to peak at speeds between 1 m/s and 2 m/s. Further speed reduction produces a decrease and then a reversal of the outlet swirl angle. In a duct with constant radius, ψ would oscillate between its initial value ψ_{in} and $180^o - \psi_{\text{in}}$ but, as shown in Figure 5.17(d), the reduction in radius provided by the contraction allows these limits to be exceeded. It is even possible to select flow conditions, for example $U_{\text{out,equiv}} = 1.66$ m/s and $\psi_{\text{in}} = 0$, which produce non-oscillating or non-reversing swirl in the test section of the wind tunnel. This phenomenon can be explained by considering the work done by the buoyancy torque over a flow-rotation angle ψ_1 to ψ_2:

$$\mathcal{W} = \int_{\psi_1}^{\psi_2} T\,d\psi = \frac{\pi}{8}\frac{\Delta\Theta}{\Theta_a}\rho_a g R^3(\sin\psi_2 - \sin\psi_1). \tag{5.43}$$

In order to obtain a non-reversing swirl in the test section, the work done as rotation angle changes from ψ_{in} to 90^o in the settling chamber and contraction has to be larger than the work required to rotate the flow from 90^o to -90^o in the test section. Therefore,

$$R_{\text{in}}^3\{\sin 90^o - \sin\psi_{\text{in}}\} > R_{\text{out}}^3\{\sin 90^o - \sin(-90^o)\}, \tag{5.44}$$

and the non-reversing criterion becomes

$$2\left(\frac{R_{\text{out}}}{R_{\text{in}}}\right)^3 < 1 - \sin\psi_{\text{in}}. \tag{5.45}$$

5.4.2.8 Effect of boundary-layer friction

Surface friction would be expected to retard the tangential velocity of buoyant swirl only within the boundary layer. The effect of friction on the flow would therefore be small and would tend to reduce the radius of the forced vortex rather than retard the bulk of the flow rotation. However, if boundary-layer friction were assumed to act directly on the bulk of the forced vortex, then its effect can be modelled very easily, if crudely, by adding another term to Equation 5.27. The tangential component of wall shear stress produced by a small angle of swirl at the periphery of the duct is

$$\tau_{w\theta} = C_f\left(\frac{1}{2}\rho U^2\right)\left(\frac{U_\phi}{U}\right) = \frac{1}{2}\rho C_f U\omega R, \tag{5.46}$$

where C_f is the wall-friction coefficient. The boundary-layer thickness is assumed to be negligible. The torque applied by $\tau_{w\theta}$ to the rim of the control volume in Figure 5.16 is then

$$dT = -\tau_{w\theta}(2\pi R\,dx)\,R = -\pi\rho C_f U R^3\omega\,dx, \tag{5.47}$$

and so, with this additional torque, Equation 5.30 becomes

$$\frac{d^2\psi}{dx^2} = \frac{\Delta\Theta}{\Theta_a}\frac{g\cos\psi}{4RU^2} - \frac{2C_f}{R}\frac{d\psi}{dx}. \tag{5.48}$$

Numerical solutions of Equation 5.48 for the same conditions as in Section 5.4.2.7 show reductions in outlet swirl angle of 4.7% at $U_{\text{out,equiv}} = 7.45$ m/s and 11% at $U_{\text{out,equiv}} = 2.00$ m/s. In each case the respective friction coefficients were assumed to be a uniformly distributed $C_f = 0.004$ and $C_f = 0.009$. The uncertainty of the assumption underlying this calculation is offset by the conclusion that neglecting boundary-layer friction does not significantly affect the accuracy of numerical simulations which are based on the forced vortex model of buoyant swirl.

5.5 Suppression of buoyant convection

From the theory in the previous section, the parameter which characterises the importance of buoyant convection within a duct is the Richardson number defined by Equation 5.12. Experimental evidence suggests that buoyant swirl excited by naturally occurring random temperature variations could significantly change the characteristics of boundary layers developed in the wind-tunnel test section. Such effects would be produced by swirl angles in the contraction of, typically, only a few degrees, and

hence by Richardson numbers in the order of 0.2. If, in order to reduce buoyancy effects to acceptable levels, it were necessary to decrease the Richardson number by a factor of say 5, the maximum allowable temperature nonuniformity in the air stream would be 0.1^o C at a test-section flow speed of 7.5 m/s and 0.005^o C at 1.6 m/s. This degree of uniformity would require very thorough mixing of the air flowing into the wind tunnel.

Initial attempts at mixing the air flow with ventilation fans arranged in various ways around the bell-mouth inlet were unsuccessful because the mixing was nonuniform, because part of the inlet flow remained in an unmixed state and because the effectiveness of mixing varied with the flow conditions in the laboratory. The results of these trials indicated that mixing would be adequate only if the air flow were mixed within the confines of a duct and then delivered to the wind-tunnel inlet through a diffuser. For this purpose a centrifugal blower with a flow capacity of about 1 m^3/s was used.

5.5.1 Effectiveness of mixing by the centrifugal blower

For the spatial distribution of a scalar quantity such as temperature or species concentration, a convenient measure of mixing effectiveness η can be obtained from the initial and final standard deviations of the distribution:

$$\eta = 1 - \frac{\sigma_{\text{final}}}{\sigma_{\text{initial}}}. \tag{5.49}$$

Hilby (1981) used a related measure of inhomogeneity based on variances rather than on standard deviations. The effectiveness and suitability of the centrifugal blower as a mixing device was therefore determined from measurements of temperature distribution at its inlet and outlet. The required inlet temperature nonuniformity was produced by placing an electric fan-heater near the blower inlet, and temperatures were measured with a hand-held Solomat MPM 2000 platinum resistance thermometer. The flow rates, which were equivalent to test-section flow speeds of 2.1, 3.6, 6.3 and 12 m/s, were measured with a Solomat vane anemometer. The temperature distributions for 3.6 m/s are shown in Figure 5.18 as a series of isothermal contours. The locations of the 50 or so individual measurements in each distribution were selected by placing the temperature sensor in the alternate spaces of a 1-mesh-per-inch wire-mesh screen at the inlet and outlet. The piecewise linear appearance of the isotherms in Figure 5.18 is mainly due to the large spacing between measurement locations and lack of refinement in the contour-drawing algorithm. Each temperature measurement is a result of time-averaging over a period of about one minute. The resolution of the thermometer was 0.1^o C.

For the result shown in Figure 5.18 ($\langle U \rangle = 3.6$ m/s) and at the higher speeds of 6.3 and 12 m/s, the effectiveness of mixing was approximately constant at $\eta = 97.5\%$. At the lowest speed ($\langle U \rangle = 2.1$m/s) a value of $\eta = 94.5\%$ indicated much poorer mixing and so, when the blower was connected to the wind tunnel, it was always operated at an r.p.m. higher than required for the temperature measurements

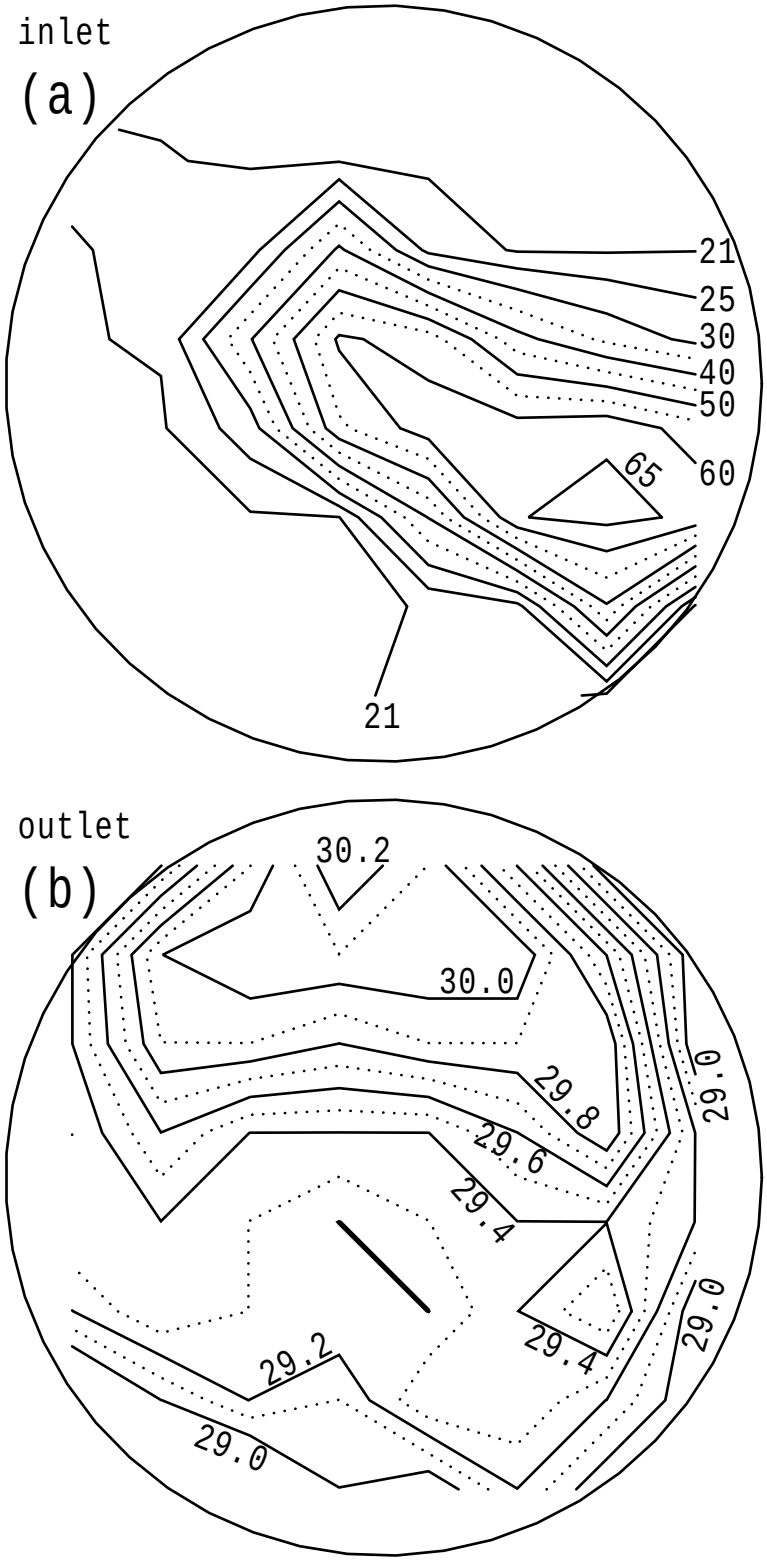

Figure 5.18: Temperature distributions at (a) inlet and (b) outlet of the centrifugal blower used for mixing the inlet air flow of the wind tunnel. Isotherms drawn as solid lines are labelled in degrees Celsius. Inlet and outlet diameters are approximately 300 mm. $\langle U \rangle \approx 3.6$ m/s

at 3.6 m/s. While $\eta = 97.5\%$ indicates very thorough mixing of the flow, for a naturally occurring temperature nonuniformity of 1^o C at the blower inlet, it is still lower than the estimated minimum requirement of $\eta = 99.5\%$ at a test section flow speed of 1.6 m/s. However, these measurements of mixing effectiveness indicate that the centrifugal blower would be able to suppress buoyant convection over at least the upper half of the wind-tunnel speed range.

5.5.2 Design of the wide-angle inlet diffuser

The purpose of the diffuser was to take the flow from the centrifugal blower through an area-expansion ratio of 15.1:1 and to deliver it to the wind-tunnel inlet as a steady attached flow with an approximately uniform velocity distribution. In addition, the diffuser had to be short so that it would fit within the available laboratory space.

In the absence of any measures to prevent boundary-layer separation, the area expansion ratio of a diffuser designed for steady flow is limited to about 2.5:1 and the maximum diffuser angle to about 5^o. In this case, where the area ratio is much larger and the diffuser angle is 45^o, development of the boundary layer within the diffuser is controlled by inlet guide vanes and a sequence of wire-mesh screens. The number and location of the screens was determined largely from the design guidelines developed by Mehta (1977). As shown in Figure 5.19, screens in the downstream half of the diffuser are clamped between flanges to ensure that they intersect the diverging walls at right angles. This and other design details such as the use of curved fairings at each end of the diffuser also follow the recommendations of Mehta.

Initial trials, in which diffuser stages 2, 3 and 4 were removed (see Figure 5.19), were conducted without any screens in stage 1 of the diffuser and the only flow control devices were the inlet guide vanes. These trials revealed a steady reversed flow over the central 20% to 30% of cross-section area at the end of stage 1. On at least one of the 8 walls, there was a boundary-layer separation which was very sensitive to changes in the inlet flow. The strength of the separation and the sensitivity to the condition of the inlet flow were greatly reduced by installing a screen immediately upstream of the guide vanes. In order to eliminate the separation and flow reversal completely, it was necessary to place screens at one third and at two thirds of the way along stage 1 of the diffuser. At this point, large perturbations of the inlet flow could still produce a noticeably nonuniform flow at the outlet of stage 1.

When the diffuser was fully assembled, further investigation of its performance became much more difficult because the flow speeds at its outlet were extremely low. However, a pulse of smoke injected at the inlet of the centrifugal blower was observed a few seconds later to emerge almost simultaneously from every part of the diffuser outlet as a uniform mist.

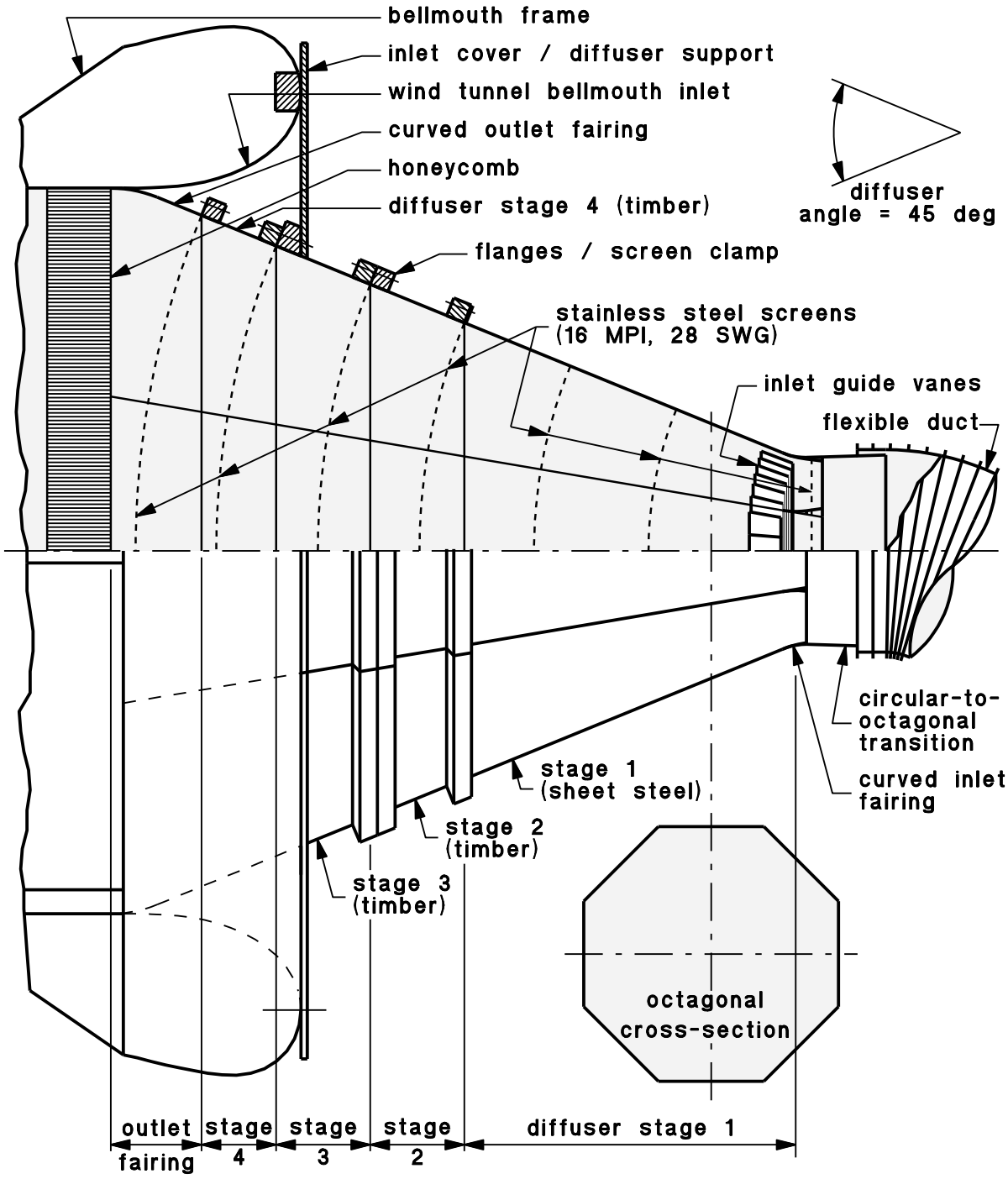

Figure 5.19: Wide-angle inlet diffuser — assembled and installed. The top half of the drawing is sectioned. The flexible duct is connected to the outlet of the centrifugal blower. Scale 1:10.

5.5.3 Evaluation of buoyant secondary flow suppression

The effectiveness of the centrifugal blower as a suppressor of naturally occurring buoyant convection has been examined for a test-section flow speed of 7.5 m/s. The flow-visualisation technique used in these tests is described in Section 5.2. At the start of a test the centrifugal blower was switched off and a single forced-vortex swirl was often detected but, in each of these cases, the swirl eventually decayed and disappeared after the centrifugal blower was switched on. The time taken for the swirl to disappear was usually between 5 and 10 minutes. The length of this time delay, which was much larger than that indicated by Figure 5.7, was attributed to the thermal inertia of the wire-mesh screens in the diffuser.

A fan-heater was then used to produce large temperature asymmetries at the blower inlet. These temperature variations were approximately the same as those shown in Figure 5.18(a). With the blower switched off, these asymmetries generated large flow disturbances in the test section at flow speeds of 4 m/s and 7.5 m/s. As expected, when the blower was switched on, the disturbances became much weaker and smaller but were not entirely removed. On removal of the heat source from the blower inlet, the disturbances decayed and disappeared.

5.5.4 Residual disturbances

After the blower and wide-angle diffuser were installed, slowly varying and rapidly fluctuating streamer deflections of the type shown in Figure 5.9(f) occurred much more frequently than in experiments performed prior to the installation. Further examples of such streamer patterns are provided in Figure 5.20. The flow which produces this type of streamer deflection has smaller length scales and much higher rotation rates than the forced vortex produced by buoyant convection. Its characteristics and behaviour are quite different from those of buoyant swirl and it can readily be distinguished from buoyancy-driven swirl by observing the streamers. These strong non-buoyant secondary flows would clearly have a large effect on the development of test-section boundary layers, and so also have to be suppressed. This problem is addressed in the next chapter.

The presence of non-buoyant secondary flows made it extremely difficult to evaluate the effectiveness of the centrifugal blower. However, natural buoyant excitation of classical forced-vortex swirl was never observed while the centrifugal blower was in use.

5.6 Summary

Weak secondary flows have been detected in the test section of an open-circuit wind tunnel by observing the patterns formed by an array of streamers. These secondary flows extended over a significant

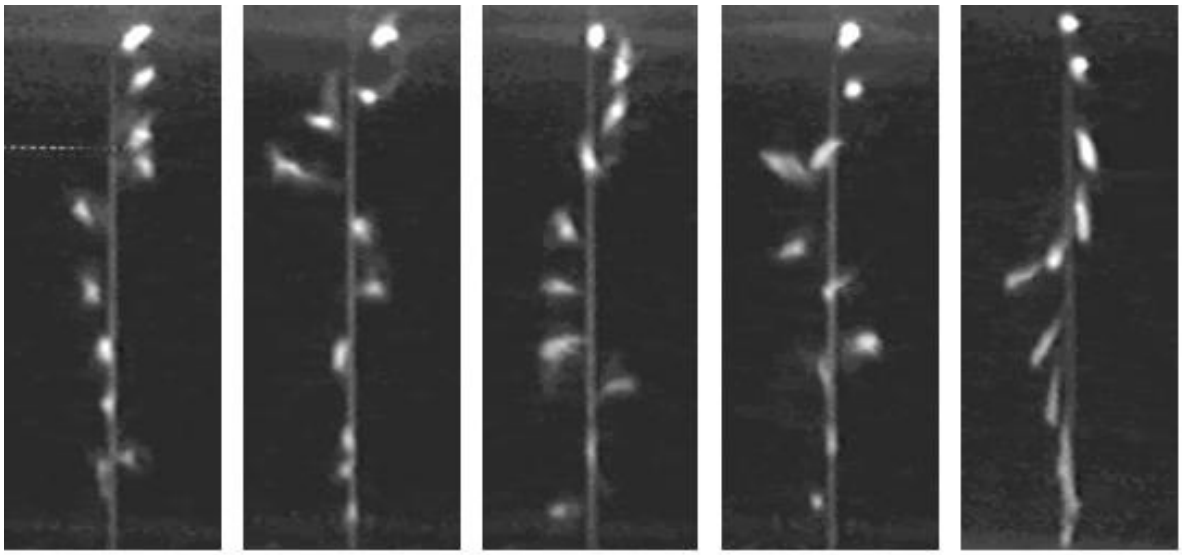

Figure 5.20: Streamer deflections produced by strong non-buoyant free stream secondary flows at a flow speed of $\langle U \rangle = 4.1$ m/s.

proportion of the test-section length and usually took the form of a single streamwise vortex occupying most of the available duct cross-section. The angle of swirl was typically one or two degrees at the periphery of the vortex. The fluctuation time-scale of the forced-vortex swirl angle was in the same order of magnitude as the time-scale of variations in boundary-layer thickness.

Further experimental investigation showed that the forced-vortex secondary flow is a form of buoyant convection generated within the settling chamber and contraction of the wind tunnel. The density variation which drives this convection is produced by temperature nonuniformity of the air drawn into the wind-tunnel inlet. The principal mode of secondary flow is a single forced vortex occupying the entire cross-section of the duct. As the temperature nonuniformity is gradually increased, the single vortex develops into a pair of steady counter-rotating vortices which then "breaks down" and produces large and rapid oscillation of the streamers.

The development of a forced vortex generated by a linear temperature distribution can be modelled mathematically as a single second-order ordinary differential equation. The analytical solution for small rotation angles in a pipe flow shows that the peripheral swirl angle is

$$\alpha = \frac{1}{4} Ri, \qquad \text{where} \qquad Ri = \frac{\Delta\Theta}{\Theta_a} \frac{gL}{U^2} \tag{5.50}$$

is the Richardson number of the flow. Numerical solutions of the differential equation indicate that swirl develops in the wind-tunnel settling chamber and in the upstream half of the contraction, but is reduced by the convergence of the duct in the remainder of the contraction. For a test-section flow

speed of 7.5 m/s and an inlet temperature nonuniformity of 1^o C, the numerical model predicts an outlet swirl angle which is very close to the experimentally measured value of 0.5^o.

Buoyant convection was effectively suppressed by mixing the wind-tunnel inlet flow in a centrifugal fan. Measurements showed that this centrifugal fan, which was similar to those used in open circuit "blower" wind tunnels, could reduce the temperature nonuniformity in an air flow by a factor of 40. The flow from the blower was delivered to the wind-tunnel bellmouth inlet through a wide-angle diffuser with an area-expansion ratio of 15.1:1.

Flow visualisation experiments also reveal the presence of a complex vortex structure which is quite different from and is much stronger than the weak single-vortex secondary flow produced by buoyant convection. The complex vortex structure is observed much more frequently after installation of the wide-angle diffuser and in the absence of buoyant convection than in the initial experiments. The first clue to the cause of this flow disturbance is provided by Figure 4.32(d) in which a pair counter-rotating Görtler vortices is apparently observed to have moved away from direct contact from the wall surface and into the free stream flow. The relationship between the weak three-dimensional separation produced by Görtler instability and the vigorous flow disturbances illustrated in Figure 5.20 is examined more closely in the next chapter.

5.7 Notation

A	cross-section area
A_{in}, A_{out}	areas of control-volume surfaces S_{in} and S_{out}
C_f	local boundary-layer skin-friction coefficient
CO_2	carbon dioxide
F	buoyancy force
F_i	$F_i = g_i$ per unit mass body force tensor due to gravity
g	gravitational acceleration
g_i	$-kg$, gravitational acceleration tensor
i, j, k	unit vectors in the x, y and z directions
k	constant of proportionality
l/d	length to diameter ratio of honeycomb cells
L	length of duct
MPI	weave density of a woven wire screen in "meshes per inch"
n	unit outward normal vector on the control-volume surface S
$\tilde{p}$	time-dependent air pressure
P	steady air pressure

P_a	time and space-averaged ambient air pressure
$P(\psi_0)$	a polynomial of ψ_0
r	displacement vector
R	radius of cylindrical duct
Re_θ	$U_0\theta/\nu$, Reynolds number based on boundary-layer momentum thickness θ
Ri	Richardson number, defined by Equation 5.12 on page 133
S	Surface of truncated conical control volume, with flat inlet surface S_{in}, flat outlet surface S_{out} and cylindrical rim S_{rim}
SWG	Standard Wire Gauge — a measure of wire diameter
t	time
T	buoyancy torque on the duct flow
U	steady air-velocity vector
U, V, W	components of steady air-velocity in x, y and z directions
U_j	steady air-velocity tensor
U_0	free stream speed in wind-tunnel test section
$U_{\text{out,equiv}}$	Flow speed at outlet of the axisymmetric wind tunnel contraction multiplied by 20.7/25. The flow rate at the contraction outlet is then equal to the flow rate produced by $U_{\text{out,equiv}}$ in the test section.
U_ϕ	tangential component of flow velocity (see Figure 5.14)
$\langle U \rangle$	bulk flow speed in the wind-tunnel test section; i.e. flow speed averaged over the cross-section area
$\tilde{u}_i$	time-dependent air-velocity tensor
dV	infinitesimal volume element, $dV = dA\,dx$
$\mathcal{W}$	work done by the buoyancy torque T over a flow-rotation angle
x	distance downstream from the start of the test section, from the origin of the boundary layer, from the start of the wind-tunnel contraction or from the start of a duct
x_j	displacement tensor
x, y, z	streamwise, vertical and lateral components of displacement from an origin
(x, r, ϕ)	cylindrical coordinate system for forced-vortex model of buoyant convection; $z = r\cos\phi$, $y = r\sin\phi$.
α	angle through which the air-velocity vector is turned by buoyant convection or swirl angle at the periphery of a forced vortex
$\Delta\theta$	elevation of air temperature above the ambient temperature, Θ_a
$\Delta\Theta$	amplitude of the variation in $\Delta\theta$ over a duct cross-section
η	$1 - \sigma_{\text{final}}/\sigma_{\text{initial}}$; effectiveness of mixing
θ	$\int_0^\infty (1 - U/U_0)(U/U_0)\,dy$, boundary-layer momentum thickness

Θ_a	ambient air temperature
μ	dynamic viscosity
ν	μ/ρ, kinematic viscosity
ρ	air density
ρ_a	ambient air density
σ_{initial}, σ_{final}	standard deviations of temperature distributions before and after mixing
$\tau_{w\theta}$	tangential component of wall shear stress
ϕ	azimuth angle in the cylindrical coordinate system (r, ϕ, x)
ψ	rotation angle of the flow or rotation angle of the temperature distribution due to buoyant convection
ψ_{in}	rotation angle of a linear temperature distribution at a duct inlet
ψ_0	nondimensional term defined by Equation 5.35 on page 138
ω	angular velocity of a forced-vortex flow
$\nabla\theta$	temperature gradient

Vectors

Vectors are indicated by **bold** typeface.

Superscripts

Variables written with a ˜ (e.g. $\tilde{u}$) are time dependent.

Subscripts

i, j, k	tensor subscripts for *x*, *y* and *z* components
in	at the inlet of a duct or control volume
out	at the outlet of a duct or control volume

Chapter 6

Three-dimensional separation in the contraction

6.1 Introduction

Velocity measurements described in earlier chapters have shown that the characteristics of the test-section turbulent boundary layer varied irregularly with time. Further experimental investigations found that these variations were associated with two-dimensional laminar boundary-layer separation within the wind-tunnel contraction, with the formation of Görtler vortices in the contraction, and with the development of large-scale buoyant swirl in the low-speed flow upstream of the test section. By a series of appropriate modifications to the contraction and inlet section of the wind tunnel, and by boundary-layer suction at the start of the test section, these flow mechanisms were suppressed so that they no longer perturbed the test-section boundary layer. Further flow-visualisation tests (Section 5.5.3) then revealed the presence of yet another type of secondary flow within the test section. This secondary flow disturbance was much stronger than that produced by buoyant convection.

Previous flow-visualisation experiments (Sections 4.12 and 5.5.4) indicated the most likely cause of the secondary flow to be a three-dimensional separation from the concave walls of the contraction. Further flow-visualisation experiments described in Sections 6.2 and 6.3, confirmed this hypothesis and pointed to measures which could be taken to prevent this type of flow separation. Successful suppression of the separation is the final step in establishing a boundary layer free of external disturbances.

6.2 Experimental investigation of flow in the test section

6.2.1 Initial observations of streamer deflection

The purpose of these experiments was to identify the cause of the flow disturbances shown in Figure 5.20. The flow-visualisation technique, relying on the lateral displacement of streamers to reveal the behaviour of the test-section flow, was initially the same as that described in Section 5.2.1.

The first part of the experiment was to examine the effect of flow speed and the suction manifold on streamer deflection. Some results of these tests are shown in Figure 6.1. In the absence of a suction flow at the start of the test section, the flow was straight, steady and free of disturbances at flow speeds in excess of about 7 m/s. When the air speed was decreased from this value the disturbance first appeared as as a small lateral displacement of the lowest streamer (Figure 6.1(a)). With further reduction in air speed, the deflection of the streamers increased and the disturbance moved towards the centre of the duct (Figures 6.1(b–e)). The pattern formed by the streamers was usually unsteady and indicated the presence of a quasi-cyclic fluctuating flow structure with a characteristic frequency in the order of 0.3 Hz to 3 Hz. The finer details of the patterns varied with with each repetition of the experiment. Each of the images in Figure 6.1 was obtained at a phase in the disturbance cycle where the streamer deflection was near a maximum.

The effect of using the suction manifold can be seen by comparing Figures 6.1(f–j) with Figures 6.1(a–e). This comparison shows that the suction flow drew the disturbance closer to the floor of the test section and decreased the maximum speed at which the disturbance could be observed, but did not suppress it or change its general behaviour. On the assumption that the flow disturbance was generated upstream of the suction manifold, these observations are entirely consistent with main actions of the manifold, which were to remove flow adjacent to the walls of the duct and to increase the flow rate upstream of the manifold.

6.2.2 Detection of flow disturbance by pulsed smoke cloud

The next step in the investigation was to determine which component of the wind tunnel was responsible for generation of the flow disturbance. Buoyant convection within the wind tunnel is driven by small temperature gradients in the air entering from the laboratory (Sections 5.3.2 and 5.4). The temperature gradients vary with time and sometimes might not produce detectable buoyant cross-flow for periods of more than an hour or so. Under these conditions, when buoyant convection was negligible, removal of the mixing fan and inlet diffuser from the wind tunnel had no effect on the formation of flow disturbances of the type shown in Figure 6.1. The settling chamber was then disconnected from

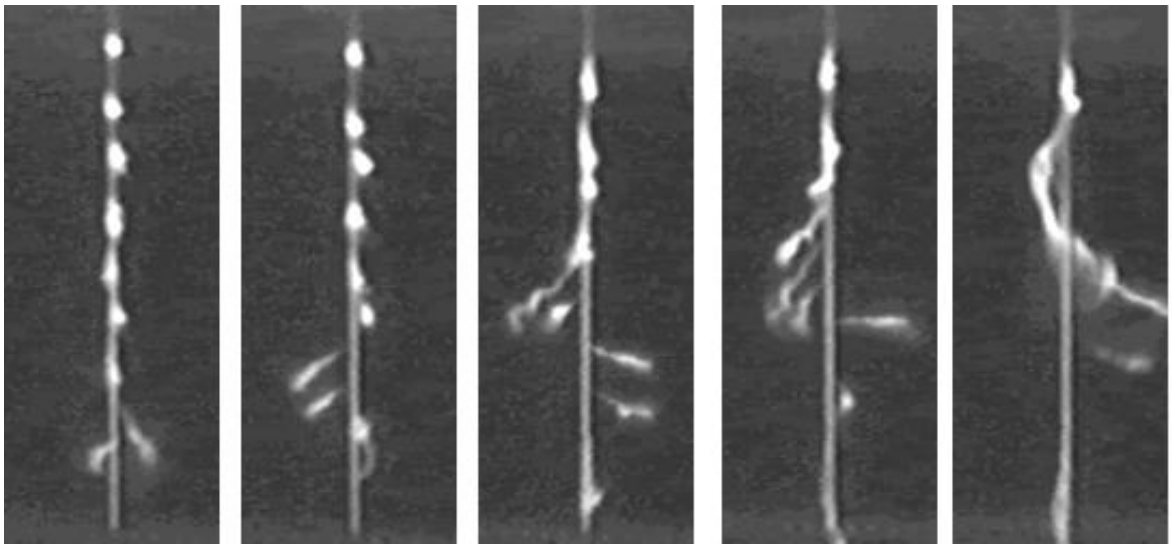

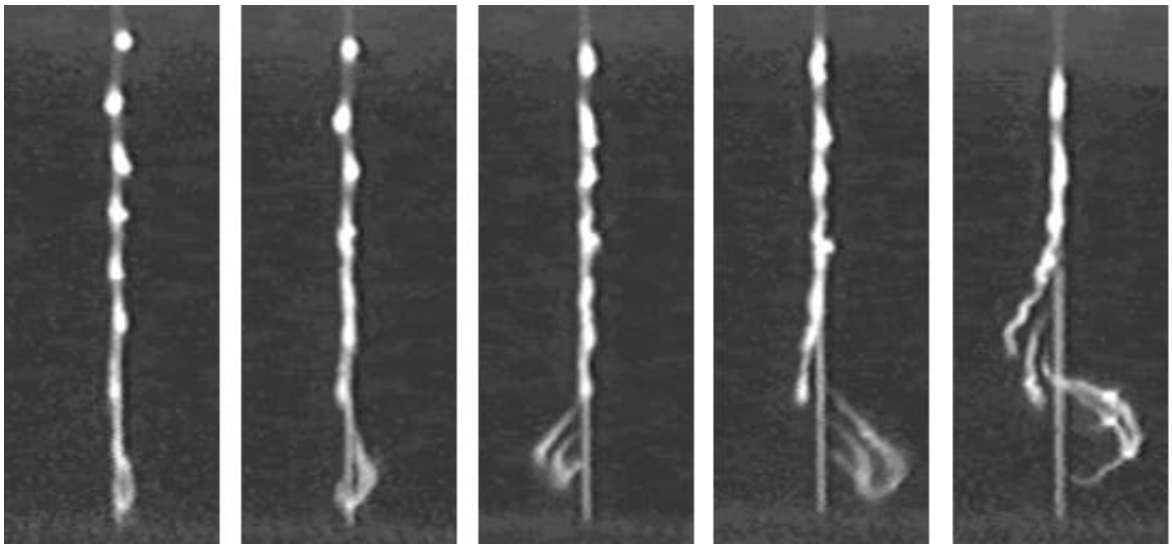

Figure 6.1: Effect of the suction manifold and changing flow speed ($\langle U \rangle$) on streamer deflection; (a–e) without suction flow; (f–j) with suction flow. The streamers are located between Port 1 and Port 2 of the test section.

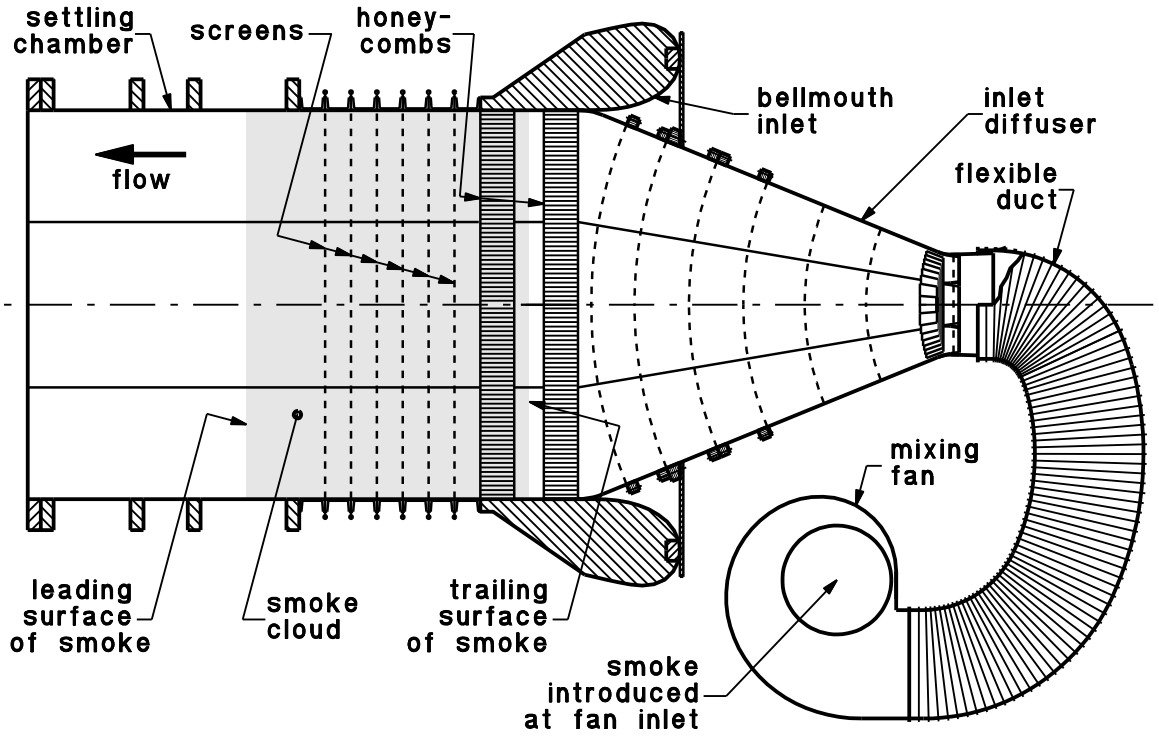

Figure 6.2: Schematic diagram of smoke flow through the inlet section of the wind tunnel. The settling chamber was disconnected from the contraction.

the contraction and the flow through the diffuser, honeycombs and screens was examined by feeding smoke into the the inlet of the mixing fan. This arrangement is shown in Figure 6.2. Smoke emerged from the screens as a uniformly dense cloud moving at an apparently steady and uniform speed over the entire duct cross-section. When the smoke flow was switched on and off at intervals of about 30 seconds, each cloud of smoke passing through the wind-tunnel inlet had fairly well defined leading and trailing surfaces which appeared to be flat and perpendicular to the flow direction. This uniformity and the absence of lingering trails behind each pulse of smoke were strong indications that the flow through the settling chamber was free of disturbances like those observed in the test section.

The inlet section of the wind tunnel was then reassembled and the same pulsed-cloud technique was used to examine the behaviour of flow emerging from the contraction. From this point on, the suction manifold was not used in any flow visualisation experiments. From the very first observations of combined smoke flow and streamer deflection, the leading and trailing surfaces of the smoke cloud appeared to have developed some definite structure during their journey through the contraction. In the leading surface of the cloud, this structure was visible as deep holes, and in the trailing surface it was visible as long tails of smoke. At a bulk flow speed of about 2.4 m/s, both of these features were visible for several seconds after the passing of the main smoke/clear-air interface. The examples of smoke and

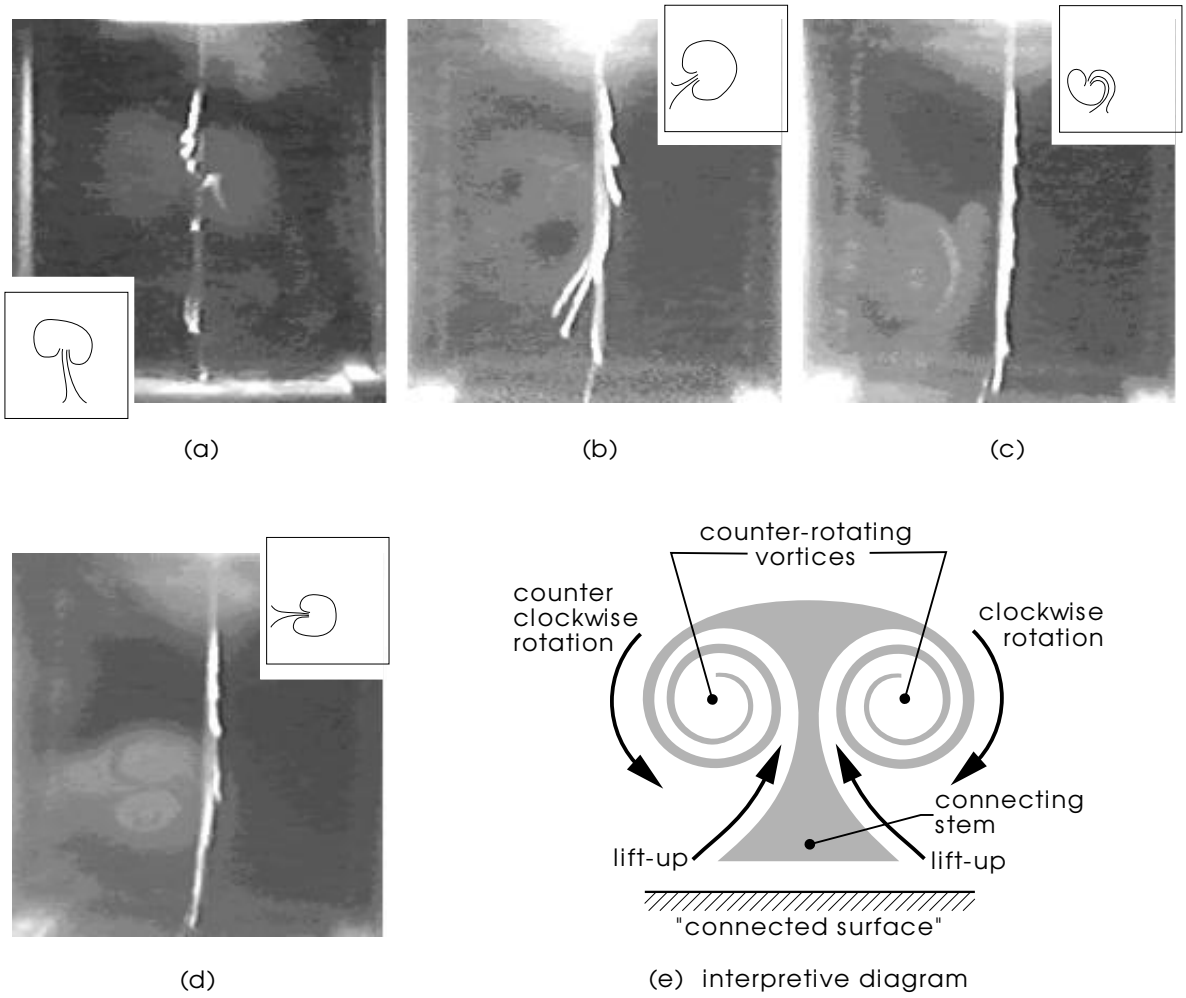

Figure 6.3: Observations of combined streamer deflection and smoke pattern at the trailing surface of a smoke cloud. As shown in the interpretive diagram (e), these images (a–d) indicate the presence of a pair of counter-rotating streamwise vortices at various locations and orientations in the test section duct. The streamers are located between Port 1 and Port 2 of the test section. Suction is not used. $\langle U \rangle \approx 2.4$ m/s

streamer patterns in Figures 6.3(a–d) show that the streamer deflections are closely correlated with the smoke patterns and that both are clearly produced by the same flow disturbance. The double circular shapes formed by the distorted surfaces of the smoke cloud indicate the presence of two streamwise vortices associated with one of the duct surfaces by a connecting “stem” (Figure 6.3(e)). The details of streamer deflection confirm that the vortices in each pair are counter-rotating in a direction which induces migration of the vortex cores away from the associated surface and, in the region between the vortices, lifts flow from that surface. As suggested by the variety of images in Figures 6.3(a–d), the location and orientation of vortices within the duct cross-section are at least partly random. At flow

speeds lower than about 4 m/s, the vortex pair frequently migrates slowly from one part of the duct cross-section to another or develop an oscillatory motion with a frequency in the order of 0.3 Hz to 3 Hz.

6.3 Three-dimensional separation in the contraction

In these experiments, the counter-rotating vortices were made visible by retardation of flow within the contraction. The only source of retarded flow in the contraction was the boundary layer on its internal surfaces, and so it was reasonable to conclude that the vortex pairs observed in the test section resulted from three-dimensional boundary-layer separation from the inner surfaces of the contraction. The existence of a two-dimensional separation would have required a zero-shear-stress line on the surface and the formation of a closed separation bubble. In this case neither of these conditions was satisfied because there were no regions of near-stagnant recirculating fluid on the internal contraction surfaces (Section 4.12.2) and because streamsurfaces in the form of counter-rotating vortex "tubes" emerged from the separation region.

6.3.1 Inadequacy of Görtler instability as a separation mechanism

The flow-visualisation experiment described in Section 4.12.3 produced evidence that Görtler vortices developed in the contraction at test-section flow speeds between 2.4 m/s and 7.4 m/s. The results shown in Figure 6.4, which were obtained in the same way as those of Figure 6.3, might therefore seem to confirm that streamwise vortices near the centre of the duct were simply pairs of Görtler vortices which had become detached from the surfaces of the contraction and had migrated away from the surface in accordance with the Biot-Savart law. However, several features in the experimental results indicate that mechanisms other than Görtler instability provided the driving force for strong three-dimensional separation in the contraction.

The first of these features was that, without deliberate stimulation from devices such as heating coils or winglets, Görtler instability had been observed to produce an array of several streamwise vortices (Figure 4.32) [Tani, 1962, Swearingen and Blackwelder, 1987]. In contrast, for flow speeds greater than about 2 m/s the detached streamwise vortex pairs shown in Figures 6.3 and 6.4 usually appeared as solitary structures. As flow speed was reduced to about 1 m/s, the simultaneous appearance of a second or third detached vortex pair occurred more frequently, and their migratory or wandering motion tended to increase. In most of these cases the additional vortex pairs originated from different contraction surfaces. With a decrease in flow speed below 1 m/s the number of vortex pairs increased further, their persistence declined, they became transitory and eventually the unsteadiness of the flow increased to

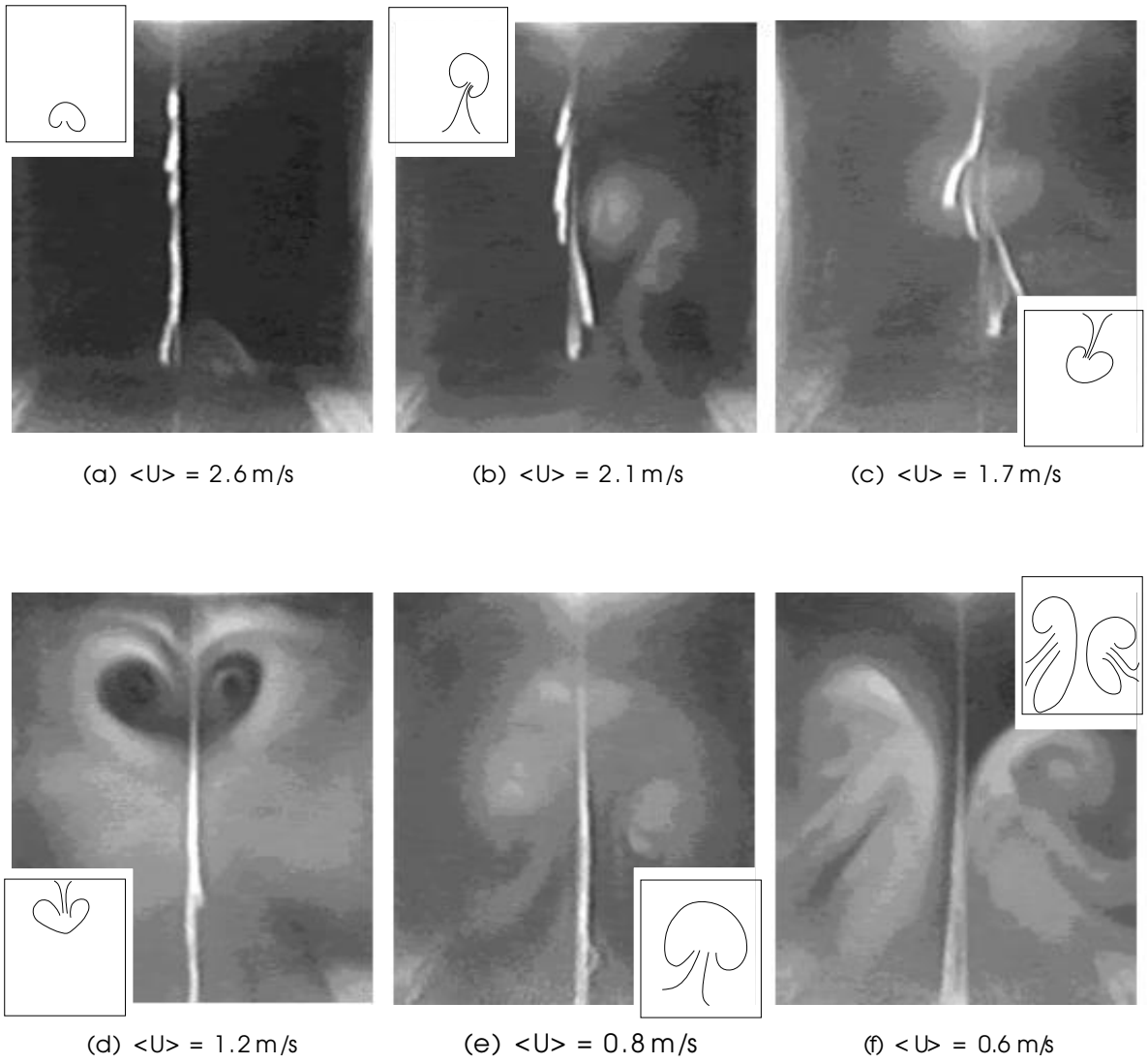

Figure 6.4: Variation in the behaviour and scale of counter-rotating streamwise vortices with decreasing flow speed. These experiments are described in Section 6.2. The streamers are located between Port 1 and Port 2 of the test section. Suction is not used.

a level at which details became unclassifiable (Figure 6.4(f)). This experimentally observed decrease in stability was the opposite of what would have been expected from a separation driven by Görtler instability because, at a fixed location in a Blasius boundary layer, the Görtler number is theoretically proportional to $U_0^{1/4}$. The theoretically calculated dependence of amplification rate on Görtler number [Görtler, 1941] then implies that a decrease in flow speed *should* have produced a weak reduction in the degree of instability and a weak reduction in the growth rate of disturbances. This would then have delayed the onset of the oscillations.

Another inconsistency with behaviour expected of Görtler vortices was the variation in size of de-

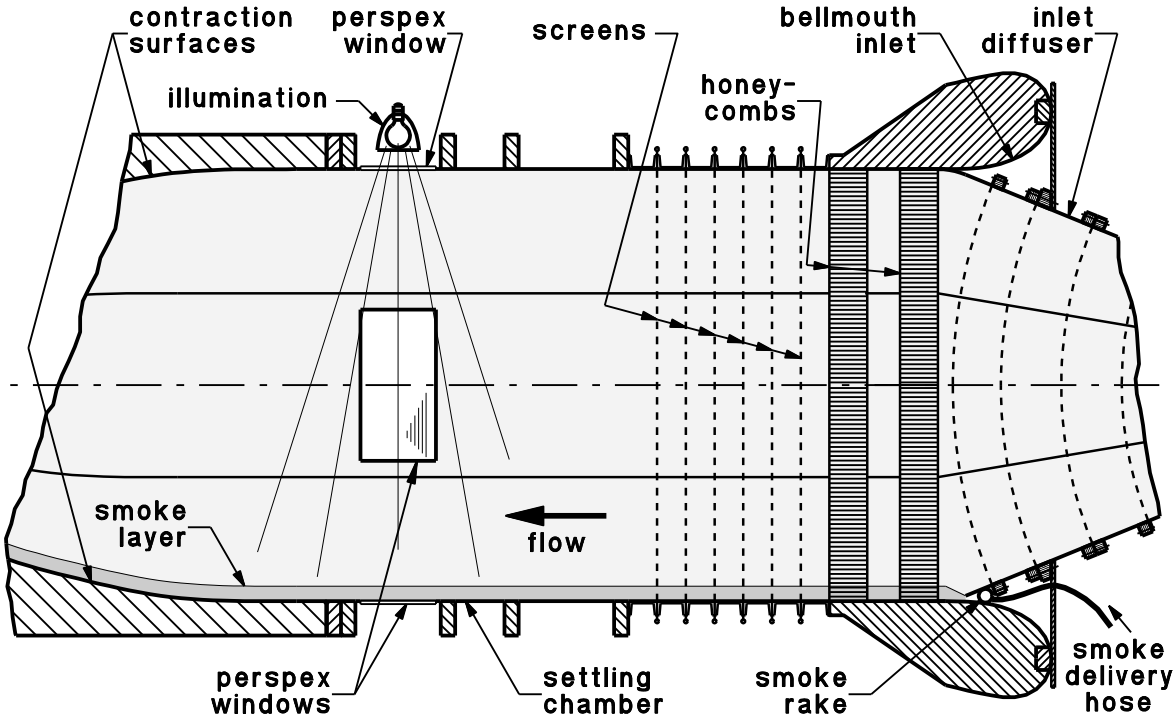

Figure 6.5: Flow-visualisation arrangement for direct observation of three-dimensional separation in the contraction. Scale 1:20

tached vortex pairs over the range of flow speeds. As illustrated in Figures 6.4(a) to 6.4(e), detached vortex pairs generally became larger as flow speed was reduced. On the other hand, the wavelength selection mechanism of Görtler instability is independent of streamwise location and is so weak [Floryan and Saric, 1984] that spacing and spanwise location of streamwise vortices are determined by pre-existing nonuniformities in the flow field [Swearingen and Blackwelder, 1986, Bippes, 1990]. Böttcher and Wedemeyer (1989) have found that the lateral wavelength of disturbances produced by a screen increases with downstream distance until, at a sufficiently large distance, it becomes constant[1]. From this point, where the lateral dimensions and locations of flow nonuniformities are fixed, the spanwise length scale of Görtler vortices is independent of flow speed.

Experimental observations described in Section 4.12.3 show that Görtler vortices were produced within the contraction throughout the upper half of the flow-speed range ($\langle U \rangle \gtrsim 5$ m/s). The pulsed-cloud technique of flow visualisation does not detect these vortices because typical vortices produced by the Görtler instability mechanism are very weak and, in comparison with the detached vortex pairs illustrated in Figures 6.3 and 6.4, do not significantly retard any part of the flow. The anomalies described in the previous two paragraphs, the large streamer deflections in the flow-visualisation images

[1]For the settling-chamber screens in the wind tunnel, the downstream distance required for the disturbance wavelength to become constant would be, according to results obtained by Böttcher and Wedemeyer (1989), between 2 mm and 44 mm.

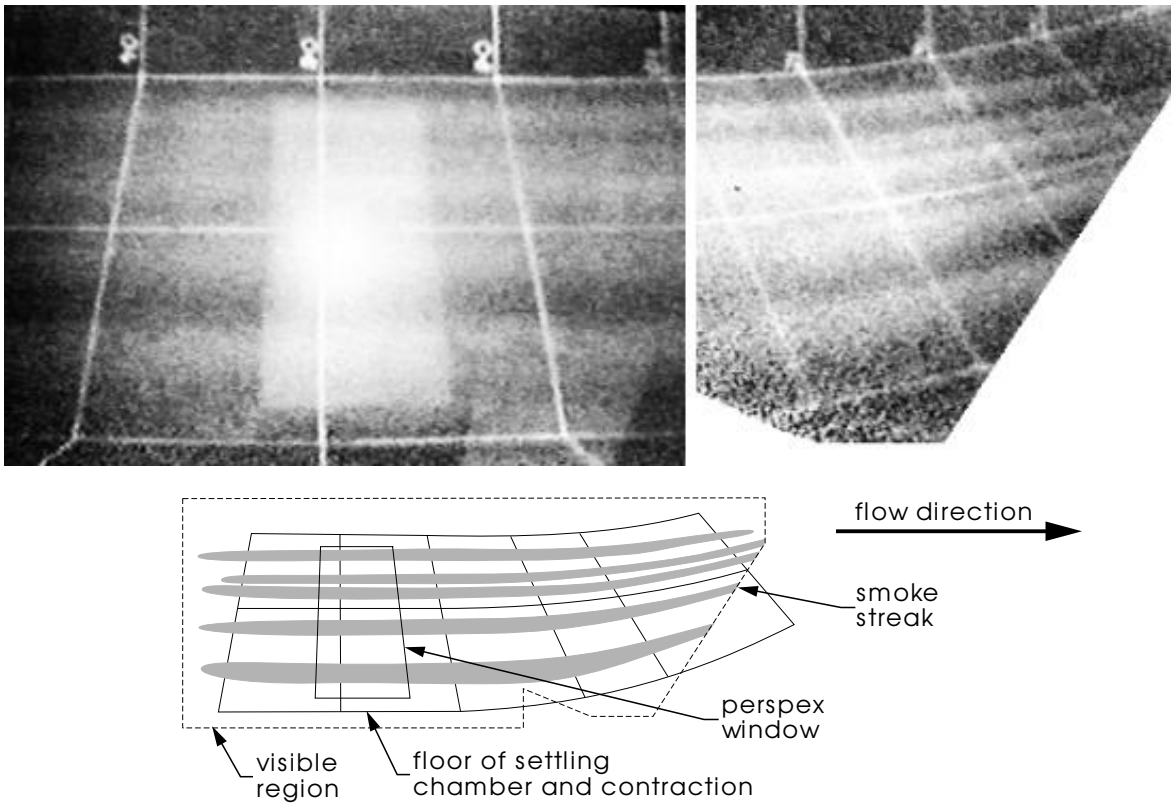

Figure 6.6: Development of low-speed streaks on the floor of the settling chamber and contraction at $\langle U \rangle = 7.8$ m/s without lifting from the surface. The behaviour of the smoke layer was observed through a side-wall window in the settling chamber.

and the substantial retardation of fluid contained within the detached vortex pairs therefore suggest the presence of a vortex-growth mechanism which is much stronger than and qualitatively different from Görtler instability.

6.3.2 Direct observation of separation in the contraction

In order to observe the process of separation in the contraction more directly, an internally flush-mounted perspex window was built into each non-diagonal side of the settling chamber and, as illustrated in Figure 6.5, smoke was injected into the boundary-layer flow from the junction of the inlet diffuser and the bellmouth. The interior of the wind tunnel was painted matt black and was illuminated through the window in the top surface of the settling chamber. The behaviour of smoke on the floor was viewed through a side-wall window. It was also possible to see the simultaneous effects on the test-section flow because the flow-visualisation arrangements shown in Figure 5.5 were still in place.

The clearest feature of the smoke layer on the floor of the wind tunnel was its lateral nonuniformity. At each of the flow speeds studied in the experiment, this nonuniformity was visible as four or five broad streaks which emerged from the final settling-chamber screen. For the highest flow speed ($\langle U \rangle = 7.8$ m/s) the smoke streaks became more distinct and more clearly separated from each other as they progressed through the settling chamber and contraction (Figure 6.6). Estimates of the Görtler number on the concave contraction surface were mostly in the range where amplification of disturbances has been observed experimentally [Floryan and Saric, 1982], and so this gradual intensification of weak flow disturbances was believed to be a product of Görtler instability. Near the downstream end of the contraction the streaks were compressed laterally by flow from the tapered diagonal surfaces so that they occupied only one half of the test section width. Observations from the test section showed that the smoke streaks remained on the floor surface and that there were no disturbances in the free stream flow.

As test section flow speed was reduced below about 4 m/s, the number of smoke streaks emerging from the settling-chamber screens remained the same, but they tended to coalesce at some stage of their journey through the contraction (Figure 6.7(a)). Lifting of smoke from the surface was frequently observed downstream of the coalescence. Although the rather primitive nature of the visualisation technique and wide variations in behaviour made detailed observations very difficult, it was clear that the most probable location of the coalescence moved upstream from the highly concave part of the contraction and then into the parallel-sided settling chamber as flow speed decreased. The coalescence of smoke streaks was always accompanied by large streamer deflections in the test section which, in earlier experiments (Figures 6.4 and 6.3), were associated with the presence of a streamwise vortex pair. Sometimes, as in Figure 6.7(b), sufficient smoke was removed from the floor to make the detached vortex pair visible from the test section. The apparently disjoint nature of the vortex structure in Figure 6.7(b) is a consequence of the near-surface streak formation by Görtler instability. The results from this experiment clearly show that the detached vortex pair observed in the test section was part of a strong three dimensional separation structure which was the dominant feature of the flow within the contraction. The strength of the separation structure was indicated by the convergence angle of the coalescing smoke streaks which, from images similar to Figure 6.7(a), was approximately 10 to 15 degrees near the start of the contraction. Strong separation was also indicated by vortex swirl angles in the test section. These were estimated from streamer deflections to be in the order of 5 to 10 degrees. On the assumption that the flow separation mechanism did not contribute significantly to the strength of the counter-rotating streamwise vortices in the favourable pressure gradient region of the contraction, conservation of angular momentum (Equation 5.42) implies that vortex swirl angles near the start of the contraction were in the order of 20 to 35 degrees.

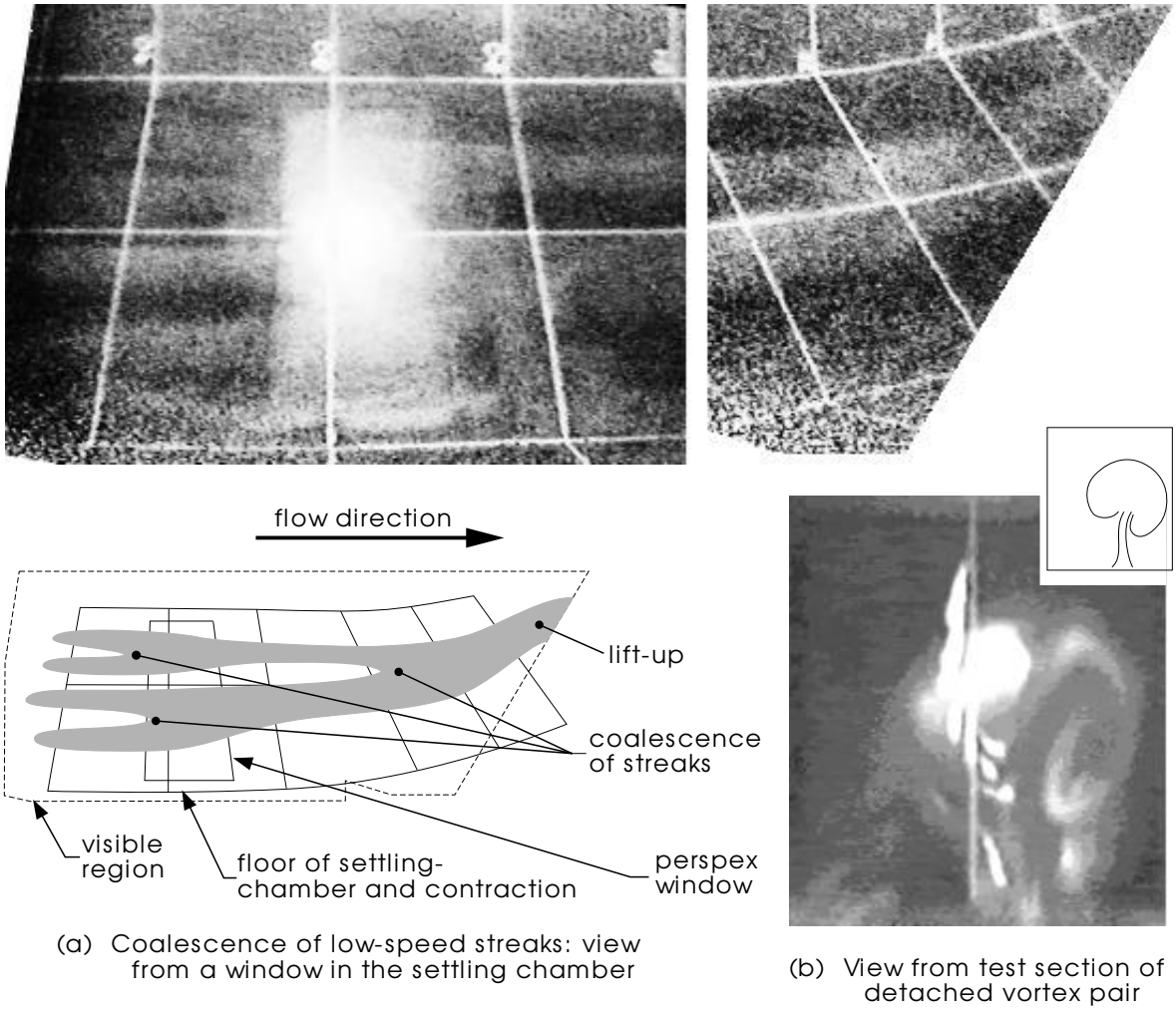

Figure 6.7: Coalescence of low speed streaks on the floor of the settling chamber and contraction at $\langle U \rangle = 1.6$ m/s. The behaviour of the smoke layer was observed through a side-wall window in the settling chamber and from the test section.

6.3.3 A conceptual model of three-dimensional separation in the contraction

At this stage of the experimental investigations, enough was known to propose a qualitative model which would explain the observed features of three-dimensional separation in the contraction.

6.3.3.1 The effect of initial flow nonuniformity

The wire-mesh screens in the settling chamber of the wind tunnel performed the important function of increasing the uniformity of the flow. However, Böttcher and Wedemeyer (1989) have shown that small variations in mesh density, which are produced during manufacture of the screens, are the source

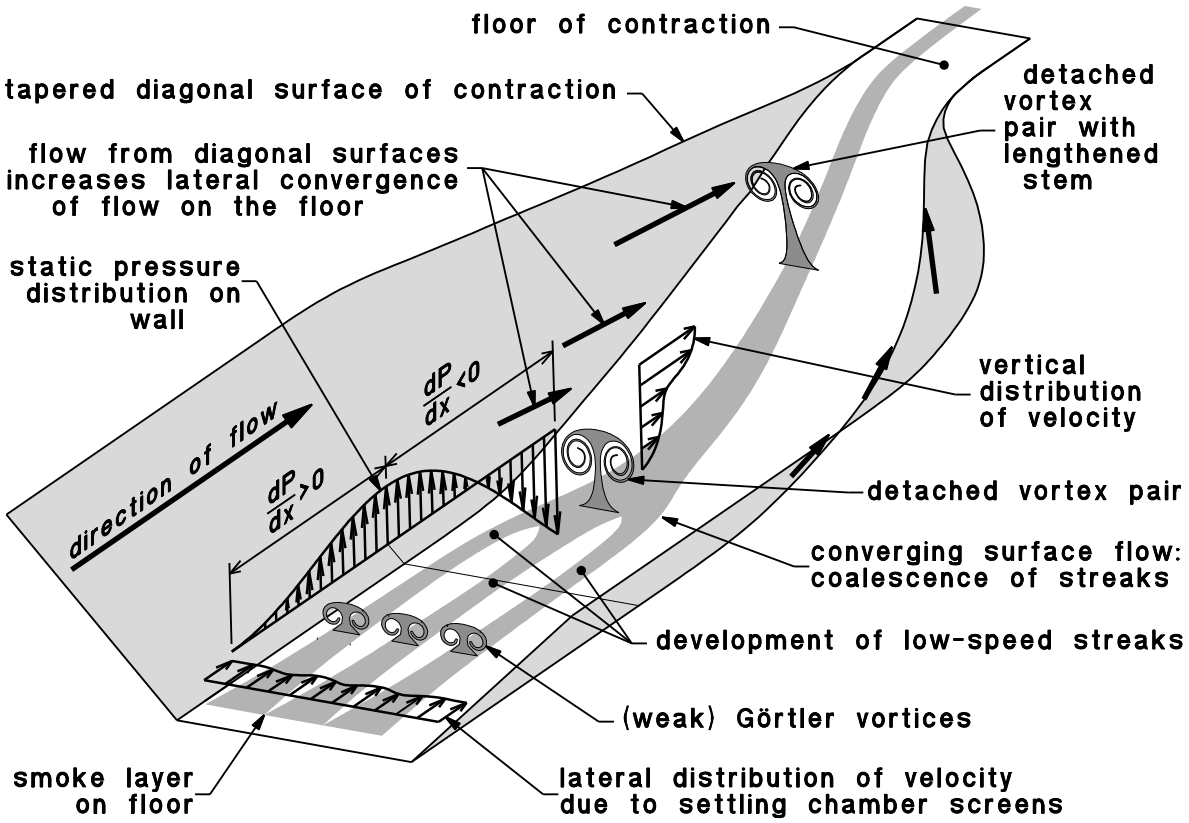

Figure 6.8: Schematic diagram of a conceptual model for three-dimensional boundary-layer separation from the contraction surface.

of low-amplitude nonuniformities in the time-averaged flow downstream of a screen. Such nonuniformities, which are fixed in space [Swearingen and Blackwelder, 1986], are likely to have been the cause of the initial lateral variations in the thickness of the smoke layer on the floor of the settling chamber (Figures 6.6 and 6.7).

The next stage leading to strong separation in the contraction was observed experimentally as the transformation of the surface smoke layer into a series of distinct streaks as it traveled through the contraction. These developing surface streaks were interpreted as accumulations of low-speed near-wall fluid in the updraught region between and beneath pairs of weak counter-rotating streamwise vortices driven by Görtler instability (Figure 6.8).

6.3.3.2 The effect of adverse streamwise pressure gradients

From the study of two-dimensional separation in Chapter 4, both adverse[2] and favourable[3] streamwise pressure gradients were known to exist within the contraction flow. Sonada and Aihara (1981) have examined the effects of streamwise pressure gradients on the development of secondary Görtler instability. The most important of their measurements were made in the updraught region between adjacent Görtler vortices where vertical distributions of mean velocity are heavily inflected. These velocity distributions have two regions of high shear, one near the wall and the other of possibly even higher shear rate near the outer edge of the boundary layer (Figure 6.9(a)). The outer shear layer is located within the top of the characteristically mushroom-shaped cross-section of the Görtler vortex pair. According to Sonada's and Aihara's experiments, favourable pressure gradients tend to suppress the growth of velocity fluctuations and so retard the development of secondary instability, while the main effect of an adverse pressure gradient is to increase the distance from the wall and the thickness of the outer shear layer, with little effect on the near-wall shear layer. The increasing distance between the near-wall and outer shear layers under the influence of an adverse pressure gradient can readily be interpreted as a migration of a vortex pair away from the wall.

In the wind tunnel, the boundary-layer flow entering the contraction first encounters an adverse pressure gradient (Figure 4.22(a), Figure 6.8) and then, in the rapidly converging part of the duct, a very favourable pressure gradient. The initial migration of a Görtler vortex pair away from the concave surface is believed to occur in the adverse pressure gradient region (Figure 6.8) in a manner very similar to that observed by Sonada and Aihara (1981). For flow speeds higher than approximately 2 m/s, detached vortex pairs in the test section were usually observed to be stationary or nearly stationary within the cross-section of the duct. This indicates that the length of the adverse pressure gradient region was insufficient to permit the development of secondary Görtler instability. It also indicates that, in accordance with the observations of Sonada and Aihara (1981), the favourable pressure gradient suppressed secondary Görtler instability, and so prevented the growth of velocity fluctuations which could eventually become turbulent. In effect, the acceleration of the flow and the vortex stretching[4] in the contraction appears to have stabilised the inflectional velocity distributions produced by the upwash between a pair of streamwise vortices. As the flow speed is reduced ($1 \lesssim \langle U \rangle \lesssim 2$ m/s), not only are vortex pairs observed to grow away from the wall at a location further upstream, but they also develop a lateral oscillatory motion within the adverse pressure gradient region. Sonada and Aihara (1981)

[2] Adverse gradient of pressure at the wall: $\dfrac{\partial P}{\partial x} > 0$

[3] Favourable gradient of pressure at the wall: $\dfrac{\partial P}{\partial x} < 0$

[4] As in Equation 5.42 (page 139), vortex stretching reduces swirl angle approximately in proportion to the reduction in duct radius. This is illustrated in Figure 5.17(a) on page 140.

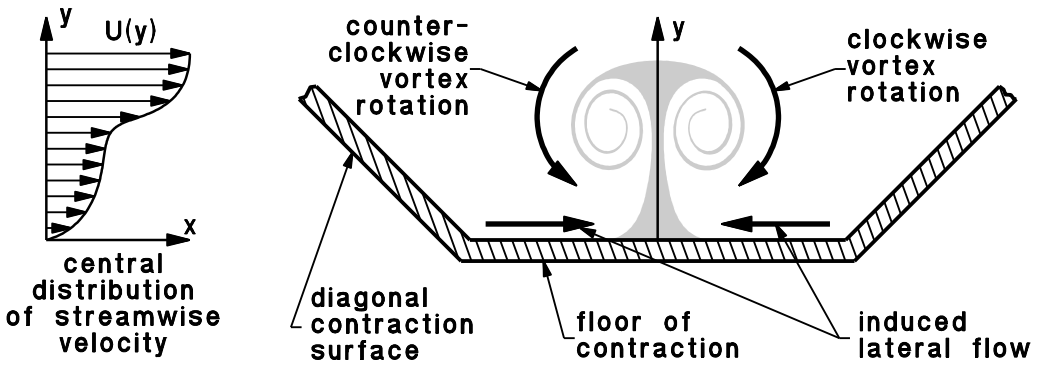

(a) flow induced by the rotation of streamwise separation vortices

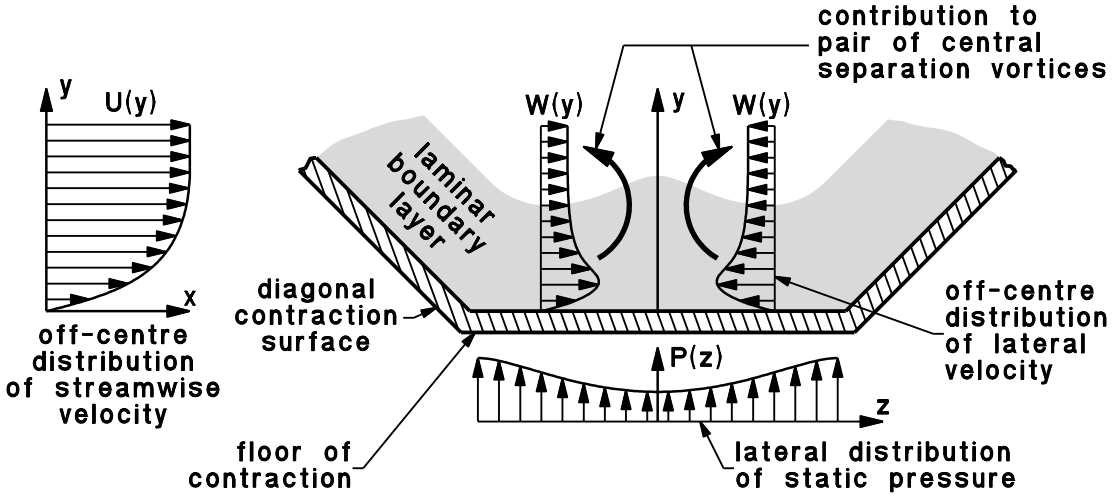

(b) skewing of the boundary layer by lateral pressure gradient —

also known as skew-induced secondary flow

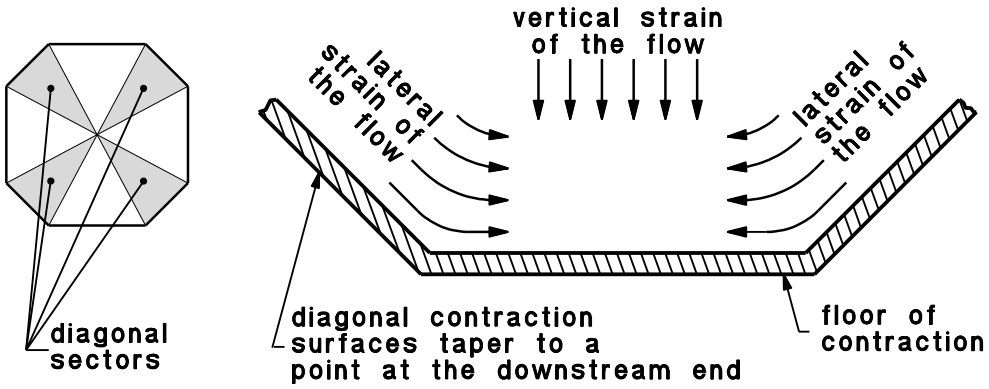

(c) flow displaced from the tapering diagonal surfaces

Figure 6.9: Schematic diagram of the mechanisms of near-wall lateral flow: lower cross-section views within the contraction. The direction of the main flow is perpendicular to the page.

have observed similar effects when changing from a zero streamwise pressure gradient to an adverse pressure gradient. The lateral oscillatory motion, which also has features similar to those seen by Peerhossaini and Wesfreid (1988), is interpreted as the sinuous or wavelike mode of secondary Görtler instability. At even lower speeds (e.g. $\langle U \rangle \approx 0.6$ m/s, Figure 6.4(f)), vortex pairs were visible only as momentarily appearing and disappearing structures, as if horseshoe-vortex structures were formed in the adverse pressure gradient region and then convected into the test section. These transient three-dimensional separations are similar to structures produced by the horseshoe-vortex mode of secondary Görtler instability.

6.3.3.3 The effect of lateral pressure gradients[5]

The measurements of Sonada and Aihara (1981) and the visualisation of near-surface flow in the contraction have shown that, when Görtler instability is augmented by the effects of an adverse streamwise pressure gradient, the resulting three-dimensional separation can be quite strong and the angle of lateral flow deflection near the surface can be quite large. Figure 6.9(a) shows how lateral flow is induced by the rotational motion in streamwise separation vortices. Bansod and Bradshaw (1972) have shown that converging lateral flows generated by *lateral* pressure gradients can also produce pairs of streamwise separation vortices. In their study, which was of the flow in an S-shaped duct, this phenomenon was particularly strong. They also reported that a similar, but less dramatic effect has been observed in non-axisymmetric wind-tunnel contractions. Welsh and Fontaine (1978) measured velocity distributions revealing the existence of this separation mechanism in the turbulent boundary layer of a contraction with a square cross-section.

Lateral pressure gradients can produce higher lateral flow velocity within a boundary layer than in the adjacent free stream. The reason for this is revealed by inspection of the equation for the lateral component of momentum:

$$U\frac{\partial W}{\partial x} + V\frac{\partial W}{\partial y} + W\frac{\partial W}{\partial z} = -\frac{1}{\rho}\frac{\partial P}{\partial z} + \nu\nabla^2 W. \tag{6.1}$$

If viscous diffusion terms ($\nu\nabla^2 W$) are ignored and the lateral deflection of the flow is small, Equation 6.1 may be simplified to

$$U\frac{\partial W}{\partial x} \approx -\frac{1}{\rho}\frac{\partial P}{\partial z}. \tag{6.2}$$

The rate of flow deflection ($\partial W/\partial x$) in the relatively low-momentum fluid (U) of the boundary layer would therefore be significantly larger than in the faster external free stream flow. As illustrated schematically in Figure 6.9(b), the result is a skewed boundary layer where the lateral velocity component has a maximum between the edge of the boundary layer and the wall. The convergence of these

[5] Lateral pressure gradient: $\frac{\partial P}{\partial z}$

lateral flows near the middle of the floor then produces counter-rotating streamwise vortices which are very similar to Görtler vortices augmented by the adverse streamwise pressure gradient (Figure 6.9(a)).

The relative importance of the augmented Görtler vortex mechanism and the skew-inducing lateral pressure gradient in the production of three-dimensional separation is unknown. However, it is quite apparent from Figure 4.32(d) that Görtler vortex pairs near the middle of the floor are reinforced by the skew-induced vorticity. Other less centrally located Görtler vortices are not reinforced in this way but can be convected towards the middle of the floor and entrained into the stronger central vortex pair.

Skewing of the boundary-layer flow can also be explained in terms of the vorticity transport equation[6] as the "skew-induced" production of streamwise vorticity by inviscid rotation of the vorticity vector. However, further discussion of this complex subject would be of doubtful relevance and, for the sake of brevity, the interested reader is simply referred to the fundamental studies by Squire and Winter (1951), Hawthorne (1951), Taylor (1959), Johnston (1960) and the more recent review by Bradshaw (1987).

6.3.3.4 The effect of tapering diagonal surfaces

The third and final lateral flow mechanism is shown schematically in Figure 6.9(c). The diagonal surfaces of the contraction taper to a point at the downstream end and so, over the length of the contraction, the fluid in the diagonal sectors flows into the sectors associated with the top surface, floor and vertical sides. The overall effect of this flow from the diagonal sectors is to ensure that, on the floor of the contraction and the other non-diagonal surfaces, the average lateral strain of the flow is the same as the average vertical strain. In this sense, the tapering of the diagonal surfaces does not produce true lateral flow.

6.3.3.5 Summary

The description advanced for the mechanism of three-dimensional separation is based on the observed behaviour of the flow in the settling chamber, contraction and test section of the wind tunnel, and, in summary, is as follows. The process of three-dimensional separation is envisaged to begin with small flow nonuniformities generated by the settling-chamber screens. Flow nonuniformities which occur within the concave boundary-layer streamlines near the start of the contraction are amplified by the

[6] The terms responsible for the generation of skew-induced vorticity are the second and third terms on the right side of the transport equation for streamwise vorticity:

$$U\frac{\partial \Omega_x}{\partial x} + V\frac{\partial \Omega_x}{\partial y} + W\frac{\partial \Omega_x}{\partial z} = \Omega_x\frac{\partial U}{\partial x} + \Omega_y\frac{\partial U}{\partial y} + \Omega_z\frac{\partial U}{\partial z} + \nu\nabla^2\Omega_x.$$

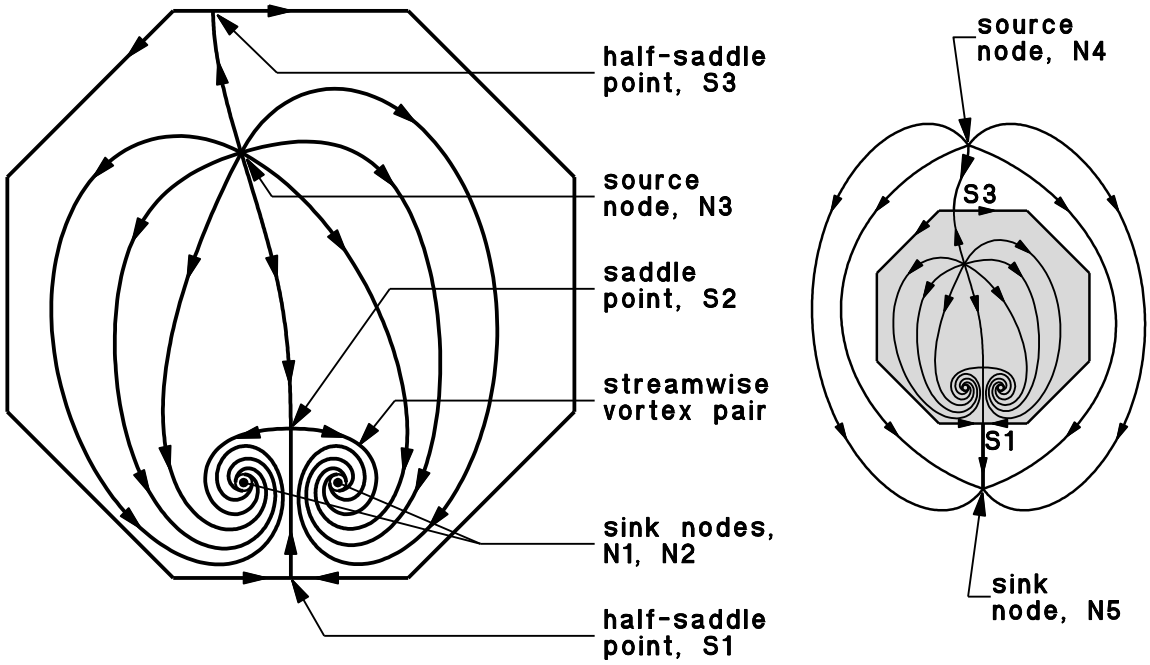

(a) necessary critical points

(b) immersion in a simple source-sink flow

Figure 6.10: Schematic diagram of cross-section topology for a three-dimensional boundary-layer separation from the contraction surface. Streamwise flow is perpendicular to the page.

Görtler instability mechanism. The development of Görtler vortices is accelerated by the presence of an adverse streamwise pressure gradient near the start of the contraction. The growth of vortex pairs near the middle of the top surface, floor and vertical sides is also assisted by lateral pressure gradients which produce converging lateral flows within the boundary layer. At very low flow speeds (typically less than about 4 m/s in the test section), one of the vortex pairs grows in strength and in size to become the dominant feature of the contraction flow and it migrates away from the wall. This dominant vortex pair is usually more or less centrally located on one of the contraction surface segments. It can produce significant lateral flows on adjacent surface segments and it alters the overall pressure distribution in a manner which, except at extremely low speeds (Figure 6.4(f)), suppresses the development of strong separation vortices on the other surface segments.

6.3.4 Topology of the three-dimensional separation

The conceptual model of the flow produced by a three-dimensional separation from the contraction surface can be developed further by identifying the critical points and streamlines associated with the streamwise separation vortices. These features are most easily shown in a cross-sectional view of the

flow. Within each vortex core of the counter-rotating pair (Figure 6.10(a)) is a spiral node (N1, N2). The vortex cores contain low-speed fluid removed from the near-wall region of the boundary layer, and this fluid has a lower velocity than the surrounding main flow. Viscous diffusion of momentum therefore produces streamwise vortex stretching which, by continuity, ensures that the vortex nodes are sinks (i.e. stable foci) rather than sources. The other critical points which are part of the detached vortex pair are a half-saddle (S1) on the wall and a full-saddle (S2) at the top of the "mushroom". Continuity requires the addition of a source node (N3), and the no-slip boundary condition requires that it be at an interior point of the flow cross-section. Another half-saddle (S3) must then be located on the wall. Enclosure of the flow cross-section in a simple source-sink flow (Figure 6.10(b)) demonstrates that the flow represented by Figure 6.10(a) satisfies the topological law for flow on simply connected surfaces:

$$[\text{Number of nodes}] - [\text{Number of saddles}] = 2 \tag{6.3}$$

[Lighthill, 1963]. The addition of a surrounding source-to-sink flow converts the half-saddles (S1 and S3) of Figure 6.10(a) into full-saddles.

The direction of flow in Figure 6.10(a) indicates that the cores of the separation vortices (N1, N2) are regions of low pressure and the source node (N3) is a region of high pressure. This redistribution of pressure by the separation flow is believed to stabilise the boundary layer on surface segments not directly associated with the separation vortices. In the experiments, this stabilising effect appears to have been sufficient to discourage the growth of additional separations very strongly at test-section flow speeds higher than about 1 m/s.

When the topological model in Figure 6.10(a) is extended to three dimensions, the streamlines become streamsurfaces and the saddle points become bifurcation lines [Hornung and Perry, 1984]. Figure 6.11 therefore describes the three-dimensional topology of flow near the streamwise separation vortices in terms of dividing streamsurfaces and bifurcations. The line derived from the half-saddle (S1) underneath the separation vortices is a negative bifurcation of the wall streamsurface where flow separates from the wall. The horizontal streamsurface from the double-sided bifurcation at S2 rolls up into the separation vortices at N1 and N2. The other half-saddle (S3, shown only in Figure 6.10(a)) represents a positive wall bifurcation where flow from the source node (N3) becomes attached to the wall.

Figure 6.10(a), Figure 6.11 and the previous discussion describe the topology of a three-dimensional separation at some distance downstream from its origin. At this location it is no longer developing rapidly under the influence of lateral and streamwise pressure gradients. In ideal circumstances, the flow geometry near the start of boundary-layer separation would be determined from the pattern of critical points on the contraction surface [Fairlie, 1980, Perry and Fairlie, 1974]. However, experiments to identify these critical points were not performed because this information was not required for suppression of the three-dimensional separation. In addition, at the required flow speeds of between

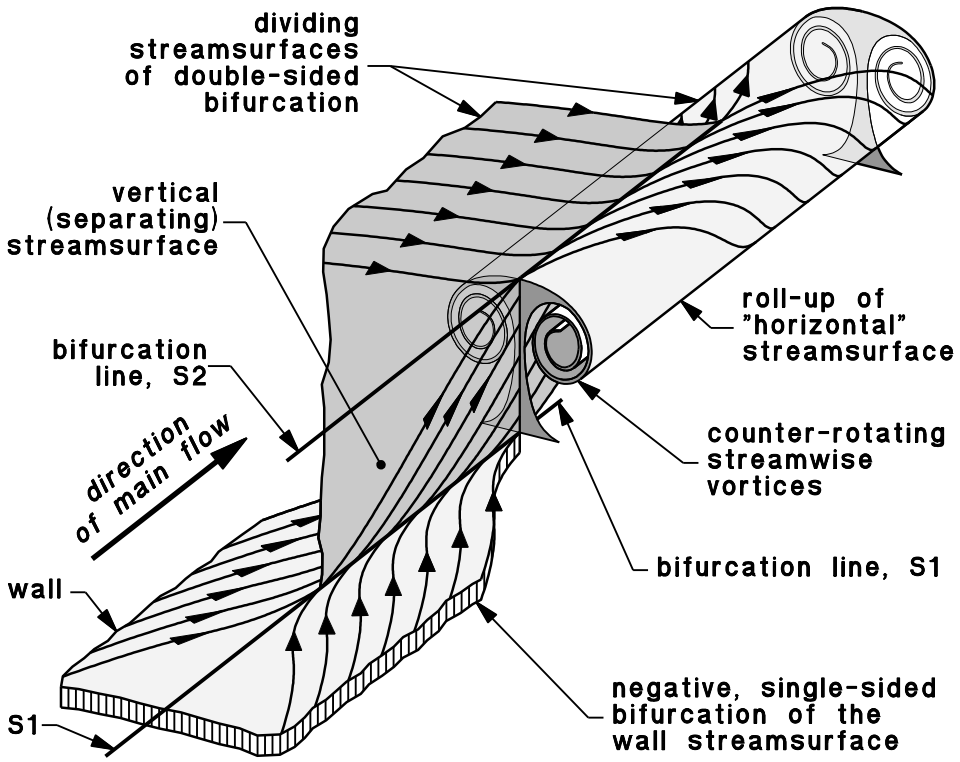

Figure 6.11: Schematic diagram of bifurcations near the streamwise separation vortices

0.05 m/s and 0.2 m/s in the settling chamber, there would be serious practical difficulties in any search for critical points with conventional surface-flow markers such as dyes or china-clay.

An alternative approach is to construct and examine several vortex-skeleton models of the separation [Perry and Hornung, 1984]. The dominant feature of each vortex-skeleton model is a pair of counter-rotating quasi-streamwise vortices near the outer edge of a thick laminar boundary layer. In the first of these models (Figure 6.12(a)) the quasi-streamwise vortex tubes, which represent counter-rotating separation vortices, are formed by rotating and stretching a small proportion of the boundary-layer vorticity. The driving force for increasing the strength of the streamwise vortices is provided by the various mechanisms discussed in Section 6.3.3. The effects of the vortex rotation and stretching are accumulated over a considerable streamwise distance, and so the surface flow topology is that of a gradually strengthening negative bifurcation. The initial strength of the bifurcation is determined by the state of the flow emerging from the settling-chamber screens.

In the second vortex-skeleton model, the streamwise separation vortices grow from source points on the wall as counter-rotating viscous tornados [Lim et al., 1980] and are convected downstream by the main flow. The resulting flow topology, which is known as an owl-face separation of the first kind [Perry and Hornung, 1984], is illustrated schematically in Figure 6.12(b). The arrangement of critical

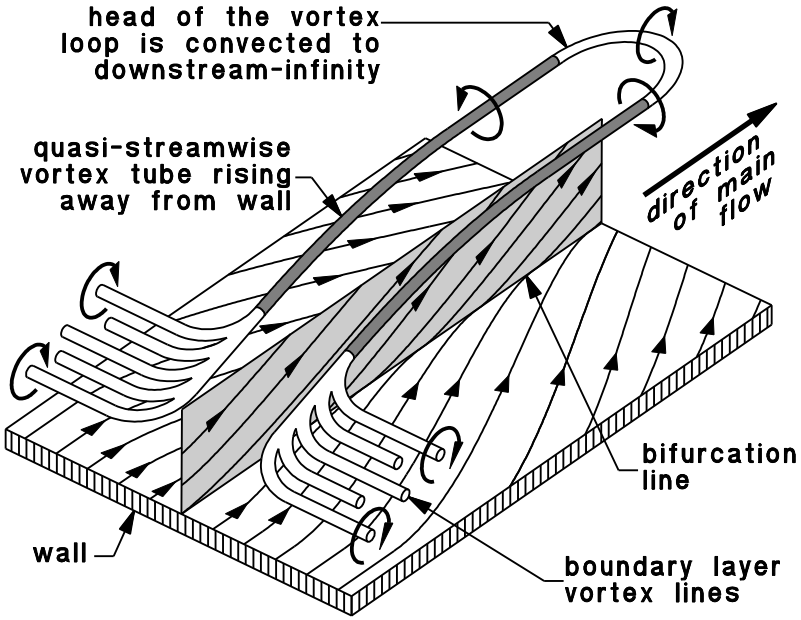

a) Formation of simple bifurcation and separation vortices by accumulated rotation and stretching of boundary-layer vorticity.

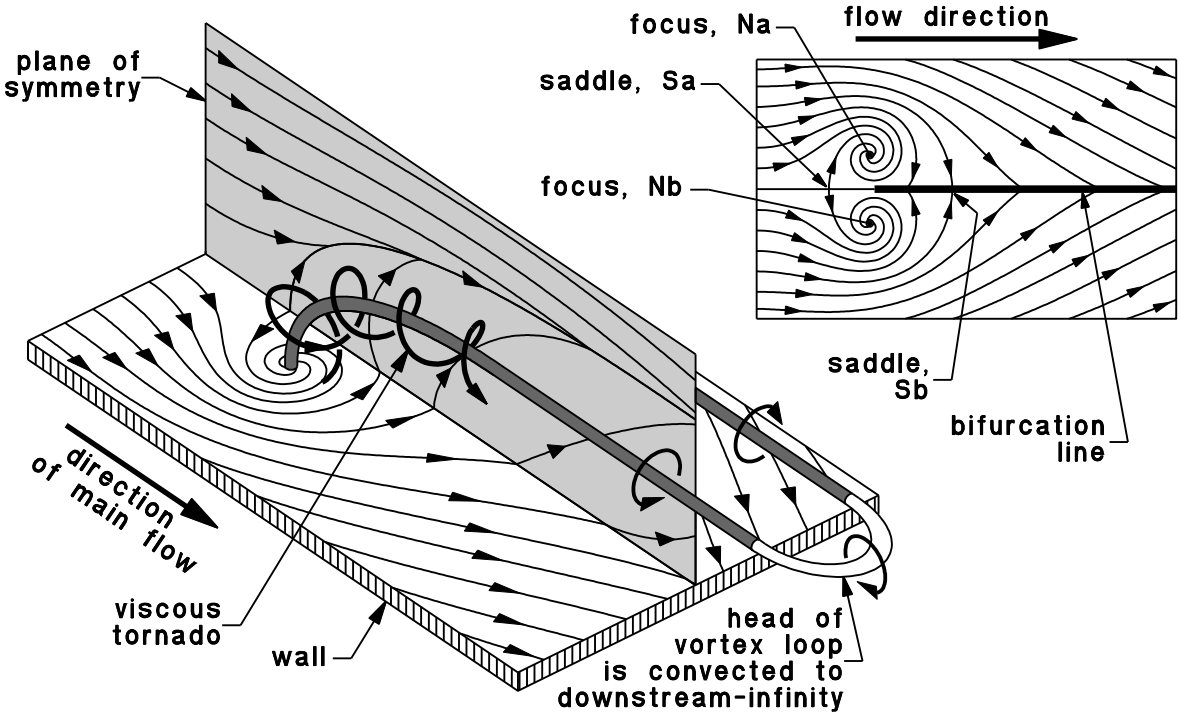

b) Owl-face separation and associated streamwise vortices.
The critical points are labelled **Na**, **Nb**, **Sa** and **Sb**.

Figure 6.12: Topologically feasible vortex-skeleton models for the initial stage of three-dimensional separation

points on the surface and the negative wall bifurcation downstream of saddle “Sa” are shown on a plan-view. Unlike the scenario in Figure 6.12(a), where the strength of the wall bifurcation increases gradually from an almost infinitesimal beginning, the wall bifurcation produced by the the owl-face separation has a well-defined upstream termination at some point between the two saddles Sa and Sb. This termination is inconsistent with the gradual streamwise development of Görtler-type vortices, and so the owl-face separation shown in Figure 6.12(b) is unlikely to represent correctly the initial development of three-dimensional separation in the wind-tunnel contraction. The first vortex-skeleton model (Figure 6.12(a)) is preferred because it is consistent with the conceptual model developed in Section 6.3.3.

6.4 Suppression of three-dimensional separation

In the conceptual model described in Section 6.3.3, three-dimensional separation originates from the nonuniformity of the flow emerging from the settling-chamber screens. Streamwise concavity of streamlines within the boundary layer then allows Görtler instability to amplify the near-wall nonuniformities so that they develop into an array of counter-rotating streamwise vortex pairs. As shown in Figure 6.11, each vortex pair is accompanied by a negative wall bifurcation and a separating streamsurface. The lateral convergence of near-wall flow towards each bifurcation line produces an accumulation of retarded fluid which is observed experimentally as a low-speed streak on the surface of the contraction (Figures 6.6 and 6.7) .

6.4.1 On the fluid mechanics associated with using screens to suppress separation

In order to suppress the unacceptable effects of three-dimensional separation, it was necessary to prevent low-speed streaks from developing to the stage where the streamwise vortices become detached from the contraction surface. Consideration of various options, which included boundary-layer suction and tangentially blown jets, indicated that the necessary control of separation would be achieved most effectively with a series of wire-mesh screens in the contraction. This is similar to the conventional practice of using screens to prevent separation in wide-angle diffusers. However, three-dimensional separation in the contraction results from the amplification of Görtler vortex structures by weak pressure gradients, while separation in wide-angle diffusers is driven by strong adverse pressure gradients and produces regions of reverse flow. These separation mechanisms are quite different, and so control of separation in the contraction could not be assured simply by following the diffuser design guidelines established by Mehta (1977). It was therefore necessary to select the number and spacing of screens empirically.

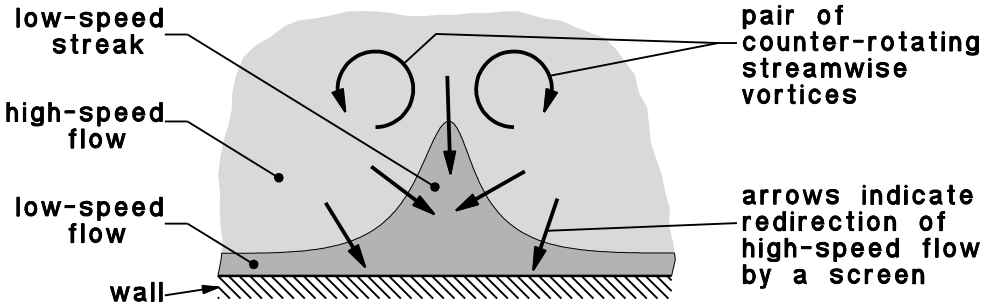

Figure 6.13: Schematic cross-section of a low-speed streak formed on the wall of the contraction. The outer region of boundary layer and the free stream is considered to be high-speed flow. Free stream flow is perpendicular to the page.

Mehta (1985) has shown that screens prevent separation by redirecting flow from regions of relatively high velocity towards regions of relatively low velocity. Flow-visualisation experiments (Section 6.3.2) indicate that typical near-wall low-speed streaks are narrow features which protrude into the outer region of high-speed flow (Figure 6.13), and so a screen might be expected to remove them very efficiently. However, the flow field immediately downstream of a screen also contains concave near-wall streamlines and small scale flow nonuniformities so that, in the absence of a sufficiently favourable streamwise pressure gradient, Görtler instability can amplify these nonuniformities and establish new low-speed streaks. If the screen is located in a region of adverse pressure gradient, low-speed streaks may again develop into three-dimensional vortex-pair separations. The final screen should therefore be located well within the favourable pressure-gradient region of the contraction.

6.4.2 Description of screens in the contraction

The screens in the contraction were made of the same 16 MPI, 28 SWG wire mesh as the screens in the wide-angle inlet diffuser (page 146). The distance between successive screens was also made the same as in the wide-angle inlet diffuser, 170 mm. After each screen was cut to the required shape and size, a 25 mm-wide flange was folded around the periphery and was reinforced with 0.25 mm thick steel shim. The screen was then permanently dished by placing it on a hard flat surface and carefully rolling a short length of heavy steel shaft[7] around its interior. The purpose of this curvature was to produce approximately perpendicular intersections of the contraction surface and the screens, and consequently to discourage excessive concavity of near-wall streamlines immediately downstream of each intersection. For initial tests, three screens were stuck by their reinforced flanges to the wall of the contraction with double-sided adhesive tape. In the final installation of five screens, which is

[7]The steel shaft was approximately 200 mm long and 150 mm in diameter

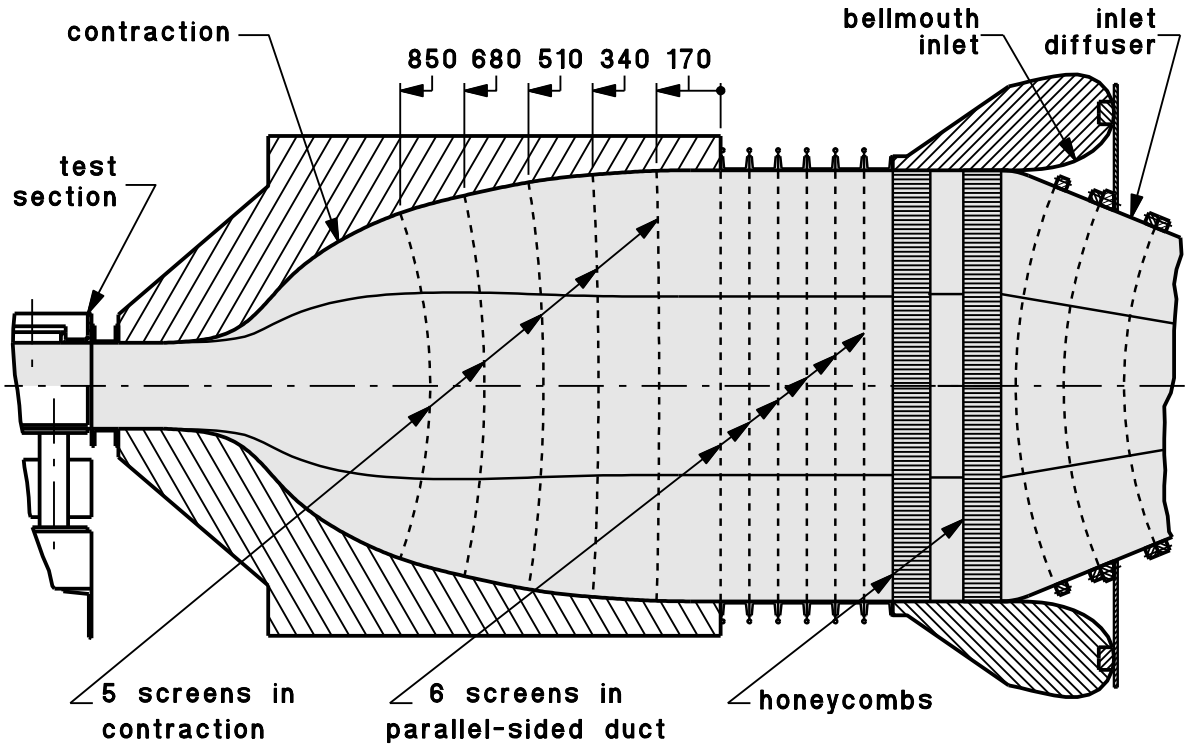

Figure 6.14: Final configuration for the inlet section of the wind tunnel, showing the location of screens in the contraction. Scale 1:20.

illustrated in Figure 6.14, the flanges were both glued and bolted in place.

As an additional measure, the settling chamber was removed and the contraction was bolted directly onto the parallel-sided section containing 6 screens (Figure 6.14). This reduced the boundary-layer thickness and the flow non-uniformity at the start of the contraction. It also decreased the length of the wind tunnel by 0.76 m.

6.4.3 Flow visualisation with screens in the contraction

Initial flow-visualisation tests were performed with three screens located 170 mm, 340 mm and 510 mm downstream from the start of the contraction. Flow visualisation was by the “pulsed smoke cloud” technique described in Section 6.2.2. Typical results from these tests are shown in Figure 6.15. The results clearly demonstrate that, although three-dimensional separation and the associated test-section flow disturbances still occurred within the required speed range of wind-tunnel operation (1 m/s to 4 m/s), the strength of the disturbances and the size of the separation vortices were significantly reduced by the presence of screens in the contraction.

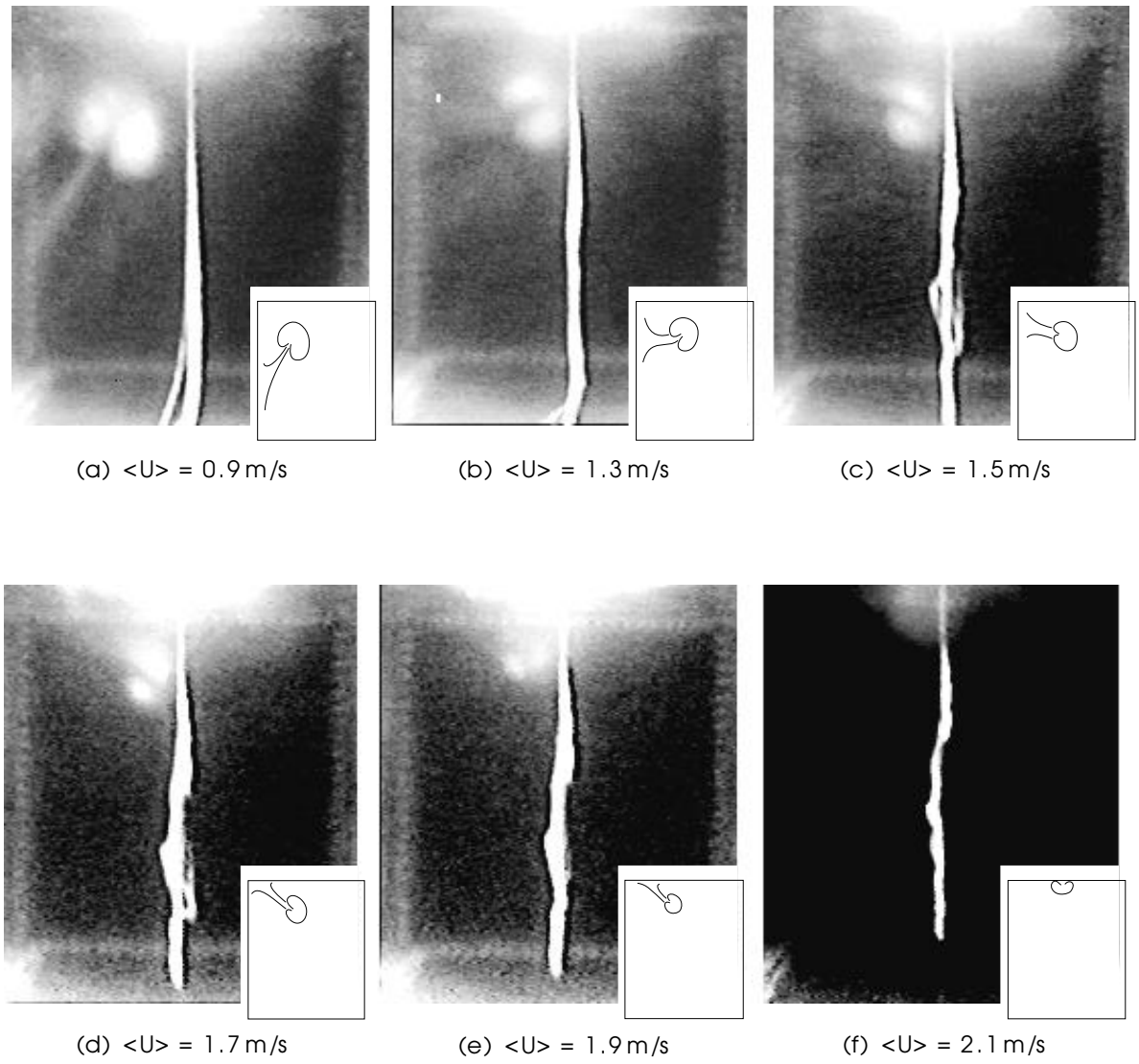

Figure 6.15: Streamwise vortex patterns due to three-dimensional separation with three screens in the contraction. Note the increasing flow speed. The suction manifold was not used. The bright patch at the top of each image is due to illumination of the flow field through test-section Port 2 (Figure 5.5). The streamers are located between Port 1 and Port 2 of the test section.

In tests of the final configuration, where the number of screens in the contraction was increased to five and flanges of the screens were fixed rather more securely to the walls, the sensitivity of the visualisation technique was increased by illuminating the flow field through slots in the test-section extension (Figure 4.31) with a much more powerful 750 Watt quartz-halogen lamp. The results of this experiment (Figure 6.16) show that large-scale separation vortices of the type shown in Figures 6.3 and 6.4 had been replaced by a small vortex pair in each corner of the duct. These vortex pairs probably result from near-wall lateral flows created by the tapering and disappearance of the diagonal surfaces

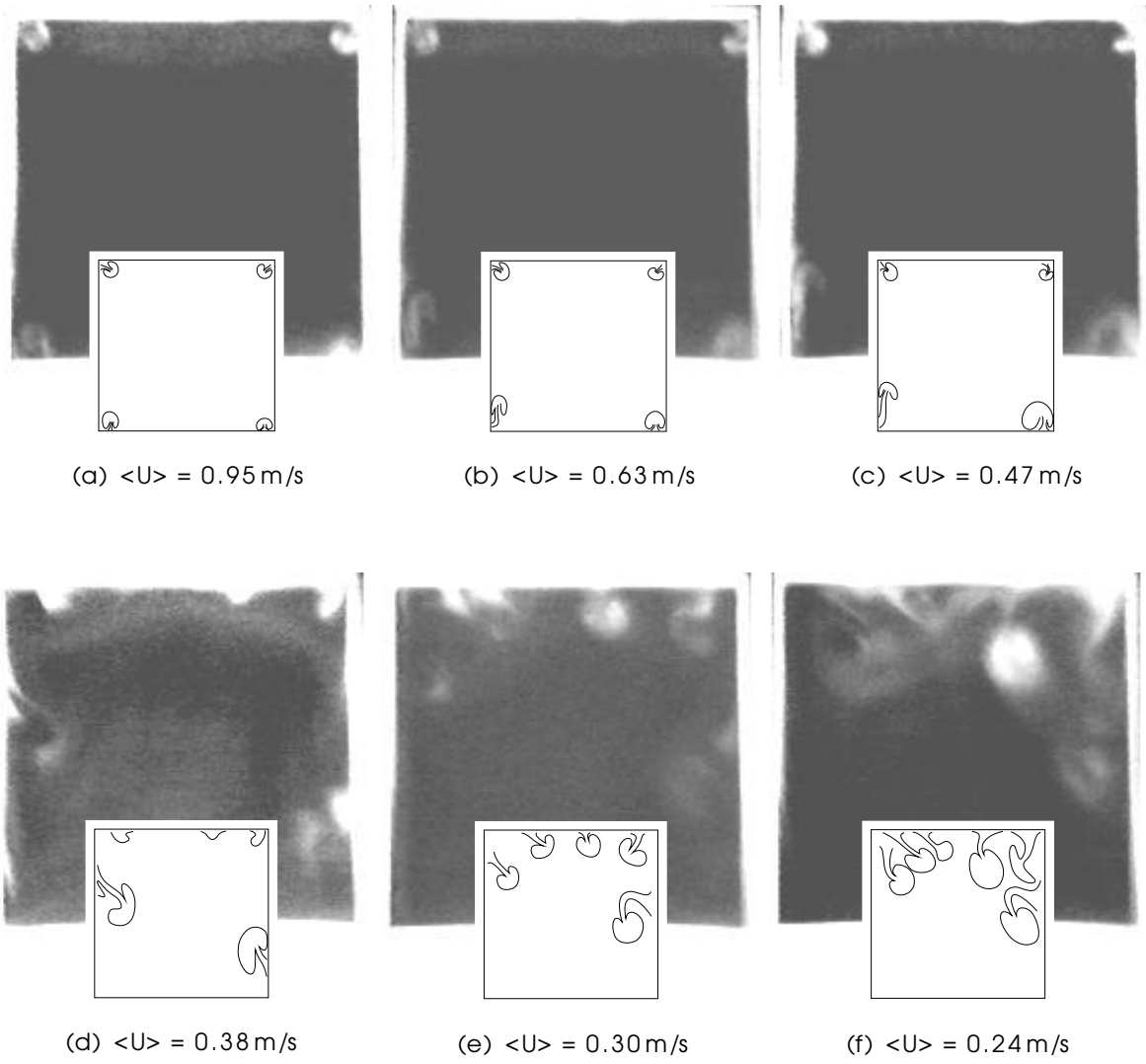

Figure 6.16: Suppression of three-dimensional separation with five screens in the contraction; flow visualisation of the flow cross-section at the contraction exit. Suction is not used.

at the downstream end of the contraction. Between the highest flow speed of 2.4 m/s and 0.95 m/s, the width and height of each vortex pair remained constant at about 15–20 mm. As flow speed was reduced further, the corner vortices became larger and, at speeds lower than about 0.5 m/s, three-dimensional separations of the type illustrated in Figure 6.12(a) began to appear in the mid-span regions of the contraction surfaces.

The results displayed in Figure 6.16 indicate that, for bulk flow speeds greater than 0.5 m/s, separation from the surface of the contraction produced no disturbances in the free stream of the test section flow. This level of performance was completely satisfactory because turbulent boundary layers were required only at flow speeds higher than 1 m/s. In this higher range of speeds, the small corner vortices

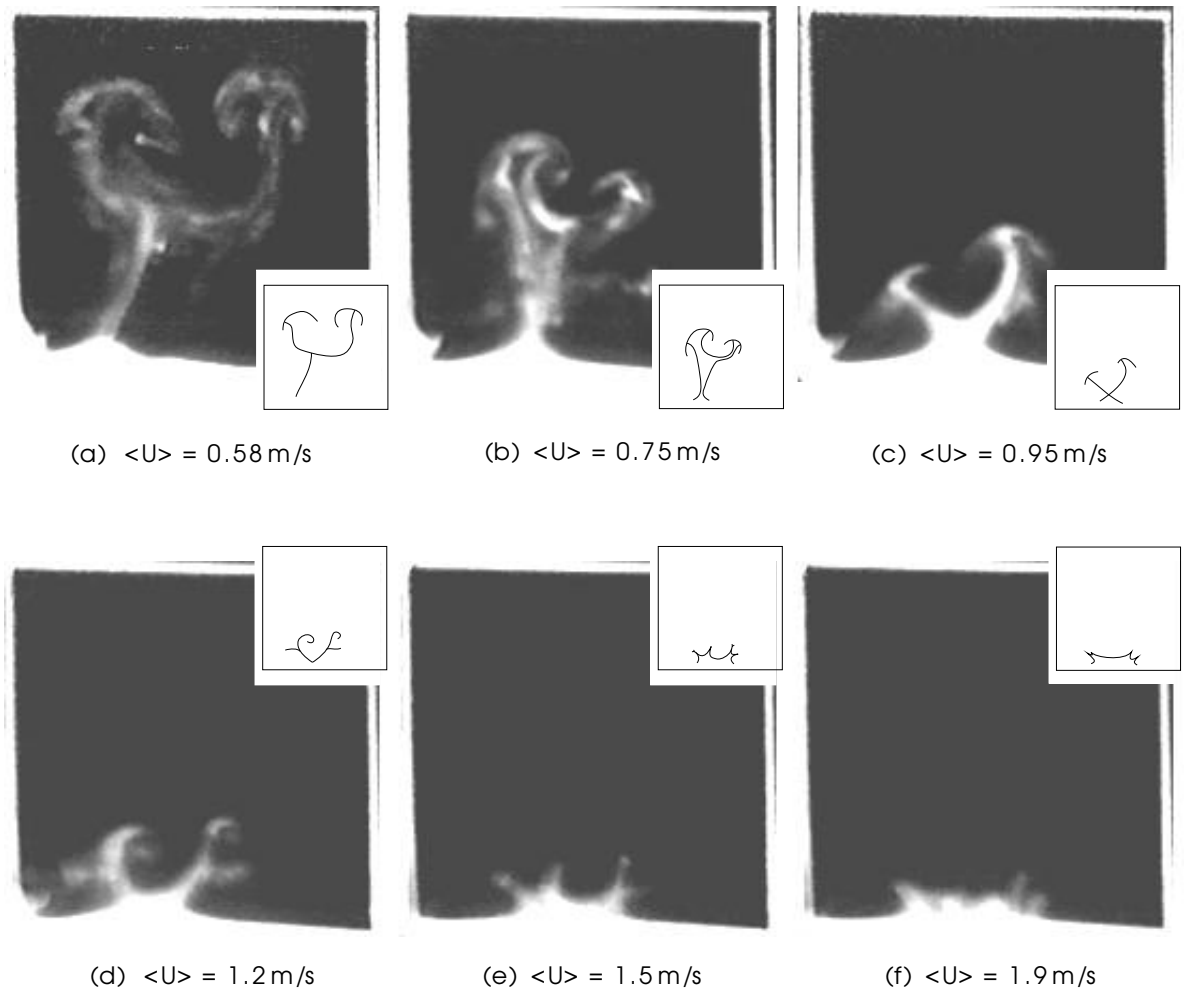

Figure 6.17: Unsteady separation induced by a layer of smoke from a horizontal rake located immediately upstream of the honeycombs and 100 mm from the floor of the wind-tunnel inlet; flow visualisation of the flow cross-section at the contraction exit. Suction is not used.

shown in Figure 6.16 were "attached" to the surface and remained well within 30 mm of the wall at the downstream end of the contraction. These small attached vortices were easily removed by the suction manifold (Section 4.13) which was installed between the contraction and the test section.

6.4.4 Observed effects of negatively buoyant smoke at extremely low speed

The flow-separation vortices shown in Figure 6.16 were stationary at all flow speeds except the two lowest ($\langle U \rangle = 0.30$ m/s and 0.24 m/s), where the negative buoyancy of smoke-oil droplets caused the smoke-filled component of the flow to fall slowly and the clear-air component of the flow to rise slowly. In experiments which required the use of smoke, flow speeds at the start of the contraction

were frequently low enough for smoke-oil droplets to induce contaminating secondary flows. For example, a simple jet of smoke introduced at the middle of the wind-tunnel bellmouth inlet would develop into train of negatively buoyant plumes. In the worst case, smoke introduced on a side-wall would fall to the floor of the contraction and form a stagnant pool without ever emerging into the test section. In another example, which is illustrated in Figure 6.17, a layer of smoke from a rake located 100 mm from the floor would apparently reveal the presence of large-scale unsteady separation in the contraction. Further investigation with different smoke flow rates conclusively demonstrated that this separation was due entirely to the presence of the smoke.

Buoyancy effects of smoke were reduced as much as possible by decreasing the smoke flow rate, but this also reduced the clarity of the flow-visualisation images.

6.4.5 Variability of turbulent boundary-layer characteristics in the test section

The measures designed to suppress separation and buoyant convection within the wind-tunnel contraction were also tested by observing the variability of turbulent boundary-layer characteristics at Port 9 of the test section with $\langle U \rangle = 1.66 \pm 0.06$ m/s. The data necessary for these observations were obtained from repeated measurements of the streamwise velocity distribution across the thickness of the boundary layer. Some tests were run with an open bellmouth inlet. Others were run with the mixing fan and inlet diffuser installed. Each test produced four separate velocity distributions. The details of the experimental procedure, the test-section flow conditions and the measurement techniques were the same as for the the measurements described in Section 5.1. Accordingly, the depth of the test section was a uniform 230 mm over its entire length, producing a small negative streamwise pressure gradient. Boundary-layer transition was produced by a single row of 4.76 mm diameter balls on the downstream edge of the suction manifold (Section 4.13.3).

Results of these test are shown in Table 6.1 and Figure 6.18. The use of the mixing fan and inlet diffuser to suppress buoyant convection within the wind tunnel reduced the standard deviation of boundary-layer characteristics by approximately an order of magnitude. Within each set of four measurements, the standard deviation of the individual measurements was used as an indication of variability. The variability of displacement, momentum and energy thicknesses decreased by a much larger factor than the variability of other characteristics listed in Table 6.1 because the wake region of the boundary layer not only makes the largest contribution to these measurements (δ^*,theta,δ_E) but is also the region most affected by secondary flow. The reductions in the standard deviation of the friction velocity (U_τ) show that even the inner region of the boundary layer was measurably contaminated by secondary flows. These results verify that the effects of buoyant convection and boundary-layer separation in the contraction can be reduced to acceptable levels.

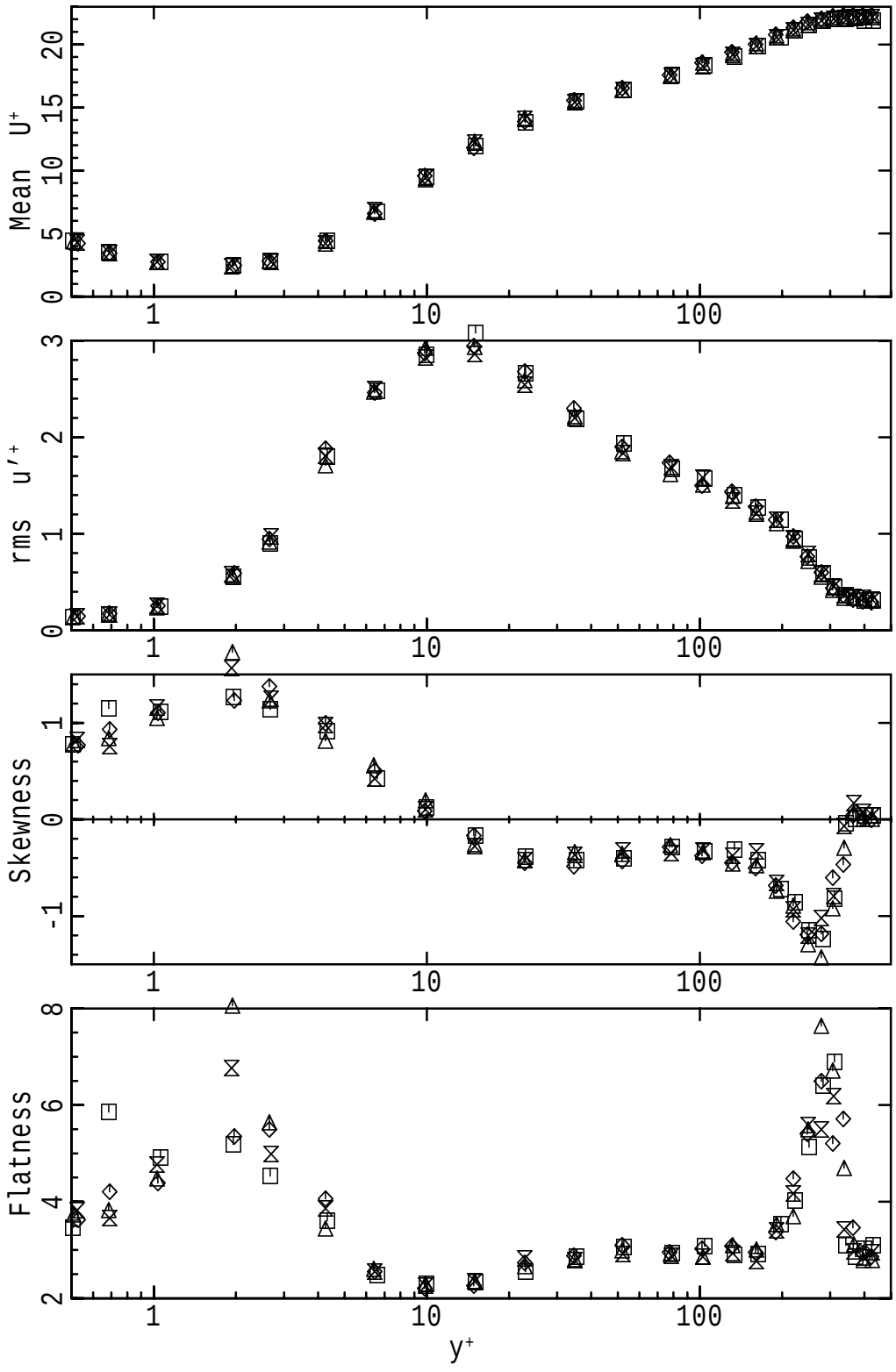

Figure 6.18: Distributions of streamwise velocity statistics measured in the boundary layer at test section Port 9 after installation of the mixing fan and inlet diffuser, and after installation of five screens in the wind-tunnel contraction; (a) mean velocity, (b) r.m.s. fluctuation, (c) skewness, (d) flatness. $\langle U \rangle = 1.67$ m/s. A different symbol is used to mark each distribution.

Table 6.1: Effect of inlet-flow mixing on the variability of turbulent boundary-layer characteristics at test section Port 9. Mean values are the average of four separate measurements. Standard deviations, which express the variability of the measurements, are expressed as percentages of the mean values.

			open bellmouth inlet		mixing fan and inlet diffuser installed	
			mean	% standard deviation	mean	% standard deviation
Distance from trip	x	m	2.53		2.53	
Free stream air speed	U_0	m/s	1.65	1.41	1.67	0.37
Friction velocity	U_τ	m/s	0.0804	1.55	0.0810	0.36
Local friction coefficient	C_f		0.00473	2.46	0.00471	0.27
Boundary-layer thickness	$\delta_{0.99}$	mm	55.6	5.6	57.6	0.70
Displacement thickness	δ^*	mm	7.46	5.8	7.57	0.28
Momentum thickness	θ	mm	5.09	5.5	5.16	0.07
Energy thickness	δ_E	mm	8.90	5.4	8.99	0.11

When the mixing fan and inlet diffuser were used, the absence of significant irregularities in the distributions of velocity statistics (Figure 6.18) also indicates an absence of extraneous disturbances to the boundary-layer flow. In particular, values of skewness and flatness in the outer region of the boundary layer, which are extremely sensitive to fluctuations in boundary-layer thickness, were measured with a high degree of repeatability.

6.5 Summary

After suppression of two-dimensional boundary-layer separation and large-scale buoyant swirl upstream of the wind-tunnel test section, visualisation experiments with streamers revealed the presence of a strong large-scale disturbance in the core of the test-section flow. Inspection of the smoke/clear-air interfaces, which were formed by feeding smoke into the wind-tunnel inlet at discrete intervals, showed that this disturbance in the test section was a pair of counter-rotating streamwise vortices. The streamwise vortices were visible in these tests because they contained significantly retarded flow, and this indicated that they were created by a three-dimensional separation of flow from the internal surface of the wind-tunnel contraction.

When a layer of smoke was introduced at the floor of the bellmouth inlet, low-speed streaks were observed in the boundary layer emerging from the settling-chamber screens. At the highest flow speeds ($\langle U \rangle = 7.8$ m/s) the low-speed streaks passed through the contraction and were observed in the test section as conventional Görtler vortices but, at speeds lower than $\langle U \rangle \approx 4$ m/s, they tended to coalesce

and then lift from the floor of the contraction. The coalescence and lift-up of smoke streaks was always associated with the presence of a streamwise vortex pair in the test section.

A conceptual model of three-dimensional separation in the contraction has been constructed from the experimental evidence. In this model, the separation process begins with small nonuniformities in the near-wall flow emerging from the settling-chamber screens. These flow nonuniformities are convected into the concave boundary layer near the start of the contraction, where they are amplified by Görtler instability and develop into a spanwise array of counter-rotating streamwise vortex pairs. Under the influence of lateral and adverse streamwise pressure gradients in this region, the diameter and rotation rate of one vortex pair increases much more than those of the other Görtler vortex pairs, and it acquires a partly self-induced motion away from the contraction surface. Experiment shows that this dominant vortex pair is usually located near the middle of a contraction surface segment, where skew-induced lateral flows are expected to converge. The vortex-diameter and rotation-rate scales are determined by the local inertial and viscid dynamics of three-dimensional separation rather than by the much weaker scaling mechanisms of Görtler instability.

Some features of three-dimensional separation in the contraction have been deduced from a study of the flow topology. The first step was to identify the critical points in a cross-section of the flow. This indicates that the separation vortices create a nonuniform pressure distribution which discourages the growth of additional separations within the contraction. Inspection of several vortex-skeleton models then suggests that the separation vortices evolve from an accumulated rotation and stretching of boundary-layer vorticity. The surface flow topology during the growth phase of the separation can therefore be described as a gradually strengthening negative bifurcation.

Three-dimensional separation was suppressed by installing a series of five wire-mesh screens at intervals of 170 mm from the start of the contraction. The screens were intended to function by preventing near-wall low speed streaks from developing to the stage where their associated streamwise vortices become detached from the surface. Flow visualisation with the screens in place showed that, for flow speeds in excess of $\langle U \rangle \approx 0.5$ m/s, the previously observed large-scale separation vortices were replaced by a small vortex pair in each corner of the duct. The small corner vortices were easily removed by suction. Repeated measurements of boundary-layer characteristics at Port 9 of the test section confirmed the absence of time-dependent disturbances.

6.6 Notation

C_f	τ_w/q_0, local skin-friction coefficient
MPI	Meshes Per Inch — units of mesh density in a screen

P	static pressure in a flow field
q_0	$\frac{1}{2}\rho U_0^2$, free stream dynamic pressure
SWG	Standard Wire Gauge — a measure of wire diameter
U, V, W	components of air velocity in the x, y and z directions
U_0	free stream speed in wind-tunnel test section
$\langle U \rangle$	bulk flow speed in the wind-tunnel test section
U^+	U/U_τ; nondimensional time-averaged value of the streamwise velocity component in a turbulent boundary layer.
U_τ	friction velocity of the boundary layer; defined by $\tau_w = \rho U \tau^2$
u'^+	u'/U_τ; nondimensional r.m.s. of the streamwise velocity fluctuation in a turbulent boundary layer.
x, y, z	streamwise, vertical and lateral components of displacement from an origin. y is usually perpendicular to a wall or reference surface.
x	distance downstream from the boundary-layer trip
y^+	yU_τ/ν; nondimensional distance from a wall on which a boundary layer is developed
δ_{99}	boundary-layer thickness; defined as the distance from the wall at which mean velocity is equal to 99% of the free stream speed
δ^*	$\int_0^\infty (1 - U/U_0)dy$; displacement thickness of the boundary layer
δ_E	$\int_0^\infty (1 - U^2/U_0^2)(U/U_0)dy$; energy thickness of the boundary layer
θ	$\int_0^\infty (1 - U/U_0)(U/U_0 dy$; momentum thickness of the boundary layer
ν	kinematic viscosity
ρ	density
τ_w	wall shear stress
$\Omega_x, \Omega_y, \Omega_z$	x, y, z components of time-averaged vorticity

Chapter 7

The test-section boundary layer

7.1 Introduction

With mixing of the wind-tunnel inlet-air flow and the installation of screens in the contraction, repeated measurements of the velocity distribution across the boundary layer at a single (x, z) location in the test section produced a very narrow range of values for the boundary-layer thickness (Section 6.4.5). The scatter in the measurements of this and other characteristics was small enough to be caused by random errors rather than by variations in boundary-layer thickness. These results, which were obtained for a bulk flow speed of 1.47 m/s, indicated satisfactory performance of the wind-tunnel inlet and contraction, even at very low air speeds.

It was then necessary to reconfigure the test section in a way which would produce a canonical turbulent boundary layer at the lowest possible flow speeds. Previous experience with boundary-layer trips on the downstream edge of the suction manifold (see Section 4.13.3 and Figure 4.33) had shown that, at very low speeds, the boundary layer tended to relaminarise over the 20% contraction near the start of the test section. This initial contraction, which allowed a divergence in the remainder of the test section, was formed by jacking up the flexible, lower surface of the test-section. The divergence was necessary to produce a boundary-layer flow with a zero streamwise pressure gradient. Any attempt to prevent relaminarisation by using a larger trip diameter would have introduced turbulence flow structures of a kind which could not be sustained by the wall turbulence mechanism. It is known that such over-stimulation of transition increases the strength (ΔU^+) of the wake component of the turbulent boundary layer [Coles, 1962] and, especially for Reynolds numbers Re_θ lower than about 1000, produces measurable changes in turbulence amplitude and structure [Erm, 1988]. The requirement for a zero streamwise pressure gradient therefore made it necessary to adjust the lower, flexible surface of the test section so that the divergence of the duct began at its upstream end without an initial

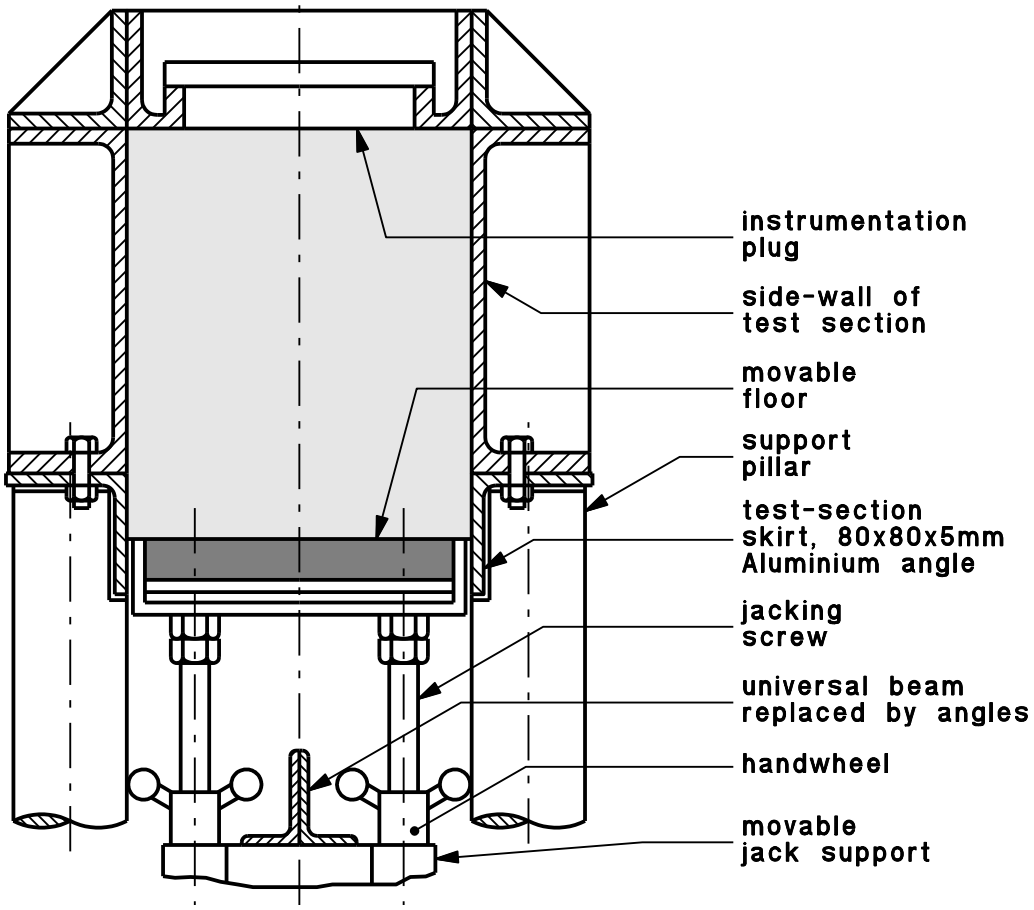

Figure 7.1: Addition of skirts to the wind-tunnel test section. The floor of the test section is below the original side walls. Scale 1:5.

contraction. In order to produce the necessary increase in the height of the duct, skirts were attached to the side-walls of the test section, as shown in Figure 7.1. The depth of the skirts was sufficient to accommodate growth of the boundary-layer displacement thickness over the full length of the test section.

For studying the small-scale structure of the turbulent boundary layer, it was desirable to operate the wind tunnel with choked flow rates corresponding to test-section flow speeds between approximately 1 m/s and 4 m/s. The remaining steps in reconfiguring the test section were to select a set of boundary-layer trips which would produce acceptable transition to turbulence over this speed range, and to minimise the streamwise pressure gradient at a single speed within this range. It was then possible to examine pertinent characteristics of the turbulent boundary layers developed on the upper surface of the test section and to assess the suitability of these boundary layers for further studies of canonical wall turbulence.

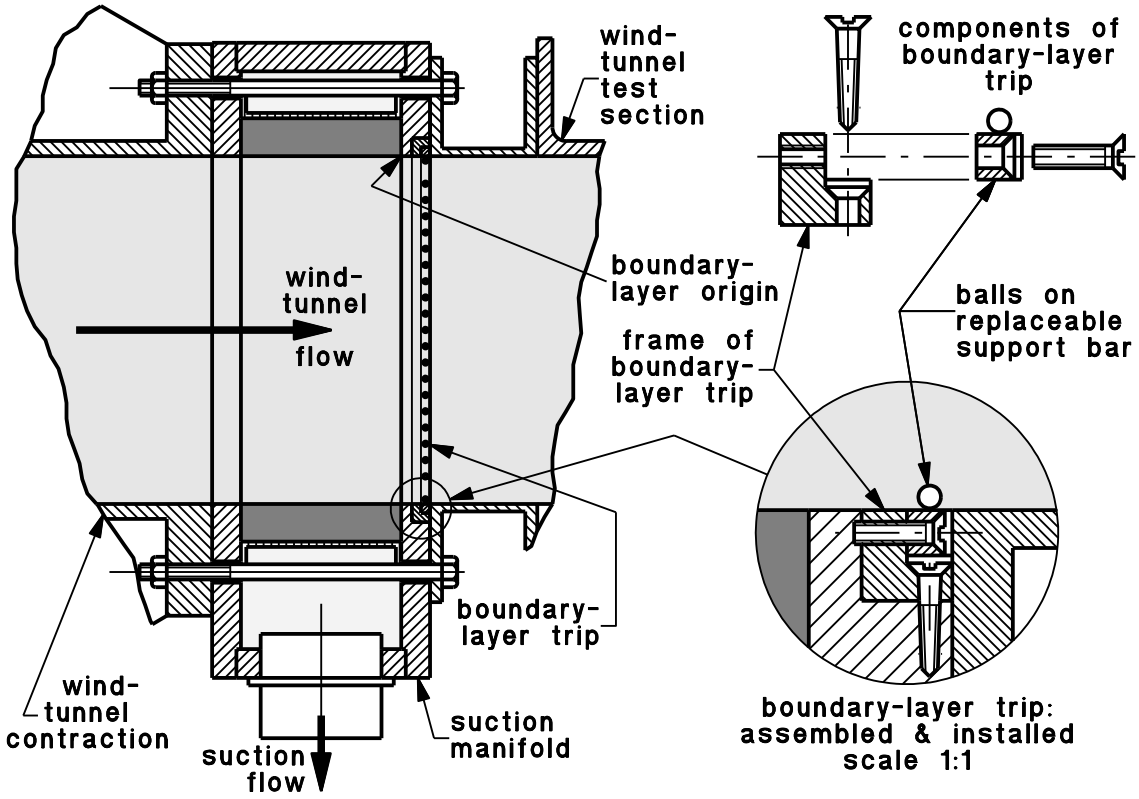

Figure 7.2: Replaceable boundary-layer trip at the downstream edge of the suction manifold. Scales 1:5 and 1:1.

7.2 Boundary-layer trip

7.2.1 Design of the trip

In earlier investigations (Section 4.13.3) boundary-layer trips consisting of a single row of spheres were found to produce thinner turbulent boundary layers than cylindrical trips. The sphere diameter required to produced transition was minimised by placing the trip as close to the boundary-layer origin as possible. It also became clear that the optimum size of the trip depends on the flow speed.

The construction details of the trips used to initiate boundary-layer turbulence are illustrated in Figure 7.2. Each trip consisted of a single row of steel balls extending right around the test-section perimeter. The balls were glued to aluminium support bars. The removable support bars were mounted in a fixed frame which was recessed into each of the four downstream edges of the suction manifold. When a trip was installed only the steel balls protruded from the wall and the ball centres were 16 mm downstream of the boundary-layer origin. Trips were made for each of the ball diameters listed in Table 7.1. These were intended to produce boundary-layer transition at flow speeds between 1 m/s and

Table 7.1: Dimensions of boundary-layer trips: ball diameters and space between ball centres.

Ball Diameter		Spacing	Number
mm	inches	mm	per side
2.38	3/32	5	45
2.78	7/64	5.5	41
3.17	1/8	6	37
3.50	—	7	32
3.97	5/32	8	27
4.76	3/16	10	22
5.56	7/32	11	20
7.14	9/32	15	14

4 m/s. The space between the centres of adjacent balls, which is also given in Table 7.1, was selected to produce a gap approximately equal to the ball diameter.

The boundary-layer trip is designed on the principle that the lateral shear ($\partial u/\partial z$) and streamwise vorticity (ω_x) generated by the flow between adjacent balls creates "transition sites" immediately downstream of the trip. The mechanism of turbulence production at these sites is believed to be similar to the mechanism which produces near-wall eruptions in the wake of a cylinder-wall junction (see Figure 1.9) [Smith et al., 1991a]. The distance between adjacent balls was selected to produce a high density of "transition sites", and therefore laterally uniform boundary-layer characteristics.

7.2.2 Experimental technique

Erm (1988) invested a very considerable effort in determining acceptable trips for the boundary layer in flows with free-stream speeds between 8 m/s and 14 m/s. The flow speed which he selected as correct for each size and style of trip was the speed at which the location of the maximum wall shear stress ceased to move further upstream as flow speed was increased. At flow speeds between 1 m/s and 4 m/s, dynamic pressures were too low for reliable and rapid measurements of the wall shear stress with a Preston tube and the available manometers, and so Erm's method of determining the correct trip size was considered to be impracticable in the present case. However, the success of Erm's work suggests that boundary-layer trips might be selected on the basis of wall shear stress measurements even when it is not possible to follow his procedure.

In the speed range 1 m/s to 4 m/s, the wall shear stress is most reliably obtained from the distribution of mean air speed within the near-wall region of the boundary layer. For each trip, the wall shear stress was measured 845 mm downstream of the boundary-layer origin over a range of six or seven different flow speeds. At least one of the speeds in each range was low enough for the boundary layer to remain

in a completely laminar state, and the remainder of each speed range extended well into the turbulent boundary-layer regime.

The experimental procedure for these measurements was, except for several refinements, the same as for the measurements reported in Sections 3.3, 4.1 and 5.1. The two most significant refinements were in the use of wall proximity effect for calibration of hot-wires (see Section 2.2.6.3) and in further development of the Clauser-chart method.

The Clauser chart, which was originally used for determining only the wall shear stress [Clauser, 1954], was adapted by Coles (1968) to find also the optimal values of the parameters δ_π and Π for his boundary-layer wake function which can be closely represented by

$$w\left(\frac{y}{\delta_\pi}\right) = \frac{2\Pi}{\kappa}\sin^2\left(\frac{\pi y}{2\,\delta_\pi}\right). \tag{7.1}$$

For selection of operating speeds of boundary-layer trips, the Coles wake function (Equation 7.1) was combined with Squire's (1948) formula for the mean velocity distribution in the near-wall region to give the following representation of the overall mean velocity distribution in the boundary layer:

$$\begin{aligned} U^+ = \frac{U}{U_\tau} &= y^+ && \text{for} \quad 0 < y^+ < y_0^+, \\ &= \frac{1}{\kappa}\ln\left(y^+ - y_0^+ + \frac{1}{\kappa}\right) + C + w\left(\frac{y^+}{\delta_\pi^+}\right) && \text{for} \quad y^+ \geq y_0^+, \end{aligned} \tag{7.2}$$

where $y_0^+ = C - \kappa^{-1}\ln\kappa$. From experimental measurements of mean velocity over the full thickness of the turbulent boundary layer, it was then possible to optimise the five parameters U_τ, κ, C, δ_π^+ and Π simultaneously. In this optimisation, the multidimensional downhill simplex method [Press et al., 1986] was used to minimize the mean square difference between the experimental data and Equation 7.2. The technique was adapted for laminar and transitional boundary layers by ignoring all parameters except U_τ and using only data from the linear near-wall region for the curve-fitting optimisation. The experimental data were not corrected for wall-proximity effect.

7.2.3 Selection of operating speeds for the boundary-layer trips

As indicated in the previous section, the primary information used for the selection of an operating speed for each boundary-layer trip is the local skin-friction coefficient C_f at a distance 845 mm downstream from the boundary-layer origin (i.e. at test-section Port 3). The results of these measurements are plotted in Figure 7.3 as a separate set of data for each trip. During transition to turbulence brought about by increasing the flow speed, the friction coefficient increases by a factor of approximately two. With the exception of the trip with 2.78-mm-diameter spheres, the rise in C_f occurs over a change in flow speed of no more than 10%. After this almost abrupt rise, C_f gradually decreases as flow speed is further increased.

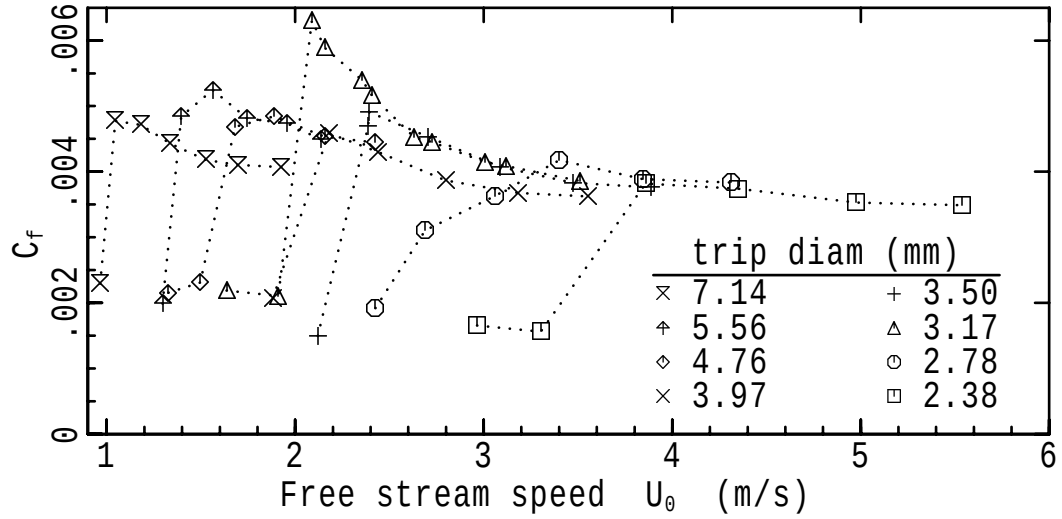

Figure 7.3: Local skin-friction coefficient for laminar-to-turbulent boundary-layer transition at test-section Port 3 ($x = 845$ mm).

The start of transition in a laminar boundary layer is readily observed on an oscilloscope as the onset of fluctuations in the hot-wire signal. By using the maximum value of C_f to define conveniently the completion of transition to turbulence, it is then possible to plot the transitional speed range as a function of trip diameter (Figure 7.4). The empirically fitted curve

$$Re_d = \frac{U_0 d}{\nu} = 423\left(\frac{x_t}{d}\right)^{0.15}, \tag{7.3}$$

where $x_t = 16$ mm is the distance from the trip centre to the boundary-layer origin, passes through the middle of nearly all the transition ranges in Figure 7.4. Over the range of trip diameters tested, it is little different from the constant, $Re_d = 533$. The weak dependence of the transition Reynolds number on trip diameter appears to result from the *decrease* in the ratio of laminar boundary-layer thickness to trip diameter (i.e. δ/d) as flow speed is decreased; because, as $Re_{x_t} = Ux_t/\nu$ decreases, the necessary trip diameter increases more rapidly than boundary-layer thickness. At the selected operating speeds, which are plotted as □ symbols in Figure 7.4, this effect also makes the Reynolds number of the trip a weakly decreasing function of diameter.

Because the skin-friction coefficient values are calculated from recordings of fluctuating velocity throughout the near-wall region, it is possible to examine the distributions of mean velocity, and the higher order statistics of velocity fluctuation[1] without additional measurements. A close examination of these data proves to be very useful for verifying the selection of operating speed, and for resolving the difficulties created by anomalous values of wall shear stress. The salient features observed in the

[1] I.e. r.m.s., skewness and flatness

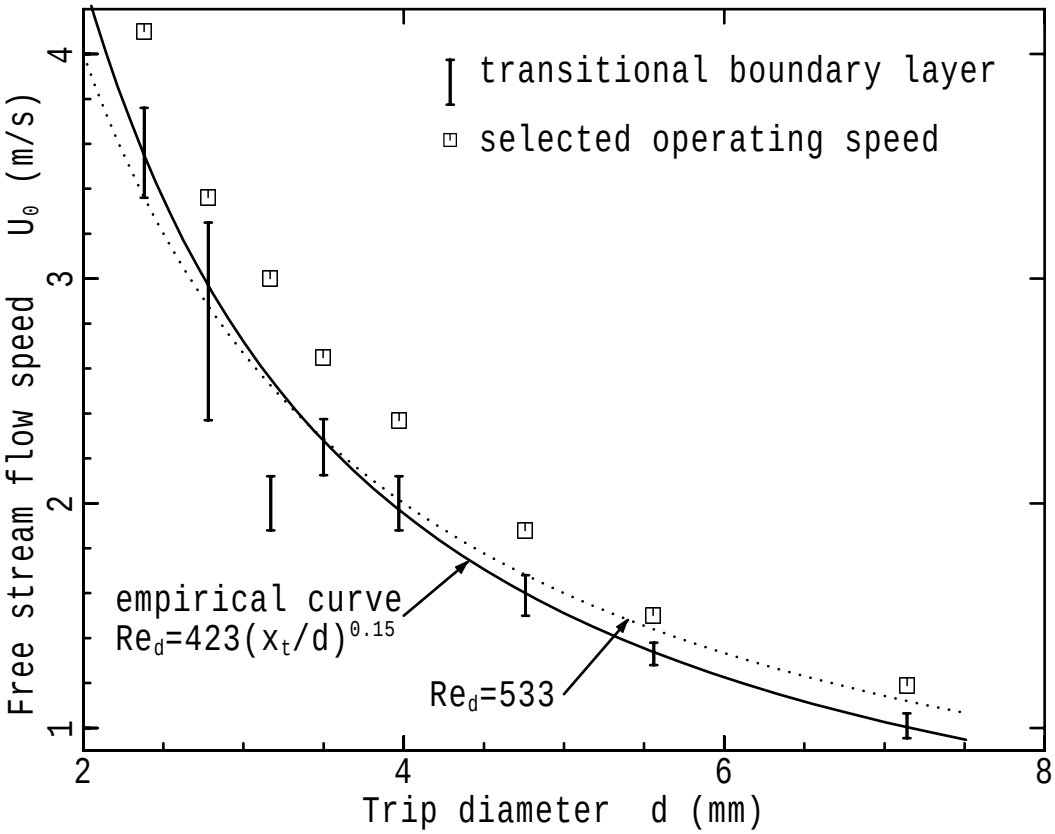

Figure 7.4: Transitional boundary-layer regime and selected operating speed for each trip diameter. The error bars span the speed range of the transitional boundary layer.

velocity statistics of laminar, transitional and low-Reynolds-number turbulent boundary layers are illustrated schematically in Figure 7.5. In this figure, laminar to turbulent transition is associated with a clockwise rotation of the mean velocity distribution, first onto the buffer region and log region of the classical "law of the wall", and then onto the wake region of the turbulent boundary layer. Purtell, Klebanoff and Buckley (1981) identify a similar final stage of wake-function adjustment as a state of underdevelopment in which outer region statistics plotted as functions of y/δ^* are different from those measured in fully developed turbulent boundary layers.

The r.m.s. velocity distributions show that velocity fluctuation levels in transitional boundary layers are almost the same as in fully turbulent boundary layers. The transitional nature of these boundary layers is sometimes also revealed by an abnormally large scatter in the data. In contrast to r.m.s. distributions, skewness and flatness are extremely sensitive indicators of transition and the development of turbulence. During transition both undergo very large, rapid changes which cease or "slow down" only when transition is complete. As shown in Figures 7.5(c) and 7.5(d), the measured skewness and flatness of "velocity fluctuations" in a laminar boundary layer are 0 and 3 respectively, because

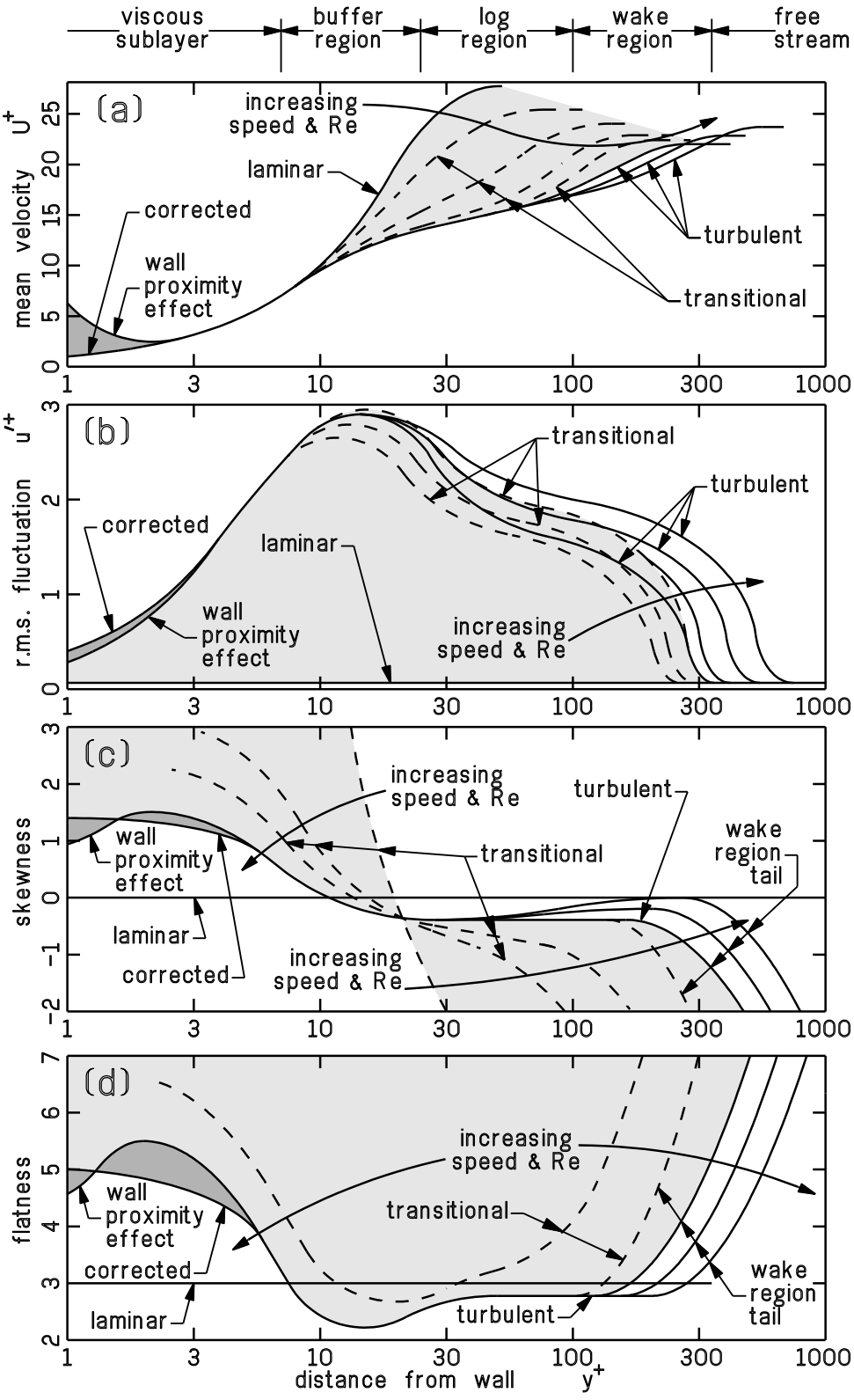

Figure 7.5: Schematic diagram of streamwise velocity statistics for laminar-to-turbulent boundary-layer transition produced by increasing flow speed. Distributions for transitional boundary layers are shown as dashed lines within the shaded regions. (a) Mean velocity; (b) r.m.s. velocity fluctuation; (c) skewness; (d) flatness.

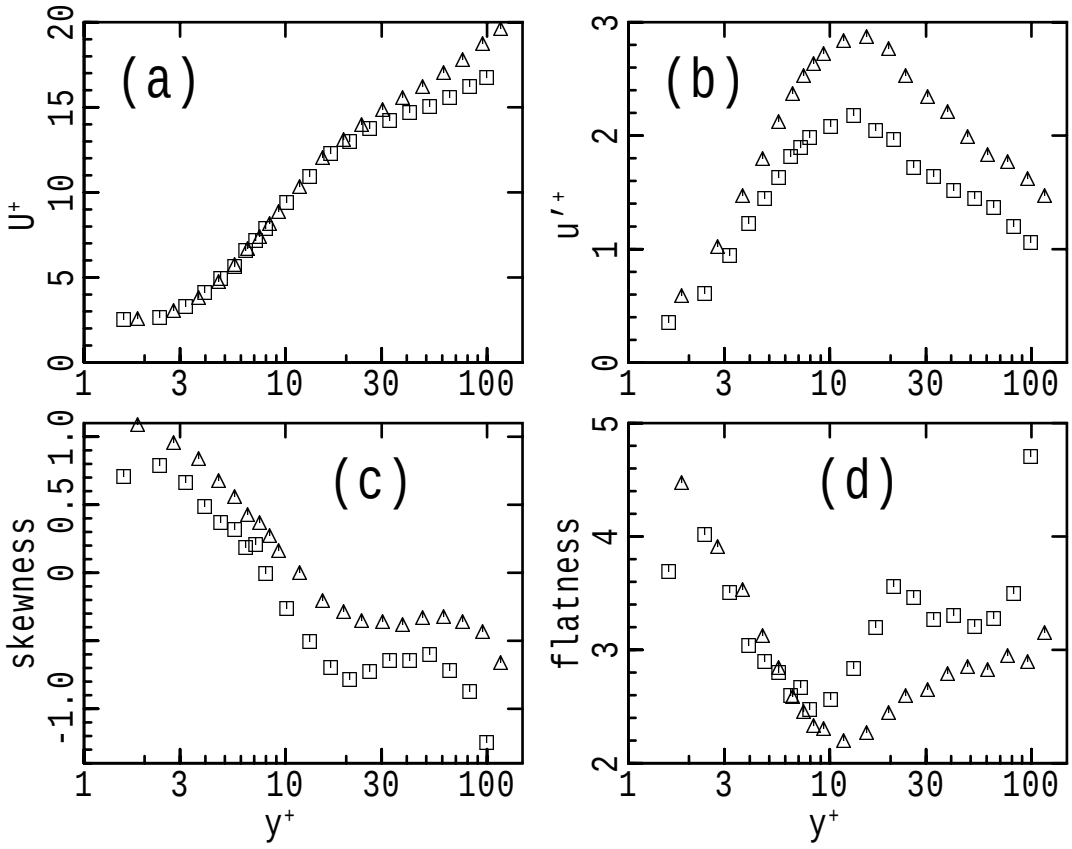

Figure 7.6: Statistics of velocity distributions at $x = 845$ mm for premature transition with a 3.17 mm trip; (a) mean velocity; (b) r.m.s. fluctuations; (c) skewness; (d) flatness. □, premature or anomalous transition at, $U_0 = 2.1$ m/s; △, normal transition at $U_0 = 3.0$ m/s.

the signal fluctuations are entirely due to random noise. With rising flow speed, the intermittency of the fluctuating velocity signal at the onset of transition produces amplitudes of skewness and flatness which are extremely large and frequently exceed the ordinate limits of Figures 7.5(c) and 7.5(d). During the increase in flow speed, skewness and flatness settle rapidly toward values typical of a turbulent boundary layer. The final stage of the transition is the formation of a "wake region tail" (Figures 7.5(c) and 7.5(d)). Increasing the Reynolds number of the turbulent boundary layer produces further adjustment of the wake region r.m.s., skewness and flatness, but these changes are much more gradual than encountered during transition.

The results shown in Figure 7.4 indicate that the 3.17 mm trip produces transition at a flow speed significantly lower than the 2.5 m/s given by Equation 7.3. Closer inspection of the experimental data does not reveal the cause of this apparently premature transition, but it does show that the resulting boundary-layer characteristics are not those of a conventional low-Reynolds-number turbulent boundary layer. For example, at test-section Port 3, the maximum C_f obtained with the 3.17 mm trip

(Figure 7.3) is much higher than for the other trip diameters. In addition, the mean and r.m.s. velocity distributions for flow speeds lower than 2.5 m/s (Figures 7.6(a) and (b)) are quite atypical of turbulent boundary layers; the mean velocity gradients in the logarithmic region and the turbulence levels are too low for the observed values of C_f. The corresponding skewness and flatness distributions in Figures 7.6(c) and (d) indicate abnormal behaviour throughout the near-wall region. However, as flow speed is increased, these anomalies gradually disappear and, at speeds higher than 2.5 m/s, the velocity statistics are indistinguishable from those of conventional wall turbulence.

7.3 Streamwise pressure gradient in the test section

In comparison with the effects of skin friction, the effects of streamwise pressure gradient on the turbulent boundary layer were reduced to a very low level by measuring the static pressure variation along the test section and then adjusting the height of the flexible lower surface of the test section. Even with the most sensitive available manometer, which was a 1 Torr MKS Baratron, extreme care was required to resolve static pressure variations along the test section. The measurement technique was the same as that outlined in Section 3.2.2.2.

The first step in the process of adjusting the pressure gradient was to change the height of the flexible lower surface so that the static pressure difference between test-section Port 1 ($x = 0.24$ m) and Port 12 ($x = 3.59$ m) was zero at a flow speed of 1.9 m/s. Both suction and a boundary-layer trip were required to produce a turbulent boundary layer. A different suction flow rate and a different trip diameter were required for each of the selected flow speeds, which ranged from 1.2 m/s to 4.1 m/s. A micrometer was used to ensure that, between the reference point at Port 1 and the reference point at Port 12, the test-section floor remained flat (but not horizontal). This established a datum for further adjustments between the two reference points. The surface profile was then changed so that, at the higher flow speed of 4.1 m/s, the streamwise pressure gradient was constant. This was a lengthy and repetitive process because, in addition to the difficulty of compensating for manometer output-voltage drift, adjustment of the surface height at one test-section port inevitably changed the static pressure at nearby ports.

After the adjustments to the lower-surface profile were complete, the distribution of static pressure was measured along the upper surface of the test section. The static pressure coefficient,

$$\Delta C_p = \frac{P - P_1}{\frac{1}{2}\rho U_0^2}, \tag{7.4}$$

where P_1 is the static pressure at test-section Port 1 and U_0 is also measured at Port 1, is plotted in Figure 7.7. As shown by additional measurements at $U_0 = 1.9$ m/s, transition is delayed until almost half-way along the test section if the suction manifold is not used. The change in boundary-layer growth rate produced by varying the flow speed is clearly smaller than the change produced by natural transi-

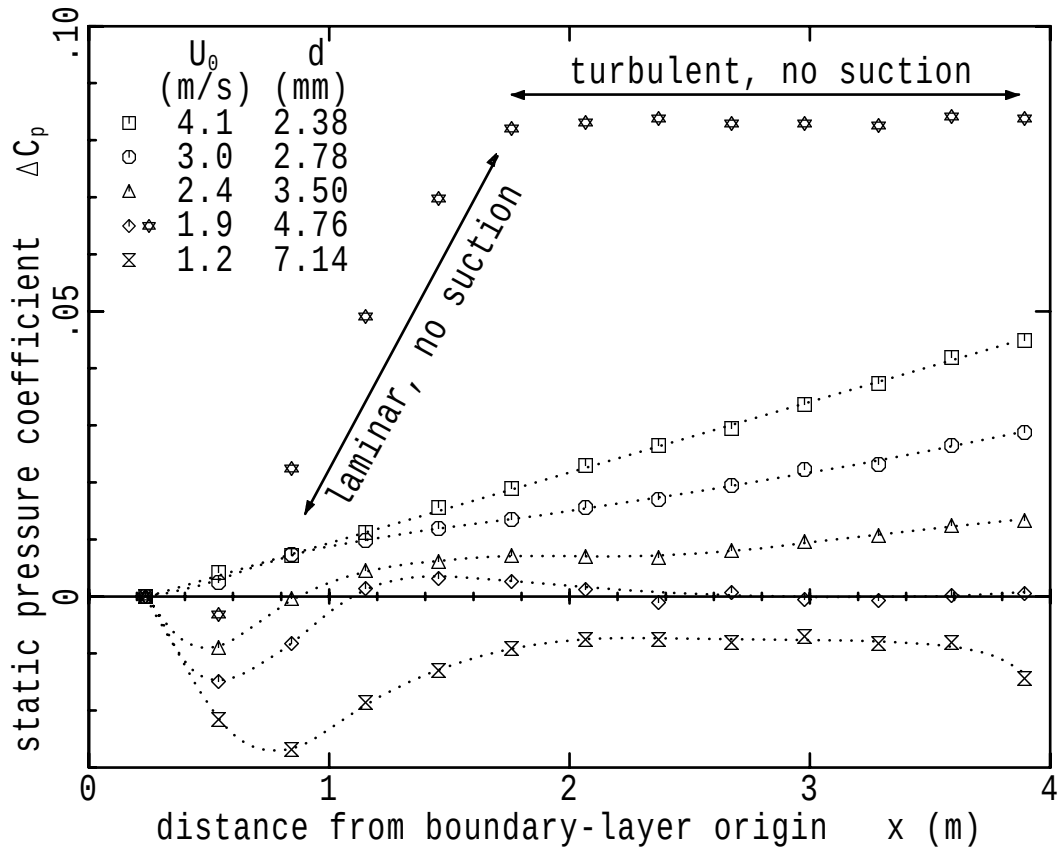

Figure 7.7: Static wall pressure distribution $\Delta C_p = (P - P_1)/\frac{1}{2}\rho U_0^2$ along the length of the test section. Flow speeds, U_0, and trip diameters, d, are given in the legend. The suction manifold was used for all but one set of measurements (✡) at $U_0 = 1.9$ m/s. The dotted "curves of best fit" were drawn manually.

tion from a laminar to a turbulent boundary layer. The pressure distribution is linear at $U_0 = 4.1$ m/s but does not remain linear as flow speed is reduced. With decreasing flow speed, the deviations from linearity near the upstream end of the test section are believed to be caused by increasing streamline curvature in the vicinity of the suction manifold. The higher streamline curvature is due to an increase in the proportion of flow removed by the suction manifold. The residual effects of the streamwise and normal pressure gradients produced by such streamline curvature can be expected to persist for downstream distances of one or two duct widths.

The hypothesis, that the suction manifold is at least partly responsible for static pressure variations near the upstream end of the test section, is reinforced by independent measurements of the free stream speed distribution along the length of the test section. These measurements are shown in Figure 7.8.

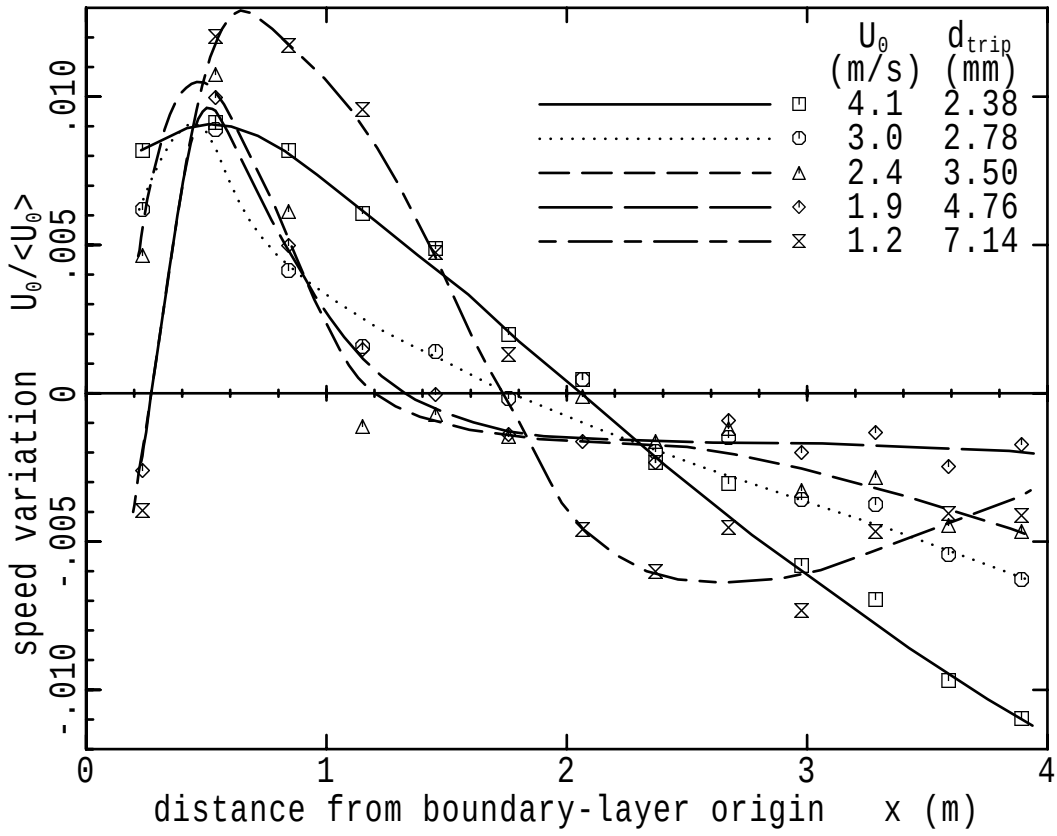

Figure 7.8: Distribution of free stream air speed along the length of the test section. $\langle U_0 \rangle$ is free stream speed averaged over the length of the test section.

7.4 Velocity fluctuations in the free stream

Velocity-fluctuation levels in the free stream flow were determined from data obtained primarily for measuring the characteristics of the test-section boundary layers. From these measurements, the r.m.s. fluctuating component of free stream flow speed was found to be approximately constant at about 0.01 m/s for all flow speeds less than 3 m/s. A slightly higher r.m.s. fluctuation of 0.015 m/s was recorded at 3.9 m/s. Comparisons between the signal from the hot-wire and the signal from a nearby microphone show that the free stream velocity fluctuations are mostly acoustic particle-velocity oscillations. The acoustic noise within the test section, which is usually at a level[2] of 95 to 100 dB, consists almost entirely of very-low-frequency "organ pipe" modes excited by compressor noise emerging from the suction manifold.

In summary, the r.m.s. intensity of velocity fluctuations in the test-section free stream decreases from 0.9% to 0.4% as the flow speed increases from 1.16 m/s to 3.9 m/s.

[2]Decibel reference pressure is 20 μPa.

7.5 Boundary-layer characteristics

Characteristics of the turbulent boundary layer developed on the upper surface of the test section were determined from velocity distributions measured on the longitudinal plane of symmetry ($z = 0$) at distances of up to 3.89 m from the boundary-layer origin. It was then possible to calculate momentum balances and to compare the boundary-layer characteristics with previously published data. Data were obtained at five test-section flow speeds between 1.1 m/s and 4.0 m/s, in each case with a trip diameter selected from Figure 7.4.

7.5.1 Experimental technique

The procedure for measuring velocity distributions was, with the addition of several refinements, the same as in Section 5.1. The main refinements were in the use of wall-proximity effect for hot-wire calibration (see Section 2.2.6.3) and, as described in Section 7.2.2, in using a development of the Clauser-chart method for simultaneous optimisation of the parameters U_τ, C, δ_π and Π. Thermal drift of the analogue instrumentation was reduced to an acceptable level by carefully choosing the time of day for the measurements and by selective ventilation of the laboratory. Of the 25 data-sampling locations of the hot-wire probe at each test-section port, about half were distributed linearly in the outer part of the boundary layer so that displacement-thickness and momentum-thickness integrals could be calculated accurately. The remainder of the sampling locations were distributed exponentially within the wall-region of the boundary layer in order to place at least a few within the viscous sublayer and to ensure that they would be distributed uniformly on a $\log y^+$ axis. Data records of 5000 samples, which were collected over a period of 30 seconds, were long enough to evaluate the mean velocity and the r.m.s. velocity fluctuation with a resolution in the order of the signal noise level. The skewness and flatness values calculated from these data were reliable enough to study the effects of scaling y with different thickness parameters in the outer region of the boundary layer.

7.5.2 Calculation of momentum balance

The conventional definitions for displacement thickness,

$$\delta_2^* = \int_0^\delta \left(1 - \frac{U(y)}{U_0}\right) dy, \tag{7.5}$$

and momentum thickness,

$$\theta_2 = \int_0^\delta \frac{U(y)}{U_0} \left(1 - \frac{U(y)}{U_0}\right) dy, \tag{7.6}$$

may be considered to be a by-product of deriving the momentum-integral equation for a two-dimensional boundary layer,

$$\frac{d\theta_2}{dx} + \frac{\theta_2}{U_0}\frac{dU_0}{dx}(H_2+2) = \frac{1}{2}C_f \tag{7.7}$$

[Duncan et al., 1970], where $H_2 = \delta_2^*/\theta_2$. For the calculation of a momentum balance from data measured in the absence of a streamwise pressure gradient, Equation 7.7 can be written most conveniently in the form

$$\theta(x_1) = \theta(x_0) + \frac{1}{2}\int_{x_0}^{x_1} C_f dx \tag{7.8}$$

[Erm, 1988], where the local skin-friction coefficient C_f is integrated over the streamwise displacement $(x_1 - x_0)$ from a starting point x_0.

The momentum-integral equation for flow in a duct with an arbitrary cross-section,

$$\frac{d\theta_d}{dx} + \frac{\theta_d}{U_0}\frac{dU_0}{dx}(H_d+2) = \frac{1}{2}\overline{C_f} - \frac{\theta_d}{\mathcal{P}}\frac{d\mathcal{P}}{dx}, \tag{7.9}$$

where $H_d = \delta_d^*/\theta_d$ and $\mathcal{P}$ is the perimeter of the duct cross-section, is derived in Appendix H. In Equation 7.9, the definitions of the momentum thickness θ_d and displacement thickness δ_d^* are adjusted to take account of the duct cross-section, and the skin-friction coefficient $\overline{C_f}$ is averaged around the cross-section perimeter (Equation H.18). If, as an approximation, the cross-sectional velocity contours of the flow in a rectangular duct are assumed to be rectangular, the appropriate expressions for the displacement and momentum thicknesses are

$$\delta_d^* = \int_0^\delta \left(1 - \frac{U}{U_0}\right)\left(1 - \frac{8y}{\mathcal{P}}\right) dy \tag{7.10}$$

and

$$\theta_d = \int_0^\delta \frac{U}{U_0}\left(1 - \frac{U}{U_0}\right)\left(1 - \frac{8y}{\mathcal{P}}\right) dy \tag{7.11}$$

respectively. Similar expressions have been obtained by Cebeci and Bradshaw (1977) for boundary layers developed in the longitudinal flows over the internal and external surfaces of a cylinder. As for a two-dimensional boundary layer, Equation 7.9 can be integrated in the streamwise direction to produce an equation which is more suitable for estimating a momentum balance from experimental data:

$$\theta_d(x_1) = \theta_d(x_0) + \frac{1}{2}\int_{x_0}^{x_1} \overline{C_f}\, dx - \int_{x_0}^{x_1} \frac{\theta_d}{U_0}\frac{dU_0}{dx}(H_d+2)\, dx - \int_{x_0}^{x_1} \frac{\theta_d}{\mathcal{P}}\frac{d\mathcal{P}}{dx}\, dx. \tag{7.12}$$

The balance of momentum in the test-section turbulent boundary layers was examined by comparing the right side of Equation 7.12 with measurements of the momentum thickness θ_d and θ_2. A reference streamwise location of $x_0 = 1.15$ m, corresponding to test-section Port 4, avoided the worst effects of any spanwise momentum-thickness variations which may have existed at positions further upstream. Values of the centreline skin-friction coefficient were used in place of the perimeter-averaged friction coefficient $\overline{C_f}$. The data of Leutheusser (1963) indicate that, in a fully developed turbulent duct flow,

the error resulting from this approximation should be less than 2% at the highest test-section flow speed of $U_0 = 3.9$ m/s. The centreline skin-friction coefficients were determined by optimising the parameters of two different mean-velocity models to fit the experimental velocity-profile data. The Coles (1968) wake function is used in both models. In the first model, the law of the wall is assumed to be

$$U^+ = \frac{1}{\kappa} \ln y^+ + C \tag{7.13}$$

with $\kappa = 0.41$ and $C = 5.0$. In the second model, the friction velocity is obtained using Spalding's (1961) formulation for the law of the wall,

$$y^+ = U^+ + e^{-\kappa C} \left[e^{\kappa U^+} - \sum_{n=0}^{4} \frac{1}{n!} (\kappa U^+)^n \right], \tag{7.14}$$

with $\kappa = 0.41$ and with the value of C optimised for each individual mean velocity distribution. Further details of these procedures and the resulting values of C_f are given in Section 7.5.4. The Spalding-Coles mean velocity model (Equations 7.14 and 7.1) is preferred over the Squire-Coles mean velocity distribution (Equation 7.2), which was used for determination of the boundary-layer trip diameter, because, in the buffer region of the boundary layer ($7 \lesssim y^+ \lesssim 30$), it agrees much more closely with the experimental measurements. Values of friction velocity calculated from the second model are effectively determined from measurements in the viscous sublayer and near-wall half of the buffer region (i.e. $y^+ \lesssim 15$), and so do not depend significantly on the momentum-thickness integral (Equation 7.11), which, in these experiments, accumulates between approximately 85% and 97% of its value from the region $y^+ \gtrsim 15$. The free stream velocity gradient (dU_0/dx) was obtained from Figure 7.8.

In Figure 7.9, the duct momentum thickness (θ_d, Equation 7.11) is shown as □ symbols. The right side of Equation 7.12 is drawn as solid lines when C_f is determined from Coles's (1968) wall function (Equation 7.13) and is drawn as dashed lines when C_f is determined from Spalding's (1961) function (Equation 7.14). These results confirm the validity of the momentum-integral equation for a duct (Equation 7.9), and also show that the effects of contaminating cross-flows in the test section are very small. When Coles's (1968) wall function is used, the overall r.m.s. difference between θ_d and the right side of Equation 7.12 is 1.64% of the momentum-thickness value at $x = 3.96$ m (i.e. near the downstream end of the test section). For the Spalding (1961) formulation the imbalance is of opposite sign and has a slightly larger r.m.s. magnitude of 1.79%. The largest r.m.s. mismatch of 2.1% occurs at the lowest flow speed ($U_0 = 1.16$ m/s) and is likely to be a consequence of residual buoyant cross-flows. Results for higher flow speeds indicate that, in the downstream half of the test section, error due to the assumptions

(1) the centreline friction coefficient is equal to the perimeter-averaged friction coefficient ($C_f = \overline{C_f}$), and

(2) cross-section contours of mean velocity are concentric rectangles

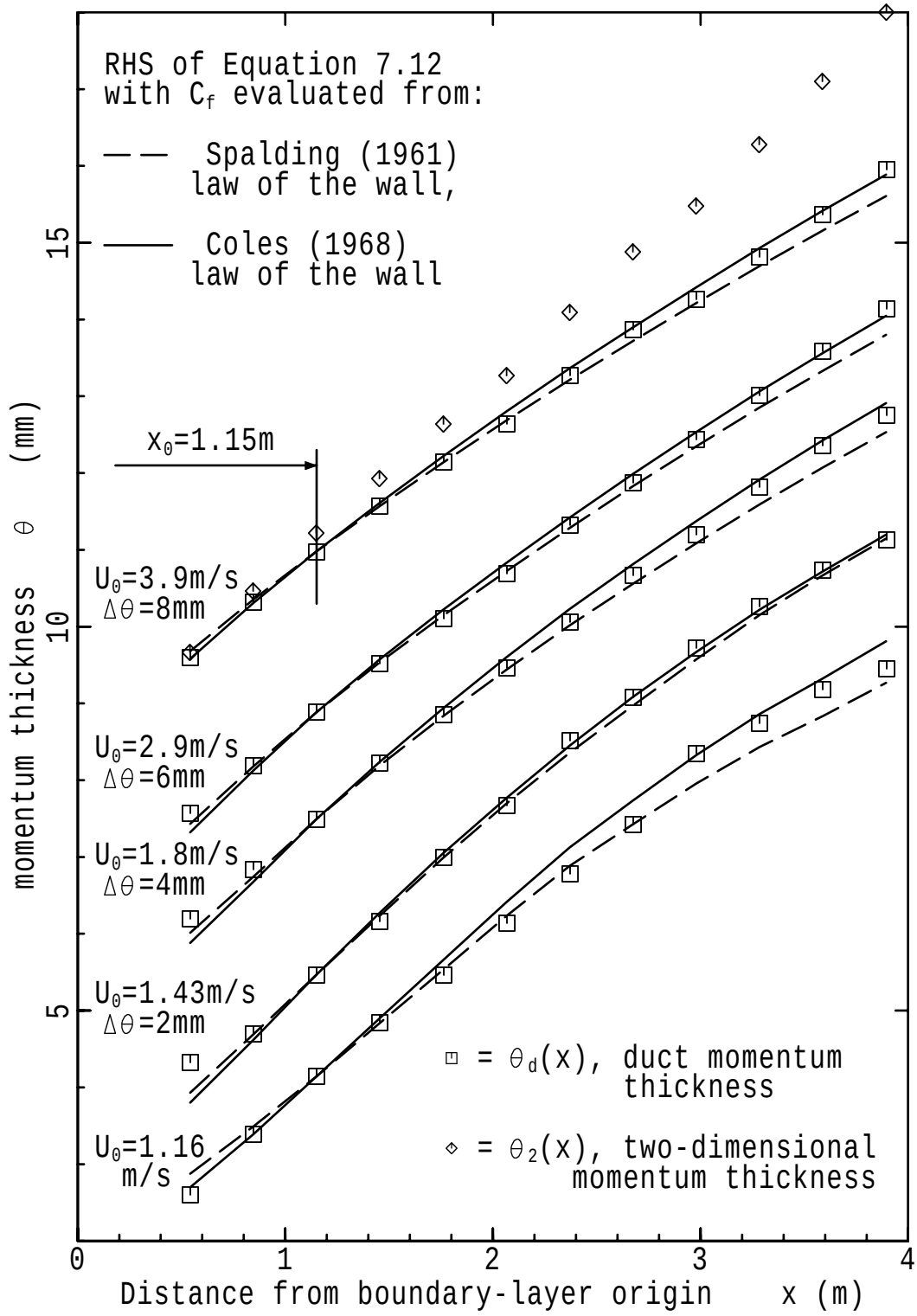

Figure 7.9: Momentum balance for test-section turbulent boundary layers with free stream flow speeds from 1.16 m/s to 3.9 m/s. Momentum thickness values (□, ◇) are compared with the right hand side of Equation 7.12 (solid and dotted lines). The origin for integration is at test-section Port 4 ($x_0 = 1.15$ mm). The vertical offset $\Delta\theta$ for each set of data is indicated under the flow-speed label as, for example, $\Delta\theta = 8$mm at $U_0 = 3.9$ m/s.

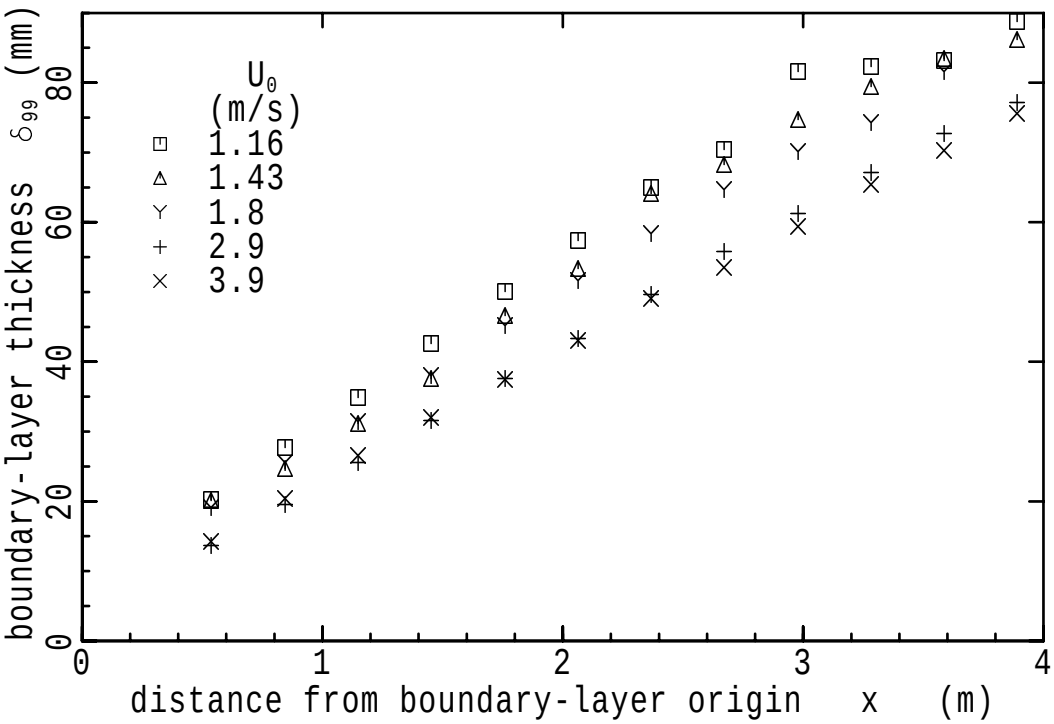

Figure 7.10: Thickness of the turbulent boundary layer developed in the test section

is generally in the order of 2%, and is not significantly larger than the errors in measuring C_f or θ_d.

The obvious mismatch shown in Figure 7.9 between the two-dimensional momentum thickness, θ_2, and the right side of Equation 7.12 at $U_0 = 3.9$ m/s also occurs at all the other flow speeds. Clearly, in cases where the boundary-layer thickness is more than about 10% of the duct height, it is inappropriate to use the two-dimensional momentum thickness for calculating the momentum balance.

7.5.3 Boundary-layer thickness

Beginning with the results of Section 3.3.2, previous experience has shown that measurements of boundary-layer thickness (δ_{99}) are extremely sensitive to time-dependence and vortex structures in the free stream flow. In addition, a large change in δ_{99} can be produced by relatively small variations in mean velocity because the mean velocity gradient near the edge of the boundary layer is very small. In a boundary layer believed to be free of external disturbances, the repeated thickness measurements of Section 6.4.5 varied by less than $\pm 2\%$. For boundary-layer thicknesses less than about 80 mm, the accuracy of the results shown in Figure 7.10 is expected to be of a similar magnitude.

For flow speeds lower than about 2 m/s, some values of δ_{99} near the downstream end of the test section are greater than 83 mm. These measurements were considered to be much less reliable than in thinner boundary layers because the hot-wire probe could not be placed further than 90 mm from the wall and it was not possible to obtain satisfactory measurements of the free stream velocity. The growth rate of the boundary layer ($d\delta_{99}/dx$) at any particular distance downstream of the boundary-layer origin decreases as flow speed increases, so that, at the downstream end of the test section, δ_{99} also decreases. A different boundary-layer trip was used for each of the free stream speeds listed in Figure 7.10, and so the less regular changes in δ_{99} with flow speed at the upstream end of the test section are probably caused by differences in details of the transitional flow which, in effect, are equivalent to unpredictable changes in the location of the boundary-layer origin. The anomaly at $x = 2.37$ m for the free stream speed of 1.43 m/s is an order of magnitude smaller than those in Figure 3.5 and, at such a low speed, could have been caused by buoyant convection due to an air-temperature nonuniformity as small as 0.01^oC. Subject to the limitations already described in this paragraph, the boundary-layer thickness varies in a generally smooth and regular fashion consistent with the development of an uncontaminated turbulent boundary layer.

7.5.4 Wall shear stress

The centreline skin-friction coefficient of the test-section boundary layer is determined from the mean velocity distributions in two different ways and the results are used in the momentum-balance calculations of Section 7.5.2. The first of these is similar to the method used by Coles (1968) in which U_τ, Π and δ_π are found by fitting the mean velocity data to the equation

$$\frac{U}{U_\tau} = \frac{1}{\kappa}\ln\left(\frac{yU_\tau}{\nu}\right) + C + \frac{2\Pi}{\kappa}\sin^2\left(\frac{\pi y}{2\delta_\pi}\right), \tag{7.15}$$

with $\kappa = 0.41$ and $C = 5.0$. In effect, the friction velocity is determined from the logarithmic part of the mean velocity distribution. The corresponding values of the friction coefficient are plotted in Figure 7.11(a) against the Reynolds number Re_{θ_2}. The two-dimensional momentum thickness, θ_2, is chosen for calculating the Reynolds number because, as demonstrated later in Section 7.5.7, outer region turbulence statistics scale much better with θ_2 than with the duct momentum thickness, θ_d. Except at the lowest free stream speed, the values of friction coefficient in Figure 7.11(a) fall within a narrow band 5% to 10% below the Coles (1962) local friction law. For flow speeds of 1.8 m/s or more, the smaller differences of 5% to 7% occur in the upstream half of the test section and the values coincide almost exactly with those obtained by Murlis et al. (1982). Under the influence of stress-induced secondary flows the difference between the C_f data and Coles's curve grows to about 10% at the downstream end of the test section.

The theoretical model used for the second method of calculating C_f combines Spalding's (1961) near-

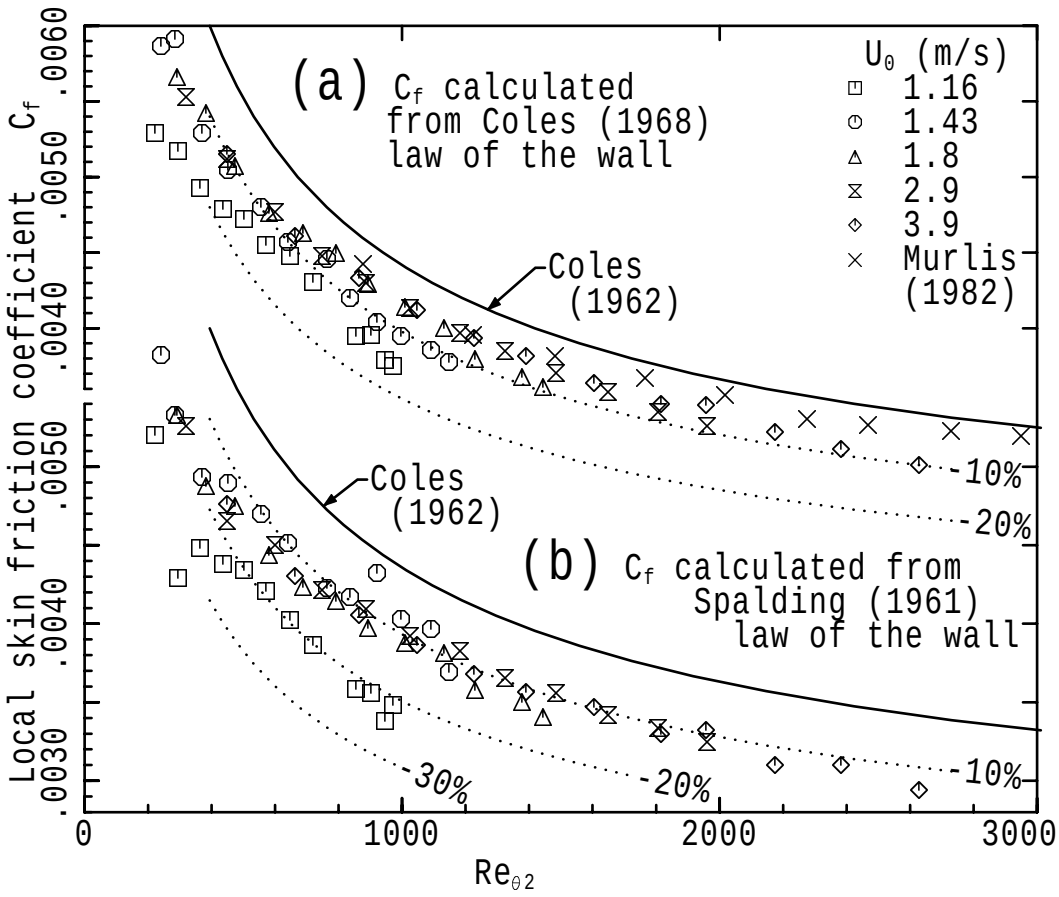

Figure 7.11: Local skin-friction coefficient of the test-section boundary layer; (a) calculated from the Coles (1968) wall function, $U^+ = \kappa^{-1} \ln y^+ + C$; (b) calculated calculated from Spalding's (1961) equation for the law of the wall. The data are compared with Coles's (1962) curve of "best fit" (solid line). The dotted lines are 10%, 20% and 30% lower than the curve of "best fit".

wall velocity distribution (Equation 7.14) with the Coles (1968) wake function, $w(y/\delta_\pi)$, defined in Equation 7.1. Von Kàrmàn's constant is assumed to have the value $\kappa = 0.41$. The remaining coefficients of the model U_τ, C, Π and δ_π are calculated by minimising the mean square difference between the experimental mean-velocity data and the theoretical model. Over all the mean-velocity data, the r.m.s. error of this curve-fitting process is $0.14U_\tau$ or 0.6% of the free stream speed. The values of skin-friction coefficient determined by this method (Figure 7.11(b)) depend almost entirely on the distribution of mean velocity measurements in the viscous sublayer and near-wall half of the buffer region (i.e. $y^+ \lesssim 15$). They are, on average, 5.6% lower than those determined from Equation 7.15 and are between 8% and 30% smaller than values given by the Coles (1962) curve of "best fit" for C_f.

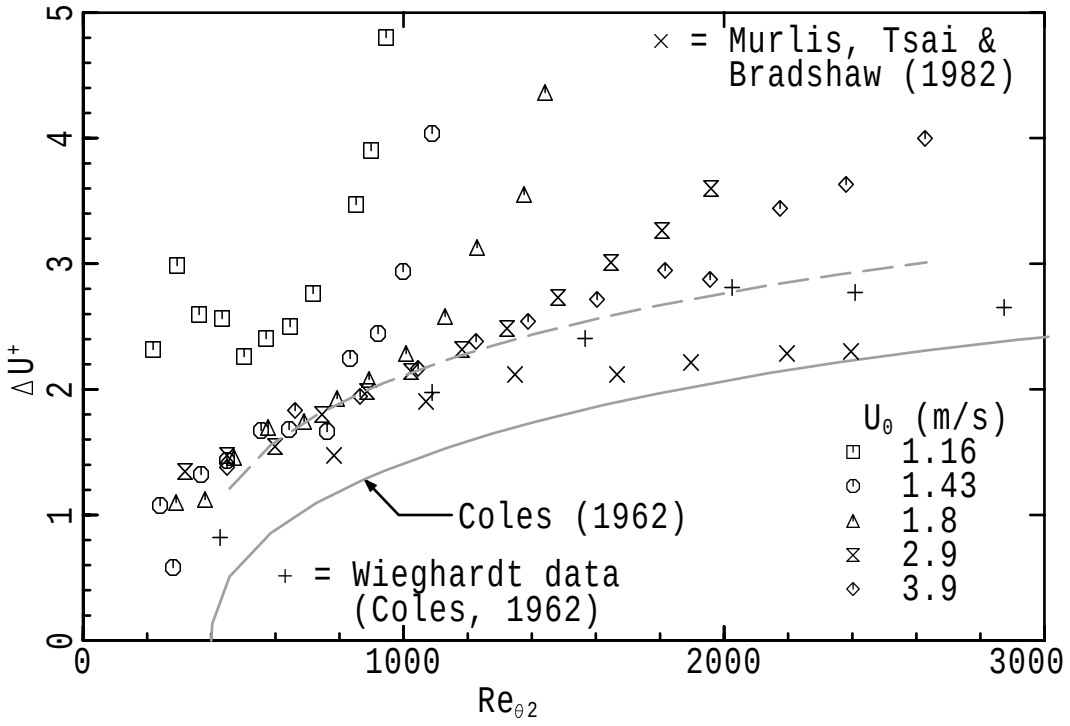

Figure 7.12: Wake strength of the test section boundary layer; compared with Coles (1962) "best fit" curve (—), Wieghardt data (+) [Coles, 1962] and Murlis et al. (1982) data (×). The dashed line is obtained by adding 0.7 to the ΔU^+ values of the Coles curve.

7.5.5 Wake region of the boundary layer

The strength of the wake contribution to the boundary layer, which is defined in terms of the wake-function amplitude, Π, as

$$\Delta U^+ = \frac{\Delta U}{U_\tau} = \frac{2\Pi}{\kappa}, \tag{7.16}$$

is described by Coles (1962) as "...distinguished by an almost exquisite sensitivity to the history and environment of a particular flow ..." and is used as the basis of the selection procedure in his identification of canonical turbulent boundary layers.

The values of wake strength shown as closed symbols in Figure 7.12 are calculated by the same process that produced the skin-friction coefficients of Figure 7.11(b). All are larger than values taken from the Coles (1962) "best fit" curve for ΔU^+. As shown by the dashed line, ΔU^+_{2D}, in Figure 7.12, the minimum difference between the present experimental data and Coles's curve is about 0.7 and occurs near the middle of the test section ($1.5 < x < 2.0$ m).

The larger difference near the upstream end of the test section ($Re_{\theta_2} < 600$) can be attributed to flow disturbances which are generated by the boundary-layer trip [Coles, 1962]. Plotting the difference be-

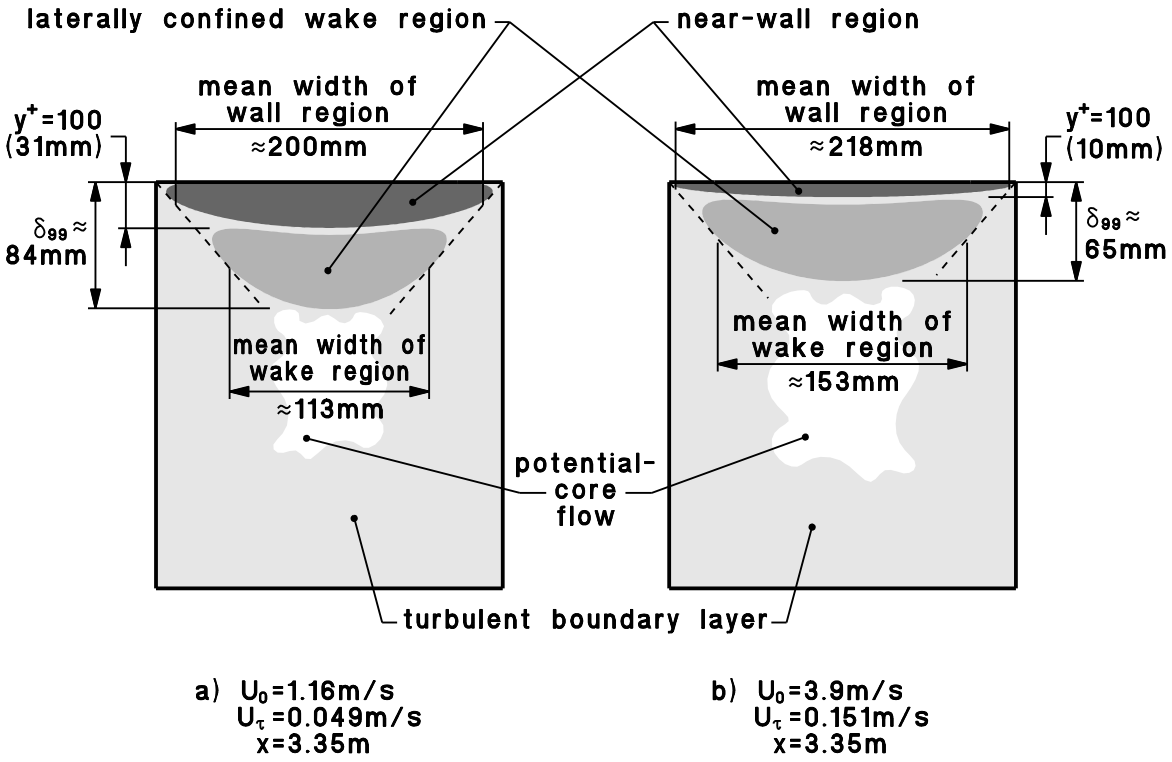

Figure 7.13: Schematic diagram of the boundary-layer cross-section at test-section Port 11 ($x = 3.305$ m), showing the spanwise widths of the wake region and wall region of the boundary layer; (a) $U_0 = 1.16$ m/s; (b) $U_0 = 3.9$ m/s.

tween experimental values and the dashed line (that is, $\Delta U^+_{XS} = \Delta U^+ - \Delta U^+_{2D}$) as a function of Re_x (Figure 7.15(b)) shows these disturbances decaying rapidly until, for Re_x between 150,000 and 200,000, they have no detectable effect on the wake strength. At the lowest flow speed of $U_0 = 1.16$ m/s, the much larger initial wake strength indicates a much less satisfactory performance of the boundary-layer trip than at higher flow speeds.

As boundary-layer thickness, δ_{99}, increases beyond about half the effective duct radius, r', ΔU^+ becomes much larger than previously published values for a two-dimensional boundary layer [Coles, 1962, Murlis et al., 1982, Purtell et al., 1981]. For the present context, where the duct cross-section is almost square, the effective radius is defined as the hydraulic radius, $2A/\mathcal{P}$, which is approximately equal to the maximum possible boundary-layer thickness or half the duct height. The explanation suggested for the larger ΔU^+ values in the test-section boundary layer is as follows. In the downstream half of the test section, the boundary-layer thickness increases from about $0.35r'$ to $0.85r'$, and so, as shown schematically in Figure 7.13, the spanwise width of the boundary-layer wake region becomes significantly less than the width of near-wall region. Therefore, in order to maintain the rate of momentum transfer which sustains the wall shear stress, the Reynolds stress in the wake region has to be significantly

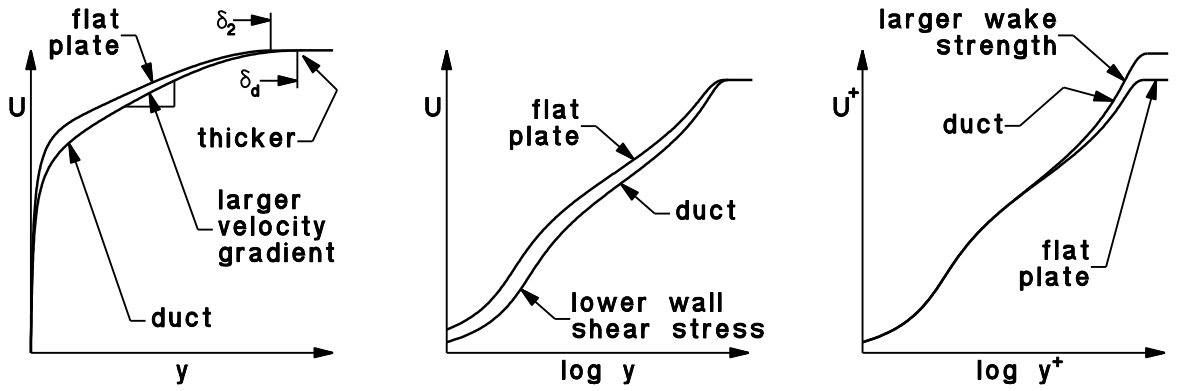

(a) dimensional y and U on linear axes

(b) dimensional y and U on semi-log axes

(c) wall-region scaling of y and U on semi-log axes

Figure 7.14: The effect of wake-region constriction on the mean velocity distribution, $U(y)$, in the turbulent boundary layer. The effect is exaggerated in this schematic diagram.

higher than in a true flat-plate boundary layer. On assuming a less than proportionate or zero increase in eddy viscosity, this higher Reynolds stress implies a larger mean velocity gradient. The velocity defect ($U_0^+ - U^+(y)$) in the wake region is therefore larger, and the wake strength (ΔU^+) is also larger than in the corresponding flat-plate boundary layer. This effect of lateral wake-region constriction on the mean velocity distribution is illustrated schematically in Figure 7.14. The lower wall shear stress shown for the duct boundary layer in Figure 7.14(b) is consistent the experimental momentum-balance results of Section 7.5.2 and Figure 7.9.

The hypothesis that lateral constriction of the wake region is responsible for elevated levels of wake strength, ΔU^+, suggests that the broken line in Figure 7.12 represents the wake strength, ΔU^+_{2D}, of a boundary layer which is thin in comparison with the cross-section dimensions of the duct. In the x-y mid-plane, such a boundary layer is two-dimensional and is not affected by the development of side-wall boundary layers. The wake strength, ΔU^+, of the relatively thick boundary layer near the downstream end of the wind-tunnel test section is significantly larger than ΔU^+_{2D} so that there is an apparent wake-strength excess,

$$\Delta U^+_{XS} = \Delta U^+ - \Delta U^+_{2D}. \tag{7.17}$$

In Figure 7.15(a), wake-strength excess is plotted as a function of the nondimensional momentum thickness, $8\theta_2/\mathcal{P}$. The $8/\mathcal{P}$ factor, which is used to nondimensionalise the momentum thickness, is equivalent to the effective radius of the duct, and $\theta_2 \approx \delta_{99}/10$ in a typical flat-plate boundary layer. A point plotted near the right-hand edge of Figure 7.15(a) therefore indicates a boundary layer occupying almost the entire cross-section of the duct. Data for $Re_x < 140{,}000$ are omitted from the graph in order to avoid showing the effects of disturbances produced by the boundary-layer trip. Repetition of exper-

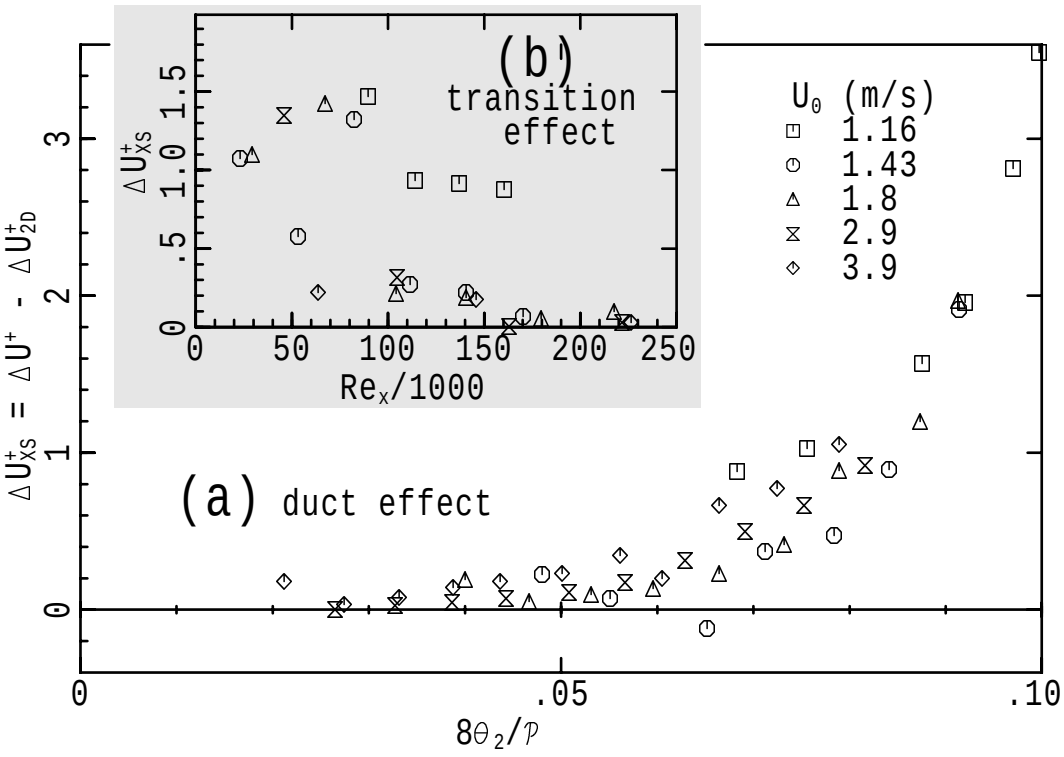

Figure 7.15: The effect of (a) duct radius and (b) transition on wake-strength excess; (a) ΔU^+_{XS}, as a function of nondimensional momentum thickness, $8\theta_2/\mathcal{P}$, with data for $Re_x < 140{,}000$ omitted; (b) ΔU^+_{XS}, as a function of Reynolds number, Re_x, with data for $8\theta_2/\mathcal{P} > 0.069$ omitted. $\mathcal{P}/8 \approx$ hydraulic radius,r'

imental procedures for $U_0 = 3.9$ m/s shows that the uncertainty in the measurements of wake strength, and hence the expected scatter in Figure 7.15(a), is in the order of ± 0.3. The collapse of data in Figure 7.15(a) is therefore sufficient to suggest that the wake strength excess, ΔU^+_{XS}, in the downstream half of the wind-tunnel test section is a function of $8\theta_2/\mathcal{P}$. A similar collapse of data is obtained when the ordinate is $\Delta U^+/\Delta U^+_{\mathrm{2D}}$. The nondimensional momentum thickness, $8\theta_2/\mathcal{P}$, serves as a measure of the lateral constriction of the boundary-layer wake region. It also indicates the proportion of the duct cross-section occupied by the boundary layer, and so may be replaced by δ_{99}/r'. The data in Figure 7.15(a) therefore support the hypothesis that lateral constriction of the wake region produces a wake-strength excess.

7.5.6 Shape factor

The shape factor $H_2 = \delta^*_2/\theta_2$ (Figure 7.16(a)) was calculated from the measurements of two-dimensional displacement thickness and momentum thickness. Where the boundary layer is thin in comparison with the effective duct radius (i.e. $\delta_{99}/r' \lesssim 0.5$), H_2 agrees closely with the measurements of Purtell et.

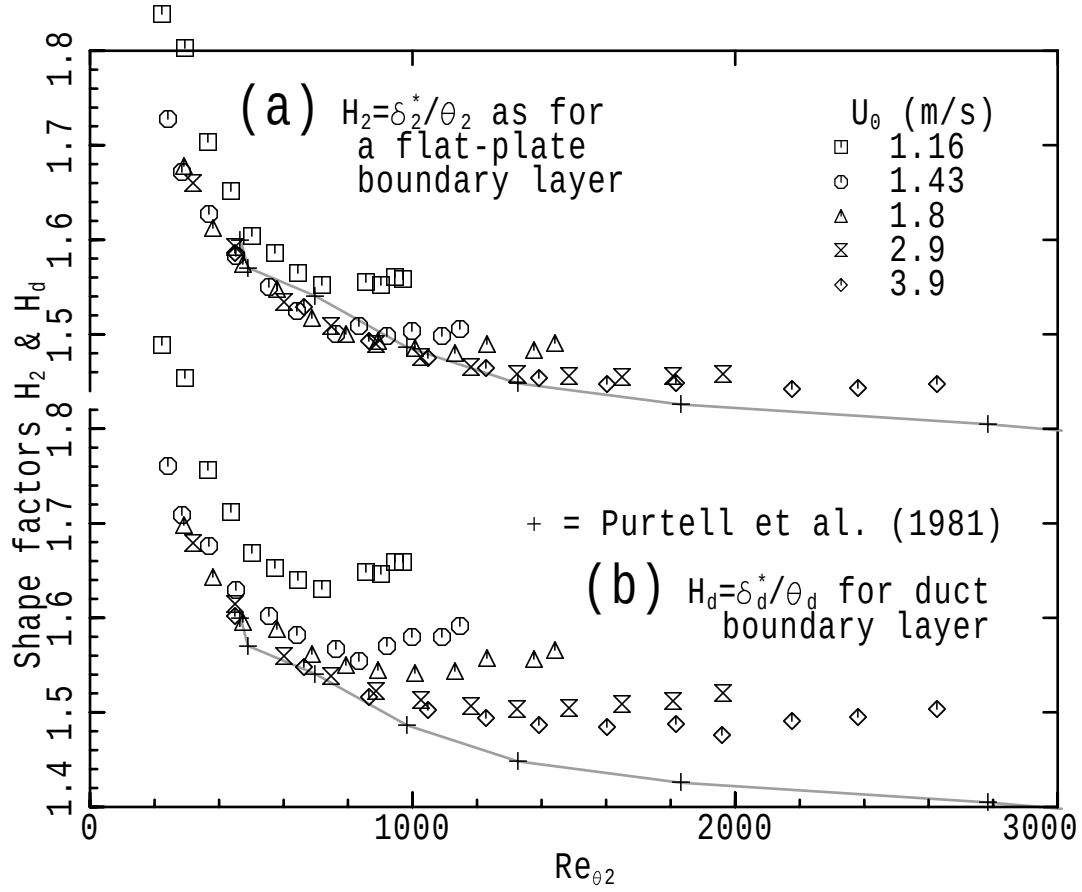

Figure 7.16: Shape factor for the test-section boundary layer; (a) $H_2 = \theta_2/\delta_2^*$ as for a flat-plate boundary layer; (b) $H_d = \theta_d/\delta_d^*$ for a duct boundary layer. The data are compared with the measurements of Purtell, Klebanoff and Buckley (1981) for a flat-plate boundary layer (+ symbols joined by straight line segments).

al. (1981) at all free stream speeds except 1.16 m/s and, as expected of a canonical flat-plate boundary layer, decreases with increasing Re_{θ_2}. Inspection of Equations 7.5 and 7.6 reveals that the wake region of the boundary layer makes a proportionately greater contribution to the momentum thickness than to the displacement thickness, and so any increase in wake-region velocity defect (or decrease in mean velocity) caused by lateral constriction of the wake increases the shape factor. The results in Figure 7.16(a) show that, where $\delta_{99}/r' \gtrsim 0.5$, this effect is sufficient to halt the conventional dependence of H_2 on Re_{θ_2}, finally causing H_2 to increase slightly with increasing distance from the boundary-layer origin. However, in comparison with the effect on wake strength, the effect of wake-region constriction on H_2 is very small.

The constricting effect of the side-wall boundary layers in the downstream half of the test section is accentuated when the shape factor is calculated from the duct displacement and momentum thicknesses

(δ_d^* and θ_d), as can be observed in Figure 7.16(b).

7.5.7 Outer region scaling of turbulence statistics

In the published literature on two-dimensional boundary layers, several different thickness parameters are used for the outer-region scaling of turbulence statistics. For example, Purtell et al. (1981) uses both displacement thickness, δ_2^*, and boundary layer thickness, δ_{99}, for nondimensionalising r.m.s. turbulence levels. For the measurements presented in this chapter there is some additional uncertainty in the selection of an outer region scaling parameter because the momentum balance and wake strength are significantly affected by the development of side-wall boundary layers in the test-section duct. In order to select the best scaling parameter, the flatness data for free stream speeds of 1.8 m/s and 3.9 m/s are plotted with a variety of scaling thicknesses. Boundary layers with a Reynolds number, Re_{θ_2}, between 288 and 2630 are represented in these graphs. The suitability of each scaling parameter is assessed on the basis of the convergence of the data to a single-valued function within the wake region of the boundary layer. The flatness factor is chosen for this trial because, of all the meaningful statistical quantities, it is the most sensitive to variations in experimental conditions and it has the steepest gradients in the wake region. From the results shown in Figure 7.17, the flat-plate momentum thickness θ_2 is clearly the best outer region scaling parameter. The poorest convergence of data, which is not shown in the figure, is obtained by scaling with the duct displacement thickness δ_d^*.

The momentum balance calculations (Section 7.5.2) demonstrate that the duct geometry is an important parameter in determining the growth rate of the test-section boundary layer. However, the success of θ_2 as a scaling parameter suggests that the wake-region eddy structure in the normal mid-plane, $z = 0$, is essentially the same as in a two-dimensional flat-plate boundary layer and that the turbulence mechanism is not changed by the presence of side-wall boundary layers. This result is also consistent with the discovery by Brundrett and Baines (1964) that, as shown in Figure 3.4(b), the dynamics of secondary flow are concentrated near the corners of the duct cross-section.

When flat-plate momentum thickness, θ_2, is used as a scaling parameter for the mean velocity distribution, acceptable convergence of the data is obtained over the region $y/\theta_2 > 2$ (Figure 7.18). The least satisfactory convergence occurs near the outer edge of the boundary layer at the downstream end of the test section because, with a boundary-layer thickness exceeding 83 mm, it was not possible to measure the free-stream velocity or momentum thickness accurately.

From Figure 7.19 it is clear that the flat-plate momentum thickness can be used for scaling the distributions of r.m.s. turbulence intensity, skewness and flatness in the wake region of the turbulent boundary layer. At $x = 0.54$m and $x = 0.86$m, where $Re_{\theta_2} < 400$, this form of scaling does not produce agreement with measurements made further downstream. For the lower free stream speed of 1.16 m/s the

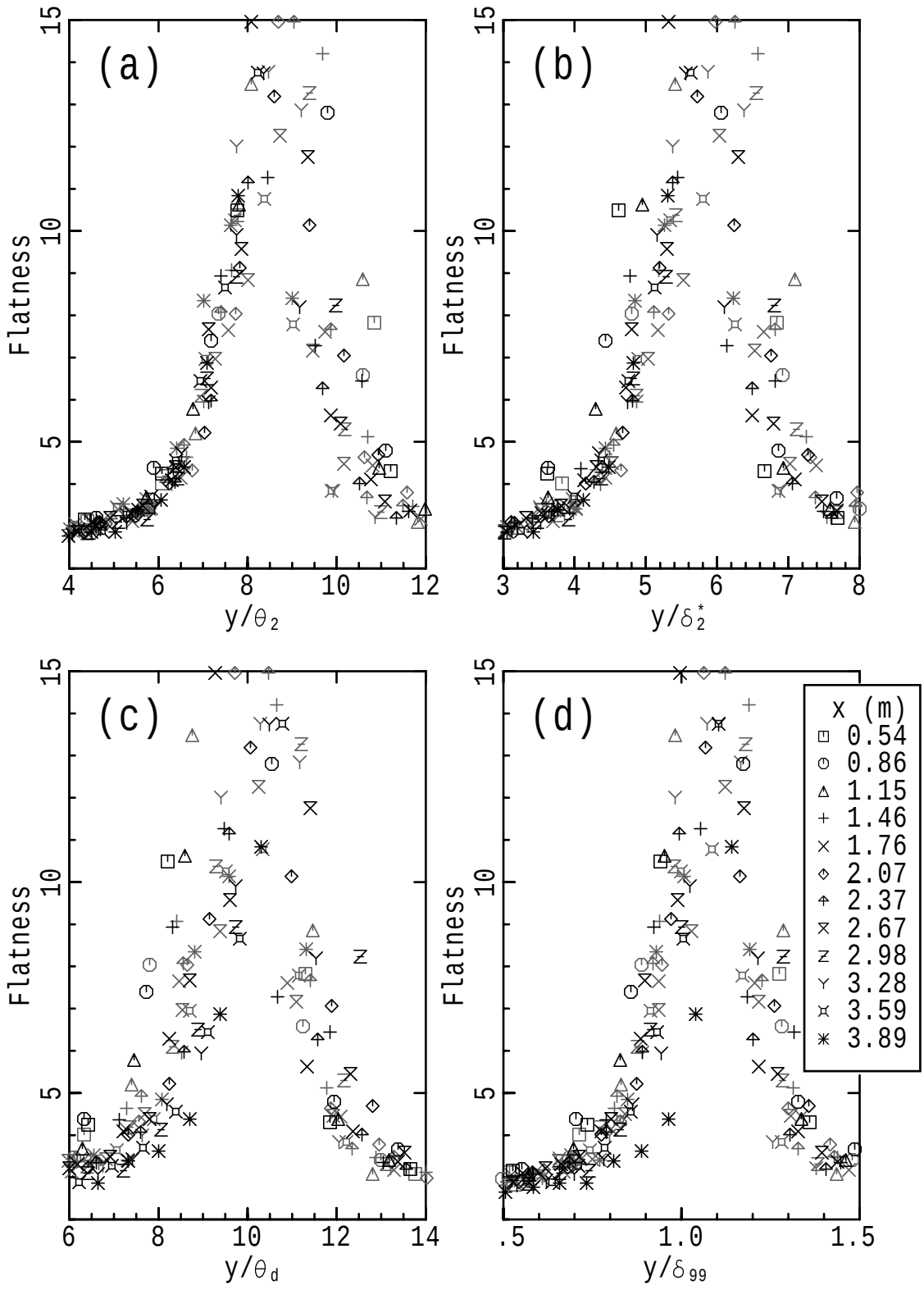

Figure 7.17: Selection of thickness parameter for scaling flatness in the outer region of the boundary layer; (a) flat-plate momentum thickness, θ_2; (b) flat-plate displacement thickness, δ_2; (c) duct momentum thickness, θ_d; (d) boundary-layer thickness, δ_{99}. The free stream speeds are $U_0 = 1.8$ m/s and $U_0 = 3.9$ m/s.

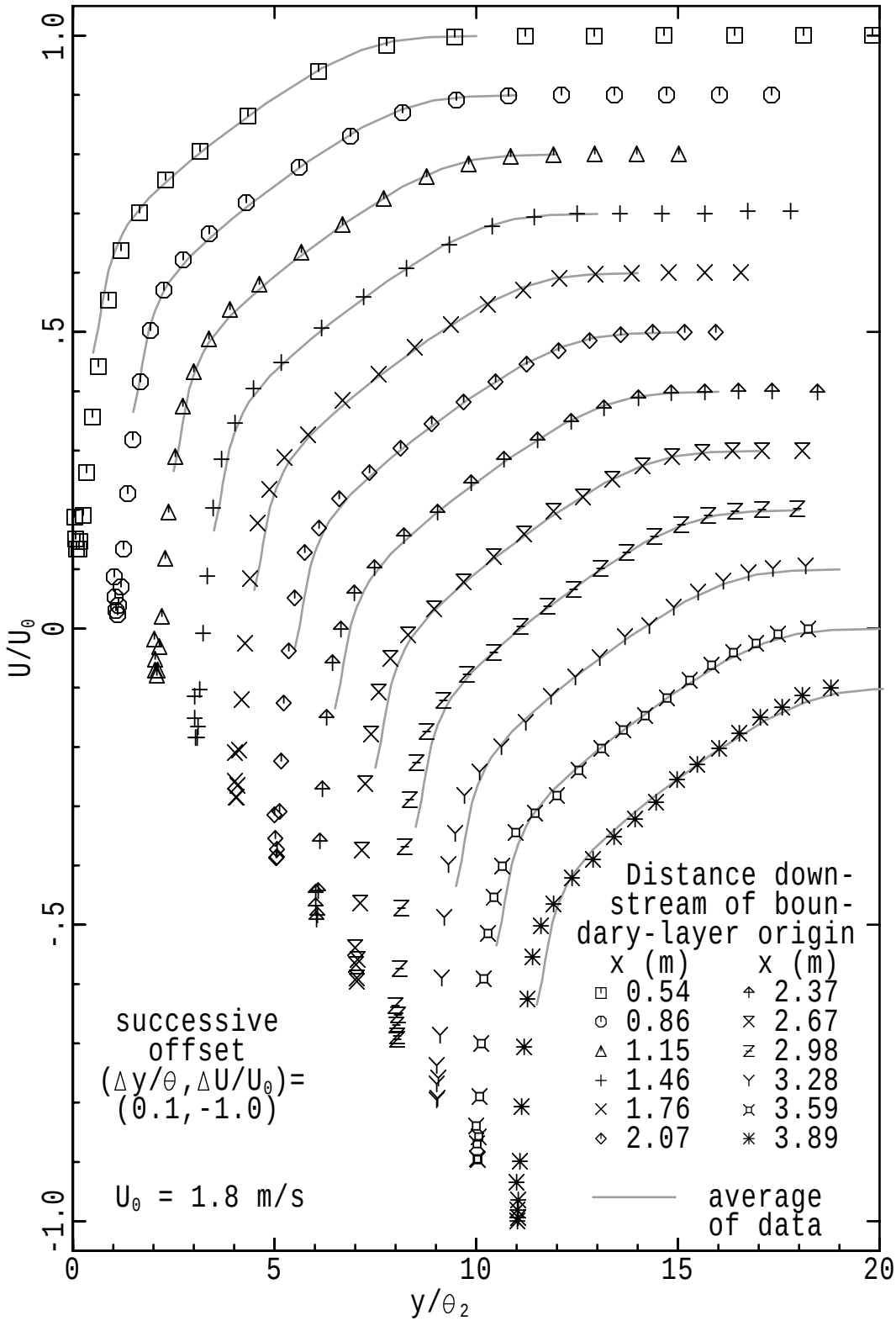

Figure 7.18: Outer region scaling of the mean velocity distribution for a free stream speed of 1.8 m/s. The scaling parameters are free stream speed U_0 and flat-plate momentum thickness θ_2. Data are successively offset by $(\Delta y/\theta_2, \Delta U/U_0) = (0.1, -1.0)$ as distance from the boundary-layer trip is increased from $x = 0.54$ m.

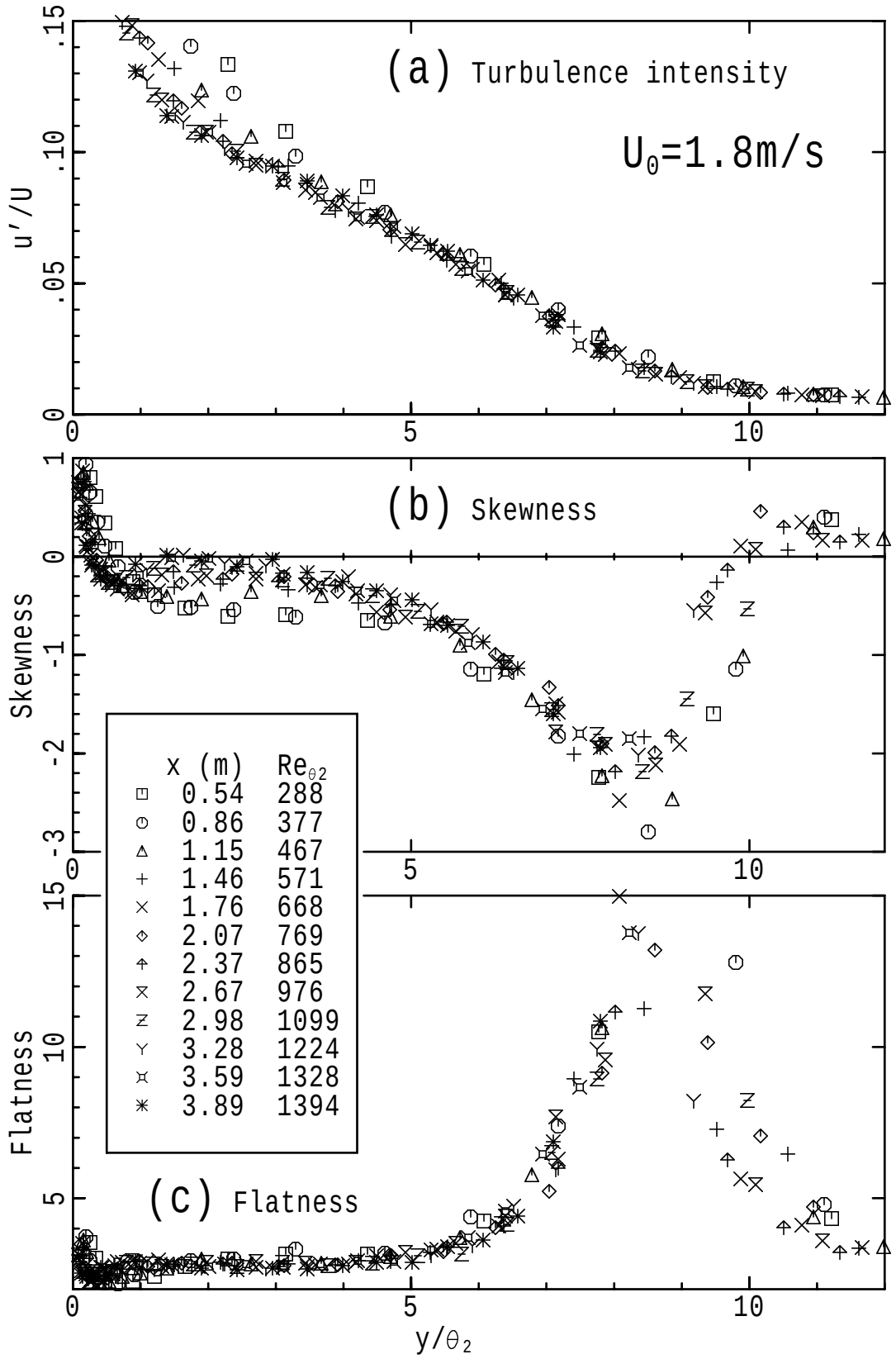

Figure 7.19: Outer region scaling of boundary-layer turbulence statistics for a free stream speed of 1.8 m/s; (a) turbulence intensity; (b) skewness; (c) flatness. Distance from the wall is scaled with flat-plate momentum thickness θ_2.

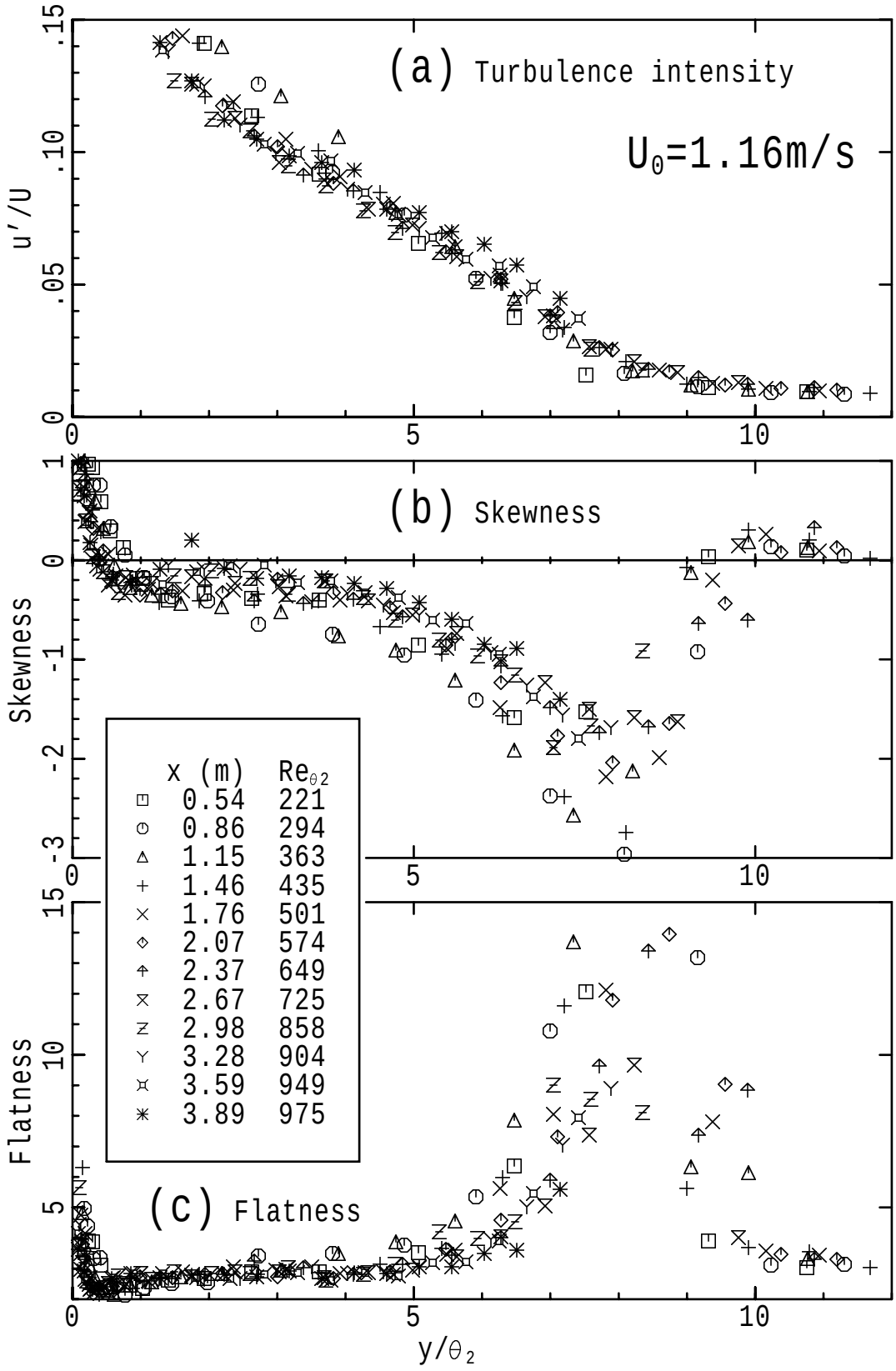

Figure 7.20: Outer region scaling of boundary-layer turbulence statistics for a free stream speed of 1.16 m/s; (a) turbulence intensity; (b) skewness; (c) flatness. Distance from the wall is scaled with flat-plate momentum thickness θ_2.

Reynolds number is generally about 24% lower than at 1.8 m/s and the lack of similarity is more obvious (Figure 7.20). The turbulence statistics for $U_0 = 1.8$ m/s and $U_0 = 1.16$ m/s also show that, except where a free stream potential flow may not exist at the downstream end of the test section ($U_0 = 1.16$ m/s), similarity based on θ_2 is well established for $Re_{\theta_2} > 400$.

7.5.8 Wall-region scaling of the mean velocity distribution

Mean velocity distributions for $U_0 = 1.8$ m/s, scaled with the wall parameters U_τ and ν, are shown in Figure 7.21. Optimal coefficients U_τ, C, δ^+ and Π for the theoretical model,

$$\begin{aligned} y^+ &= U_w^+ + e^{-\kappa C}\left[e^{\kappa U_w^+} - \sum_{n=0}^{4}\frac{1}{n!}(\kappa U_w^+)^n\right] \\ U_w^+ &= U^+ - \frac{2\Pi}{\kappa}\sin^2\left(\frac{\pi y}{2\delta_\pi}\right), \end{aligned} \tag{7.18}$$

have been determined for each of the measured mean-velocity distributions. This model is obtained by combining Spalding's (1961) equation for the law of the wall (Equation 7.14) with Coles's (1968) wake function (Equation 7.1). The results of the curve fitting, which are drawn as solid lines in Figure 7.21, indicate that there is usually very close agreement between the experimental data and the model (Equation 7.18) everywhere except $y^+ < 2.5$. In particular, the agreement within the buffer region ($7 < y^+ < 30$) is much better than that obtained with Squire's (1948) law of the wall, and the values calculated for the friction velocity are consequently more reliable. Over all the mean-velocity data (1.16 m/s $\leq U_0 \leq$ 3.9 m/s), the r.m.s. difference between Equation 7.18 and the data is $0.14U_\tau$ or 0.6% of the free stream speed.

In Figure 7.22, the additive coefficient C for the Spalding-Coles model of the mean-velocity distribution is plotted as a function of Reynolds number Re_{θ_2}. The general trend of the data, which is towards lower values of C with increasing Reynolds number, is perhaps best described by the least-squares linear-regression curve

$$C' = 9.0 - 1.08\log_{10} Re_{\theta_2}. \tag{7.19}$$

Scatter in the values of C effectively prevents any meaningful attempt either to fit a higher-order polynomial to the $(\log_{10} Re_{\theta_2}, C)$ coordinate data, or to use an ordinate transformation which produces a limiting value of $C = 5.00$ at infinite Reynolds number. The curve representing Equation 7.19 in Figure 7.22 has a value of $C' = 5.00$ at $Re_{\theta_2} = 5000$.

The effect of wall proximity on the hot-wire anemometer used in the measurements is clearly visible in the viscous sublayer as a departure from the linear mean velocity distribution $U^+ = y^+$. Data contaminated by wall-proximity effect were not used for the calculation of displacement or momentum thickness, even though it has been established that the effect of wall proximity on these calculations

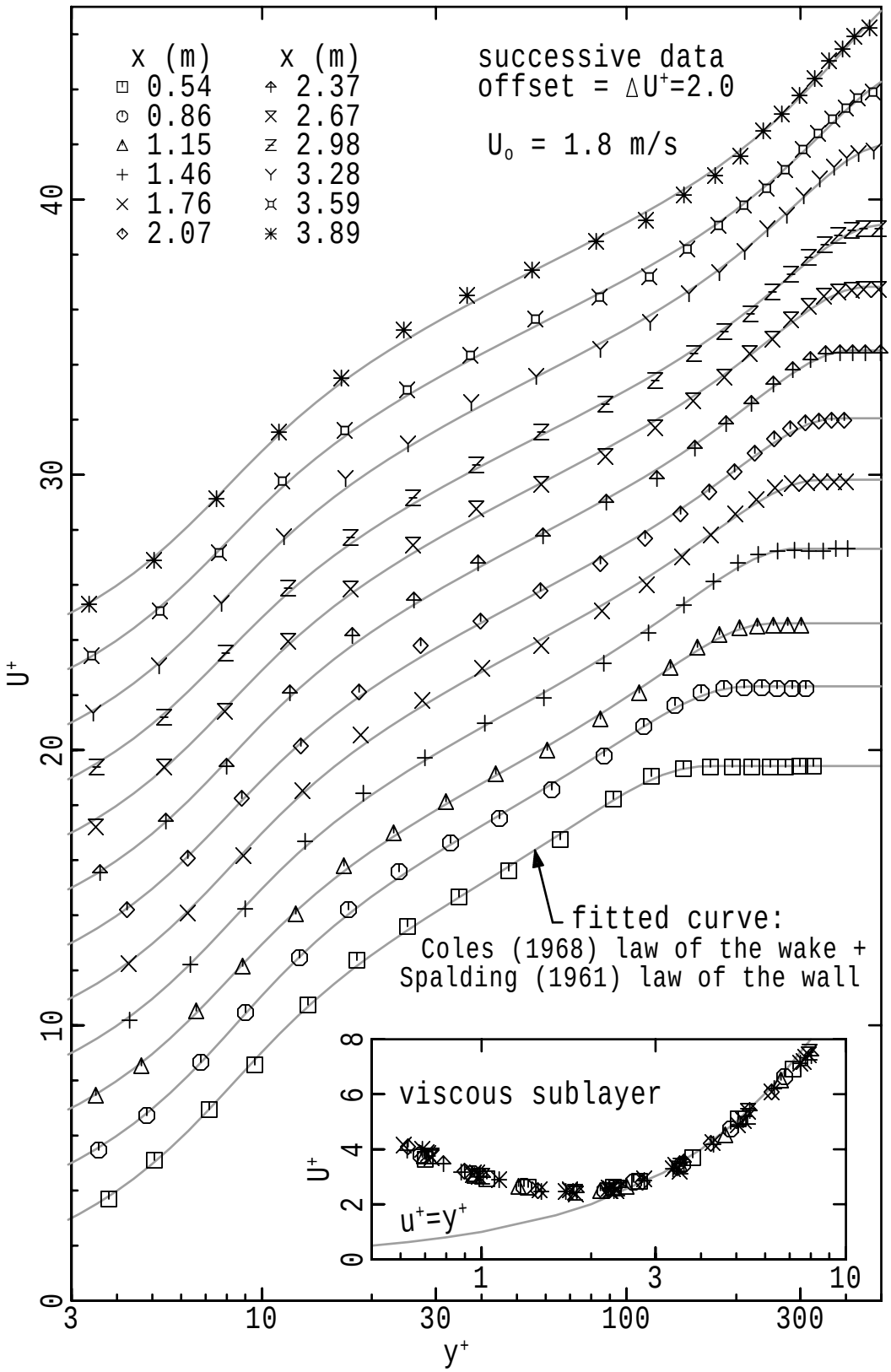

Figure 7.21: Wall-region scaling of the mean velocity distribution for a free stream speed of 1.8 m/s. Data are successively offset by $\Delta U^+ = 2$ with increasing distance from the boundary-layer trip. U_τ is calculated from the Spalding-Coles model of the mean velocity distribution.

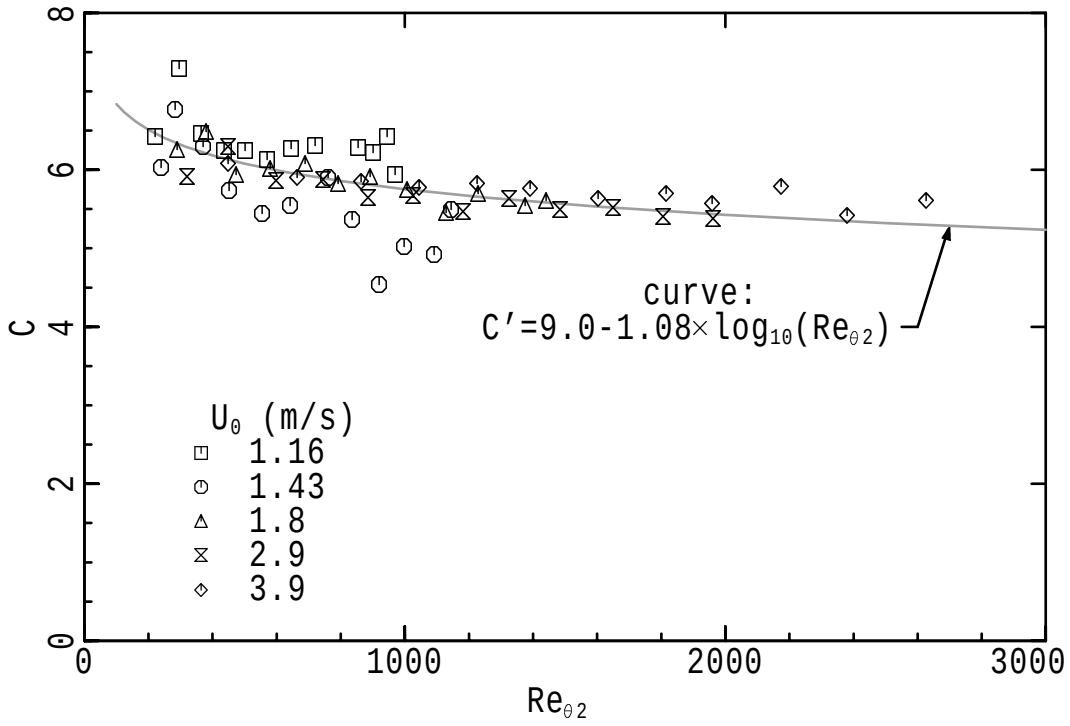

Figure 7.22: Additive coefficient C for the Spalding-Coles model of the mean-velocity distribution. The solid line $C' = 9.0 - 1.08\log_{10} Re_{\theta_2}$ is a least squares fit to the $(\log_{10} Re_{\theta_2}, C)$ data.

was only about 0.5%.

7.5.9 Wall-region similarity of turbulence statistics

The overall shape of the r.m.s. fluctuating velocity distribution, shown in Figures 7.23(a) and 7.24(a), and its dependence on Reynolds number in the logarithmic region are typical of low-Reynolds-number flat-plate turbulent boundary layers [Purtell et al., 1981, Wei and Willmarth, 1989, Antonia et al., 1992]. Close inspection of these results reveals no visible dependence on Reynolds number in the region between the wall and the location of maximum turbulence level at $y^+ \approx 13$ if the Reynolds number, Re_{θ_2}, is higher than 400. For $Re_{\theta_2} \lesssim 400$, the turbulence levels in this region are slightly lower than at higher Reynolds numbers. Examination of r.m.s. turbulence distributions for other free stream speeds (Appendix I) also shows that the region of similarity does not extend any further from the wall than $y^+ \approx 13$ as the Reynolds number Re_{θ_2} increases beyond 400.

Comparison of Figures 7.19 and 7.23 shows that the scatter of skewness and flatness measurements in the sublayer region $y^+ < 3$ is considerably larger than the scatter of approximately equal skewness and flatness values in the wake region of the boundary layer. The uncertainty of the measurements is

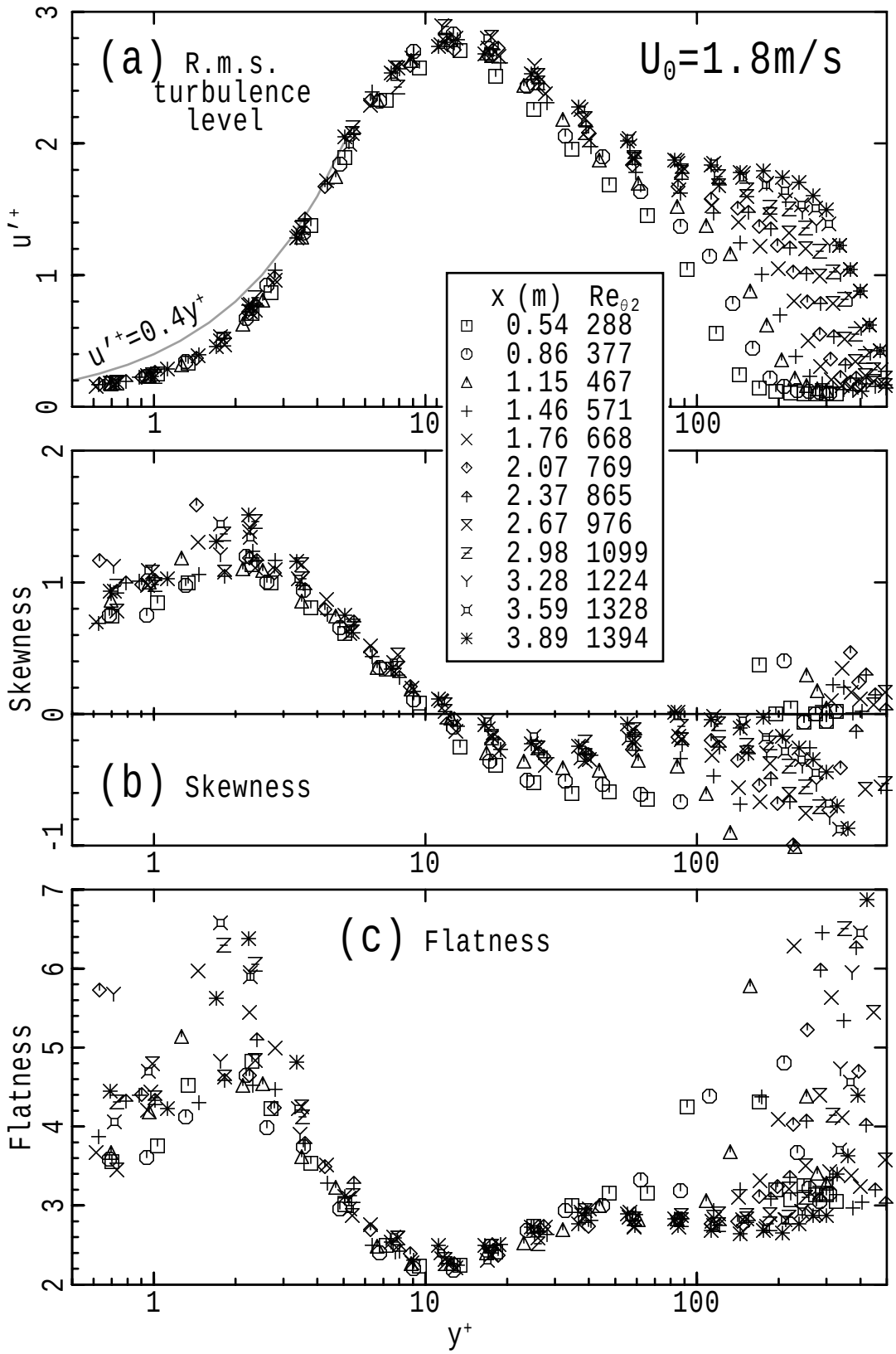

Figure 7.23: Wall-region scaling of boundary-layer turbulence statistics for a free stream speed of 1.8 m/s; (a) r.m.s. turbulence level; (b) skewness; (c) flatness. U_τ is calculated from the Spalding-Coles model of the mean velocity distribution.

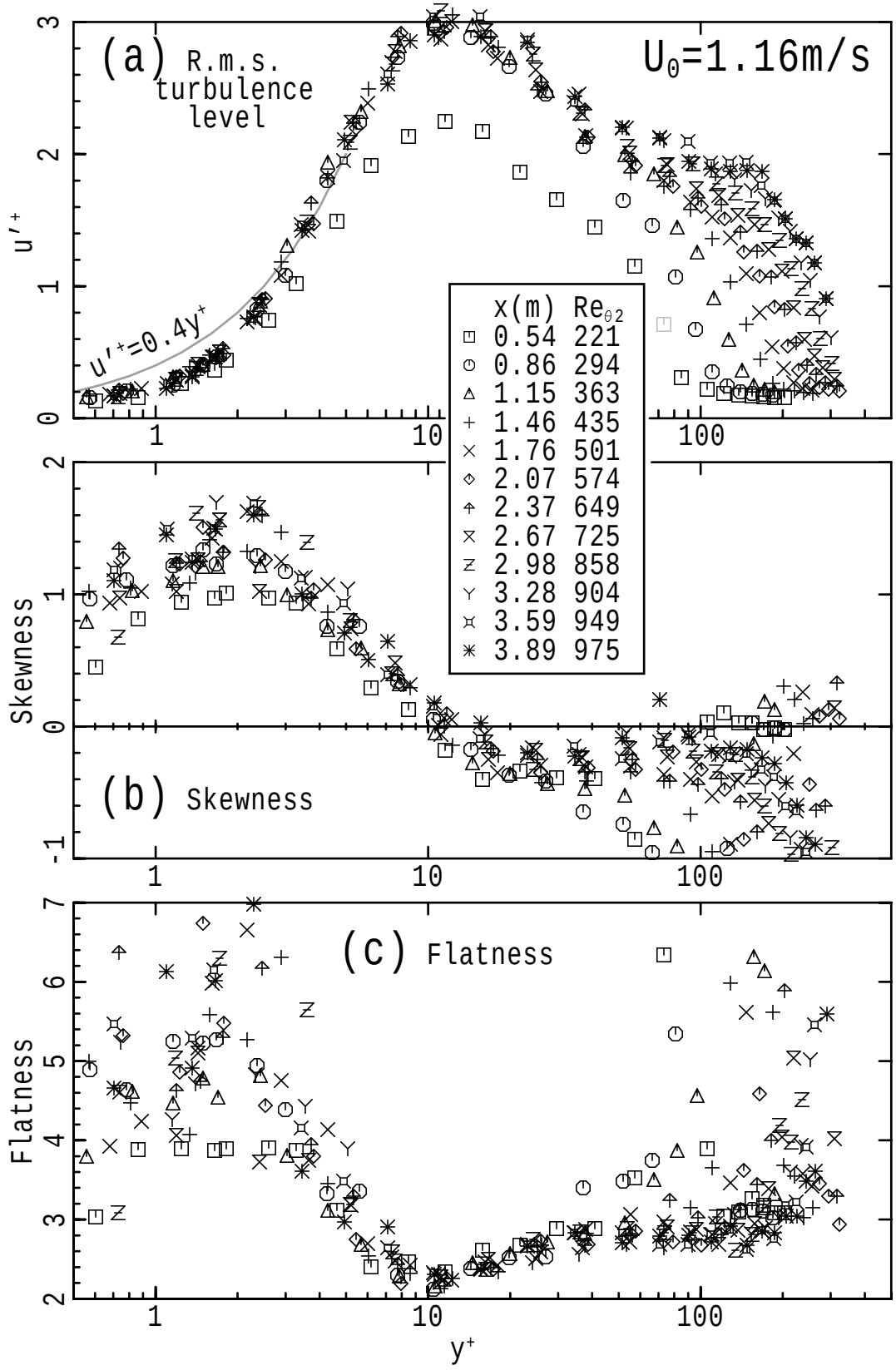

Figure 7.24: Wall-region scaling of boundary-layer turbulence statistics for a free stream speed of 1.16 m/s; (a) r.m.s. turbulence level; (b) skewness; (c) flatness. U_τ is calculated from the Spalding-Coles model of the mean velocity distribution.

larger in the viscous sublayer because, with the much lower mean velocities, the frequency of events contributing significantly to skewness and flatness is approximately an order of magnitude lower than in the wake region. This explanation is supported by a significant decrease in the observed scatter as free stream speed is increased and also by the results shown in Figures 3.9 and 3.10 where the duration of data sampling is four times longer. The primary requirement of the experiment, which is to measure mean velocity at a large number of x and y locations within a reasonable length of time, therefore tends to be incompatible with the secondary requirement for measurements of sublayer skewness and flatness.

From the results for $Re_{\theta_2} \gtrsim 400$ in Figures 7.23, 7.24 and Appendix I, skewness and flatness appear to be independent of Reynolds number in the region $4 < y^+ < 13$. Dimensional reasoning suggests that the region of similarity should extend to the wall, but the scatter of the measurements is too large for this to be confirmed by direct observation. At Reynolds numbers lower than about 400, skewness and flatness in the region $y^+ < 13$ are slightly smaller than at higher Reynolds numbers. This effect is most noticeable for $y^+ < 3$ where skewness and flatness are much more sensitive to variations in turbulence structure than elsewhere in the near-wall region. Flatness values show no detectable dependence on Reynolds number in the buffer and log-law regions of the boundary layer.

Both Wei and Willmarth (1989) and Antonia et al. (1992) have demonstrated that turbulence statistics scaled on near-wall parameters depend on Reynolds number in the region between $y^+ = 15$ and the wake region of a turbulent channel flow. In addition, from direct numerical simulations of turbulent channel flow at two different Reynolds numbers ($Re_{\theta_2} \approx 350$ and $Re_{\theta_2} \approx 800$), Antonia and Kim (1992) observed a change in the wall values of many statistical turbulence quantities, including those which were normalised using the wall parameters U_τ, ν and y^+ (e.g. u'^+/y^+, $\omega_z'^+$).

The measurements of turbulence statistics presented in this chapter are consistent with the findings of Wei and Willmarth (1989) and Antonia et al. (1992). Within the viscous sublayer, Reynolds number dependence like that observed by Antonia and Kim (1992), is apparent only at the upstream end of the test section ($x = 0.54$) where $Re_{\theta_2} \lesssim 400$. This failure of similarity based on wall variables at $Re_{\theta_2} \lesssim 400$ indicates that a significant proportion of near-wall turbulence events extend through the full thickness of the boundary layer and interact strongly with the free-stream flow. Similarly, the failure of wake-region scaling based on flat-plate momentum thickness θ_2, which also occurs at $Re_{\theta_2} \lesssim 400$, implies that large-scale turbulence motions are directly influenced by the presence of the wall.

7.5.10 An interpretation of some features of skewness and flatness distributions

7.5.10.1 Wake region of the boundary layer

In the wake region, large-scale turbulence eddies interact with and entrain higher speed fluid from the free stream [Bradshaw, 1971] so that, with measurements approaching the outer edge of the boundary layer, the increasing predominance of the free stream in an intermittently turbulent flow is responsible for increasing flatness and decreasing skewness of the streamwise velocity signal. The maximum amplitudes of skewness and flatness measured at the outer edge of the boundary layer are determined by the duration of data sampling and by uncontrolled secondary flows such as buoyant rotation rather than by the structure of wake-region turbulence.

7.5.10.2 Positive skewness near the outer edge of the boundary layer

The positive skewness just beyond the edge of the boundary layer ($10 < y/\theta_2 < 12$) (Figure 7.19(b)), is believed to be a residual effect of flow acceleration around the "roughness" elements in the boundary-layer trip. The turbulence level in this region is no more than 50% higher than in the free stream, and, in the velocity signal $\tilde{u}(t)$, the fluctuations responsible for the positive skewness are not visually distinguishable from free stream turbulence. Comparison of data in Figure 7.19(b) with corresponding data points in Figure 7.19(c) shows that the velocity fluctuations causing positive skewness also elevate the flatness.

7.5.10.3 Maxima in the viscous sublayer

In the region $10 < y^+ < 15$, zero skewness and a flatness minimum of about 2.3 coincide approximately with the maximum turbulence level. As the measuring position is moved closer to the wall, the effect of increasingly intermittent "sweep" events ($u > 0$, $v < 0$) is to elevate both skewness and flatness. The maxima at $y^+ \approx 2$ are artifacts of wall-proximity effect on the hot-wire probe. Results in Figures 10.11 and 10.12 show that, when wall-proximity error is removed from the hot-wire signal, both skewness and flatness are significantly decreased in the region $1 < y^+ < 3$ and the maximum values then occur at the wall.

7.5.10.4 Zero-skewness between $y^+ = 100$ and the wake region

As the measuring position is moved further from the wall, beyond $y^+ \approx 12$, eruptive spires observed as "ejection" events ($u < 0$, $v > 0$) contribute negatively to the skewness of the velocity signal. This

effect persists to $y^+ \approx 100$ which, for $Re_{\theta_2} = 1400$, is at start of the wake region. At the junction of the log-region and the wake region[3], the skewness of the streamwise velocity in a boundary layer with $Re_{\theta_2} \gtrsim 1400$ is effectively zero. This marks a region where direct turbulence interactions with near-wall eruptions (Section 1.2.5) and with irrotational fluid from the free stream are very weak. For lower Reynolds numbers, the region influenced by near-wall eruptions overlaps with the wake region, where interaction between turbulent and irrotational (free stream) fluid also produces negative skewness. In these circumstances, some vortices formed by roll-up of near-wall eruptions would be able to entrain fluid from the free stream without undergoing further evolution by processes such as vortex stretching or self-induced motion (Section 1.2.3). At higher Reynolds numbers, the existence of a zero-skewness region between $y^+ = 100$ and the wake region suggests that vortices produced by near-wall eruptions interact with irrotational fluid only after they have evolved to a location further from the wall.

7.6 Summary and conclusions

7.6.1 Introduction: test-section flow environment

Evidence presented in Chapters 4, 5 and 6 shows that buoyant flow rotation and various types of separation within the inlet section of an open-circuit wind tunnel can produce unsteadiness in the characteristics of the test-section boundary layers. These phenomena are especially troublesome at the very low test-section flow speeds ($U_0 \leq 4$ m/s) required for the investigation of near-wall turbulence with conventionally-sized hot-wire probes. The measurements of boundary-layer thickness and the final flow visualisation studies described in Chapter 6 show that the flow defects can be successfully eliminated by making a series of modifications to the inlet section of the wind tunnel. Finally, to meet the requirement that the turbulent wall layers conform as closely as possible with the ideal of the canonical turbulent boundary layer, it was necessary to induce an acceptable form of boundary-layer transition near the start of the test section and then to remove or minimise the streamwise pressure variation within the test section.

Acceptable transition is induced by a boundary-layer trip consisting of a single spanwise row of balls located 16 mm downstream from the start of the test-section. This type of trip produces satisfactory boundary-layer turbulence at a flow speed 10% to 20% higher than the transition speed U_t given by the empirical formula

$$Re_d = \frac{U_t d}{\nu} = 423 \left(\frac{x_t}{d} \right)^{0.15}. \tag{7.20}$$

The transition mechanism may be similar to that which generates eruption spires in the wake of a cylinder-wall junction [Smith et al., 1991a].

[3] e.g. $y^+ \approx 100$ in Figure 7.23

After the selection of suitable boundary-layer trips, it was possible to adjust the flexible lower surface of the test-section so that, for all flow speeds between 1 m/s and 4 m/s, the static pressure nonuniformity along the length of the test section is less than 4% of the initial free stream dynamic pressure. Experimental evidence (Figures 7.7 and 7.8) suggests that the dominant causes of the remaining nonuniformity are the flow-speed dependence of boundary-layer growth rate and the flow-speed dependence of streamline curvature near the suction manifold.

Tests were then performed to determine the regions of test-section turbulent boundary-layer which were free of contamination by secondary lows and could be regarded as representing the ideal canonical turbulent boundary layer.

7.6.2 Momentum balance of the test-section boundary layer

The streamwise component of velocity was measured across the thickness of the turbulent boundary layer and along the length of the test section for five flow speeds between 1 m/s and 4 m/s. The momentum balances and boundary-layer thicknesses calculated from these data show that, for a flow speed of 1.8 m/s or more, the effects of residual flow irregularities in and upstream of the wind-tunnel contraction are too small to be detected. Even at lower speeds, these effects are at least an order of magnitude smaller than observed prior to inlet-flow mixing and prior to the installation of screens in the wind-tunnel contraction.

The results presented in Section 7.5.2 validate both the momentum-integral equation for a duct flow (Equation 7.9) and the momentum-balance of the boundary-layer developed in the test section. For the particular example studied in this chapter, where the duct cross-section is nearly square, cross-sectional contours of mean velocity are assumed to be concentric rectangles and the centreline friction coefficient, C_f, is used in place of the perimeter-averaged friction coefficient, $\overline{C_f}$. Over the length of the test-section duct ($L/r' \approx 36$), the errors resulting from these assumptions are generally in the order of 2% of the final momentum thickness.

Momentum-balance calculations which assume a two-dimensional flat-plate boundary layer do not produce correct results when the boundary-layer thickness is more than about 10% of the duct height.

7.6.3 Characteristics of the test-section mid-plane boundary layer

Evaluation of skin-friction coefficient C_f, wake strength ΔU^+ and shape factor H_2 is considered to be a necessary part of assessing whether the test-section boundary layer is useful as a representative of canonical wall turbulence, in which case the variables would be essentially functions of the two-dimensional Reynolds number Re_{θ_2}. With the possible exception of results obtained for the lowest

flow speed, the C_f, ΔU^+ and H_2 characteristics agree sufficiently well with the published research data for two-dimensional turbulent boundary layers [Coles, 1962, Purtell et al., 1981, Murlis et al., 1982] to indicate that the dominant mechanisms in the mid-plane boundary layers are those of canonical boundary-layer turbulence. In the downstream half of the test section, where the boundary-layer thickness, δ_{99}, exceeds approximately half of the effective duct radius, ΔU^+ and H_2 display the effects of a wake-region constricted by the side-wall boundary layers. Boundary-layer characteristics measured at the lowest flow speed ($U_0 = 1.16$ m/s) are also affected by flow disturbances from the boundary-layer trip. In comparison with higher flow speeds ($U_0 > 1.16$ m/s), the abnormally high wake strength, large shape factor and low skin friction in the upstream half of the test section indicate a deficit of momentum in the near-wall region which may be caused by an incorrectly sized or incorrectly proportioned boundary-layer trip.

Measurements of spanwise variation in wall shear stress, referred to in Section 3.2.3, indicate that, compared with a flat-plate boundary layer, stress-induced secondary flow reduces C_f by an amount increasing from zero to about 5% over the downstream half of the test section. Skin-friction coefficients are calculated from experimental data using two different methods. In the first method, Coles's (1968) equation for the law of the wall (with $\kappa = 0.41$, $C = 5.0$) produces C_f values which are between 5% and 10% lower than those given by the Coles (1962) "best fit" curve and agree more closely with the data of Murlis et al. (1982). In the second method, Spalding's (1961) law-of-the-wall function is combined with the Coles (1968) wake function, and the coefficient C is adjusted to optimise agreement between the experimental data and the mean-velocity model. Skin-friction coefficients obtained in this way are, on average, 5.7% lower than those calculated using the Coles's (1968) function for the law of the wall.

At the low Reynolds number of these experiments, the values of the law-of-the-wall coefficient C are generally higher than the conventional $C = 5.0$. When the values of C are plotted as a function of Reynolds number, their behaviour is best described by the least-squares linear-regression relationship,

$$C' = 9.0 - 1.08 \log_{10} Re_{\theta_2}, \tag{7.21}$$

which has a value of $C' = 5.00$ at $Re_{\theta_2} = 5000$.

At all flow speeds except the lowest, the shape factor H_2 of the boundary layer agrees very closely with the measurements of Purtell et al. (1981) when $\delta_{99}/r' \lesssim 0.5$. In the downstream half of the test section where $\delta_{99}/r' \gtrsim 0.5$, lateral constriction of the wake region produces values of H_2 slightly higher than expected for a two-dimensional flat-plate boundary layer.

Measurements presented in Section 7.5.5 reinforce the findings of Coles (1962) that, during the initial development of a turbulent boundary-layer ($Re_{\theta_2} \lesssim 600$), wake strength ΔU^+ is extremely sensitive to the presence of a boundary-layer trip. At higher Reynolds numbers, ΔU^+ is a function of Re_{θ_2}

if the boundary-layer thickness is small in comparison with the effective radius of the duct (i.e. if $\delta_{99}/r' \lesssim 0.5$). As the boundary layer develops further and becomes very thick ($\delta_{99}/r' \gtrsim 0.5$), its wake region is squeezed laterally by side-wall boundary layers and ΔU^+ becomes larger than the value, ΔU^+_{2D}, expected for a flat-plate boundary layer. Experimental evidence (Figure 7.15(a)) suggests the increase or excess in wake strength, ΔU^+_{XS}, is primarily a function of $8\theta_2/\mathcal{P}$ or equivalently δ_{99}/r', so that

$$\Delta U^+ = \Delta U^+_{2D}(Re_{\theta_2}) + \Delta U^+_{XS}\left(\frac{\delta_{99}}{r'}\right). \tag{7.22}$$

7.6.4 Outer and inner region scaling

Of all the parameters[4] examined in this study, the best outer region scaling parameter for distance from the wall is the two-dimensional momentum thickness θ_2. Except for the measurements in boundary layers with $Re_{\theta_2} < 400$ or with momentum thicknesses too large to measure accurately, scaling with θ_2 leads to a similarity of mean velocity, r.m.s., skewness and flatness distributions throughout the wake region of the boundary layer. The success of θ_2 as a wake-region scaling parameter is further evidence that the wake-region eddy structure of the mid-plane boundary layers is the same as in a two-dimensional flat-plate boundary layer.

As observed in several other investigations [Purtell et al., 1981, Wei and Willmarth, 1989], [Antonia et al., 1992], the apparent wall-region similarity of mean velocity distributions scaled on wall variables does not extend to measurements of turbulence statistics. When scaled on wall variables, r.m.s. velocity distributions are dependent on Reynolds number for all values of y^+ greater than 13. Between the turbulence peak at $y^+ = 13$ and the wake region, the skewness depends on Reynolds number only when $Re_{\theta_2} \lesssim 1400$. Flatness shows no detectable dependence on Reynolds number in the buffer and logarithmic regions of the boundary layer.

In boundary layers with $Re_{\theta_2} \gtrsim 400$, no Reynolds number dependence was observed in the r.m.s., skewness or flatness of streamwise velocity fluctuations between the wall and $y^+ = 13$. However, because scatter of skewness and flatness measurements within the inner part of the viscous sublayer ($y^+ < 4$) was rather large, the existence in this region of similarity based on wall variables was inferred from observed similarity in the outer part of the sublayer ($4 < y^+ < 7$) where measurements were much more accurate. In cases where $Re_{\theta_2} \lesssim 400$, the lack of both wall-region similarity and outer-region similarity indicates that the boundary-layer turbulence is not yet developed to the stage where there are distinct near-wall and wake regions. Under these conditions, the behaviour of turbulence throughout the boundary layer depends simultaneously on both wall variables ($U_\tau, \nu/U_\tau$) and on outer region variables (U_0, θ_2).

[4] δ_{99}, θ_2, θ_d, δ_2 and δ_d

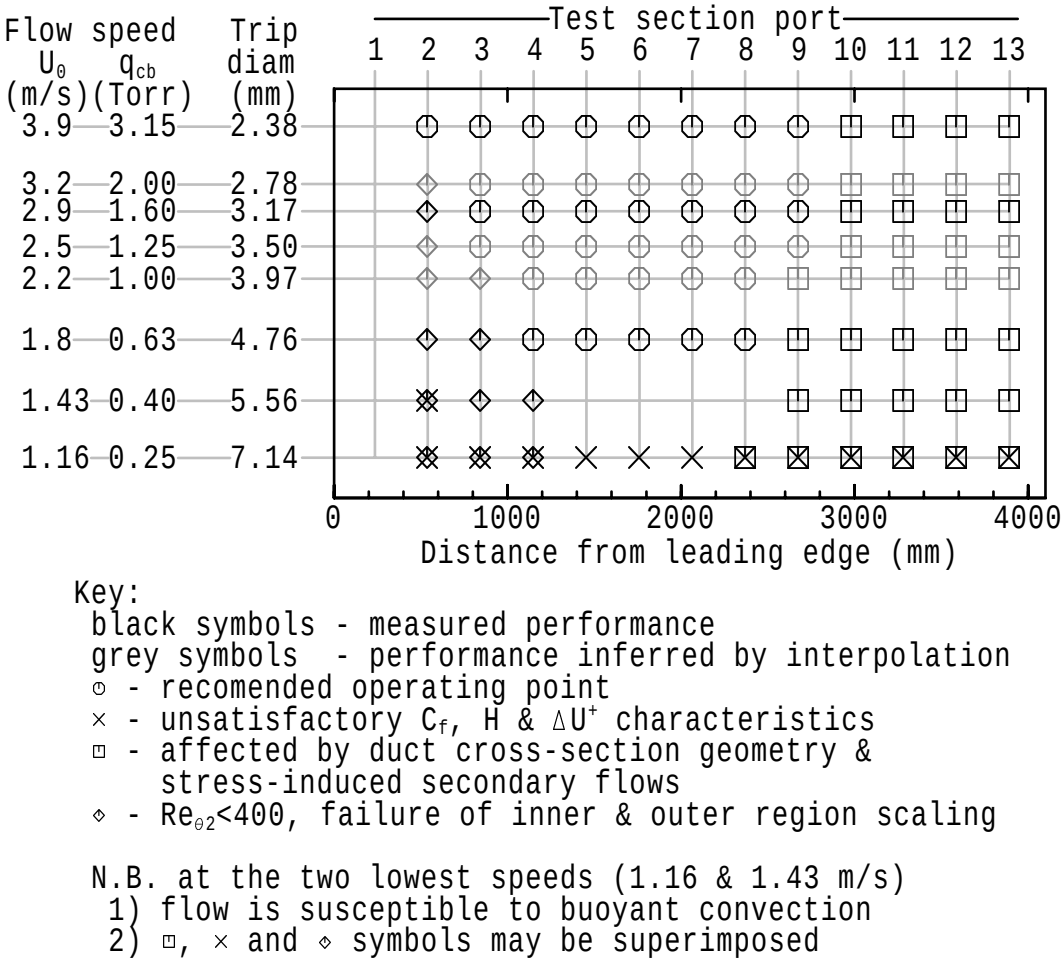

Figure 7.25: Summary of mid-plane boundary-layer behaviour; showing free stream speeds (vertical axis) and locations (horizontal axis) most suitable for investigating canonical wall turbulence. Plotting symbols are used to indicate the varying condition of the turbulent boundary layer. q_{cb} is the centreline dynamic pressure in the pipe flow upstream of the sonic choke centrebody.

7.6.5 Evaluation of the test-section boundary layer

For a free-stream speed of 1.8 m/s or more, measurements of boundary-layer thickness and momentum balance in the test section of the wind tunnel have demonstrated an absence of contamination by buoyant cross-flows or by separation in the contraction. At lower speeds these effects were an order of magnitude smaller than observed when no action was taken to eliminate them. Measurements of boundary-layer characteristics and a demonstration of wake-region similarity have shown that, in the logarithmic and wake regions, the turbulence mechanisms were those of the canonical turbulent boundary layer.

The conclusion is that, subject to some limitations, the boundary layer developed along the mid-plane

of a duct is a suitable representative of a two-dimensional canonical boundary layer with an essentially unaltered wall-turbulence mechanism. The selection of free stream speeds and distance downstream from the boundary-layer origin is constrained by the need to avoid

(1) the residual susceptibility, in conventional low-turbulence wind tunnels, to the effects of buoyant convection at very low free stream speeds (lower than 1.5 m/s in the present investigation),

(2) Reynolds numbers (Re_{θ_2}) lower than 400 where, due to inadequately developed turbulence, distinct near-wall and wake regions of the boundary layer do not exist,

(3) the effects of duct cross-section geometry in which the spanwise width of the wake region is significantly reduced by the development of thick side-wall boundary layers and stress-induced secondary flows reduce shear stress at the wall centrelines.

In this particular study, the optimum boundary-layer flow is obtained where, at free stream speeds between 1.8 m/s and 3.9 m/s, the boundary-layer thickness is less than half the effective duct radius and the Reynolds number (Re_{θ_2}) is higher than 400 (Figure 7.25).

7.7 Notation

A	cross-section area of the test-section duct
C	constant or offset parameter for the logarithmic mean velocity distribution near the wall: $U^+ = \kappa^{-1} \ln y^+ + C$
C'	value of C determined from a line-of-best-fit to the experimental data
C_f	local skin-friction coefficient
$\overline{C_f}$	skin-friction coefficient averaged around the cross-section perimeter of the test-section duct
ΔC_p	$\Delta P / \frac{1}{2}\rho U_0^2$, coefficient of static wall pressure distribution
d	diameter of trip balls
H_2	δ_2^*/θ_2, shape factor for flat-plate two-dimensional boundary layer
H_d	δ_d^*/θ_d, shape factor for the boundary layer in a duct
L	useful length of test-section duct
P	static wall pressure
$\mathcal{P}$	perimeter of the cross-section of the test-section duct
q_{cb}	centreline dynamic pressure in the pipe flow upstream of the sonic choke centrebody
r'	effective radius of a duct. In a square duct, this is the hydraulic radius, $2A/\mathcal{P}$, or half the duct height.
Re_d	$U_0 d/\nu$, Reynolds number of the boundary-layer trip
Re_θ, Re_{θ_2}	$U_0\theta_2/\nu$, Reynolds number of a two-dimensional flat-plate boundary layer — based on momentum thickness θ_2.

U	streamwise (i.e. x) component of mean fluid velocity
U_0	speed of the main free stream flow (outside the boundary layer)
$\langle U_0 \rangle$	free stream speed averaged over the length of the test section
U_τ	friction velocity of the boundary layer; defined by wall shear stress $\tau_w = \rho U_\tau^2$
U_t	free stream speed at which a boundary-layer trip produces transition
$\tilde{u}(t)$	velocity signal recorded as a function of time
u, v	velocity fluctuation in x and y directions
u'	r.m.s. of the streamwise velocity fluctuations
$w(y/\delta_\pi)$	the Coles wake function (Equation 7.1)
x	distance downstream from the origin of the test-section boundary layer
x_t	distance from the porous surface of the suction manifold to the boundary-layer trip
x_0, x_1	these locations are limits of integration along the length of the test section
y	distance from the wall
y_0^+	$C - \kappa^{-1} \ln \kappa$
z	spanwise displacement from the $x-y$ plane of symmetry in the test section
ΔU	strength of the wake component of the turbulent boundary layer
ΔU_{2D}	component of Coles (1962) wake strength due to flat-plate boundary-layer turbulence; function of Re_{θ_2}
ΔU_{XS}	component of Coles (1962) wake strength due to lateral constriction of the wake region by side-wall boundary layers; function of δ_{99}/r' or $8\theta_2/\mathcal{P}$
δ	boundary-layer thickness
δ_{99}	boundary-layer thickness defined as the distance from the wall at which $U = 0.99U_0$
δ_π	boundary-layer thickness parameter for the Coles wake function
δ^*, δ_2^*	displacement thickness of a two-dimensional flat-plate boundary layer (Equation 7.5)
δ_d^*	displacement thickness of a duct boundary layer (Equation 7.10)
θ, θ_2	momentum thickness of a two-dimensional flat-plate boundary layer (Equation 7.6)
θ_d	momentum thickness of a duct boundary layer (Equation 7.11)
κ	Von Kàrmàn constant ($\kappa = 0.41$) for the law of the wall: $U^+ = \kappa^{-1} \ln y^+ + C$
ν	kinematic viscosity
Π	amplitude parameter for Coles wake function
ρ	density
τ_w	wall shear stress
ω_x	streamwise component of vorticity fluctuations
ω_z'	spanwise component of r.m.s. vorticity fluctuation

Superscripts

Variables which have a superscript $^+$ are nondimensionalised using the viscous flow variables U_τ and ν, e.g. $U^+ = U/U_\tau$ and $y^+ = yU_\tau/\nu$.

Part II

Wall-proximity effect

Chapter 8

Introduction

Boundary-layer mean velocity distributions presented in earlier chapters contain measurements of mean velocity which reach a minimum value and then increase as the hot-wire probe is moved toward the wall. This failure to measure within the viscous sublayer a mean velocity consistent with $U^+ = y^+$ is a consequence of "wall-proximity effect". Wall-proximity effect comprises a number of wall-induced aerodynamic and thermal effects. Many investigations published over a period of more than thrty years have been aimed at correcting air speed measurements distorted by wall-proximity effect. The fact that no satisfactory theoretical model and no completely satisfactory correction method have emerged from this work is testimony to the complexity of the phenomenon. Three methods for empirically correcting velocity data from the viscous sublayer are described in Chapter 10. These methods have been developed from an analysis of the heat transfer from a hot-wire, and from the work of Oka and Kostic (1972), and Bhatia, Durst and Jovanovic (1982).

8.1 Aerodynamic perturbation

8.1.1 The effect of probe geometry

The aerodynamic perturbation of the flow field around the active part of a hot-wire filament is a function of probe geometry, probe orientation in the flow, shear rate in the fluid and distance from the wall. If, in the course of an experiment, the direction of the flow field relative to the probe does not change, and the flow is shear-free, any effect of flow-field distortion at the filament is taken into account by calibrating the probe. However, the flow conditions are usually not of this ideal form, and so it is necessary to construct a probe which produces minimum flow perturbation at the filament. Compte-Bellot, Strohl and Alcaraz (1971) and Dahm and Rasmussen (1969) have investigated the effect of

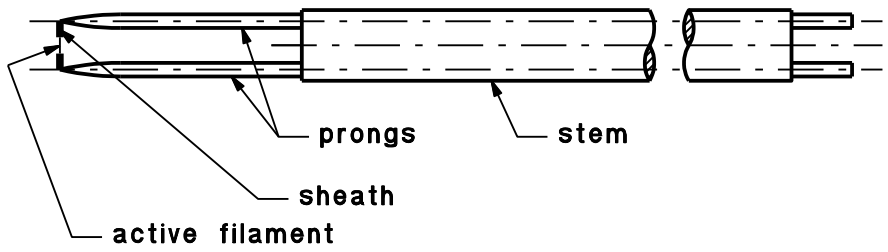

Figure 8.1: Components of a typical single-hot-wire probe

probe geometry on the velocity measurement by rotating the probe about the filament axis in a uniform flow field. Both reported that the sensitivity to flow direction is reduced by increasing the length of the prongs and the spacing between them. In these experiments, the active filament length was constant, and the remainder of the hot-wire length was covered with a sheath of silver or copper — as is the usual practice (Figure 8.1). Compte-Bellot et al. measured the relative importance of the perturbation caused by stem, prong and wire sheath by comparison with a reference probe, and showed that the perturbation caused by the sheath is negligible. They also showed that the disturbance caused by the prongs is usually several times greater than the disturbance caused by the stem. The results of Dahm and Rasmussen (1969) indicate that the most important factor in optimising the probe geometry is the distance separating the active part of the hot-wire filament from the prongs. A sheath length of at least 5 prong diameters is required to remove the active filament from the flow disturbance generated by the prongs. In order to remove the filament from the influence of the probe stem, a typical probe with a filament diameter of about 5 microns and a prong spacing of between 2 mm and 4 mm should have prongs between 10 and 20 mm long.

8.1.2 The effect of shear

The work of Polyakov and Shindin (1979), Van Thinh (1969), and Krishnamoorthy, Wood, Chambers and Antonia (1983) indicates that the shear due to proximity of a wall can greatly increase the distorting effect of the probe geometry on the flow field at the filament. In the experiments of Polyakov and Shindin(1979), Van Thinh(1969), and Krishnamoorthy et al. (1983), mean velocity within the boundary layer was measured with the prongs of a hot-wire probe inclined at various angles to the stream direction. In each case the authors concluded that, in order to minimise the measurement error, the pitch angle of the prongs should be less than five degrees. Van Thinh (1969) also showed that the error decreases as the length of the filament, together with the prong spacing, is increased; that is, as the middle of the filament is “moved” away from the prongs and out of the distorted flow field.

The reasons for this additional effect of wall proximity are that

(1) the confining presence of the wall increases the flow-field distortion caused by the probe stem and prongs, and

(2) the inclination of the prongs puts the body of the probe and prongs in a region of much higher flow speed than the sensing element. Some of the higher speed flow around the stem and prongs is deflected toward the surface.

Both of these effects increase the flow speed measured at the filament. The first effect is expected to be less important than the second and does not require shear; that is, it does not require a stationary wall.

The above discussion of aerodynamic distortion does not include the effect of the hot-wire filament element itself upon the flow. Milthorpe and Wood (1983) have calculated the flow field around an infinitely long wire in the viscous sublayer using a finite element method. By independently varying the shear rate around the wire and the distance from the wall, it was found that a high shear rate ($\frac{d}{U}\frac{dU}{dy} = 0.13$) significantly distorts the wake of the wire and deflects it away from the wall, toward the higher speed flow. However, proximity of the wall largely suppresses this deflection of the wake. The effect of the distortion on the rate of heat transfer from the wire was not evaluated but, from the evidence provided, it appears likely that the heat flow would be significantly affected only if the wire were within a few diameters of the wall.

8.2 Thermal effects

Thermal disturbances due to wall proximity take the form of a heat flow to the wall from the fluid surrounding the hot-wire. This heat flow to the wall can be expected to reduce the temperature of the thermal wake downstream of the hot-wire. For a hot-wire operated at constant temperature, the thermal component of wall-proximity effect is observed experimentally as an increase in voltage across the hot-wire filament and therefore as an increase in the rate of heat transfer from the wire. This increased heat loss is indistinguishable from the effect of increasing the flow speed.

Many studies of the increased heat loss due to the presence of a nearby wall have been published. One of the most often cited is by Wills (1962), who found that, at a fixed distance from the wall in a laminar channel flow, the additional heat loss is constant provided that the Reynolds number of the hot-wire filament, Re_d, is greater than 0.1. The resulting increase in the Nusselt number of the filament was expressed as a function of y/d, and this function formed the basis for a correction procedure. When applied to a turbulent boundary layer with the same friction velocity, this procedure over-corrected, and only one half of the correction was required. Walker (1983) and Nishioka (1973) have used this method of correction successfully in laminar boundary layers. However, many attempts [Walker, 1983, Hebbar, 1980, Zaric, 1972, Krishnamoorthy et al., 1985] to use it for correcting wall-

proximity effect in turbulent boundary layers have produced unsatisfactory results. Oka and Kostic (1972) have measured velocity distributions in the near-wall and viscous-sublayer regions of a turbulent channel flow with a probe which avoids aerodynamic interference effects from the prongs and stem. When non-dimensionalised on wall-friction scales, the error in the sublayer mean velocity measurement, ΔU^+, was found to be a function of y^+ only, that is,

$$\Delta U^+ = f(y^+), \tag{8.1}$$

for channel-flow Reynolds numbers ranging from 11,700 to 64,000. The channel-flow Reynolds number was defined as $Re_H = \langle U \rangle H / 2\nu_\infty$ where $\langle U \rangle$ is the bulk flow speed and H is the smaller of the duct cross-section dimensions (either width or height). The correction curve for the mean velocity was constructed by assuming $U^+ = y^+$ for $y^+ < 5$, and then subtracting this assumed profile from the mean velocity measurements. Oka and Kostic used the velocity error, ΔU^+, successfully to correct mean velocity measurements in the vicinity of a two-dimensional roughness element. Hebbar (1980) adopted this method to correct mean velocity data obtained from a three-dimensional boundary layer over a small range of friction velocities. The scatter of his corrected velocity data was quite large for $y^+ < 2$, but this may have been due to experimental error in measuring the distance from the wall, or because the minimum distance from the wall was only about 4 wire diameters. The results of Oka and Kostic (1972), Zemskaya, Levitsky, Repik and Sosedko (1979) and Janke (1986) indicate that, when it is expressed in the form of Equation 8.1, the velocity error due to conduction of heat to the wall is independent of the Reynolds number of the flow (Re_H for a duct, Re_θ for a boundary layer with momentum thickness θ). Only the measurements of Azad and Burhanuddin (1984) show a significant and regular variation in ΔU^+ with changing Reynolds number, Re_θ.

Andreopoulos, Durst, Zaric and Jovanovic (1984) have measured the mean, r.m.s., skewness and flatness statistics of the streamwise velocity in a turbulent boundary layer over a range of Reynolds numbers, $3{,}600 < Re_\theta < 15{,}500$. Measurements were made over almost the full thickness of the boundary layer, with a minimum distance from the wall of $y^+ = 2.8$. It is claimed in this paper that wall-proximity effect can be avoided by using a thermally non-conducting wall material. However, careful comparisons of their mean velocity data with the measurements of Krishnamoorthy et al. (1985), Azad and Burhanuddin (1984), and with the results presented in earlier chapters of this thesis, suggest that Andreopoulos et al. (1984) have insufficient data over the range $0 < y^+ < 5$ to justify this claim.

Other measurements presented by Zemskaya et al. (1979) have indicated that the velocity error, $\Delta U^+ = f(y^+)$, is the same for both laminar and turbulent boundary layers. They also showed that the velocity error depends on the hot-wire diameter, and obtained approximate collapse of results onto a single curve by using an empirical relationship of the form

$$\Delta U^+ \left[\frac{d^*}{d}\right]^{0.15} = f\left(y^+ \left[\frac{d^*}{d}\right]^{0.15}\right), \tag{8.2}$$

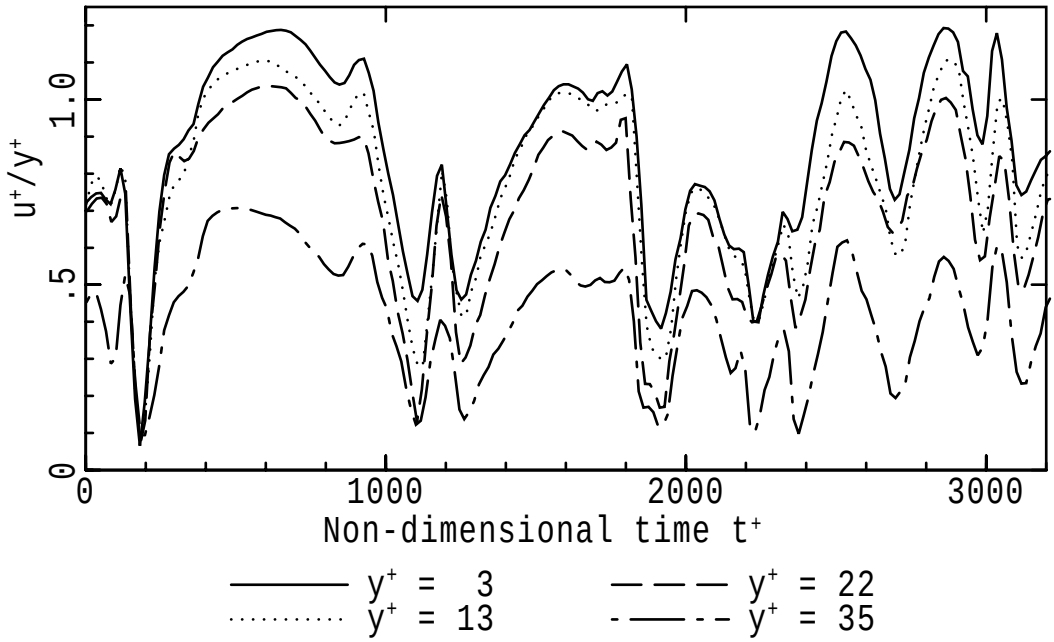

Figure 8.2: Velocity-time record from a "ladder" hot-wire array [Willmarth and Lu, 1972].

where d^* is a reference diameter. In this case, the range of hot-wire diameters was from 3.4 μm to 41.6 μm. Krishnamoorthy et al. (1983, 1985) performed experiments to determine the effect of wire diameter and overheat ratio, a, on the measurement of mean velocity in the viscous sublayer. They found that a reduction of overheat ratio to $a = 0.06$, or of wire diameter from 5 μm to 0.63 μm decreased the velocity error, but in no case was the minimum value in the measured velocity distribution reduced by more than about 30%. Krishnamoorthy et al. (1985) also measured the r.m.s., skewness and flatness distributions of streamwise velocity fluctuations in the sublayer. The measurements of r.m.s. fluctuating velocity appear not to have been influenced by wall proximity, and agree closely with the data of Eckelmann (1974) and Andreopoulos et al. (1984). However, the interpretation of the skewness and flatness measurements is more uncertain. For $y^+ < 3$, the skewness and flatness results depend on hot-wire diameter, but not on the overheat ratio. They are larger than those of Eckelmann, whose values are free of wall-proximity effect, but because they fall between Eckelmann's and Andreopoulos' results, it is not possible without more experimental data to conclude that the difference is due to wall-proximity effect.

Bhatia et al. (1982) modelled the heat conduction from a hot-wire to a wall numerically. They used the results of the numerical modelling as the basis of a method for removing the effect of wall-proximity error from mean velocity measurements. In that study, the instantaneous velocity distribution in the sublayer was assumed to be linear with y. In a paper on Reynolds shear stress, Willmarth and Lu (1972) present some velocity-time records obtained from a "ladder" hot-wire array. These results, which are reproduced with non-dimensional coordinates in Figure 8.2, strongly support Bha-

tia's (1982) linearity assumption. Linearity of the instantaneous sublayer velocity distribution permits the instantaneous velocity field to be non-dimensionalised using the instantaneous friction velocity, $\tilde{u}_\tau$. In addition, the hot-wire was assumed by Bhatia et al. (1982) to have such a small diameter that its presence did not change the the flow field in the sublayer, and it was assumed to have infinite length so that the fluid and heat flows were two-dimensional. The steady-state energy equation was solved for both thermally conducting and non-conducting walls, and the results expressed the velocity measurement error, $\Delta\tilde{u}^+$, as a function of $\tilde{y}^+$. For the high conductivity wall, the results of the numerical model were used for correcting experimental measurements of mean velocity. This procedure, which required a separate iteration for each individual data sample, appeared to be quite successful. In the case of a thermally non-conducting wall, the numerical results produced negligible wall-proximity effect, and the experimental data showed a significantly smaller wall-proximity effect than for a conducting wall. However, from our own experience and that of several other workers [Alfredsson et al., 1988, Polyakov and Shindin, 1979, Turan et al., 1987] we do not believe that, as Bhatia et al. (1982) have concluded, heat transfer to a wall of material with low thermal conductivity can be neglected.

The experiments of Janke (1986), in which particular care was taken to measure the distance from the hot-wire filament to the wall and particular care was taken to calibrate the hot-wire accurately at low speeds, confirm the conclusions of Oka and Kostic (1972). Equation 8.1 was recast as a function of Uy/ν_∞ to give a direct relationship between the measured mean velocity, U_m and the actual mean velocity, U:

$$\frac{U_m y}{\nu_\infty} = g\left(\sqrt{\frac{Uy}{\nu_\infty}}\right) = \sqrt{\frac{Uy}{\nu_\infty}}\, f\left(\sqrt{\frac{Uy}{\nu_\infty}}\right) + \frac{Uy}{\nu_\infty}. \tag{8.3}$$

The related functions f and g were determined from measurements. Janke concluded that the similarity, which he and Zemskaya et al. (1979) found between $U_m^+(y^+)$ in the sublayer of turbulent boundary layers and $U_m^+(y^+)$ in laminar boundary layers, was due to the very small curvature of the function g in Equation 8.3. Janke also observed that the finite non-zero value of the ordinate $U_m y/\nu_\infty$ at $Uy/\nu_\infty = 0$ implies an inverse proportionality ($U_m \propto 1/y$), which can be used for extending a hot-wire calibration towards zero velocity. By using the linear relationship between wall shear stress and the velocity gradient in the sublayer, Wagner (1990) rewrote Janke's velocity correction formula in terms of wall shear stress. Then he used it for calibrating the probes and measuring the instantaneous wall shear stress.

8.3 Summary

Wall-proximity effect can be resolved into two components, one aerodynamic and one thermal. The aerodynamic component, which is due to perturbation of the velocity field around the hot-wire filament

by the other parts of the probe, is a function of probe geometry, probe orientation and shearing of the flow. In extreme cases, it may be detected well within the buffer region of the turbulent boundary layer. The principal features of probes which produce a negligible level of aerodynamic wall-proximity error are

(1) prongs which are aligned at an angle of less than five degrees from the mean flow direction [van Thinh, 1969, Polyakov and Shindin, 1979, Krishnamoorthy et al., 1983], and

(2) an active hot-wire filament which is sufficiently remote from the prongs and the probe body [van Thinh, 1969, Dahm and Rasmussen, 1969, Compte-Bellot et al., 1971].

The thermal component of wall-proximity effect is due to heat transfer from the hot-wire filament to the wall. For a fluid with a Prandtl number in the order of unity (e.g. air), heat flow to the wall is usually significant only if the hot-wire filament is placed within the viscous sublayer. Thermal wall-proximity error can be expressed as a non-dimensional velocity-error function, $\Delta U^+ = f(y^+)$, which is independent of Reynolds number (Re_θ or Re_H) and is the same in both turbulent and laminar boundary layers [Oka and Kostic, 1972, Zemskaya et al., 1979, Janke, 1987]. This velocity-error function has been used for correcting measurements of the mean velocity distribution over surfaces where there are spatial variations in wall shear stress [Oka and Kostic, 1972, Hebbar, 1980]. Bhatia et al. (1982) have developed an iteration procedure which calculates the wall shear stress and simultaneously removes wall-proximity error from the velocity data. They also assumed linearity of the instantaneous velocity distribution within the viscous sublayer, and so were able to demonstrate the correction of a fluctuating velocity signal.

Wall-proximity effect, which is most clearly visible as the velocity error ΔU^+, can be changed significantly by varying parameters such as overheat ratio or hot-wire diameter [Zemskaya et al., 1979, Krishnamoorthy et al., 1985]. The variability of the skewness and flatness in the viscous sublayer [Eckelmann, 1974, Andreopoulos et al., 1984, Krishnamoorthy et al., 1985] is also fairly large, but is without an obvious explanation. In contrast, the apparent lack of variation in the measurements of r.m.s. velocity fluctuations, u', within the viscous sublayer indicates that the effect of wall proximity on u' is relatively small.

8.4 Notation

a	overheat ratio of the hot-wire filament; $a = \dfrac{\text{operating resistance}}{\text{cold resistance}} - 1$
d	diameter of the hot-wire filament.
d^*	reference diameter used by Zemskaya et al. (1979) for correlating the effect of varying the diameter of the hot-wire filament
f, g	used to denote a function representing the wall-proximity error

H	the smaller of duct cross-section dimensions (width or height)
Re_d	Ud/ν_f, Reynolds number of a hot-wire filament
Re_H	$U_a H/2\nu_\infty$, Reynolds number of the flow in a duct
Re_θ	$U\theta/\nu_\infty$, Reynolds number of a boundary layer
$\langle U \rangle$	bulk flow speed; i.e. average flow speed over a duct cross-section
u	streamwise component of the flow-velocity vector
u_m	flow speed as measured by a hot-wire probe; i.e. not corrected for wall-proximity effect
y	distance between the hot-wire filament and the wall
Δu	$u_m - u$, measurement error due to wall-proximity effect
θ	momentum thickness of a boundary layer
ν	kinematic viscosity

superscripts

$^+$	scales the quantity on the viscous flow variables U_τ and ν_∞, e.g. $U^+ = \bar{U}/U_\tau$ and $\tilde{y}^+ = y\tilde{u}_\tau/\nu_\infty$.
$\tilde{}$	used for indicating a quantity which may vary as a function of time, e.g. $\tilde{u}$.

subscripts

$_f$	for properties of the fluid evaluated at the film temperature $T_f = T_\infty + \Delta T/2$
$_\infty$	for properties of the fluid far field

Upper case is used for indicating time-averaged or constant values. All physical quantities are expressed in SI units.

Chapter 9

Analysis

9.1 Heat flows

The purpose of the analysis presented here is to develop a model for the heat flow from a hot-wire filament which is placed near a wall. This model will then be used as the basis of correction procedures which can remove the wall-proximity error from the measurement of flow speed in the viscous sublayer. It is assumed that the aerodynamic effects of wall proximity have been reduced to an insignificant level by appropriate design of the probe.

The total heat flow rate from a hot-wire in the viscous sublayer is

$$\tilde{q}_{\text{total}} = \tilde{q}_{\text{conv}} + \tilde{q}_{\text{wall}}, \tag{9.1}$$

where $\tilde{q}_{\text{wall}}$ is the rate of heat transfer to the wall and $\tilde{q}_{\text{conv}}$ is that part of the heat flow which is convected far downstream by the fluid and is *not* transferred to the wall. The ˜ symbol indicates quantities which can vary as a function of time. It is also assumed that heat transfer from the hot-wire filament is entirely by conduction and that radiation heat loss is negligible. Simple estimates for a tungsten wire at an overheat ratio[1] of 0.5 show the radiation loss to be less than 0.1% of the total heat loss from the wire. The heat flow $\tilde{q}_{\text{total}}$, which is interpreted experimentally as a measured flow speed $\tilde{u}_m$, can then be written as

$$\tilde{q}_{\text{total}} = \frac{A\Delta T\, k_f}{d}\, Nu_d\left(\frac{\tilde{u}_m d}{\nu_f}, Pr_f\right), \tag{9.2}$$

where $A = \pi dl$ is the surface area of the hot-wire filament, ΔT is the nominal temperature of the filament above the distant fluid temperature, d is the filament diameter, k_f is thermal conductivity of

[1] The overheat ratio, a, is the increase in filament resistance caused by electrical heating divided by its resistance at the ambient temperature of the fluid.

the fluid, and ν_f is kinematic viscosity of the fluid at the film[2] temperature. The Nusselt number, Nu_d, defines the hot-wire calibration and is traditionally written as a function of the filament Reynolds number, $\tilde{Re}_d = \tilde{u}_m d/\nu_f$, and fluid Prandtl number, $Pr_f = c_f \mu_f / k_f$.

Similarly, the convected heat flow to the fluid can be written as

$$\tilde{q}_{\text{conv}} = \frac{A \Delta T \, k_f}{d} \tilde{Nu}_c, \tag{9.3}$$

where the convection Nusselt number $\tilde{Nu}_c = \tilde{h}_c d/k_f$ is a function of as yet undetermined parameters. When the distance between the hot-wire and the wall is sufficient to prevent heat transfer to the wall, the convection Nusselt number reduces to the hot-wire calibration (i.e. $\tilde{Nu}_c = \tilde{Nu}_d$).

The Nusselt number of heat transfer to the wall,

$$\tilde{Nu}_w = \frac{\tilde{h}_w y}{k_f}, \tag{9.4}$$

is initially defined in terms of the distance from the wall, y, because heat flow from the hot-wire filament to the wall depends more strongly on y than on other readily apparent length scales such as l or d. On the basis of this definition, the heat flow to the wall is

$$\tilde{q}_{\text{wall}} = \frac{A \Delta T \, k_f}{y} \tilde{Nu}_w. \tag{9.5}$$

The results obtained from dimensional and order analysis are independent of the parameter chosen as a length scale for $\tilde{Nu}_w$. If a different parameter, such as d, is used as a length scale for $\tilde{Nu}_w$, the same results can be obtained from dimensional and order analysis, but, as demonstrated in Section 9.5.3, different aspects of interpretation are advanced by the consequent rearrangement of nondimensional groups.

By substituting Equations 9.2, 9.3 and 9.5 into Equation 9.1, we obtain

$$Nu_d(\tilde{Re}_{d,m}, Pr_f) = \tilde{Nu}_c + \frac{d}{y} \tilde{Nu}_w. \tag{9.6}$$

Equation 9.6 is the basis for a general heat-transfer model which describes wall-proximity effect. The next stage in the analysis is to determine the parameters of $\tilde{Nu}_c$ and $\tilde{Nu}_w$. By deleting those parameters which remain constant within a typical set of sublayer velocity measurements (for example, those related to ambient fluid properties, wall-material properties and probe geometry), it is then possible to develop a simplified semi-empirical formula from Equation 9.6. With empirical coefficients determined from uncorrected velocity data, this formula can be used for correcting sublayer turbulence signals from the hot-wire anemometer.

[2]The film temperature is chosen to represent the condition of the fluid field in the vicinity of the hot-wire filament and is initially defined as the mean of the ambient fluid temperature and the temperature of the filament surface.

9.2 Dimensional analysis

The first step in the dimensional analysis is to write the coefficient of heat transfer to the wall $\tilde{h_w}$ as a function of dimensional parameters which describe the flow field geometry, fluid properties and wall material properties. Hot-wire diameter d, length l, distance from the wall y and time t are clearly parameters. If the velocity distribution in the viscous sublayer is assumed to be linear at any instant, that is, if $\tilde{u}(y,t) = \tilde{\tau}_w(t)\, y/\mu_\infty$, the flow field is characterised by the instantaneous wall shear stress $\tilde{\tau}_w$, or by the friction velocity $\tilde{u}_\tau$. From the non-dimensional governing energy equation which is presented later in this section as Equation 9.19, it is clear that if the effects of viscous dissipation are to be modelled, the temperature difference ΔT must also be a parameter of the function. If the fluid surrounding the hot-wire is a gas, the temperature variation in the fluid may be expected to produce significant variations in the fluid properties. By including fluid properties evaluated at both the film temperature (thermal conductivity k_f, kinematic viscosity μ_f, density ρ_f, specific heat c_f) and the ambient fluid temperature (k_∞, ν_∞, ρ_∞, c_∞) as parameters, a mechanism is introduced for defining a single temperature which is representative of the fluid temperature field near the hot-wire and the adjacent wall. It might then be possible to select a representative temperature which permits successful modelling of effects such as variation of overheat ratio. Properties of the wall material at the ambient fluid temperature (i.e. thermal conductivity k_w, specific heat c_w, density ρ_w) are also included as parameters of the function, so that

$$\tilde{h}_w = h_1(d, l, y, t, \tilde{u}_\tau, \Delta T, k_w, c_w, \rho_w, k_f, c_f, \nu_f, \rho_f, k_\infty, c_\infty, \nu_\infty, \rho_\infty). \tag{9.7}$$

Four fundamental dimensions are used in this function, and so the 18 parameters can be reduced to 14 by forming non-dimensional groups. The parameters y, k_∞, ν_∞ and ρ_∞ have been used to non-dimensionalise all the remaining parameters to obtain

$$\frac{\tilde{h}_w y}{k_\infty} = Nu_{1w}\left(\frac{d}{y}, \frac{l}{y}, \frac{t\nu_\infty}{y^2}, \frac{\tilde{u}_\tau y}{\nu_\infty}, \frac{\Delta T k_\infty y^2}{\rho_\infty \nu_\infty^3}, \frac{k_w}{k_\infty}, \frac{c_w \nu_\infty \rho_\infty}{k_\infty}, \right.$$
$$\left. \frac{\rho_w}{\rho_\infty}, \frac{k_f}{k_\infty}, \frac{c_f \nu_\infty \rho_\infty}{k_\infty}, \frac{\nu_f}{\nu_\infty}, \frac{\rho_f}{\rho_\infty}, \frac{c_\infty \nu_\infty \rho_\infty}{k_\infty}\right). \tag{9.8}$$

The parameters of Equation 9.8 are clearly not in the simplest or most physically appropriate form. The first step in simplifying them is to write the parameter $\tilde{u}_\tau y/\nu_\infty$ as $\tilde{y}^+$, and to write the parameter $c_\infty \nu_\infty \rho_\infty / k_\infty$ as the Prandtl number Pr_∞. Any other parameters containing y or $\nu_\infty \rho_\infty / k_\infty$ can then be expressed in terms of $\tilde{y}^+$ and Pr_∞:

$$\frac{\tilde{h}_w y}{k_\infty} = Nu_{2w}\left(\frac{d}{y}, \frac{l}{y}, \tilde{y}^+, \frac{k_w}{k_\infty}, \frac{c_w}{c_\infty} Pr_\infty, \frac{\rho_w}{\rho_\infty}, \frac{c_\infty \Delta T}{\tilde{u}_\tau^2} \frac{\tilde{y}^{+2}}{Pr_\infty}, \frac{\tilde{t}^+}{\tilde{y}^{+2}}, \frac{k_f}{k_\infty}, \frac{c_f}{c_\infty} Pr_\infty, \frac{\nu_f}{\nu_\infty}, \frac{\rho_f}{\rho_\infty}, Pr_\infty\right), \tag{9.9}$$

where $\tilde{t}^+ = t\tilde{u}_\tau^2/\nu_\infty$. Parameters can also be simplified by combining them with others. For example, in order to be more consistent with the hot-wire calibration relation (Equation 9.2), the left hand side of Equation 9.8 can be replaced by $\tilde{h}_w y/k_f$ because k_f/k_∞ is also a parameter. The parameter

$\tilde{t}^+/\tilde{y}^{+2}$ can be replaced by $\tilde{t}^+$, the Prandtl number can be removed from the parameters containing c_f and c_w, and the parameter containing ΔT can be simplified to an Eckert number, $Ec = \tilde{u}_\tau^2/(c_\infty \Delta T)$ [Schlichting, 1968], so that

$$\frac{\tilde{h}_w y}{k_f} = Nu_{3w}\left(\frac{d}{y}, \frac{l}{y}, \tilde{y}^+, \frac{k_w}{k_\infty}, \frac{c_w}{c_\infty}, \frac{\rho_w}{\rho_\infty}, Ec, \tilde{t}^+, \frac{k_f}{k_\infty}, \frac{c_f}{c_\infty}, \frac{\nu_f}{\nu_\infty}, \frac{\rho_f}{\rho_\infty}, Pr_\infty\right). \tag{9.10}$$

The Nusselt number of heat convection, Nu_c, has the same parameters as Nu_w because both the heat flow to the wall and the heat flow convected away by the fluid depend on the temperature distribution in the fluid around the hot-wire filament; i.e.

$$\frac{\tilde{h}_c d}{k_f} = Nu_{3c}\left(\frac{d}{y}, \frac{l}{y}, \tilde{y}^+, \frac{k_w}{k_\infty}, \frac{c_w}{c_\infty}, \frac{\rho_w}{\rho_\infty}, Ec, \tilde{t}^+, \frac{k_f}{k_\infty}, \frac{c_f}{c_\infty}, \frac{\nu_f}{\nu_\infty}, \frac{\rho_f}{\rho_\infty}, Pr_\infty\right). \tag{9.11}$$

9.3 Order analysis

An appreciation of the physical significance and the relative importance of many of the parameters in Equations 9.10 and 9.11 can be obtained by a qualitative examination of the heat transfer from a hot-wire filament.

9.3.1 Probe geometry

The nondimensional geometric parameters of heat flow from the hot-wire filament are d/y and l/y. Because the filament is in the viscous sublayer, $U^+ = y^+$. The ratio d/y can then be written as

$$\frac{d}{y} = \frac{\tilde{u}d}{\nu_f}\frac{\nu_\infty}{\tilde{u}_\tau y}\frac{\tilde{u}_\tau}{\tilde{u}}\frac{\nu_f}{\nu_\infty} = \frac{\tilde{Re}_d}{\tilde{y}^{+2}}\frac{\nu_f}{\nu_\infty}, \tag{9.12}$$

where $\tilde{u}$ is the local instantaneous fluid speed a distance y from the surface. The factors $\tilde{y}^+$ and ν_f/ν_∞ are already parameters of Equations 9.10 and 9.11, and so d/y may simply be replaced by the Reynolds number, $\tilde{Re}_d = \tilde{u}d/\nu_f$, which characterises the velocity shear due to the hot-wire filament and is evaluated at the fluid-film temperature.

For the heat conduction from the hot-wire filament to the wall to be considered two-dimensional, the ratio l/y would have to be large (e.g. greater than 10). Within the viscous sublayer ($y^+ < 5$) this requirement becomes $l^+ \gtrsim 50$. However, if the signal fluctuations are not to be significantly affected by spatial averaging of the turbulence, the criterion $l^+ < 20$ must be satisfied [Ligrani and Bradshaw, 1987a]. Therefore it is not permissible to assume that the heat flow from a probe which measures sublayer turbulence accurately is two dimensional, and the parameter l/y cannot be removed from Equation 9.16. However, as we shall see in Section 9.5.2, it might be expressed more appropriately as l/d.

Table 9.1: Properties of selected fluids and wall-materials at 20^oC

	density ρ kg/m^3	specific heat c $J/kg/K$	thermal conductivity k $W/m/K$	thermal diffusivity α $10^{-6}m^2/s$	kinematic viscosity ν $10^{-6}m^2/s$	Prandtl number Pr
aluminium	2707	896	204	84.1		
copper	8954	383	386	112.0		
mild-steel	7833	465	54	14.8		
granite	2640	820	2.8	1.29		
glass	2700	840	0.78	0.344		
polythene	917	2303	0.335	0.158		
perspex	1185	1465	0.21	0.143		
PVC	1535	1382	0.138	0.0651		
polypropylene	904	1926	0.117	0.0672		
polystyrene	1065	1340	0.105	0.0736		
cork	160	1880	0.043	0.014		
glycerine	1264	2386	0.286	0.0948	1180	12500
engine oil	888	1880	0.145	0.00087	900	10400
water	998	4180	0.6022	0.144	1.010	7.00
air	1.2096	1006	0.0257	21.1	15.83	0.750

9.3.2 Properties of the wall material

Now we consider the role of the parameter containing the thermal conductivity of the wall, k_w. The thermal resistance to heat conduction through the fluid scales with $y/(k_f dl)$ and, by analogy with radial conduction from the axis of a cylinder, the thermal resistance of a wall with a fixed geometry scales with $1/(k_w l)$. The representative temperature elevation of the part of the wall receiving heat from the fluid is therefore in the order of

$$\Delta T_w = O(\Delta T \frac{k_f d}{k_w y + k_f d}). \tag{9.13}$$

The distance from the filament to the wall is usually at least one order of magnitude greater than the filament diameter, and the thermal conductivity of even the best solid insulators (i.e. those without cavities) is at least several times greater than that of air (Table 9.1). Therefore $\Delta T_w \ll \Delta T$, and the dependence of heat flow to the wall on k_w is likely to be weak. In particular, the temperature of a metal wall is essentially constant, uniform and equal to the ambient fluid temperature.

A comparison of uncorrected mean velocity profiles for various wall materials is shown in Figure 9.1. Because of the variation in hot-wire diameters, operating temperatures and probe geometries, and because the data are adjusted to force $U^+ = y^+$ in the region $4 < y^+ < 5$, the diagram should be interpreted with caution. Nevertheless, it is evident that although the wall-proximity error, ΔU^+, can be reduced by using an insulating wall material, the reduction factor is orders of magnitude less than the

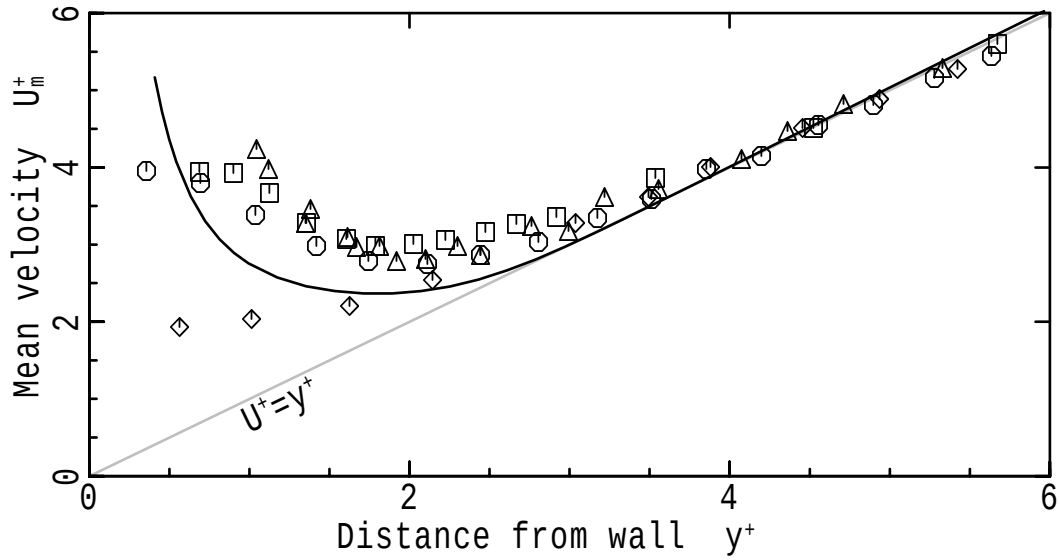

		d (μm)	ΔT (^oC)	wall material	k_w $W/m/K$
□	Krishnamoorthy (1985)	5	190	aluminium	204
◯	Hebbar (1980)	3.8	167	aluminium	204
△	Zemskaya (1979)	4.4	223	steel	54
◇	Alfredsson (1988)	2.5	190	cork	0.043
—	present results	5	104	polystyrene	0.105

Figure 9.1: Comparison of uncorrected mean velocity measurements in the sublayer for various wall materials. The data from each of these experiments have been shifted vertically to ensure $U^+ = y^+$ in the region $4 < y^+ < 5$.

variation in wall conductivity and ΔU^+ cannot be reduced to insignificance; k_w/k_∞ and k_f/k_∞ are therefore retained as parameters of Nu_w and Nu_c. Measurements of Turan, Azad and Atamanchuk (1987) indicate that heat flow to the wall depends much more on wall conductivity when the flow speed is reduced to zero.

Heat flow within the wall is governed by the thermal diffusion equation,

$$\rho_w c_w \frac{\partial \tilde{T}}{\partial t} = \frac{\partial}{\partial x_i}\left(k_w \frac{\partial \tilde{T}}{\partial x_i}\right). \tag{9.14}$$

When thermal conductivity (k_w) is distributed uniformly, ρ_w, c_w and k_w may be combined and written as the thermal diffusivity, $\alpha_w = k_w/(\rho_w c_w)$. This, however, does not permit the parameter k_w/k_∞ to be removed from Equation 9.10 or combined with other parameters because, as shown by Equation 9.13, k_w is one of the variables determining the surface temperature of the wall. On the other hand, the density (ρ_w) and the specific heat (c_w) in Equation 9.14 can only affect the transient or unsteady component of the temperature distribution, and they are multiplied together to form the single parameter, $\rho_w c_w$. In Equation 9.10, the dependence of $\tilde{h}_w y/k_f$ on ρ_w and c_w is therefore on the product $\rho_w c_w$ rather than the

two separate parameters, and since

$$\frac{\rho_w}{\rho_\infty}\frac{c_w}{c_\infty} = \frac{\alpha_\infty}{\alpha_w}\frac{k_w}{k_\infty}, \tag{9.15}$$

the ratios ρ_w/ρ_∞ and c_w/c_∞ can be replaced by α_w/α_∞. Equation 9.10 then becomes

$$\frac{\tilde{h}_w y}{k_f} = Nu_{4w}\left(\tilde{Re}_d, \frac{l}{d}, \tilde{y}^+, \frac{k_w}{k_\infty}, \frac{\alpha_w}{\alpha_\infty}, \tilde{t}^+, Ec, \frac{k_f}{k_\infty}, \frac{c_f}{c_\infty}, \frac{\rho_f}{\rho_\infty}, \frac{\nu_f}{\nu_\infty}, Pr_\infty\right). \tag{9.16}$$

9.3.3 Time scales

We now look at the time scales which characterise unsteady heat flow to the wall. They are as follows.

(1) The convection time scale. The results of Bhatia et al. (1982) give some indication that most of the heat transfer to the wall occurs downstream of the wire, but within a distance comparable to the distance between the filament and the wall. Consequently, the typical residence time of a fluid "particle" within the thermal wake of the hot-wire filament is $t_{\text{conv},f} \approx \nu_\infty/\tilde{u}_\tau^2$ or $t^+_{\text{conv},f} \approx 1$.

(2) Thermal diffusion time scale in the fluid. The time scale for conduction of heat to the wall from a hot-wire filament in the sublayer is $t_{\text{diff},f} = y^2/\alpha_f$ or $t^+_{\text{diff},f} = Pr_\infty {y^+}^2 \alpha_\infty/\alpha_f$. The experimental data of Oka and Kostic (1972), Hebbar (1980) and Krishnamoorthy et al. (1983,1985) indicate that the maximum distance at which significant heat transfer to the wall occurs is $y^+ \approx 4$. For air ($Pr = 0.7$), the thermal diffusion time scale in the fluid is therefore at most in the order of $t^+_{\text{diff},f} \approx 10$.

(3) Thermal diffusion time scale in the wall. The time scale for diffusion within the wall of heat from the hot-wire is $t_{\text{diff},w} = y^2/\alpha_w$ or $t^+_{\text{diff},w} = Pr_\infty {y^+}^2 \alpha_\infty/\alpha_w$. By selecting from a wide range of fluids and wall-materials it is possible to obtain values of $t^+_{\text{diff},w}$ from about 0.01 to 10^6.

(4) Time scale of turbulence, t^+_{turb}. The Kolmogorov dissipation time scale in the sublayer is the same as the viscous time scale ν_∞/U_τ^2 (or $t^+_{\text{diss},f} = 1$). The most rapid velocity fluctuations actually observed in the sublayer are about one order of magnitude slower than this, and so $t^+_{\text{turb}} \gtrsim 10$.

The time scale of thermal diffusion within the wall cannot affect the perturbations of the temperature field in the fluid if the Prandtl number of the fluid is high enough to suppress heat flow to the wall (Section 9.3.4), if the surface temperature elevation is small compared with the wire overheat temperature, or if the time scale is long enough to ensure a virtually constant wall surface temperature distribution (e.g. $t^+_{\text{diff},w} > 100$). The convection and thermal diffusion time scales in the fluid are about the same as or shorter than that of the most rapid turbulence fluctuations and so, because it can change at least as rapidly as the velocity field, the temperature field is always at or close to a state of equilibrium. The temperature field therefore conforms to the requirements of the momentum (Navier-Stokes) equations without any significant "thermal lag" effects. In the viscous sublayer, the instantaneous velocity distribution is assumed to be linear, so that, when the momentum equations are non-dimensionalised on instantaneous wall variables, all time-dependence is expressed through the instantaneous friction

velocity, $\tilde{u}_\tau$. In this form, the momentum equations become "locally" independent of time and there is no time-derivative term. Consequently, with the possible exception of cases where a hot-wire filament is very close ($y^+ \ll 1$) to a low conductivity surface (e.g. perspex) in a low Prandtl number, low thermal diffusivity fluid (e.g. water), the time parameter t^+ need not be included in the thermal model of wall-proximity effect. The parameter α_w/α_∞, which permits modelling the effect of wall temperature fluctuations on the heat flow rate, is also removed so that Equation 9.16 becomes a steady-state description :

$$\frac{\tilde{h}_w y}{k_f} = Nu_{5w}\left(\tilde{Re}_d, \frac{l}{d}, \tilde{y}^+, \frac{k_w}{k_\infty}, Ec, \frac{k_f}{k_\infty}, \frac{c_f}{c_\infty}, \frac{\rho_f}{\rho_\infty}, \frac{\nu_f}{\nu_\infty}, Pr_\infty\right). \tag{9.17}$$

9.3.4 Viscous dissipation

The significance of viscous dissipation in heat transfer from a hot-wire filament can be assessed by an order analysis of the heat-transport equation for an incompressible fluid,

$$\rho c\left(\frac{\partial \tilde{T}}{\partial t} + \tilde{u}_i\frac{\partial \tilde{T}}{\partial x_i}\right) = \frac{\partial}{\partial x_i}\left(k\frac{\partial \tilde{T}}{\partial x_i}\right) + \frac{\mu}{2}\left(\frac{\partial \tilde{u}_i}{\partial x_j} + \frac{\partial \tilde{u}_j}{\partial x_i}\right)^2. \tag{9.18}$$

con-vection | thermal conduction | heat addition from viscous dissipation

The reasoning of the previous section (Section 9.3.3) indicates that the effect of the time dependent term, $\rho c\partial\tilde{T}/\partial t$ is negligible. If Equation 9.18 is nondimensionalised using the scale variables $\tilde{u}_\tau$, $\nu/\tilde{u}_\tau$ and ΔT,

$$\frac{\nu_\infty}{\nu}\tilde{u}_i^+\frac{\partial \tilde{\theta}}{\partial x_i^+} = \frac{1}{Pr}\left[\frac{\partial^2\tilde{\theta}}{\partial x_i^{+2}} + \frac{\partial}{\partial x_i^+}\ln\left(\frac{k}{k_\infty}\right)\frac{\partial\tilde{\theta}}{\partial x_i^+}\right] + \frac{1}{2}Ec\left[\frac{\partial\tilde{u}_i^+}{\partial x_j^+} + \frac{\partial\tilde{u}_j^+}{\partial x_i^+}\right]^2, \tag{9.19}$$

where the unsubscripted fluid properties (ν, Pr and k) are functions of temperature and hence functions of location. The characteristic Reynolds number of flow described by this equation is

$$Re = \frac{\tilde{u}_\tau(\nu_\infty/\tilde{u}_\tau)}{\nu_\infty} = 1. \tag{9.20}$$

The significance of viscous dissipation is related to the product of the Eckert number, $Ec = \tilde{u}_\tau^2/(\Delta T)$, and the square of the maximum characteristic velocity gradient in the flow.

The main features of the velocity and temperature fields around a hot wire in wall proximity are an externally imposed viscous-sublayer shear flow and a local shear flow due to the presence of the hot-wire filament. The steepest temperature gradients and velocity gradients occur in the local shear flow region of the filament itself rather than in the viscous sublayer. Evaluation of the Oseen solution for the drag of a cylinder [Lighthill, 1963, Section IV.5.2] indicates that, at typical Reynolds numbers, the thickness of the shear-flow region around a hot-wire filament varies approximately in accordance with

$$\frac{\delta}{d} \propto (Re_d)^{-0.8}. \tag{9.21}$$

When the filament is placed in the viscous sublayer, this expression can be nondimensionalised with wall variables:

$$\delta^+ \approx C_1 \left(\frac{\nu_\infty}{\nu_f} y^+ \right)^{-0.8} d^{+0.2} \tag{9.22}$$

where C_1 is a constant of proportionality. If all variables except y^+ are evaluated for typical hot-wire operating conditions and absorbed into the constant,

$$\delta^+ \approx C_2 y^{+-0.8} \tag{9.23}$$

and C_2 is in the order of five. Similarly, the thickness of the thermal diffusion region (i.e. "thermal boundary layer") around the hot-wire filament, which depends on Péclet number rather than Reynolds number, varies according to

$$\delta_T^+ \approx C_2 \left(y^+ Pr \right)^{-0.8}. \tag{9.24}$$

The nondimensional velocity scale for the shear-flow region around a hot-wire filament in the viscous sublayer is U^+ $(= y^+)$. In all media except liquid metals, nearly all of the temperature drop from $T_\infty + \Delta T$ to T_∞ occurs within this shear-flow region, and so the appropriate temperature scale is ΔT.

It is now possible to evaluate the order of magnitude of the term on the left hand side of Equation 9.19 for a hot-wire operating under typical conditions in air:

$$\frac{\nu_\infty}{\nu} \tilde{u}_i^+ \frac{\partial \tilde{\theta}}{\partial x_i^+} = O\left(y^+ \frac{1}{C_2} \left(y^+ Pr \right)^{0.8} \right) = O(0.04 \rightarrow 3), \tag{9.25}$$

for $0.5 \lesssim y^+ \lesssim 5$. Under the same conditions, the derivative part of the viscous dissipation term is

$$\left[\frac{\partial \tilde{u}_i^+}{\partial x_j^+} + \frac{\partial \tilde{u}_j^+}{\partial x_i^+} \right]^2 = O\left(\left[\frac{y^+}{C_2 y^{+-0.8}} \right]^2 \right) = O(0.003 \rightarrow 13), \tag{9.26}$$

and the Eckert number, Ec, is in the order of 10^{-7} to 10^{-5}. The right hand term in Equation 9.19 is therefore at least four orders of magnitude smaller than the other terms, and Ec is not required as a parameter in Equation 9.17. Since specific heat (c) appears only in the viscous dissipation term, the parameter c_f / c_∞ may also be discarded. One may observe that density is not an explicit parameter in Equation 9.19, but since this equation must be solved simultaneously with the Navier-Stokes equations in order to calculate the velocity-vector and temperature fields, the parameter ρ_f / ρ_∞ should be retained in Equation 9.17.

9.3.5 Prandtl number

Equation 9.24 shows that, in high Prandtl number fluids (e.g. glycerine, oil), the thermal diffusion region (i.e. the "thermal boundary layer") around a hot-wire filament is much thinner than the smallest realisable distance, y^+, between the filament and the wall. In these flows, hot-wire and hot-film

anemometry in the viscous sublayer is free from wall-proximity effect [Bakewell and Lumley, 1967, Eckelmann, 1974].

Without the viscous dissipation term, Equation 9.19 can be written as

$$\tilde{u}_i^+ \frac{\partial \tilde{\theta}}{\partial x_i^+} = \frac{1}{Pr} \frac{\nu}{\nu_\infty} \left[\frac{\partial^2 \tilde{\theta}}{\partial x_i^{+2}} + \frac{\partial}{\partial x_i^+} \ln\left(\frac{k}{k_\infty}\right) \frac{\partial \tilde{\theta}}{\partial x_i^+} \right]. \tag{9.27}$$

Clearly, an increase in local viscosity, ν, which is due, for example, to an increase in hot-wire temperature, can produce the same effect as a decrease in local Prandtl number. For a gas, it is also clear that, because $\nu_\infty/\nu < 1$ and Pr is independent of temperature, wall-proximity error cannot be reduced to a level which avoids the need for correcting the velocity measurement — even if the overheat ratio is decreased to almost zero. In flat-plate thermal boundary layers, Žukauskas and Šlančiauskas (1987, Section 4.3) have measured significant distortion of velocity and temperature distributions resulting from the temperature dependence of fluid properties.

9.3.6 Operating conditions

The number of independent non-dimensional parameters required in a general model of wall-proximity effect has now been reduced from 13 to 8:

$$\frac{\tilde{h}_w y}{k_f} = Nu_{6w}\left(\tilde{Re}_d, \frac{l}{d}, \tilde{y}^+, \frac{k_w}{k_f}, \frac{k_f}{k_\infty}, \frac{\rho_f}{\rho_\infty}, \frac{\nu_f}{\nu_\infty}, Pr_\infty\right). \tag{9.28}$$

The parameter list can be reduced still further if the hot-wire operates within a restricted range of conditions. For example, the parameter k_w/k_f can be removed if the wall is always of metal.

The ratios k_f/k_∞, ρ_f/ρ_∞ and ν_f/ν_∞ represent the distribution of the fluid properties k, ρ and ν in the vicinity of the hot-wire filament and the adjacent wall. To a very good approximation they are functions only of temperature and so, if the hot-wire is driven by a constant temperature bridge circuit at a particular overheat ratio, k_f/k_∞, ρ_f/ρ_∞ and ν_f/ν_∞ can effectively be cast as functions of $\tilde{Re}_d$, l/d and $\tilde{y}^+$. We then have a different set of functions,

$$\frac{\tilde{h}_w y}{k_f} = Nu_{7w}\left(\tilde{Re}_d, \frac{l}{d}, \tilde{y}^+, \frac{k_w}{k_\infty}, Pr_\infty\right) \tag{9.29}$$

$$\frac{\tilde{h}_c d}{k_f} = Nu_{7c}\left(\tilde{Re}_d, \frac{l}{d}, \tilde{y}^+, \frac{k_w}{k_\infty}, Pr_\infty\right), \tag{9.30}$$

for each distinct working fluid and hot-wire operating temperature.

9.4 Simple heat-transfer model

The parameter list in Equations 9.29 and 9.30 shows that a complete thermal model of wall-proximity effect must take into account the probe location and geometry, the flow speed, the fluid properties and

the thermal conductivity of the wall material. With the possible exception of the wall conductivity, all of these factors have a strong influence on the wall-proximity error. The construction of a general model from experimental or simulation data would be a large and difficult process. Fortunately this is unnecessary because wall conductivity, probe geometry and ambient fluid properties usually do not change within any particular set of measurements. Under these more restrictive conditions the parameters l/d, k_w/k_f and Pr_∞ of Equations 9.29 and 9.30 become constants. Absorbing these parameters and further limiting the scope of the Nusselt-number functions Nu_w and Nu_c allows the expression for total heat flow from the hot-wire to be written as

$$Nu_d(\tilde{Re}_{d,m}) = Nu_c(\tilde{Re}_d, \tilde{y}^+) + \frac{d}{y} Nu_w(\tilde{y}^+, \tilde{Re}_d). \tag{9.31}$$

This relation still has two unknown functions and so is not immediately useful for removing wall-proximity error. However, if the convection Nusselt number Nu_c is assumed to be independent of distance from the wall, and therefore to be a function of the single parameter $\tilde{Re}_d$, it is possible to calculate values of Nu_w from experimental mean-velocity data. This assumption reduces Nu_c to the (free-air) hot-wire calibration, Nu_d. Figure 9.2 shows the values of Nu_w obtained from Krishnamoorthy's (1985) data for the effects of varying overheat ratio and varying hot-wire diameter. If allowance is made for experimental uncertainty a curve which is independent of Re_d,

$$Nu_w(y^+) = e^{-P(y^+)}, \tag{9.32}$$

where $P(y^+)$ is a polynomial of y^+, can be fitted quite successfully to the data by evaluating the fluid "film" properties at the hot-wire temperature.

For these calculations of Nu_w the hot-wire calibration is assumed to be

$$Nu_d(\tilde{Re}_d) = \left(\frac{T_f}{T_\infty}\right)^{0.17} \left(A + B\tilde{Re}_d^n\right), \tag{9.33}$$

where $A = 0.24$ and $B = 0.56$ are taken from Collis and Williams (1959). The actual values chosen for A and B are unimportant because A is an additive constant on both sides of Equation 9.31, and B is then a multiplicative constant for Nu_w. For hot-wire diameters from 0.63 μm to 5 μm in Figure 9.2(b) the values of n are, for the purpose of this calculation, spaced evenly over the range 0.62 to 0.45 used by Krishnamoorthy. For varying overheat ratio, where $d = 5$ μm, $n = 0.45$.

The results shown in Figure 9.2 seem to suggest that Equation 9.6 can be simplified to

$$Nu_d(\tilde{Re}_{d,m}) = Nu_d(\tilde{Re}_d) + \frac{d}{y} Nu_w(\tilde{y}^+), \tag{9.34}$$

where both $Nu_d(\tilde{Re}_d)$ and $Nu_w(\tilde{y}^+)$ can be determined from measurements. If the hot-wire calibration is in the form of Equation 9.33, Equation 9.34 can be written as

$$\frac{\tilde{u}_m^+}{\tilde{u}^+} = \left[\frac{1}{B}\frac{\tilde{d}^+}{\tilde{y}^+}\left(\tilde{y}^+\tilde{d}^+\frac{\nu_\infty}{\nu_f}\right)^{-n}\left(\frac{T_\infty}{T_f}\right)^{0.17} Nu_w(\tilde{y}^+) + 1\right]^{1/n}, \tag{9.35}$$

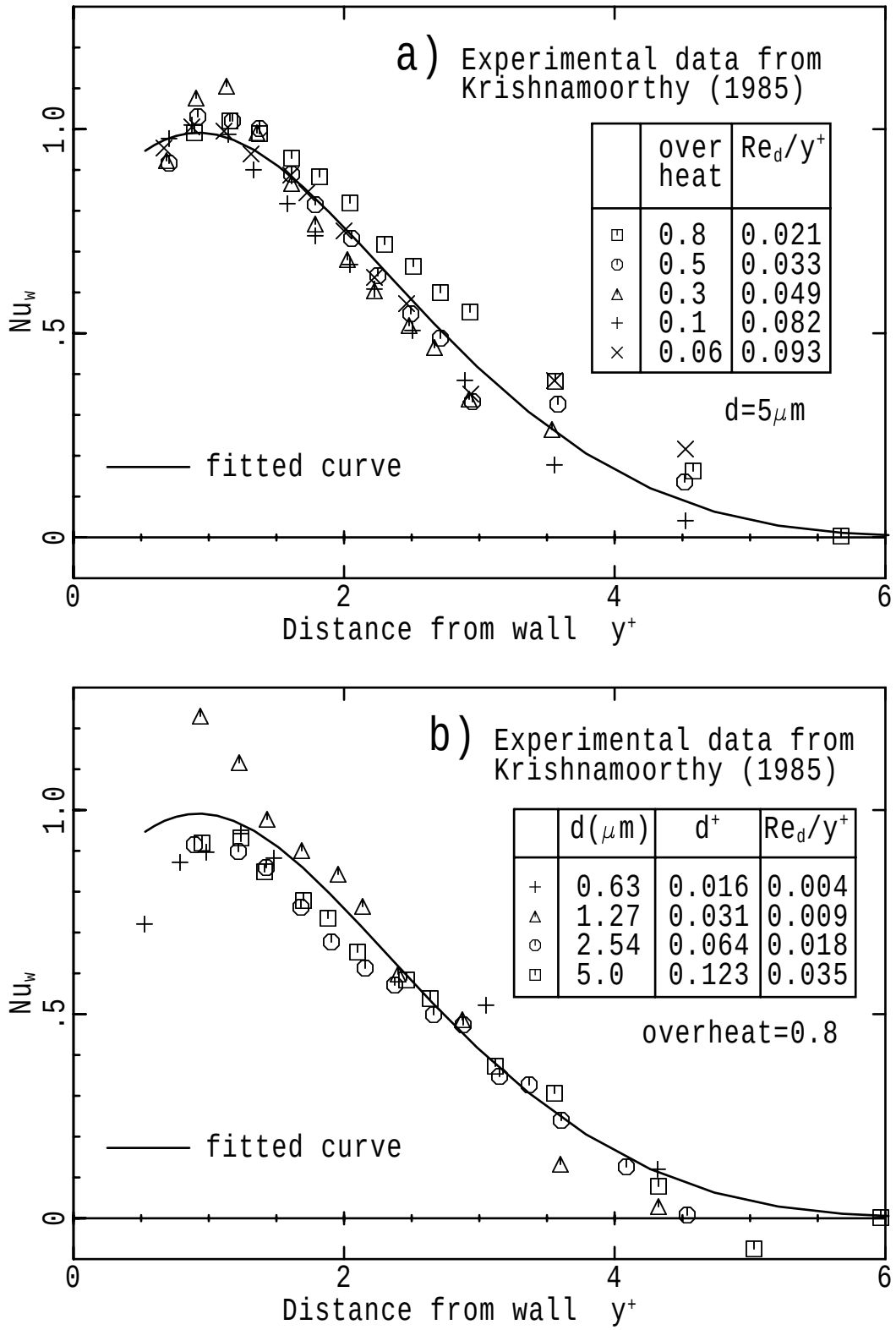

Figure 9.2: Nusselt number of heat transfer to the wall – inferred from Krishnamoorthy's (1985) data on the effect of (a) overheat ratio and (b) hot-wire diameter. Fluid properties are evaluated at the hot-wire temperature. The fitted curve is $Nu_w = e^{-P(y^+)}$, where $P(y^+) = 0.2859 - 0.6516y^+ + 0.4433y^{+2} - 0.0739y^{+3} + 0.0069y^{+4}$.

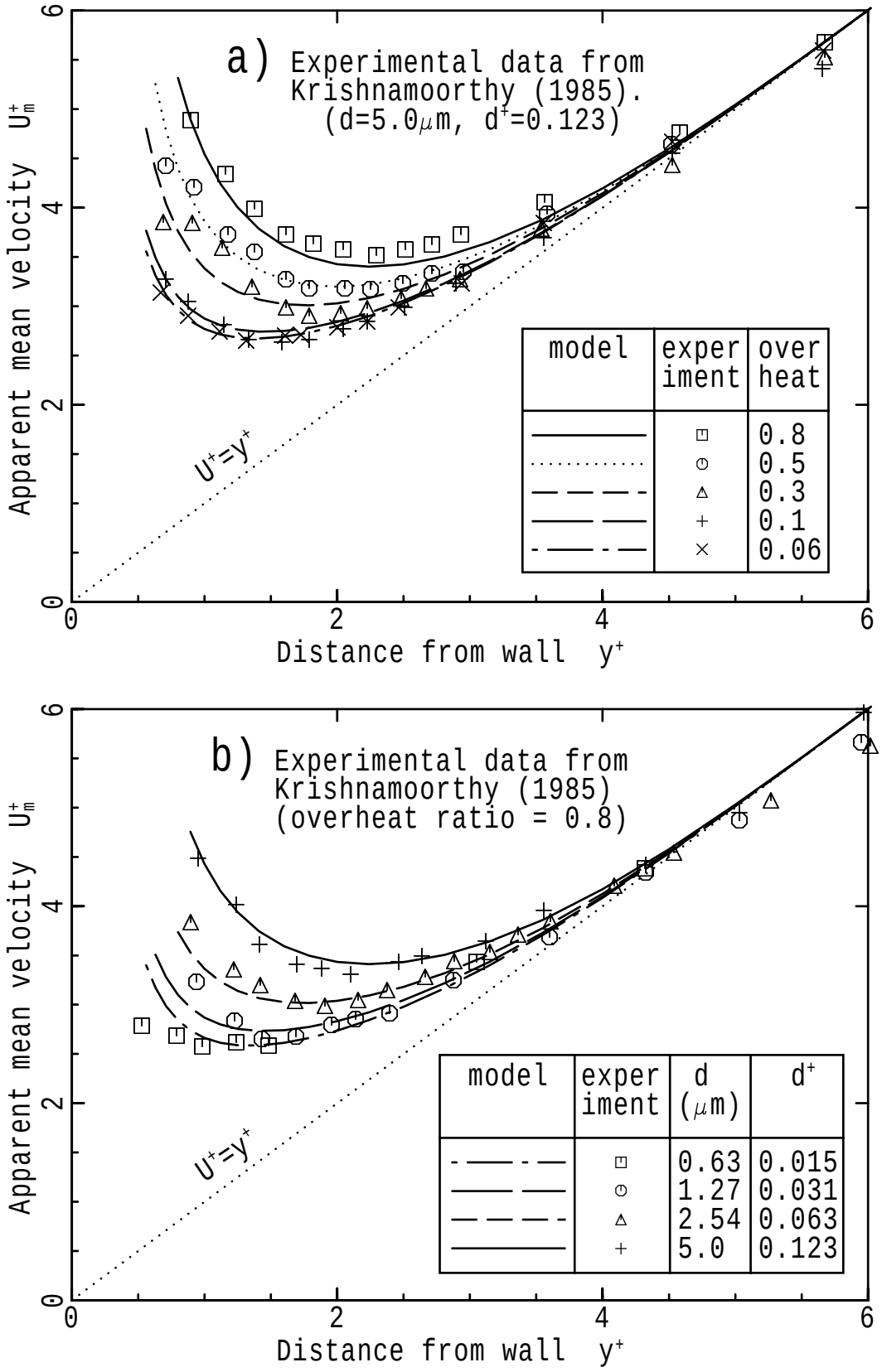

Figure 9.3: Comparison of the simple heat-transfer model with the experimental data of Krishnamoorthy et al. (1985) for the effect of varying (a) overheat ratio and (b) hot-wire diameter. $Nu_w(y^+)$ is obtained from the fitted curve of Figure 9.2.

where $\tilde{u}^+ = \tilde{y}^+$, and it can be used for predicting the effects on the velocity measurement of changing overheat ratio, wire diameter, friction velocity and filament material. Comparison of these predictions with measurements recorded in the research literature is useful for evaluating this simple heat-transfer model.

Varying overheat ratio. As shown in Figure 9.3(a), the effect of varying overheat ratio is modelled fairly accurately by evaluating fluid properties at the nominal hot-wire temperature. The effect of changing overheat ratio would therefore appear to arise almost entirely from the dependence of kinematic viscosity (and hence Reynolds number) on temperature. In comparison, the direct effect of changing temperature through the factor $(T_f/T_\infty)^{0.17}$ is smaller by about one order of magnitude.

Varying hot-wire diameter. For the effect of varying hot-wire diameter, the level of agreement between the model and the experimental data of Krishnamoorthy et al. (1985) is almost the same as for the effect of varying overheat ratio (Figure 9.3(b)). In Figure 9.4(a) the behaviour of the simple heat-transfer model is compared with data obtained by Zemskaya et al. (1979) for a range of filament diameters. For diameters less than 10 μm there is quite reasonable agreement between the model and the experimental data, but for 22.4 μm and 41.6 μm the sensitivity of the experimentally measured velocity, U_m^+, to changes in diameter is significantly less than the sensitivity predicted by the model.

Varying friction velocity. Oka & Kostic (1972), Zemskaya et al. (1979) and Janke (1986) have shown that if all parameters except distance from the wall and air speed (i.e. friction velocity) are fixed, U_m^+ is a function of only y^+. Inspection of Equation 9.35, where $\tilde{u}_m^+$ is a function of $\tilde{d}^+$, $\tilde{y}^+$ and ν_∞/ν_f, reveals that the simple heat-transfer model (Equation 9.34) is inconsistent with this well established experimental result. This disagreement between the model and the measurements of Zemskaya et al., which reveal no dependence on the free stream air speed in excess of the scatter of the data, is illustrated in Figure 9.4(b).

Different hot-wire materials. The 90%Pt–10%Rh alloy Wollaston wire used by Krishnamoorthy et al. (1985) has a much smaller temperature coefficient of resistivity (0.0016) than the other common hot-wire materials, tungsten (0.0048) and platinum (0.0039). Hot-wires, which are of different materials but are operated at the same overheat ratio, should therefore produce different velocity measurements because they are at different temperatures. However, the effect predicted by Equation 9.35 of replacing Krishnamoorthy's 90%Pt–10%Rh wire with tungsten and platinum wires (Figure 9.5) is not supported by the observations of Krishnamoorthy et al. (1985) who reported that changing the hot-wire material did not significantly alter the measured velocity, U_m^+. This seems to be quite an anomalous result because, as far as the mechanism of heat

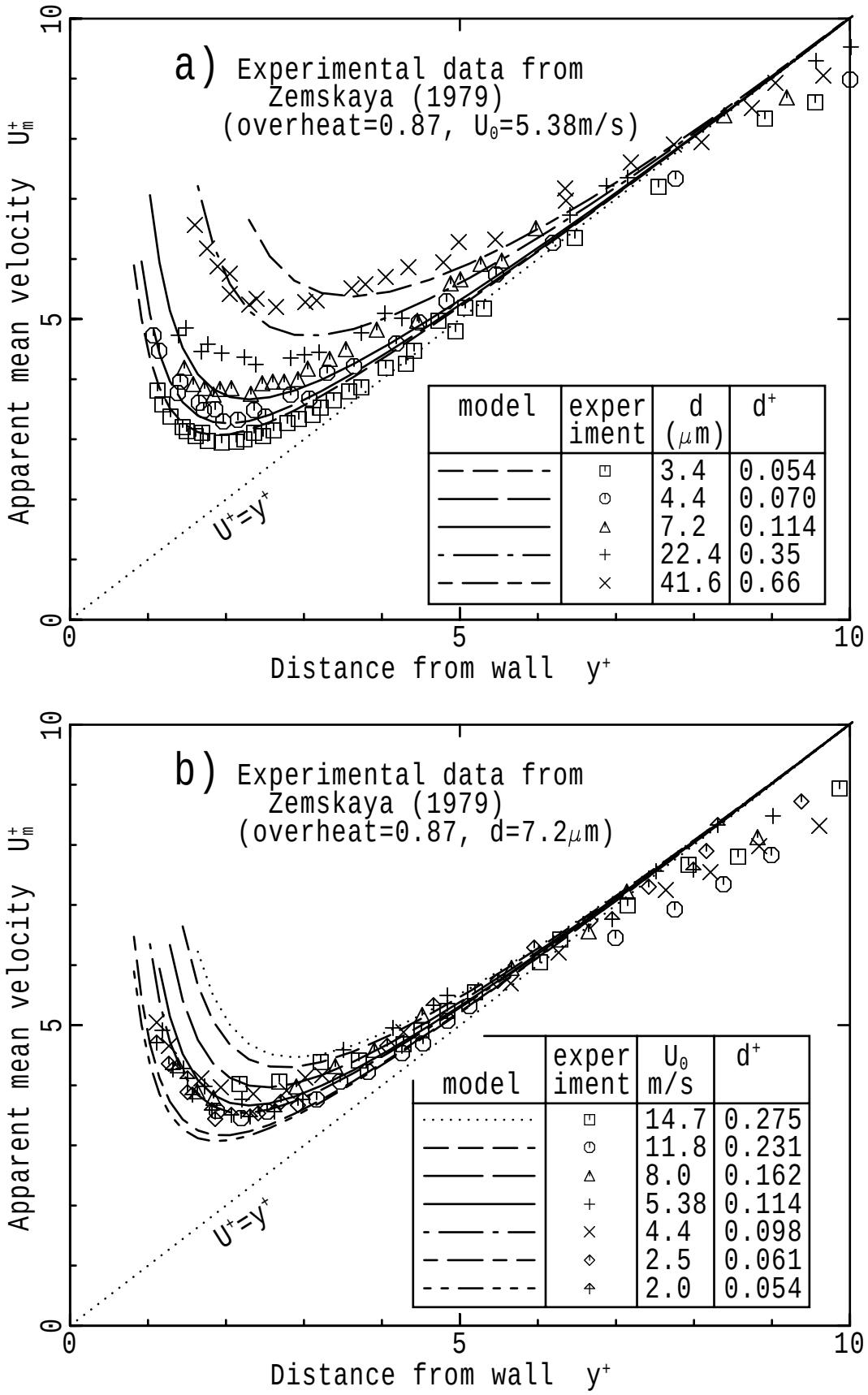

Figure 9.4: Comparison of the simple heat-transfer model with the experimental data of Zemskaya et al. (1979) for the effect of varying a) hot-wire diameter, d, and b) free stream air speed, U_0.

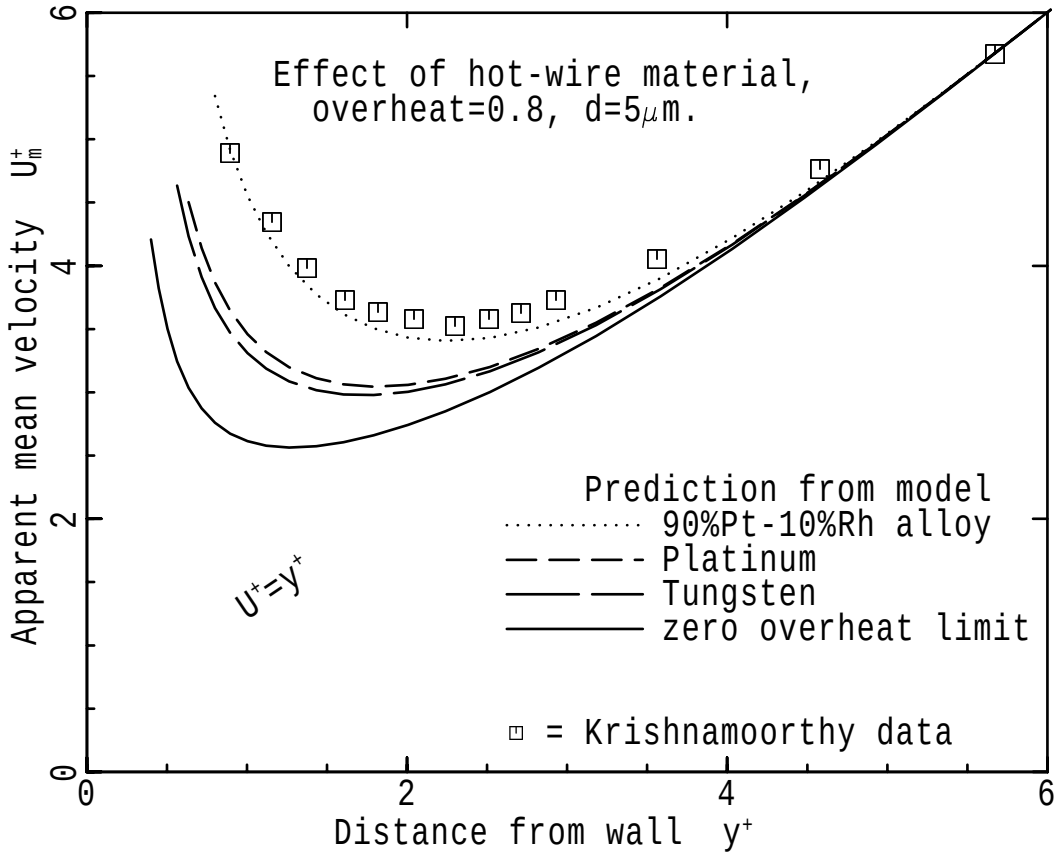

Figure 9.5: Prediction of the effect of changing the hot-wire material from 90%Pt-10%Rh alloy to Platinum and Tungsten. Curves are obtained from Equation 9.34.

transfer is concerned, changing the wire material and changing the overheat ratio are simply two different ways of changing the surface temperature of the hot-wire filament. The solid curve labelled “zero overheat limit” in Figure 9.5 represents the limiting minimum wall-proximity effect which is not physically realisable, but, according to the model, can be approached by reducing the overheat ratio towards zero or by increasing the hot-wire temperature coefficient of resistivity towards infinity.

In testing a model of wall-proximity effect against experimental data, one must recognise that it is very difficult to obtain accurate measurements of the low speeds and small distances from the wall which are typical of the viscous sublayer. The data processing technique therefore should be made as tolerant of experimental error as possible, and detailed comparisons with the experimental data should be interpreted with caution. This uncertainty is increased by the possibility that the hot-wire calibration formula, Equation 9.33, becomes less accurate as the flow around the hot-wire approaches the buoyant convection regime. One common fault in sublayer mean-velocity data is a failure to satisfy the fundamental requirement $U_m^+ = y^+$ at distances from the wall where wall-proximity error is negligible

(usually $3 < y^+ < 6$). In each of the Figures 9.2 to 9.5 the friction velocity has been adjusted by an empirical factor which forces $U^+ = y^+$. Almost identical results are obtained by the alternative but in principle unsatisfactory approach of assuming $U^+ = my^+$ where m is a constant close to but not equal to one.

The simple heat-transfer model seems to predict the effect of changing overheat ratio fairly well. However, modelling the effect of diameter changes is more fragile and modelling the effect of friction-velocity variations is unsuccessful.

9.5 Modified heat-transfer model

9.5.1 Matching the model with the data

Another difficulty with the simple heat-transfer model of wall-proximity effect (i.e. Equation 9.34) is that it does not produce credible r.m.s. levels, skewness or flatness of the streamwise velocity when it is used for "correcting" data from the turbulent viscous sublayer. This makes it necessary to review the assumptions underlying the simple heat-transfer model, that

(1) the heat flow to the wall (i.e. Nu_w) can be represented by a correction function of the form $f(\tilde{y}^+)$ and

(2) that the convected heat flow (Nu_c) is unaffected by wall proximity.

In an effort to find a better model of wall-proximity effect, many different Nusselt-function pairs, such as

$$Nu_c = \left(\frac{T_f}{T_\infty}\right)^{0.17} (A + BRe_d^n)\left(1 - Ce^{-y^{+2}}\right) \tag{9.36}$$

$$Nu_w = \frac{1}{\sqrt{d^+}}\, f_1(y^+), \tag{9.37}$$

have been tested against the experimental data of Krishnamoorthy et al. (1985). These Nusselt functions are required not only to produce the same changes in ΔU_m^+ as the Krishnamoorthy data when the overheat ratio and hot-wire diameter are varied, but are also required to make ΔU_m^+ independent of friction velocity (U_τ).

In the particular example defined by Equations 9.36 and 9.37, convected heat flow (Nu_c) is reduced below the hot-wire calibration (Nu_d) by the factor $1 - Ce^{-y^{+2}}$. This is intended to model the confining effect of the wall and the effect of fluid shear. With $C = \frac{2}{3}$, Equation 9.36 reduces to the free-air calibration at large y^+ and to one third of the free-air calibration when the hot-wire is very close to the wall. Equations 9.36 and 9.37 behave in a manner generally consistent with the measurements of Krishnamoorthy (1985) and they also produce a velocity error, ΔU^+, which is independent of U_τ.

However, the presence of the additional parameter d^+, which may be written as

$$d^+ = \left(\frac{\nu_f}{\nu_\infty}\right)\frac{Re_d}{y^+}, \tag{9.38}$$

makes them inconsistent with the three-parameter model (Equation 9.31) deduced from the dimensional analysis.

In general it has not been possible to model the effects of varying four different experimental parameters (overheat ratio, d, U_τ, y^+) with only the two nondimensional parameters, Re_d and y^+. This difficulty indicates that, in a heat-transfer model of wall-proximity effect, it is necessary to use at least one, and possibly two more parameters from those listed in Equation 9.28.

9.5.2 Heat-transfer mechanism at low Reynolds number

At conventional Reynolds numbers (Re_d of more than 1000 or so) the boundary layer formed on a cylinder with its axis normal to the flow is very thin in comparison with the cylinder diameter. In contrast, the Reynolds number of a hot-wire filament used for measurements in the viscous sublayer is typically in the range 0.003 to 0.3, and the boundary layer around the filament is expected to have a thickness which is at least an order of magnitude larger than the filament diameter (Equation 9.23). A Prandtl number in the order of unity ensures that the kinematic and thermal boundary layers are of approximately equal thickness, and so, if there is heat transfer to the wall ($Nu_w > 0$), the boundary layer of the hot-wire must bridge the gap between the filament and the wall. For such a thick boundary layer, the flow within a distance of one or two diameters of the wire is so retarded by viscosity that the dominant mechanism of heat transfer within this inner region is one of thermal diffusion [Langmuir, 1912, Bradshaw, 1971]. This thermal diffusion tends to be omni-directional in the x-y plane because it is driven by an essentially radial temperature gradient. Heat removal by laminar convection becomes significant only outside this inner diffusion region, in the outer region of the kinematic boundary layer around the filament. The relative importance of these two heat-transfer mechanisms at any location within the thermal boundary layer of the hot-wire filament is determined principally by the local Péclet number

$$\tilde{Pe} = \frac{\tilde{u}r}{\tilde{\alpha}}, \tag{9.39}$$

where $\tilde{u}$ is the air speed in the undisturbed wall sublayer, r is radial distance from the hot-wire axis and $\tilde{\alpha}$ is the local thermal diffusivity. The velocity distribution in the viscous sublayer ensures that the inner diffusion region is heavily skewed towards the wall and its size (e.g. $\sqrt{\text{area}}$) is inversely proportional to distance from the wall. For a hot-wire filament at these very low Reynolds numbers, the inner diffusion region is very thick, and the effective l/d ratio for convective outer-region heat transfer is much lower than the actual l/d ratio. If the effective l/d ratio is so low that the heat flux field in the outer convective

region is significantly three dimensional, the convective heat transfer cannot be described adequately by a function of only Re_d and y^+.

Champagne, Sleicher & Wehrmann (1967) have measured the convection Nusselt number, Nu_d, as a function of the Reynolds number, Re_d, for several l/d ratios. Their results indicate that it might be possible to model the effects of changing l/d ratio approximately by writing the coefficients A and B of the hot-wire-calibration relation (Equation 9.33) as functions of l/d. In adopting this suggestion the Nusselt-number functions can be written in a form which guarantees independence of U_m^+ from the friction velocity:

$$Nu_d\left(\tilde{Re}_{d,m}, \frac{l}{d}\right) = \left(\frac{T_f}{T_\infty}\right)^{0.17}\left(A + B\tilde{Re}_{d,m}^n\right), \tag{9.40}$$

$$Nu_c\left(\tilde{Re}_d, \tilde{y}^+, \frac{l}{d}\right) = \left(\frac{T_f}{T_\infty}\right)^{0.17}\left(A + B\left[1 - Ce^{-\tilde{y}^{+2}}\right]\tilde{Re}_d^n\right) \tag{9.41}$$

and

$$Nu_w\left(\tilde{Re}_d, \tilde{y}^+\right) = Re_d^{n-1} y^+ f(y^+), \tag{9.42}$$

where the calibration coefficient A can be any function of l/d, $n = 0.45$, and B is a monotonically increasing function of l/d selected to produce the desired dependence of U_m^+ on hot-wire diameter. The coefficient C in Equation 9.41, which is given a value of $\frac{2}{3}$, provides for attenuation of convective heat transfer by wall proximity.

9.5.3 Behaviour of the modified heat-transfer model

At this point it is useful to change the scaling length of Nu_w from y to d, and so change the definition from that given in Equation 9.4 to

$$\tilde{Nu}_w = \frac{\tilde{h}_w d}{k_f}. \tag{9.43}$$

The thermal balance, Equation 9.6, is then simplified to

$$Nu_d(\tilde{Re}_{d,m}, Pr_f) = \tilde{Nu}_c + \tilde{Nu}_w, \tag{9.44}$$

and Equation 9.42 becomes

$$Nu_w\left(\tilde{Re}_d, \tilde{y}^+, \frac{\nu_f}{\nu_\infty}\right) = \left(\frac{\nu_f}{\nu_\infty}\right)^s \tilde{Re}_d^n \frac{1}{\tilde{y}^+} f(\tilde{y}^+), \tag{9.45}$$

where, in the first instance, $s = 1$. If the Nusselt numbers in Equation 9.44 are replaced by the appropriate expressions from Equations 9.40, 9.41 and 9.45,

$$\left(\frac{T_f}{T_\infty}\right)^{0.17} B\tilde{Re}_{d,m}^n = \left(\frac{T_f}{T_\infty}\right)^{0.17} B\left[1 - Ce^{-\tilde{y}^{+2}}\right]\tilde{Re}_d^n + \left(\frac{\nu_f}{\nu_\infty}\right)^s Re_d^n \frac{1}{y^+} f(y^+). \tag{9.46}$$

On ignoring the weak effect of the temperature ratio, it is immediately clear that attenuation of Nu_c by wall proximity is experimentally indistinguishable from a change in Nu_w, which represents the

heat transferred to the wall. With $C = 0$, Nu_w represents both the heat transferred to the wall and the attenuation of heat convected away by the flow. The independence of $\Delta U^+(y^+)$ from the friction velocity is easily verified by substituting $d^+U^+\nu_\infty/\nu_f$ for the Reynolds number in Equation 9.46.

In Figure 9.6 the behaviour of the model defined by Equations 9.44, 9.40, 9.41 (with $C = 0$) and 9.45 is compared with the experimental data of Krishnamoorthy et al. (1985). The solid and dashed lines representing the model are obtained by fitting a single function of the form

$$f(y^+) = e^{-P(y^+)} \tag{9.47}$$

to all of Krishnamoorthy's (1985) data. The experimental data themselves are plotted in the figure as various symbols.

When the film temperature is defined in the conventional manner as $T_f = T_\infty + 0.5\Delta T$, optimal modelling for the effect of varying overheat ratio is achieved with a viscosity-ratio exponent $s = 0.67$. The requirement for a non-zero value of s indicates that wall-proximity effect depends significantly on distribution of fluid properties around the hot-wire filament. Unfortunately, there is no acceptable definition for a representative film temperature which permits the dependence on fluid properties to be absorbed into the Reynolds number. With the values of hot-wire calibration coefficient B tabulated in Figure 9.6(c), the modified heat-transfer model produces essentially the same range of velocity measurements as the experiments. The selected values of B (Figure 9.7) are consistent with a function of l/d which converges to a finite limiting value at $l/d = \infty$. The effect of varying friction velocity is not shown in Figure 9.6 because the algebraic form of the functions defining the model (Equations 9.40, 9.41 and 9.42) guarantees that U_m^+ is independent of friction velocity.

For the sake of simplicity in the calculations, all the dependence on l/d is incorporated into the calibration coefficient B. This is sufficient to demonstrate that an apparent dependence of wall-proximity effect on filament diameter might actually be a dependence on the l/d ratio, but it is unlikely to produce an accurate model for the behaviour of the Nusselt-number functions. For example, if Nu_d and Nu_c depend on l/d, then, in general, so does Nu_w. Unfortunately, apart from an indication that the calibration coefficient A is increased by end conduction losses [Champagne et al., 1967], there are no experimental data which quantify the dependence of these Nusselt numbers on l/d.

9.6 Summary and conclusions

In a dimensional analysis of the heat flow from a hot-wire filament in a viscous sublayer, Nusselt numbers are considered as functions of the dimensionless parameters $\tilde{y}^+$, $\tilde{Re}_d$, l/d, k_w/k_f, Pr_∞, k_f/k_∞, ρ_f/ρ_∞, and ν_f/ν_∞. If wall conductivity, probe geometry, hot-wire temperature and ambient fluid

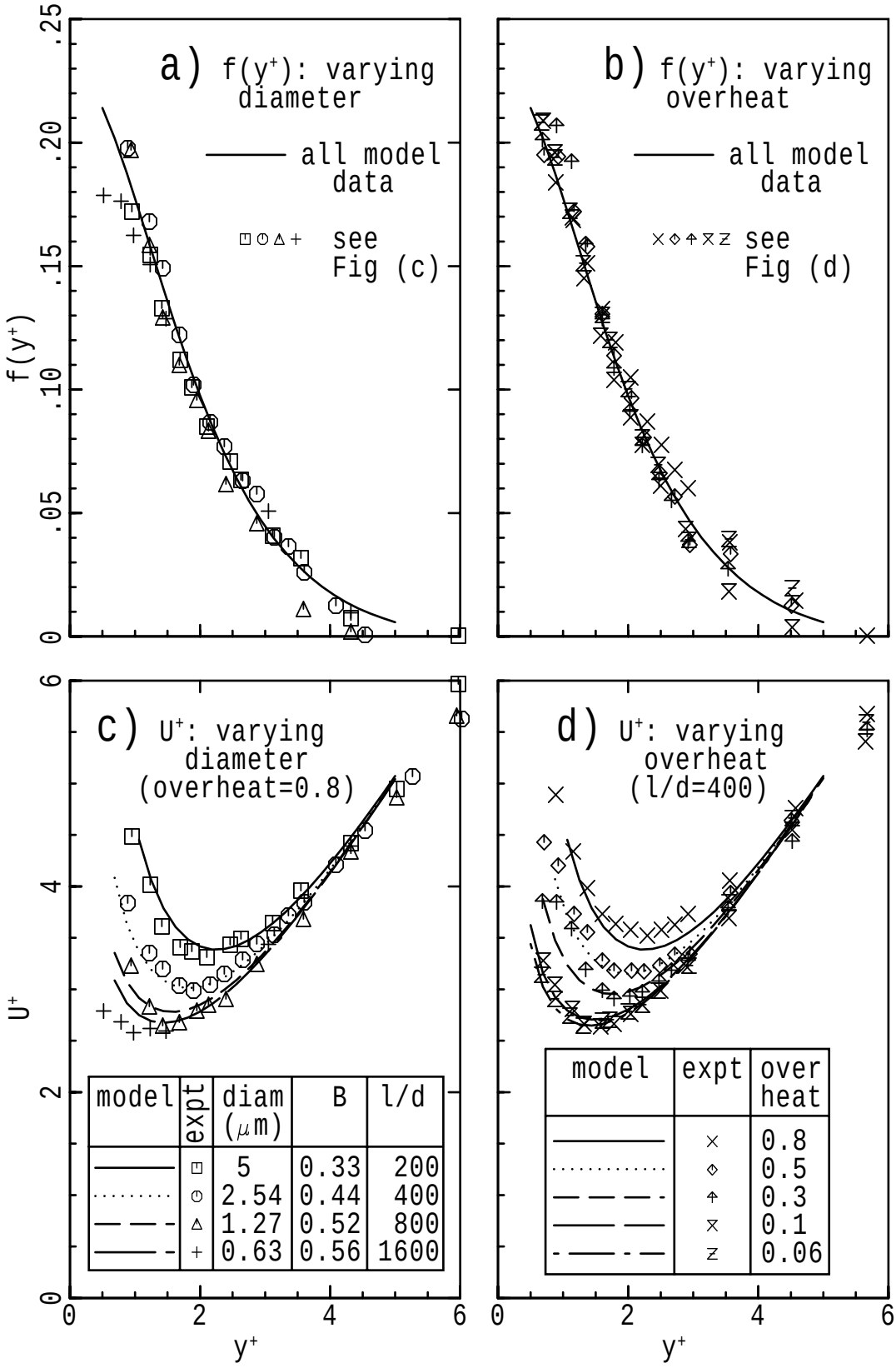

Figure 9.6: Function $f(y^+)$ and measured velocity U_m^+ for a modified heat-transfer model constructed to match the results of Krishnamoorthy (1985) for varying hot-wire diameter ((a) & (c)) and overheat ratio ((b) & (d)).

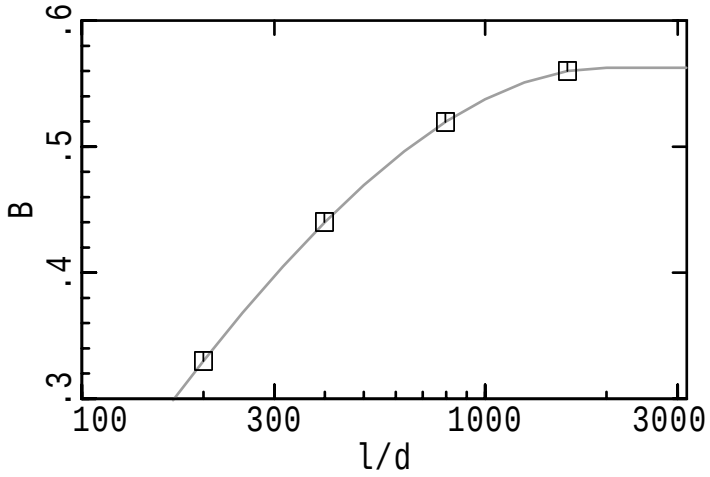

Figure 9.7: Variation of the values selected for the hot-wire calibration coefficient, B, as a function of the estimated l/d ratio. These values, indicated by □ symbols, are used for the calculation of Figure 9.6. The trend is shown by a curve fitted to the $(l/d, B)$ coordinates.

properties do not change, the Nusselt numbers depend only on $\tilde{y}^+$ and $\tilde{Re}_d$. If the hot-wire overheat ratio is changed, it is necessary to include a parameter such as ν_f/ν_∞ which can account for the effects of local variations in temperature-dependent fluid properties. In order to model the effect of changing the filament diameter, it is also necessary to retain the parameter l/d. Thermal wall-proximity effect can then be described by

$$Nu_d\left(\tilde{Re}_{d,m}, \frac{l}{d}\right) = Nu_c\left(\tilde{Re}_d, \tilde{y}^+, \frac{l}{d}, \frac{\nu_f}{\nu_\infty}\right) + Nu_w\left(\tilde{Re}_d, \tilde{y}^+, \frac{l}{d}, \frac{\nu_f}{\nu_\infty}\right), \tag{9.48}$$

where Nu_d is the hot-wire calibration, Nu_c represents heat convected to the fluid far field and Nu_w represents heat flow to the wall.

Two theoretical models of the heat flow are derived from the dimensional analysis. The first, which is called the "simple heat-transfer" model, assumes a simplified heat-transfer relationship of the form

$$Nu_d(\tilde{Re}_{d,m}) = Nu_d(\tilde{Re}_d) + \frac{d}{y} Nu_w(\tilde{y}^+). \tag{9.49}$$

This model cannot satisfy the criterion $\Delta U^+ = f(y^+)$ for fixed probe geometry, and it cannot correctly predict the effect of changing the filament diameter. The second or "modified heat-transfer" model, which is a much larger subset of Equation 9.48, is constrained to satisfy $\Delta U^+ = f(y^+)$ by making Nu_w proportional to Re_d^n, where n is the Reynolds-number exponent of the hot-wire calibration (Equation 9.40). For the purpose of correcting velocity measurements in the viscous sublayer, the effects of wall proximity on Nu_c can then be transferred to Nu_w. The results of comparing the model with the experimental data of Krishnamoorthy et al. (1985) suggest that dependence on the

viscosity-ratio parameter can be removed from Nu_c and written into Nu_w as the factor $(\nu_f/\nu_\infty)^{0.67}$, so that $Nu_c(\tilde{Re}_d, l/d) = Nu_d(\tilde{Re}_d, l/d)$. If the probe geometry remains unchanged, the l/d parameter can be ignored and the form of the "modified heat-transfer" model used for correction of experimental data becomes

$$Nu_d(\tilde{Re}_{d,m}) = Nu_d(\tilde{Re}_d) + \left(\frac{\nu_f}{\nu_\infty}\right)^{0.67} \tilde{Re}_d^n \frac{1}{\tilde{y}^+} f(\tilde{y}^+). \tag{9.50}$$

The variation of wall-proximity error with hot-wire filament diameter is due to the geometric parameter, l/d, which controls the three-dimensionality of the outer, convective heat-flow field around the filament. Examination of the non-dimensional heat-transport equation (Equation 9.27) reveals that temperature-dependent viscosity changes in the vicinity of the hot-wire filament are equivalent to inversely proportional changes in Prandtl number. Decreasing the filament diameter or overheat ratio cannot, therefore, reduce wall-proximity effect enough to avoid the need for correcting sublayer velocity measurements. In practice, reducing hot-wire diameter and overheat ratio can lead to greatly increased experimental difficulties, for example, increased thermal drift, poor frequency response, instability of the C.T.A. bridge and extreme fragility of the probes. In ideal circumstances, wall-proximity effect is best avoided by selecting a fluid with a very high Prandtl number.

9.7 Notation

a	overheat ratio of the hot-wire filament; $a = \dfrac{\text{operating resistance}}{\text{cold resistance}} - 1$
A, B	0.24 and 0.56 respectively, coefficients for the Collis and Williams (1959) hot-wire calibration relation
A	πdl, surface area of the hot-wire filament
c	specific heat
C	an attenuation coefficient of trial functions for the convection Nusselt number, Nu_c
C_1, C_2	constants of proportionality in approximations for the thickness of the kinematic and thermal "boundary-layer" around the hot-wire filament
d	diameter of the hot-wire filament
Ec	$U_\tau^2/(c_\infty \Delta T)$, an Eckert number for heat transfer within the viscous sublayer
f	functions of y^+ which are used for describing the velocity error or Nusselt number of heat transfer to the wall
h_c	heat-transfer coefficient for heat convected far downstream from a hot-wire filament
h_w	coefficient for heat transfer from the hot-wire filament to the wall
k	thermal conductivity
l	active length of hot-wire filament

m	slope of the experimentally measured non-dimensional mean velocity distribution in the viscous sublayer, $U^+ = my^+$
n	velocity exponent for a hot-wire calibration; usually $n = 0.45$
Nu_c	$h_c d/k_f$, Nusselt number for heat which is convected far downstream from a hot-wire filament and is *not* eventually transferred to the wall
Nu_d	hd/k_f, Nusselt number for heat transfer from a cylinder; i.e. hot-wire calibration
Nu_w	$h_w y/k_f$ or $h_w d/k_f$, Nusselt number for heat transfer from a hot-wire filament to a solid wall
$O(x)$	within an order of magnitude of x
$P(y^+)$	polynomials used for approximating Nu_w
Pe	Ud/α, Péclet number
Pr	$c\mu/k$, Prandtl number
q_{conv}	the part the heat flow from a hot-wire filament which is convected far downstream by the fluid and is *not* eventually transferred to the wall
q_{total}	total heat flow rate from a hot-wire filament
q_{wall}	heat-transfer rate from hot-wire filament to the wall
Re_d	Ud/ν_f, Reynolds number of a hot-wire filament
r	(radial) distance from axis of the hot-wire filament
s	exponent of viscosity ratio; $(\nu_f/\nu_\infty)^s$ is used for modelling the effect of changing hot-wire temperature
t	time
T	fluid temperature
U_0	speed of a free stream flow
u	streamwise component of the velocity vector u
u_i	velocity tensor
u_τ	$\sqrt{\tau_w/\rho_f}$, friction velocity of a boundary layer
x_i	location tensor
y	distance between the hot-wire filament and the wall
α	$k/\rho c$, thermal diffusivity
ΔT	nominal temperature of the hot-wire filament above the ambient fluid temperature
ΔT_w	temperature of the wall-surface above the ambient fluid temperature
Δu	$u_m - u$, error in measured velocity due to wall-proximity effect
δ	thickness of the shear-flow region around the hot-wire filament
δ_T	thickness of the thermal-diffusion region (or thermal "boundary layer") around the hot-wire filament
θ	$\tilde{T}/\Delta T$, non-dimensional temperature of the fluid

μ	dynamic viscosity
ν	kinematic viscosity
ρ	density
τ_w	wall shear stress generated by the boundary layer

superscripts

$^+$	scales the quantity on the viscous flow variables U_τ and ν_∞, e.g. $U^+ = U/U_\tau$ and $\tilde{y}^+ = y\tilde{u}_\tau/\nu_\infty$
$\tilde{}$	used for indicating a quantity which may vary as a function of time.

subscripts

$_f$	for properties of the fluid - evaluated at the film temperature, which is usually defined as $T_f = T_\infty + \Delta T/2$
$_{i,j}$	tensor subscripts 1,2 or 3 for vector components.
$_m$	indicates a quantity as measured (i.e. not corrected for wall-proximity effect).
$_w$	for properties of the wall material.
$_{1...9}$	used for distinguishing similar or related functions.
$_\infty$	for properties of the fluid far field.

Upper case is used for indicating time-averaged or constant values. All physical quantities are expressed in SI units.

Chapter 10

Correction of experimental data

10.1 Correction methods

Three methods of correcting for the thermal component of wall-proximity effect are described in this chapter. The first is a "velocity-error" method based on the experimental observation $\Delta U^+ = f(y^+)$ and developed from the work of Oka and Kostic (1972), and Bhatia et al. (1982). The second technique is derived from the simple heat-transfer model presented in Section 9.4. The third correction method is based on a modified heat-transfer model (Section 9.5) designed to overcome the deficiencies of the second method. This is done by using the parameters l/d and ν_f/ν_∞ to decouple the effects of varying hot-wire diameter and overheat ratio from the effect of varying air speed, and by selecting Nusselt functions which satisfy the criterion $\Delta U^+ = f(y^+)$. All three methods are consistent with the main result of the dimensional and order analysis in Chapter 9 (Equation 9.48). In each case a correction function $f(y^+)$ is formulated from the experimental data. The correction function is then applied via a correction algorithm to each sample in the velocity data stream. It is assumed that the aerodynamic effects of wall proximity are avoided through appropriate design of the hot-wire probe. The results from applying each of these methods are presented and discussed in Section 10.3.

10.1.1 Velocity-error method

Oka and Kostic (1972) and Hebbar (1980) have treated wall-proximity effect as a velocity error, and so have used a correction of the form

$$U^+ = U_m^+ - \Delta U^+(y^+). \tag{10.1}$$

They calculated the error ΔU^+ by assuming a sublayer mean velocity distribution $U^+ = y^+$ for the two-dimensional flat-plate turbulent boundary layer. With an independently determined wall-shear

stress, the mean velocity measurements in more complex flows could then be corrected. Bhatia et al. (1982) also used a velocity-error formulation (Equation 10.1) but, because their error was calculated from a numerical solution of the energy equation, they were able to obtain by iteration a correction for each sampled value of the instantaneous velocity and a correction for the instantaneous friction velocity. Acharya and Escudier (1984) have since shown that, by recasting the velocity error into the form

$$\frac{\Delta U}{U_m} = F\left(\frac{yU_m}{\nu_\infty}\right), \tag{10.2}$$

the velocity correction can be found without iteration and without measurement of the friction velocity.

10.1.1.1 Formulating the correction function

The first step in calculating a useful velocity-error function of the form $\Delta U^+(y^+)$ is to obtain (using the hot-wire probe) a reliable measurement of the uncorrected mean-velocity distribution in the viscous sublayer and buffer regions of the turbulent boundary layer. These data are non-dimensionalised with wall variables, and so are presented as a function of y^+. As a check for absence of aerodynamic effects, the measurement should show that the effects of wall proximity are confined to the viscous sublayer region, $y^+ < 5$. The next step is to calculate the error in the velocity measurement by subtracting an estimate for the actual mean velocity from the data. Oka and Kostic (1972) and Hebbar (1980) assumed $U^+ = y^+$. However, unless the friction velocity has been deduced directly from the mean velocity gradient in the sublayer, which can be quite difficult if the sublayer measurements are dominated by the wall-proximity effect, this assumption may not produce a velocity error, ΔU^+, which tends to zero as distance from the wall increases. A convenient way of overcoming this problem is to calculate the error with

$$\Delta U^+ = U_m^+ - my^+. \tag{10.3}$$

The coefficient m is chosen by fitting the straight line $U^+ = my^+$ to the experimental data over the region where wall-proximity effect is negligible, typically $3 < y^+ < 7$, so that ΔU^+ becomes zero as the hot-wire filament moves away from the wall and out of wall proximity. It should be emphasised that the factor m is only a means of improving the usefulness of imperfect experimental data, and that for reliable experimental data m should be very close to one.

After applying Equation 10.3 to obtain the ΔU^+ data, it is necessary to fit a suitable analytic formula so that the velocity error can be evaluated at arbitrary distance from the wall. Various rational functions of the form

$$\Delta U^+ = f(y^+) = y^{+j} P_1(y^+), \tag{10.4}$$

which contain a polynomial $P_1(y^+)$ selected by a least-squares process, have been tested. While the best choice for the value of j appears to be $j = -1$, all of these functions fail because the fitting error

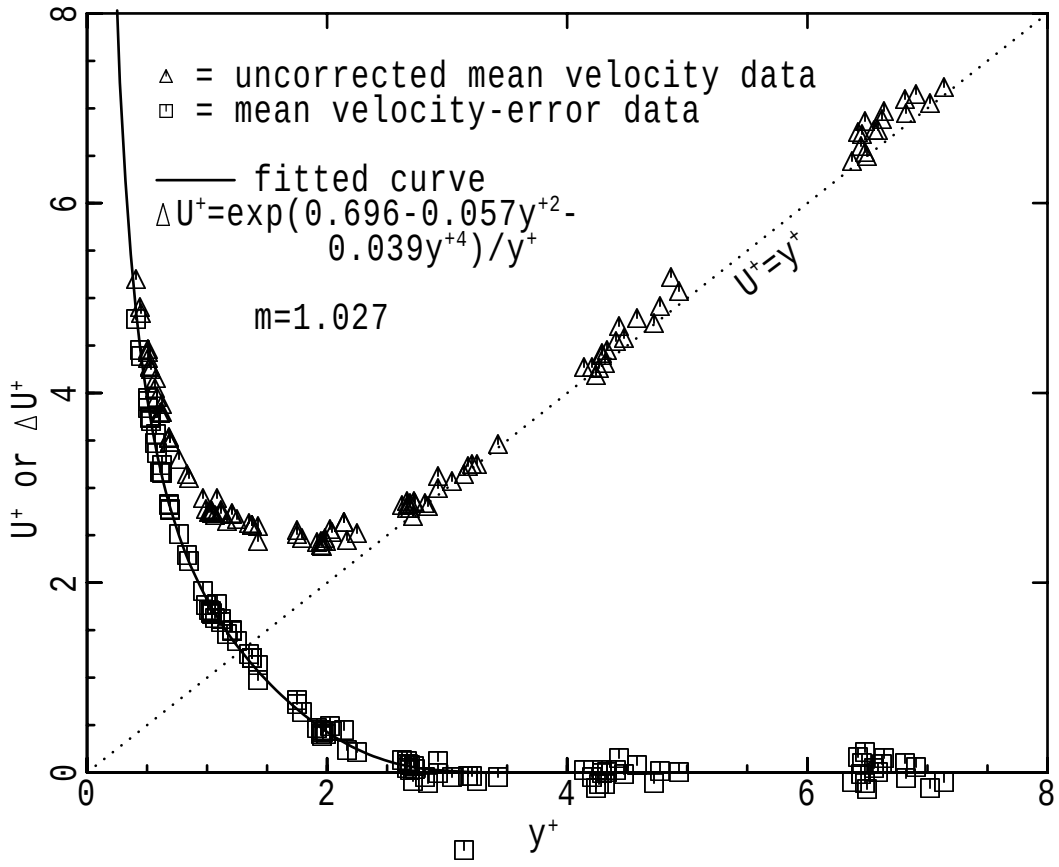

Figure 10.1: Measurement error calculated from experimental data, showing typical mean-velocity measurements, inferred velocity distribution, wall-proximity error and fitted error curve in the viscous sublayer.

at the ends of the domain cannot be controlled properly. For acceptable results with a wide range of experimental data, the selected function $f(y^+)$ should have an asymptote proportional to y^{-1} at the wall and an asymptote of zero at a large distance from the wall. The curve-fitting technique can then be directed at minimising the fitting error in the mid-range of the data without sacrificing accuracy at the ends of the domain. The y^{-1} asymptote at the wall is consistent with the observation of Zemskaya et al. (1979) and of Janke (1987) that $U_m^+ y^+$ approaches a constant value when the velocity error, ΔU^+, becomes much larger than the actual velocity, U^+. The function eventually chosen to represent the velocity error is

$$\Delta U^+ = f(y^+) = \frac{1}{y^+} e^{-P_2(y^{+2})}, \tag{10.5}$$

where $P_2(y^{+2})$ is a polynomial. The process of calculating the measurement error from experimental data is illustrated in Figure 10.1. The velocity-error data are calculated from experimental velocity distributions using Equation 10.3, and a curve of the form Equation 10.5 is fitted to them. In practice, the polynomial $P_2(y^{+2})$ for Equation 10.5 never needs to be of order greater than two, whereas the

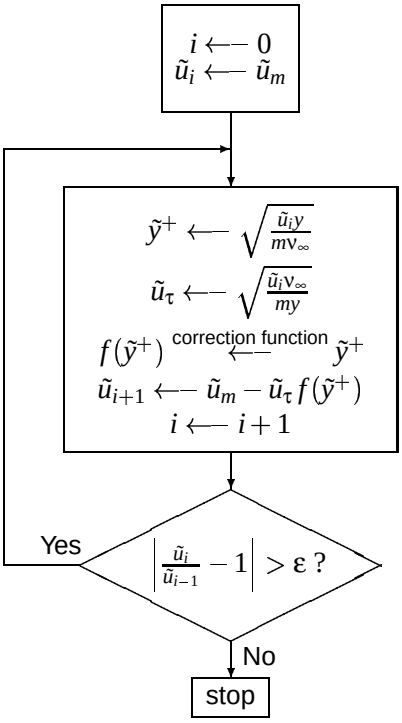

Figure 10.2: Flow-chart of iteration procedure for the velocity error model

rational function, Equation 10.4, frequently requires a polynomial of order 5 or more, and even then produces inferior results.

10.1.1.2 The data correction process

In terms of the velocity error $\Delta U^+ = f(y^+)$, the dependent and independent variables in Equation 10.2 are

$$\frac{\Delta U}{U_m} = \frac{f(y^+)}{f(y^+) + y^+} \tag{10.6}$$

and

$$\frac{yU_m}{\nu_\infty} = y^+ (f(y^+) + y^+) \tag{10.7}$$

respectively, and so Acharya's reformulation of the measurement error (Equation 10.2) can be written as the parametric equation

$$\left(\frac{yU_m}{\nu_\infty}, \frac{\Delta U}{U_m}\right) = \left(y^+ \left[f(y^+) + y^+\right], \frac{f(y^+)}{f(y^+) + y^+}\right), \tag{10.8}$$

where the parameter is y^+. If this is modified to take account of imperfect experimental data (Equation 10.3),

$$\left(\frac{yU_m}{\nu_\infty}, \frac{\Delta U}{U_m}\right) = \left(y^+ \left[f(y^+) + my^+\right], \frac{f(y^+)}{f(y^+) + my^+}\right) \tag{10.9}$$

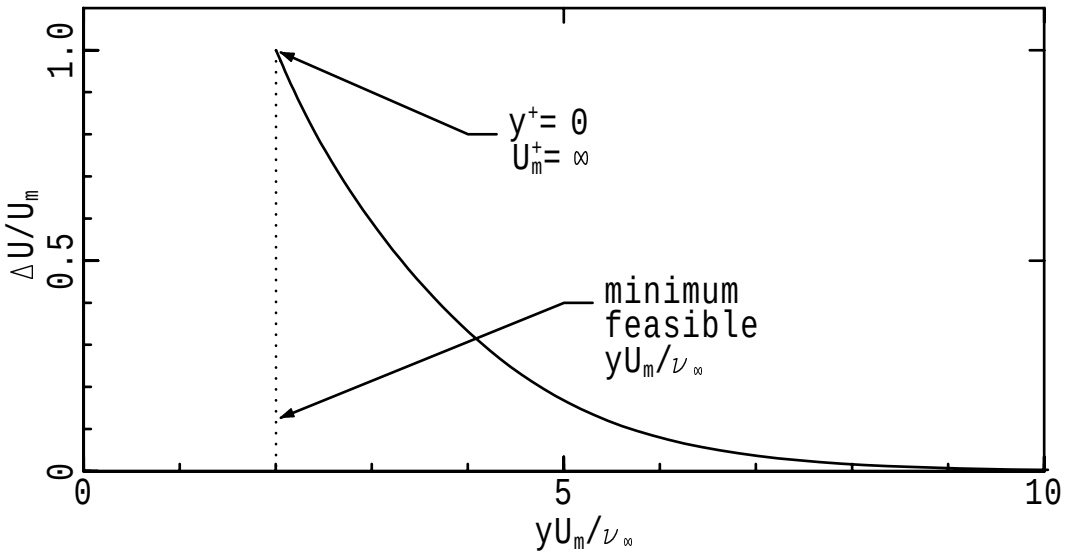

Figure 10.3: Look-up table for correcting wall-proximity error; prepared from the data in Figure 10.1.

can be used to generate a look-up table of $\Delta U/U_m$ versus yU_m/ν_∞. The correction procedure is to calculate yU_m/ν_∞ and then interpolate an approximate value for the required correction, $\Delta U/U_m$, from the table. If necessary, the accuracy of the estimate produced by interpolation can be refined by the iteration method of Bhatia et al. (1982). A flow-chart for this iteration algorithm is shown in Figure 10.2. Tests for non-convergence are incorporated into the software but are not shown in the flow-chart. This correction procedure (i.e. interpolation from a table followed by iterative refinement), is used for producing the corrected velocity results presented in Section 10.3. A correction procedure consisting only of Bhatia's iteration converges to an accuracy of about one in 20,000 in 12 to 18 iterations. In contrast, use of linear interpolation from a table of 100 coordinate pairs requires only 2 or 3 refining iterations to achieve the same accuracy. Another advantage of using the look-up table is that the table has a well defined minimum abscissa, yU_m/ν_∞, at which $\Delta U/U_m = 1$. This is illustrated in Figure 10.3 by plotting a look-up table which is calculated from the mean-velocity measurements of Figure 10.1. If a velocity measurement produces an abscissa smaller than the minimum feasible value, which is shown as a vertical dotted line in Figure 10.3, correction for wall-proximity effect cannot be performed and the iteration procedure diverges. Thus, the feasibility of correction can be tested without actually waiting for the iteration to diverge.

10.1.1.3 Adjusting $f(y+)$ for formulation-from-turbulence error

One difficulty with this method of correcting for wall-proximity effect is that the correction is calculated from time-averaged velocity data, but it is applied to each individual data sample. As a conse-

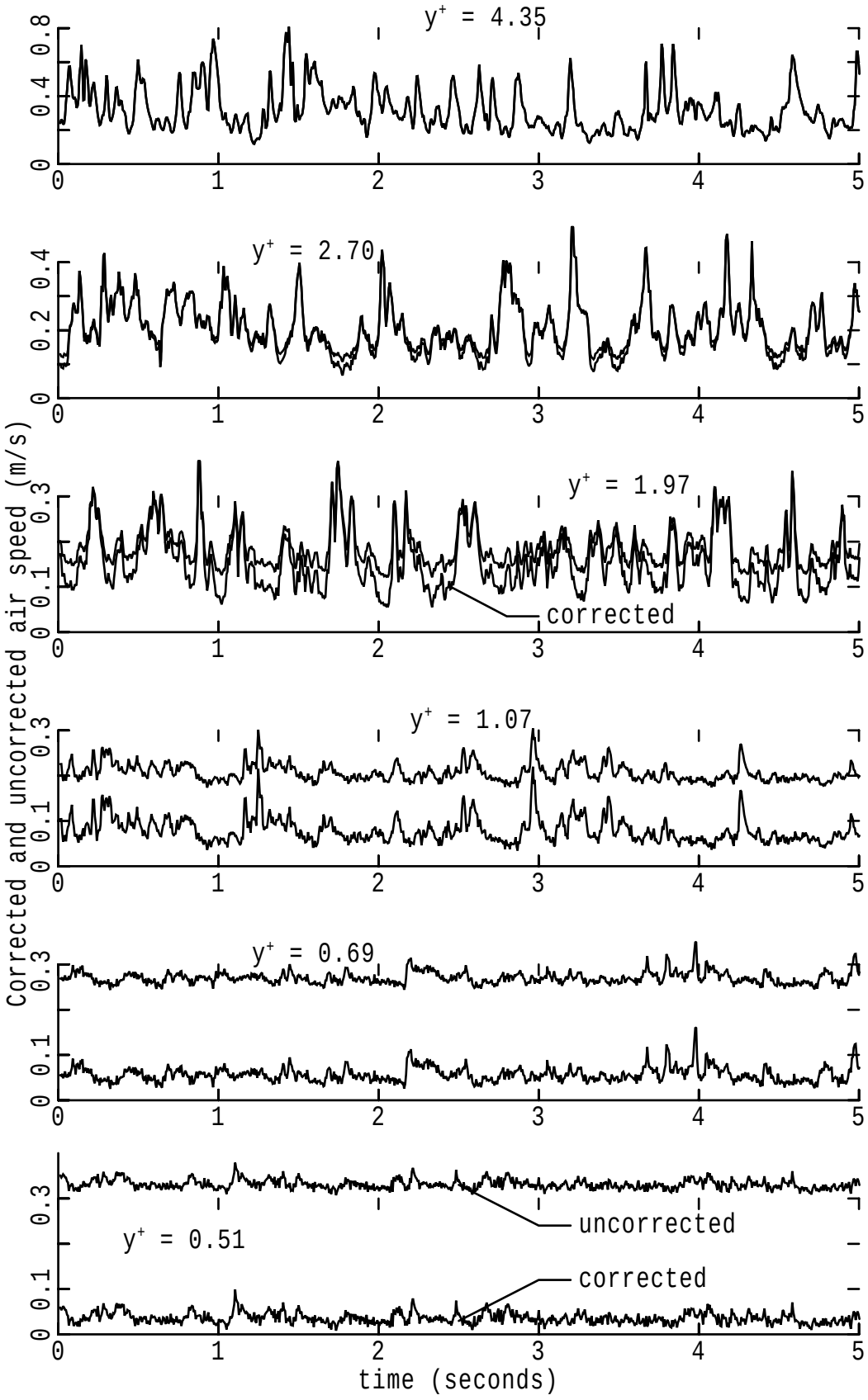

Figure 10.4: Comparison of the uncorrected and corrected velocity signals. The upper trace in each graph is the uncorrected signal. The lower trace is the corrected signal.

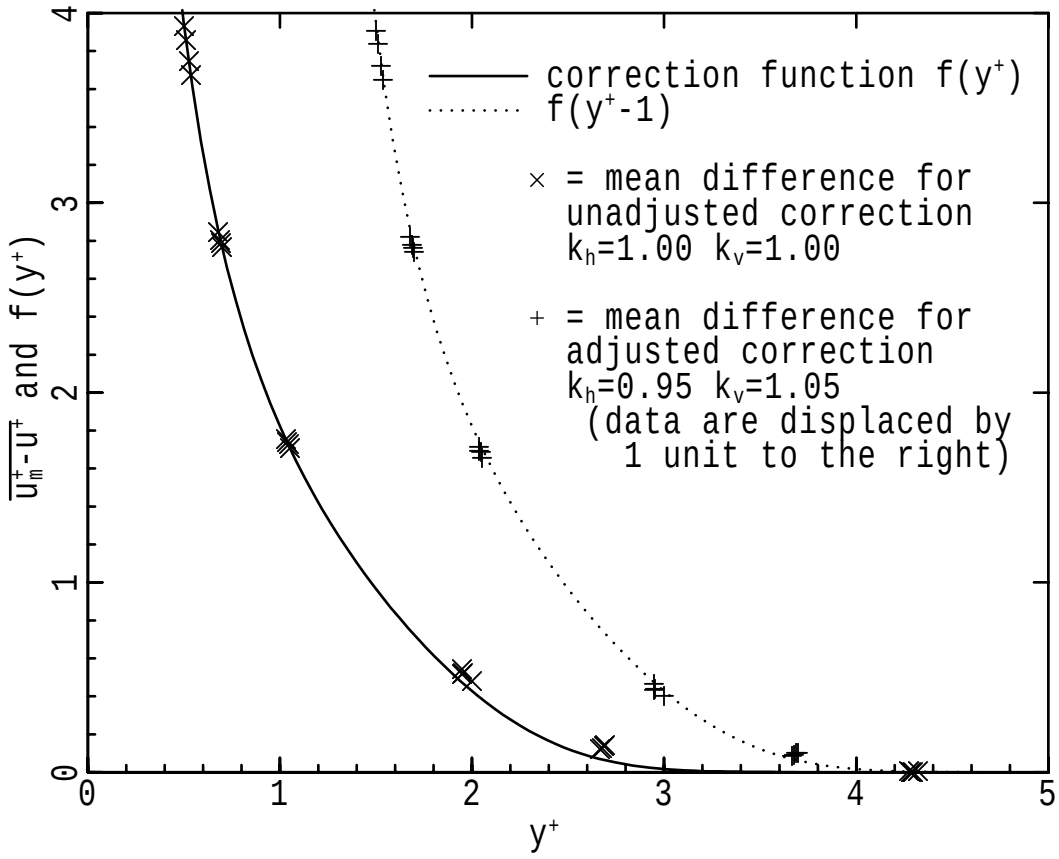

Figure 10.5: Comparison of the unadjusted and adjusted correction functions with the mean difference between corrected and uncorrected signals

quence, the highly non-linear nature of $f(y^+)$ virtually guarantees that the time-average of the applied correction, $\overline{\tilde{u}_\tau f(\tilde{y}^+)}$, is not exactly the same as the correction, $U_\tau f(y^+)$, implied by the error in the measured mean velocity. In other words, there is a small error in the correction function, $f(y+)$, because the function is derived from measurements in a turbulent boundary layer rather than a laminar boundary layer. Figure 10.4, which shows the effect of the correction process on the velocity signal from the hot-wire probe, indicates the reason for this deficiency. If the probe is placed at a distance from the wall where the correction function $f(y^+)$ is small compared with the velocity fluctuation (e.g. $y^+ = 2.70$ and 1.97), only the smaller velocity values in the signal are altered by the correction process. This occurs because, for each data sample, the correction function f is evaluated at an instantaneous $\tilde{y}^+$ which depends on the instantaneous friction velocity $\tilde{u}_\tau$, which in turn depends on the instantaneous air speed $\tilde{u}$; i.e. $\tilde{y}^+ = \tilde{u}_\tau y/\nu_\infty$ where $\tilde{u}_\tau = \sqrt{\tilde{u}\nu_\infty/y}$. In the cases where the correction process does not change the data, the instantaneous $\tilde{y}^+$ is high enough to produce an error $f(\tilde{y}^+)$ equal to zero. For the smaller sampled air speed values, the instantaneous $\tilde{y}^+$ used to evaluate $f(\tilde{y}^+)$ is less than the y^+ calculated from the time-averaged friction velocity, and so the amount of correction is much greater than

indicated by $f(y^+)$. The overall effect is to generate a slightly larger correction than is actually necessary. This can be seen by comparing the $\times$ symbols with the accompanying curve in Figure 10.5. The portion of the correction function $f(y^+)$ required for correcting the signals at $y^+ = 2.70$ and $y^+ = 1.97$ is highly curved (i.e. nonlinear), whereas at $y^+ = 0.69$ and $y^+ = 0.51$ a much smaller, more linear portion of the correction function is used, and the mean value of the correction agrees very closely with the correction function. One readily observed effect of applying a correction to the data is an increase in the r.m.s. velocity fluctuation. The increase in fluctuation occurs over the whole of the region in which wall-proximity effect can be detected.

If the mismatch of the type shown in Fig 10.5 is to be avoided, it is necessary to provide some means of adjusting any correction function, $f(y^+)$, derived from turbulent boundary-layer data. A convenient form of adjustment is to make use of "horizontal" and "vertical" dilation factors k_h and k_v so that

$$\Delta U^+ = k_v f(\frac{y^+}{k_h}). \tag{10.10}$$

For the purpose of determining $f(y^+)$ from the mean velocity distribution (using the method described above), k_h and k_v are set equal to one. The function $f(y^+)$ is tested by using it to correct the data stream which was used to formulate it, and then comparing it graphically with the mean value of the difference between the corrected and uncorrected signals, $(\overline{\tilde{u}_m - \tilde{u}})/U_\tau$, at each probe position. This comparison is shown as the $\times$ symbols and the solid curve in Figure 10.5. The values of k_h and k_v are then adjusted until the difference between the two sets of data shown on the graph is minimised. The result of using the approximately optimal values of dilation factors, $k_h = 0.95$ and $k_v = 1.05$, is shown as the $+$ symbols and the dashed line in Figure 10.5. It is clear from the figure that, while the adjustment resulting from these dilation factors is small, it should produce a better approximation to the "true" correction function, and it should lead to better estimates of sublayer turbulence statistics.

In ideal circumstances, the need for the dilation factors k_h and k_v can be avoided by calculating the correction function from a velocity distribution measured in a laminar boundary layer and then applying the correction to the turbulent boundary-layer data. In practice this requires an apparatus which can produce both laminar and turbulent boundary layers with approximately equal friction velocities.

10.1.2 Simple heat-transfer method

The simple heat-transfer model developed and examined in Section 9.4 was obtained from dimensional and order analysis by additionally assuming that the Nusselt number of heat transfer to the wall is independent of hot-wire Reynolds number and that the Nusselt number of heat convected away by the fluid is unaffected by wall proximity. This model can be used to construct a correction method which is similar to the velocity-error method in that a correction function is calculated from measurement of

mean velocity in the viscous sublayer, and the correction function is used in an iteration which simultaneously produces a corrected velocity signal and an instantaneous friction-velocity signal. Although it is clear from Section 9.4 that the simple heat-transfer model is less than completely satisfactory, as a further test, it is useful to observe the effect of a possibly faulty correction method on the turbulence signal.

If the heat conduction loss from the ends of the hot-wire filament can be ignored (i.e. $l/d > 200$), the heat transfer to the fluid is equal to the electrical power dissipation within the filament; and for a hot-wire operated at constant temperature, Equation 9.6 becomes

$$\tilde{v}_{w,m}^2 = \frac{(1+a)R_w k_f A \Delta T}{d}\left[Nu_c(\tilde{Re}_d, \tilde{y}^+) + \frac{d}{y} Nu_w(\tilde{y}^+, \tilde{Re}_d)\right], \tag{10.11}$$

where $\tilde{v}_{w,m}$ is the voltage across the hot-wire filament, a is the overheat ratio of the filament and R_w is its cold electrical resistance. It is known that neither the temperature nor the resistance of the hot-wire filament is perfectly constant [Perry and Morrison, 1971], but the fluctuations are so small that in practice they can be neglected. When the additional restrictions on Nu_c and Nu_w implied by the simple heat-transfer model are applied, Equation 10.11 becomes

$$\tilde{v}_{w,m}^2 = \tilde{v}_w^2 + \frac{(1+a)R_w k_f A \Delta T}{y} Nu_w(\tilde{y}^+), \tag{10.12}$$

where $\tilde{v}_w$ is the corrected voltage across the hot-wire filament. For fixed experimental conditions and for a particular hot-wire probe operated at fixed overheat ratio, the parameters R_w, k_f, ΔT and a can be absorbed into the Nusselt-number function $Nu_w(\tilde{y}^+)$, which becomes a correction function, $f(\tilde{y}^+)$. The anemometer output voltage, $\tilde{v}$, is proportional to the voltage across the hot-wire filament, $\tilde{v}_w$, and if this constant of proportionality is also absorbed into $f(\tilde{y}^+)$,

$$\tilde{v}_m^2 = \tilde{v}^2 + \frac{1}{y} f(\tilde{y}^+). \tag{10.13}$$

The form of $f(y^+)$ used for correcting the anemometer voltage (i.e. to calculate $\tilde{v}$) is

$$f(\tilde{y}^+) = e^{-P_3(\tilde{y}^+)}, \tag{10.14}$$

where the coefficients of the polynomial $P_3(\tilde{y}^+)$ are determined by applying the least-squares technique to a graph showing values of $ln[y(V_m^2 - V^2)]$ as a function of y^+. The data for this graph are obtained from V_m, which is the mean output voltage of the constant temperature anemometer, and from V, which is the anemometer voltage calculated from the assumption of a mean velocity distribution, $U^+ = my^+$. As for correction using the velocity-error method, the coefficient m is chosen to ensure that $f(y^+)$ vanishes at the edge of the sublayer. Equation 10.13 is implemented as the iterative correction procedure detailed in Figure 10.6(a). The final step in formulating the correction function is to compensate for the effects of calculating the correction function from time-averaged turbulence data. This is done by

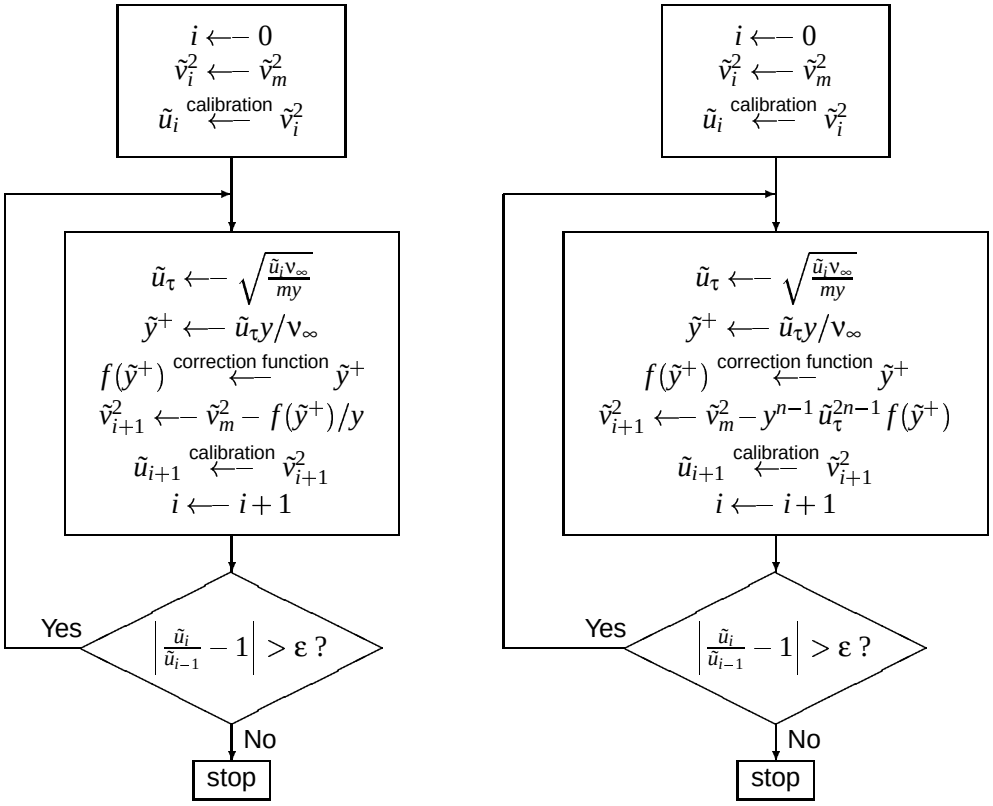

a) Simple heat-transfer model b) Modified heat-transfer model

Figure 10.6: Flow-charts of iteration procedures for heat-transfer models

selecting horizontal and vertical dilation factors (k_h and k_v) in the same way as for the velocity-error method.

This correction procedure uses the hot-wire calibration and, in addition to correcting for wall-proximity effect, also converts the anemometer output voltage into air speed. It does not assume any particular form of hot-wire calibration relation and, in the software, the hot-wire calibration is passed to the correction procedure as an opaque or "black-box" function.

10.1.3 Modified heat-transfer method

10.1.3.1 Correction formula

The equations which define the modified heat-transfer model (i.e. Equations 9.44, 9.40, 9.41 and 9.45) are converted into a correction formula in the same way as for the simple heat-transfer model. All constants in these equations except C and n are absorbed into the correction function ($f(\tilde{y}^+)$) and, as shown previously in Section 9.5.3, C becomes zero without loss of generality. The resulting correction

formula is

$$\tilde{v}_m^2 = \tilde{v}^2 + y^{n-1}\tilde{u}_\tau^{2n-1} f(\tilde{y}^+). \tag{10.15}$$

For the results of Section 10.3, where the hot-wire data is linearised using the Siddal-Davies (1972) relation, the assumed value of n in Equation 10.15 is 0.45.

10.1.3.2 Correction procedure

The correction procedure for the modifed heat-transfer model is the iteration shown in the flowchart of Figure 10.6(b). The correction function, $f(\tilde{y}^+)$, has the same general form as the correction function for the simple heat-transfer method (Equation 10.14). Compensation for the effects of calculating the correction function from time-averaged turbulence data takes the same form as for the other two correction methods.

10.1.3.3 Equivalence of the modified heat-transfer and velocity-error models

The sensitivity of the correction method to a small change in n has been studied by calculating the r.m.s., skewness and flatness of velocity fluctuations corrected using first $n = 0.45$ and then $n = 0.5$. From the results of this study, the effect of changing n is clearly negligible in the region $y^+ \gtrsim 1$. At smaller distances from the wall, the observed effect is of approximately the same magnitude as the uncertainty due to experimental error.

By writing the empirical correction function $f(\tilde{y}^+)$ in Equation 9.45 as $e^{-P(\tilde{y}^+)}$, substituting the result into Equation 9.46 and assuming $n = 0.5$, it is easy to show that the non-dimensional velocity error

$$\Delta\tilde{u}^+ = \left(\frac{\tilde{u}_m^+}{\tilde{u}^+} - 1\right)\tilde{y}^+ \tag{10.16}$$

reduces to an expression of the form

$$\Delta\tilde{u}^+ = \frac{1}{\tilde{y}^+} e^{-P_5(\tilde{y}^+)} + e^{-P_6(\tilde{y}^+)} + \tilde{y}^+ e^{-P_7(\tilde{y}^+)}, \tag{10.17}$$

where P_5, P_6 and P_7 are polynomials. As $\tilde{y}^+$ approaches zero, Equation 10.17 becomes proportional to $1/\tilde{y}^+$ and as $\tilde{y}^+$ becomes large it approaches zero. With appropriate selection of a "best fit" polynomial $P_8(\tilde{y}^+)$, the velocity error can therefore be represented by

$$\Delta\tilde{u}^+ = \frac{1}{\tilde{y}^+} e^{-P_8(\tilde{y}^+)} \tag{10.18}$$

which is the same as the correction formula for the velocity-error model. The modified heat-transfer model may therefore be considered equivalent to the velocity-error model.

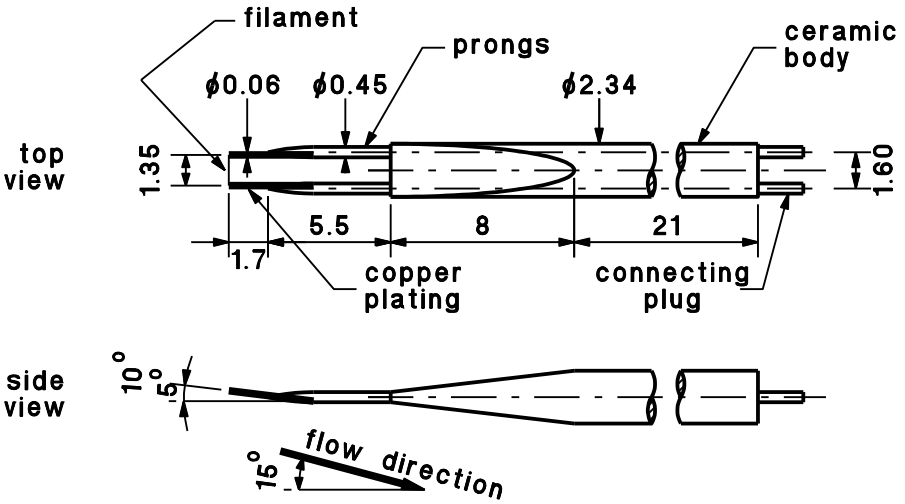

Figure 10.7: Hot-wire probe

10.2 Experimental details

The results presented in the next section were obtained by reprocessing the experimental data acquired for testing the effectiveness of buoyant swirl suppression (Section 6.4.5). The experimental equipment, instrumentation, software, procedure and data processing techniques have been described in earlier chapters, and so only the details relevant to the wall-proximity effect phenomenon are reported here.

The experimental data consist of sixteen boundary-layer velocity distributions measured at a distance of 2.53 m downstream from the boundary-layer origin. The free stream speed was 1.67 m/s. The depth of the test section was a uniform 230 mm along its entire length so that the pressure gradient was produced entirely by boundary-layer growth. In order to reduce heat transfer to the wall and to increase the proportion of the viscous sublayer free of wall-proximity effect, the surface of the plug carrying the hot-wire probe was thermally insulated with a 0.5 mm-thick sheet of high-impact-strength polystyrene. Unlike a reduction of overheat ratio or hot-wire diameter, the presence of the wall insulation introduced no deleterious side-effects. The details of the hot-wire probe, which are shown in Figure 10.7, do not strictly conform to the recommendations of Section 8.1 for avoiding the aerodynamic perturbations due to probe geometry, but the data obtained from it show that the wall-proximity effect was confined to the viscous sublayer, and so indicate that aerodynamic effects were negligible. The probe was designed to keep the prongs well away from the active part of the hot-wire filament and also to allow the filament to be placed very close to the wall.

The single continuous data record from each probe location consists of 5,000 samples with a sampling interval of 6 milli-seconds. The total of 80,000 data samples obtained for each probe location is suf-

ficient for reasonably accurate measurement of the high values of skewness or flatness in the viscous sublayer. The measurement of air speed in the viscous sublayer is very sensitive to the quality of the hot-wire calibration because the data of interest are heavily biased toward the lower extreme of the calibration range. It is therefore important to provide calibration data at flow speeds typical of those in the viscous sublayer.

10.3 Results and discussion

Properties of the turbulent boundary layer 2.53 m downstream from its origin are listed in Table 10.1. The values of displacement (δ_2^*), momentum (θ_2) and energy thickness (δ_{E2}) have been calculated from both the corrected and the uncorrected velocity data. The variation in these thicknesses (δ_2^*, θ_2 and δ_{E2}) caused by changing from one correction method to another is only about 0.001 mm, which is much less than experimental error. The variation produced by not correcting for wall-proximity effect and by simply ignoring the measurements with detectable wall-proximity error is about 0.003 mm. The distributions of mean, r.m.s. fluctuation, skewness and flatness of the streamwise velocity component across the full thickness of the turbulent boundary layer are shown in Figure 6.18. These have not been corrected for wall-proximity effect. The features shown in these graphs are typical of what is expected from a low-Reynolds-number turbulent boundary layer. When the data are presented in this manner on a logarithmic horizontal scale, the effect of heat transfer from the hot-wire to the wall is clearly visible in the mean velocity distribution, but it is very difficult to judge whether or not there is any effect on the r.m.s. fluctuation. It is also difficult to make any prediction of the influence of wall-proximity effect on the measurement of skewness or flatness simply by considering the nature of the correction process.

The mean values of the uncorrected and corrected streamwise velocity data are shown in Figure 10.8. The extent of agreement between the corrected data and the ideal mean velocity distribution, $U^+ = y^+$,

Table 10.1: Properties of the turbulent boundary layer

Distance downstream of origin	x	2.53 m
Free stream air speed	U_0	1.65 m/s
Friction velocity	U_τ	0.0754 m/s
Local friction coefficient	C_f	0.00416
Boundary-layer thickness	δ_{99}	57.6 mm
Displacement thickness	δ_2^*	9.52 mm
Momentum thickness	θ_2	6.43 mm
Energy thickness	δ_{E2}	11.30 mm
Shape factor	$H_2 = \delta_2^*/\theta_2$	1.480
Reynolds number	Re_{θ_2}	698

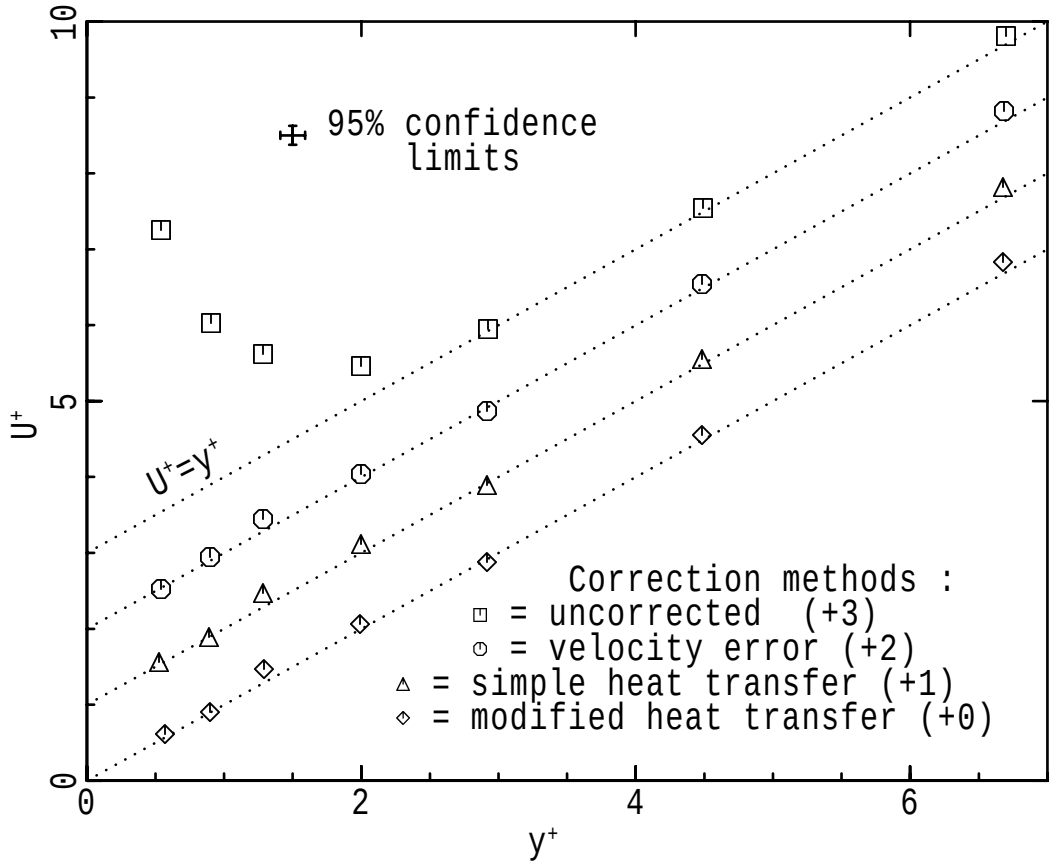

Figure 10.8: Mean of corrected and uncorrected streamwise velocity in the viscous sublayer. The values in parentheses in the legend are the vertical displacements of the data.

depends on the scatter in the uncorrected data and on the accuracy of the estimated error functions. For all models the corrected values agree quite well with the ideal mean velocity profile throughout the viscous sublayer; and the results for all three cases are almost exactly the same. The accuracy of the results in Figure 10.8 and in subsequent graphs of turbulence statistics is indicated by error bars showing the estimated width of the 95% confidence intervals.

Figure 10.9 shows the effect of the correction process on the measurement of r.m.s. fluctuating streamwise velocity. The evidence from Figure 10.4 that the corrected values of r.m.s. fluctuation can be greater than the uncorrected values is reinforced quite clearly in Figure 10.9. Ideally, measured r.m.s. velocity fluctuation in the viscous sublayer should be proportional to distance from the wall, but the uncorrected data have pronounced curvature in the region $0 < y^+ < 3$ and so clearly do not satisfy this condition. The velocity-error and modified heat-transfer correction methods significantly improve the linearity of the r.m.s. profile data. Smooth curves fitted to data from the MPI oil-channel and the MIT wind-tunnel experiments of Alfredsson et al. (1988) are included in Figure 10.9. The measurements

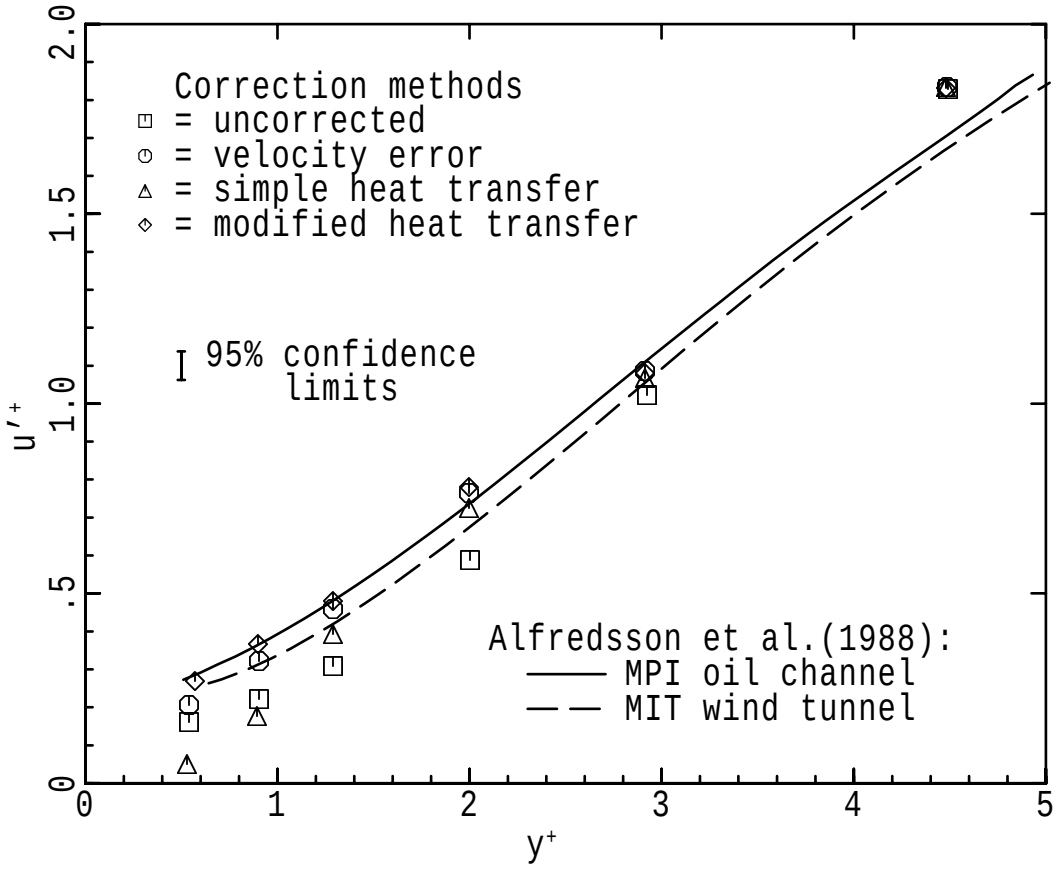

Figure 10.9: R.m.s. fluctuating streamwise velocity in the viscous sublayer

from the MIT wind-tunnel boundary layer are modified by the wall-proximity effect and the r.m.s. profile has the same sort of positive curvature in the region $1 < y^+ < 3$ as the uncorrected results (□) shown in the figure. When the wall-proximity effect is absent, as is the case for the MPI oil channel experiments, the curvature of the r.m.s. sublayer profile is significantly lower. For the velocity-error and modified heat-transfer models, a straight line of best fit to the r.m.s. data crosses the horizontal axis no further from the origin than $y^+ \approx 0.2$. These small discrepancies may be attributed to experimental error. A similar line of best fit to the r.m.s. data corrected using the simple heat-transfer model crosses the horizontal axis at a significantly greater distance from the origin ($y^+ \approx 0.5$). This is a strong indication that the simple heat-transfer model is faulty.

The faulty axis intercept (at $y^+ \approx 0.5$) of the r.m.s. values from the simple heat-transfer model is caused by the increased sensitivity of the hot-wire probe at lower air speeds. This can be explained with the aid of Figure 10.10 which shows the steps required to correct the velocity signal at $y^+ = 0.51$. The uncorrected velocity signal, which is marked with an "A" in the figure, is first converted to a voltage-squared signal (B) using the hot-wire calibration. Because the correction function $f(\tilde{y}^+)$ is essentially

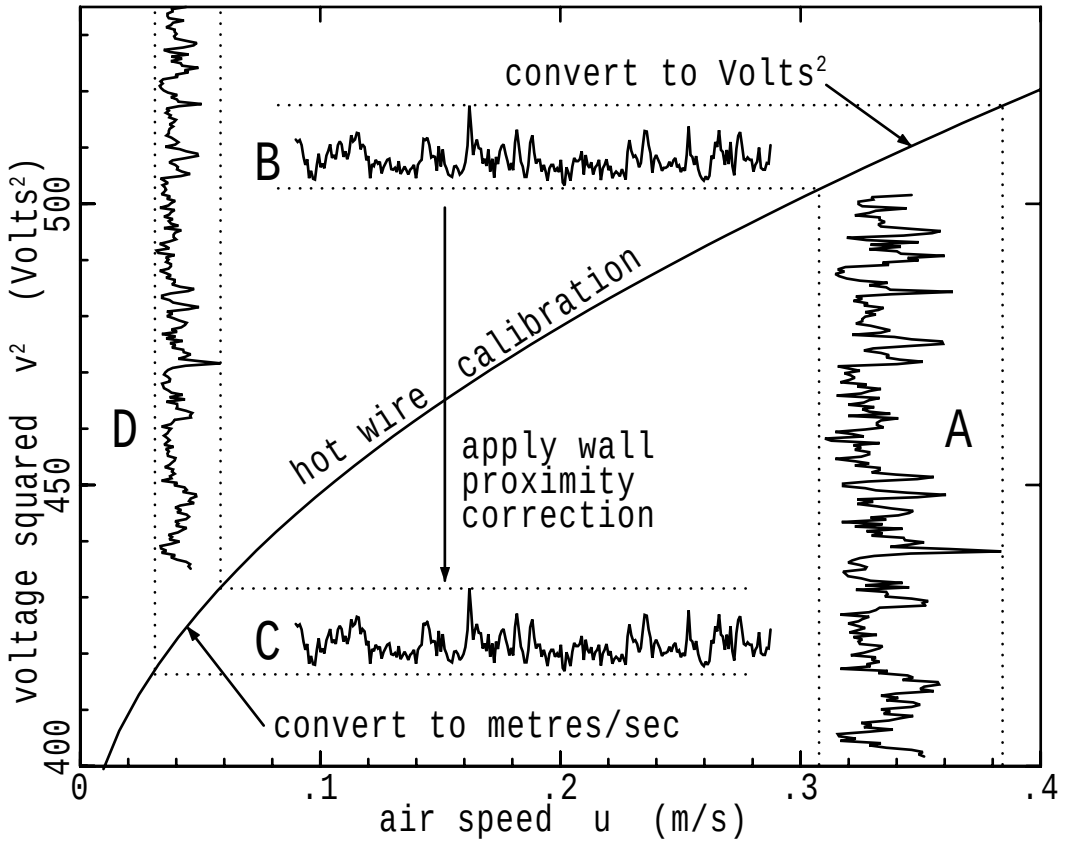

Figure 10.10: The mechanism of correction with the simple heat-transfer model at $y^+ = 0.51$, where $f(\tilde{y}^+)$ is essentially constant. A) uncorrected velocity vs. time signal; B) uncorrected voltage squared vs. time; C) corrected voltage squared vs. time; D) corrected velocity signal vs. time.

constant at this distance from the wall, the correction process is approximately a translation in the voltage-squared domain and does not significantly change the amplitude of voltage fluctuation. Finally, the corrected voltage-squared (C) is converted back to a velocity signal (D). The increased slope of the calibration curve at the lower (corrected) air speed results in the amplitude of velocity fluctuation being greatly reduced by the correction process. In contrast, at larger distances from the wall where the correction function has a small value (e.g. at $y^+ = 1.97$ or $y^+ = 2.70$), approximately the same part the calibration curve is used for both the forward and reverse conversions in the correction process. Only the smaller velocity data values are changed by the correction process, and so the amplitude of velocity fluctuation is increased. The results of correction with the modified heat transfer-model are different because the correction function has a different shape and the correction process cannot be represented as a translation along the voltage-squared axis.

The skewness distribution of the uncorrected and corrected streamwise velocity signals is shown in Figure 10.11. The corresponding distributions of flatness and relative turbulence intensity, u'/U, are

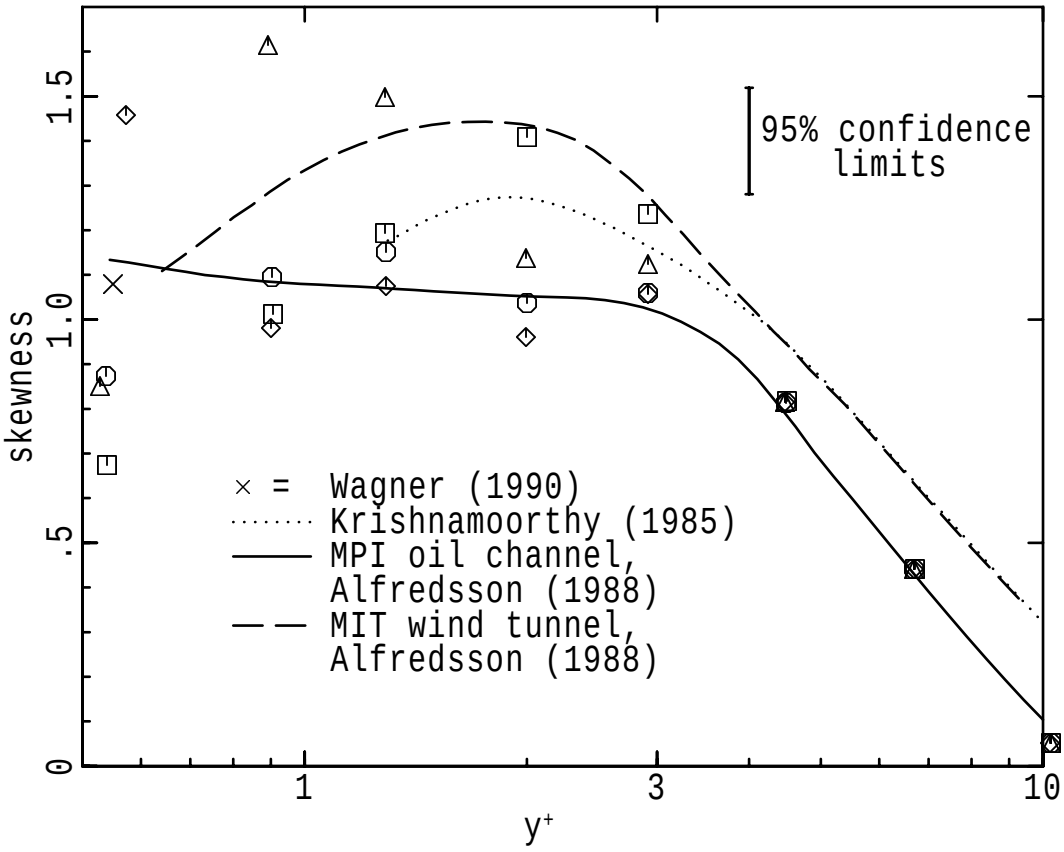

Figure 10.11: Skewness of streamwise velocity in the viscous sublayer. The correction methods are □: uncorrected, ◯: velocity-error, △: simple heat-transfer, ◇: modified heat-transfer.

shown in Figures 10.12 and 10.13 respectively. The data in Figures 10.11, 10.12 and 10.13 are presented in the same way as for the r.m.s. velocity distributions in Figure 10.9. All correction methods significantly change the distributions of skewness, flatness and relative turbulence intensity in the viscous sublayer. The results from the velocity-error method are almost the same as those from the modified heat-transfer method but are quite different from the results produced by the simple heat-transfer method. For example, the skewness of the uncorrected velocity signal has a maximum of 1.4 at $y^+ \approx 2$ and a limiting value of about 0.6 at the wall. The velocity-error and modified heat-transfer methods produce a broad skewness maximum of about 1.1 over the interval $0.9 < y^+ < 2$, and the simple heat-transfer method produces a narrower maximum of about 1.6 at $y^+ \approx 0.9$. The corrected skewness measurements closest to the wall (i.e. at $y^+ = 0.54$) should be considered rather less reliable than the measurements further from the wall because

(1) signal-to-noise ratios are relatively low,

(2) the calculation of skewness is very sensitive to erroneous velocity data caused by occasional failure of the correction iteration to converge, and

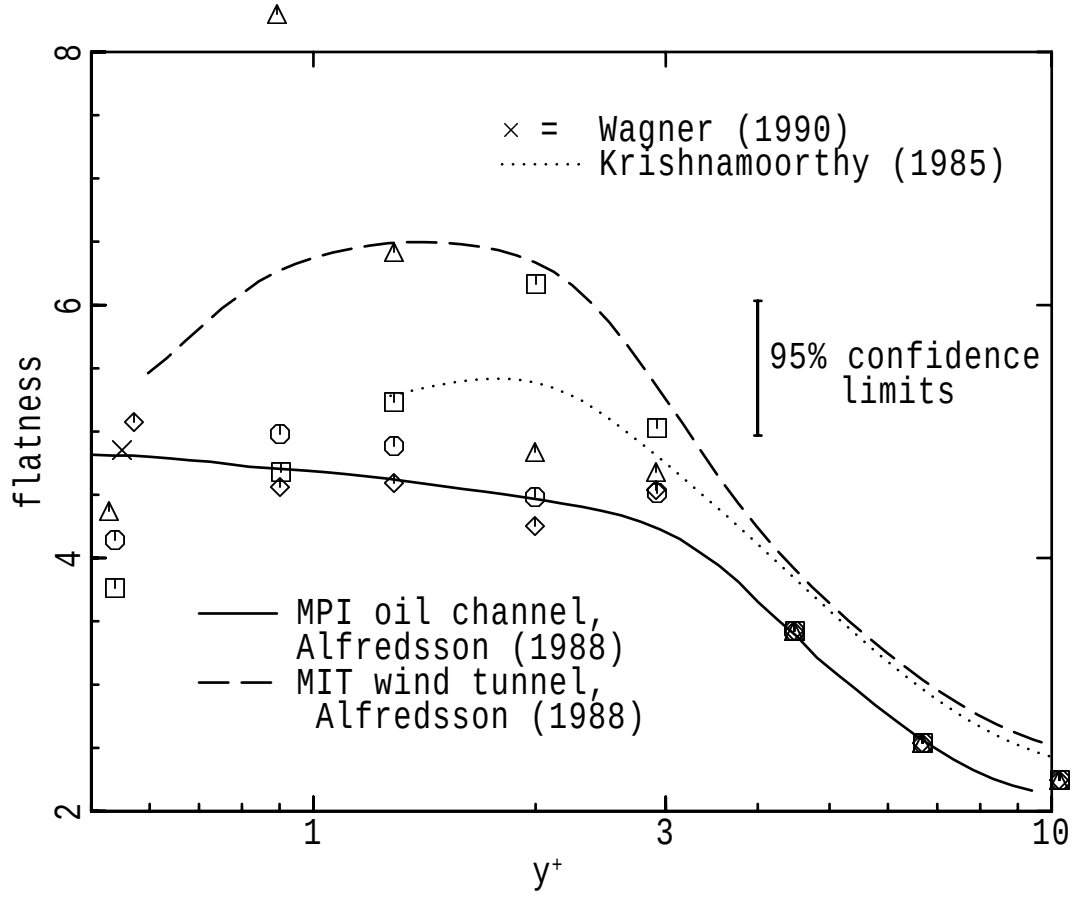

Figure 10.12: Flatness of streamwise velocity in the viscous sublayer. The correction methods are □: uncorrected, ◯: velocity-error, △: simple heat-transfer, ◇: modified heat-transfer.

(3) the correction process, which is essentially a subtraction, amplifies errors, especially when the corrected signal is an order of magnitude or more smaller than the uncorrected signal.

Figure 10.12 shows that the effects of the correction process on the flatness of the velocity signal are similar to the effects on skewness. For $y^+ > 1$ correction of the data by the velocity-error and modified heat-transfer methods produces skewness and flatness which agree closely with the MPI oil channel measurements of Alfredsson et al. (1988) and with Wagner's (1990) values for skewness and flatness (1.08 and 4.8 respectively) of wall shear stress. The skewness and flatness of the uncorrected data and the data corrected using the simple heat-transfer method agree with neither the uncorrected measurements of Krishnamoorthy et al. (1985) nor Alfredsson's MIT wind-tunnel data.

The values obtained for relative turbulence intensity (i.e. r.m.s. divided by mean velocity) again show (in Figure 10.13) that the closest agreement with Alfredsson's MPI oil channel data is obtained by correction with the velocity-error and modified heat-transfer methods. This agreement is significant and substantial. Wagner's (1990) value of between 0.36 and 0.37 for the turbulence wall shear stress intensity and similar values from Castro, Dianat and Bradbury (1987) confirm these measurements. The

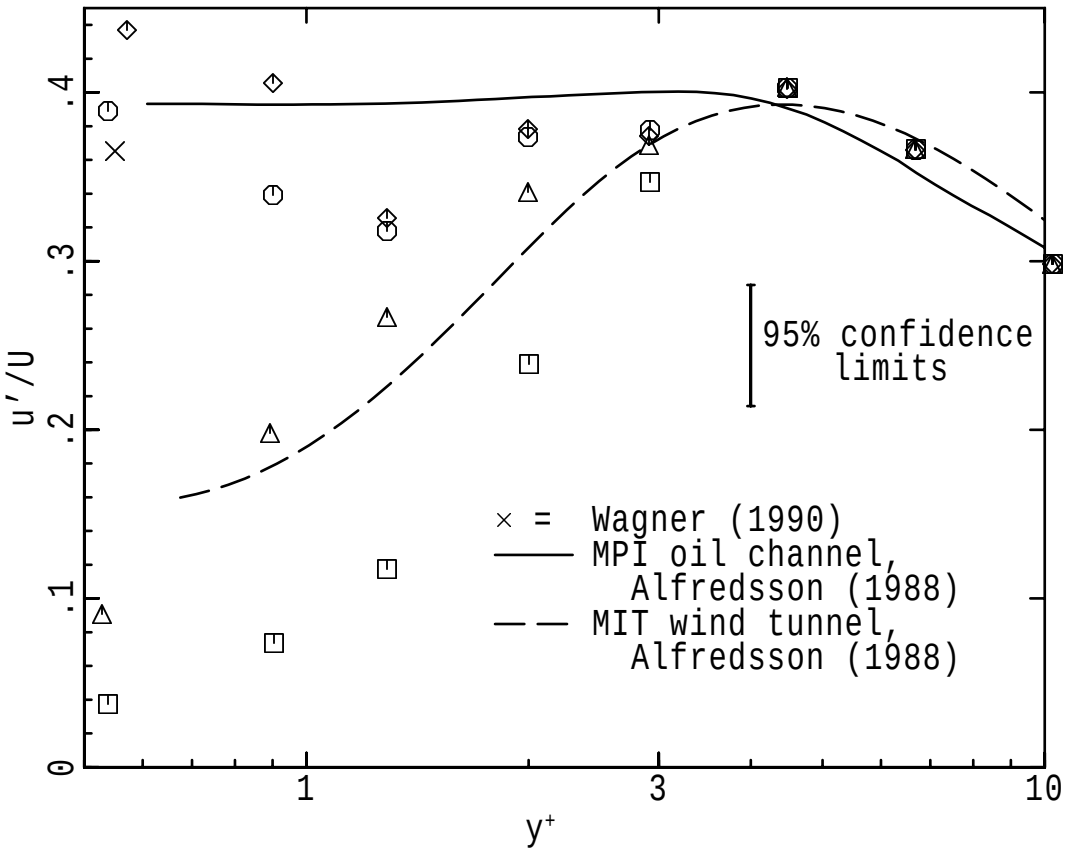

Figure 10.13: Relative turbulence intensity of streamwise velocity in the viscous sublayer. The correction methods are □: uncorrected, ◯: velocity-error, △: simple heat-transfer, ◇: modified heat-transfer.

values of turbulence intensity at $y^+ = 1.3$ are lower than expected because the corresponding values of corrected mean velocity (Figure 10.8) are significantly greater (15%) than required by the relationship $U^+ = y^+$. All correction methods assume that, in the viscous sublayer, the instantaneous velocity is proportional to distance from the wall (page 241). Although this assumption directly implies a constant value of relative turbulence intensity, Figure 10.13 clearly shows that the correction processes have not forced constant turbulence intensity on the corrected experimental data. In fact, the large change in values produced by correction with the simple heat-transfer model over the range $0 < y^+ < 4$, again indicates that this model does not work.

The results presented in Figures 10.9 to 10.13 indicate that the velocity-error and modified heat-transfer models of wall-proximity effect can be used successfully for correcting measurements of instantaneous velocity in the viscous sublayer. Both of these models rely on the experimental observation by Oka and Kostic (1972), Zemskaya et al. (1979) and Janke (1986) that

$$\Delta U^+ = f(y^+). \tag{10.19}$$

Although some success has been achieved on the basis of this relationship we have not been able to derive it theoretically and, until an independent non-empirical verification of Equation 10.19 can be found, a residual doubt about its general validity must remain. For correction of sublayer-velocity data the velocity-error model is preferred over the modified heat-transfer model because the correction process is easier to apply, does not use the hot-wire calibration, requires an order of magnitude fewer arithmetic operations and is more robust. However, despite its usefulness, the model is incomplete because it provides no insight into the physics of wall-proximity effect and it cannot be used for studying the effect of varying any experimental parameter (e.g. hot-wire diameter or overheat ratio) except friction velocity.

The modified heat-transfer model has the advantage that it can predict the effect of changing the overheat ratio of the hot-wire. In principle, predicting the effect of changing hot-wire diameter with this model is possible, but in order to do so, detailed knowledge is required of how the Nusselt numbers Nu_d, Nu_c and Nu_w depend on the length-to-diameter ratio of the hot-wire filament.

In addition to the faults revealed in Section 9.4, the simple heat-flow model is unable to produce correct r.m.s. fluctuation, skewness, flatness or relative turbulence intensity values for velocity in the viscous sublayer. Therefore, it is useful only for demonstrating that different models of wall-proximity effect can generate different corrections to the turbulence-velocity data.

The r.m.s., skewness, flatness and relative intensity of the streamwise turbulence velocity component in the viscous sublayer have also been measured by Eckelmann (1974), Andreopoulos et al. (1984), Krishnamoorthy et al. (1985), Alfredsson et al. (1988) and Wagner (1990), but significantly different results were obtained from each wind tunnel or flow channel. The work presented here suggests that, in every case where the measurements were made in air, these earlier results are unavoidably contaminated by the effects of wall proximity and a properly applied correction would produce the same results as from the oil channel of Eckelmann (1974) and Alfredsson et al. (1988). The differences between these earlier measurements considerably inhibit interpretation of the measurements in terms of turbulence structure in the viscous sublayer. The elevation of skewness and flatness within the sublayer ($y^+ < 5$) to levels much higher than in the logarithmic region of the boundary layer is caused by intermittent regions of high speed ($u' > 0$) fluid, which are conventionally known as sweeps, approaching the wall ($v' < 0$). If skewness and flatness maxima occur at some distance from the wall ($y^+ > 0$), one might conclude that the sweeps are prevented from reaching the wall or are attenuated by an as yet undiscovered turbulence mechanism operating within the viscous sublayer. However, the weight of evidence now indicates that maximum values of flatness and skewness occur at the wall. This suggests that such a turbulence mechanism does not exist and that attenuation of high speed sweeps within the sublayer is entirely by viscous diffusion.

10.4 Summary and conclusions

Three methods have been developed for removing wall-proximity error from hot-wire anemometry in the viscous sublayer of a turbulent boundary layer. All methods are consistent with or are a subset of Equation 9.48, all assume linearity of the instantaneous velocity distribution in the viscous sublayer, and all use correction functions, $f(\tilde{y}^+)$, which are determined from mean velocity measurements. Application of these correction methods to experimental data shows that heat flow to the wall changes not only the measurements of mean velocity, but also the measurements of velocity fluctuation. The effects on the measured skewness and flatness of fluctuating velocity are quite significant even in the region where the effect on the mean velocity measurement is small. The results indicate that, in the viscous sublayer, the corrected distributions of skewness, flatness and relative turbulence intensity have maxima at the wall of 1.1, 4.7 and 0.39 respectively. Because skewness and flatness are indicators of the amplitude and intermittency of boundary-layer sweep events, the location of these maxima at $y^+ = 0$ suggests that sweeps are attenuated by simple viscous diffusion rather than by any active turbulence mechanism within the sublayer.

The first correction method is developed from the work of Oka and Kostic (1972) and Bhatia et al. (1982). Provided that probe geometry, fluid properties, wall-material properties and overheat ratio do not change, it assumes a velocity error which depends only upon $\tilde{y}^+$. Correction of the velocity signal is therefore based on the formula,

$$\tilde{u}_m^+ = \tilde{u}^+ + f(\tilde{y}^+), \tag{10.20}$$

where

$$f(\tilde{y}^+) = \frac{1}{\tilde{y}^+} e^{-P_2(\tilde{y}^{+2})}. \tag{10.21}$$

In the region $1 < y^+ < 4$, data corrected by this velocity-error method have r.m.s., skewness, flatness and relative turbulence-intensity distributions which agree well with experimental data believed to be free of wall-proximity error. Of the three correction methods this is the simplest, fastest and most robust, but it provides the least scope for investigating the physics of wall-proximity effect.

The second correction method is derived from a dimensional analysis of heat flow from the hot-wire filament by additionally assuming that the Nusselt number of heat transfer to the wall (Nu_w) depends only upon $\tilde{y}^+$, that the Nusselt number of convection to the fluid (Nu_c) is unaffected by wall proximity and that wall-proximity error is not affected by changes in l/d. These assumptions lead to a correction formula for the anemometer output voltage,

$$\tilde{v}_m^2 = \tilde{v}^2 + \frac{1}{y} f(\tilde{y}^+), \tag{10.22}$$

with $f(\tilde{y}^+) = e^{-P_3(\tilde{y}^+)}$. The hot-wire calibration is used for required voltage-to-velocity and velocity-to-voltage transformations. This simple heat-transfer model can predict the effects of varying overheat

ratio and hot-wire diameter with fair success, but it cannot produce the invariance of $\Delta U^+(y^+)$ with changing air speed, and it does not produce credible turbulence statistics when used for correcting experimental data.

The third correction method is based on a modified heat-transfer model which is designed to overcome the difficulties of the simple heat-transfer model. This is done by selecting Nusselt-number functions which allow the heat balance (Equation 9.48) to satisfy the criterion $\Delta U^+ = f(y^+)$. The correction formula then becomes

$$\tilde{v}_m^2 = \tilde{v}^2 + y^{n-1}\tilde{u}_\tau^{2n-1} f(\tilde{y}^+), \tag{10.23}$$

where $f(\tilde{y}^+) = e^{-P_4(\tilde{y}^+)}$ and $n = 0.45$ is the velocity exponent of the Collis and Williams (1959) hot-wire calibration. The turbulence statistics of data corrected by the modified heat-transfer method are essentially the same as those from the velocity-error method because, with a small change to $n = 0.5$, these two correction methods are mathematically equivalent.

10.5 Notation

a	overheat ratio of the hot-wire filament; $a = \dfrac{\text{operating resistance}}{\text{cold resistance}} - 1$
A	πdl, surface area of the hot-wire filament
C_f	local skin-friction coefficient
d	diameter of the hot-wire filament
f	functions of y^+ which describe the velocity error or Nusselt number of heat transfer to the wall
F	velocity-error function formulated by Acharya and Escudier (1984) (Equation 10.2)
H_2	δ_2^*/θ_2, shape factor for flat-plate two-dimensional boundary layer
j	integer trial exponent for y^+ in a function which approximates the velocity error, Δu
k	thermal conductivity
k_h, k_v	adjustment factors for the effect of calculating the correction function from turbulent boundary-layer data
l	active length of hot-wire filament
m	slope of the experimentally measured non-dimensional mean velocity distribution in the viscous sublayer, $U^+ = my^+$
n	velocity exponent for a hot-wire calibration; usually $n = 0.45$
Nu_c	$h_c d/k_f$, Nusselt number for heat which is convected far downstream from a hot-wire filament and is *not* eventually transferred to the wall

Nu_d	hd/k_f, Nusselt number for heat transfer from a cylinder; i.e. hot-wire calibration
Nu_w	$h_w y/k_f$, Nusselt number for heat transfer from a hot-wire filament to a solid wall
$P(y^+)$	polynomials used for approximating Nu_w
R_w	cold electrical resistance of the hot-wire filament
Re_d	Ud/ν_f, Reynolds number of a hot-wire filament
Re_{θ_2}	$U\theta_2/\nu_\infty$, Reynolds number of a boundary layer
t	time
U_0	speed of a free stream flow
u	streamwise component of the velocity vector u
u_m	instantaneous flow speed measured by the hot-wire anemometer without correcting for wall-proximity affect
u_τ	$\sqrt{\tau_w/\rho_f}$, friction velocity of a boundary layer
u', v'	x and y components of the r.m.s. velocity fluctuation
v	anemometer output voltage
v_m	anemometer output voltage from a hot-wire subject to wall-proximity effect
v_w	voltage across the hot-wire filament
y	distance between the hot-wire filament and the wall
ΔT	nominal temperature of the hot-wire filament above the ambient fluid temperature
Δu	$u_{\text{meas}} - u$, error in measured velocity due to wall-proximity effect
δ_{99}	boundary-layer thickness defined as the distance from the wall at which $U = 0.99U_0$
δ_2^*	displacement thickness of a two-dimensional flat-plate boundary layer (Equation 7.5)
δ_{E2}	energy thickness of a two-dimensional flat-plate boundary layer
ε	predetermined figure-of-merit for terminating the correction iteration
θ_2	momentum thickness of a two-dimensional flat-plate boundary layer (Equation 7.6)
ν	kinematic viscosity
ρ	density
τ_w	wall shear stress generated by the boundary layer

superscripts

$^+$	scales the quantity on the viscous flow variables U_τ and ν_∞, e.g. $U^+ = U/U_\tau$ and $\tilde{y}^+ = y\tilde{u}_\tau/\nu_\infty$
$\tilde{}$	used for indicating a quantity which may vary as a function of time.
$\overline{}$	indicates time averaging

subscripts

f	for properties of the fluid - evaluated at the film temperature, which is sometimes defined as $T_f = T_\infty + \Delta T/2$
i	iteration counter
$1...8$	used for distinguishing similar or related functions.
∞	for properties of the fluid far field.

Upper case is used for indicating time-averaged or constant velocity. All physical quantities are expressed in SI units.

Part III

Conclusions

Chapter 11

Research findings

11.1 Introduction

The flow conditions in an open-circuit wind tunnel have been adjusted to permit experimental investigations into the mechanisms of low-Reynolds number boundary-layer turbulence. In order to use conventionally-sized hot-wire probes for such investigations, it is necessary to develop a well-behaved canonical turbulent boundary layer at free stream speeds of no more than 4 m/s. As a result of the constraints on flow speed and flow uniformity, a number of undesirable features can occur in wind-tunnel flows of this type. These include:

(1) quasi two-dimensional separation of the laminar boundary-layer in the upstream part of the inlet contraction (Chapter 4);
(2) formation of Görtler vortices on the concave surfaces of the inlet contraction (Chapter 4);
(3) strong three-dimensional boundary-layer separation from the concave surfaces of the inlet contraction due to the cumulative effect of weak wall-pressure gradients on laminar Görtler-vortex flow (Chapter 6);
(4) large-scale buoyant flow rotation caused by atmospheric temperature non-uniformities in conjunction with extremely low inlet flow speeds (Chapter 5).

All of these flow defects can be successfully eliminated by making a series of modifications to the inlet section of the wind tunnel. The modifications required are:

(1) changes to the shape of the inlet region of the contraction (for (1) above);
(2) installation of screens in the contraction and boundary-layer suction at the start of the test section (for (2) and (3) above); and
(3) an installation for thoroughly mixing the inlet air to remove temperature non-uniformities, before the air enters the wind-tunnel contraction (for (4) above).

Implementation of these measures, which are illustrated in Figure 11.1, leads to a steady uniform free stream flow with laminar boundary layers at the start of the test section, and subsequently this flow becomes a steady uniform duct flow with turbulent wall boundary layers. Over a limited range of flow speeds and locations, these boundary layers have characteristics typical of the canonical turbulent boundary layer.

The primary instrument for investigating the details of turbulent boundary-layer flow was the hot-wire anemometer. When a hot-wire filament is located within the viscous sublayer of the turbulent boundary layer, heat transfer from the hot-wire filament to the wall produces significant errors in the measurements of both the mean and the fluctuating velocity components. Methods have been developed for removing this error, which is known as wall proximity-effect, from the hot-wire signal.

11.2 Quasi two-dimensional separation

Most wind-tunnel contractions are designed on the assumption that their internal boundary layers are turbulent. In cases where flow speeds are reduced to such an extent that these boundary layers are laminar, the boundary layers may separate from the surfaces and so produce regions of near-stagnant surface flow. Although the regions of near-stagnant separated flow may cover a large proportion of the internal contraction surface, they are typically an order of magnitude thinner than the overlying laminar boundary layer. The area of surface covered by the separation region is inversely related to flow speed. Potential flow simulations show that the separation is produced by adverse pressure gradients near the start of the contraction. Performance indicators from the simulations are improved significantly by changing the cross-section geometry of the contraction inlet from square to octagonal and by reducing the streamwise concavity of the near-inlet contraction surfaces. These modifications, which incorporate a transition from octagonal to square cross-section over the length of the contraction, are sufficient to prevent quasi two-dimensional separation of the laminar boundary layer.

The potential flow simulations demonstrate that, when the design objective is to avoid laminar separation, the most important geometric parameters are the degree of cross-section symmetry and the streamwise curvature of the wall near the start of the contraction. The inlet:outlet area ratio is a much less important parameter. The simulation results quantify earlier observations that the degree of symmetry in the duct cross-section controls the amplitude of cross flows [Downie et al., 1984], and that the near-inlet pressure rise is produced by local streamwise concavity of the contraction surface [Mikhail, 1979]. The significance of near-wall cross-flows is indicated by the r.m.s. spanwise variation in the amplitude of the pressure rise near the start of the contraction. For an octagonal cross-section geometry this spanwise variation in maximum pressure is 4.5 times smaller than for a square contraction. The spanwise average of the rise in wall-pressure near the contraction inlet depends much more

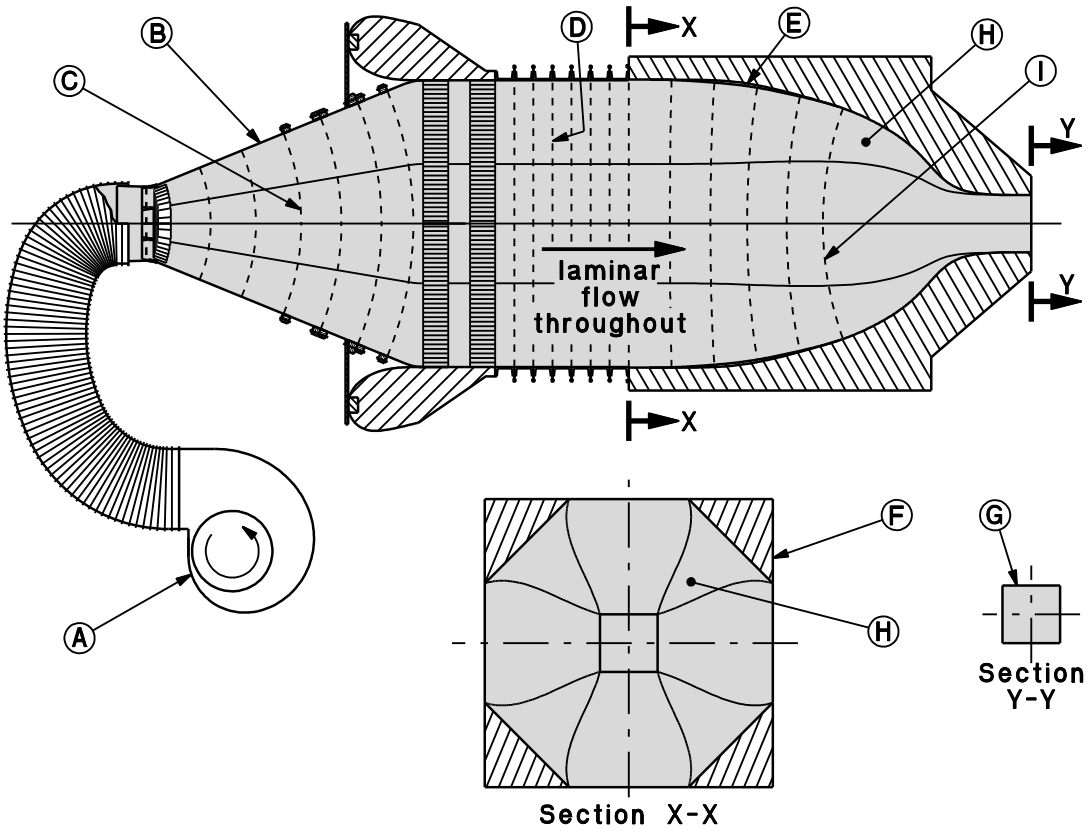

A	centrifugal blower reduces temperature nonuniformities by a factor of 40
B	wide-angle diffuser delivers well mixed air flow to the wind tunnel
C	screens prevent separation in the diffuser
D	Reynolds number of the screens is too low for vortex shedding, and so the traditional settling chamber, which provides additional development length for boundary layers and buoyant convection, is not required
E	contraction profile is modified to reduce concavity
F	cross-section of the contraction inlet is changed from square to octagonal in order to reduce three-dimensionality of flow near the contraction inlet
G	square cross-section of the contraction outlet matches the shape of the test section
H	octagonal to square transition
I	dished screens prevent three-dimensional separation in the contraction

Figure 11.1: Design features of a wind-tunnel inlet for very low flow speed

on streamwise wall curvature than on cross-section geometry.

Thwaites's method has been used for estimating the streamwise development of the laminar boundary layer, and the Thwaites pressure-gradient parameter, m, is used as an indicator of separation. The change from square to octagonal cross-section geometry reduces the maximum value of m by 43%[1]. Only small profile adjustments are required to decrease the maximum surface concavity by a factor of two and so reduce the maximum value of m by a further 65%. Comparison of a two-dimensional contraction with a three-dimensional contraction shows that an increase in area ratio does not necessarily make separation more likely. For example, in a two-dimensional contraction with an area ratio of 5, the maximum Thwaites parameter is about 25% *higher* than in the corresponding octagonal contraction which has the same profile and an area ratio of 25.

11.3 Buoyant flow rotation

The weak secondary flow produced by buoyant convection in a duct can be detected from the patterns formed in the end-on view of an array of streamers. This secondary flow develops at very low flow speeds and so, in an open-circuit wind tunnel, is most likely to occur in the settling chamber and contraction. When the amplitude of temperature nonuniformity is small, buoyant rotation usually consists of a single forced vortex occupying most of the available duct cross-section. As temperature nonuniformity at the duct inlet is increased, the single swirl vortex can develop into a pair of steady counter-rotating vortices and, for even larger temperature differences, the buoyant convection becomes unsteady.

For the purpose of developing a simple mathematical model of buoyant swirl, air temperature may be assumed to vary linearly across the width of the duct inlet and the duct cross-section may be assumed to be circular. If the inlet is open to the atmosphere and the cross-section is octagonal, these are reasonable first order approximations. The mathematical solution for the rotation angle of the temperature distribution, ψ, in a duct of length L and variable radius $R(x)$ is obtained by applying the conservation law for angular momentum to a cylindrical control volume. The result is a second order ordinary differential equation:

$$\frac{d^2\psi}{d(x/L)^2} = \frac{L}{4R(x)} Ri \cos\psi, \tag{11.1}$$

where the Richardson number, Ri, is defined as

$$Ri = \frac{\Delta\theta}{\Theta_a} \frac{gL}{U^2}. \tag{11.2}$$

If, from an initial value of $\psi = 0$, the temperature distribution in a duct of constant radius is rotated

[1] All comparisons of Thwaites parameter, m, are for a test-section flow speed of 1.5 m/s.

through only a small angle, the analytical solution of Equation 11.1 for the swirl angle α is

$$\tan\alpha = \frac{R}{L}\frac{d\psi}{d(x/L)} = \frac{1}{4}Ri. \tag{11.3}$$

For a final rotation angle of 1 radian, the error in this solution is 10%. A more complicated analytical solution is obtained for larger rotation angles. In order to simulate buoyant swirl within a duct of varying radius, $R(x)$, Equation 11.1 can be solved numerically. The numerical solutions for buoyant flow in the open-circuit wind tunnel agree very closely with the available experimental data. They verify that rotation of the flow can develop in the wind-tunnel settling chamber and in the upstream half of the contraction. In the remainder of the contraction the swirl angle is reduced by the narrowing of the duct. The numerical solutions demonstrate that the solutions for swirl angle and flow rotation angle are oscillatory functions of streamwise distance, x, but also shows that, under certain conditions, a contraction in a duct can prevent reversal of the swirl direction.

Buoyant convection is most readily suppressed by providing the duct with a well-mixed inlet flow. In the particular example of the open-circuit wind tunnel, the flow is mixed with a centrifugal fan and is then delivered to the wind-tunnel inlet through a wide-angle diffuser. The effect of the centrifugal fan is to reduce the nonuniformity of the air-flow temperature distribution by a factor of about 40.

11.4 Three-dimensional separation

In the absence of two-dimensional laminar boundary-layer separation and large-scale buoyant swirl, flow conditions sometimes permit three-dimensional separation from the concave internal surfaces of a wind-tunnel contraction. This type of three-dimensional separation produces a pair of strong counter-rotating streamwise vortices which occupy a significant proportion of the core flow in the contraction and downstream duct. Direct observations of flow upstream of the contraction show that low-speed streaks evolve in the boundary layer downstream of the settling chamber screens (item D in Figure 11.1). At flow speeds too high for three-dimensional separation, the low-speed streaks pass through the contraction and are observed in the downstream duct as conventional Görtler vortices but, at lower speeds, they tend to coalesce and then lift from the surface of the contraction. The coalescence and lift-up of low-speed streaks is always associated with the presence of a large streamwise vortex pair.

In the conceptual model constructed from this experimental evidence, the separation process begins with small nonuniformities in the near-wall flow emerging from the settling chamber screens. These flow nonuniformities are convected into the concave boundary layer near the start of the contraction, where they are amplified by Görtler instability and develop into a spanwise array of counter-rotating streamwise vortex pairs. Mid-way between the vortices in each sufficiently developed vortex pair,

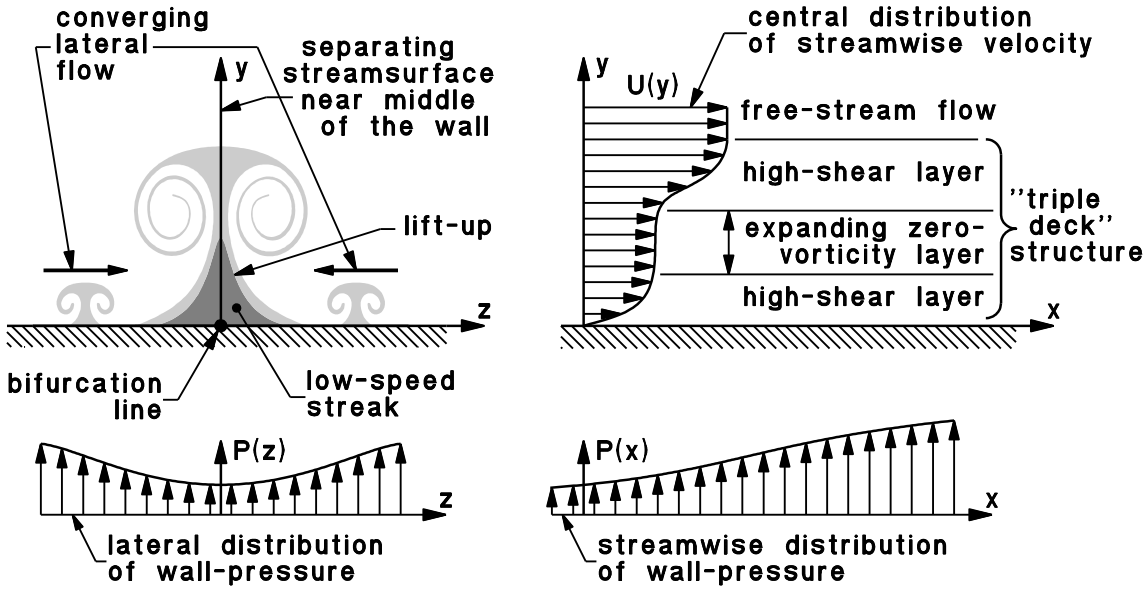

(a) cross-section view — flow is perpendicular to the page

(b) side view of the separating streamsurface

Figure 11.2: Schematic diagram illustrating the mechanisms of three-dimensional separation.

the velocity distribution across the thickness of the boundary layer contains one region of high shear adjacent to the wall and another adjacent to the free stream (Figure 11.2(b)). Between the two regions of high shear, there is a region of very low or zero vorticity. This "triple deck" structure [Elliot et al., 1983, Cowley et al., 1990] of the laminar boundary layer is also believed to be the initial stage of eruptive spire separation in turbulent boundary layers and is therefore a fundamental part of the wall-turbulence mechanism [Smith et al., 1991b]. With the assistance of the adverse streamwise pressure gradient near the start of the wind-tunnel contraction, the low-vorticity part of the "triple deck" structure increases in thickness and lifts the outer high-shear layer further away from the surface. This effect is observed as a lift-up of the underlying low-speed streak and as a migration of the streamwise vortex pair away from the wall of the contraction. The lift-up of the low-speed streak is the central feature of a three-dimensional separation which can be described topologically as a gradually strengthening negative bifurcation of the wall streamsurface. The three-dimensionality of flow in the contraction, which is due to the non-axisymmetry of the cross-section, ensures that the wall pressure not only rises with increasing distance from the start of the contraction, but also rises with increasing lateral distance from the centreline of each surface segment[2] (Figure 11.2(a)). On each side of the surface segment, this spanwise pressure gradient deflects flow laterally towards the centreline and produces spanwise velocity components which are higher within the lower speed flow of the boundary layer than in the free stream. Together with skewing of the boundary layer, the resulting convergence of

[2]For example, one of the surface segments is the floor of the contraction

lateral flows significantly increases the strength of the negative bifurcation nearest the surface centre-line, and also significantly increases the diameter and rotation rate of the associated streamwise vortex pair. This dominant separation structure, which contains the streamwise vortex pair and the negative wall-surface bifurcation, produces near-wall secondary flows and alters the pressure distribution within the contraction in a way which discourages the growth of additional separations. Buoyant swirl is also observed to discourage three-dimensional separation.

A series of wire-mesh screens located within the concave region of the contraction can prevent the low speed streaks between streamwise vortex pairs from developing to the stage where the vortices detach from the surface. Flow-visualisation experiments show that six wire-mesh screens installed at intervals of 170 mm from the start of a 20.7:1 contraction prevent three-dimensional separation at exit-flow speeds higher than 0.5 m/s. The effect of the screens is to replace the previously observed large-scale separation vortices with a much smaller vortex pair in each corner of the exit duct. These small corner vortices are easily removed by wall suction at the contraction outlet.

11.5 The test-section boundary layer

The final steps required for establishing a turbulent boundary layer in the test section at flow speeds between 1 m/s and 4 m/s were to produce acceptable laminar-to-turbulent transition and to minimise the streamwise pressure gradient. A single hot-wire probe was then used for measuring the distribution of the streamwise velocity component in the boundary layer developed along the x-y mid-plane of the test surface. These measurements made it possible to examine several characteristics of the mid-plane boundary layer and to evaluate the suitability of this boundary layer for further studies of canonical wall turbulence.

11.5.1 Transition and streamwise pressure distribution

A satisfactory form of boundary-layer transition can be induced by a trip comprising a single spanwise row of spheres. Placing the trip immediately downstream of the boundary-layer origin produces transition at the lowest possible flow speed. In the absence of a leading edge, a boundary-layer origin may be defined by using suction through a porous surface to remove the boundary layer immediately upstream of the trip. Measurements of wall shear stress 850 mm downstream of the trip then show that, for spheres of diameter d located at $x_t = 16$ mm, the boundary layer is in transition at a flow speed, U_t, given by the formula:

$$Re_d = \frac{U_t d}{\nu} = 423 \left(\frac{x_t}{d} \right)^{0.15}. \tag{11.4}$$

Satisfactory boundary-layer turbulence is produced at flow speeds 10% to 20% higher than the transition speed U_t. The selection of operating speeds is assisted by inspecting the statistics of the velocity fluctuations in the boundary-layer. The distributions of skewness and flatness are particularly useful for determining the state of the boundary layer because, in laminar and turbulent boundary layers, they are well-established and have a relatively low sensitivity to changing flow speed whereas, in transitional boundary layers, values of skewness and flatness are very large and are extremely sensitive to changes in flow speed.

11.5.2 Characteristics of the mid-plane boundary layers in a duct

Measurements of skin-friction coefficient, shape factor and wake strength indicate that the mechanisms of turbulence in the mid-plane boundary layers of a square duct are essentially the same as in a two-dimensional flat-plate boundary layer. These characteristics are indistinguishable from those of a flat-plate boundary layer if the boundary-layer thickness, δ_{99}, is less than half the effective duct radius[3], r'. The effects of a larger boundary-layer thickness (i.e. $\delta_{99}/r' \gtrsim 0.5$) are observed in both the near-wall and wake regions of a duct boundary layer as departures from the conventional behaviour of a two-dimensional boundary layer (Figure 11.3).

The skin friction coefficient, C_f, depends on the behaviour of flow in the near-wall region. In the near-wall x-y mid-plane of a duct with a square or nearly square cross-section, stress-induced secondary flow produces a mean velocity component away from the wall which is in the order of 0.3% of the free stream speed [Brundrett and Baines, 1964, Melling and Whitelaw, 1976]. Measurements indicate that, as a boundary layer increases in thickness to occupy most of the available duct cross-section, this secondary flow reduces C_f by up to about 5%. On the other hand, the flat-plate shape factor, H_2, depends primarily on the behaviour of flow in the wake region of the boundary layer. In locations where $\delta_{99}/r' \gtrsim 0.5$, lateral constriction of the wake region by the growth of side-wall boundary layers produces values of H_2 only slightly higher than expected of a two-dimensional flat-plate boundary layer.

During the initial development of the turbulent boundary layer, the nondimensional wake strength, ΔU^+, is increased by flow disturbances from the boundary-layer trip. If the trip is well designed, these effects decay rapidly and are usually undetectable at $Re_x > 150{,}000$. Between the trip-affected region and the location where $\delta_{99}/r' \approx 0.5$, the behaviour of the wake strength is the same as in a two-dimensional flat-plate boundary layer, and so it is a function of Reynolds number, $\Delta U^+_{2D}(Re_{\theta_2})$. In boundary layers thicker than $r'/2$, lateral constriction of the wake region by the side-wall boundary layers produces a wake-strength excess, ΔU^+_{XS}, which increases the wake strength to values significantly

[3] In a square duct, the effective duct radius is the hydraulic radius or half the height of the duct cross-section.

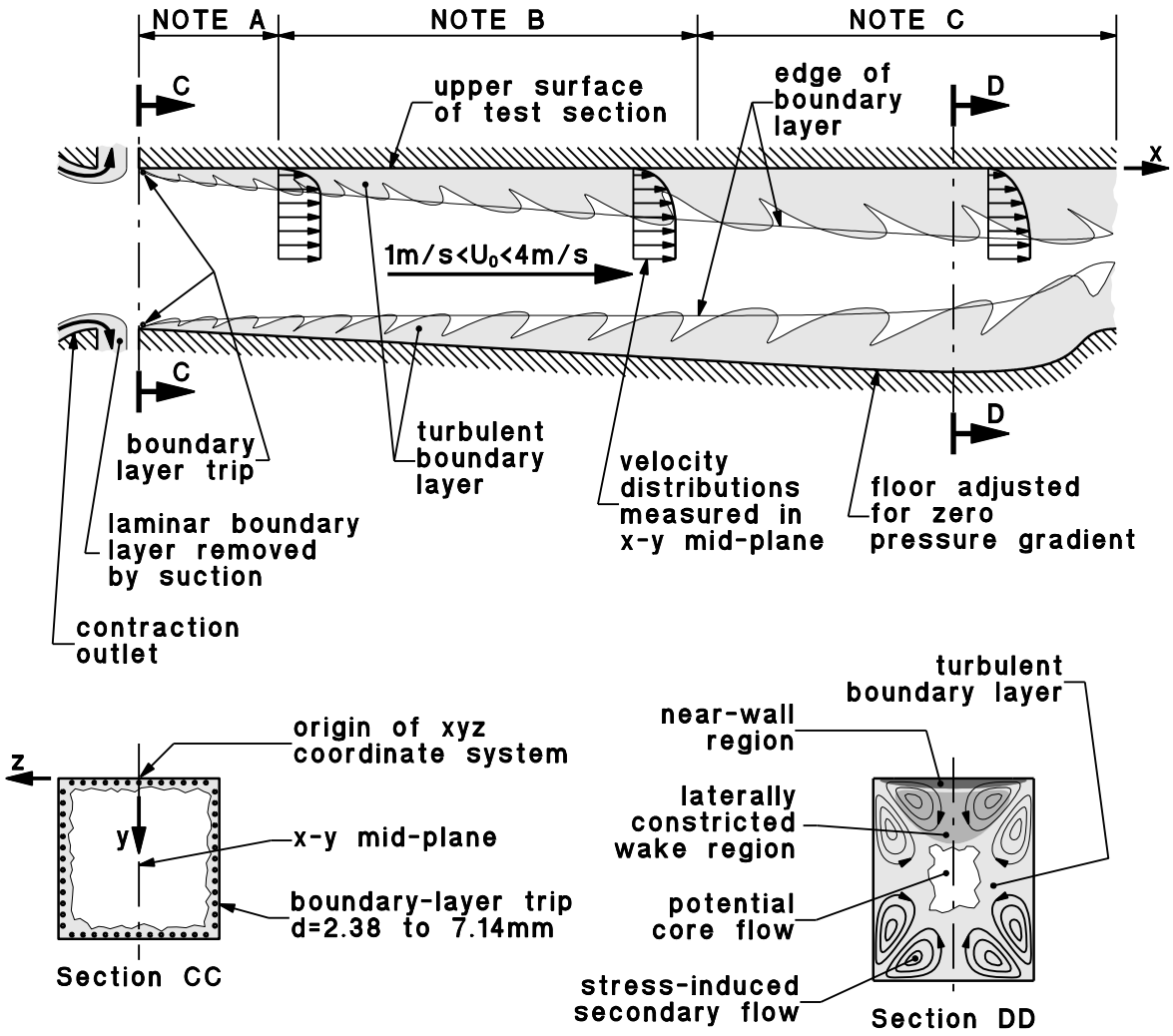

NOTES			
	test section Ports	criterion	comments
A	1 – 2/3	$Re_{\theta_2} < 400$	lack of wall-region and wake-region similarity
B	2/3 – 8/9	$\delta_{99}/r' \lesssim 0.5$	thin boundary layer good approximation to flat-plate boundary layer
C	9/10 – 15	$\delta_{99}/r' \gtrsim 0.5$	thick boundary layer lateral constriction of wake region increases H_2 and ΔU^+ C_f is reduced by stress-induced secondary flows

Figure 11.3: Schematic diagram of flow in the test section of the wind tunnel

larger than ΔU^+_{2D}. Experimental results suggest that ΔU^+_{XS} depends on the proportion of the duct cross-section occupied by the boundary layer. The total wake strength is therefore given by

$$\Delta U^+ = \Delta U^+_{2D}(Re_{\theta_2}) + \Delta U^+_{XS}\left(\frac{\delta_{99}}{r'}\right). \tag{11.5}$$

The mean-velocity model

$$\begin{aligned} y^+ &= U^+_w + e^{-\kappa C}\left[e^{\kappa U^+_w} - \sum_{n=0}^{4}\frac{1}{n!}(\kappa U^+_w)^n\right] \\ U^+_w &= U^+ - \frac{2\Pi}{\kappa}\sin^2\left(\frac{\pi y}{2\delta_\pi}\right) \\ \kappa &= 0.41, \end{aligned} \tag{11.6}$$

which is derived from Spalding's (1961) law of the wall and Coles's (1968) law of the wake, conforms to the experimental data with an overall r.m.s. error of $0.006U_0$. As Reynolds number increases, the coefficient C follows a generally decreasing trend which is best described by

$$C = 9.0 - 1.08\log_{10}Re_{\theta_2}. \tag{11.7}$$

The momentum-integral equation for flow in a duct with an arbitrary cross-section is

$$\frac{d\theta_d}{dx} + \frac{\theta_d}{U_0}\frac{dU_0}{dx}(H_d + 2) = \frac{1}{2}\overline{C_f} - \frac{\theta_d}{\mathcal{P}}\frac{d\mathcal{P}}{dx}. \tag{11.8}$$

This may be integrated with respect to x and, in the particular example where the duct cross-section is square or nearly square, a momentum balance may be estimated from velocity distribution and surface friction measurements in the x-y mid-plane of the duct. Over a development length of 15 duct heights from the boundary-layer origin, the measured r.m.s. error in momentum balance is about 2% of the final momentum thickness. In these calculations, it is assumed that

(1) the centreline friction coefficient is equal to the perimeter-averaged friction coefficient ($C_f = \overline{C_f}$) [Leutheusser, 1963], and

(2) cross-section contours of mean velocity are concentric rectangles.

The second assumption allows displacement thickness and momentum thickness of the duct mid-plane boundary layer to be evaluated using

$$\delta^*_d = \int_0^\delta \left(1 - \frac{U}{U_0}\right)\left(1 - \frac{8y}{\mathcal{P}}\right)dy \tag{11.9}$$

and

$$\theta_d = \int_0^\delta \frac{U}{U_0}\left(1 - \frac{U}{U_0}\right)\left(1 - \frac{8y}{\mathcal{P}}\right)dy \tag{11.10}$$

respectively.

When the conventional momentum integral equation for the two-dimensional flat-plate boundary layer,

$$\frac{d\theta_2}{dx} + \frac{\theta_2}{U_0}\frac{dU_0}{dx}(H_2 + 2) = \frac{1}{2}C_f \tag{11.11}$$

[Duncan et al., 1970], is used for calculating the momentum balance of thick duct boundary layers, balance errors can be in the order of 25%. It is therefore recommended that the two-dimensional momentum integral equation (Equation 11.11) not be used for momentum-balance calculations if $\delta_{99}/r' \gtrsim 0.2$.

11.5.3 Turbulence behaviour in the mid-plane boundary layer

The best outer-region scaling parameter for distance from the wall, y, is the flat-plate momentum thickness, θ_2. All the other outer-region scaling parameters examined in this study produce an inferior collapse of the data. Scaling with θ_2 produces similarity of wake-region mean velocity and wake-region turbulence statistics in boundary layers with Reynolds numbers, Re_{θ_2}, larger than 400. This success of θ_2 as a wake-region scaling parameter is not restricted to strictly flat-plate boundary layers; it applies equally to thin ($\delta_{99}/r' \lesssim 0.5$) and to thick ($\delta_{99}/r' \gtrsim 0.5$) mid-plane boundary layers in a square or nearly square duct. It suggests that the local wake-region dynamics of the mid-plane duct boundary layer are essentially the same as those in a two-dimensional flat-plate boundary layer.

General wall-region similarity of statistics derived from streamwise velocity fluctuations is restricted to the region between $y^+ = 13$ and the wall. Wall-region similarity of flatness and skewness extends through the log-law region to the inner edge of the wake region but, for skewness, this extended similarity is only observed when $Re_{\theta_2} \gtrsim 1400$. At lower Reynolds numbers, direct interaction between near-wall eruptions and irrotational fluid from the free stream flow causes the extended similarity of skewness to degenerate into a Reynolds-number dependence. Unusually low values of r.m.s., skewness and flatness statistics within the viscous sublayer and buffer region indicate failure of wall-region similarity for $Re_{\theta_2} \lesssim 400$.

In well developed turbulent boundary layers, similarity based on the wall variables U_τ and ν occurs in the region close to the wall where interaction between turbulence and the free stream is very weak. Likewise, wake-region similarity occurs where large-scale turbulence motions interact only very indirectly with the wall. However, at Reynolds numbers lower than 400, these normally weak interactions are strong enough to invalidate both wake-region similarity and wall-region similarity, and the development of conventional boundary-layer turbulence may be considered incomplete because it is not possible to divide the boundary layer into separate near-wall and wake regions.

11.5.4 Constraints on satisfactory performance of the wind tunnel

The behaviour of the centreline boundary layer in a duct with a square cross-section most closely approximates that of a canonical turbulent boundary layer where boundary-layer thickness is less than 50% of the effective duct radius and where the Reynolds number, Re_{θ_2}, is higher than 400. In boundary

layers thicker than half the effective duct radius, the wake-region characteristics H_2 and ΔU^+ are changed by lateral constriction of the wake region, and C_f is reduced by stress-induced secondary flows. Wall region and wake region similarity fail at Reynolds numbers (Re_{θ_2}) lower than 400. The lower limit of flow speed for a well-behaved boundary layer in the duct is determined by the onset of buoyant cross-flows and flow separation which may have their sources in the flow conditions far upstream of the duct segment under consideration.

11.6 Wall-proximity effect in hot-wire anemometry

Wall-proximity effect is the error in air speed measurement produced by placing a hot-wire probe close to a solid boundary. It is a result of aerodynamic distortion of the flow by the probe and conduction of heat from the hot-wire to the wall. The aerodynamic component of the error can be reduced to a negligible level by correct geometrical design of the hot-wire probe. The thermal component can be suppressed only by selecting a working fluid with a very high Prandtl number. In cases where this cannot be done, reliable measurements of turbulence in the viscous sublayer can be obtained by correcting the data from the hot-wire.

Dimensional analysis has shown that, in experiments where wall conductivity, probe geometry, hot-wire temperature and ambient fluid properties do not change, the only parameters of the Nusselt-number functions describing heat transfer to the wall (Nu_w) and to the fluid (Nu_c) are $\tilde{y}^+$ and $\tilde{Re}_d$. Changes in wall-proximity error caused by altering the hot-wire overheat ratio are due to the temperature dependence of kinematic viscosity, and are equivalent to the effect of changing the Prandtl number of the fluid.

Three methods have been developed for removing wall-proximity error from measurements with hot-wires in the viscous sublayer of a turbulent boundary layer. All methods use correction functions (f_1, f_2 or f_3) determined from mean velocity measurements and assume a linear instantaneous velocity distribution. The first method is based on the observation that, for fixed probe geometry, fluid properties, wall-material properties and overheat ratio, the error in mean velocity measurement is given by the single-parameter function $\Delta U^+ = f_1(y^+)$. The necessary correction to the data is determined by solving

$$\tilde{u}_m^+ = \tilde{u}^+ + f_1(\tilde{y}^+). \tag{11.12}$$

This method produces viscous sublayer turbulence statistics which agree well with other experimental data believed to be free of wall-proximity errors, but provides very little scope for investigating the physics of wall-proximity effect.

The second correction method is derived from the dimensional analysis of heat flow from a hot-wire

filament and assumes a simplified heat-transfer relationship of the form

$$Nu_d(\tilde{Re}_{d,m}) = Nu_d(\tilde{Re}_d) + \frac{d}{y} Nu_w(\tilde{y}^+), \tag{11.13}$$

where Nu_d is the hot-wire calibration. The resulting correction formula for the anemometer output voltage, $\tilde{v}_m$ is

$$\tilde{v}_m^2 = \tilde{v}^2 + \frac{1}{y} f_2(\tilde{y}^+). \tag{11.14}$$

This simple heat-transfer model predicts the effects of varying overheat ratio and hot-wire diameter with fair success, but it does not produce the required invariance of $\Delta U^+ = f_1(y^+)$ with changing air speed, and it does not produce credible turbulence statistics when used for correcting experimental data.

For the third correction method, the heat-transfer model is constrained to satisfy $\Delta U^+ = f(y^+)$ by making Nu_w proportional to Re_d^n, where n is the Reynolds-number exponent of the hot-wire calibration. For the purpose of removing wall-proximity error, the effects of wall proximity on Nu_c can then be transferred to Nu_w. The required effect of varying the hot-wire filament diameter can be achieved with an additional parameter, l/d, which controls the three-dimensionality of the outer, convective heat-flow field around the hot-wire filament. The parameter l/d decouples the effect of varying diameter from the effect of varying air speed. On the basis of correlation with the experimental data of Krishnamoorthy et al. (1985), it is suggested that the effect of varying overheat ratio can be modelled by making Nu_w proportional to $(\nu_f/\nu_\infty)^{0.67}$. For a fixed probe geometry, the "modified heat-transfer" model then becomes

$$Nu_d(\tilde{Re}_{d,m}) = Nu_d(\tilde{Re}_d) + \left(\frac{\nu_f}{\nu_\infty}\right)^{0.67} \tilde{Re}_d^n \frac{1}{\tilde{y}^+} f(\tilde{y}^+), \tag{11.15}$$

and the corresponding correction formula for the anemometer output voltage is

$$\tilde{v}_m^2 = \tilde{v}^2 + \left(\frac{\nu_f}{\nu_\infty}\right)^{0.67} y^{n-1} \tilde{u}_\tau^{2n-1} f_3(\tilde{y}^+). \tag{11.16}$$

The turbulence statistics of data corrected by this method are essentially the same as those from the velocity-error method because, given a fixed overheat ratio and $n = 0.5$, these two correction methods are mathematically equivalent. However, this method has the advantage that it can allow for the effect of varying overheat ratio.

11.7 Notation

A	cross-section area of a duct
C	additive coefficient for Coles's (1968) law of the wall, $U^+ = \kappa^{-1} \ln y^+ + C$.
C_f	Local skin friction coefficient

$\overline{C_f}$	Local skin friction coefficient averaged around the cross-section perimeter of a duct.
d	diameter of spheres used in a boundary-layer trip, or diameter of a hot-wire filament
f_1, f_2, f_3	error functions which describe wall-proximity effect
g	gravitational acceleration
H_2	δ_2^*/θ_2, shape factor for two-dimensional flat-plate boundary layer
H_d	δ_d^*/θ_d shape factor for the boundary layer in a duct
l	active length of a hot-wire filament.
L	length of duct
m	Thwaites parameter (Equation 4.4, page 80)
Nu_c	$h_c d/k_f$, Nusselt number for heat which is convected far downstream from a hot-wire filament and is *not* eventually transferred to the wall
Nu_d	hd/k_f, Nusselt number for heat transfer from a cylinder; i.e. hot-wire calibration
Nu_w	$h_w y/k_f$, Nusselt number for heat transfer from a hot-wire filament to a solid wall
$\mathcal{P}$	perimeter of a duct cross-section
r'	effective radius of a duct. In a square duct, this is the hydraulic radius, $2A/\mathcal{P}$, or half the duct height.
$R(x)$	possibly varying radius of an axisymmetric duct
Re_d	$U_0 d/\nu$, Reynolds number of the boundary-layer trip, or Reynolds number of the hot-wire filament
Re_x	$U_0 x/\nu$, Reynolds number of a boundary layer — based on distance from the boundary-layer origin, x.
Re_{θ_2}	$U_0\theta/\nu$, Reynolds number of a flat-plate boundary layer — based on momentum thickness θ_2.
Ri	Richardson number, defined by Equation 11.2 on page 294
U	x component of time-averaged flow velocity
U_0	free stream speed in the wind-tunnel test section
U_t	free stream speed at which a boundary-layer trip produces transition
U_w^+	law-of-the-wall component of streamwise velocity
U_τ	time-averaged friction velocity of the boundary layer; defined by the wall-shear stress, $\tau_w = \rho U_\tau^2$
$\tilde{u}$	x component of instantaneous flow velocity
$\tilde{u}_m$	instantaneous flow speed measured by the hot-wire anemometer without correcting for wall-proximity affect
$\tilde{u}_\tau$	instantaneous friction velocity, defined by $\tilde{\tau}_w = \rho\tilde{u}_\tau^2$

$\tilde{v}$	anemometer output voltage corresponding to a flow velocity, $\tilde{u}$, which is corrected for wall-proximity effect
$\tilde{v}_m$	anemometer output voltage from a hot-wire subject to wall-proximity effect
x	distance downstream from the boundary-layer origin
x_t	distance from the boundary-layer origin to the boundary-layer trip
y	distance from the test-section wall
α	swirl angle at the periphery of a forced vortex
ΔU^+	$f_1(y^+)$, error in velocity measurement due to wall- proximity effect
ΔU^+	$2\Pi/\kappa$, Coles (1962) wake strength
ΔU^+_{2D}	component of Coles (1962) wake strength due to flat-plate boundary-layer turbulence; function of Re_{θ_2}
ΔU^+_{XS}	component of Coles (1962) wake strength due to lateral compression by side-wall boundary layers; function of δ_{99}/r'
$\Delta\theta$	elevation of air temperature above the ambient temperature Θ_a
δ_{99}	boundary-layer thickness defined as the distance from the wall at which $U = 0.99U_0$
δ^*_2	displacement thickness of a two-dimensional flat-plate boundary layer (Equation 7.5)
δ^*_d	displacement thickness of the boundary layer developed in a duct with a rectangular cross-section (Equation 11.9)
δ_π	boundary-layer thickness parameter for the Coles wake function
Θ_a	ambient air temperature
θ_2	momentum thickness of a two-dimensional flat-plate boundary layer (Equation 7.6)
θ_d	momentum thickness of the boundary layer developed in a duct with a rectangular cross-section (Equation 11.10)
κ	Von Kàrmàn constant ($\kappa = 0.41$) for the law of the wall: $U^+ = \kappa^{-1}\ln y^+ + C$
ν	kinematic viscosity
Π	amplitude parameter for Coles wake function
ψ	rotation angle of the flow or rotation angle of the temperature distribution due to buoyant convection

Superscripts

Variables which have a superscript $^+$ are nondimensionalised using the viscous flow variables U_τ and ν, e.g. $U^+ = U/U_\tau$ and $y^+ = yU_\tau/\nu$.

Superscript $\tilde{}$ is used for indicating a quantity which may vary as a function of time.

subscripts

f	for properties of the fluid - evaluated at the film temperature, which is sometimes defined as $T_f = T_\infty + \Delta T/2$
∞	for ambient properties of the fluid

References

[Acarlar and Smith, 1987a] Acarlar, M. S. and Smith, C. R. (1987a). A study of hairpin vortices in a laminar boundary layer. Part 1. Hairpin vortices generated by a hemisphere protuberance. *Journal of Fluid Mechanics*, 175:1–41.

[Acarlar and Smith, 1987b] Acarlar, M. S. and Smith, C. R. (1987b). A study of hairpin vortices in a laminar boundary layer. Part 2. Hairpin vortices generated by fluid injection. *Journal of Fluid Mechanics*, 175:42–83.

[Acharya and Escudier, 1984] Acharya, M. and Escudier, M. P. (1984). A direct formulation of correlations for wall-proximity corrections of hot-wire measurements. *Experiments in Fluids*, 2:135–136.

[Aihara et al., 1984] Aihara, Y., Tomita, Y., and Ito, A. (1984). Generation, development and distortion of longitudinal vortices in boundary layers along concave and flat plates. In Kozlov, V. V., editor, *Proceedings of IUTAM Symposium on Laminar-turbulent transition,*, pages 447–453, Novosibirsk, USSR. IUTAM, Springer-Verlag.

[Alfredsson et al., 1988] Alfredsson, P. H., Johansson, A. V., Haritonidis, J. H., and Eckelmann, H. (1988). The fluctuating wall-shear stress and the velocity field in the viscous sublayer. *Physics of Fluids*, 31(5):1026–1033.

[Andreopoulos et al., 1984] Andreopoulos, J., Durst, F., Zaric, Z., and Jovanovic, J. (1984). Influence of Reynolds number on characteristics of turbulent wall boundary layers. *Experiment in Fluids*, 2:7–16.

[Antonia and Bisset, 1990] Antonia, R. A. and Bisset, D. K. (1990). Spanwise structure in the near-wall region of a turbulent boundary layer. *Journal of Fluid Mechanics*, 210:437–458.

[Antonia and Kim, 1992] Antonia, R. A. and Kim, J. (1992). Low Reynolds number effects on near-wall turbulence. In *Eleventh Australasian Fluid Mechanics Conference*, pages 817–820. University of Tasmania.

[Antonia et al., 1992] Antonia, R. A., Teitel, M., Kim, J., and Browne, L. W. B. (1992). Low-Reynolds-number effects in a fully developed turbulent channel flow. *Journal of Fluid Mechanics*, 236:579–605.

[Azad and Burhanuddin, 1984] Azad, R. S. and Burhanuddin, S. (1984). Measurements of some features of turbulence in wall-proximity. *Experiments in Fluids*, 1:149–160.

[Bakewell and Lumley, 1967] Bakewell, H. P. and Lumley, J. L. (1967). Viscous sublayer and adjacent wall region in turbulent pipe flow. *Physics of Fluids*, 10(9):1880–1889.

[Bansod and Bradshaw, 1972] Bansod, P. and Bradshaw, P. (1972). The flow in s-shaped ducts. *Aeronautical Quarterly*, 23(2):131–140.

[Beattie and Green, 1983] Beattie, D. R. H. and Green, W. J. (1983). A simplified and accurate method of describing non-turbulent transport of momentum in turbulent flow theory. In *Proceedings, 8th Australasian Fluid Mechanics Conference*, pages 10A.5–10A.9. University of Newcastle.

[Bernard and Berger, 1984] Bernard, P. S. and Berger, B. S. (1984). Balance of turbulent energy in the linear wall region of channel flow. *American Institute of Aeronautics and Astronautics Journal*, 22(2):306–308.

[Bhatia et al., 1982] Bhatia, J. C., Durst, F., and Jovanovic, J. (1982). Corrections of hot-wire anemometer measurements near walls. *Journal of Fluid Mechanics*, 122:411–431.

[Bies and Hansen, 1988] Bies, D. A. and Hansen, C. H. (1988). *Engineering Noise Control*, chapter 9. Unwin Hyman, Sydney & London, 1st edition.

[Bippes, 1990] Bippes, H. (1990). Experimental results on the Görtler instability problem and comparison with theoretical approaches. In *First Euromech Symposium on Görtler vortex flows*, page 261, Nantes, France.

[Bippes and Görtler, 1972] Bippes, H. and Görtler, H. (1972). Three-dimensional disturbances in the boundary layer along a concave wall. *Acta Mechanica*, 14:251–267.

[Blackwelder, 1981] Blackwelder, R. F. (1981). *Hot-Wire and Hot-Film Anemometers*, volume 18(A) of *Methods of Experimental Physics: Fluid Dynamics*, pages 259–314. Academic Press, New York.

[Blackwelder and Kaplan, 1976] Blackwelder, R. F. and Kaplan, R. E. (1976). On the wall structure of the turbulent boundary layer. *Journal of Fluid Mechanics*, 76(1):89–112.

[Böttcher and Wedemeyer, 1989] Böttcher, J. and Wedemeyer, E. (1989). The flow downstream of screens and its influence on the flow in the stagnation region of cylindrical bodies. *Journal of Fluid Mechanics*, 204:501–522.

[Bradshaw, 1965] Bradshaw, P. (1965). The effect of wind-tunnel screens on nomimally two dimensional boundary layers. *Journal of Fluid Mechanics*, 22:679–687.

[Bradshaw, 1971] Bradshaw, P. (1971). *An introduction to turbulence and its measurement*. Pergamon Press.

[Bradshaw, 1987] Bradshaw, P. (1987). Turbulent secondary flows. *Annual Review of Fluid Mechanics*, 19:53–74.

[Bradshaw and Wong, 1972] Bradshaw, P. and Wong, F. Y. F. (1972). The reattachment and relaxation of turbulent shear layer. *Journal of Fluid Mechanics*, 52:113–135.

[Brundrett and Baines, 1964] Brundrett, E. and Baines, W. D. (1964). The production and diffusion of vorticity in duct flow. *Journal of Fluid Mechanics*, 19:375–394.

[Cantwell, 1981] Cantwell, B. J. (1981). Organized motion in turbulent flow. *Annual Review of Fluid Mechanics*, 13:457–515.

[Castro et al., 1987] Castro, I. P., Dianat, M., and Bradbury, L. J. S. (1987). The pulsed wire skin-friction measurement technique. In *Turbulent shear flows 5, selected papers from Fifth International Symposium on Turbulent Shear Flows*, pages 278–290. Springer-Verlag.

[Cebeci and Bradshaw, 1977] Cebeci, T. and Bradshaw, P. (1977). *Momentum transfer in boundary layers*. Hemisphere Publishing Corporation, Washington.

[Champagne et al., 1967] Champagne, F. H., Sleicher, C. A., and Wehrmann, O. H. (1967). Turbulence measurements with inclined hot-wires. Part 1. Heat transfer experiments with inclined hot-wire. *Journal of Fluid Mechanics*, 28(1):153–175.

[Cheers, 1945] Cheers, F. (1945). Note on wind-tunnel contractions. Reports and Memoranda 2137, Aeronautical Research Council.

[Chmielewski, 1974] Chmielewski, G. E. (1974). Boundary-layer considerations in the design of aerodynamic contractions. *Journal of Aircraft*, 11(8):435–438.

[Clauser, 1954] Clauser, F. H. (1954). Turbulent boundary layers in adverse pressure gradients. *Journal of the Aeronautical Sciences*, 21(2):91–108.

[Cohen and Ritchie, 1962] Cohen, M. J. and Ritchie, N. J. B. (1962). Low-speed three-dimensional contraction design. *Journal of the Royal Aeronautical Society*, 66:231–236.

[Coles, 1962] Coles, D. E. (1962). A manual of experimental boundary layer practice for low speed flow. Appendix A to Rand Report TR-403-PR, National Advisory Committee on Aeronautics.

[Coles, 1968] Coles, D. E. (1968). The young person's guide to the data. In *1968 AFOSR-IFP-Stanford Conference on Computation of Turbulent Boundary Layers*, pages 1–45.

[Collis and Williams, 1959] Collis, D. C. and Williams, M. J. (1959). Two dimensional convection from heated wires at low Reynolds number. *Journal of Fluid Mechanics*, 6:357–389.

[Compte-Bellot, 1976] Compte-Bellot, G. (1976). Hot-wire anemometry. *Annual Review of Fluid Mechanics*, 8:209–231.

[Compte-Bellot et al., 1971] Compte-Bellot, G., Strohl, A., and Alcaraz, E. (1971). On aerodynamic disturbances caused by single hot-wire probes. *A.S.M.E. Transactions, Journal of Applied Mechanics*, 38:767–774.

[Corino and Brodkey, 1969] Corino, E. R. and Brodkey, R. S. (1969). A visual investigation of the wall region in a turbulent flow. *Journal of Fluid Mechanics*, 37(1):1–30.

[Corrsin and Kistler, 1954] Corrsin, S. and Kistler, A. (1954). The free stream boundaries of turbulent flows. Technical Note 3133, National Advisory Committee on Aeronautics.

[Cowley et al., 1990] Cowley, S. J., van Dommelen, L. L., and Lam, S. T. (1990). On the use of Langrangian variables in descriptions of unsteady boundary-layer separation. *Philosophical Transactions of the Royal Society of London*, 333:343–378.

[Curle, 1962] Curle, N. (1962). *The Laminar Boundary Layer Equations*. Oxford Univerity Press.

[Dahm and Rasmussen, 1969] Dahm, M. and Rasmussen, C. G. (1969). Effect of wire mounting system on hot-wire probe characteristics. *DISA Information*, 7:19–24.

[Deissler, 1969] Deissler, R. G. (1969). Direction of maximum turbulent vorticity in a shear flow. *Physics of Fluids*, 12(2):426–427.

[Doligalski and Walker, 1984] Doligalski, T. L. and Walker, J. D. A. (1984). The boundary layer induced by a convected two-dimensional vortex. *Journal of Fluid Mechanics*, 139:1–28.

[Downie et al., 1984] Downie, J. H., Jordinson, R., and Barnes, F. H. (1984). On the design of three-dimensional wind tunnel contractions. *Aeronautical Journal*, 88(4):287–295.

[Duncan et al., 1970] Duncan, W. J., Thom, A. S., and Young, A. D. (1970). *Mechanics of Fluids*. Edward-Arnold (publishers) Ltd., London, 2nd edition.

[Eckelmann, 1974] Eckelmann, H. (1974). The structure of the viscous sublayer and the adjacent wall region in a turbulent channel flow. *Journal of Fluid Mechanics*, 65:439–459.

[Elliot et al., 1983] Elliot, J. W., Cowley, S. J., and Smith, F. T. (1983). Breakdown of boundary layers: (i) on moving surfaces; (ii) in self-similar unsteady flow; (iii) in fully unsteady flow. *Geophysical and Astrophysical Fluid Dynamics*, 25:77–138.

[Erm, 1988] Erm, L. P. (1988). *Low-Reynolds-number turbulent boundary layers*. PhD dissertation, University of Melbourne, Department of Mechanical and Manufacturing Engineering.

[Ersoy and Walker, 1985] Ersoy, S. and Walker, J. D. A. (1985). Viscous flow induced by counter-rotating vortices. *Physics of Fluids*, 28(9):2687–2698.

[Ersoy and Walker, 1987] Ersoy, S. and Walker, J. D. A. (1987). The boundary layer due to a three-dimensional vortex loop. *Journal of Fluid Mechanics*, 185:569–598.

[Fage and Townend, 1932] Fage, A. and Townend, H. C. H. (1932). An examination of turbulent flow with an ultramicroscope. *Proceedings of the Royal Society of London, Series A*, 135:656–677.

[Fairlie, 1980] Fairlie, B. D. (1980). Flow separation on bodies of revolution at incidence. In *Proceedings, 7th Australasian Hydraulics and Fluid Mechanics Conference*, pages 338–341, Brisbane, Queensland. Institution of Engineers, Australia, Pergamon.

[Floryan and Saric, 1982] Floryan, J. M. and Saric, W. S. (1982). Stability of Görtler vortices in boundary layers. *American Institute of Aeronautics and Astronautics*, 20(3):316–324.

[Floryan and Saric, 1983] Floryan, J. M. and Saric, W. S. (1983). Effects of suction on the Görtler instability of boundary layers. *American Institute of Aeronautics and Astronautics Journal*, 21(12):1635–1639.

[Floryan and Saric, 1984] Floryan, J. M. and Saric, W. S. (1984). Wavelength selection and growth of Görtler vortices. *American Institute of Aeronautics and Astronautics Journal*, 22(11):1529–1538.

[Freymuth, 1977] Freymuth, P. (1977). Frequency response and electronic testing for constant temperature hot-wire anemometers. *Journal of Physics E (Scientific Instruments)*, 10:705–709.

[Freymuth and Fingerson, 1977] Freymuth, P. and Fingerson, L. M. (1977). Electronic testing of frequency response for thermal anemometers. *TSI Quarterly*, 3:5–12.

[Gaster, 1971] Gaster, M. (1971). Vortex shedding from circular cylinders at low Reynolds numbers. *Journal of Fluid Mechanics*, 46(4):749–756.

[Gavrilakis, 1992] Gavrilakis, S. (1992). Numerical simulation of low-Reynolds-number turbulent flow through a straight square duct. *Journal of Fluid Mechanics*, 244:101–129.

[Gerich and Eckelmann, 1982] Gerich, D. and Eckelmann, H. (1982). Influence of end plates and free ends on the shedding frequency of circular cylinders. *Journal of Fluid Mechanics*, 122:109–121.

[Görtler, 1940] Görtler, H. (1940). Über den Einfluß der Wandkrümmung auf die Entstehung der Turbulenz. *Zeitschrift für Angewandte Mathematik und Mechanik*, 20(3):138–147.

[Görtler, 1941] Görtler, H. (1941). Instabilität laminarer Grenzchichten an konkaven Wänden gegenüber gewissen dreidimensionalen Störungen. *Zeitschrift für Angewandte Mathematik und Mechanik*, 21(4):250–252.

[Grant, 1958] Grant, H. L. (1958). The large eddies of turbulent motion. *Journal of Fluid Mechanics*, 4:149–190.

[Grass, 1971] Grass, A. J. (1971). Structural features of turbulent flow over smooth and rough boundaries. *Journal of Fluid Mechanics*, 50(2):233–255.

[Guezennec et al., 1989] Guezennec, Y. G., Piomelli, U., and Kim, J. (1989). On the shape and dynamics of wall structures in turbulent channel flow. *Physics of Fluids A*, 1(4):764–767.

[Gupta et al., 1971] Gupta, A. K., Laufer, J., and Kaplan, R. E. (1971). Spatial structure in the viscous sublayer. *Journal of Fluid Mechanics*, 50(3):493–512.

[Hall, 1983] Hall, P. (1983). The linear development of Görtler vortices in growing boundary layers. *Journal of Fluid Mechanics*, 130:41–58.

[Hawthorne, 1951] Hawthorne, W. R. (1951). Secondary circulation in fluid flow. *Proceedings of the Royal Society of London, Series A*, 206:374–387.

[Head and Bandyopadhyay, 1981] Head, M. R. and Bandyopadhyay, P. (1981). New aspects of turbulent boundary layer structure. *Journal of Fluid Mechanics*, 107:297–338.

[Hebbar, 1980] Hebbar, K. S. (1980). Wall-proximity corrections for hot-wire readings in turbulent flows. *DISA Information*, 25:15–17.

[Hilby, 1981] Hilby, J. W. (1981). Definition and measurement of the degree of mixing in liquid mixtures. *International Chemical Engineering*, 21(2):197–204.

[Hinze, 1975] Hinze, J. O. (1975). *Turbulence: An introduction to its mechanism and theory*. McGraw-Hill Book Co., New York, 2nd edition.

[Hollasch and Gebhart, 1972] Hollasch, K. and Gebhart, B. (1972). Calibration of constant-temperature hot-wire anemometers at low velocities in water with variable fluid temperature. *A.S.M.E. Transactions, Journal of Heat Transfer*, 94:17–22.

[Hon and Walker, 1991] Hon, T. L. and Walker, J. D. A. (1991). Evolution of hairpin vortices in a shear flow. *Computers and Fluids*, 20(3):343–358.

[Hornung and Perry, 1984] Hornung, H. and Perry, A. E. (1984). Some aspects of three-dimensional separation. Part 1: Streamsurface bifurcations. *Zeitschrift für Flugwissenschaften und Weltraumforschung*, 8(2):77–87.

[Janke, 1987] Janke, G. (1987). Hot wire in wall proximity. In *Advances in Turbulence 1, Proceedings of the Third European Turbulence Conference, Lyon 1986*, pages 488–498, New York, Berlin. Springer-Verlag.

[Jiminez and Moin, 1991] Jiminez, J. and Moin, P. (1991). The minimal flow unit in near-wall turbulence. *Journal of Fluid Mechanics*, 225:213–240.

[Johansson and Alfredsson, 1983] Johansson, A. V. and Alfredsson, P. H. (1983). Effects of imperfect spatial resolution on measurements of wall-bounded turbulent shear flows. *Journal Of Fluid Mechanics*, 137:409–421.

[Johansson et al., 1986] Johansson, A. V., Alfredsson, P. H., and Eckelmann, H. (1986). On the evolution of shear-layer structures in near-wall turbulence. In *Advances in Turbulence 1, Proceedings of the First European Turbulence Conference*, pages 383–390. Springer-Verlag.

[Johnston, 1960] Johnston (1960). On the three-dimensional turbulent boundary layer generated by secondary flow. *Journal of Basic Engineering, Transactions A.S.M.E. Series D*, 82(1):233–248.

[Kastrinakis et al., 1977] Kastrinakis, E. G., Wallace, J. M., Willmarth, W. W., Ghorashi, B., and Brodkey, R. S. (1977). On the mechanism of boundary turbulent shear flows. *Lecture Notes in Physics*, 75:190–204.

[Kim et al., 1971] Kim, H. T., Kline, S. J., and Reynolds, W. C. (1971). The production of turbulence near a smooth wall in a turbulent boundary layer. *Journal of Fluid Mechanics*, 50(1):133–160.

[Kim, 1983] Kim, J. (1983). On the structure of wall-bounded turbulent flows. *Physics of Fluids*, 26(8):2088–2097.

[Kim, 1985] Kim, J. (1985). Turbulence structure associated with the bursting event. *Physics of Fluids*, 28(1):52–58.

[Kim, 1987] Kim, J. (1987). Evolution of a vortical structure associated with the bursting event in a channel flow. In *Turbulent Shear Flows 5, selected papers from Fifth International Symposium on Turbulent Shear Flows*, pages 221–233. Springer-Verlag.

[Kim et al., 1987] Kim, J., Moin, P., and Moser, R. (1987). Turbulence statistics in fully developed channel flow at low Reynolds number. *Journal of Fluid Mechanics*, 177:133–166.

[Kim and Spalart, 1987] Kim, J. and Spalart, P. R. (1987). Scaling of the bursting frequency in turbulent boundary layers at low Reynolds numbers. *Physics of Fluids*, 30(11):3326–3328.

[King, 1914] King, L. V. (1914). On the convection of heat from small cylinders in a stream of fluid: determination of the convective constants of small platinum wires with applications to hot-wire anemometry. *Philosophical Transactions of the Royal Society of London, Series A*, 214:373–432.

[Klebanoff, 1957] Klebanoff, P. S. (1957). Characteristics of turbulence in a boundary layer with zero pressure gradient. Technical Report 1247, National Advisory Committee for Aeronautics.

[Kline et al., 1967] Kline, S. J., Reynolds, W. C., Schraub, F. A., and Runstadler, P. W. (1967). The structure of turbulent boundary layer. *Journal of Fluid Mechanics*, 30(4):741–773.

[Komoda, 1967] Komoda, H. (1967). Nonlinear development of disturbance in a laminar boundary layer. *Physics of Fluids*, 10(9):S87–S94.

[König et al., 1990] König, M., Eisenlohr, H., and Eckelmann, H. (1990). The fine structure in the Strouhal-Reynolds number relationship of the laminar wake of a circular cylinder. *Physics of Fluids A*, 2(9):1607–1614.

[Kovasznay, 1949] Kovasznay, L. S. G. (1949). Hot-wire investigation of the wake behind cylinders at low Reynolds numbers. *Proceedings of the Royal Society of London, Series A*, 198:174–190.

[Kovasznay, 1970] Kovasznay, L. S. G. (1970). The turbulent boundary layer. *Annual Review of Fluid Mechanics*, 2:95–112.

[Kreplin and Eckelmann, 1979a] Kreplin, H.-P. and Eckelmann, H. (1979a). Behaviour of the three fluctuating velocity components in the wall region of a turbulent channel flow. *Physics of Fluids*, 22(7):1233–1239.

[Kreplin and Eckelmann, 1979b] Kreplin, H.-P. and Eckelmann, H. (1979b). Propagation of perturbations in the viscous sublayer and adjacent wall region. *Journal of Fluid Mechanics*, 95(2):305–322.

[Kreyszig, 1972] Kreyszig, E. (1972). *Advanced Engineering Mathematics*. John Wiley and Sons, Inc, New York, London, Sydney, Toronto, third edition.

[Krishnamoorthy and Antonia, 1988] Krishnamoorthy, L. V. and Antonia, R. A. (1988). Turbulent kinetic energy budget in the near-wall region. *American Institute of Aeronautics and Astronautics Journal*, 26(3):300–302.

[Krishnamoorthy et al., 1983] Krishnamoorthy, L. V., Wood, D. H., Chambers, A. J., and Antonia, R. A. (1983). Wall effect on a hot wire in a turbulent boundary layer. In *Proceedings, 8th Australasian Fluid Mechanics Conference*, pages 6B13–6B16. University of Newcastle.

[Krishnamoorthy et al., 1985] Krishnamoorthy, L. V., Wood, D. H., Chambers, A. J., and Antonia, R. A. (1985). Effect of wire diameter and overheat ratio near a conducting wall. *Experiments in Fluids*, 3:121–127.

[Langmuir, 1912] Langmuir, I. (1912). Convection and conduction of heat in gases. *Physical Review*, 34(6):401–422.

[Lanspeary, 1986] Lanspeary, P. V. (1986). Mean and fluctuating velocity in a low Reynolds number boundary layer. In *Proceedings, 9th Australasian Fluid Mechanics Conference*, pages 618–621. The University of Auckland.

[Laufer, 1954] Laufer, J. (1954). The structure of turbulence in fully developed pipe flow. Technical Report 1174, National Advisory Committee on Aeronautics.

[Leutheusser, 1963] Leutheusser, H. J. (1963). Turbulent flow in rectangular ducts. *American Society of Civil Engineers, Journal of the Hydraulics Division*, 89(HY 3):1–19.

[Lighthill, 1963] Lighthill, M. J. (1963). *Laminar Boundary Layers*, Chapter II, pages 76–82. Oxford University Press, Amen House, London E.C.4.

[Ligrani and Bradshaw, 1987a] Ligrani, P. M. and Bradshaw, P. (1987a). Spatial resolution and measurement of turbulence in the viscous sublayer using subminiature hot-wire probes. *Experiments in Fluids*, 5:407–417.

[Ligrani and Bradshaw, 1987b] Ligrani, P. M. and Bradshaw, P. (1987b). Subminiature hot-wire sensors: Development and use. *Journal of Physics E (Scientific Instruments)*, 20:323–332.

[Lim, 1971] Lim, K. B. (1971). *Pressure Fluctuations in Turbulent Flows Under the Effects of Mean Pressure Gradients*. PhD thesis, University of Adelaide, Department of Mechanical Engineering.

[Lim et al., 1980] Lim, T. T., Chong, M. S., and Perry, A. E. (1980). The viscous tornado. In *Proceedings, 7th Australasian Hydraulics and Fluid Mechanics Conference*, pages 250–253, Brisbane, Queensland. Institution of Engineers, Australia, Pergamon.

[Liu et al., 1983] Liu, D. G., Fei, J. G., Yu, Y. J., and Li, G. (1983). *Collection of Fortran Algorithms*. Defence Industry Press Inc., Beijing.

[Lomas, 1986] Lomas, C. G. (1986). *Fundamentals of hot wire anemometry*. Cambridge University Press, Cambridge [Cambridgeshire] ; New York.

[Mehta, 1977] Mehta, R. D. (1977). The aerodynamic design of blower tunnels with wide-angle diffusers. *Progress in Aerospace Sciences*, 18:59–120.

[Mehta, 1985] Mehta, R. D. (1985). Turbulent boundary layer perturbed by a screen. *American Institute of Aeronautics and Astronautics Journal*, 23(9):1335–1342.

[Melling and Whitelaw, 1976] Melling, A. and Whitelaw, J. H. (1976). Turbulent flow in a rectangular duct. *Journal Of Fluid Mechanics*, 78(2):289–315.

[Mikhail, 1979] Mikhail, M. N. (1979). Optimum design of wind-tunnel contractions. *American Institute of Aeronautics and Astronautics Journal*, 17(5):471–477.

[Milthorpe and Wood, 1983] Milthorpe, J. F. and Wood, D. H. (1983). Numerical simulation of hot-wire behaviour in the viscous sublayer. In *Proceedings, 8th Australasian Fluid Mechanics Conference*, pages 6B5–6B8. University of Newcastle.

[Moin and Kim, 1982] Moin, P. and Kim, J. (1982). Numerical investigation of turbulent channel flow. *Journal of Fluid Mechanics*, 118:341–377.

[Moin and Kim, 1985] Moin, P. and Kim, J. (1985). The structure of the vorticity field in turbulent channel flow. Part 1. Analysis of instantaneous fields and statistical correlations. *Journal of Fluid Mechanics*, 155:441–464.

[Moin and Moser, 1989] Moin, P. and Moser, R. D. (1989). Characteristic-eddy decomposition of turbulence in a channel. *Journal of Fluid Mechanics*, 200:471–509.

[Morel, 1975] Morel, T. (1975). Comprehensive design of axisymmetric wind tunnel contractions. *A.S.M.E. Transactions, Journal of Fluids Engineering*, 87(2):225–233.

[Murlis et al., 1982] Murlis, J., Tsai, H. M., and Bradshaw, P. (1982). The structure of turbulent boundary layers at low Reynolds numbers. *Journal of Fluid Mechanics*, 122:13–56.

[Nishioka, 1973] Nishioka, M. (1973). Hot-wire technique for measuring velocities at extremely low wind-speed. *Bulletin of the Japan Society of Mechanical Engineers*, 16:1887–1899.

[Nishioka and Sato, 1974] Nishioka, M. and Sato, H. (1974). Measurements of velocity distributions in the wake of a circular cylinder at low Reynolds numbers. *Journal of Fluid Mechanics*, 65(1):97–112.

[Nychas et al., 1973] Nychas, S. G., Hershey, H. C., and Brodkey, R. S. (1973). A visual study of turbulent shear flow. *Journal of Fluid Mechanics*, 61(3):513–540.

[Offen and Kline, 1974] Offen, G. R. and Kline, S. J. (1974). Combined dye-streak and hydrogen-bubble visual observations of a turbulent boundary layer. *Journal of Fluid Mechanics*, 62(2):223–239.

[Offen and Kline, 1975] Offen, G. R. and Kline, S. J. (1975). A proposed model of the bursting process in turbulent boundary layers. *Journal of Fluid Mechanics*, 70(2):209–228.

[Oka and Kostic, 1972] Oka, S. and Kostic, Z. (1972). Influence of wall proximity on hot-wire velocity measurements. *DISA Information*, 13:29–33.

[Pao, 1965] Pao, Y. (1965). Structure of turbulent velocity and scalar fields at large wavenumbers. *Physics of Fluids*, 8(6):1063–1075.

[Papangelou, 1993] Papangelou, A. (1993). A "robust " vortex shedding anemometer. *Experiments in Fluids*, 14:208–210.

[Peerhossaini and Wesfreid, 1988] Peerhossaini, H. and Wesfreid, J. E. (1988). On the inner structure of streamwise Görtler rolls. *International Journal of Heat and Fluid Flow*, 9(1):12–18.

[Peridier et al., 1991a] Peridier, V. J., Smith, F. T., and Walker, J. D. A. (1991a). Vortex-induced boundary-layer separation. Part 1. The unsteady limit problem $Re \rightarrow \infty$. *Journal of Fluid Mechanics*, 232:99–131.

[Peridier et al., 1991b] Peridier, V. J., Smith, F. T., and Walker, J. D. A. (1991b). Vortex-induced boundary-layer separation. Part 2. Unsteady interacting boundary-layer theory. *Journal of Fluid Mechanics*, 232:133–165.

[Perry, 1982] Perry, A. E. (1982). *Hot wire Anemometry*. Clarendon Press, Oxford.

[Perry and Chong, 1982] Perry, A. E. and Chong, M. S. (1982). On the mechanism of wall turbulence. *Journal of Fluid Mechanics*, 119:173–217.

[Perry and Fairlie, 1974] Perry, A. E. and Fairlie, B. D. (1974). Critical points in flow patterns. *Advances in Geophysics*, 18 B:299–315.

[Perry et al., 1986] Perry, A. E., Henbest, S., and Chong, M. S. (1986). A theoretical and experimental study of wall turbulence. *Journal of Fluid Mechanics*, 165:163–199.

[Perry and Hornung, 1984] Perry, A. E. and Hornung, H. (1984). Some aspects of three-dimensional separation. Part 2: Vortex skeletons. *Zeitschrift für Flugwissenschaften und Weltraumforschung*, 8(3):155–160.

[Perry and Morrison, 1971] Perry, A. E. and Morrison, G. L. (1971). A study of the constant temperature hot-wire anemometer. *Journal of Fluid Mechanics*, 47(3):577–599.

[Piomelli et al., 1993] Piomelli, A. U., Ong, B. L., Wallace, C. J., and Ladhari, D. F. (1993). Reynolds stress and vorticity in turbulent wall flows. *Applied Scientific Research*, 51:365–370.

[Polyakov and Shindin, 1979] Polyakov, A. F. and Shindin, S. A. (1979). Hot-wire anemometer measurement of mean velocity very close to a wall. *Journal of Engineering Physics*, 36:644–648.

[Praturi and Brodkey, 1978] Praturi, A. K. and Brodkey, R. S. (1978). A stereoscopic visual study of coherent structures in turbulent shear flow. *Journal of Fluid Mechanics*, 89(2):251–272.

[Press et al., 1986] Press, W. H., Flannery, B. P., Teukolsky, S. A., and Vetterling, W. T. (1986). *Numerical Recipes: the art of Scientific Computing*. Cambridge University Press, 1st edition.

[Purtell et al., 1981] Purtell, L. P., Klebanoff, P. S., and Buckley, F. T. (1981). Turbulent boundary layer at low Reynolds number. *Physics of Fluids*, 24(5):802–811.

[Robinson, 1991] Robinson, S. K. (1991). The kinematics of turbulent boundary layer structure. Technical Memorandum 103859, National Aeronautics and Space Administration.

[Roshko, 1954] Roshko, A. (1954). On the development of turbulent wakes from vortex streets. Technical Report 1191, National Advisory Committee on Aeronautics.

[Schlichting, 1968] Schlichting, H. (1968). *Boundary Layer Theory*. McGraw-Hill, 6th edition.

[Schubauer, 1954] Schubauer, G. B. (1954). Turbulent processes as observed in boundary layer and pipe. *Journal of Applied Physics*, 25(2):188–196.

[Schubauer and Skramstad, 1943] Schubauer, G. B. and Skramstad, H. K. (1943). Laminar-boundary-layer oscillations and transition on a flat plate. Technical Report 909, National Advisory Committee on Aeronautics.

[Schubauer and Skramstad, 1947] Schubauer, G. B. and Skramstad, H. K. (1947). Laminar boundary-layer oscillations and stability of laminar flow. *Journal of the Aeronautical Sciences*, 14(2):69–78.

[Siddall and Davies, 1972] Siddall, R. G. and Davies, T. W. (1972). An improved response equation for hot-wire anemometry. *International Journal of Heat and Mass Transfer*, 1:367–368.

[Smith et al., 1991a] Smith, C. R., Fitzgerald, J. P., and Greco, J. J. (1991a). Cylinder end-wall vortex dynamics. *Physics of Fluids, A*, 3:2031.

[Smith and Metzler, 1983] Smith, C. R. and Metzler, S. P. (1983). The characteristics of low speed streaks in the near-wall region of a turbulent boundary layer. *Journal of Fluid Mechanics*, 129:27–54.

[Smith and Schwartz, 1983] Smith, C. R. and Schwartz, S. P. (1983). Observation of streamwise rotation in the near-wall region of a turbulent boundary layer. *Physics of Fluids*, 26(3):641–652.

[Smith et al., 1991b] Smith, C. R., Walker, J. D. A., Haidari, A. H., and Sobrun, U. (1991b). On the dynamics of near-wall turbulence. *Philosophical Transactions of the Royal Society of London*, 336:131–175.

[Smoliakov and Tkachenko, 1983] Smoliakov, A. V. and Tkachenko, V. M. (1983). *The measurement of turbulent fluctuations: An introduction of hot-wire anemometry and related transducers*. Springer-Verlag, Berlin ; New York.

[Sonada and Aihara, 1981] Sonada, T. and Aihara, Y. (1981). Effects of pressure gradient on the secondary instability of Görtler vortices. Paper 81-0197, American Institute of Aeronautics and Astronautics.

[Spalart, 1988] Spalart, P. R. (1988). Direct simulation of a turbulent boundary layer up to $Re_\theta = 1410$. *Journal of Fluid Mechanics*, 187:61–98.

[Spalart and Leonard, 1987] Spalart, P. R. and Leonard, A. (1987). Direct numerical simulation of equilibrium turbulent boundary layers. In *Turbulent Shear Flows 5, selected papers from Fifth International Symposium on Turbulent Shear Flows*, pages 235–252. Springer-Verlag.

[Spalding, 1961] Spalding, D. B. (1961). A single formula for the "law of the wall". *A.S.M.E. Transactions, Journal of Applied Mechanics*, 28(3):455–458.

[Squire, 1948] Squire, H. (1948). Reconsideration of the theory of free turbulence. *Philosophical Magazine, 7th Series*, 39:1–20.

[Squire and Winter, 1951] Squire, H. B. and Winter, K. G. (1951). The secondary flow in a cascade of airfoils in a nonuniform stream. *Journal of the Aeronautical Sciences*, 18(4):271–277.

[Swearingen and Blackwelder, 1986] Swearingen, J. D. and Blackwelder, R. F. (1986). Spacing of streamwise vortices on concave walls. *American Institute of Aeronautics and Astronautics Journal*, 24(10):1706–1709.

[Swearingen and Blackwelder, 1987] Swearingen, J. D. and Blackwelder, R. F. (1987). The growth and breakdown of streamwise vortices in the presence of a wall. *Journal of Fluid Mechanics*, 182:255–290.

[Tani, 1962] Tani, I. (1962). Production of longitudinal vortices in the boundary layer along a concave wall. *Journal of Geophysical Research*, 67(8):3075–3080.

[Tani and Aihara, 1969] Tani, I. and Aihara, Y. (1969). Görtler vortices and boundary layer transition. *Zeitschrift für angewandte Mathematik und Physik*, 20(5):609–618.

[Taylor, 1959] Taylor, E. S. (1959). The skewed boundary layer. *Journal of Basic Engineering, Transactions A.S.M.E. Series D*, 81(3):297–304.

[The Mathworks, Inc., 1995] The Mathworks, Inc. (1995). *Matlab version 4 User's Guide*. Prentice-Hall, London.

[Theodorsen, 1952] Theodorsen, T. (1952). Mechanism of turbulence. In *Proceedings of the 2nd Midwestern Conference on Fluid Mechanics*, Columbus, Ohio. Ohio State University.

[Thomas, 1977] Thomas, A. S. W. (1977). *Organized Structures in the Turbulent Boundary Layer*. PhD thesis, University of Adelaide, Department of Mechanical Engineering.

[Thwaites, 1949] Thwaites, B. (1949). Approximate calculation of the laminar boundary layer. *Aeronautical quarterly*, 1(4):245–280.

[Townsend, 1951] Townsend, A. A. (1951). The structure of the turbulent boundary layer. *Proceedings of the Cambridge Philosophical Society*, 47(2):375–395.

[Townsend, 1956] Townsend, A. A. (1956). *The structure of turbulent shear flow*. Cambridge University Press, 1st edition.

[Townsend, 1976] Townsend, A. A. (1976). *The structure of turbulent shear flow*. Cambridge University Press, 2nd edition.

[Tritton, 1959] Tritton, D. J. (1959). Experiments on the flow past a circular cylinder at low Reynolds numbers. *Journal of Fluid Mechanics*, 6:547–567.

[Turan et al., 1987] Turan, O., Azad, R. S., and Atamanchuk, T. M. (1987). Wall effect on the hot-wire signal without flow. *Journal of Physics E (Scientific Instruments)*, 20:1278–1280.

[Utami and Ueno, 1987] Utami, T. and Ueno, T. (1987). Experimental study on the coherent structure of turbulent open-channel flow using visualization and picture processing. *Journal of Fluid Mechanics*, 174:399–440.

[van Dommelen and Cowley, 1990] van Dommelen, L. L. and Cowley, S. J. (1990). On the Lagrangian description of unsteady boundary layer separation. Part 1. General theory. *Journal of Fluid Mechanics*, 210:593–626.

[van Thinh, 1969] van Thinh, N. (1969). On some measurements made by means of a hot-wire in a turbulent flow near a wall. *DISA Information*, 7:13–18.

[von Kàrmàn, 1921] von Kàrmàn, T. (1921). Über laminare und turbulente Reibung. *Zeitschrift für Angewandte Mathematik und Mechanik*, 1(4):233–252.

[Wagner, 1990] Wagner, P. M. (1990). The use of near-wall hot-wire probes for time-resolved skin-friction measurements. In *Advances in Turbulence 3, Proceedings of the Third European Turbulence Conference*. Springer-Verlag.

[Walker, 1983] Walker, G. J. (1983). Wall-proximity corrections for hot-wire readings. In *Proceedings, 8th Australasian Fluid Mechanics Conference*, pages 6B9–6B12, Newcastle, N.S.W. University of Newcastle.

[Wallace, 1982] Wallace, J. M. (1982). On the structure of bounded turbulent shear flow: A personal view. *Developments in Theoretical and Applied Mechanics*, 11:509–521.

[Wallace, 1984] Wallace, J. M. (1984). Observations on the nature and mechanism of the bounded turbulent shear flow structure. *Proceedings of IUTAM Conference: Turbulence and Chaotic Phenomena in Fluids*, pages 447–452.

[Wallace, 1985] Wallace, J. M. (1985). The vortical structure of bounded turbulent shear flow. *Lecture Notes in Physics*, 235:253–268.

[Wallace et al., 1977] Wallace, J. M., Brodkey, R. S., and Eckelmann, H. (1977). Pattern recognized structures in bounded turbulent shear flows. *Journal of Fluid Mechanics*, 83(4):673–693.

[Wallace et al., 1972] Wallace, J. M., Eckelmann, H., and Brodkey, R. S. (1972). The wall region in turbulent shear flow. *Journal of Fluid Mechanics*, 54(1):39–48.

[Watmuff, 1986] Watmuff, J. H. (1986). Wind-tunnel contraction design. In *Proceedings, 9th Australasian Fluid Mechanics Conference*, pages 472–475. University of Auckland.

[Watmuff, 1989] Watmuff, J. H. (1989). The effects of feedback amplifier characteristics on constant temperature hot-wire anemometer systems. In *Proceedings, 10th Australasian Fluid Mechanics Conference*, pages 15.33–15.36. University of Melbourne.

[Wei and Willmarth, 1989] Wei, T. and Willmarth, W. W. (1989). Reynolds-number effects on the structure of a turbulent channel flow. *Journal of Fluid Mechanics*, 204:57–95.

[Welsh and la Fontaine, 1978] Welsh, M. C. and la Fontaine, R. F. (1978). A small wind tunnel for acoustic resonance studies. Technical Report TR 20, Division of Mechanical Engineering, Commonwealth Scientific and Industrial Research Organisation, Highett, Victoria.

[Weske and Plantholt, 1953] Weske, J. R. and Plantholt, A. H. (1953). Discrete vortex systems in the transition range of fully developed flow in a pipe. *Journal of the Aeronautical Sciences*, 20:716–718.

[Williamson, 1988] Williamson, C. H. K. (1988). Defining a universal and continuous Strouhal-Reynolds number relationship for the laminar vortex shedding of a circular cylinder. *Physics of Fluids*, 31(10):2742–2744.

[Williamson, 1989] Williamson, C. H. K. (1989). Oblique and parallel modes of vortex shedding in the wake of a circular cylinder at low Reynolds numbers. *Journal of Fluid Mechanics*, 206:579–627.

[Willmarth, 1974] Willmarth, W. W. (1974). Structure of turbulence in boundary layers. *Advances in Applied Mechanics*, 15:159–254.

[Willmarth, 1975] Willmarth, W. W. (1975). Pressure fluctuations beneath turbulent boundary layers. *Annual Review of Fluid Mechanics*, 7:13–38.

[Willmarth and Lu, 1972] Willmarth, W. W. and Lu, S. S. (1972). Structure of the Reynolds stress near the wall. *Journal of Fluid Mechanics*, 55:65–92.

[Willmarth and Sharma, 1984] Willmarth, W. W. and Sharma, L. K. (1984). Study of turbulent structure with hot wires smaller than the viscous length. *Journal of Fluid Mechanics*, 142:121–149.

[Willmarth and Tu, 1967] Willmarth, W. W. and Tu, B. J. (1967). Structure of turbulence in the boundary layer near the wall. *Physics of Fluids*, 10(9):s134–s137.

[Willmarth et al., 1976] Willmarth, W. W., Winkel, R. E., Sharma, L. K., and Bogar, T. J. (1976). Axially symmetric turbulent boundary layers. *Journal of Fluid Mechanics*, 76:35–64.

[Wills, 1962] Wills, J. A. B. (1962). The correction of hot-wire readings for proximity to a solid boundary. *Journal of Fluid Mechanics*, 12:388–396.

[Wyngaard, 1968] Wyngaard, J. C. (1968). Measurement of small-scale turbulence structure with hot-wires. *Journal of Physics E (Scientific Instruments)*, 1:1105–1108.

[Zang, 1991] Zang, T. A. (1991). Numerical simulation of the dynamics of tubulent boundary layers: perspectives of a transition simulator. *Philosophical Transactions of the Royal Society of London*, 336:95–102.

[Zaric, 1972] Zaric, Z. (1972). Wall turbulence studies. *Advances in Heat Transfer*, 8:285–350.

[Zemskaya et al., 1979] Zemskaya, A. S., Levitskiy, V. N., Repik, Y. U., and Sosedko, Y. P. (1979). Effect of the proximity of the wall on hot-wire readings in laminar and turbulent boundary layers. *Fluid Mechanics – Soviet Research*, 8(1):133–141.

Appendix A

Dissipation scales near the wall

The selection of hot-wire dimensions and free-stream speed for accurate measurement of velocity spectra in the turbulent boundary layer requires estimation of the dissipation scales. For the near-wall region these estimates can be obtained by applying a series of conventional approximations to the basic turbulence-energy equation.

In tensor notation, a general form of the turbulence-energy equation is

$$\underset{\substack{\text{convection}\\ \text{by mean flow}}}{U_j \frac{\partial}{\partial x_j}\left(\frac{\overline{u_i^2}}{2}\right)} = \underset{\substack{\text{pressure, kinetic, gradient}\\ \text{diffusion}}}{-\frac{\partial}{\partial x_j}\left(\frac{\overline{u_j p}}{\rho} + \frac{1}{2}\overline{u_i u_j u_i} - 2\nu\overline{u_i s_{ij}}\right)} - \underset{\substack{\text{produc-}\\ \text{tion}}}{\overline{u_i u_j} S_{ij}} - \underset{\substack{\text{dissi-}\\ \text{pation}}}{2\nu\overline{s_{ij}^2}} \tag{A.1}$$

[Hinze, 1975] where x_i is the displacement tensor, U_i (u_i) is the mean (fluctuating) velocity tensor, and S_{ij} (s_{ij}) is the mean (fluctuating) shear tensor. The terms containing viscosity are frequently written as

$$\frac{\nu}{2}\frac{\partial^2}{\partial x_j^2}\overline{u_i^2} - \overline{\nu\left(\frac{\partial u_i}{\partial x_j}\right)^2}. \tag{A.2}$$

In a two-dimensional boundary layer, the mean lateral velocity component W and mean lateral derivatives $\overline{\partial/\partial x_3}$ are zero. In comparison with derivatives normal to the wall, streamwise derivatives are extremely small, and so the streamwise transport terms may be neglected. When expressed using the more familiar (U,V,W) velocity and (x,y,z) displacement notation, the resulting approximation for the turbulence-energy equation in the near-wall region of the two-dimensional turbulent boundary layer is

$$0 = \underset{\text{diffusion}}{-\frac{\partial}{\partial y}\left(\frac{\overline{vp}}{\rho} + \overline{qv} - \nu\frac{\partial}{\partial y}\overline{q}\right)} - \underset{\text{production}}{\overline{uv}\frac{\partial U}{\partial y}} - \underset{\text{dissipation}}{\varepsilon}, \tag{A.3}$$

where $q = u_i^2/2$ is the turbulence energy.

Measurements by Laufer (1954) and Schubauer (1954) indicate that, except in the viscous sublayer and buffer regions of the boundary layer, the transport terms of the turbulence-energy equation are much

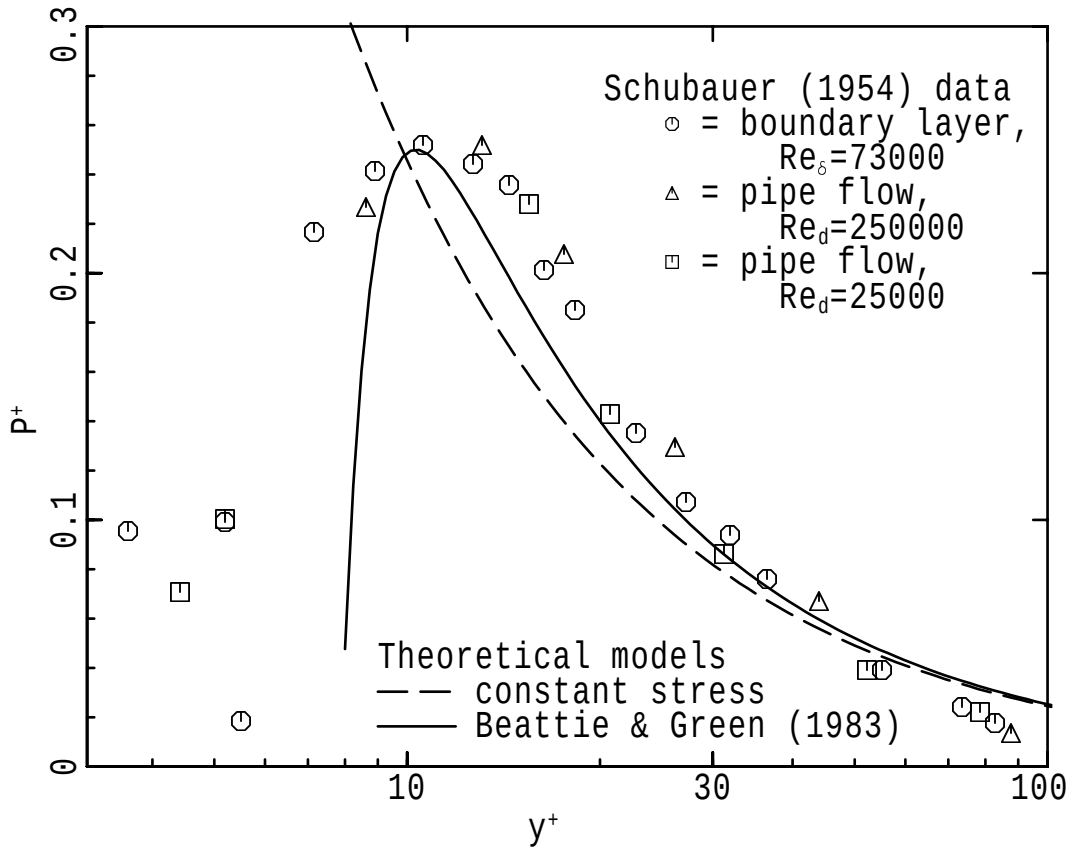

Figure A.1: Predicted and measured turbulence-energy production near the wall

smaller than the production term and the dissipation term. In the region $y^+ > 30$, the turbulence-energy equation therefore simplifies to

$$\varepsilon \approx \overline{uv}\frac{\partial U}{\partial y}. \tag{A.4}$$

The dissipation length, velocity and time scales, the Kolmogorov scales, which are defined as

$$\eta = \left(\frac{\nu^3}{\varepsilon}\right)^{1/4}, \qquad \upsilon = (\nu\varepsilon)^{1/4} \qquad \text{and} \qquad \tau = \sqrt{\frac{\nu}{\varepsilon}} \tag{A.5}$$

respectively, can then be written in terms of the non-dimensional turbulence-energy production

$$P^+ = \frac{\nu}{U_\tau^4}\,\overline{uv}\,\frac{\partial U}{\partial y} \tag{A.6}$$

as

$$\eta^+ = \frac{\eta U_\tau}{\nu} = P^{+-1/4}, \tag{A.7}$$

$$\upsilon^+ = \frac{\upsilon}{U_\tau} = P^{+1/4}, \tag{A.8}$$

$$\tau^+ = \frac{U_\tau^2 \tau}{\nu} = P^{+-1/2}. \tag{A.9}$$

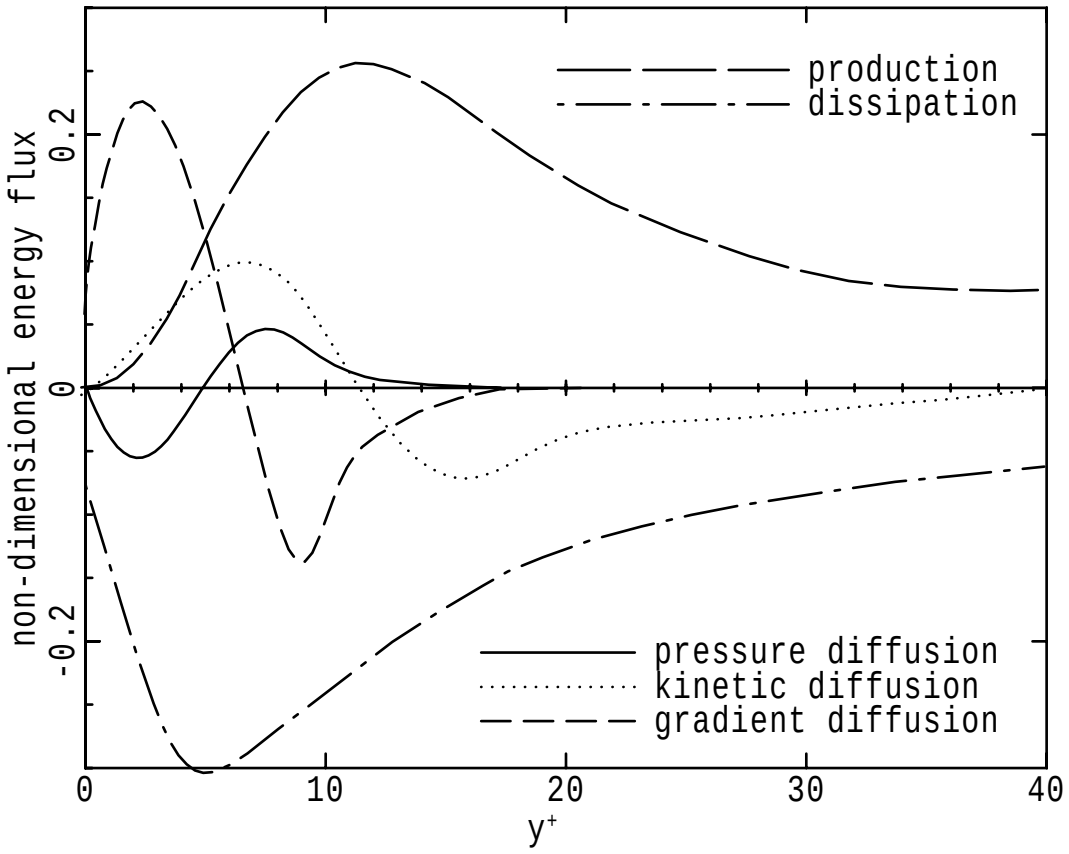

Figure A.2: Turbulence kinetic energy budget in the near-wall region (from Krishnamoorthy and Antonia, 1988)

In the logarithmic region of the boundary layer $\overline{uv} \approx U_\tau^2$ and the mean velocity gradient is $U_\tau/(\kappa y)$, so that

$$\varepsilon^+ \approx P^+ \approx \frac{1}{\kappa y^+}. \tag{A.10}$$

The semi-empirical reasoning of Beattie and Green (1983) has produced an improved estimate of the production term:

$$P^+ = \frac{\kappa(y^+ - 7.87)}{[\kappa(y^+ - 7.87) + 1]^2} \tag{A.11}$$

for $y^+ \gtrsim 10$ (Figure A.1).

Experimental measurements by Laufer (1954) and Schubauer (1954) have shown that, in the buffer and viscous sublayer regions, the diffusion terms of Equation A.3 contribute significantly to the turbulence-energy budget. Laufer's measurements of the dissipation term, which assumed Taylor's hypothesis and isotropy of the turbulence, were adjusted by Townsend (1956) for the effect of large intensity gradients near the wall. Bernard and Berger (1984) used the data of Eckelmann (1974) and of Kreplin and Eckelmann (1979) to evaluate the Taylor expansion coefficients of the terms in Equation A.3, and so

were able to improve the estimates for the energy-budget terms in the region $y^+ \leq 2$. From temperature measurements in a turbulent boundary layer flowing over a heated wall, Krishnamoorthy and Antonia (1988) determined all the terms in the temperature-variance transport equation. On the basis of the similarity between thermal and velocity turbulence, they then proposed that the relationship between the kinetic diffusion and production terms in velocity turbulence is the same as the relationship between the kinetic diffusion and production terms in thermal turbulence.

The near-wall turbulence-energy budget resulting from these developments is shown in Figure A.2. Figure A.3 compares Kolmogorov scales calculated from Equations A.7, A.8 and A.9 with Kolmogorov scales calculated from the dissipation data in Figure A.2. In Figure A.3 the extreme values of the dissipation length, time and velocity scales are $\eta^+_{min} = 1.35$, $\tau^+_{min} = 1.81$ and $\upsilon^+_{max} = 0.74$ respectively at $y^+ = 5$.

A.1 Notation

p	fluctuating component of pressure
P	time-averaged pressure
q	$u_i^2/2$; turbulence energy
S_{ij}	time-averaged shear tensor
s_{ij}	fluctuating component of shear tensor
U_i	time-averaged velocity tensor
u_i	fluctuating component of velocity tensor
U, V, W	x, y and z components of time-averaged velocity
u, v, w	x, y and z components of fluctuating velocity
x_i	displacement tensor
x, y, z	streamwise, normal and spanwise components of displacement
ε	energy dissipation rate
η	dissipation length scale
κ	constant coefficient for the logarithmic mean velocity distribution near the wall: $U^+ = \kappa^{-1} \ln y^+ + C$
ν	kinematic viscosity
ρ	density
υ	dissipation velocity scale
τ	dissipation time scale

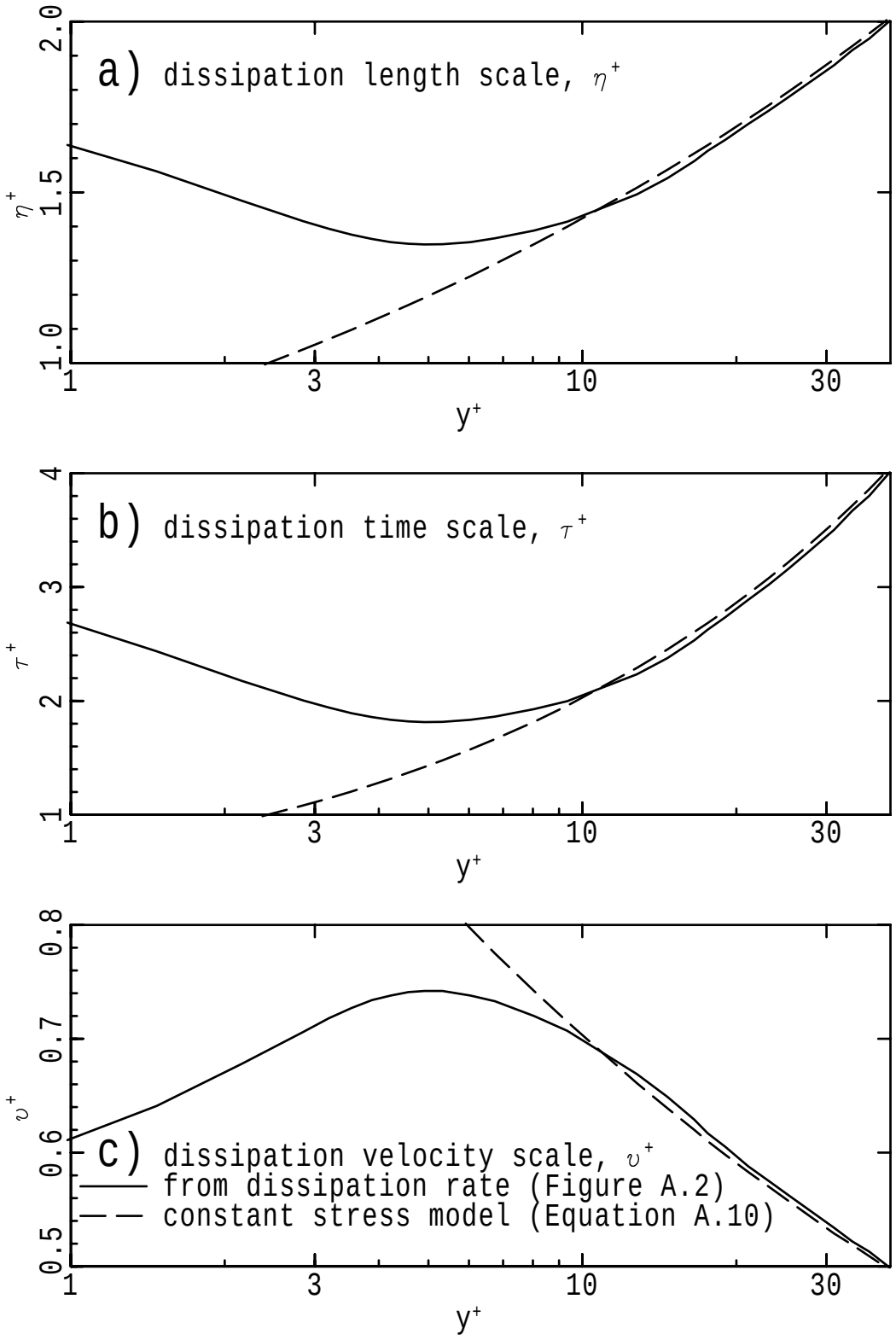

Figure A.3: Estimates of Kolmogorov scales in the near-wall region

Superscripts

Variables which have a superscript $^+$ are nondimensionalised using the viscous flow variables U_τ and ν, e.g. $U^+ = U/U_\tau$ and $y^+ = yU_\tau/\nu$.

Appendix B

Flow rate control

The variable-throat-area sonic choke, which controlled the flow rate in the wind-tunnel test section, consisted principally of a sliding centrebody in a section of pipe with a nozzle at its upstream end (Figure B.1). The original centrebody was replaced by another of larger diameter in order both to reduce the regulated flow rate and to increase the speed range.

The location of the original choke centrebody could be adjusted to give a minimum throat area ratio of $(A^*/A) = 0.0531$, corresponding to a bulk-flow velocity of 10.7 m/s in the 228 mm $\times$ 228 mm test section. The maximum bulk-flow velocity was limited to 20 m/s by the power of the main drive motor.

The location of the larger centrebody could be adjusted to produce a throat area ratio of as small as $(A^*/A) = 0.00285$, corresponding to a test section flow speed of only 0.56 m/s, but in practice the lowest flow speed at which choked flow occurred was about 1.0 m/s. With the larger centrebody the highest possible bulk-flow velocity in the test section was 9.6 m/s. The nose profile of the larger centrebody was formed according to the relations

$$\begin{array}{rcll} r & = & 46.81\left(1-\left[1-\frac{x}{147.0}\right]^{1.5}\right)^{1/1.5}\,\text{mm} & \text{for} \quad 0.0\,\text{mm} \le x \le 114.5\,\text{mm} \\ & & 50.84\left(1-1.576\left[1-\frac{x}{254.5}\right]^{2.6}\right)^{1/2.6}\,\text{mm} & 114.5\,\text{mm} \le x \le 120\,\text{mm} \\ & & 50.84\,\text{mm} & x \ge 254.5\,\text{mm} \end{array} \qquad \text{(B.1)}$$

where r is centrebody radius and x is distance downstream from the nose of the centrebody (Figure B.1). An attempt was made to minimise the rate of change of Mach number in the region of the throat by modelling the sonic-choke behaviour as a one dimensional inviscid compressible flow.

At flow rates lower than 0.30 kg/s, which is equivalent to a flow speed of 4.7 m/s in the test section, the flow over the compressor blades stalled. The resulting loss in pressure ratio across the compressor caused the flow through the control nozzle to become unchoked. To overcome this problem, an auxiliary flow from the laboratory was introduced between the variable-area sonic choke and the com-

pressor. The auxiliary flow was matched to atmosphere with a bellmouth inlet and the flow rate was limited by a fixed-area sonic choke to 0.35 kg/s (Figure 2.1).

Notation

A^*/A	ratio of sonic-choke throat (i.e. minimum) area to cross-section area of wind-tunnel test section
r	radius of sonic-choke centrebody — is a function of x
x	distance downstream from the nose of the sonic-choke centrebody

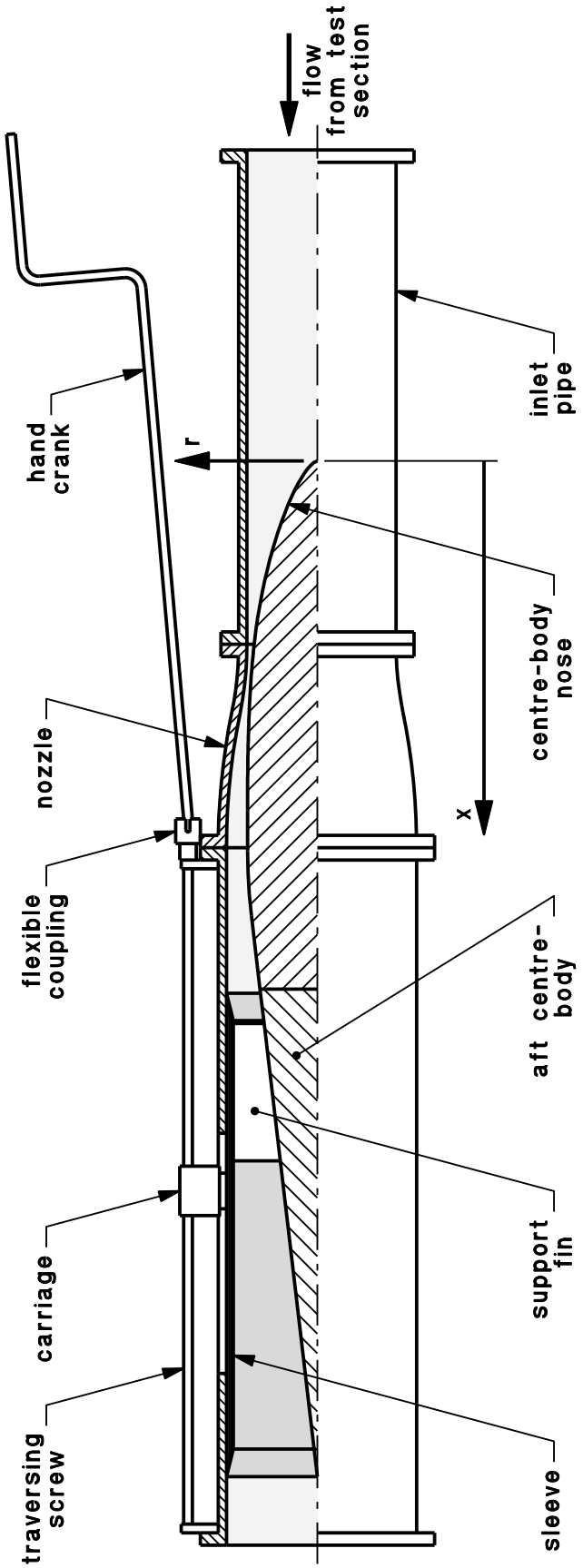

Figure B.1: Variable -throat-area sonic choke with large sliding centrebody. Scale 1:5

Figure B.1: Variable-throat-area sonic choke with large sliding centrebody. Scale 1:5

Appendix C

Exhaust diffuser and silencer

When operating at its full speed of 10–12,000 rpm the wind-tunnel drive compressor produced noise levels higher than 120 dB in the exhaust flow. The noise, which was in the 2 kHz and 4 kHz octave bands, consisted mostly of pure tones at the compressor blade-passing frequency and at the first few harmonic frequencies. Without an effective exhaust silencer it was therefore not possible to operate the wind tunnel. The silencer shown in Figure C.1, which is essentially a duct lined with sound absorbing material, was designed in accordance with guidelines provided by Dr. D. A. Bies

Design charts [Bies and Hansen, 1988] indicated that the attenuation rate of a correctly sized and lined duct can be larger than 5 dB per sound wavelength and so, for frequencies in excess of 2 kHz, the required level of attenuation could be achieved in a very short length of duct. A set of 6 splitter plates, each packed with fibreglass wool, was used to reduce the effective width of the acoustic channel in the silencer. One wall of each splitter plate was perforated steel sheet. A splitter-plate thickness of twice the channel width provided a broad attenuation bandwidth. The purpose of the large duct cross-section was to ensure an air flow speed through the silencer of less than 10 m/s, and so avoid damage to the sound-absorbing material.

The length of the diffuser (Figure C.1), which connects the compressor outlet to the silencer inlet, was limited by the height of the laboratory ceiling to about 1300 mm. For the required inlet:outlet area ratio of 1:6.25, the 5.7^o half angle of the diffuser was larger than that needed for optimal pressure recovery and the flow at the compressor outlet was quite non-uniform. A cluster of guide vanes was therefore installed at the diffuser inlet in order to improve the uniformity of the flow and to discourage separation from the walls of the diffuser.

The attenuation of the silencer was estimated to be well over 40 dB in the 2 kHz and 4 kHz octave bands, and after installation the dominant source of exhaust noise was from transmission through the walls of the diffuser. By covering the diffuser and silencer with a 50 mm thick fibreglass-wool blanket, the level of high frequency noise in the laboratory was reduced by a further 10 dB.

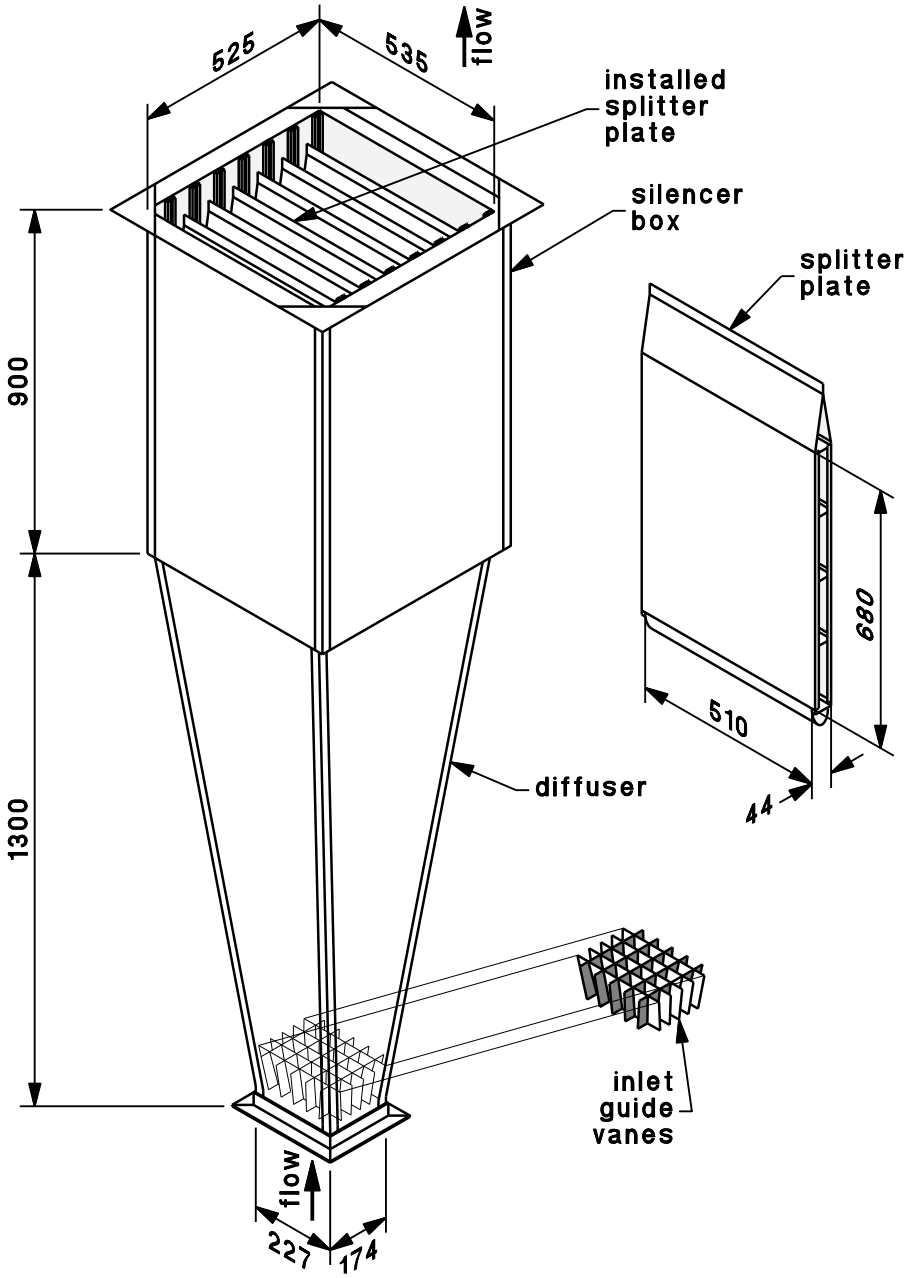

Figure C.1: Exhaust diffuser and silencer for the boundary layer wind tunnel. Scale 1:20

Appendix D

Multi-directional traverse mechanism

The multi-directional traverse mechanism shown in Figure D.1 gave three translational and two rotational degrees of freedom to a probe. Like the simple traverse described in Section 2.2.7, it could be placed in any of the ports in the wind-tunnel test section with nothing more than the probe stem extending beneath the face of the instrumentation plug. The main sub-assemblies of the traverse were

1. the plug and base plate, and
2. the tower and probe stem.

The plug and base plate controlled the location at which the probe stem emerged into the test-section flow. The entire plug rotated on the base plate. Within the plug, the probe stem could be translated in a straight line parallel to the test section surface. The mechanism which performed the translation is shown schematically in Figure D.2. It used two counter-rotating disks geared together one inside the other so that the surface of the test section remained sealed and free of any discontinuity when the mechanism was in motion. Near the periphery of the plug there was also a hole which could be used to place a second or auxiliary probe in the flow. By the combined rotation of the plug and the translation, it was possible to move the main probe in both the streamwise and spanwise directions relative to the auxiliary probe.

The tower and probe stem (Figure D.3) provided the probe sensors with a further 3 degrees of freedom of motion. Vertical motion of the probe was produced by driving a large carriage up and down the shafts of the tower. A smaller carriage which rode inside the larger carriage gave a more restricted vertical motion to a second, concentric stem. This second stem could be used for pitching the probe or could carry another set of probes. Finally, the probe stem could be rotated about its own vertical axis.

All motions of the traverse except the plug rotation were driven by 6 Volt 2 Watt d.c. electric motors through multistage epicyclic gearboxes. The plug rotation was driven by a 3 Watt synchronous motor. The motion produced by each motor was monitored by reading potentiometers which were attached to the traverse.

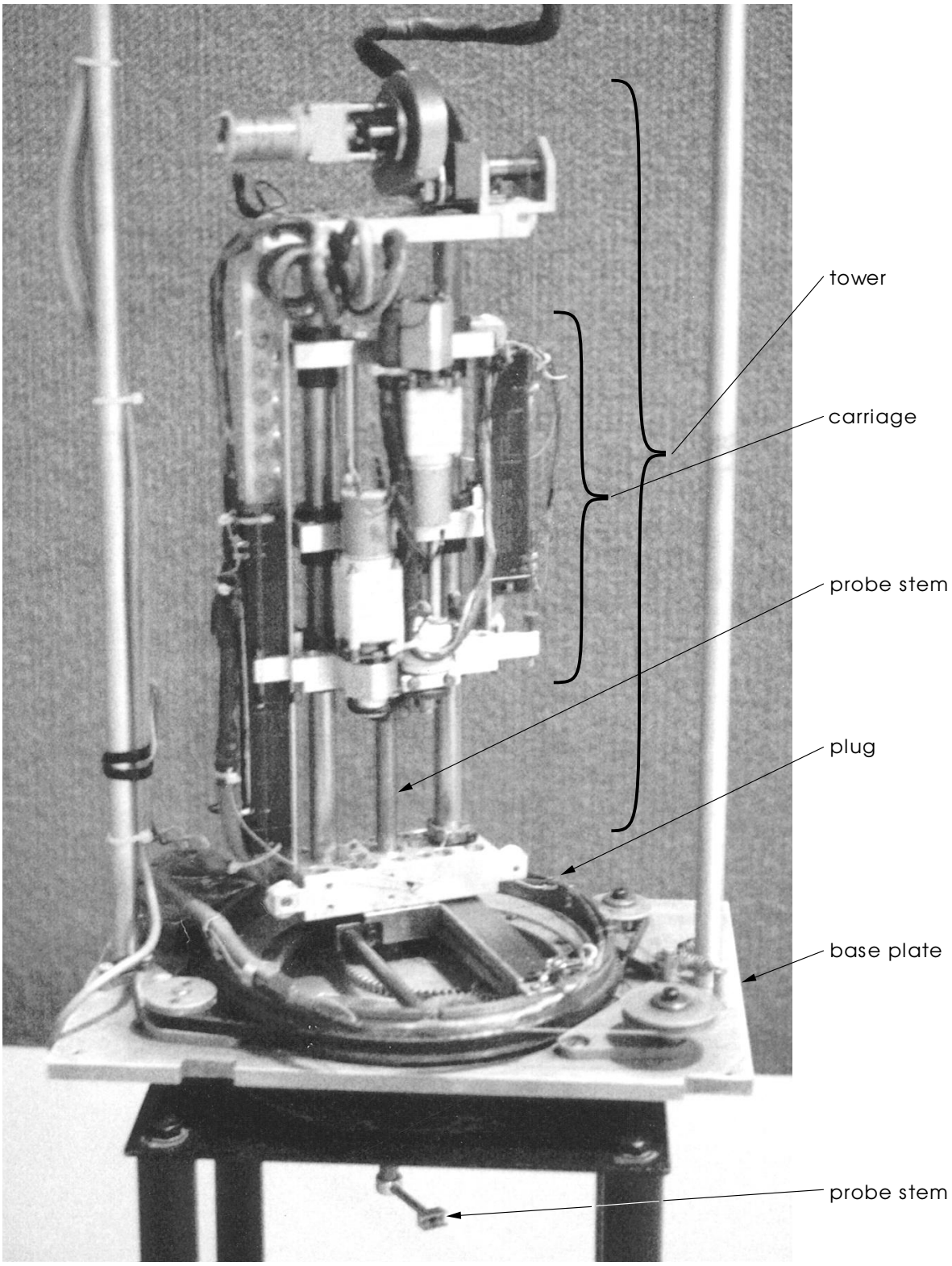

Figure D.1: Multi-directional probe traverse mechanism

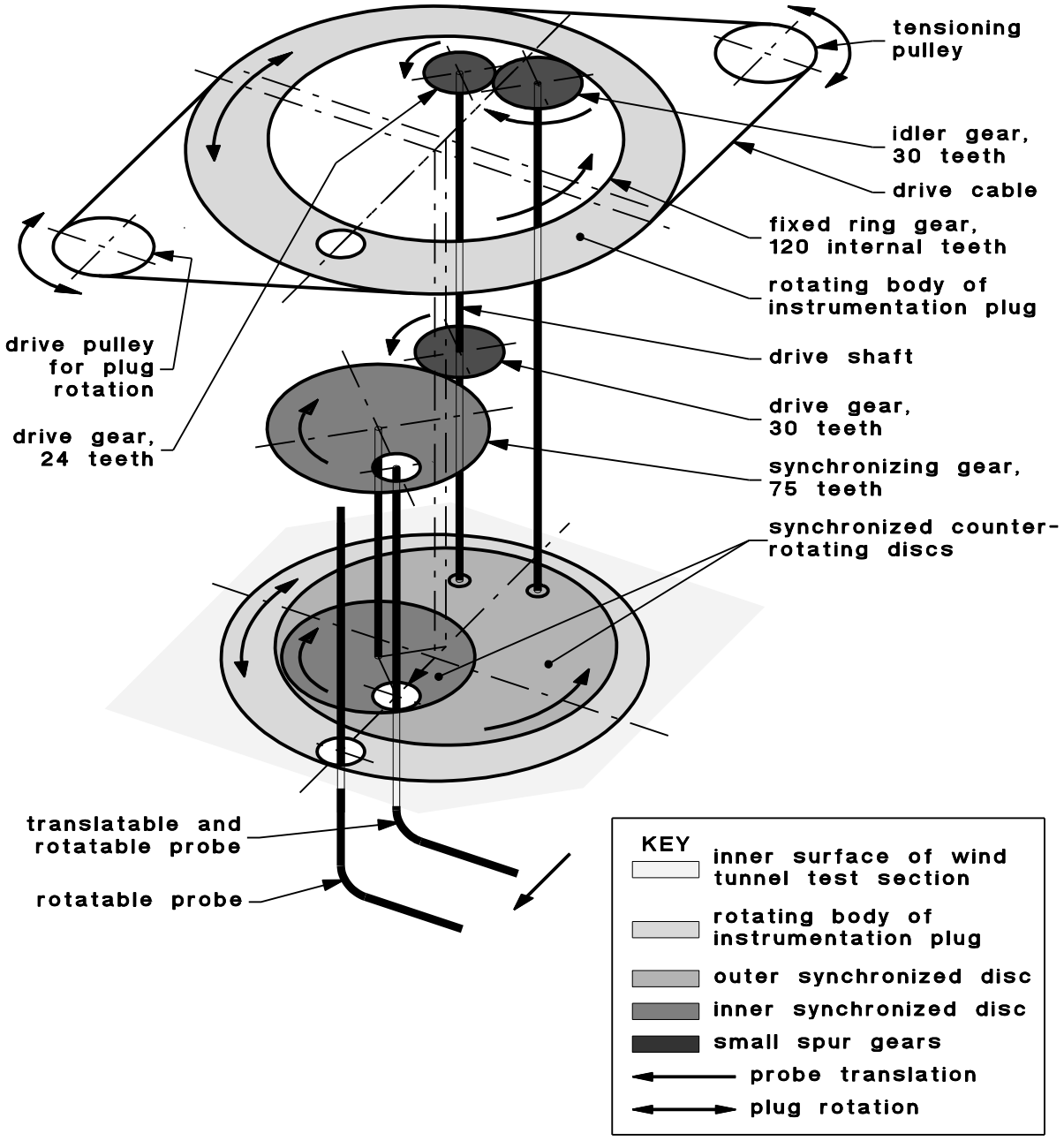

Figure D.2: Exploded schematic diagram of the horizontal translation and plug rotation mechanisms of the multi-directional probe traverse

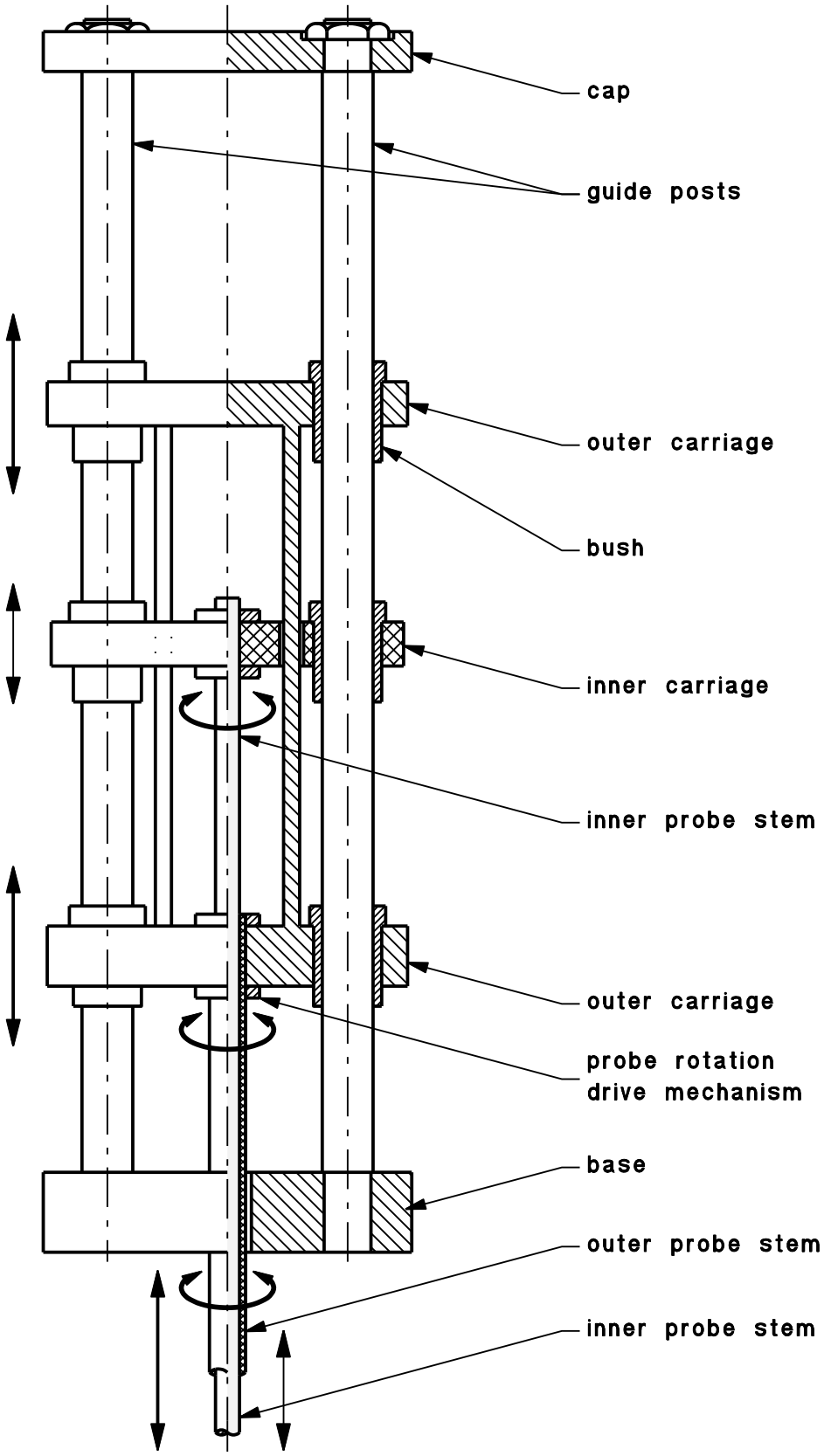

Figure D.3: Simplified diagram of the tower mechanism of the multi-directional probe traverse

Appendix E

Data acquisition system

Control and data interfaces to the data acquisition hardware were provided by an SBC100M microcomputer which, in turn, was controlled by an MS-DOS personal computer with an Intel 8088 processor. The SBC100M controlled two analogue-to-digital (A/D) converters and 2 megabytes of external RAM which was used for data storage. It also drove the probe traverse mechanism and copied data to the personal computer.

The SBC100M contained a 8-bit Zilog Z80A microprocessor, 64 kilobytes of RAM, two RS232 serial ports and a pair of 8-bit parallel ports on an S100 bus. Additional parallel ports (Intel 8255 chips) were provided by three SPC-29 peripheral interface cards. The external RAM was marketed by its suppliers as a rapid-access disk drive and so was known as a "Quasi Disk". The CP/M operating system was used to load and start a control program which was stored on an 8-inch floppy disk drive. The major elements of the data acquisition system are shown schematically in Figure E.1. The arrangement of peripheral devices around the SBC100M is shown in Figure E.2.

E.1 Analogue to digital converters

The data acquisition system was equipped with a fast DAS250A A/D converter and a slower DAS1128 A/D converter. The input to each of these converters was multiplexed from sixteen analogue data channels. Both had 12 bit precision. The fast A/D converter, which had a conversion time of less than four microseconds, was used for sampling the rapidly fluctuating signals from hot-wire anemometers. It received status and timing signals (start convert etc.) from a MPF-1 MicroProfessor single-printed-circuit-card microcomputer which was specially adapted for the job by the addition of a timing circuit. The data from the fast A/D converter were passed through a data-packing circuit and were stored temporarily on the 2 megabyte "Quasi Disk" RAM via a special DMA card. The data-packing circuit

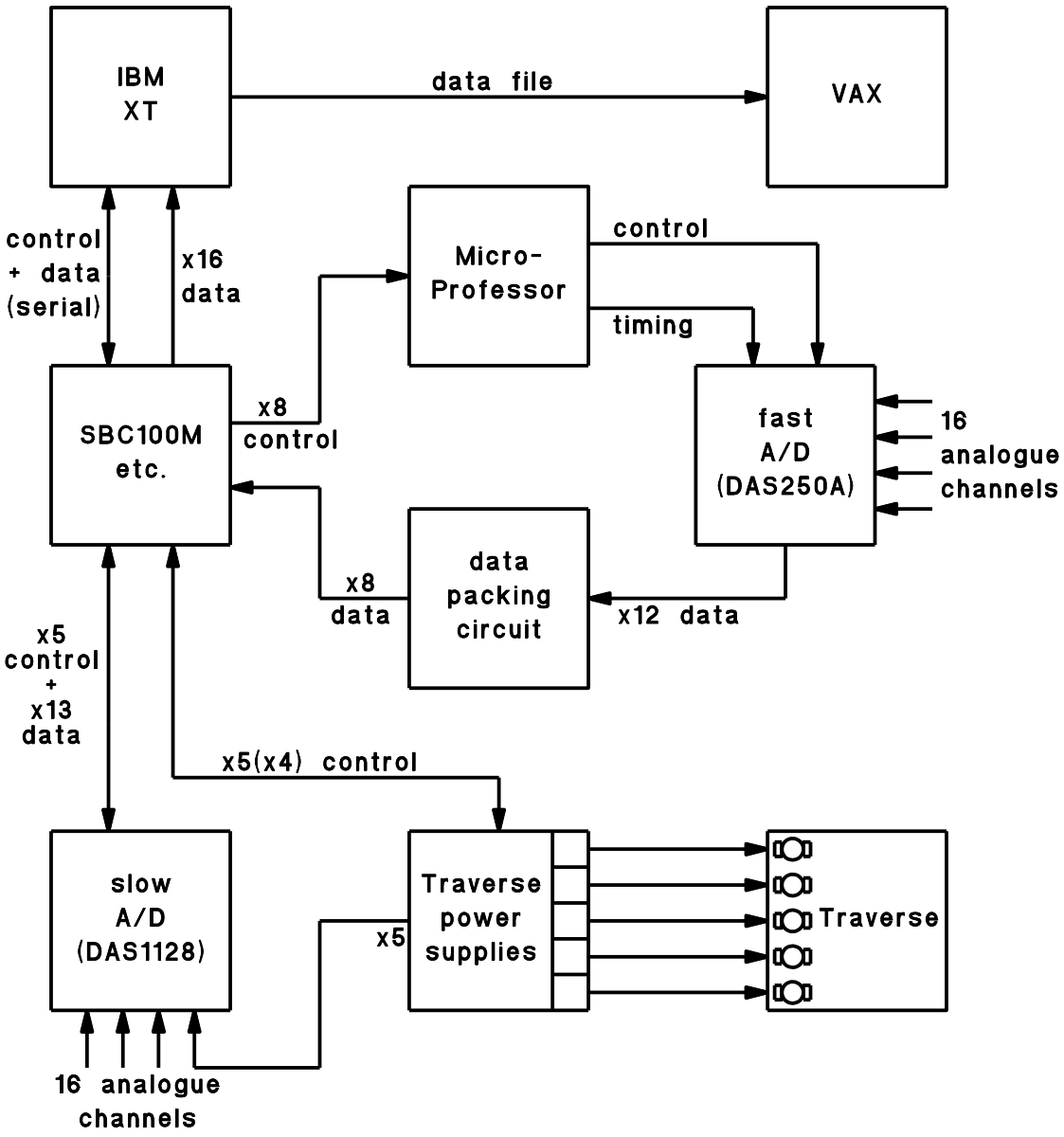

Figure E.1: Major elements of the data acquisition system. "$\times 8, \times 16 \ldots$"etc. indicate the number of parallel data lines for each link between elements of the system.

copied each pair of 12-bit data samples into 3 bytes and so, in comparison with usual requirement for 2 bytes per sample, increased the data storage capacity by 33%. The SBC100M began the data collection process by specifying and starting the MicroProfessor's timing sequence. It then primed the DMA card, gave control of the S100 bus to the DMA card and halted. After the MicroProfessor had stopped the A/D converter and after data transfer to the "Quasi Disk" had finished, the DMA card sent a non-maskable interrupt to restart the SBC100M. Some of the major system components such as the MicroProfessor timing circuit, the data packing circuit and the DMA card were designed and

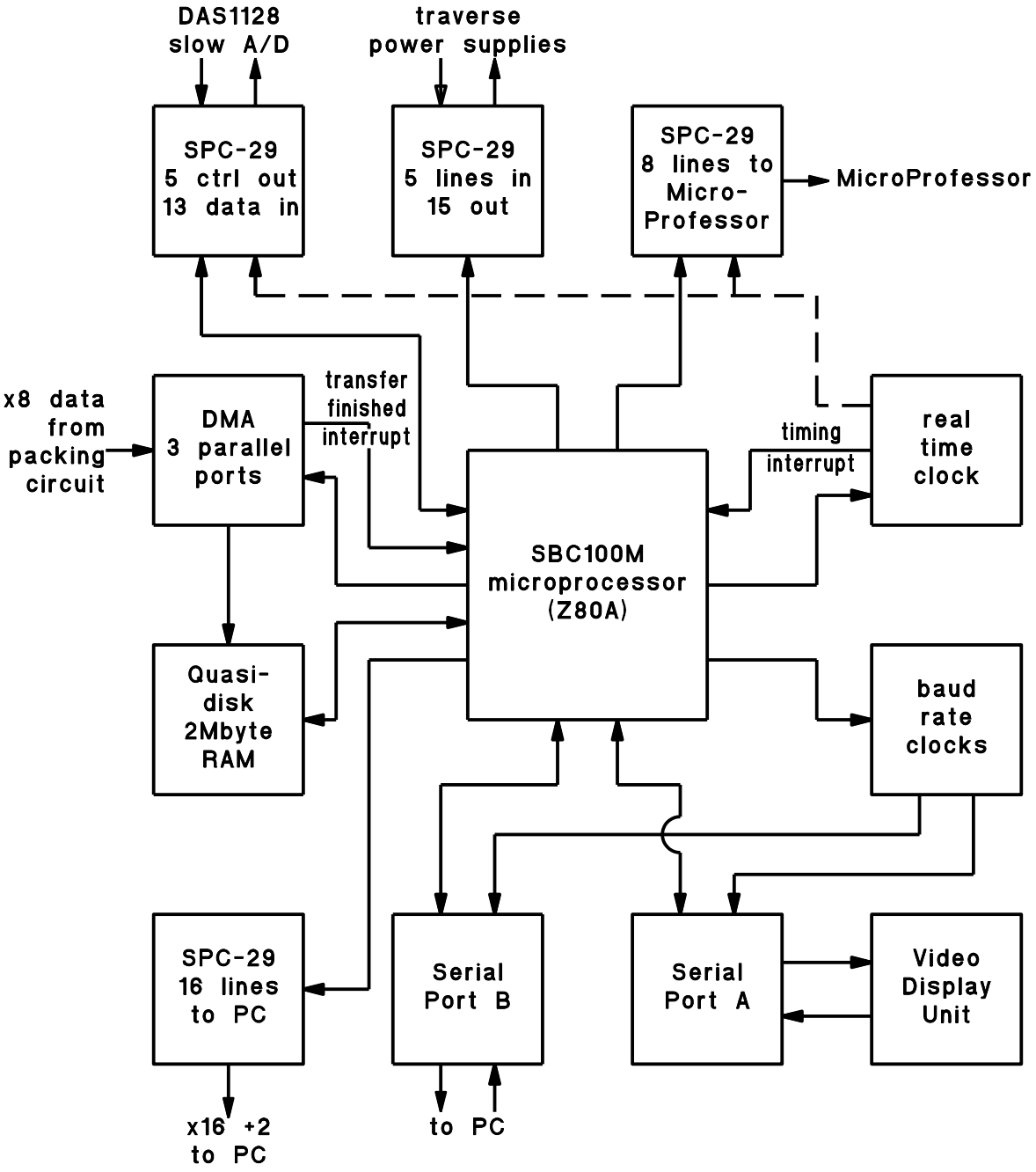

Figure E.2: SBC100M - single board microcomputer real-time system controller

assembled by the electronics technicians of the Department of Mechanical Engineering.

The slower A/D converter, which had a conversion time of 20 microseconds, was controlled by the SBC100M through an SPC-29 peripheral devices card. It was used for sampling slowly-varying signals such as those from electronic manometers and probe traverse potentiometers. Data from this A/D converter were stored in the SBC100M 64-kilobyte memory before they were sent to the personal computer.

E.2 Traverse control

As shown in Figure E.1, each motor in the probe traverse mechanisms had a separate control unit. Each traverse control unit received speed and direction commands from three parallel ports driven by the SBC100M microcomputer. A fourth parallel port was used to read the limit switches placed at the extremes of traverse motion. The SBC100M obtained information on the traverse position by using the slow A/D converter to read the position-indicating potentiometers which were attached to the traverse mechanisms. When the SBC100M was adjusting the location of an anemometer probe, it simply drove the traverse to a specified set of potentiometer voltage readings. The personal computer had the task of transforming the probe location coordinates into potentiometer readings. It performed the reverse transformations when determining the probe location.

E.3 Control programs for the microprocessors

Both the SBC100M and the MicroProfessor microcomputers contained an 8-bit Z80 microprocessor CPU. The program for the MPF-1 MicroProfessor was written in Z80 assembler and stored in EPROM. It received and executed lists of commands from its keypad or from a parallel port (Z80-PIO) connection with the SBC100M. The program for the SBC100M was also written in Z80 assembler because the easier alternative of a higher level language was not available at the time. However, the use of assembler offered the advantages of considerably more compact code, accurate prediction of execution speed, very efficient programming of interface devices, and access to interrupt control and interrupt routines. The SBC100M program could be controlled from a display terminal, or by the personal computer. Its structure was essentially the same as that of the MicroProfessor program. It had a similar command syntax, but a different set of command functions.

Table E.1: Main routines in the data acquisition program

Routine	Description
initialize	Open the data file and allow documentation of the experiment.
calibrate	Procedures to calibrate hot-wire probes, electronic manometers and probe traverses – with predetermined acquisition parameters.
acquire data	The user must specify this part of the procedure in detail, possibly with repetition in which some parameters are variables.
display data	The acquisition parameters are displayed in tabular form. Data from the A/D converters is displayed graphically.
close	Close the data file.

E.4 Communications with the data acquisition hardware

The personal computer issued instructions to the SBC100M through an RS232 serial line. Data were copied from temporary storage in the SBC100M memory or the "Quasi Disk" RAM, to the personal computer through this serial line, or more often through a much faster 16-bit parallel line. The personal computer copied the incoming data to a binary file on a hard disk drive. On conclusion of an experiment, the data were transferred from the personal computer through another RS232 serial line or through an Ethernet connection.

E.5 Data acquisition program for the personal computer

The data acquisition program for the personal computer automated the data collection procedure, and so relieved the experimenter of most of the workload generated by the complexity of the data acquisition system, especially during tedious and complicated calibration procedures. It was flexible enough to perform a wide variety of experiments, and it could vary experimental parameters by executing multiply-nested loops which were similar in nature to the Fortran "do" loop. In addition to running an experiment "manually", the program could write command procedures for itself, which it could later execute with minimal intervention from the operator. This command redirection facility formed an outer shell. Each routine in the next layer of the program was designed to perform a major item of experimental procedure such as a probe calibration, repetitive data acquisition, or data retrieval. These routines are listed in Table E.1.

E.6 Data-file structure

The data files produced by the data acquisition program were organized as sequences of modules, each module containing the data produced by one of the routines listed in Table E.1. Each "calibrate" or "acquire-data" module was broken into labelled blocks. Data from each A/D converter or movement of the traverse mechanism were contained in a separate sub-block within the block. Label or header records at the beginning of each module, block and sub-block contained peripheral information about the experimental conditions and procedure, e.g. acquisition rates, amount of data, calibration values, traverse positions.

E.7 Instrumentation amplifier

Instrumentation amplifiers were used to match the C.T.A. bridge output to the input of the A/D converter. They were d.c. coupled and had from -10 volts to $+10$ volts of offset adjustment available at the input. The amplifier gain could be varied continuously from 1 to 125. The amplitude attenuation of the frequency response from 0 Hz to 25 kHz was about 0.1 dB, and no change in the the group delay could be measured over this frequency range.

A low-pass filter was built onto the same printed circuit card as each amplifier. The filters were specifically designed to eliminate SCR[1] noise from the main drive controller of the wind tunnel, with negligible signal attenuation, and with negligible phase distortion of the signal. The SCR noise had a characteristic frequency of about 200 kHz. The filters could be switched out of the circuit if they were not required. They were 6 pole Bessel filters with a 3 dB cut-off frequency of 18 kHz. In order to avoid signal distortion, the component values in each filter were adjusted carefully to achieve a phase lag proportional to frequency (i.e. constant group delay) over the range 0 Hz to 25 kHz.

The data acquisition system performed several functions in addition to that of sampling data at high speed. These other functions required sampling of steady or very slowly changing signals. The amplifiers which matched the slowly changing signals to the input of the A/D converter did not need a wide frequency bandwidth. In these cases, an amplifier response which rolled-off at very low frequencies filtered out more unwanted noise than one with a high bandwidth. Accordingly, the instrumentation amplifiers used with these signals were equipped with simple two-pole low-pass filters with a cut-off frequency of 18 Hz. Their d.c. gain and offset voltage ranges were similar to those of the wide-band amplifiers.

[1] SCR = silicon control rectifier

Appendix F

Introduction to analysis software

The computer programs which were written for analysis of experimental data and presentation of the results performed four basic functions. These functions were

1. manipulation and inspection of files produced by the data acquisition program,
2. interpretation of calibration data and generation of calibration relations for hot-wire probes and electronic manometers,
3. processing and interpretation of boundary-layer data, and
4. graphical presentation of experimental results.

A large proportion of the code was written as object-library routines in order to facilitate software management and maintenance. The main source-code files for these object-libraries are listed in Table F.1 and Table F.2.

F.1 Initial manipulation and inspection of data files

Before any analysis of a data file, it was necessary to remove a simple fault due to differences between the MS-DOS and VMS file systems. This initial correction, was performed by a program called DIRCVT.

Various kinds of equipment failure during an experiment could produce meaningless or damaged data-file records, or even incomplete data files. The utility program called PATCH was able to repair these faults by copying selected parts of one or more data files into a new data file.

The program RAWLOOK was used to inspect (i.e. plot or tabulate) the contents of data files and perform elementary statistical or spectral analysis.

F.2 Interpretation of calibration data

The program CALBAR would search in a data file for calibration data associated with an electronic manometer and would then create a calibration file which contained the information necessary for converting the manometer signal into pressure readings. This conversion process was performed by routines from the object library BARLIB.

The much more complex task of interpreting hot-wire calibration data and generating appropriate calibration relations was done by program called CALHW1. The calibration files from CALHW1 were used by HW1LIB library routines for changing the hot-wire signals into air-speed measurements.

F.3 Processing boundary-layer data

Of the programs used for processing boundary-layer data, the most important were and PROX_LAW and PRF. PRF was used for calculating boundary-layer characteristics such as skin-friction coefficients, momentum thicknesses, shape factors and Reynolds numbers. It was also used for tabulating and plotting spatial distributions of nondimensional velocity statistics.

PROX_LAW was written for developing semi-empirical functions which described the error due to wall-proximity effect. With these functions PRF was able to remove wall-proximity effect from the hot-wire signals.

F.4 Graphical presentation of results

Throughout this research project it was essential to have an efficient method of presenting results in a graphical form. A program called ILGPLOT was written for this purpose before either personal computers or graphics software became generally available. ILGPLOT is a general purpose program for plotting on two-dimensional Cartesian (x-y) axes. It has produced all but one of the graphs in this thesis.

Table F.1: C source-code files for graphics device drivers

Source code file	Description
clip.c	two- and three-dimensional rectangular clipping
dev_comm.c	source code common to all device drivers
dummy_g.c	dummy graphics device — for debugging
error.c	error reporting
f77_g.c	Sun Fortran-to-C binding routines
f77_vms_g.c	VAX Fortran-to-C binding routines
hpgl_g.c	HPGL device driver
ps_g.c	PostScript device driver
t_device.c	graphics-device selector
v500_g.c	Visual 500 device driver

Table F.2: Fortran library source-code files

Source code file	Description
barlib.for	converts electronic manometer output into pressure measurements
blm.for	calculates boundary-layer mean velocity distributions from model parameters
bly_delta.for	calculates boundary-layer thickness, momentum thickness etc.
f77_math.for	mathematical functions
f77_num.for	numerical methods; e.g. optimisation, integration, interpolation, matrix inversion, root-finding, averaging, curve-fitting
f77_sig.for	signal processing; e.g. FIR filtering, spectral analysis, correlation, probability density
f77_ute.for	utility routines; e.g. file access, string processing, data input
graph.for	graphical editing of data
hw1lib.for	converts hot-wire signal into air-speed measurement
hpispp.for	HPISPP-like interface to low-level graphics device drivers
ilglib.for	high-level graphics routines
maclib.mar	VAX assembler routines for DEC–IEEE numeric conversions and unpacking 12-bit data from the A/D converter
qu_tau.for	calculates model parameters (U_τ, κ, C, Π, δ_Π) for boundary-layer mean velocity distributions
qvkvs.for	vortex-shedding anemometry
rdflib.for	provides access to binary (“raw”) data files written by the data acquisition program
wallprox.for	models and corrects the hot-wire anemometry error produced by by wall-proximity effect

Appendix G

Octagonal-to-square transition in a contraction

In a wind-tunnel contraction, conversion of the duct cross-section from square to octagonal can be achieved by building a fillet in each corner of the original square cross-section (Figure G.1, inlet cross-section). Transition back to a square cross-section at the contraction outlet is then required in order to match the geometry of the wind-tunnel test section. The width d of the corner fillets is therefore tapered to zero at the contraction outlet. The formulae chosen for this taper are given as functions of the ratio

$$h_r(x) = \frac{h(x) - h_o}{h_i - h_o}. \tag{G.1}$$

where all the symbols on the right hand side are defined in Figure G.1. The three taper formulae, with symbols defined in Figure G.1, are as follows:

fillet taper, the diagonal width of the fillet is a linear function of the cross-section height,

$$d_d(x) = d_i h_r(x)$$

floor taper, the width of the floor of the contraction is a function of the cross-section height,

$$f_f(x) = (f_i - f_o)h_r(x) + f_o,$$

where $f_i = d_i$ at the inlet, and $f_o = 2h_o$ at the outlet;

mixed taper: the taper of the fillets is calculated by making the floor width $f_m(x)$ a weighted average of the floor widths for the fillet taper and the floor taper. If the weight of the fillet taper component is $h_r(x)$, and the weight of the floor taper component is $1 - h_r(x)$, then

$$f_m(x) = h_r(x)\, f_d(x) + (1 - h_r(x))\, f_f(x).$$

The effect of this weighting is to generate a taper similar to the fillet taper near the inlet, and similar to the floor taper near the contraction outlet.

The effect of each taper formula on the shape of the contraction is best illustrated by comparing outlet-end views of the finite element mesh, as shown in Figure G.2.

Notation

$d(x)$	diagonal width of the fillet insert in the octagonal-to-square contraction
$f(x)$	width of the floor of the octagonal-to-square contraction
$h(x)$	horizontal or vertical distance from the axis of the contraction to the contraction surface
$h_r(x)$	contraction height ratio (Equation G.1, page 349)

subscripts

$_d$	for the fillet and floor width (d_d and f_d) of an octagonal-to-square contraction with a fillet taper rule
$_f$	for the fillet and floor width (d_f and f_f) of an octagonal-to-square contraction with a floor taper rule
$_i$	for inlet dimensions of the contraction (h_i, d_i and f_i)
$_m$	for the fillet and floor width (d_m and f_m) of an octagonal-to-square contraction with a mixed taper rule
$_o$	for outlet dimensions of the contraction (h_o, d_o and f_o)

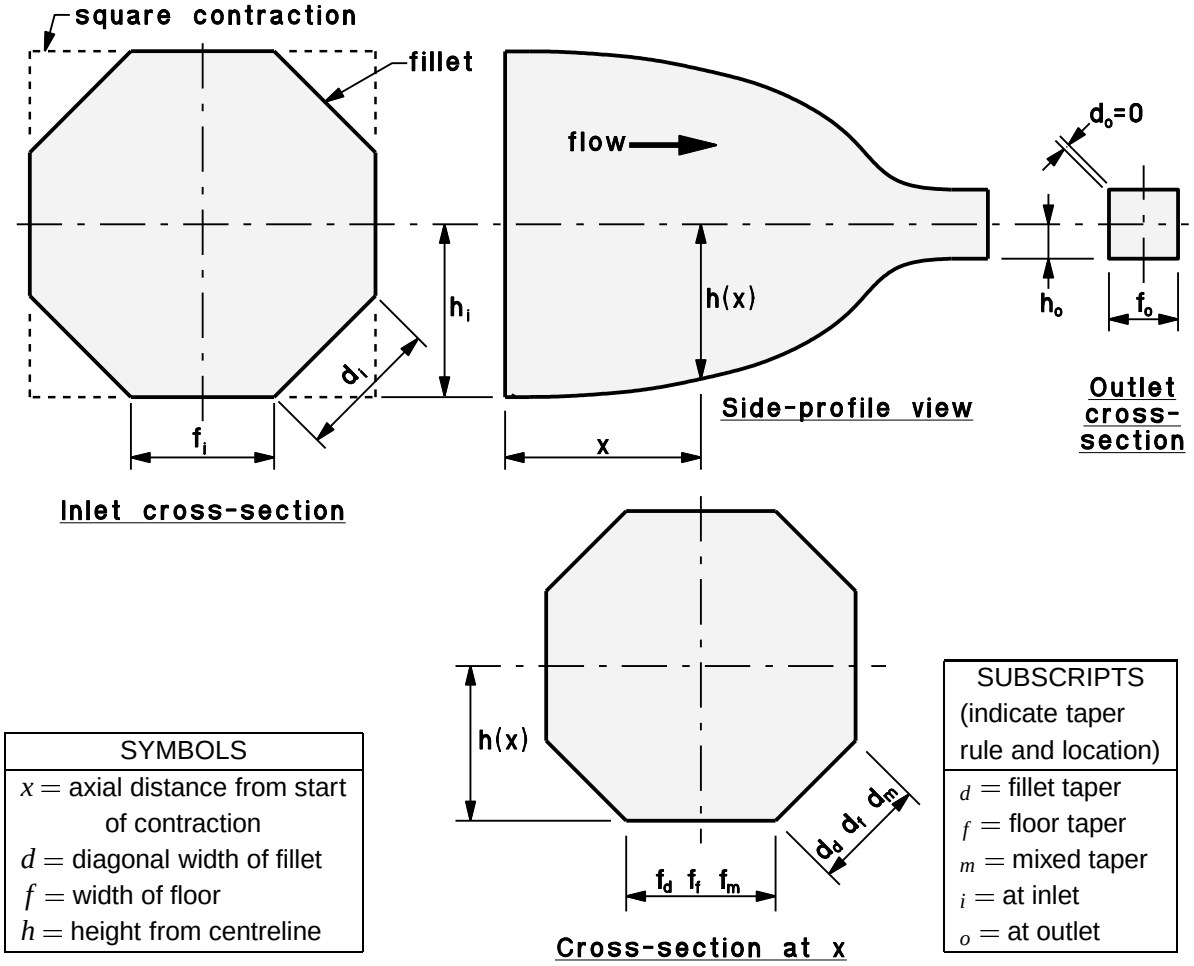

Figure G.1: Symbols used for defining the taper rules.

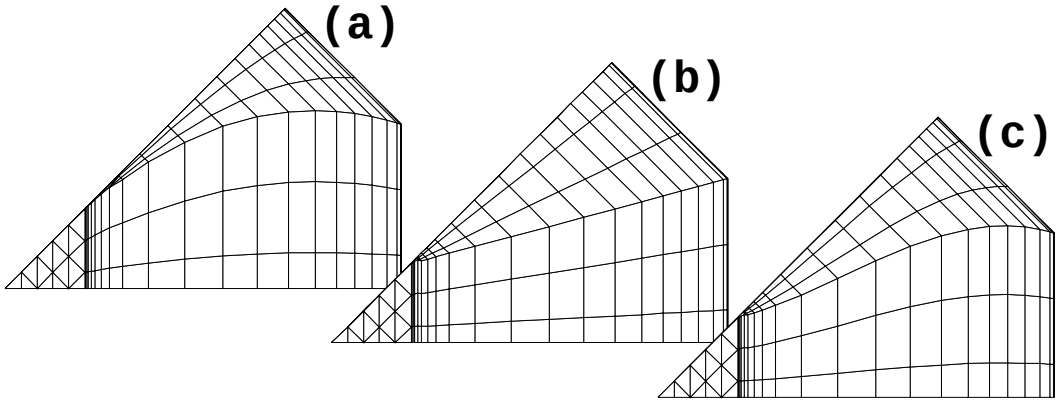

Figure G.2: The effect of different taper rules on the shape of the octagonal to square contraction: views from the outlet end of the finite element mesh; (a) fillet taper; (b) “floor” taper; (c) mixed taper.

Appendix H

Momentum integral equation for a duct

This derivation of the momentum integral equation for flow in a duct is included with the kind permission of its author, Dr. M. K. Bull.

H.1 Arbitrary duct cross-section

The continuity equation for incompressible flow at streamwise location x in a duct may be written as an integral over the cross-section area A:

$$\int_A U\, dA' = \mathcal{V} = \text{constant}, \tag{H.1}$$

where U is the streamwise component of velocity. The displacement area of the duct boundary layer may be defined as

$$A_{\delta^*} = \int_A \left(1 - \frac{U}{U_0}\right) dA', \tag{H.2}$$

where U_0 is the speed of the central potential flow. Similarly, the momentum area of the duct boundary layer is

$$A_\theta = \int_A \frac{U}{U_0}\left(1 - \frac{U}{U_0}\right) dA'. \tag{H.3}$$

The displacement area may also be written in terms of the volume-flow rate $\mathcal{V}$:

$$A_{\delta^*} = A - \frac{\mathcal{V}}{U_0}. \tag{H.4}$$

If it is assumed that pressure is constant over the duct cross-section, the net pressure force on a cross-section control volume of streamwise thickness dx (Figure H.1) is

$$-A\frac{dP}{dx}\,dx. \tag{H.5}$$

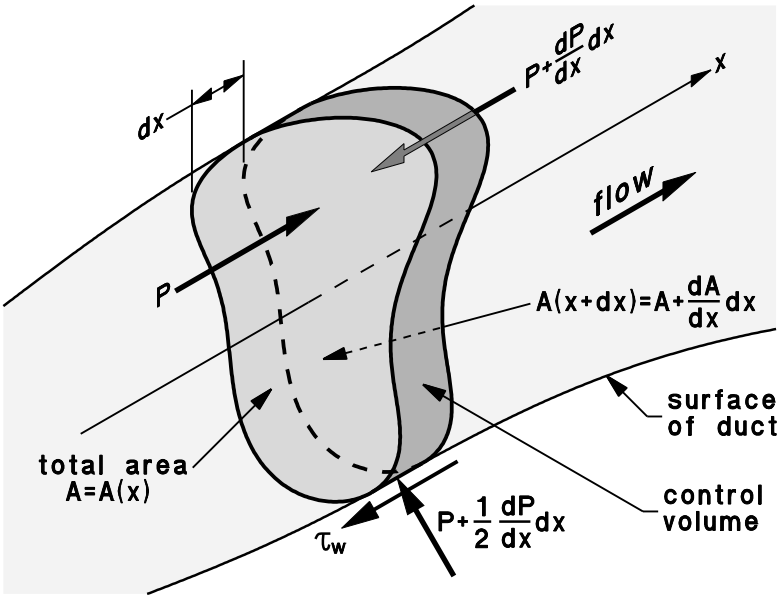

Figure H.1: Schematic diagram of a control volume in a duct of arbitrary cross-section.
$A =$ total cross-section area, $P =$ pressure, $\tau_w =$ wall shear stress, $dx =$ length of control volume.

The momentum balance for the control volume is therefore

$$\rho \int_{A(x+dx)} U^2\, dA' - \rho \int_{A(x)} U^2\, dA' = -A\frac{dP}{dx}\,dx - dx \oint_{\mathcal{P}} \tau_w\, d\mathcal{P}', \tag{H.6}$$

where $\mathcal{P}$ is the perimeter of the duct and τ_w is the wall shear stress, or

$$\frac{d}{dx}\int_A U^2\, dA' = -\frac{A}{\rho}\frac{dP}{dx} - \frac{1}{\rho}\oint_{\mathcal{P}} \tau_w\, d\mathcal{P}'. \tag{H.7}$$

The integral on the left hand side can be expressed in terms of the momentum and displacement areas:

$$\begin{aligned}\int_A U^2\, dA' &= -\int_A U(U_0 - U)\, dA' + \int_A (UU_0 - U_0^2)\, dA' + \int_A U_0^2\, dA' \\ &= -U_0^2\,(A_\theta + A_{\delta^*} - A),\end{aligned} \tag{H.8}$$

so that Equation H.7 becomes

$$\frac{d}{dx}\left[U_0^2\,(A_\theta + A_{\delta^*} - A)\right] = \frac{A}{\rho}\frac{dP}{dx} + \frac{1}{\rho}\oint_{\mathcal{P}} \tau_w\, d\mathcal{P}'. \tag{H.9}$$

Using the product rule of differentiation to expand the left hand side and removing the terms which are zero by continuity gives

$$U_0^2\left\{\frac{dA_\theta}{dx} + \frac{A_\theta}{U_0}\frac{dU_0}{dx}\left(\frac{A_{\delta^*}}{A_\theta} + 2\right)\right\} - U_0 A\frac{dU_0}{dx} = \frac{A}{\rho}\frac{dP}{dx} + \frac{1}{\rho}\oint_{\mathcal{P}} \tau_w\, d\mathcal{P}'. \tag{H.10}$$

The Bernoulli equation is then used to convert the streamwise pressure-gradient to a free-stream velocity gradient:

$$\frac{A}{\rho}\frac{dP}{dx} = -AU_0\frac{dU_0}{dx} \tag{H.11}$$

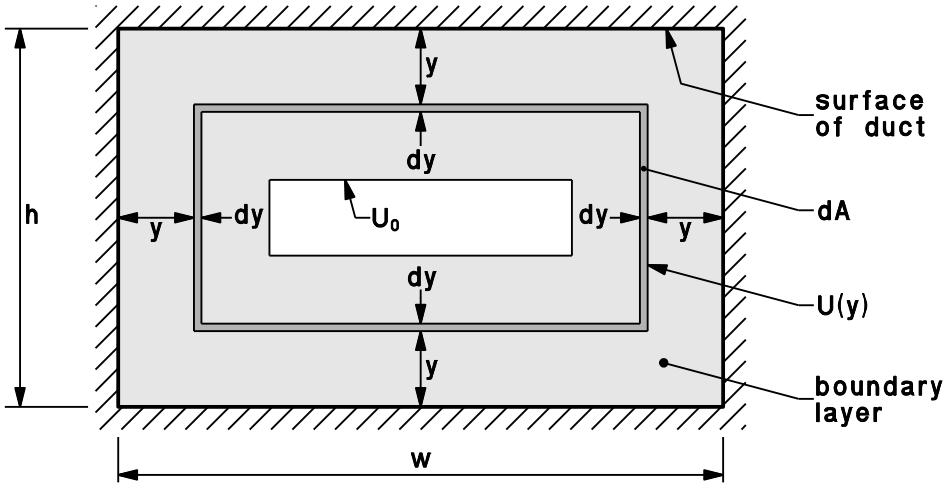

Figure H.2: Cross-section of a rectangular duct showing the elemental cross-section area dA and the assumed mean velocity distribution $U = U(y)$.

so that, in terms of momentum area A_θ and displacement area A_{δ^*}, the momentum integral equation is

$$\frac{dA_\theta}{dx} + \frac{A_\theta}{U_0}\left(\frac{A_{\delta^*}}{A_\theta} + 2\right)\frac{dU_0}{dx} = \frac{1}{\rho}\oint_{\mathcal{P}}\left(\frac{\tau_w}{\rho U_0^2}\right)d\mathcal{P}'. \tag{H.12}$$

Division by $\mathcal{P}$ and use of the quotient rule of differentiation,

$$\frac{d}{dx}\left(\frac{A_\theta}{\mathcal{P}}\right) = \frac{1}{\mathcal{P}}\frac{dA_\theta}{dx} - \frac{A_\theta}{\mathcal{P}}\frac{1}{\mathcal{P}}\frac{d\mathcal{P}}{dx}, \tag{H.13}$$

in Equation H.12 gives

$$\frac{d}{dx}\left(\frac{A_\theta}{\mathcal{P}}\right) + \left(\frac{A_\theta}{\mathcal{P}}\right)\frac{1}{\mathcal{P}}\frac{d\mathcal{P}}{dx} + \left(\frac{A_\theta}{\mathcal{P}}\right)\frac{1}{U_0}\frac{dU_0}{dx}\left[\frac{(A_{\delta^*}/\mathcal{P})}{(A_\theta/\mathcal{P})} + 2\right] = \frac{1}{\mathcal{P}}\oint_{\mathcal{P}}\left(\frac{\tau_w}{\rho U_0^2}\right)d\mathcal{P}', \tag{H.14}$$

or

$$\frac{d\theta_d}{dx} + \frac{\theta_d}{U_0}\frac{dU_0}{dx}\left[\frac{\delta_d^*}{\theta_d} + 2\right] = \frac{1}{2}\overline{C_f} - \frac{\theta_d}{\mathcal{P}}\frac{d\mathcal{P}}{dx}, \tag{H.15}$$

where

$$\theta_d = \frac{A_\theta}{\mathcal{P}} \tag{H.16}$$

$$\delta_d^* = \frac{A_{\delta^*}}{\mathcal{P}} \tag{H.17}$$

$$\frac{1}{2}\overline{C_f} = \frac{1}{\mathcal{P}}\oint_{\mathcal{P}}\left(\frac{\tau_w}{\rho U_0^2}\right)d\mathcal{P}'. \tag{H.18}$$

Finally,

$$\frac{d\theta_d}{dx} + \frac{\theta_d}{U_0}\frac{dU_0}{dx}(H_d + 2) = \frac{1}{2}\overline{C_f} - \frac{\theta_d}{\mathcal{P}}\frac{d\mathcal{P}}{dx}, \tag{H.19}$$

where $H_d = \delta_d^*/\theta_d$.

H.2 Rectangular duct cross-section

If, as an approximation, it is assumed that the velocity contours in a rectangular duct are concentric rectangles so that time-averaged velocity is a function only of distance from the nearest wall ($U = U(y)$), the elemental area dA of the duct cross-section can be written as

$$\begin{aligned} dA &= 2[(w-2y)+(h-2y)]dy \\ &= (\mathcal{P}-8y)dy \end{aligned} \tag{H.20}$$

where w is the duct width, h is the duct height and the perimeter is $\mathcal{P} = 2(w+h)$ (Figure H.2). The momentum thickness then becomes

$$\begin{aligned} \theta_d &\approx \frac{1}{\mathcal{P}} \int_0^\delta \frac{U}{U_0} \left(1 - \frac{U}{U_0}\right) (\mathcal{P} - 8y)\, dy \\ &\approx \int_0^\delta \frac{U}{U_0} \left(1 - \frac{U}{U_0}\right) \left(1 - \frac{8y}{\mathcal{P}}\right) dy, \end{aligned} \tag{H.21}$$

where δ is the boundary-layer thickness. Similarly, the displacement thickness is

$$\delta_d^* \approx \int_0^\delta \left(1 - \frac{U}{U_0}\right) \left(1 - \frac{8y}{\mathcal{P}}\right) dy. \tag{H.22}$$

H.3 Notation

A	$A(x)$; total cross-section area of the duct
A_{δ^*}	displacement area of the duct boundary layer, defined by Equation H.2
A_θ	momentum area of the duct boundary layer, defined by Equation H.3
$\overline{C_f}$	skin friction averaged around the perimeter of the duct cross-section
H_d	δ_d^*/θ_d
h	height of a rectangular duct cross-section
P	pressure
$\mathcal{P}$	perimeter of the duct cross-section
U	streamwise component of velocity
U_0	speed of the central potential flow
$\mathcal{V}$	volume-flow rate in the duct
w	width of a rectangular duct cross-section
x	streamwise location
δ	boundary-layer thickness
δ_d^*	$A_{\delta^*}/\mathcal{P}$, displacement thickness of a duct boundary layer
θ_d	$A_\theta/\mathcal{P}$, momentum thickness of a duct boundary layer

ρ	density
τ_w	wall shear stress

Appendix I

Turbulence statistics of the test-section boundary layer

This appendix contains graphs of turbulence statistics obtained from the test-section boundary layer at free stream flow speeds of 1.43 m/s, 2.9 m/s and 3.9 m/s. These results, which supplement Figures 7.19, 7.20, 7.23 and 7.24 in Chapter 7, are scaled on the flat-plate momentum thickness (Figures I.1, I.2 and I.3) and also on wall variables (Figures I.4, I.5 and I.6). All results with outer region scaling, including those in Figures 7.19 and 7.20, may be compared by superposition of the figures. Results nondimensionalised with wall-region parameters can be compared in the same way.

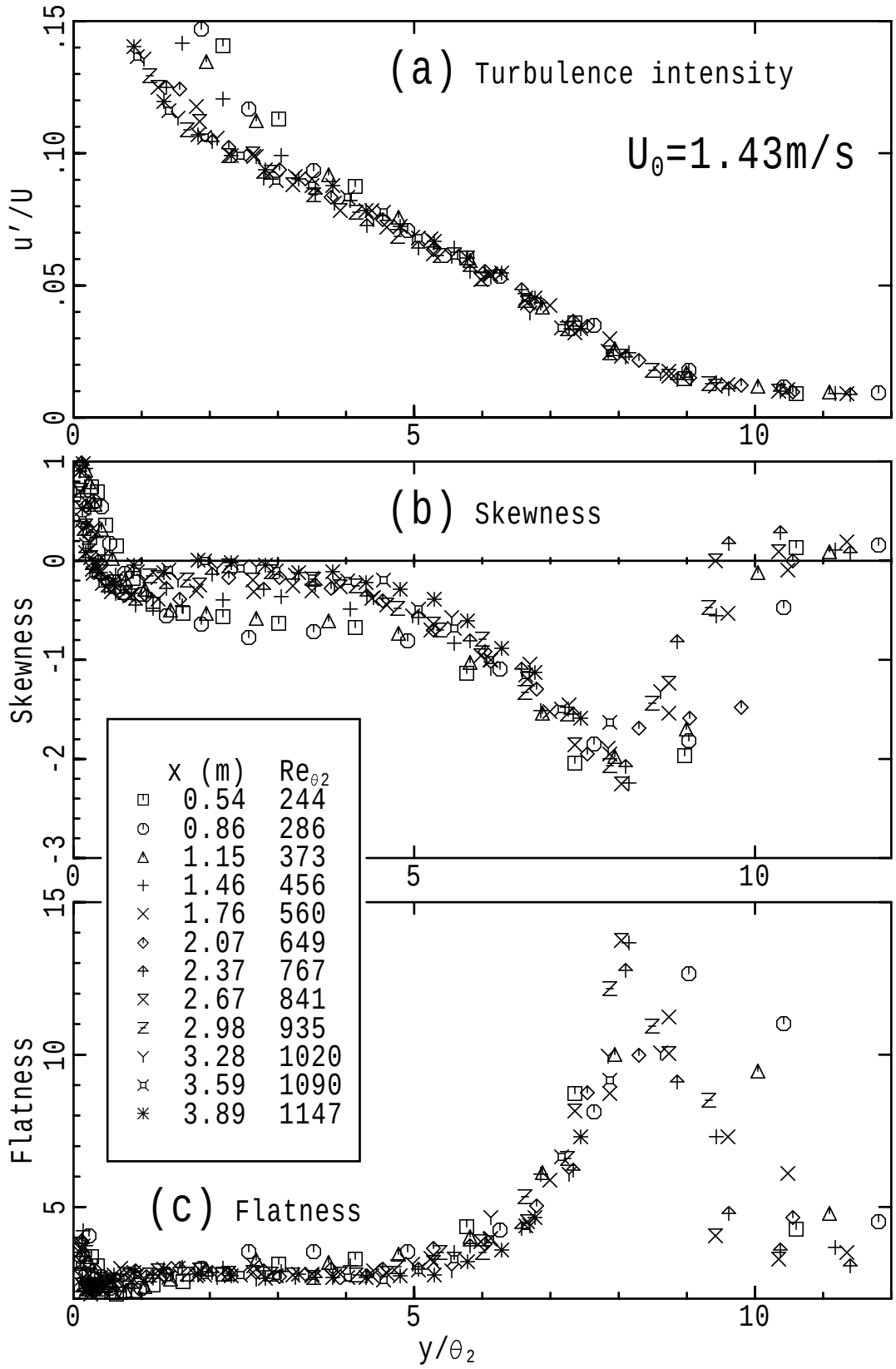

Figure I.1: Outer region scaling of boundary-layer turbulence statistics for a free stream speed of 1.43 m/s; (a) turbulence intensity; (b) skewness; (c) flatness. Distance from the wall is scaled with flat-plate momentum thickness.

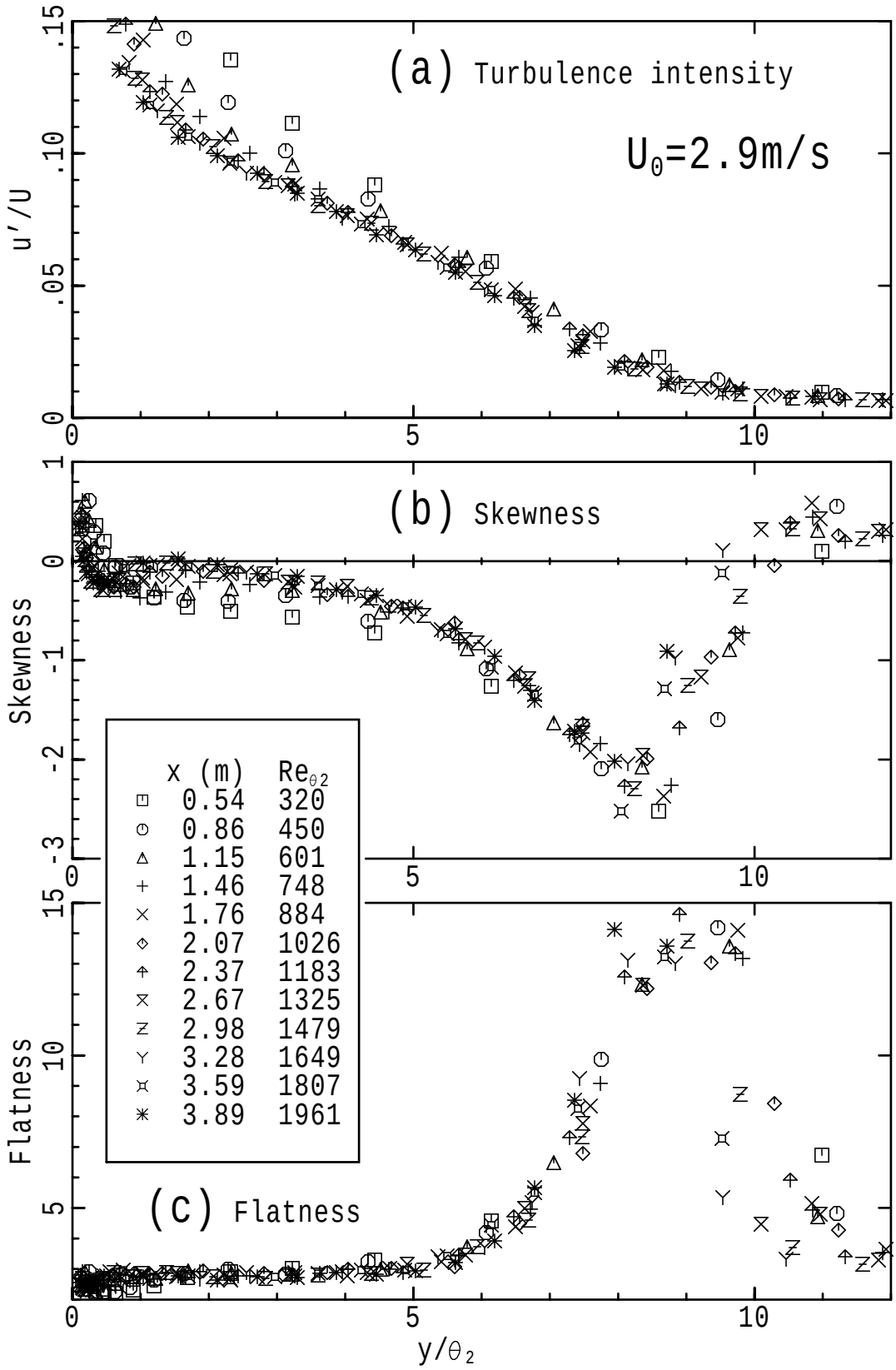

Figure I.2: Outer region scaling of boundary-layer turbulence statistics for a free stream speed of 2.9 m/s; (a) turbulence intensity; (b) skewness; (c) flatness. Distance from the wall is scaled with flat plate momentum thickness.

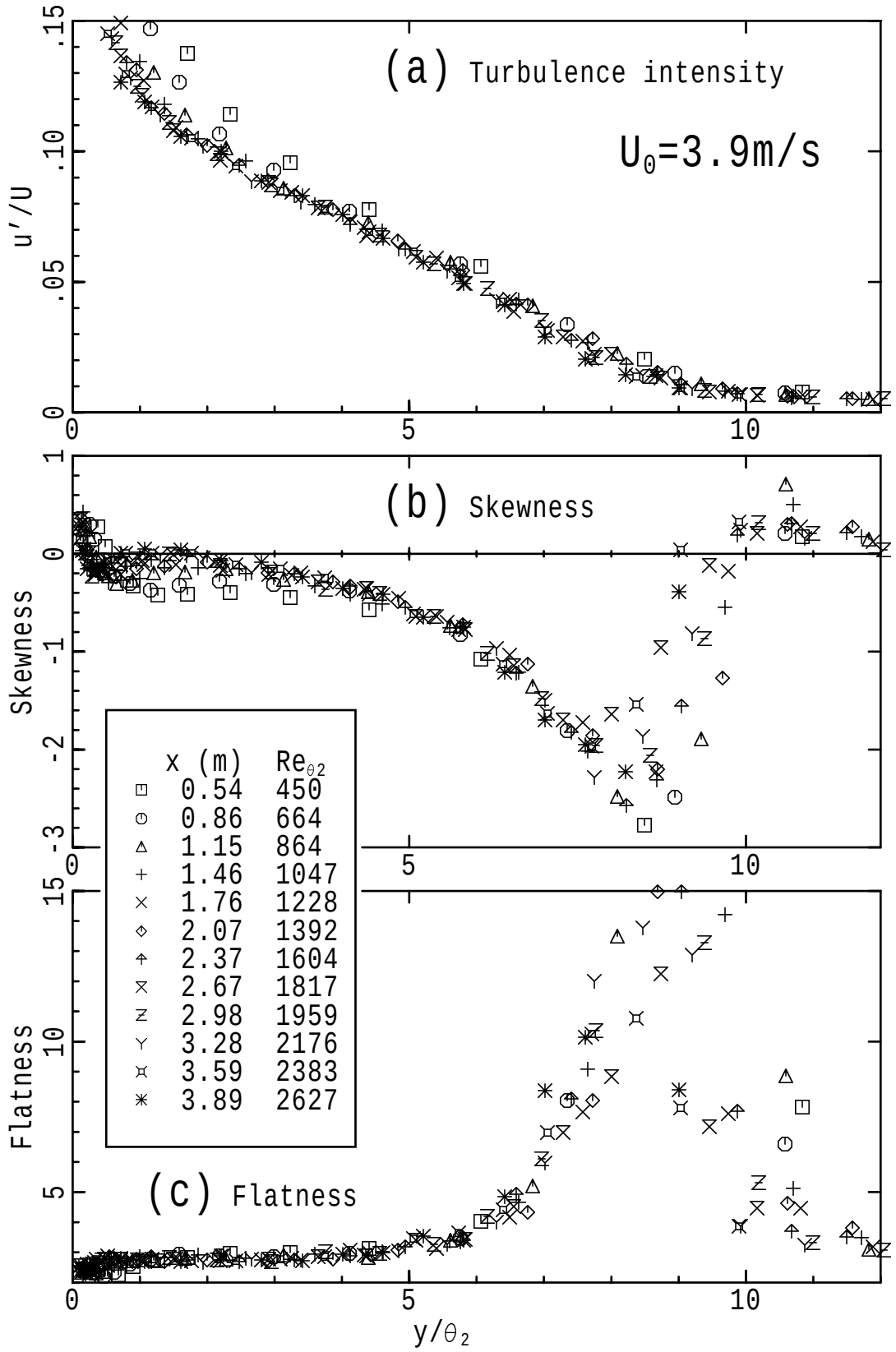

Figure I.3: Outer region scaling of boundary-layer turbulence statistics for a free stream speed of 3.9 m/s; (a) turbulence intensity; (b) skewness; (c) flatness. Distance from the wall is scaled with flat-plate momentum thickness.

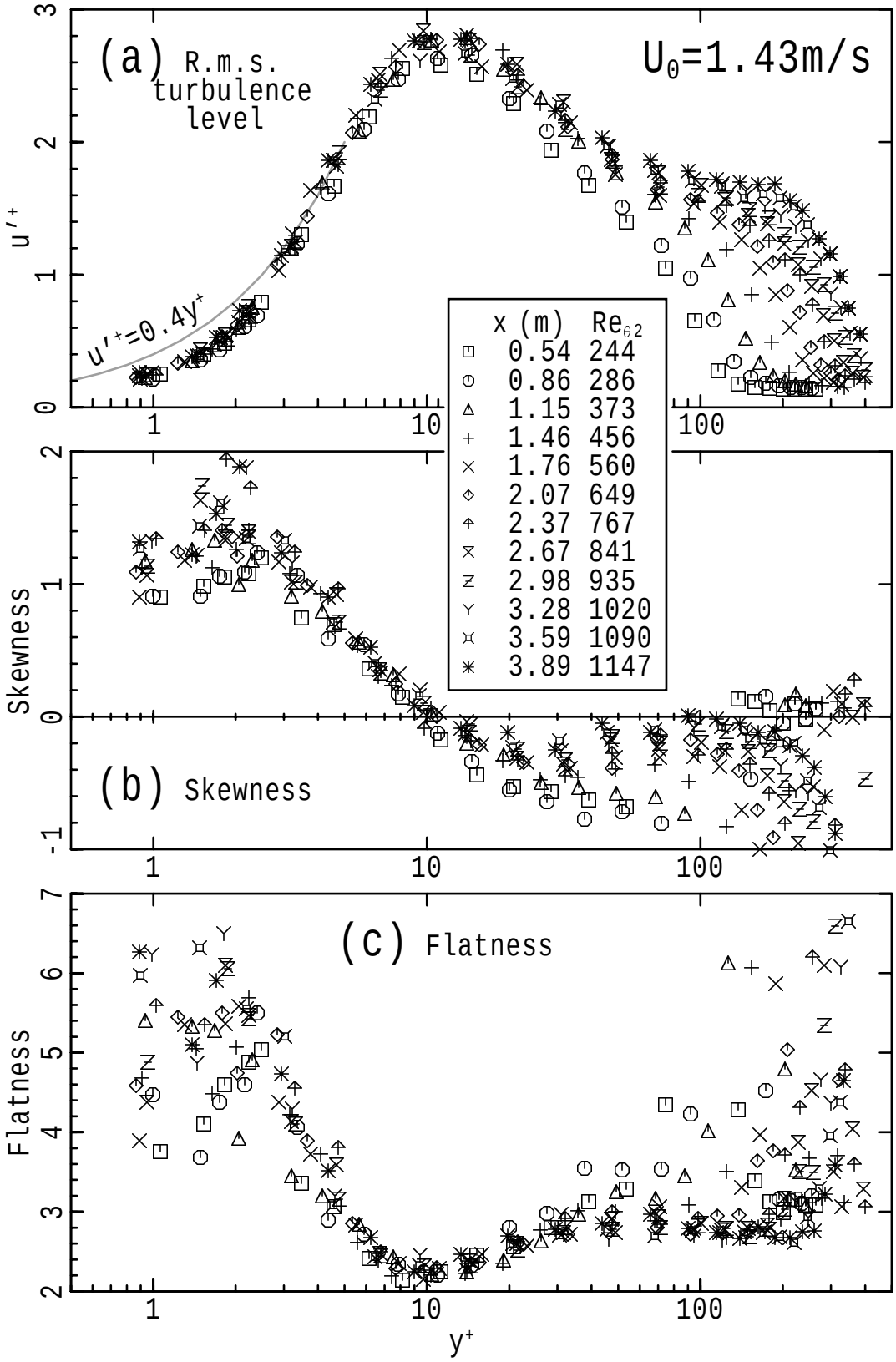

Figure I.4: Wall-region scaling of boundary-layer turbulence statistics for a free stream speed of 1.43 m/s; (a) r.m.s. turbulence level; (b) skewness; (c) flatness. U_τ is calculated from the Spalding-Coles model of the mean velocity distribution.

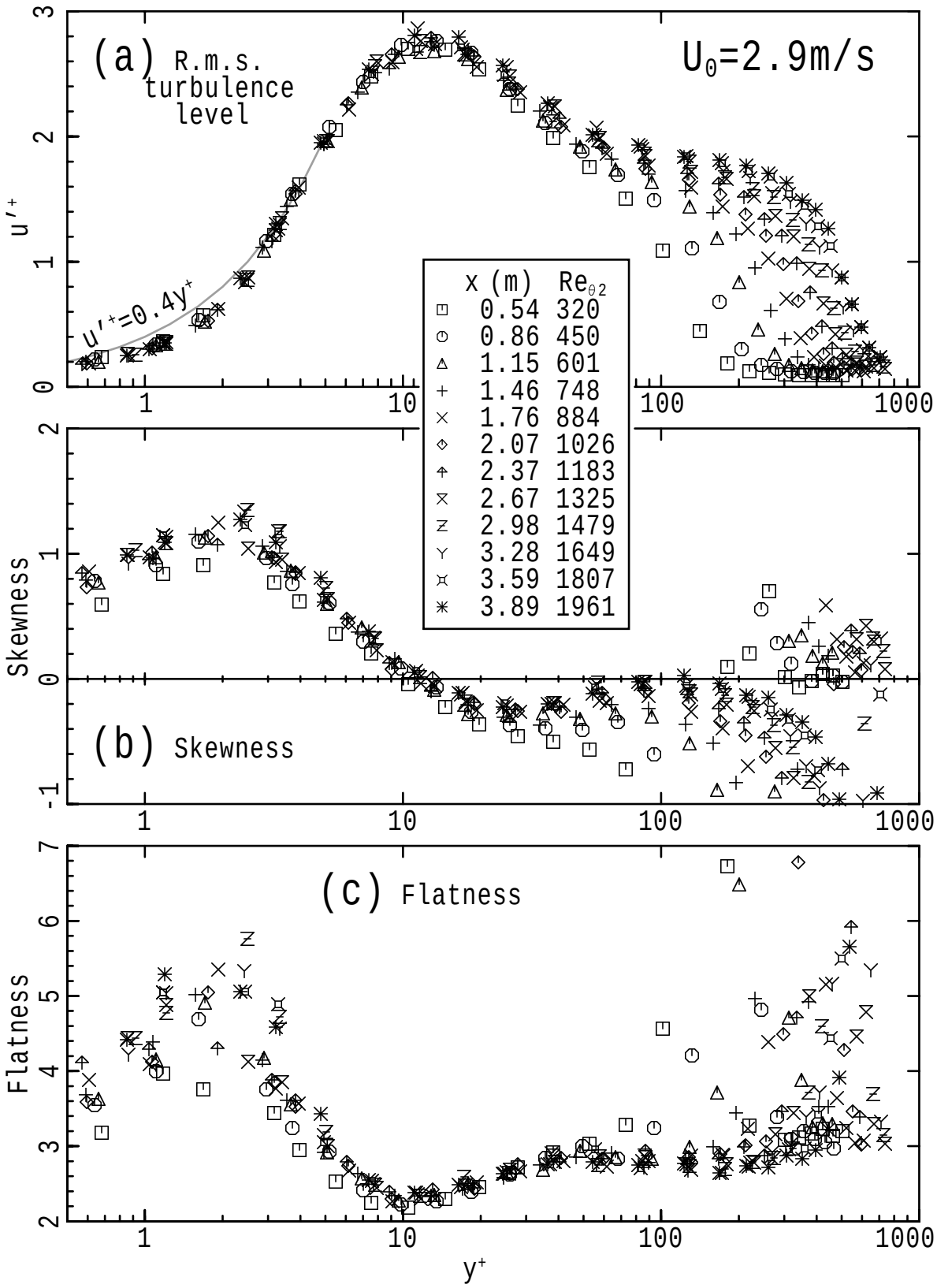

Figure I.5: Wall-region scaling of boundary-layer turbulence statistics for a free stream speed of 2.9 m/s; (a) r.m.s. turbulence level; (b) skewness; (c) flatness. U_τ is calculated from the Spalding-Coles model of the mean velocity distribution.

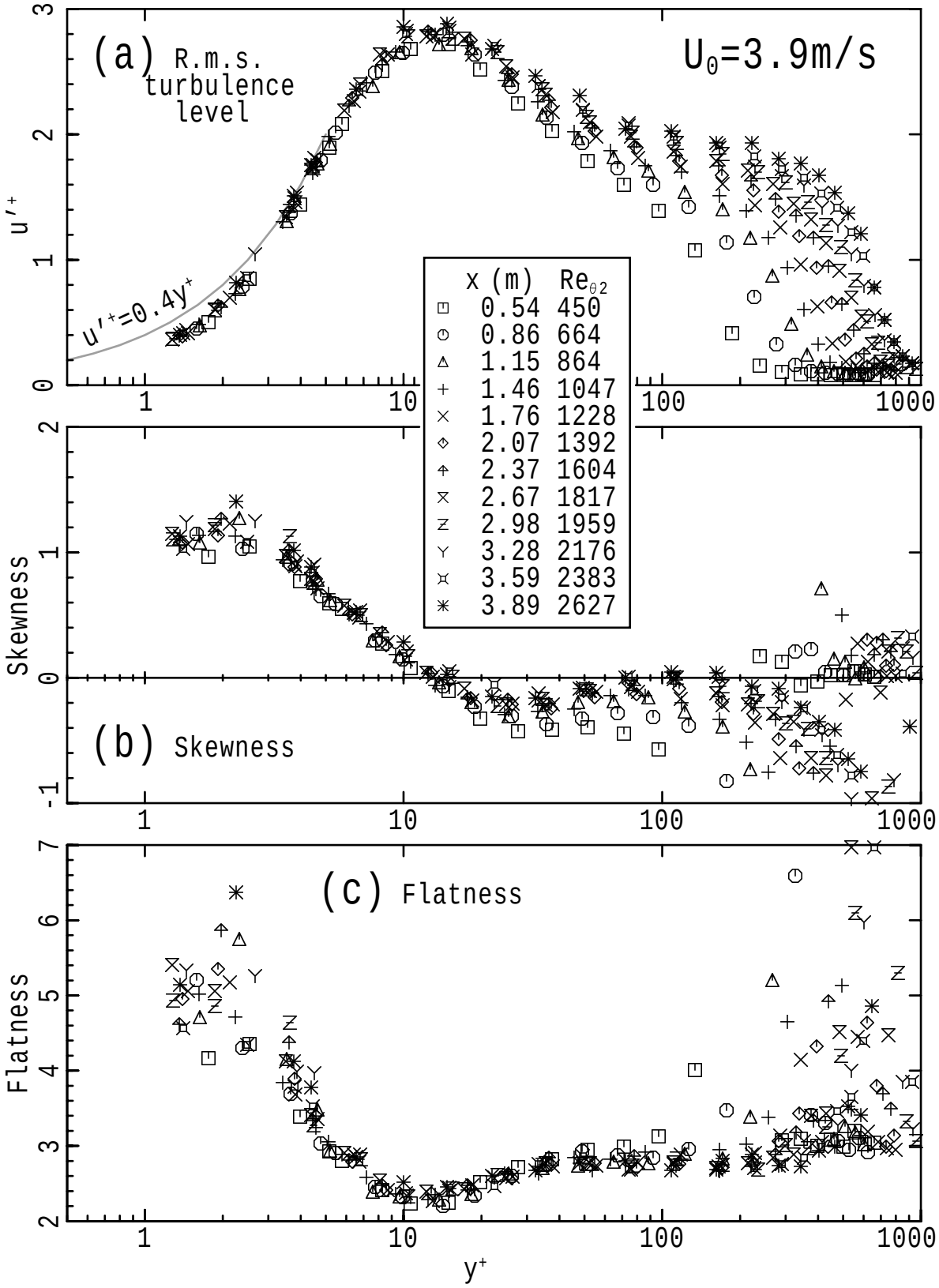

Figure I.6: Wall-region scaling of boundary-layer turbulence statistics for a free stream speed of 3.9 m/s; (a) r.m.s. turbulence level; (b) skewness; (c) flatness. U_τ is calculated from the Spalding-Coles model of the mean velocity distribution.